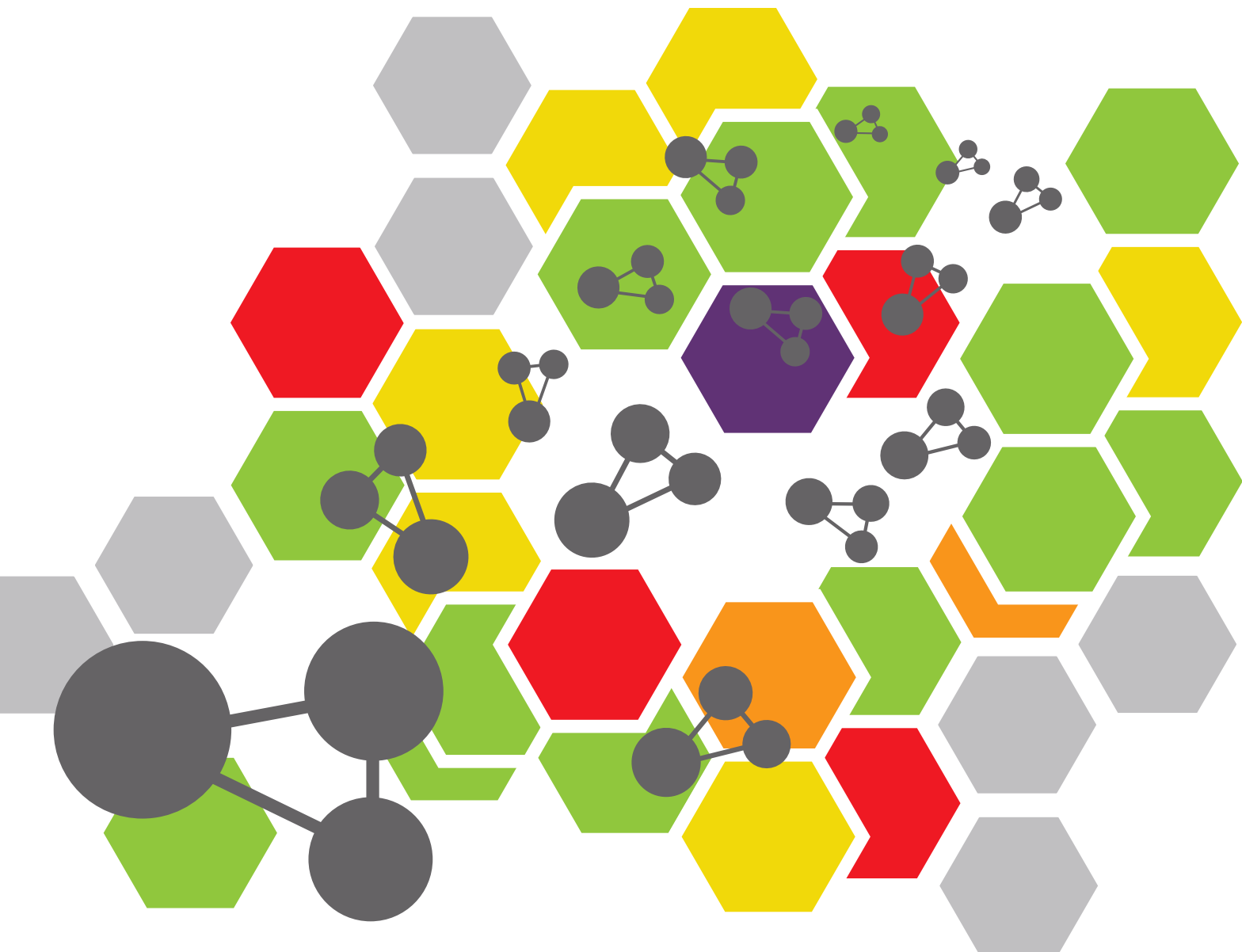
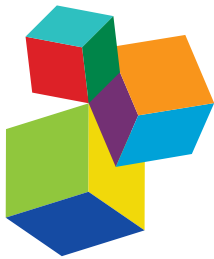


# MULTISENSOR SYSTEMS FOR ANALYSIS OF LIQUIDS AND GASES: TRENDS AND DEVELOPMENTS

EDITED BY: Larisa Lvova and Dmitry Kirsanov  
PUBLISHED IN: *Frontiers in Chemistry*





#### Frontiers Copyright Statement

© Copyright 2007-2019 Frontiers Media SA. All rights reserved.

All content included on this site, such as text, graphics, logos, button icons, images, video/audio clips, downloads, data compilations and software, is the property of or is licensed to Frontiers Media SA ("Frontiers") or its licensees and/or subcontractors. The copyright in the text of individual articles is the property of their respective authors, subject to a license granted to Frontiers.

The compilation of articles constituting this e-book, wherever published, as well as the compilation of all other content on this site, is the exclusive property of Frontiers. For the conditions for downloading and copying of e-books from Frontiers' website, please see the Terms for Website Use. If purchasing Frontiers e-books from other websites or sources, the conditions of the website concerned apply.

Images and graphics not forming part of user-contributed materials may not be downloaded or copied without permission.

Individual articles may be downloaded and reproduced in accordance with the principles of the CC-BY licence subject to any copyright or other notices. They may not be re-sold as an e-book.

As author or other contributor you grant a CC-BY licence to others to reproduce your articles, including any graphics and third-party materials supplied by you, in accordance with the Conditions for Website Use and subject to any copyright notices which you include in connection with your articles and materials.

All copyright, and all rights therein, are protected by national and international copyright laws.

The above represents a summary only. For the full conditions see the Conditions for Authors and the Conditions for Website Use.

ISSN 1664-8714  
ISBN 978-2-88945-721-2  
DOI 10.3389/978-2-88945-721-2

#### About Frontiers

Frontiers is more than just an open-access publisher of scholarly articles: it is a pioneering approach to the world of academia, radically improving the way scholarly research is managed. The grand vision of Frontiers is a world where all people have an equal opportunity to seek, share and generate knowledge. Frontiers provides immediate and permanent online open access to all its publications, but this alone is not enough to realize our grand goals.

#### Frontiers Journal Series

The Frontiers Journal Series is a multi-tier and interdisciplinary set of open-access, online journals, promising a paradigm shift from the current review, selection and dissemination processes in academic publishing. All Frontiers journals are driven by researchers for researchers; therefore, they constitute a service to the scholarly community. At the same time, the Frontiers Journal Series operates on a revolutionary invention, the tiered publishing system, initially addressing specific communities of scholars, and gradually climbing up to broader public understanding, thus serving the interests of the lay society, too.

#### Dedication to Quality

Each Frontiers article is a landmark of the highest quality, thanks to genuinely collaborative interactions between authors and review editors, who include some of the world's best academicians. Research must be certified by peers before entering a stream of knowledge that may eventually reach the public - and shape society; therefore, Frontiers only applies the most rigorous and unbiased reviews.

Frontiers revolutionizes research publishing by freely delivering the most outstanding research, evaluated with no bias from both the academic and social point of view. By applying the most advanced information technologies, Frontiers is catapulting scholarly publishing into a new generation.

#### What are Frontiers Research Topics?

Frontiers Research Topics are very popular trademarks of the Frontiers Journals Series: they are collections of at least ten articles, all centered on a particular subject. With their unique mix of varied contributions from Original Research to Review Articles, Frontiers Research Topics unify the most influential researchers, the latest key findings and historical advances in a hot research area! Find out more on how to host your own Frontiers Research Topic or contribute to one as an author by contacting the Frontiers Editorial Office: [researchtopics@frontiersin.org](mailto:researchtopics@frontiersin.org)

# MULTISENSOR SYSTEMS FOR ANALYSIS OF LIQUIDS AND GASES: TRENDS AND DEVELOPMENTS

Topic Editors:

**Larisa Lvova**, Università degli Studi di Roma Tor Vergata Roma, Italy

**Dmitry Kirsanov**, Saint Petersburg State University Saint Petersburg, Russia

Nowadays the application of multisensor systems for the analysis of liquids and gases is becoming more and more popular in analytical chemistry. Such systems, also known as "electronic tongues" and "electronic noses" are based on various types of chemical sensors and biosensors with different transduction principles combined with multivariate data processing protocols. These instruments received significant interest due to their simplicity, low costs and the possibility to obtain reliable chemical information from complex unresolved analytical signals. A distinct feature of electronic tongues and noses is that they can be calibrated for prediction of complex integral features in samples, like e.g. taste, odor, toxicity, geographical origin, general conformity with certain standards, etc. – the tasks that otherwise would require involvement of complex analytical instrumentation, human or animal sensory panels. In the present eBook the original research and review articles in the area of multisensor approach are collected. They dedicated to the novel sensor materials development, measuring techniques evaluation, electronics, data processing protocols and practical applications. An editorial foreword article is followed by the researches authored by leading scientists in the field of chemical sensors and artificial sensing systems. With this eBook we hope to inspire further interest and new research efforts in this exciting area.

**Citation:** Lvova, L., Kirsanov, D., eds. (2019). Multisensor Systems for Analysis of Liquids and Gases: Trends and Developments. Lausanne: Frontiers Media. doi: 10.3389/978-2-88945-721-2

# Table of Contents

## SECTION 1

### INTRODUCTION

- 05 Editorial: Multisensor Systems for Analysis of Liquids and Gases: Trends and Developments**  
Larisa Lvova and Dmitry Kirsanov

## SECTION 2

### GENERAL INFORMATION

- 07 Combining two Selection Principles: Sensor Arrays Based on Both Biomimetic Recognition and Chemometrics**  
Wim Cuypers and Peter A. Lieberzeit

## SECTION 3

### NOVEL SENSIG MATERIALS AND MULTISENSOR PLATFORMS FOR LIQUID PHASE ANALYSIS

- 17 Multisensor Systems by Electrochemical Nanowire Assembly for the Analysis of Aqueous Solutions**  
Konstantin G. Nikolaev, Yury E. Ermolenko, Andreas Offenhäusser, Sergey S. Ermakov and Yulia G. Mourzina
- 33 Solid-Contact Potentiometric Sensors and Multisensors Based on Polyaniline and Thiocalixarene Receptors for the Analysis of Some Beverages and Alcoholic Drinks**  
Michail Sorvin, Svetlana Belyakova, Ivan Stoikov, Rezeda Shamagsumova and Gennady Evtugyn
- 49 Graphene FET Array Biosensor Based on ssDNA Aptamer for Ultrasensitive  $Hg^{2+}$  Detection in Environmental Pollutants**  
Jiawei Tu, Ying Gan, Tao Liang, Qiongwen Hu, Qian Wang, Tianling Ren, Qiyong Sun, Hao Wan and Ping Wang
- 58 A Fluorescent Sensor Array Based on Heteroatomic Macroyclic Fluorophores for the Detection of Polluting Species in Natural Water Samples**  
Larisa Lvova, Fabrizio Caroleo, Alessandra Garau, Vito Lippolis, Luca Giorgi, Vieri Fusi, Nelsi Zaccheroni, Marco Lombardo, Luca Prodi, Corrado Di Natale and Roberto Paolesse
- 68 Toward a Hybrid Biosensor System for Analysis of Organic and Volatile Fatty Acids in Fermentation Processes**  
Désirée L. Röhlen, Johanna Pilas, Markus Dahmen, Michael Keusgen, Thorsten Selmer and Michael J. Schöning
- 79 SPRi-Based Biosensing Platforms for Detection of Specific DNA Sequences Using Thiolate and Dithiocarbamate Assemblies**  
Marcin Drozd, Mariusz D. Pietrzak and Elżbieta Malinowska

- 91** *Monitoring the Phenolic Ripening of Red Grapes Using a Multisensor System Based on Metal-Oxide Nanoparticles*

Celia Garcia-Hernandez, Cristina Medina-Plaza, Cristina Garcia-Cabezon, Yolanda Blanco, Jose A. Fernandez-Escudero, Enrique Barajas-Tola, Miguel A. Rodriguez-Perez, Fernando Martin-Pedrosa and Maria L. Rodriguez-Mendez

## SECTION 4

### MULTISENSOR SYSTEMS FOR GASES

- 99** *Thermally Driven Selective Nanocomposite PS-PHB/MGC Nanofibrous Conductive Sensor for air Pollutant Detection*

Joshua Avossa, Emiliano Zampetti, Fabrizio De Cesare, Andrea Bearzotti, Giuseppe Scarascia-Mugnozza, Giuseppe Vitiello, Eyal Zussman and Antonella Macagnano

- 113** *Peptide Modified ZnO Nanoparticles as gas Sensors Array for Volatile Organic Compounds (VOCs)*

Marcello Mascini, Sara Gaggiotti, Flavio Della Pelle, Corrado Di Natale, Sinazo Qakala, Emmanuel Iwuoha, Paola Pittia and Dario Compagnone

## SECTION 5

### FEATURE SELECTION AND CALIBRATION UPDATES IN MULTISENSOR ANALYSIS

- 122** *A Practical Method to Estimate the Resolving Power of a Chemical Sensor Array: Application to Feature Selection*

Luis Fernandez, Jia Yan, Jordi Fonollosa, Javier Burgués, Agustin Gutierrez and Santiago Marco

- 136** *Calibration Update and Drift Correction for Electronic Noses and Tongues*

Alisa Rudnitskaya

## SECTION 6

### ELECTRONICS AND FABRICATION TECHNOLOGY OF MULTISENSOR SYSTEMS

- 153** *Advances in the Electronics for Cyclic Voltammetry: the Case of Gas Detection by Using Microfabricated Electrodes*

Giorgio Pennazza, Marco Santonico, Luca Vollero, Alessandro Zompanti, Anna Sabatini, Nandeesh Kumar, Ivan Pini, William F. Quiros Solano, Lina Sarro and Arnaldo D'Amico

- 166** *3D Printed e-Tongue*

Gabriel Gaál, Tatiana A. da Silva, Vladimir Gaál, Rafael C. Hensel, Lucas R. Amaral, Varlei Rodrigues and Antonio Riul Jr



# Editorial: Multisensor Systems for Analysis of Liquids and Gases: Trends and Developments

Larisa Lvova<sup>1\*</sup> and Dmitry Kirisanov<sup>2\*</sup>

<sup>1</sup> Department of Chemical Sciences and Technology, University 'Tor Vergata', Rome, Italy, <sup>2</sup> Institute of Chemistry, St. Petersburg State University, St. Petersburg, Russia

**Keywords:** chemical sensors, electronic tongue (e-tongue), chemometrics, multisensory systems, electronic nose (e-nose)

## Editorial on the Research Topic

### Multisensor Systems for Analysis of Liquids and Gases: Trends and Developments

The Research Topic is devoted to the recent advances in the development of multisensor systems for analysis of liquids and gases. These artificial systems are known as "electronic tongues" and "electronic noses" since the inspiration for their development was found in human taste and olfaction systems, and they have been actively employed in the last two decades as effective, simple, fast, and inexpensive analytical tools for various analytical tasks. The popularity of these tools is mainly due to the two following reasons: (1) they allow quantification of complex integral quality parameters in liquids and gases, like e.g., taste descriptors; (2) they are typically much more simple and less expensive compared to the majority of modern instrumental analytical methods, yet capable of providing meaningful and important information on quantitative and qualitative composition of the samples.

Despite the high interest and wide distribution of artificial sensory systems nowadays, we cannot say that the field is fully mature: there are still many aspects to be developed and understood, from sensing materials composition, system construction and employed experimental set-ups to the details on measuring techniques, data processing methods, calibration procedures, and practical applications. The dedicated efforts are necessary for the understanding of all these aspects in order to put the multisensor systems into a common routine laboratory practice. Of course, the present research collection does not cover the whole range of advancements in the field, however it highlights certain very interesting contributions on diverse aspects of electronic tongues and noses and we hope, this will inspire further interest and new research efforts in this exciting area.

The Research Topic contains the collection of 14 original contributions: 11 research papers, two reviews, and one mini review dedicated to the different aspects related to the development and application of chemical sensors in the multisensor analysis. The mini review of Cuypers and Lieberzeit reports on the sensor arrays combining chemoselectivity and chemometrics based on biomimetic approaches in order to maximize chemical selectivity of a final device. The main aims of such systems development are: the improvement of analytical quality of quantitative data and a deeper understanding of the natural olfaction processes. The review of Rudnitskaya describes various methods for drift correction and calibration update in multisensor systems—a very important issue both for routine practical application of such systems and for scientific experiments. The contribution from the group of Sorvin et al. represents an overview of solid-state polyaniline-based potentiometric sensors and multisensor systems doped with thiocalixarene receptors for analysis of beverages. The application of these compounds has a great potential in multisensor analysis. In the study of Mascini et al. group ZnO nanoparticles were modified with computationally selected peptides, which is quite a new concept in sensor studies gaining

## OPEN ACCESS

### Edited and reviewed by:

Ashok Mulchandani,  
University of California, Riverside,  
United States

### \*Correspondence:

Larisa Lvova  
larisa.lvova@uniroma2.it  
Dmitry Kirisanov  
d.kirisanov@gmail.com

### Specialty section:

This article was submitted to  
Analytical Chemistry,  
a section of the journal  
Frontiers in Chemistry

Received: 15 October 2018

Accepted: 13 November 2018

Published: 28 November 2018

### Citation:

Lvova L and Kirisanov D (2018)  
Editorial: Multisensor Systems for  
Analysis of Liquids and Gases: Trends  
and Developments.  
*Front. Chem.* 6:591.  
doi: 10.3389/fchem.2018.00591

popularity. Such a modification allowed constructing the gas sensors with pronounced sensitivity toward volatile organic compounds. The group of Garcia-Hernandez et al. which has done a lot of research in voltammetric multisensor systems for wine analysis here reports on an interesting development of this concept for monitoring the phenolic ripening of red grapes. Quite a timely research from the group of Gaál et al. describes the way we can benefit from 3D printing technology in multisensor system construction. Drozd et al. together with colleagues reports on surface plasmon resonance biosensing platforms that can be adopted in the future for multisensing in biological applications. The contribution from Fernandez et al. addresses the field where much work remains to be done—the evaluation of the analytical figures of merit for multisensor systems. The paper deals with the protocol to assess the resolving power of sensor array. The studies in this direction are absolutely necessary for the development of the meaningful comparison protocols to select between various multisensor systems. The contribution of Lvova et al. is devoted to the application of heteroatomic macrocyclic fluorophores (diaza-crown ether, metallocorrole and pyridinophanes) for development of a fluorescent sensor array with a nice potential for environmental applications. The paper by Nikolaev et al. reports on a new procedure to develop chip-based nanoelectrochemical sensor arrays based on the directed electrochemical nanowire assembly (DENA) and their utility for non-enzymatic analysis of hydrogen peroxide, glucose, and ethanol. Such systems can be especially attractive for healthcare applications. The group of Röhlen et al. has developed the concept of hybrid biosensor with application for biogas process monitoring. Normally biosensors are not in the focus of multisensor systems development as they typically

have quite high selectivity; however the benefits of multisensor arrangement can become important in complex multicomponent media. Pennazza et al. has shown how the advanced electronics and additional operative conditions can improve the analytical performance of sensor arrays in particular based on the advances in the electronics for cyclic voltammetry. The contribution from the group of Tu et al. describes the development of quite popular concept of aptamer-based sensing toward the detection of hazardous mercury ions in environmental samples. Avossa et al. has investigated the idea of tuning working temperature to modify both the sensitivity and the selectivity of nanocomposite conductive gas sensors showing a good promise for practical application of this principle in air pollutant detection.

The Editors hope that this collection will be of a great interest to the Frontiers audience and will inspire significant progress in the field of multisensor systems for chemical analysis.

## AUTHOR CONTRIBUTIONS

All authors listed have made a substantial, direct and intellectual contribution to the work, and approved it for publication.

**Conflict of Interest Statement:** The authors declare that the research was conducted in the absence of any commercial or financial relationships that could be construed as a potential conflict of interest.

Copyright © 2018 Lvova and Kirsanov. This is an open-access article distributed under the terms of the Creative Commons Attribution License (CC BY). The use, distribution or reproduction in other forums is permitted, provided the original author(s) and the copyright owner(s) are credited and that the original publication in this journal is cited, in accordance with accepted academic practice. No use, distribution or reproduction is permitted which does not comply with these terms.



# Combining Two Selection Principles: Sensor Arrays Based on Both Biomimetic Recognition and Chemometrics

Wim Cuypers and Peter A. Lieberzeit\*

Department of Physical Chemistry, Faculty for Chemistry, University of Vienna, Vienna, Austria

## OPEN ACCESS

**Edited by:**

Larisa Lvova,  
Università degli Studi di Roma Tor  
Vergata, Italy

**Reviewed by:**

Chih-Ching Huang,  
National Taiwan Ocean University,  
Taiwan

Lorenzo Maria Mosca,  
Northwestern University,  
United States

**\*Correspondence:**

Peter A. Lieberzeit  
peter.lieberzeit@univie.ac.at

**Specialty section:**

This article was submitted to  
Analytical Chemistry,  
a section of the journal  
Frontiers in Chemistry

**Received:** 27 March 2018

**Accepted:** 12 June 2018

**Published:** 02 August 2018

**Citation:**

Cuypers W and Lieberzeit PA (2018) Combining Two Selection Principles: Sensor Arrays Based on Both Biomimetic Recognition and Chemometrics. *Front. Chem.* 6:268. doi: 10.3389/fchem.2018.00268

Electronic noses mimic smell and taste senses by using sensor arrays to assess complex samples and to simultaneously detect multiple analytes. In most cases, the sensors forming such arrays are not highly selective. Selectivity is attained by pattern recognition/chemometric data treatment of the response pattern. However, especially when aiming at quantifying analytes rather than qualitatively detecting them, it makes sense to implement chemical recognition via receptor layers, leading to increased selectivity of individual sensors. This review focuses on existing sensor arrays developed based on biomimetic approaches to maximize chemical selectivity. Such sensor arrays for instance use molecularly imprint polymers (MIPs) in both e-noses and e-tongues, for example, to characterize headspace gas compositions or to detect protein profiles. Other array types employ entire cells, proteins, and peptides, as well as aptamers, respectively, in multisensor systems. There are two main reasons for combining chemoselectivity and chemometrics: First, this combined approach increases the analytical quality of quantitative data. Second, the approach helps in gaining a deeper understanding of the olfactory processes in nature.

**Keywords:** electronic noses and tongues, biomimetics, molecular imprinting, aptamers, protein-based receptors, cells as sensing elements

## BACKGROUND

### Electronic Noses and Tongues

The terms “electronic nose” (e-nose) and “electronic tongue” (e-tongue) are used to denote devices that detect smell and taste, respectively, similar to their mammalian counterparts. The tongue and the nose constitute chemical senses (Baldwin et al., 2011; Wilson, 2012; Cui et al., 2018; Dung et al., 2018), whereas all other perceptions, including hearing, sight, and touch, respond to physical stimuli. Mammalian sensing has several advantages which include its unique ability to distinguish odors and tastes as well as its high sensitivity to toxic compounds such as thiols. Nonetheless, it also has some inherent limitations. Firstly, mammalian sensing is not quantitative. Secondly, both the senses are restricted to physiological conditions, thus limiting possible technological application. Thirdly, odor and taste perception varies among individuals and also depend on external factors that may lead to different results at different times for a given person. Some factors include the age and health conditions of test subjects, and environmental conditions, such as temperature, and/or smoking habits. Standardizing human

olfactory and sensory data, therefore, becomes close to impossible. Finally, the olfactory sense tires over time, that is it loses sensitivity. To overcome these limitations, e-noses and e-tongues make it possible to obtain standardized, intersubjective, and quantitative information. Furthermore, they also sense analytes that are harmful to living organisms, such as toxic gases or solutions (Arshak and Harris, 2004; Baldwin et al., 2011; Wilson, 2012; Dung et al., 2018). E-noses and e-tongues usually comprise a sensor array (Shurmer and Gardner, 1992; Hong et al., 1996) which are described in the following paragraphs.

### Electronic Noses

The working mechanism of an e-nose is most conveniently explained via its natural counterpart, i.e., nose (Figure 1). First of all, the compounds from the environment are taken up by the olfactory organ of a subject. These volatile compounds (VCs) reach the olfactory epithelium, where they bind to an olfactory receptor. This generates an action potential in the respective neuron, which is transmitted to the brain. Here, the responses are collected and organized into patterns, allowing the subject to recognize the specific odorant (Schaller et al., 1998; Rinaldi, 2007; Baldwin et al., 2011; Ko and Park, 2016).

Similarly, an e-nose consists of an array of receptors that are able to bind the particular (groups of) VCs. The resulting array response is processed by using pattern recognition techniques to generate an output signal. Although individual sensors are usually not highly selective, their combined signals allow the characterization of the samples in their entirety. The main difference between natural and artificial noses is that olfaction in mammals requires a phase transition from the gaseous environment into the liquid mucus of the nose.

The use of e-noses has been reported in a wide range of applications, mostly in healthcare. Prominent areas of application are in the identification of lung cancer (Dragonieri et al., 2012; Bikov et al., 2014), kidney disorders (Di Natale et al., 1999), and heart failure (Voss et al., 2012). The food industry is another notable field of application. Controlling and monitoring ripening and spoilage processes is extremely valuable to guarantee food safety and quality (Cagnasso et al., 2010; Xu et al., 2016; Wojnowski et al., 2017). Other examples of uses of e-noses include the identification of the flavoring of wine (Macias et al., 2012) and beer (Pearce et al., 1993), fruit ripening, freshness of fish and meat (Najam ul et al., 2012), and dairy products (Gutiérrez, 2011). Environmental uses of electronic noses (Baby et al., 2000) are in water and soil quality assessments.

### Electronic Tongues

E-tongues work in liquid environments and can be compared with their human analog: The human gustatory organ contains structures called papillae, and each papilla comprises thousands of taste buds (Latha and Lakshmi, 2012). These taste buds in turn consist of 50–100 individual taste receptors. Each tastant senses differently in such a way that they have distinct mechanisms for triggering action potentials. These signals are sent to the gustatory cortex via cranial nerves which lead to pattern recognition in the brain. For an e-tongue, any substance needs to be

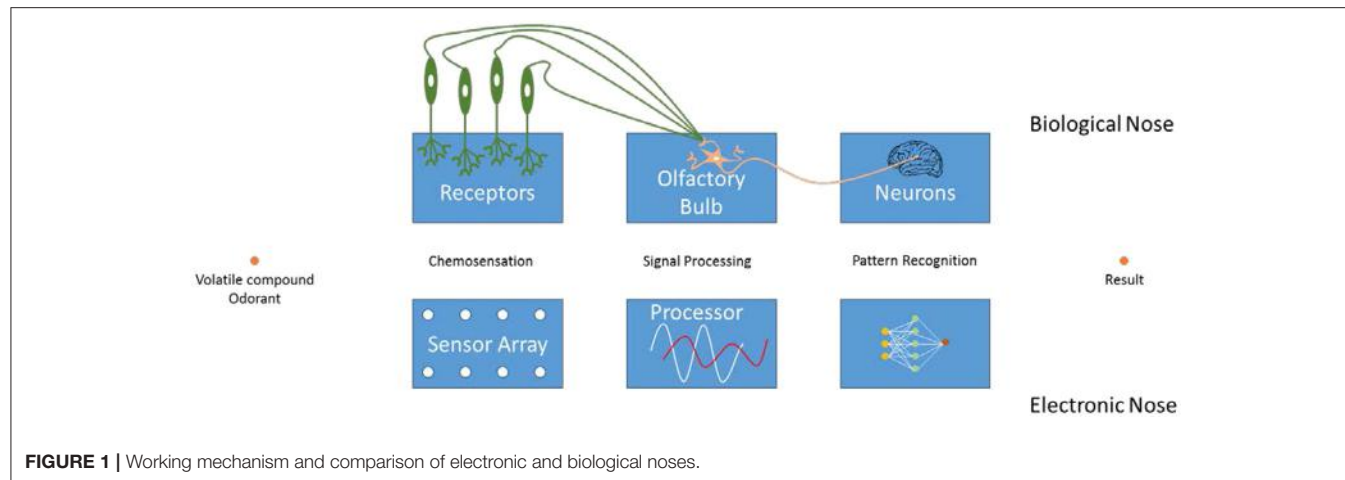
dissolved in the liquid phase to enable detection. Binding of analytes to the distinct sensors is paired with some kind of selectivity. A unique fingerprint arises and is analyzed through pattern recognition and/or through multivariate data analysis.

### Biomimetic Recognition

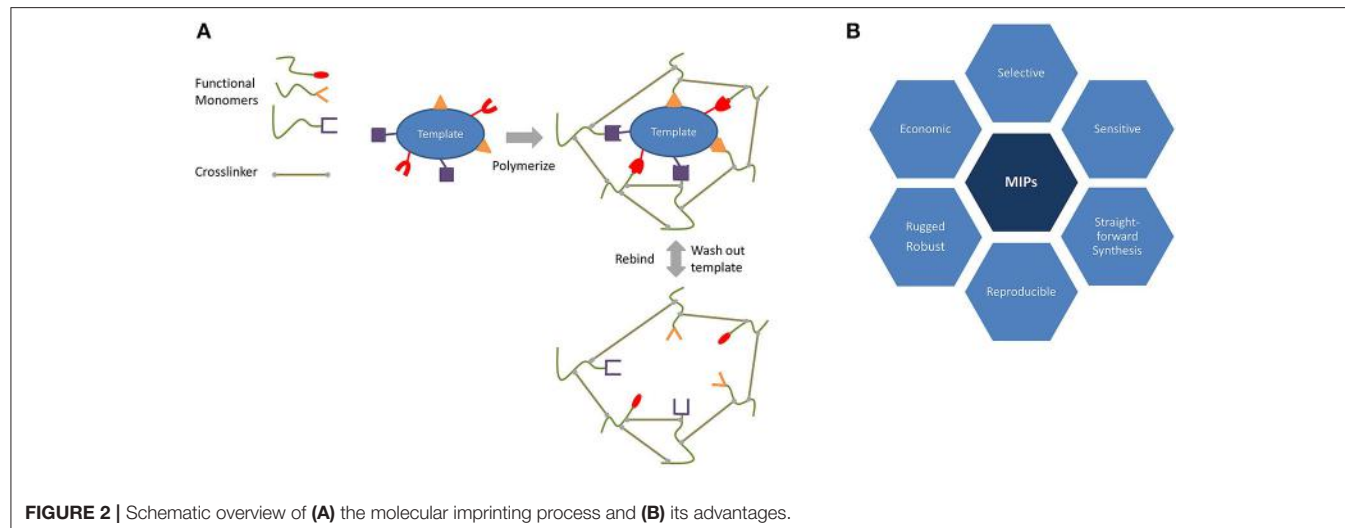
Biomimicry overcomes the limitations imposed by natural recognition by imitating nature and implementing its working mechanisms (Hussain et al., 2013; Hwang et al., 2015) in artificial systems. During the past few decades, substantial attention has been paid to the durability and sustainability of such “smart materials” in areas such as architecture, engineering, and medicine. For instance, one of the earliest inventions goes back to the fifteenth century when Leonardo da Vinci proposed a model of a “flying machine” based on a bird. Modern-day materials chemistry, for example, has been creating synthetic nanoscale materials such as carbon nanotubes, reverse micelles, and surfactant vesicles. Several other strategies aim at selective recognition, such as aptamers. Aptamers are (short) artificial oligonucleotides that typically comprise 20–40 nucleobases which selectively bind to defined epitopes (Gotrik et al., 2016; Zhuo et al., 2017). Finally, molecular imprinting leads to a class of biomimetic materials, known as molecularly imprinted polymers (MIPs), which attract substantial interest especially in analytics (Hussain et al., 2013). By mimicking enzyme–substrate complexes, MIPs benefit from the high selectivity between a target and a polymer.

Figure 2A sketches the imprinting process. During the first step of MIP synthesis, a target species—the template—and functional monomer(s) preform a complex (Haupt and Mosbach, 2000; Chunta et al., 2015), either via covalent bonds or noncovalent ones. The advantage of the former approach is that the template is strongly bound to a monomer, and this leads to highly selective materials with narrow affinity distribution. Removing the template from the final polymer, however, can be challenging because it involves the breaking of the said covalent bond. Noncovalent imprinting makes use of weaker (noncovalent) interactions between the functional monomer and the template, such as hydrogen bonds, dipole–dipole interactions, and van der Waals forces. These usually make it easier to remove the template from the polymeric matrix. In both the cases, the removal of the template generates cavities which are suitable for selectively recognizing the target of interest.

In addition to the functional monomer, MIPs also require crosslinking to achieve rigid, three-dimensional networks and thus to ensure stability. After polymerization, the template is finally removed from the matrix and leaves behind adapted cavities that are suitable for rebinding it. In a nutshell, it can be said that MIPs mimic natural recognition entities through the effects of binding and rebinding the targets of interest. The origin of MIP dates back to 1931, when Polyakov and his team generated silica materials which exhibited selective binding toward the solvent used during synthesis (Polyakov, 1931; Alexander et al., 2006). However, it took until the seventies and eighties of the twentieth century to establish some of the most remarkable breakthroughs by the groups of G. Wulff and K. Mosbach,



**FIGURE 1** | Working mechanism and comparison of electronic and biological noses.



**FIGURE 2** | Schematic overview of (A) the molecular imprinting process and (B) its advantages.

respectively. Their use of organic polymers opened a whole new world for template recognition (Alexander et al., 2006).

Compared to natural species, such as enzymes or antibodies, MIPs have some fundamental advantages, as summarized in Figure 2B. These are their low production cost, long storage time, and their ruggedness. Furthermore, they are usually stable in larger ranges of pH and temperature compared to their biological counterparts. Finally, they are usually chemically more resistant and inert toward many solvents thus allowing detection of a broad spectrum of analytes, from small molecules (neurotransmitters, amino acids, and ions) to large species (bacteria, viruses, and cells). In addition, MIPs can also be synthesized for templates that cannot be addressed by antibodies or enzymes (Haupt and Mosbach, 2000; Chunta et al., 2015; Wackerl and Lieberzeit, 2015; Chen et al., 2016).

## IMPLEMENTATION OF MIPs IN ELECTRONIC NOSES AND TONGUES

Electronic noses and tongues conventionally rely on low-affinity sensors and use pattern recognition to obtain selectivity,

afterwards. They usually consist of arrays of said sensors, each of which is affine toward a range of analytes. It may seem counterintuitive to use highly selective receptor elements, such as MIPs, in this context. Hence, it took until the beginning of the twenty-first century to see the first publications in that area (Dickert et al., 2004; Lieberzeit et al., 2008; Iqbal et al., 2010). Those experiments were guided by the interest to achieve quantitative multianalyte sensing, rather than generating data patterns to correctly assign sensor array responses to predefined clusters.

### MIP-Based Electronic Noses

The first MIP-based electronic nose was reported in 2004 (Dickert et al., 2004). It was comprised of a device for continuous surveillance of composting processes based on a six-electrode quartz crystal microbalance (QCM) coated with both molecularly imprinted polymers and affinity materials. Polymers were chosen for their interaction properties with the respective analyte: polyurethane-based MIP toward short-chain alcohols, nonpolar polystyrene MIP toward limonene, a terpene, and two different MIPs based on each of those

systems to detect acetic ester vapors to reflect their “ambivalent” functionality. Water vapor was detected by a copolymer of polyvinyl alcohol and acrylic acid leading to affinity interactions. The beauty and power of the MIP approach can be seen by the following example in detail. Although polystyrene MIP for limonene and ethyl acetate (EtAc) are chemically similar, the corresponding sensors respond differently toward those VCs, as seen in **Figure 3**. The EtAc sensor gives rise to a distinct response pattern determined by its vapor content, whereas this is almost invisible for the limonene MIP. Overall, the MIPs lead to a very high selectivity of individual sensors. Consequently the sensor array very accurately reproduced the time-dependent VOC patterns in the composter headspace as determined by gas chromatography–mass spectrometry (GC-MS) over long-term composting procedures, lasting for 1 week.

The real-life feasibility of the system was demonstrated in 2008 (Lieberzeit et al., 2008) through monitoring composting processes over a longer time, up to 6 weeks, after the quantitative calibration of the e-nose, which took a week. Therefore, it turned out to be possible to not only follow trend lines but also to quantify VCs, pine composting is one such example. **Figure 4** shows the respective concentration profiles obtained by the e-nose and GC-MS during a measuring cycle lasting for 6 weeks.

**Figure 5** displays the selectivity pattern of a similar set-up used for the detection and quantification of terpenes elaborated by distinct *Lamiaceae* species (Iqbal et al., 2010), namely rosemary, basil, and sage. The array allowed for distinguishing between the profiles of fresh and dried herbs, respectively.

Hawari et al. developed a MIP-based e-nose to distinguish the ripening stages of mango during harvesting (Hawari et al., 2012, 2013) based on the detection of  $\alpha$ -pinene emissions. Through this indicator, they defined the ripeness stage for optimal harvest maturity. Coating MIPs onto interdigital electrodes is followed by capacitance measurements. Thirty minutes after exposure to ripe mangos, the authors observed an increasing emission of pinene. However, the signal fell back a few minutes later. After 45 minutes from the start of the measurement, the signal coming from terpenes increased sharply. As seen in **Figure 6**, the signal decreases again 1 h after initial exposure. Because of these findings, Hawari et al. stated that  $\alpha$ -pinene sensors had been created in a unified way such that this technique can be applied to other types of terpenes as well.

In 2016, Shinohara et al. fabricated molecularly imprinted filtering absorbents (MIFA) for sensing gas odor molecules (Shinohara et al., 2016). These MIFAs combine a high absorptive capacity with a selective filtering procedure. Because of this synergy, superior control of absorption and odor detection can be achieved. Polydimethylsiloxane (PDMS), divinyl benzene (DVB), polyvinyl alcohol (PVA), polyethylene glycol (PEG), and polyvinyl chloride (PVC) were used as absorbent materials. Absorption of ten gases and their dependence on diethyl phthalate (DOP; a plasticizer) was measured using solid-phase microextraction (SPME) followed by GC-MS. Moreover, absorption capacities of MIFAs based on methacrylic acid (MAA) and polyacrylic acid (PAA) were evaluated toward alcohols (heptanol and nonanol) and fatty acids (heptanoic acid and nonanoic acid). Results demonstrated the superior performance

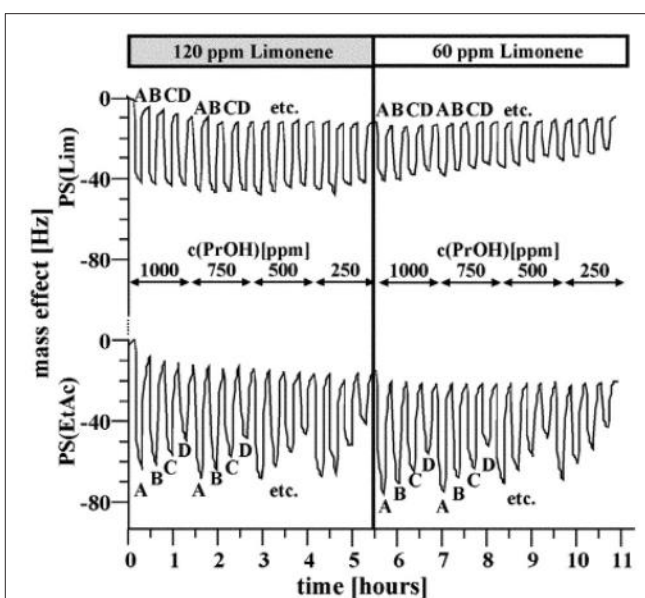


**FIGURE 3** | Detail of the frequency responses for the limonene sensor and the ethyl acetate sensor based on polystyrene toward different gas mixtures with the following analyte contents: limonene 120 and 60 ppm; propanol 250–1000 ppm; ethyl acetate: A: 3000 ppm, B: 2250 ppm, C: 1500 ppm, D: 750 ppm. Reproduced with permission from (Dickert et al., 2004) © RSC, Royal Society of Chemistry.

of rigid MAA compared to flexible PAA in all the cases. Coupling multiple affinity sensors gives rise to discrimination of gases using pattern recognition.

Instead of using organic polymers, Liu et al. employed sol-gel materials for detecting volatile aldehyde vapors (Liu et al., 2017). These metabolic byproducts play an important role in oxidative stress as well as in cancer. Such molecularly imprinted sol-gel (MISG) materials were targeting hexanal, nonanal, and benzaldehyde and could be implemented in an e-nose system. Using a five-channel array, the three distinct vapors could be separated at low concentrations by means of principal component analysis (PCA). Finally, a randomly selected array was used for qualitative comparison.

## MIP-Based Electronic Tongues

Using MIPs is not limited to the gas phase. Takeuchi and coworkers developed a MIP-based array to classify proteins (Takeuchi et al., 2007; Huynh and Kutner, 2015) via e-tongue in aqueous solution. They used acrylic acid and 2-dimethylaminoethyl methacrylate as functional monomers and glycosyloxyethyl methacrylate as a crosslinker. Cytochrome c, ribonuclease A, and  $\alpha$ -lactalbumin all demonstrated the highest affinity toward their respective synthesized MIP (**Figure 7**). The affinities of both albumin and myoglobin were analyzed for reference. They both showed more binding toward the nonimprinted polymer than to any of the three MIPs on both the tested polymers. **Figure 8** displays the PCA profiling results of these five protein groups. It turned out that the acrylate-based polymer is more suitable for correct classification of all the

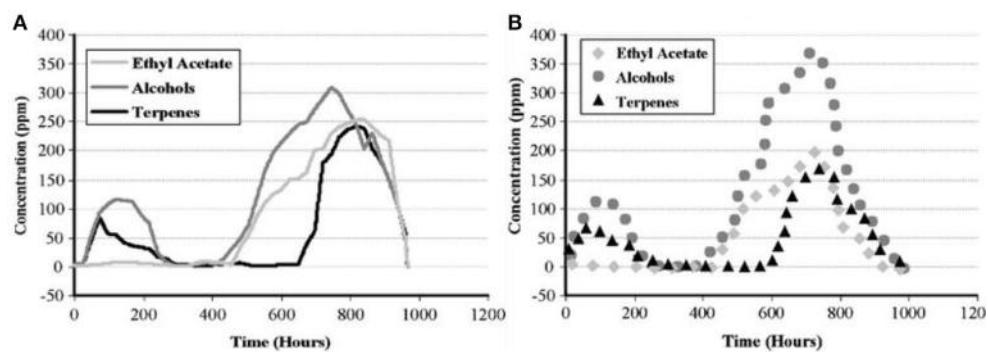


**FIGURE 4 | (A)** Mass-sensitive measurements of pine decomposition. **(B)** Corresponding GC-MS validation data. Adapted with permission from Lieberzeit et al. (2008) © Springer Nature.

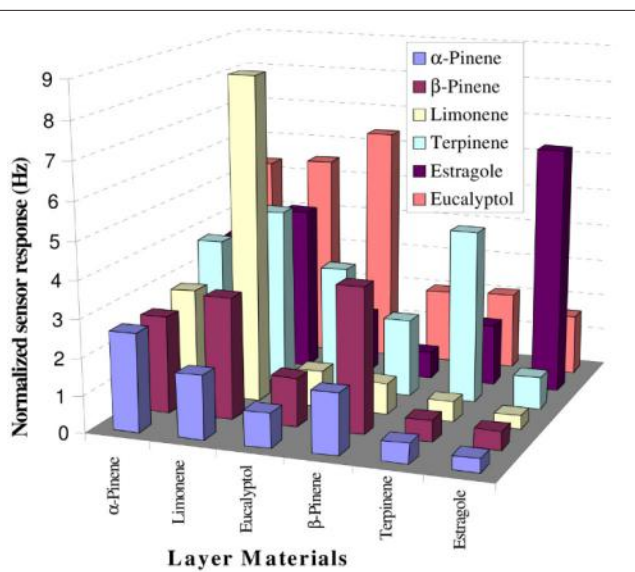


**FIGURE 5 |** Responses of different MIP-based sensors toward terpenes. Reproduced from Iqbal et al. (2010) Creative Commons License CC-BY3.0.

five proteins. It is noteworthy that albumin and myoglobin can be distinguished from the other proteins and from each other despite the fact that no MIPs were generated for either of them. This approach very clearly shows that combining “chemical” and “chemometric” selectivity indeed adds value to the system.

Feng and colleagues implemented an e-nose to distinguish clenbuterol from its metabolites: 4-aminohippuric acid (AHA) and 4-hydroxymandelic acid (HMA) (Feng et al., 2017). In 2010, clenbuterol received considerable attention in the media for its use as a doping agent in professional sports. It is a performance-enhancing drug that leads to enhanced muscle strength (George et al., 2006). In addition, it acts as a bronchodilator. Detection of very low concentrations, thus, provide a valuable tool in the battle against doping. The results showed that each MIP displays the highest affinity toward the respective target species. In this case, the authors used ethylene glycol dimethacrylate (EGDMA) as a monomer. After the imprinting process, QCM experiments

were performed to determine the amount of uptake of the  $\beta$ -2 agonist and its analogs. This led to three distinct clusters that did not overlap; thus, distinguishing the three compounds. Overall, the method resulted in a limit of detection around  $\text{LoD} = 3.0 \text{ ng/mL}$ .

## E-NOSES AND E-TONGUES RELYING ON NONPOLYMERIC BIOMIMETICS

As previously mentioned, there is only a limited number of sensor array papers describing the use of highly selective sensors. Apart from molecularly imprinted polymers, only a few other strategies have been reported, partly relying on natural species and partly on truly biomimetic ones.

### Cells

Using living cells to generate selectivity in sensing is, comparably, a new concept. It is intriguing because it makes use of the species that is usually first exposed to a given environment. The reaction to external stimuli is rapidly followed by a response. Moreover, during this process, cells preserve their essential working mechanism. One example by Wang et al. integrates olfactory and gustatory cells with a light-addressable potentiometric sensor (LAPS) to mimic human smell and taste (Wang et al., 2007). For this purpose, olfactory neurons are grown onto the silicon dioxide chip constituting the device. The LAPS is built up in two parts, namely (1) an electrolyte insulator ( $\text{SiO}_2$ ) and (2) a semiconductor (Si). Laser light shines onto the immobilized cells. Exposure to drugs triggers action potentials that are observed through changes in the bias voltage. These are picked up by the LAPS and are converted into a corresponding photocurrent. Different concentrations (1, 25, and  $50 \mu\text{M}$ ) of acetic acid were added to the chip as a feasibility test to study the stimulation of the mitral cells. This resulted in concentration-dependent elevated frequency responses upon addition of acetic acid solutions. Next, taste buds were successfully placed onto LAPS chips. Four basic tastants, namely sodium chloride ( $\text{NaCl}$ ) for “salty,” hydrochloric acid ( $\text{HCl}$ ) for “sour,” sucrose for “sweet,” and magnesium sulfate ( $\text{MgSO}_4$ ) for “bitter,” were administered. Changes in photocurrent underwent fast Fourier transformation

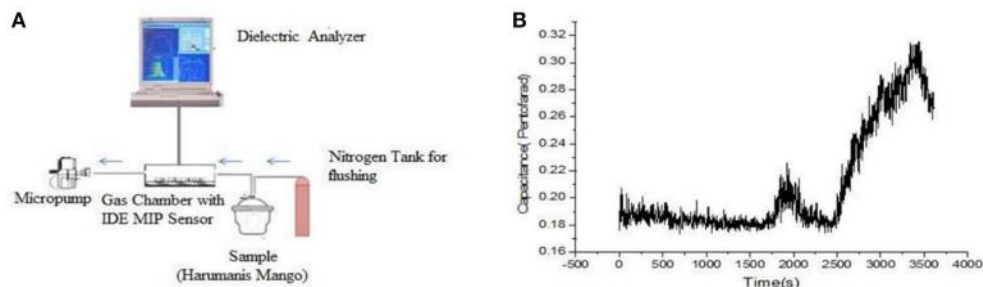


**FIGURE 6 | (A)** Set-up of mango VC detection device. **(B)** Emission profile of  $\alpha$ -pinene in time. Reproduced from Hawari et al. (2013) Creative Commons License CC-BY-NC-ND 3.0.

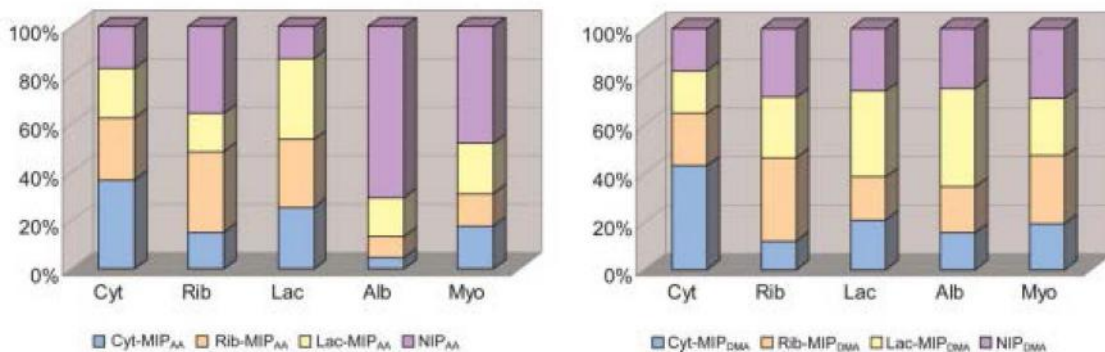


**FIGURE 7 |** Fingerprints of five proteins tested based upon AA-based and DMA-based polymers. Cyt, cytochrome C; Rib, ribonuclease A; Lac,  $\alpha$ -lactalbumin; Alb, albumin; Myo, myoglobin. The total amount of proteins bound corresponds to 100%. Reproduced with permission from Takeuchi et al. (2007) © RSC, Royal Society of Chemistry.

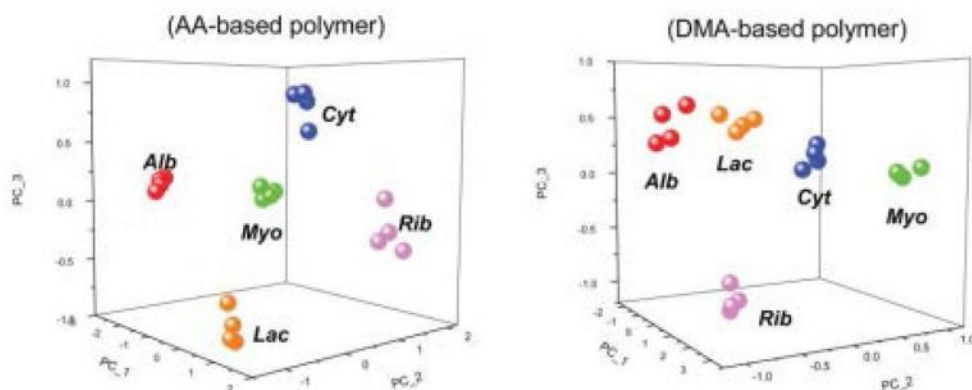


**FIGURE 8 |** PCA score plots showing the discrimination of four trials of five different proteins based upon the bound amounts of AA-based and DMA-based polymers. Cyt, cytochrome C; Rib, ribonuclease A; Lac,  $\alpha$ -lactalbumin; Alb, albumin; Myo, myoglobin. Alb and Myo are non-templated proteins. Alb and Myo are non-templated proteins. Reproduced with permission from Takeuchi et al. (2007) © RSC, Royal Society of Chemistry.

(FFT) analysis. Characteristic peaks resulting from this approach contain information about the corresponding taste profile. Very recently, a report showed a very special case of cell-based e-noses by linking a microelectrode array to the olfactory bulb of a mouse *in vivo* (Gao et al., 2018). In a similar way, the

authors achieved high selectivity and sensitivity toward odorants containing benzene rings that reached down to  $10^{-5}$  M in the case of trinitrotoluene (TNT). However, the extent to which such an approach can still be regarded “biomimetic” is of course questionable.

## Enzymes

It is well known that enzymes can be implemented as recognition elements in sensors. The blood-glucose sensor based on glucose oxidase is the most famous example of such an approach. Although many research groups have reported enzymatic biosensors so far, only few of them are implemented into e-noses or e-tongues.

As a first example, Keller and his group developed an amperometric enzyme-based biosensor to detect umami by monitoring the amount of L-glutamate in tomato specimens (Pauliukaite et al., 2006). L-glutamate oxidase was linked onto an electrode followed by exposing the sensor to increasing concentrations of glutamate. This led to concentration-dependent sensor signals and a detection limit of  $50\text{ }\mu\text{M}$ . Combining multiples of these biosensors would overcome the restriction to quantitative detection. It opens up the opportunity for qualitative measurements, i.e., discrimination among different tastants.

An already established enzyme-based e-tongue was developed by Busch et al. (2006). Tyrosinase and peroxidase were used to verify the presence or absence of phenolic compounds that are characteristic for bitterness in virgin olive oil. Correlation coefficients of 0.82 and 0.87 could be achieved for describing the relationship between tyrosinase- and peroxidase-based biosensors on the one hand and phenol content on the other. Moreover, measurements were highly repeatable, revealing a residual standard deviation (rsd) of 6%.

In 2005, Dock and his group developed an e-tongue to assess wastewater quality through chemometrics (Tønning et al., 2005) based on enzymatically modified screen-printed platinum electrodes. The sensor system targets different factors, such as chemical oxygen demand (COD) and inhibition of nitrification. Furthermore, enzyme-based amperometry forms the basis of detection. Combining an eight-sensor array together with PCA leads to clear discrimination between four different wastewater samples (untreated, alarm, alert, and normal water). The temporal drift of individual sensor signals could be overcome by using the entire array's response pattern.

## Proteins and Peptides

Most recognition elements in nature are based on proteins; hence, using them in sensors is also logical. The best examples

are, of course, enzyme electrodes and immunosensors. However, there is a beautiful example for mimicking human olfaction. In 2012, Lee et al. published the development of a human-like nanobioelectronic nose with comparable sensitivity and selectivity as its natural counterpart (Lee et al., 2012). They incorporated olfactory receptor proteins onto carboxylated polypyrrole nanotubes (CPNTs) and performed resistance measurements on these systems. They achieved a detection limit of approximately 0.02 parts per trillion (ppt) for helional gas. Hence, detecting gaseous molecules in a similar fashion as the human nose was feasible.

It is well-known that the functionality of most proteins is located on a clearly defined fraction of the respective chain/structure. Hence, constructing sensors based on short peptide chains is possible. An example of an e-tongue based on such peptide structures has been reported for detecting different dioxins (Mascini et al., 2004); in this case, biomimetic traps comprising pentapeptides were developed and coated onto QCMs. The corresponding sensor array determined the components of a mixture comprising three dioxins in a highly selective manner in a concentration range of 1–20 parts per billion (ppb). The main focus of the system in this case was to determine several dioxins simultaneously, rather than undertaking sequential measurements.

## Aptamers

The overwhelming majority of aptamers comprises RNA oligomers or single-stranded DNA oligomers that are less than a hundred nucleobases long (Eifler, 2014; Zhuo et al., 2017). Aptamers are produced through the “selection of ligands by exponential enrichment” abbreviated as SELEX (Sun and Zu, 2015; Zhuo et al., 2017). **Figure 9** describes the working mechanism of aptamers; they bind their targets with comparable selectivity similar to antibodies binding the antigens. Within the scope of this review, Eifler (2014) reported an electronic nose in combination with a biosensor for the detection of deoxynivalenol (DON). DON is a toxic secondary metabolite released by *Fusarium* species. In a first step, an electronic nose, based on metalloporphyrins, was established to detect DON. Cross-validation studies showed that the correct classification rate between infested and noninfested species reached 83%. In addition, it was feasible to distinguish between two levels of

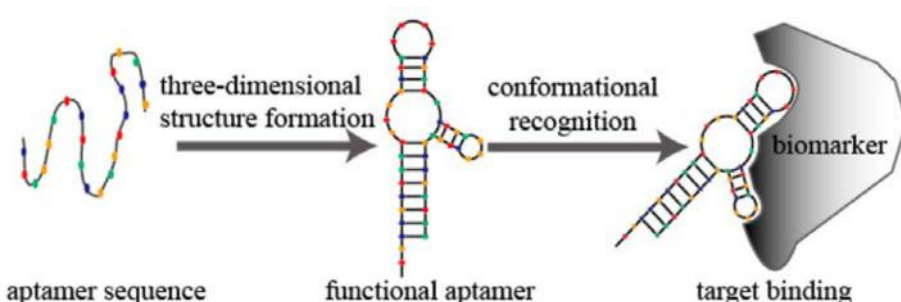


**FIGURE 9** | Schematic diagram of aptamer conformational recognition of targets to form an aptamer–target complex. From Sun and Zu (2015), CC-BY.

infections and between two fungal species with classification rates of 91% and 94%, respectively. However, this approach was not strong enough to quantitatively determine the DON levels. Therefore, a 78-base aptamer was selected and implemented to bind DON, despite other molecular species interfering. This made it possible to quantitatively detect DON, despite very strong matrix effects. In conclusion, one can say that, in the concrete case, only the combined effort of a sensor array and a selective sensor is allowed for achieving the necessary selectivity and sensitivity.

In a similar approach, an array consisting of ion-selective field-effect transistors (ISFETs) coated with aptamer was used to detect vanillin in foods and beverages without sample pretreatment (Andrianova et al., 2017). Vanillin is not only useful in fragrance and flavoring but can also evoke allergic reactions, making the need for detection inevitable (van Assendelft, 1987). At first, hybridized DNA was present on an ISFET surface. Addition of vanillin led to the dissociation of the DNA probe. The outcome was a concentration-dependent change in the surface potential. Through this method of signal amplification, a 15-fold better limit of detection could be reached. As already discussed in the previous case, the strength of the system lies in the fact that multiple sensors are used to generate a signal.

Du et al. (2013) reported odor detection using a piezoelectric biosensor coated with an olfactory receptor-based tag aptamer. First, a QCM surface was coated with anti-His towards the His-tagged olfactory receptor of *C. elegans*, ODR-10. QCM results revealed high binding responses of the sensor toward diacetyl, the natural ligand of ODR-10. This example can be the starting point of artificial designed arrays that can detect desirable volatiles, opening up very interesting potential applications in mimicking olfaction.

## CONCLUSIONS AND OUTLOOK

Overall, only a very limited number of sensor arrays published use selective detection. A short Scopus research report, as of June 2018, revealed more than 100,000 publications dealing with “chemical sensor,” almost 6,000 for “electronic nose,” and only some 270 for “electronic nose” combined with “highly selective.” Of these, less than 200 papers reported on combining molecular imprinting or biomimicry with electronic noses or tongues. Expanding the search toward the entire supramolecular analytical chemistry reveals that the topic of this review covers only a small yet an important part of sensor science. This

seems logical because the rationale behind developing electronic noses and tongues is to use sensors with broadband chemical response and generate selectivity *in silico* via chemometric treatment afterwards. When aiming at sample classification, for instance, when recognizing/distinguishing odors, such an approach indeed makes sense. The main application scenario for arrays comprising inherently highly selective sensors is to detect multiple analytes in a simultaneous manner. Indeed, most examples for such e-noses in the literature have exactly that goal in mind, whether it may be by detecting different dioxins or for aiming at different tastants. In terms of future potential, aiming at implementing cells/tissues into sensor arrays similarly to the existing e-noses and e-tongues is highly interesting. The detailed recognition mechanism remains unclear in this case. Useful information, thus, requires chemometric analysis of the data. However, the approach allows using the responses of exactly the type of cells that first come into contact with a given pollutant in the living systems. Therefore, such cells are most useful to mimic first response *in vivo* without the need for carrying out animal experiments. This does not only lead to more reliable data but also circumvents ethical issues related to animal experiments. A slightly different and ethically more problematic approach aims at interfacing the actual (mammalian) olfaction organs with an artificial sensor array to use the respective animal as recognition “species.” Although it is interesting from the scientific point of view due to the deeper insight into the processes of olfaction and tasting, applying such approaches on a commercial scale is of course impossible. Finally, one could think about an application scenario, in which natural recognition is fully replaced by biomimetic one. This would open up ways to establish bioassays—e.g., for assessing toxicological parameters—on fully artificial systems. The beauty of the approach—especially compared to single-sensor measurements—lies in the fact that this would allow for testing the influence of a certain species toward a range of targets and (bio) receptors.

## AUTHOR CONTRIBUTIONS

WC undertook the initial literature research and wrote the first version of the manuscript after having discussed the outline/structure with PL. He also participated in iterative steps on earlier version of the manuscript. PL laid out the general structure of the article, corrected, and extended versions, as well as added literature and topics and prepared the final edited version of the manuscript.

## REFERENCES

- Alexander, C., Andersson, H. S., Andersson, L. I., Ansell, R. J., Kirsch, N., Nicholls, I. A., et al. (2006). Molecular imprinting science and technology: a survey of the literature for the years up to and including 2003. *J. Mol. Recognit.* 19, 106–180. doi: 10.1002/jmr.760
- Andrianova, M., Komarova, N., Grudtsov, V., Kuznetsov, E., and Kuznetsov, A. (2017). Amplified detection of the aptamer-vanillin complex with the use of bsm dna polymerase. *Sensors* 18:49. doi: 10.3390/s18010049
- Arshak, K., Lyons, G. M., Harris, J., and Clifford, S. (2004). A review of gas sensors employed in electronic nose applications. *Sens. Rev.* 24, 181–198. doi: 10.1108/02602280410525977
- Baby, R. U., Cabezas, M. D., and de Reca, N. W. (2000). Electronic nose: a useful tool for monitoring environmental contamination. *Sens. Actuators B Chem.* 69:2148. doi: 10.1016/S0925-4005(00)00491-3
- Baldwin, E. A., Bai, J., Plotto, A., and Dea, S. (2011). Electronic noses and tongues: applications for the food and pharmaceutical industries. *Sensors* 11, 4744–4766. doi: 10.3390/s110504744

- Bikov, A., Hernadi, M., Korosi, B. Z., Kunos, L., Zsamboki, G., Sutto, Z., et al. (2014). Expiratory flow rate, breath hold and anatomic dead space influence electronic nose ability to detect lung cancer. *BMC Pulm. Med.* 14:202. doi: 10.1186/1471-2466-14-202
- Busch, J. L., Hrncirik, K., Bulukin, E., Boucon, C., and Mascini, M. (2006). Biosensor measurements of polar phenolics for the assessment of the bitterness and pungency of virgin olive oil. *J. Agric. Food Chem.* 54, 4371–4377. doi: 10.1021/jf060103m
- Cagnasso, S., Falasconi, M., Previdi, M. P., Franceschini, B., Cavalieri, C., Sberveglieri, V., et al. (2010). Rapid screening of *Alicyclobacillus acidoterrestris* spoilage of fruit juices by electronic nose: a confirmation study. *J. Sens.* 2010:143173. doi: 10.1155/2010/143173
- Chen, L., Wang, X., Lu, W., Wu, X., and Li, J. (2016). Molecular imprinting: perspectives and applications. *Chem. Soc. Rev.* 45, 2137–2211. doi: 10.1039/C6CS00061D
- Chunta, S., Suedee, R., and Lieberzeit, P. A. (2015). Low density lipoprotein sensor based on molecularly imprinted polymer. *Anal. Chem.* 88, 1419–1425. doi: 10.1021/acs.analchem.5b04091
- Cui, S., Ling, P., Zhu, H., and Keener, H. M. (2018). Plant pest detection using an artificial nose system: a review. *Sensors* 18:E378. doi: 10.3390/s18020378
- Di Natale, C., Mantini, A., Macagnano, A., Antuzzi, D., Paolesse, R., and D'Amico, A. (1999). Electronic nose analysis of urine samples containing blood. *Physiol. Meas.* 20, 377–384.
- Dickert, F. L., Lieberzeit, P. A., Achatz, P., Palfinger, C., Fassnauer, M., Schmid, E., et al. (2004). QCM array for on-line-monitoring of composting procedures. *Analyst* 129, 432–437. doi: 10.1039/b315356h
- Dragonieri, S., van der Schee, M. P., Massaro, T., Schiavulli, N., Brinkman, P., Pinca, A., et al. (2012). An electronic nose distinguishes exhaled breath of patients with Malignant Pleural Mesothelioma from controls. *Lung Cancer* 75, 326–331. doi: 10.1016/j.lungcan.2011.08.009
- Du, L., Wu, C., Peng, H., Zou, L., Zhao, L., Huang, L., et al. (2013). Piezoelectric olfactory receptor biosensor prepared by aptamer-assisted immobilization. *Sens. Actuators B Chem.* 187, 481–487. doi: 10.1016/j.snb.2013.02.009
- Dung, T. T., Oh, Y., Choi, S. J., Kim, I. D., Oh, M. K., and Kim, M. (2018). Applications and advances in bioelectronic noses for odour sensing. *Sensors* 18:E103. doi: 10.3390/s18010103
- Eifler, J. (2014). *Electronic Nose-Based Fusarium Detection and Deoxynivalenol Aptamer Development*. Göttingen.
- Feng, F., Zheng, J., Qin, P., Han, T., and Zhao, D. (2017). A novel quartz crystal microbalance sensor array based on molecular imprinted polymers for simultaneous detection of clenbuterol and its metabolites. *Talanta* 167, 94–102. doi: 10.1016/j.talanta.2017.02.001
- Gao, K., Li, S., Zhuang, L., Qin, Z., Zhang, B., Huang, L., et al. (2018). *In vivo* bioelectronic nose using transgenic mice for specific odor detection. *Biosens. Bioelectron.* 102, 150–156. doi: 10.1016/j.bios.2017.08.055
- George, I., Xydas, S., Mancini, D. M., Lamanca, J., DiTullio, M., Marboe, C. C., et al. (2006). Effect of clenbuterol on cardiac and skeletal muscle function during left ventricular assist device support. *J. Heart Lung Transplant.* 25, 1084–1090. doi: 10.1016/j.healun.2006.06.017
- Gotrik, M. R., Feagin, T. A., Csordas, A. T., Nakamoto, M. A., and Soh, H. T. (2016). Advancements in aptamer discovery technologies. *Acc. Chem. Res.* 49, 1903–1910. doi: 10.1021/acs.accounts.6b00283
- Gutiérrez, L. F. (2011). [Assessment of dairy products quality by means of electronic nose]. *Arch. Latinoam. Nutr.* 61, 189–199.
- Haupt, K., and Mosbach, K. (2000). Molecularly imprinted polymers and their use in biomimetic sensors. *Chem. Rev.* 100, 2495–2504. doi: 10.1021/cr990099w
- Hawari, H. F., Samsudin, N. M., Ahmad, M. N., Shakaff, A. Y. M., Ghani, S. A., Wahab, Y., et al. (2012). Array of MIP-based sensor for fruit maturity assessment. *Proced. Chem.* 6, 100–109. doi: 10.1016/j.proche.2012.10.135
- Hawari, H. F., Samsudin, N. M., Md Shakaff, A. Y., Ghani, S. A., Ahmad, M. N., Wahab, Y., et al. (2013). Development of interdigitated electrode molecular imprinted polymer sensor for monitoring alpha pinene emissions from mango fruit. *Proced. Eng.* 53, 197–202. doi: 10.1016/j.proeng.2013.02.026
- Hong, H.-K., Shin, H. W., Yun, D. H., Kim, S.-R., Kwon, C. H., Lee, K., et al. (1996). Electronic nose system with micro gas sensor array. *Sens. Actuators B Chem.* 36, 338–341. doi: 10.1016/S0925-4005(97)80092-5
- Hussain, M., Wackerlig, J., and Lieberzeit, P. A. (2013). Biomimetic strategies for sensing biological species. *Biosensors* 3, 89–107. doi: 10.3390/bios3010089
- Huynh, T. P., and Kutner, W. (2015). Molecularly imprinted polymers as recognition materials for electronic tongues. *Biosens. Bioelectron.* 74, 856–864. doi: 10.1016/j.bios.2015.07.054
- Hwang, J., Jeong, Y., Park, J. M., Lee, K. H., Hong, J. W., and Choi, J. (2015). Biomimetics: forecasting the future of science, engineering, and medicine. *Int. J. Nanomed.* 10, 5701–5713. doi: 10.2147/IJN.S8364
- Iqbal, N., Mustafa, G., Rehman, A., Biedermann, A., Najafi, B., Lieberzeit, P. A., et al. (2010). QCM-arrays for sensing terpenes in fresh and dried herbs via bio-mimetic MIP layers. *Sensors* 10, 6361–6376. doi: 10.3390/s100706361
- Ko, H. J., and Park, T. H. (2016). Bioelectronic nose and its application to smell visualization. *J. Biol. Eng.* 10:17. doi: 10.1186/s13036-016-0041-4
- Latha, R. S., and Lakshmi, P. K. (2012). Electronic tongue: an analytical gustatory tool. *J. Adv. Pharm. Technol.* 3, 3–8. doi: 10.4103/2231-4040.93556
- Lee, S. H., Kwon, O. S., Song, H. S., Park, S. J., Sung, J. H., Jang, J., et al. (2012). Mimicking the human smell sensing mechanism with an artificial nose platform. *Biomaterials* 33, 1722–1729. doi: 10.1016/j.biomaterials.2011.11.044
- Lieberzeit, P. A., Rehman, A., Najafi, B., and Dickert, F. L. (2008). Real-life application of a QCM-based e-nose: quantitative characterization of different plant-degradation processes. *Anal. Bioanal. Chem.* 391, 2897–2903. doi: 10.1007/s00216-008-2222-6
- Liu, C., Wyszyński, B., Yatabe, R., Hayashi, K., and Toko, K. (2017). Molecularly imprinted sol-gel-based QCM sensor arrays for the detection and recognition of volatile aldehydes. *Sensors* 17:E382. doi: 10.3390/s17020382
- Macías, M. M., Manso, A. G., Orellana, C. J., Velasco, H. M., Caballero, R. G., and Chamizo, J. C. (2012). Acetic acid detection threshold in synthetic wine samples of a portable electronic nose. *Sensors* 13, 208–220. doi: 10.3390/s130100208
- Mascini, M., Macagnano, A., Monti, D., Del Carlo M., Paolesse, R., Chen, B., et al. (2004). Piezoelectric sensors for dioxins: a biomimetic approach. *Biosens. Bioelectron.* 20, 1203–1210. doi: 10.1016/j.bios.2004.06.048
- Najam ul, H., Ejaz, N., Ejaz, W., and Kim, H. S. (2012). Meat and fish freshness inspection system based on odor sensing. *Sensors* 12, 15542–15557. doi: 10.3390/s121115542
- Pauliukaite, R., Zhlyyak, G., Citterio, D., and Spichiger-Keller, U. E. (2006). L-glutamate biosensor for estimation of the taste of tomato specimens. *Anal. Bioanal. Chem.* 386, 220–227. doi: 10.1007/s00216-006-0656-2
- Pearce, T. C., Gardner, J. W., Friel, S., Bartlett, P. N., and Blair, N. (1993). Electronic nose for monitoring the flavour of beers. *Analyst* 118, 371–377. doi: 10.1039/AN9931800371
- Polyakov, M. V. (1931). Adsorption properties and structure of silica gel. *Zhurnal Fizieskoj Khimii Akademii SSSR* 2, 799–805.
- Rinaldi, A. (2007). The scent of life. The exquisite complexity of the sense of smell in animals and humans. *EMBO Rep.* 8, 629–633. doi: 10.1038/sj.embor.7401029
- Schaller, E., Bosset, J. O., and Escher, F. (1998). 'Electronic Noses' and their application to food. *LWT Food Sci. Technol.* 31, 305–316. doi: 10.1006/fstl.1998.0376
- Shinohara, S., Chiayomaru, Y., Sassa, F., Liu, C., and Hayashi, K. (2016). Molecularly imprinted filtering adsorbents for odor sensing. *Sensors* 16:E1974. doi: 10.3390/s16111974
- Shurmer, H. V., and Gardner, J. W. (1992). Odour discrimination with an electronic nose. *Sens. Actuators B Chem.* 8, 1–11. doi: 10.1016/0925-4005(92)85001-D
- Sun, H., and Zu, Y. (2015). A highlight of recent advances in aptamer technology and its application. *Molecules* 20, 11959–11980. doi: 10.3390/molecules200711959
- Takeuchi, T., Goto, D., and Shimomori, H. (2007). Protein profiling by protein imprinted polymer array. *Analyst* 132, 101–103. doi: 10.1039/B614532A
- Tønning, E., Sapelnikova, S., Christensen, J., Carlsson, C., Winther-Nielsen, M., Dock, E., et al. (2005). Chemometric exploration of an amperometric biosensor array for fast determination of wastewater quality. *Biosens. Bioelectron.* 21, 608–617. doi: 10.1016/j.bios.2004.12.023
- van Assendelft, A. H. (1987). Adverse drug reactions checklist. *Br. Med.J. (Clin. Res. Ed.)* 294, 576–577.
- Voss, A., Witt, K., Fischer, C., Reulecke, S., Poitz, W., Kechagias, V., et al. (2012). Smelling heart failure from human skin odor with an electronic nose. *Conf. Proc. IEEE Eng. Med. Biol. Soc.* 2012, 4034–4037. doi: 10.1109/EMBC.2012.634685

- Wackerlig, J., and Lieberzeit, P. (2015). Molecularly imprinted polymer nanoparticles in chemical sensing - synthesis, characterisation and application. *Sens. Actuators B Chem.* 207, 144–157. doi: 10.1016/j.snb.2014.09.094
- Wang, P., Liu, Q., Zhang, W., Cai, H., and Xu, Y. (2007). Design of biomimetic electronic nose and electronic tongue. *Sens. Mater.* 19, 309–323.
- Wilson, A. D. (2012). Review of electronic-nose technologies and algorithms to detect hazardous chemicals in the environment. *Proced. Technol.* 1, 453–463. doi: 10.1016/j.protcy.2012.02.101
- Wojnowski, W., Majchrzak, T., Dymerski, T., Gebicki, J., and Namieśnik, J. (2017). Portable electronic nose based on electrochemical sensors for food quality assessment. *Sensors* 17:2715. doi: 10.3390/s17122715
- Xu, S., Lü, E., Lu, H., Zhou, Z., Wang, Y., and Yang, J. (2016). Quality detection of litchi stored in different environments using an electronic nose. *Sensors* 16:E852. doi: 10.3390/s16060852
- Zhuo, Z., Yu, Y., Wang, M., Li, J., Zhang, Z., Liu, J., et al. (2017). Recent advances in SELEX technology and aptamer applications in biomedicine. *Int. J. Mol. Sci.* 18:E2142. doi: 10.3390/ijms18102142

**Conflict of Interest Statement:** The authors declare that the research was conducted in the absence of any commercial or financial relationships that could be construed as a potential conflict of interest.

Copyright © 2018 Cuypers and Lieberzeit. This is an open-access article distributed under the terms of the Creative Commons Attribution License (CC BY). The use, distribution or reproduction in other forums is permitted, provided the original author(s) and the copyright owner(s) are credited and that the original publication in this journal is cited, in accordance with accepted academic practice. No use, distribution or reproduction is permitted which does not comply with these terms.



# Multisensor Systems by Electrochemical Nanowire Assembly for the Analysis of Aqueous Solutions

Konstantin G. Nikolaev<sup>1,2,3</sup>, Yury E. Ermolenko<sup>3</sup>, Andreas Offenhäusser<sup>1,2</sup>, Sergey S. Ermakov<sup>3</sup> and Yulia G. Mourzina<sup>1,2\*</sup>

<sup>1</sup> Institute of Complex Systems ICS-8, Forschungszentrum Jülich GmbH, Jülich, Germany, <sup>2</sup> JARA-FIT, Jülich, Germany,

<sup>3</sup> Institute of Chemistry, St. Petersburg State University, St. Petersburg, Russia

## OPEN ACCESS

### Edited by:

Larisa Lvova,  
Università degli Studi di Roma Tor  
Vergata, Italy

### Reviewed by:

Wei-Lung Tseng,  
National Sun Yat-sen University,  
Taiwan

Maria Rachele Guascito,  
University of Salento, Italy

### \*Correspondence:

Yulia G. Mourzina  
y.mourzina@fz-juelich.de

### Specialty section:

This article was submitted to  
Analytical Chemistry,  
a section of the journal  
Frontiers in Chemistry

Received: 15 March 2018

Accepted: 08 June 2018

Published: 29 June 2018

### Citation:

Nikolaev KG, Ermolenko YE, Offenhäusser A, Ermakov SS and Mourzina YG (2018) Multisensor Systems by Electrochemical Nanowire Assembly for the Analysis of Aqueous Solutions. *Front. Chem.* 6:256. doi: 10.3389/fchem.2018.00256

The development of electrochemical multisensor systems is driven by the need for fast, miniature, inexpensive, analytical devices, and advanced interdisciplinary based on both chemometric and (nano)material approaches. A multicomponent analysis of complex mixtures in environmental and technological monitoring, biological samples, and cell culture requires chip-based multisensor systems with high-stability sensors. In this paper, we describe the development, characterization, and applications of chip-based nanoelectrochemical sensor arrays prepared by the directed electrochemical nanowire assembly (DENA) of noble metals and metal alloys to analyze aqueous solutions. A synergic action of the electrode transducer function and electrocatalytic activity of the nanostructured surface toward analytes is achieved in the assembled metal nanowire (NW) sensors. Various sensor nanomaterials (Pd, Ni, Au, and their multicomponent compositions) can be electrochemically assembled on a single chip without employing multiple cycles of photolithography process to realize multi-analyte sensing applications as well as spatial resolution of sensor analysis by this single-chip multisensor system. For multi-analyte electrochemical sensing, individual amperometric signals of two or more nanowires can be acquired, making use of the specific electrocatalytic surface properties of the individual nanowire sensors of the array toward analytes. To demonstrate the application of a new electrochemical multisensor platform, Pd-Au, Pd-Ni, Pd, and Au NW electrode arrays on a single chip were employed for the non-enzymatic analysis of hydrogen peroxide, glucose, and ethanol. The analytes are determined at low absolute values of the detection potentials with linear concentration ranges of  $1.0 \times 10^{-6}$  –  $1.0 \times 10^{-3}$  M ( $\text{H}_2\text{O}_2$ ),  $1.5 \times 10^{-7}$  –  $2.0 \times 10^{-3}$  M (glucose), and  $0.7 \times 10^{-3}$  –  $3.0 \times 10^{-2}$  M (ethanol), detection limits of  $2 \times 10^{-7}$  M ( $\text{H}_2\text{O}_2$ ),  $4 \times 10^{-8}$  M (glucose), and  $5.2 \times 10^{-4}$  M (ethanol), and sensitivities of  $18 \mu\text{A M}^{-1}$  ( $\text{H}_2\text{O}_2$ ),  $178 \mu\text{A M}^{-1}$  (glucose), and  $28 \mu\text{A M}^{-1}$  (ethanol), respectively. The sensors demonstrate a high level of stability due to the non-enzymatic detection mode. Based on the DENA-assembled nanowire electrodes of a compositional diversity, we propose a novel single-chip electrochemical multisensor platform, which is promising for acquiring complex analytical signals for advanced data processing with chemometric techniques aimed at the development of electronic tongue-type multisensor systems for flexible multi-analyte monitoring and healthcare applications.

**Keywords:** electrochemical sensor, sensor array, metal nanowire assembly, multisensor system, non-enzymatic, glucose, ethanol, hydrogen peroxide

## INTRODUCTION

Electrochemical sensors and biosensors are widely used in clinical and pharmaceutical analysis, biomedical investigations, food quality assessments, as well as technological and environmental process monitoring due to their accuracy, selectivity, short response time, cost-effectiveness, applicability for multiparametric analysis, real-time *in situ* and *in vivo* measurements, and high spatial resolution achievable by miniaturization. Ongoing research in the field of electrochemical sensors and their operation principles leads to the development of new types of sensors and extends the range of possible applications. In particular, the need for flexible multi-analyte determinations in analyses of gas and liquid media has driven the research and development of new sensor materials, electrochemical multisensor arrays, electronic nose- and electronic tongue-type systems (Persaud and Dodd, 1982; Di Natale et al., 1995; Vlasov et al., 1999, 2005, 2010; Maistrenko et al., 2011; Kirsanov et al., 2013; Peris and Escuder-Gilabert, 2013; Voitechović et al., 2018).

For the multicomponent analysis of complex mixtures, electrochemical multisensor systems can be composed of sensors selective to individual analytes. In this case, individual sensors do not affect the accuracy of the determinations of other sensors of the multisensor system. The development of such multisensor arrays is required for miniaturization, lower costs, more reliable sensor analysis, and spatial resolution. In many cases, redox processes in amperometric and voltamperometric sensor applications on unmodified bare electrodes are hindered by the slow electrode kinetics and high overpotentials that must be applied for electrochemical conversion. As a consequence, the co-oxidation or reduction of many electroactive species present in natural samples can occur, causing unwanted interferences during detection which are difficult to distinguish. A wide range of materials and compounds with selective binding and/or electrocatalytic properties, which favor the thermodynamics and kinetics of specific redox processes, have been used to lower the absolute value of the response potential and improve the sensitivity and selectivity of these types of sensors (Yogeswaran and Chen, 2008; Budnikov et al., 2012; Thiagarajan et al., 2014; Komkova et al., 2017). These include enzymes as biocatalysts (Heller and Feldman, 2008; Koposova et al., 2014, 2015; Nikolaev et al., 2015; Rocchitta et al., 2016; Quesada-González and Merkoçi, 2017; Bandodkar et al., 2018). However, there are some general problems associated with highly selective electrochemical sensors, where selectivity is achieved by enzymes such as the low stability of biosensors, restricted measurement conditions, the use of onerous immobilization procedures, and mediators, as well as poor compatibility with nanotechnology processing. Non-enzymatic sensors, which are proposed as an alternative to enzyme biosensors (Park et al., 2006; Toghill and Compton, 2010), often suffer from slow electrode kinetics, high overpotentials, and insufficient selectivity. The latter problem might possibly be resolved through the use of multisensor systems in combination with chemometric techniques. In this case, a multisensor system may include less selective or non-selective sensors

with non-linear and multiparametric dependencies of the sensor signals on the component concentrations. A complex multiparametric signal of a multisensor system needs to be processed with chemometric techniques to obtain multiple analytical signals or non-parametric and non-quantitative information, as in the case of electronic nose and electronic tongue multisensor systems (Di Natale et al., 1995; Vlasov et al., 1999, 2010; Maistrenko et al., 2011; Panchuk et al., 2016). There are also some general problems with respect to electrochemical (bio) sensor analysis such as the need for new sensor materials and high-resolution sensor arrays. Therefore, multicomponent sensor analysis is advanced interdisciplinary based on chemometric and (nano)material approaches.

Electrochemical sensors based on metallic, carbonaceous, and composite nanomaterials help to advance the concept of non-enzymatic miniaturized electrochemical sensors (Chen et al., 2013, 2014; Guascito et al., 2013; Wang et al., 2016; Tee et al., 2017; Nikolaev et al., 2018) due to the electrocatalytic effects of surfaces and signal amplification techniques and could replace enzyme-based biosensors in various analytical applications. This leads to the improvement of sensor stability in fabrication and long-term use, cost-effectiveness, compatibility with nanotechnology, and could extend applications of sensors and multisensor systems. The development of electrochemical non-enzymatic sensors based on nanomaterials has been reviewed in a series of recent publications (Park et al., 2006; Chen et al., 2014; Jie et al., 2015; Zhang and Lieber, 2016; Gnana Kumar et al., 2017; Power et al., 2018).

Metal nanowires have become essential building blocks for the development of advanced, miniaturized non-enzymatic electrochemical sensors (Shaidarova and Budnikov, 2011; Chen et al., 2013, 2014; Koposova et al., 2013, 2015; Suib, 2013; Chen and Ostrom, 2015; Muratova et al., 2016). The improved electrocatalytic properties of the sensor metal nanomaterials in comparison with bulk materials are related to their high surface areas and energy, the preferential orientation of crystallographic planes, lattice defects at the surfaces, and the presence of pores, sharp edges, and nanoscale junctions. Different methods are available for the synthesis of metallic nanowires: chemical reduction from solutions, lithography technologies, the assembly by electromagnetic field forces, the template-based approach, CVD, laser deposition, etc. (Cheng et al., 2005; Nagashima et al., 2007; Kisner et al., 2011; Xing et al., 2012; Ji et al., 2013; Panov et al., 2017). Often, binary or more complex multicomponent systems demonstrate a higher (electro) catalytic activity due to synergic or electronic effects (Koper, 2004; Wang et al., 2008; Shaidarova and Budnikov, 2011; Guascito et al., 2013; Yang et al., 2013; Chen and Ostrom, 2015).

Recently, a method of the directed electrochemical nanowire assembly (DENA) was proposed for metal nanowires (Cheng et al., 2005, 2011; Talukdar et al., 2006; Ozturk et al., 2007a,b; Kawasaki and Arnold, 2011; Flanders et al., 2012; Ji et al., 2013; Zhang et al., 2013; Yi et al., 2014; Nikolaev et al., 2017). The method is based on the directional growth of metal nanowires and nanodendrites under the action of an AC voltage of high-frequency and a DC offset voltage applied between a pair of

pre-structured electrodes. Using this method, different metal nanowire compositions can be electrodeposited on a chip and connected to the external circuitry in a single step. Important advantages of DENA, such as application at room temperature and atmosphere, spatial resolution, fast rates of the directional electrodeposition of metal nanostructures, and low costs have yet to be fully explored for electrochemical sensors and multisensor systems. In our recent work, we explore the DENA approach for a novel class of electrochemical multisensor systems in electrolyte solutions (Nikolaev et al., 2017, 2018). A synergic action of the electrode transducer function of the assembled Pd-Au nanowires and the electrochemical activity of the nanowire surface toward hydrogen peroxide reduction is achieved in the proposed multisensor system (Nikolaev et al., 2018). The detection of hydrogen peroxide in cardiomyocyte-like HL-1 cells using a non-enzymatic Pd-Au nanowire multisensor array prepared by DENA was also demonstrated (Nikolaev et al., 2018). The DENA method has been applied to create nanostructures of platinum (Kawasaki and Arnold, 2011), gold (Ozturk et al., 2007a; Nikolaev et al., 2017), palladium (Nikolaev et al., 2018), as well as Au-Pt (Cheng et al., 2011) and Au-Ag (Ji et al., 2014) compositions. Such materials can enable the detection of a number of analytes (Koposova et al., 2014; Ermakov et al., 2016; Nikolaev et al., 2017).

In this paper, we describe the development, characterization, and application of the chip-based nanoelectrochemical multisensor platform prepared by DENA for the analysis of liquid media. A single-chip multisensor system is composed of an array of Pd-Au, Pd-Ni, Pd, and Au NW electrodes prepared without employing multiple cycles of photolithography process to realize a multiplicity of the NW sensor compositions on a single chip. Individual amperometric signals of two or more nanowires can be acquired, making use of the specific electrocatalytic surface properties of the individual nanowire sensors of the array for the electrochemical detection. The multisensor system was employed for the non-enzymatic analysis of hydrogen peroxide, glucose, and ethanol. The proposed nanoelectrochemical multisensor platform is promising for acquiring complex analytical signals for advanced data processing with chemometric techniques for flexible multi-analyte monitoring and healthcare applications.

## MATERIALS AND METHODS

### Chemicals

Potassium tetrachloropalladate (II), palladium (II) chloride, gold (III) chloride trihydrate, nickel (II) chloride, disodium phosphate, hydrogen peroxide ( $\geq 30\%$ ), HEPES (4-(2-hydroxyethyl)-1-piperazineethanesulfonic acid), sodium dihydrogen phosphate, propanol, acetone, and other chemicals were obtained from Sigma-Aldrich. The substances were of analytical grade purity and used without further purification. The photoresists and developer for the photolithography were obtained from MicroChem Corp. and MicroChemicals GmbH. Solutions of analytes were prepared directly before measurements. All solutions were prepared using distilled water.

### Electrode Synthesis by Directed Electrochemical Nanowire Assembly

The growth microelectrodes (source and ground electrodes), **Figure 1**, for the electrodeposition of the nanowires of various compositions by DENA were structured on the substrates and produced using thin-film technologies in an ISO 5 cleanroom as described in detail (Nikolaev et al., 2018). Briefly, wafers of single-crystal boron-doped n-Si with (111) surface orientation were employed as substrates for fabricating electrochemical sensors. The silicon wafers were oxidized to produce a silicon dioxide layer of 1000 nm thickness using a Tempress oxidation furnace. These Si/SiO<sub>2</sub> wafers were further used as carriers for the deposition of the growth microelectrodes by photolithography and lift-off processes.

After dehydration at 180°C for 20 min, the Si/SiO<sub>2</sub> wafers were coated with a LOR 3B photoresist to produce a layer of 5  $\mu\text{m}$ , baked for 5 min, and subsequently coated with an AZ nLOF 2020 photoresist to produce a layer of 2  $\mu\text{m}$ . A photoresist stack was used instead of a single photoresist layer to achieve a better control over the geometry of the growth microelectrodes and contact lines. After pre-baking at 115°C for 90 s, the Si/SiO<sub>2</sub> wafers with a photoresist stack were exposed at 325 watt using a photolithography mask at Mask Süss MA-6 (Hg-vapor lamp 350 W). Exposure time was optimized as 1.4 s. After exposure, the wafers were post-exposure baked at 115°C for 90 s. The wafers with an exposed photoresist stack were subsequently developed by AZ<sup>®</sup> 326 (MIF, 2.38% TMAH in H<sub>2</sub>O) for 1 min to produce structured photoresist layers for subsequent metallization and lift-off processes.

Thin metal layers of titanium for adhesion (10 nm) and gold (100 nm) were deposited on the Si/SiO<sub>2</sub> wafers with pre-structured photoresist layers by means of an electron beam evaporation using a Pfeiffer PLS 500 equipment. Afterwards, the wafers were lifted off using acetone to remove sacrificial photoresist polymer layers. The wafers were then cleaned in isopropanol and distilled water.

Subsequently, DENA of nanowires and nanodendrites was performed on the Si/SiO<sub>2</sub> wafers with metal bond pads, contact lines, and growth electrodes prepared by photolithography and lift-off processes as described above. The nanowires and nanodendrites of various metal and bimetallic compositions were assembled between growth electrodes using an Agilent Trueform Series Waveform Generator 33600. The optical microscope Leica DMLB was used for fixing and observation of DENA.

### Analysis by Scanning Electron Microscopy and Energy-Dispersive X-Ray Spectroscopy

The nanoelectrodes were characterized by scanning electron microscopy using a Magellan<sup>TM</sup> XHR SEM equipped with an energy-dispersive X-ray spectroscopy (EDX) detector system, and a Magellan<sup>TM</sup> XHR SEM equipped with a focused ion beam (FIB) setup.

## Electrochemical Measurements

To be used in aqueous solutions, the contact lines and growth electrodes of the nanowire electrode arrays prepared by DENA need to be protected by an isolation layer. An isolation layer of polyimide was produced by means of an aligned photolithography procedure. The channels with arrays of the assembled nanowire electrodes were left free from the isolation polyimide layer for contact with aqueous solutions. Additionally, the bond pads were left open for making electrical contacts to the external circuit. The wafers were diced into  $13 \times 13$  mm chips. A glass ring with a radius of about 8 mm was attached on top of each chip to make an electrochemical cell compartment and accommodate the electrolyte solution for electrochemical experiments using polydimethylsiloxane (PDMS, 10:1, Sylgard). The bond pads were left outside the glass ring.

Electrochemical experiments were performed using a three-electrode electrochemical cell placed in a dark Faraday cage and controlled by a potentiostat-galvanostat AUTOLAB (PGSTAT 302, The Netherlands). The electrochemical cell was made of a coiled platinum auxiliary electrode, an Ag/AgCl reference electrode (3 M KCl, DRIREF-450, World Precision Instruments), and the desired working electrode. The electrochemical cell was covered with a PDMS top cover, which incorporated apertures for the electrodes and argon supply. The solutions and electrochemical cell were purged with argon to remove oxygen and kept under argon atmosphere during the experiments. All experiments were at  $22 \pm 1^\circ\text{C}$ . A detection limit of sensors was estimated using a signal to noise (S/N) ratio of 3.

## RESULTS AND DISCUSSION

### Growth and Characterization of the Nanoelectrochemical Sensors

In a typical experiment on the nanowire assembly, the growth electrodes, **Figure 1**, were connected to the AC/DC voltage

generator via bond pads and a small volume of the metal salt solution of about  $5 \mu\text{l}$  was positioned across the electrode gap. A square wave potential of the defined frequency and a DC voltage offset were applied across the electrode gap. Experimentally optimized growth parameters and solution compositions are shown in **Table 1**. DENA was detected in real time by optical microscopy (a video of the nanowire assembly process is available in Supporting Information).

Nanowire shape and compositions vary with the composition of the electrodeposition solution, electrode gap, and AC/DC parameters, as shown for example in **Figures 2–4**. The nanodendrite electrodes with an overall diameter from 50 nm to several micrometers were obtained by DENA in our studies. The details of the growth mechanism were discussed in Bockris and Despic (1970), Cheng et al. (2005), Ozturk et al. (2007a,b), Kawasaki and Arnold (2011), Ji et al. (2013), and Nikolaev et al. (2018). For the multisensor system, several types of electrodes, i.e., Pd, Au, Pd-Au, and Pd-Ni, were grown on a single chip.

**Figure 3** shows an example of a Pd electrode, **Figures 3A,B**, and two examples of Pd-Au nanodendrite electrodes. A Pd-Au nanodendrite electrode in **Figures 3G–L** was obtained by

**TABLE 1** | The experimentally optimized parameters for the directed electrochemical nanowire electrode assembly.

Composition	Growth parameters	
	AC, DC parameters	Solution composition
Au	45 MHz 18 V <sub>pp</sub> , 1 V <sub>DC</sub>	$1 \times 10^{-2}$ M HAuCl <sub>4</sub> in H <sub>2</sub> O
Pd	45 MHz 17 V <sub>pp</sub> , 1.5 V <sub>DC</sub>	$1 \times 10^{-2}$ M K <sub>2</sub> PdCl <sub>4</sub> in H <sub>2</sub> O
Pd-Au	40 MHz 17 V <sub>pp</sub> , 1.5 V <sub>DC</sub>	$5 \times 10^{-3}$ M K <sub>2</sub> PdCl <sub>4</sub> , $5 \times 10^{-3}$ M HAuCl <sub>4</sub> in water or PBS
Pd-Ni	38 MHz 15 V <sub>pp</sub> , 2.5 V <sub>DC</sub>	$2.5 \times 10^{-3}$ M PdCl <sub>2</sub> , $7.5 \times 10^{-3}$ M NiCl <sub>2</sub> in 0.1 M HEPES buffer

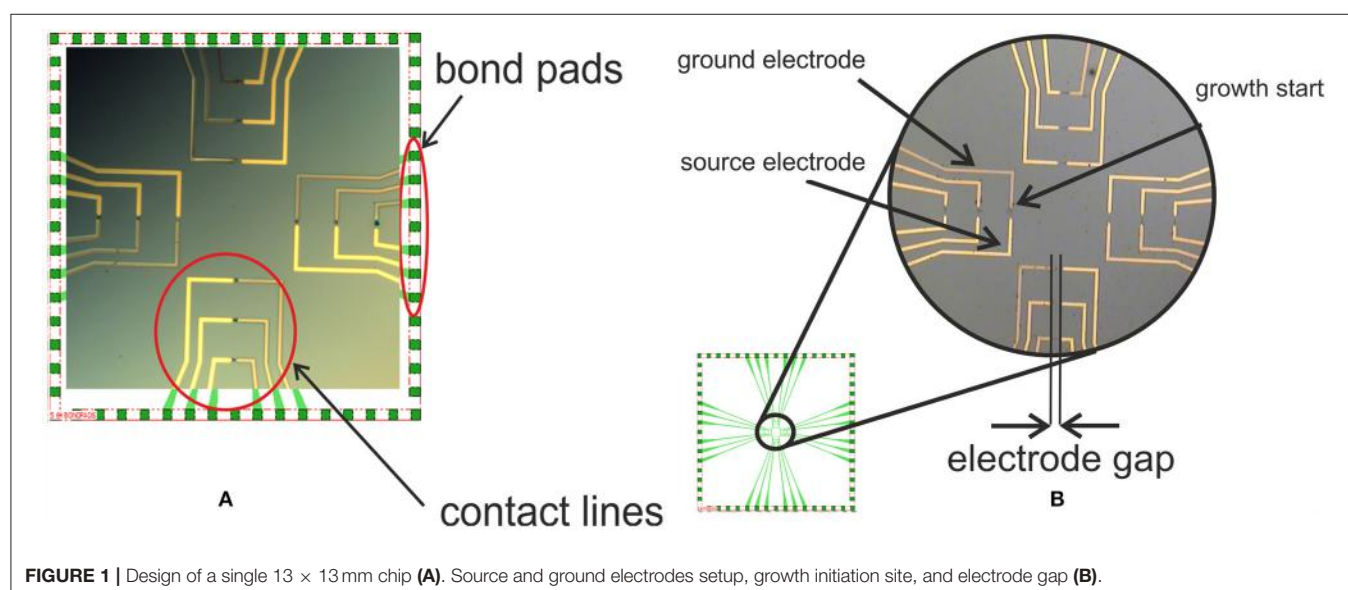
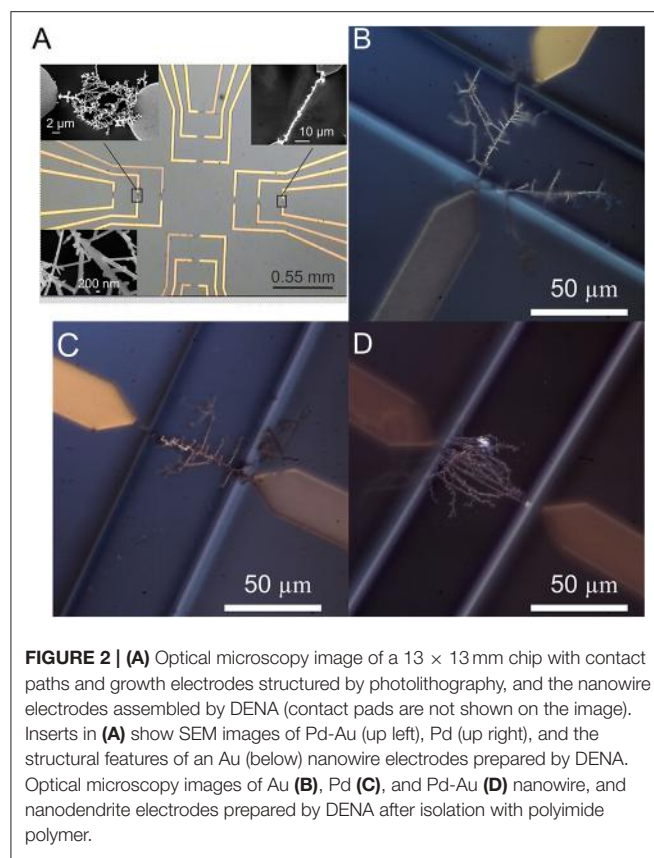


**FIGURE 1** | Design of a single  $13 \times 13$  mm chip (A). Source and ground electrodes setup, growth initiation site, and electrode gap (B).



deposition from  $5 \times 10^{-3}$  M  $\text{HAuCl}_4$  and  $5 \times 10^{-3}$  M  $\text{PdCl}_2$  in a 0.05 M phosphate buffer solution (PBS) of pH 8 at 38 MHz, 17 V<sub>pp</sub>, and 1.5 V DC offset. According to the EDX elemental mapping and spectrum of the nanowire composition, gold and palladium were homogeneously distributed throughout the cross-section and length of the Pd-Au nanodendrite electrode. The element content was found to constitute 55.5 and 44.5% for Au and Pd, respectively, while Pd accounted for about 60% in a Pd-Au nanodendrite electrode in **Figures 3c-f** in case of deposition from water solution. The nanodendrite electrodes have typically an electrochemically active surface area of thousands of  $\mu\text{m}^2$  (Nikolaev et al., 2018).

The co-deposition of Pd and Ni was carried out at 38 MHz, 15 V<sub>pp</sub>, and 2.5 V DC offset in a solution of  $2.5 \times 10^{-3}$  M  $\text{K}_2\text{PdCl}_4$  and  $7.5 \times 10^{-3}$  M  $\text{NiCl}_2$  positioned across a 50  $\mu\text{m}$  electrode gap, as shown in **Figure 4**. The chemical composition of as-prepared Pd-Ni electrode was determined using an EDX analysis. **Figures 4C,B** show the corresponding EDX spectrum and mapping of Pd (red) and Ni (green), respectively.

## Electroanalytical Measurements

### Detection of Glucose

The metal nanodendrite electrodes prepared by DENA were further characterized by cyclic voltammetry in 0.1 M PBS (pH 7.2) or 0.1 M KOH, **Figures 5A, 6A, 7A**. In a number of cases, the current-voltage curves indicated that the connections between

the nanowire electrodes and growth electrodes were destroyed during the isolation procedure. Therefore, these electrodes were not used for further experiments.

The electrochemical activities of different nanodendrite electrode surfaces prepared by DENA toward glucose oxidation were studied to evaluate the feasibility of their application for glucose sensing, **Figures 5–7**. Non-enzymatic glucose electrochemical sensors have been presented and discussed in a number of recent reviews and articles (Toghill and Compton, 2010; Chen and Ostrom, 2015; Jin et al., 2015; Pourbeyram and Mehdizadeh, 2016; Liu et al., 2017; Quesada-González and Merkoçi, 2017; Shabnam et al., 2017; Barragan et al., 2018). The electrochemical measurements for the Au NW electrode were performed in a 0.1 M PBS at pH 7.2, **Figure 5**. Cyclic voltammograms of the electrodes were recorded in a potential range of 0–1.2 V (vs. Ag/AgCl), **Figure 5A**. As shown in **Figure 5A**, the CV of the Au NW electrode in the absence of glucose displays the characteristic features of a gold electrode surface. The gold cathodic peak potential after anodic oxidation in the positive (anodic) scan was at about +0.45 V for the Au nanodendrite electrode, **Figure 5A** (black line). Cyclic voltammogram in a  $10^{-2}$  M solution of glucose displays an anodic current due to oxidation of glucose in an anodic (forward) scan at about +0.29 V and an electrocatalytic oxidation current at about +0.17 V in a cathodic (reverse) scan, **Figure 5A** (blue dashed line). In the reverse (cathodic) potential sweeping, the reduction of the oxidized gold surface occurs, meaning that the active sites on the electrode surface are regenerated and accessible for the glucose oxidation. According to this, anodic current of the glucose oxidation with a new peak at about +0.17 V is observed in a reverse scan, **Figure 5A** (blue dashed line). The Au NW non-enzymatic sensor demonstrated a linear concentration range of  $1 \times 10^{-4}$ – $5 \times 10^{-3}$  M with a sensitivity of  $0.03 \mu\text{A M}^{-1}$  and a lower limit of detection of  $3.3 \times 10^{-5}$  M glucose. Selectivity of the Au NW sensor in the presence of fructose, sucrose, and ascorbic acid is shown in Figure S1.

Mechanisms of non-enzymatic electrocatalysis of glucose oxidation on metal electrode surfaces has generated much interest over the years for applications in glucose sensors and glucose-oxygen biofuel cells (Nikolaeva et al., 1983; Vassilyev et al., 1985; Makovos and Liu, 1986; Burke, 1994; Heller and Feldman, 2008; Pasta et al., 2010; Toghill and Compton, 2010). However, the electrocatalytic behavior of gold electrodes in this process is complex and although many studies were published and a series of mechanisms were proposed, the mechanism of the glucose oxidation process remains uncertain. The processes of electrocatalytic transformations on electrode surfaces generally proceed via the adsorption of the analyte to the surface of the electrode via suitable bonds, which should be formed or broken during catalytic process (Pletcher, 1984) and involve the d-electrons and d-orbitals of the metal electrodes surface. Most notably is that electrocatalytic oxidation of glucose is favored on the oxidized metal surfaces of surface oxides or hydroxides and it was noted that electrooxidation of a number of organic molecules including glucose coincided with the  $\text{OH}_{\text{ads}}$  formation (Toghill and Compton, 2010). The concept that the oxide mediator species were involved in the electrocatalytic oxidation processes

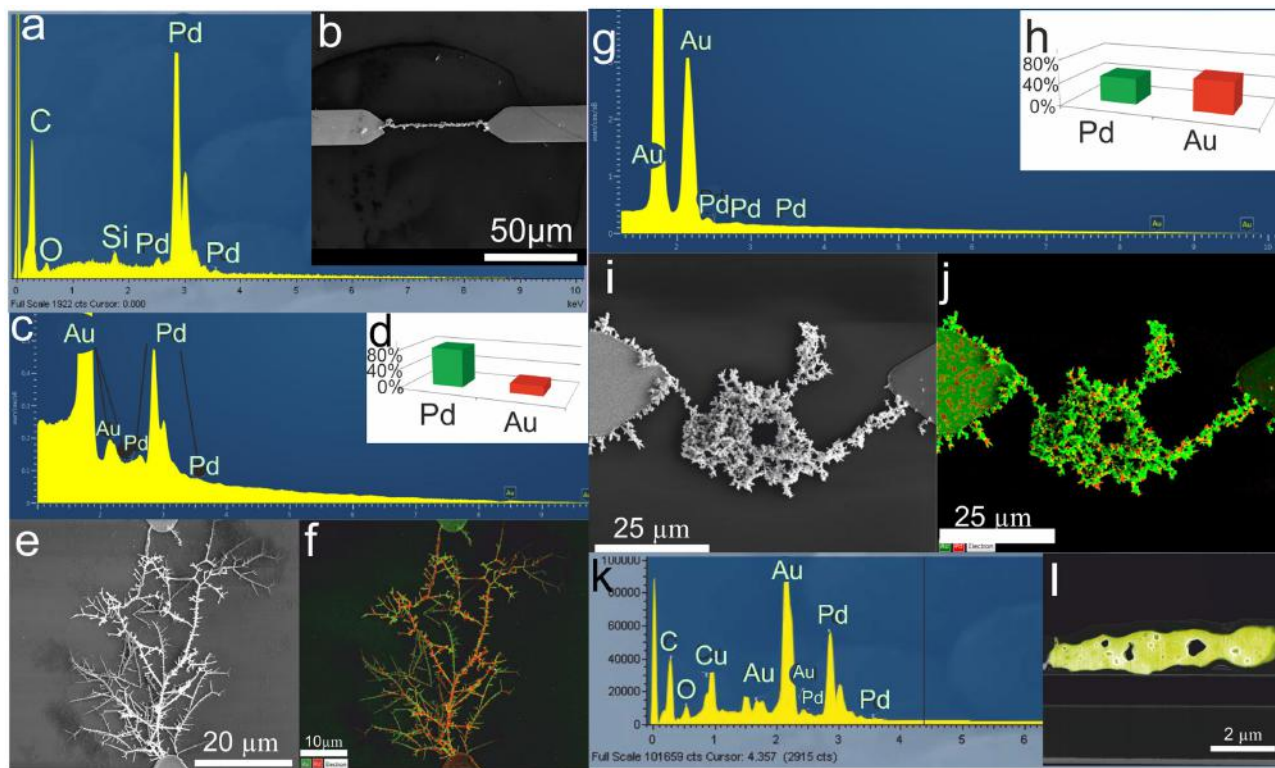
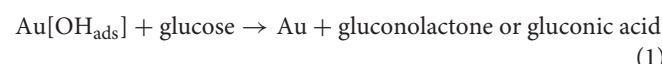


**FIGURE 3 |** (a) EDX spectrum of a Pd NW electrode, (b) SEM micrograph of the Pd NW electrode shown in (a). The Pd NW electrode was synthesized by electrodeposition from a Pd (ac)<sub>2</sub> solution. (c) EDX spectrum of a Pd-Au nanodendrite electrode and (d) histogram of the Pd and Au element content in the Pd-Au nanodendrite shown in (e) the SEM micrograph. (f) SEM micrograph of the same Pd-Au nanodendrite electrode with elemental mapping (Pd-green, Au-red). The Pd-Au nanodendrite electrode was electrochemically assembled in a  $5 \times 10^{-3}$  M HAuCl<sub>4</sub> and  $5 \times 10^{-3}$  M K<sub>2</sub>PdCl<sub>4</sub> water solution at 45 MHz, 17 V<sub>pp</sub>, and 1.5 V DC offset. (g) EDX spectrum of a Pd-Au nanodendrite electrode and (h) histogram of the Pd and Au element content in the Pd-Au nanodendrite electrode shown in (i) the SEM micrograph. (i) EDX elemental mapping of the same Pd-Au nanodendrite electrode (Pd-green, Au-red). (k) EDX spectrum of the lamella (cross section) of the Pd-Au nanodendrite electrode. (l) EDX elemental mapping of the same lamella of the Pd-Au nanodendrite electrode. The structure was synthesized by electrodeposition from  $5 \times 10^{-3}$  M HAuCl<sub>4</sub> and  $5 \times 10^{-3}$  M PdCl<sub>2</sub> dissolved in PBS, pH 8, at 38 MHz, 17 V<sub>pp</sub>, and 1.5 V DC offset. Reprinted by permission from: Springer, J. Solid State Electrochemistry, Bimetallic nanowire sensors for extracellular electrochemical hydrogen peroxide detection in HL-1 cell culture, Konstantin G. Nikolaev, Vanessa Maybeck, Elmar Neumann, Sergey S. Ermakov, Yury E. Ermolenko, Andreas Offenbässer, Yulia G. Mourzina © (2017), advance online publication, 28.11.2017 (doi: 10.1007/s10008-017-3829-3).

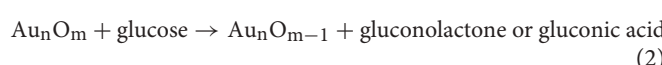
at electrodes was postulated earlier by Bagotzky and Vassilyev (1967) for the process of methanol oxidation on Pt. Burke (1994) discussed the premonolyer incipient hydrous oxide layer formed in a premonolayer oxidation step on the metal electrode surface and its role on the electrocatalytic processes at noble metal electrode/aqueous solution interface. The author introduced the “Incipient Hydrous Oxide Adatom Mediator” theory, where OH<sub>ads</sub> oxy-species on noble metal electrode surfaces might act as mediators of many electrocatalytic processes. It is thus believed that incipient hydrous gold oxide, which is formed by chemisorption of OH<sup>-</sup> to the surface of a gold electrode mediates electrocatalytic processes at a gold electrode. This hydrous gold oxide premonolayer may favor the process of the removal of the hemiacetalic hydrogen atom from the glucose molecule (Park et al., 2006) and mediates oxidation of the adsorbed species. Therefore electrocatalytic effect is more pronounced at higher pH, since the reversible adsorption of oxygen in the form of OH<sub>ads</sub> on the gold electrode surfaces is negligible in acidic media

(Vassilyev et al., 1985). Therefore, non-enzymatic glucose sensors based on metallic nanostructures are mostly used in alkaline solutions.

Nikolaeva et al. (1983) and Vassilyev et al. (1985) proposed a mechanism, in which an electrochemically formed gold oxide on the gold electrode surface possessed a catalytic effect on the process of glucose electrooxidation. It is thus supposed that a chemisorption of glucose at the hydrous gold oxide takes place and the adsorbed glucose is then oxidized by the adsorbed hydroxide anions, like it is schematically shown in Equations (1,2), and a scheme in Figure 5A:



or



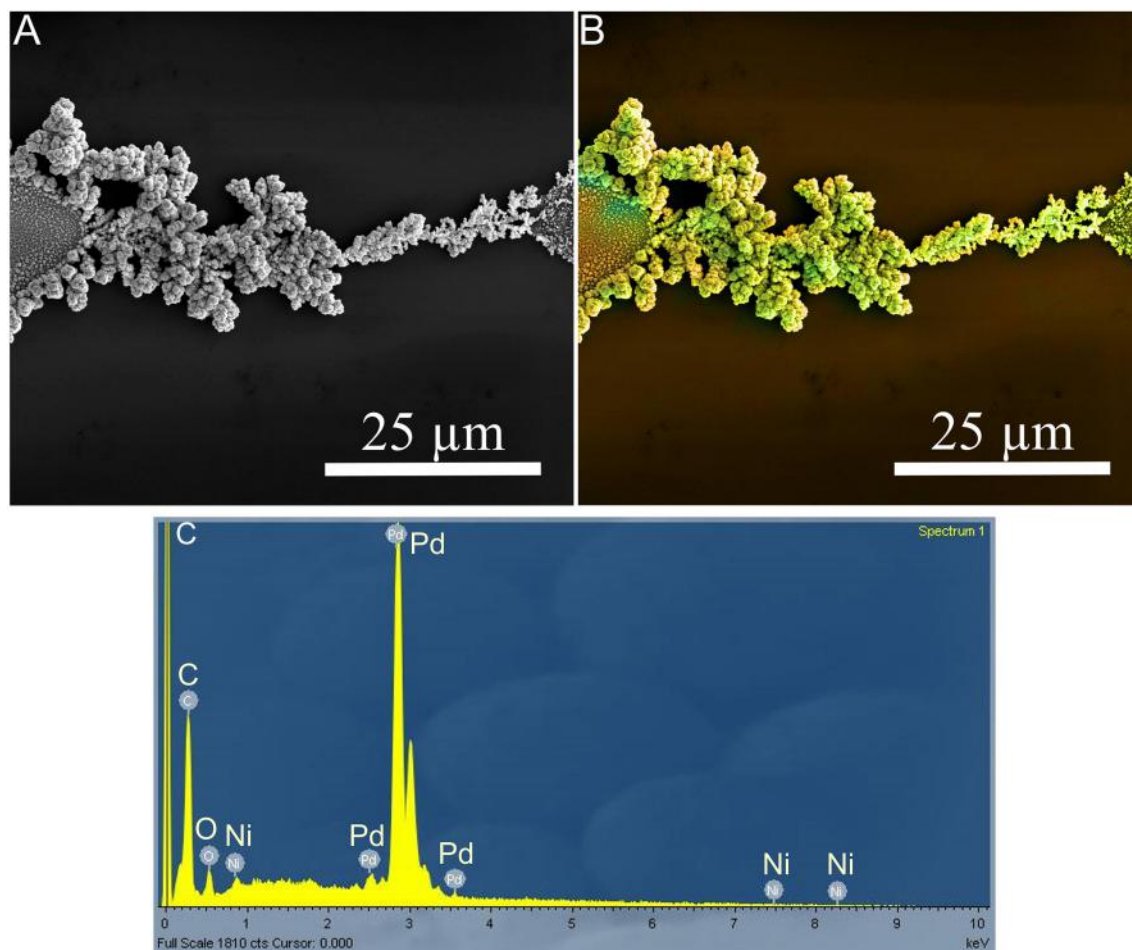
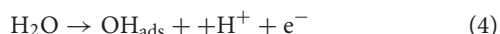
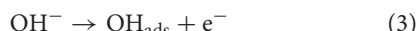


**FIGURE 4 | (A)** SEM micrograph, **(B)** EDX map (Pd is red, Ni is green), and **(C)** EDX spectrum of the Pd-Ni nanodendrite electrode. This structure was synthesized at 38 MHz, 15 V<sub>pp</sub>, and 2.5 V DC offset.

The mechanism was further elaborated by Makovos and Liu (1986), which observed an anodic current during the cathodic scan in cyclic voltammetry and the dependence of the peak current values on the concentration of glucose. A common final step in Nikolaeva et al. (1983) and Makovos and Liu (1986) was a rapid electrochemical regeneration of the gold surface oxy-species as illustrated in Equations (3–5), and scheme in Figure 5:

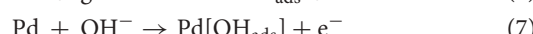


or



The mechanism of direct electrocatalytic glucose oxidation on Pd electrocatalysts was reported and is summarized in Equations (6–8) (Vassilyev et al., 1985; Becerik and Kadirgan, 1992; Cai et al.,

2013; Chen et al., 2015):



In a reverse (cathodic) scan, Figure 6B, the reduction of Pd oxide and reformation of active hydrous oxide species,  $\text{Pd}(\text{OH})_x$ , occurs after about 0.01 V in alkaline medium. The regenerated active sites of Pd hydroxide species carry out glucose oxidation reaction again and the anodic peak of glucose re-occurs.

Nickel electrodes were also investigated as catalysts for the electrooxidation of organic substances in alkaline medium, where the oxidized component of the  $\text{Ni}(\text{OH})_2/\text{NiOOH}$  redox couple is a catalytic component (Fleischmann et al., 1971; Toghill and Compton, 2010). It is supposed that the removal of the hemiacetalic hydrogen atom is the rate determining step of the process of glucose electrooxidation at nickel oxyhydroxide. Thus, the oxidation of glucose to gluconolactone in an alkaline solution

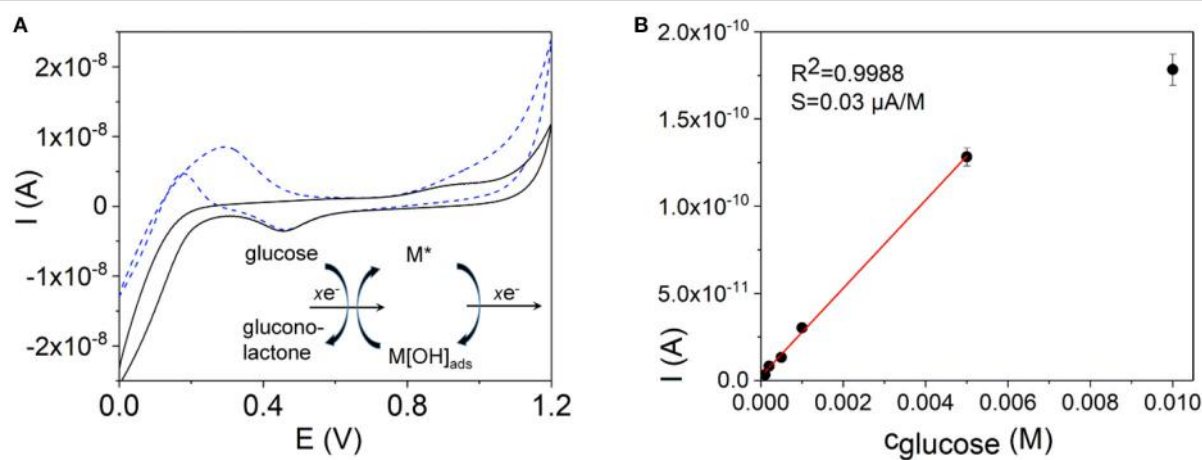


**FIGURE 5 | (A)** Cyclic voltammograms of an Au NW electrode in a  $0.1 \text{ M PBS}$ , pH 7.2, (black line) and in a  $1 \times 10^{-2} \text{ M}$  solution of glucose in PBS (blue dashed line). Insert in **(A)** shows a scheme of the oxidation and reduction processes at the metal electrode surface during oxidation of glucose. **(B)** A calibration curve as a current dependence on the concentration of glucose. The calibration curve was obtained by means of amperometry at  $E_{\text{det}} = +0.35 \text{ V}$  (vs.  $\text{Ag}/\text{AgCl}$ ) using an Au NW electrode prepared by DENA as a working electrode.

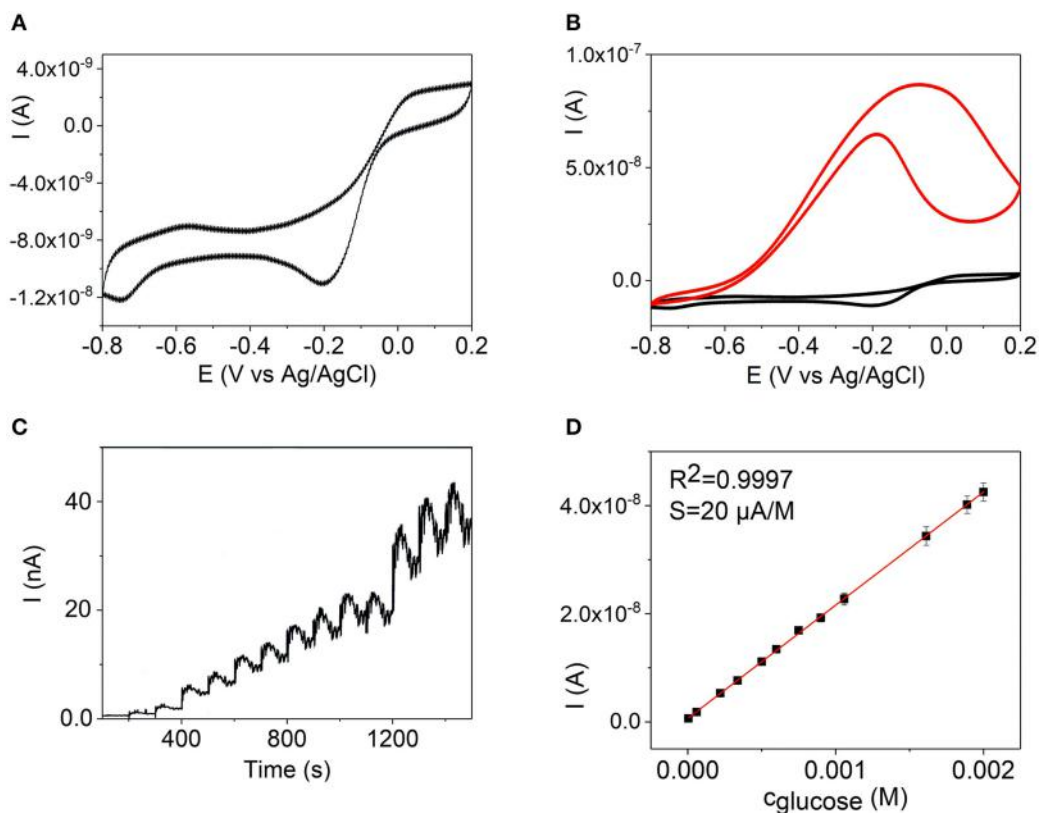
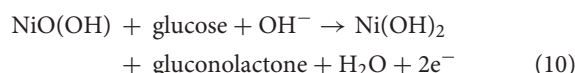


**FIGURE 6 |** Cyclic voltammograms of a Pd NW electrode in  $0.1 \text{ M KOH}$  (black line) **(A)** and with addition of  $2.0 \times 10^{-3} \text{ M}$  of glucose (red line) **(B)**. **(C)** Amperometric detection of glucose on a Pd NW electrode in  $0.1 \text{ M KOH}$  at  $-0.15 \text{ V}$  with additions of glucose up to  $2.0 \times 10^{-3} \text{ M}$ . **(D)** Calibration curve as a dependence of the oxidation current on the concentration of glucose at  $-0.15 \text{ V}$  at a Pd NW electrode,  $0.1 \text{ M KOH}$ .

is catalyzed by the Ni(II/III) redox couple of the electrode surface in accordance with reactions (9–10) (Toghill and Compton, 2010; Li et al., 2014):



Non-enzymatic electrodes based on electrocatalysis, which rely on bimetallic systems, may offer electrodes, in which the catalytic and electronic benefits of the components synergistically combine to reach particular electronic and catalytic properties (Vassilyev et al., 1985; Wang et al., 2008; Toghill and Compton, 2010; Shaidarova and Budnikov, 2011; Zhang et al., 2011; Si et al., 2013; Yang et al., 2013; Chen and Ostrom, 2015). A high surface area of the nanodendrite electrodes provides active sites for the electrocatalytic reaction. Moreover, the dendritic metals have many nanostructured features such as sharp edges and nanoscale junctions rendering them a high activity.

**Figures 6A,B, 7A,B** show the CV curves of Pd and Pd-Ni NW electrodes in the absence and presence of  $2.0 \times 10^{-3}$  M glucose in 0.1 mol L<sup>-1</sup> KOH. In order to evaluate the sensitivity of the sensors to glucose, amperometric responses of the Au, Pd,

and Pd-Ni nanodendrite electrodes to the changes of the glucose concentration were studied. The amperometric measurements were made in a constantly stirred 0.1 M solution of potassium hydroxide with successive additions of glucose every 100 s, **Figures 6C, 7C**. As can be seen in **Figures 6D, 7D**, well-defined amperometric currents were proportional to the concentration of glucose in a concentration range of  $5.0 \times 10^{-6}$  to  $2.0 \times 10^{-3}$  M for the Pd NW electrode and  $1.5 \times 10^{-7}$  to  $2.0 \times 10^{-3}$  M for the Pd-Ni NW electrode, respectively.

Series of CVs experiments were performed to evaluate linear concentration ranges, LODs, sensitivities, and regression coefficients. The experiments were performed in 0.1 M KOH for Pd, **Figure 6**, and Pd-Ni, **Figure 7**, electrodes, and in 0.1 M PBS for the Au NW electrode, **Figure 5**. **Table 2** summarizes the analytical characteristics of the Au, Pd, and Pd-Ni nanodendrite electrodes assembled by DENA in our studies for the detection of glucose. As shown in **Table 3**, the calibration graphs were linear in concentration ranges  $1.0 \times 10^{-4}$ – $5.0 \times 10^{-3}$  M for the Au NW electrode,  $5.0 \times 10^{-6}$ – $2.0 \times 10^{-3}$  M for the Pd electrode, and  $1.5 \times 10^{-7}$ – $2.0 \times 10^{-3}$  M for the Pd-Ni nanodendrite electrode. The LODs were  $3.3 \times 10^{-5}$  M,  $1.3 \times 10^{-6}$  M, and  $4.0 \times 10^{-8}$  M for Au, Pd, and Pd-Ni electrodes, respectively ( $S/N = 3$ ). Regression coefficients for all electrodes compositions were not <0.9988. Electrodes sensitivities in linear concentration ranges

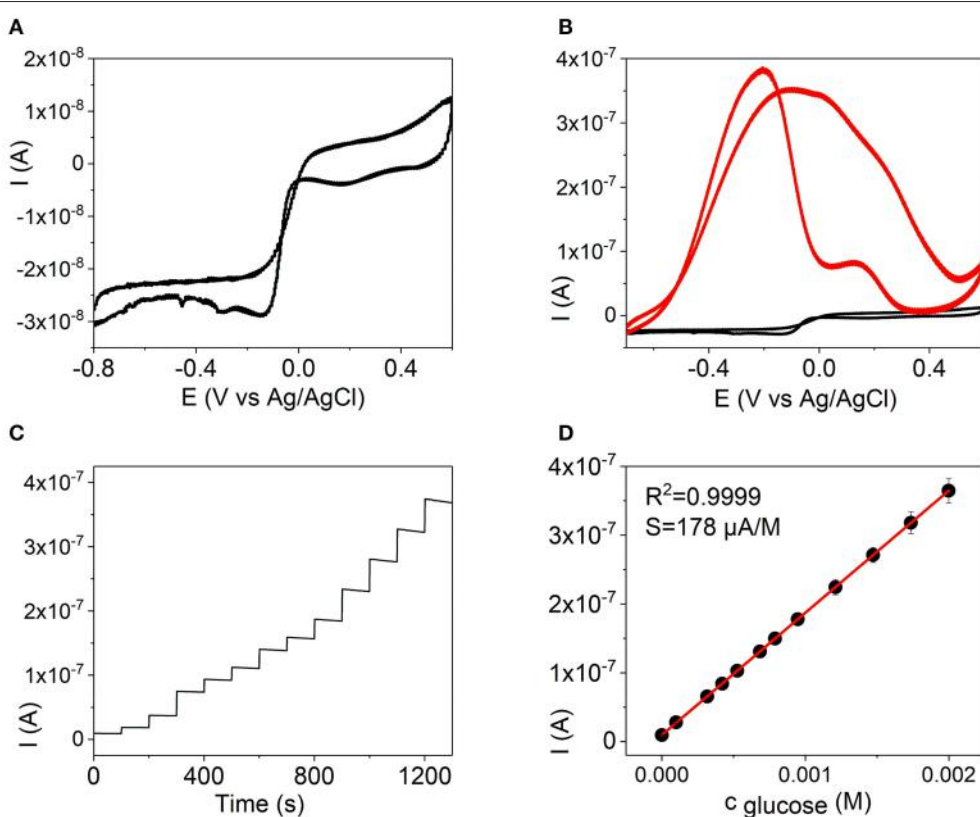


**FIGURE 7** | Cyclic voltammograms of a Pd-Ni NW electrode in 0.1 M KOH (A) and in 0.1 M KOH (black line) with addition of  $2.0 \times 10^{-3}$  M glucose (red line) (B). (C) Amperometric detection of glucose on a Pd-Ni NW in 0.1 M KOH at  $-0.15$  V with additions of glucose up to  $2.0 \times 10^{-3}$  M. (D) Calibration curve as a current dependence on the concentration of glucose at  $-0.15$  V at a Pd-Ni NW electrode, 0.1 M KOH.

were found to be 0.03, 20, and 178  $\mu\text{A M}^{-1}$  for Au-, Pd-, and Pd-Ni nanodendrite electrodes, respectively.

One can see from **Table 2** that although all three compositions demonstrate sensor properties with respect to glucose, the Pd-Ni composition provided better analytical characteristics, i.e., the lowest LOD, a higher sensitivity, and a broader linear concentration range. We suppose that this performance is due to the bimetallic composition of the electrode and a complex synergic electrocatalytic mechanism. Similar effects of the improved electrochemical sensor performance, e.g., significantly higher currents and as a consequence, a higher sensitivity of determination of hydrogen peroxide were observed for microwires of Au-Cu prepared by laser-induced metal deposition from solution in comparison with Au microwires (Panov et al., 2017). The enhanced electrocatalytic activity of two-component or more complex compositions of electrode materials in comparison with individual pure metal surfaces was also discussed (e.g., Koper, 2004; RodriGuez-Nieto et al., 2004; Shaidarova and Budnikov, 2011; Guascito et al., 2013; Yang et al., 2013). This effect may be due to bifunctional or synergic effect, the ligand or electronic effect with variations of electronic and catalytic properties of elements in composite materials compared with pure metals (Koper, 2004; RodriGuez-Nieto et al., 2004; Shaidarova and Budnikov, 2011), and formation of various phases and crystal defects in multicomponent systems leading to more electrocatalytically active surfaces. However, molecular understanding of bimetallic electrocatalysis and explanation of the experimentally observed enhanced electrocatalytic performance of bimetallic and multicomponent systems in comparison with individual metal surfaces require further detailed investigations in each case (Koper, 2004).

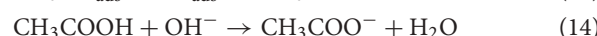
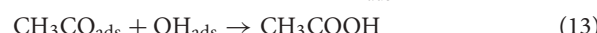
## Ethanol Detection

Further characterization of the NW electrodes prepared by DENA included the study of their electrocatalytic performance in the oxidation of ethanol. Ethanol electrooxidation on metal and composite electrodes has been discussed in a number of reviews and articles (Azevedo et al., 2005; Chen and Ostrom, 2015; Liu et al., 2015; Shishov et al., 2016; Cinti et al., 2017). Ethanol electrooxidation was reported to be most effective on the Pd-containing electrodes in alkaline media due to the electrocatalytic activity of Pd (Liu et al., 2007; Ksar et al., 2009; Chen and Ostrom, 2015). As it was discussed above, metal oxy-species on the electrode surface are supposed to mediate the electrooxidation of ethanol on Pd electrodes. It was shown that Pd had no activity for ethanol oxidation in acid media (Liu et al., 2007). Therefore,

**TABLE 2** | Analytical characteristics of the nanodendrite electrodes prepared by DENA for the detection of glucose.

Electrode	$E_{\text{det, V}}$	Linear range, M	LOD, M	Sensitivity, $\mu\text{A M}^{-1}$
Au	0.35 V(PBS)	$1.0 \times 10^{-4} - 5.0 \times 10^{-3}$	$3.3 \times 10^{-5}$	0.03
Pd	-0.15(KOH)	$5.0 \times 10^{-6} - 2.0 \times 10^{-3}$	$1.3 \times 10^{-6}$	20
Pd-Ni	-0.15(KOH)	$1.5 \times 10^{-7} - 2.0 \times 10^{-3}$	$4.0 \times 10^{-8}$	178

in the following, results for the Pd-containing NW electrodes prepared by DENA in 0.1 M KOH solution are presented. The oxidation sequence for ethanol oxidation in alkaline media may be summarized as follows:



**Figures 8, 9** show voltammograms of the Pd- and Pd-Ni NW electrodes prepared by DENA in 0.1 M KOH without and with successive additions of ethanol. The current-voltage curves in the presence of ethanol display two well-defined anodic current peaks: one on the forward (anodic) potential scan and another one on the reverse (cathodic) sweeping (Gutiérrez et al., 2007; Ksar et al., 2009), **Figures 8A, 9A**. The appearance of a symmetric anodic peak in the forward scan at about  $-0.070$  V corresponds to the ethanol electrooxidation process. In the reverse scan, oxidation of the incompletely oxidized and adsorbed on the electrode surface intermediate carbonaceous species, which are produced in the forward anodic scan, results in the appearance of the asymmetric anodic peak at about  $-0.300$  V for Pd- and  $-0.230$  V for Pd-Ni NW electrodes.

The characteristics of the NW sensors for ethanol detection based on the electrocatalytic oxidation of ethanol are presented in **Table 3** and **Figures 8, 9**. A linear calibration range of  $7.0 \times 10^{-4} - 3.0 \times 10^{-2}$  M ( $R^2 = 0.9999$ ), detection limit of  $2.2 \times 10^{-4}$  M ( $S/N = 3$ ), and a sensitivity of  $1.5 \mu\text{A M}^{-1}$  were found for the Pd NW electrodes. For the Pd-Ni NW electrodes, a similar linear calibration range of  $7.0 \times 10^{-4} - 3.0 \times 10^{-2}$  M ( $R^2 = 0.9998$ ) with a detection limit of  $5.2 \times 10^{-4}$  M, and a sensitivity of  $28 \mu\text{A M}^{-1}$  were observed in alkaline media.

## Hydrogen Peroxide Detection

Further characterization of the metal NW electrodes prepared by DENA included the study of their performance in the reduction of hydrogen peroxide, thereby Pt- and Pd-based electrocatalysts generally demonstrate high catalytic activity for the electrochemical reduction of hydrogen peroxide (Chen and Ostrom, 2015). Non-enzymatic hydrogen peroxide electrochemical sensors have been discussed in a number of recent reviews and articles (Chen et al., 2014; Chen and Ostrom, 2015; Naveen et al., 2016; Plauck et al., 2016; Wang et al., 2016; Komkova et al., 2017; Nikolaev et al., 2018).

Electrochemical reduction of hydrogen peroxide on several nanodendrite electrode surfaces was studied to evaluate these

**TABLE 3** | Analytical characteristics of the ethanol detection with the nanodendrite electrodes prepared by DENA.

Electrode	$E_{\text{det, V}}$	Linear range, M	LOD, M	Sensitivity, $\mu\text{A M}^{-1}$
Pd	-0.3	$7.0 \times 10^{-4} - 3.0 \times 10^{-2}$	$2.2 \times 10^{-4}$	1.5
Pd-Ni	-0.25	$7.0 \times 10^{-4} - 3.0 \times 10^{-2}$	$5.2 \times 10^{-4}$	28

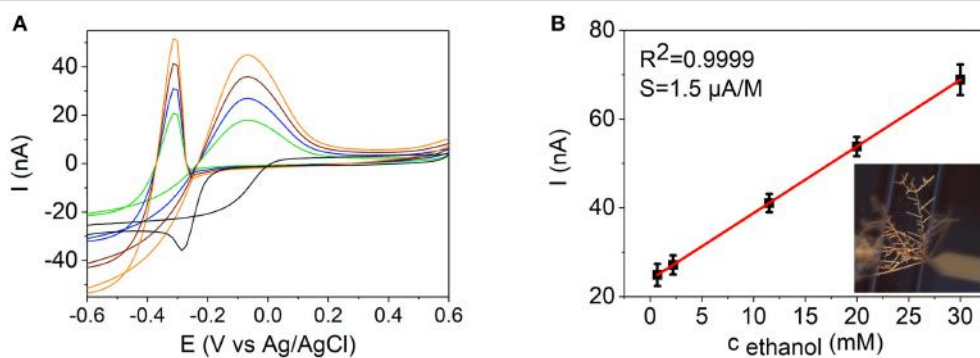


**FIGURE 8 | (A)** Cyclic voltammograms of a Pd NW electrode in a 0.1 M KOH (black line) with additions of ethanol up to  $3.0 \times 10^{-2}$  M. **(B)** Dependence of the anodic current on the concentration of ethanol at  $-0.3\text{ V}$  in 0.1 M KOH at the Pd NW electrode. Insert in **(B)** shows the Pd nanodendrite electrode used for the detection.

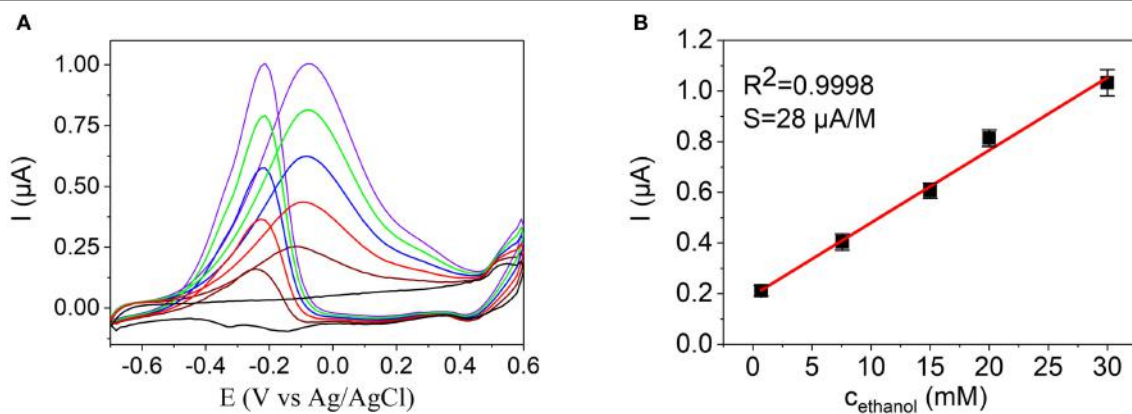


**FIGURE 9 | (A)** Cyclic voltammograms of a Pd-Ni NW electrode in a 0.1 M KOH (black line) with additions of ethanol up to  $3.0 \times 10^{-2}$  M. **(B)** Calibration curve of the Pd-Ni NW sensor as a dependence of the anodic current on the concentration of ethanol at  $-0.25\text{ V}$  in 0.1 M KOH.

electrode materials with regard to their application in hydrogen peroxide sensing. The electrochemical measurements were performed at pH 7.2 maintained with 0.1 M PBS, **Figure 10**. The current-voltage curves, which were recorded in 0 mM (black line) and 10 mM (red line) solutions of hydrogen peroxide on the Pd-Au nanodendrite electrode, and the corresponding electrode are shown in **Figures 10c,f**, respectively. As can be seen, the Pd-Au electrode demonstrates high electrochemical activity toward hydrogen peroxide reduction at these conditions with a half-wave reduction potential of about  $-0.125\text{ V}$  (vs. Ag/AgCl). Additionally, analytical characteristics of the sensors in terms of linear concentration range, sensitivity, and detection limit were studied by amperometry, where a detection potential of as low as  $-0.05\text{ V}$  was selected, **Figures 10d,e**. A low absolute value of the detection potential for the amperometric measurements was used to show the feasibility of the sensor application for the analysis of reactive oxygen species and oxygen metabolism in biological systems (Mason, 1957; Calas-Blanchard et al., 2014). The Pd-Au NW sensor demonstrates a high sensitivity of  $18 \mu\text{A M}^{-1}$  in a wide linear concentration range of  $10^{-6}$ – $10^{-3}$  M of hydrogen peroxide at this detection potential, **Table 4**. Selectivity of the sensor response to a number of

interfering substances was evaluated, **Figure S2**. The response of the sensor to  $1 \mu\text{M}$  hydrogen peroxide decreased to  $<50\%$  in the presence of  $1.5 \times 10^{-4}$  M ascorbate,  $1 \times 10^{-4}$  M dopamine, and  $5 \times 10^{-4}$  M uric acid. Thus, our results show that high concentrations of these substances exhibit interfering effect on the determination of hydrogen peroxide, however, do not distort the response to hydrogen peroxide essentially, which allows to use the developed sensors and multisensor systems in the presence of these interfering substances. The interfering effect is due to the redox behavior of the substances on electrodes and reduction of hydrogen peroxide by these interfering substances (Ames et al., 1981; Lowry and O'Neill, 1992; Deutsch, 1998; Zhao and Kim, 2016). Similar effects were discussed in Lowry and O'Neill (1992).

**Table 4** summarizes the analytical characteristics of the Pd-Au, Au, and Pd nanodendrite electrodes assembled by DENA. It can be seen, that the Pd-Au NW electrodes show a wide linear range with higher sensitivity, and a lower detection limit in comparison with the Au and Pd NW electrodes. Essentially, these analytical characteristics were achieved at a significantly lower absolute value of the detection potential than in a series of previous works (Chen et al., 2013, 2014; Goran et al., 2015; Huang

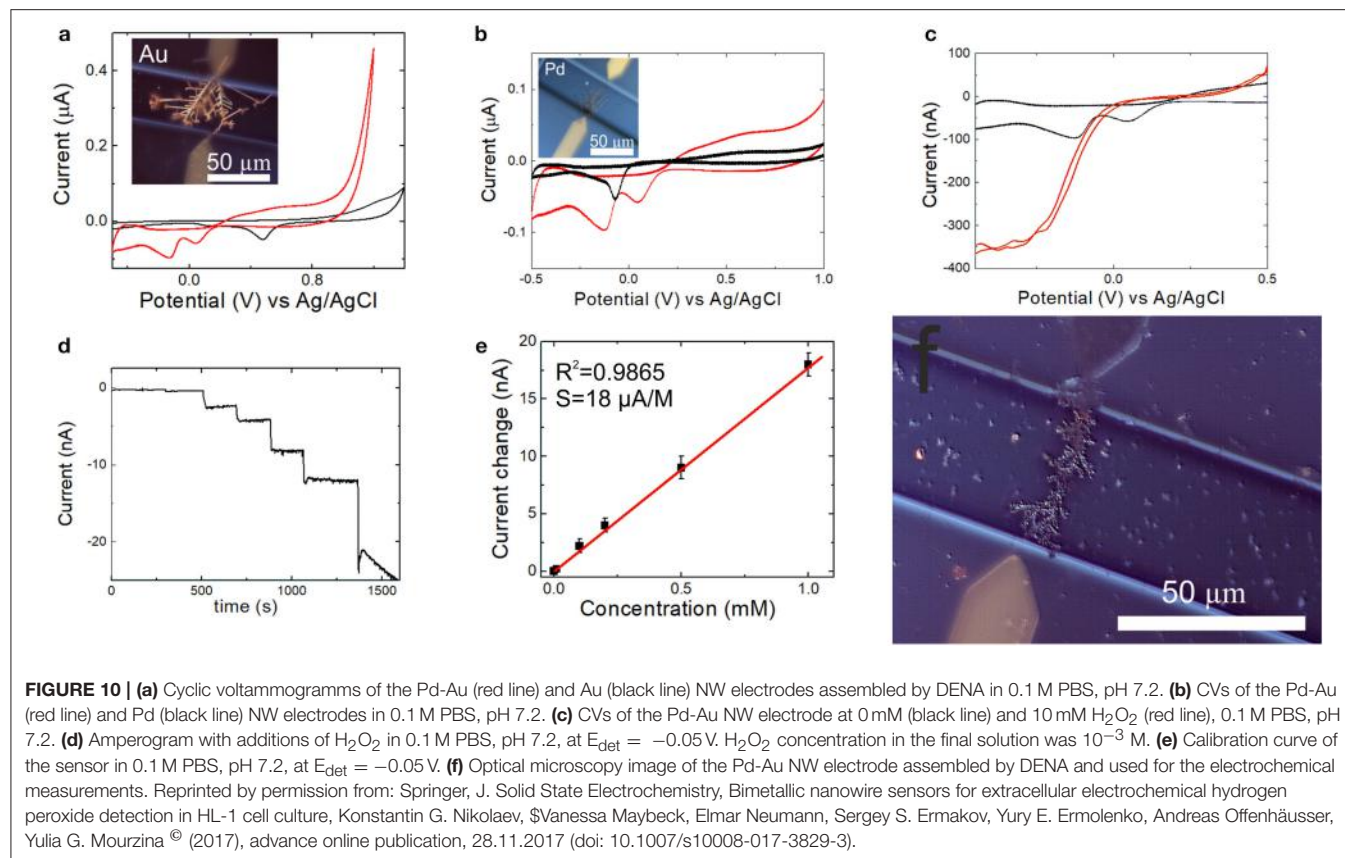


**TABLE 4 |** Analytical characteristics of the detection of hydrogen peroxide in solutions with Au-, Pd-, and Pd-Au nanodendrite electrodes electrodeposited by DENA, 0.1 M PBS.

Metal/alloy	Linear range, M	LOD, M	Sensitivity, $\text{A M}^{-1}$
Au	$2 \times 10^{-4} - 1 \times 10^{-2}$	$5.9 \times 10^{-5}$	$5.7 \times 10^{-7}$
Pd	$1 \times 10^{-5} - 7.9 \times 10^{-3}$	$6.0 \times 10^{-6}$	$5.4 \times 10^{-7}$
Pd-Au	$1 \times 10^{-6} - 1 \times 10^{-3}$	$2.4 \times 10^{-7}$	$1.8 \times 10^{-5}$

et al., 2015), thus emphasizing high activity of these new sensor nanomaterials toward electrochemical reduction of  $\text{H}_2\text{O}_2$ .

Analytical performance of the DENA-prepared non-enzymatic electrochemical sensors in electrolyte solutions offer wide linear concentrations intervals, low detection limits, and additional benefits resulting from the multiplicity of possible material compositions, spatial resolution, and durability of the sensors. While fabrication of enzymatic and most non-enzymatic sensors employs drop-casting of the nanostructures prepared by different methods and other onerous immobilization procedures on the glassy carbon electrodes or other supports, the DENA sensors presented in this investigation do not involve modification of the electrode surfaces as well as the sensor response is not affected by the surface protection (surface-capping) agents from the chemical synthesis of the nanostructures. Hence, the sensors are stable to

the detachment of components, which makes them favorable for *in vivo* analysis, minimizes drift of the sensor response, and thereby improves the stability. Furthermore, significantly lower absolute values of the detection potentials than in many previous investigations (Azevedo et al., 2005; Chen et al., 2013, 2014; Goran et al., 2015; Huang et al., 2015; Jin et al., 2015; Pourbeyram and Mehdizadeh, 2016; Shishov et al., 2016; Shabnam et al., 2017) demonstrate that the DENA-metal NW electrodes possess high activity for the electrochemical redox processes of a number of substances such as glucose, ethanol, and hydrogen peroxide, which are both important analytes and components of the fuel cell electrochemistry. Possible approaches to compensate for a generally lower selectivity of the non-enzymatic design in comparison with enzymatic biosensors can be involvement of the separation methods as well as realization of the voltamperometric “electronic tongue”-type multisensor systems, where non-selective signals of multisensor arrays are processed by chemometric techniques.

## CONCLUSIONS

Advances in nanotechnology, nanomaterials, and chemometric methods provide new opportunities for innovative electrochemical non-enzymatic sensors, multisensor systems, and multicomponent analysis. In this paper, we discuss DENA of nanowire electrochemical sensors and sensor arrays of

metals and bimetallic compositions for the development of a single-chip multisensor system for the solution analysis. Various sensor nanomaterials (Pd, Ni, Au, and their multicomponent compositions) were electrochemically assembled on a single chip and at the same time connected to the external circuit without employing repetitive cycles of photolithography. The structural features of the DENA-assembled electrodes were of 50 nm to several  $\mu\text{m}$  in diameter as found by SEM analysis. The nanostructures were characterized by EDX analysis with elemental mapping to confirm the presence of elements. Individual amperometric signals of the DENA-assembled NW electrodes of different compositions were analyzed to make use of the specific electrochemical surface properties and show their successful application as functional sensor devices. Characteristics of non-enzymatic electrooxidation or electroreduction of analytes (glucose, ethanol, and hydrogen peroxide) varied significantly depending on the NW electrode composition. For example, Pd-Ni nanowire sensors based on non-enzymatic glucose oxidation were characterized by a linear concentration range of  $1.5 \times 10^{-7} - 2.0 \times 10^{-3}$  M glucose ( $R^2 = 0.9999$ ) with a LOD of  $4.0 \times 10^{-8}$  M, and a sensitivity of  $178 \mu\text{A M}^{-1}$  at a low value of the detection potential of  $-0.15$  V. Pd- and Pd-Ni NW sensors demonstrated a similar linear calibration range of  $7.0 \times 10^{-4} - 3.0 \times 10^{-2}$  M for ethanol determination with a higher sensitivity of  $28 \mu\text{A M}^{-1}$  at  $-0.25$  V for the Pd-Ni nanodendrite electrode. Pd-Au nanowire sensors based on the non-enzymatic hydrogen peroxide reduction demonstrated a linear concentration range of  $10^{-6} - 10^{-3}$  M  $\text{H}_2\text{O}_2$  with a LOD of  $3 \times 10^{-7}$  M, and a sensitivity of  $18 \mu\text{A M}^{-1}$  at a low absolute value of the detection potential of  $-0.05$  V. Thus, a novel single-chip electrochemical multisensor platform can be proposed based on the DENA-metal nanowire electrodes of a compositional diversity. We anticipate that DENA-nanomaterials will find a wide range of applications as electrochemical sensors and multisensor systems in the fields

of high-resolution multicomponent monitoring in fundamental biology, pharmacology, biomedicine, catalysis, and microfuel cells to realize the synergistic effects of electrocatalytic materials. Possible approach to compensate for a generally lower selectivity of the non-enzymatic design in comparison with enzymatic biosensors can be realization of the voltamperometric electronic tongue-type multisensor systems, where non-selective signals of multisensor arrays are processed by chemometric techniques.

## AUTHOR CONTRIBUTIONS

KN made substantial contributions to design, acquisition, analysis, and interpretation of data, and participated in drafting the article. YE and SE made substantial contributions to conception, analysis, and interpretation of data, and participated in drafting the article. AO made substantial contributions to conception and interpretation of data, and participated in drafting the article. YM made substantial contributions to conception, design, acquisition, analysis, and interpretation of data, and participated in drafting the article. All authors gave final approval of the submitted manuscript.

## ACKNOWLEDGMENTS

KN was supported by DAAD (Migration Mendeleev Forschungsstipendium grant number 50024759). Thanks are due to E. Brauweiler-Reuters, M. Prömpers, Dr. E. Neumann, Dr. A. Savenko for support with photolithography process and structural analysis.

## SUPPLEMENTARY MATERIAL

The Supplementary Material for this article can be found online at: <https://www.frontiersin.org/articles/10.3389/fchem.2018.00256/full#supplementary-material>

## REFERENCES

- Ames, B. N., Cathcart, R., Schwiers, E., and Hochstein, P. (1981). Uric acid provides an antioxidant defense in humans against oxidant- and radical-caused aging and cancer: a hypothesis. *Proc. Natl. Acad. Sci. U.S.A.* 78, 6858–6862. doi: 10.1073/pnas.78.11.6858
- Azevedo, A. M., Prazeres, D. M. F., Cabral, J. M. S., and Fonseca, L. P. (2005). Ethanol biosensors based on alcohol oxidase. *Biosens. Bioelectron.* 21, 235–247. doi: 10.1016/j.bios.2004.09.030
- Bagotzky, V. S., and Vassilyev, Y. B. (1967). Mechanism of electro-oxidation of methanol on the platinum electrode. *Electrochim. Acta* 12, 1323–1343. doi: 10.1016/0013-4686(67)80047-1
- Bandodkar, A. J., Imani, S., Nuñez-Flores, R., Kumar, R., Wang, C., Mohan, A. M. V., et al. (2018). Re-usable electrochemical glucose sensors integrated into a smartphone platform. *Biosens. Bioelectron.* 101, 181–187. doi: 10.1016/j.bios.2017.10.019
- Barragan, J. T. C., Kogikoski, S., Da Silva, E. T. S. G., and Kubota, L. T. (2018). Insight into the electro-oxidation mechanism of glucose and other carbohydrates by CuO-based electrodes. *Anal. Chem.* 90, 3357–3365. doi: 10.1021/acs.analchem.7b04963
- Becerik, I., and Kadirgan, F. (1992). The electrocatalytic properties of palladium electrodes for the oxidation of d-glucose in alkaline medium. *Electrochim. Acta* 37, 2651–2657. doi: 10.1016/0013-4686(92)87065-8
- Boekris, J. O. M., and Despic, A. R. (1970). “The mechanism of deposition and dissolution of metals,” in *Physical Chemistry*, ed H. Eyring (New York, NY: Academic Press), 611–723.
- Budnikov, G. K., Evtugin, G. A., and Maistrenko, V. N. (2012). *Modified Electrodes for Voltamperometry in Chemistry, Biology and Medicine*. Moscow: Binom.
- Burke, L. D. (1994). Premonolayer oxidation and its role in electrocatalysis. *Electrochim. Acta* 39, 1841–1848. doi: 10.1016/0013-4686(94)85173-5
- Cai, Z.-X., Liu, C.-C., Wu, G.-H., Chen, X.-M., and Chen, X. (2013). Palladium nanoparticles deposit on multi-walled carbon nanotubes and their catalytic applications for electrooxidation of ethanol and glucose. *Electrochim. Acta* 112, 756–762. doi: 10.1016/j.electacta.2013.09.040
- Calas-Blanchard, C., Catanante, G., and Noguer, T. (2014). Electrochemical sensor and biosensor strategies for ROS/RNS detection in biological systems. *Electroanalysis* 26, 1277–1286. doi: 10.1002/elan.201400083
- Chen, A., and Ostrom, C. (2015). Palladium-based nanomaterials: synthesis and electrochemical applications. *Chem. Rev.* 115, 11999–12044. doi: 10.1021/acs.chemrev.5b00324
- Chen, C.-C., Lin, C.-L., and Chen, L.-C. (2015). Functionalized carbon nanomaterial supported palladium nano-catalysts for electrocatalytic

- glucose oxidation reaction. *Electrochim. Acta* 152, 408–416. doi: 10.1016/j.electacta.2014.11.116
- Chen, S. H., Yuan, R., Chai, Y. Q., and Hu, F. X. (2013). Electrochemical sensing of hydrogen peroxide using metal nanoparticles: a review. *Microchim. Acta* 180, 15–32. doi: 10.1007/s00604-012-0904-4
- Chen, X. M., Wu, G. H., Cai, Z. X., Oyama, M., and Chen, X. (2014). Advances in enzyme-free electrochemical sensors for hydrogen peroxide, glucose, and uric acid. *Microchim. Acta* 181, 689–705. doi: 10.1007/s00604-013-1098-0
- Cheng, C., Gonela, R. K., Gu, Q., and Haynie, D. T. (2005). Self-assembly of metallic nanowires from aqueous solution. *Nano Lett.* 5, 175–178. doi: 10.1021/nl048240q
- Cheng, Y., Yu, G., Tang, L., Zhou, Y., and Zhang, G. (2011). Self-assembled dendritic nanowires of Au–Pt alloy through electrodeposition from solution under AC fields. *J. Cryst. Growth* 334, 181–188. doi: 10.1016/j.jcrysgro.2011.08.024
- Cinti, S., Basso, M., Moscone, D., and Arduini, F. (2017). A paper-based nanomodified electrochemical biosensor for ethanol detection in beers. *Anal. Chim. Acta* 960, 123–130. doi: 10.1016/j.aca.2017.01.010
- Deutsch, J. C. (1998). Ascorbic acid oxidation by hydrogen peroxide. *Anal. Biochem.* 255, 1–7. doi: 10.1006/abio.1997.2293
- Di Natale, C., D’amicco, A., Vlasov, Y., Legin, A., and Rudnitskaya, A. (1995). “Multicomponent analysis of heavy metal cations and inorganic anions by a non-selective chalcogenide glass sensor array,” in *Proceedings of the International Conference Eurosensors IX* (Stockholm), 512.
- Ermakov, S. S., Nikolaev, K. G., and Tolstoi, V. P. (2016). Analytical possibilities of Layer-by-Layer sensors. *Russ. Chem. Rev.* 85, 880–900. doi: 10.1070/RCR4605
- Flanders, B. N., Talukdar, I., Ozturk, B., and Thapa, P. (2012). *Method of Making an Electrochemical Nanowire Assembly and Attaching Cells Thereto*. United States patent 8137526. United States, The Board of Regents for Oklahoma State University, Stillwater, OK. Available online at: <http://www.freepatentsonline.com/8137526.html>
- Fleischmann, M., Korinek, K., and Pletcher, D. (1971). The oxidation of organic compounds at a nickel anode in alkaline solution. *J. Electroanal. Chem. Interfac. Electrochem.* 31, 39–49. doi: 10.1016/S0022-0728(71)80040-2
- Gnana Kumar, G., Amala, G., and Gowtham, S. M. (2017). Recent advancements, key challenges and solutions in non-enzymatic electrochemical glucose sensors based on graphene platforms. *RSC Adv.* 7, 36949–36976. doi: 10.1039/C7RA02845H
- Goran, J. M., Phan, E. N. H., Favela, C. A., and Stevenson, K. J. (2015). H<sub>2</sub>O<sub>2</sub> detection at carbon nanotubes and nitrogen-doped carbon nanotubes: oxidation, reduction, or disproportionation? *Anal. Chem.* 87, 5989–5996. doi: 10.1021/acs.analchem.5b00059
- Guascito, M. R., Chirizzi, D., Malitesta, C., Siciliano, T., and Tepore, A. (2013). Te oxide nanowires as advanced materials for amperometric nonenzymatic hydrogen peroxide sensing. *Talanta* 115, 863–869. doi: 10.1016/j.talanta.2013.06.032
- Gutiérrez, M. C., Hortigüela, M. J., Amarilla, J. M., Jiménez, R., Ferrer, M. L., and Del Monte, F. (2007). Macroporous 3D architectures of self-assembled MWCNT surface decorated with Pt nanoparticles as anodes for a direct methanol fuel cell. *J. Phys. Chem. C* 111, 5557–5560. doi: 10.1021/jp0714365
- Heller, A., and Feldman, B. (2008). Electrochemical glucose sensors and their applications in diabetes management. *Chem. Rev.* 108, 2482–2505. doi: 10.1021/cr068069y
- Huang, Y., Ferhan, A. R., Dandapat, A., Yoon, C. S., Song, J. E., Cho, E. C., et al. (2015). A strategy for the formation of gold–palladium suprananoparticles from gold nanoparticles of various shapes and their application to high-performance H<sub>2</sub>O<sub>2</sub> sensing. *J. Phys. Chem. C* 119, 26164–26170. doi: 10.1021/acs.jpcc.5b008423
- Ji, J., Li, P., Sang, S., Zhang, W., Zhou, Z., Yang, X., et al. (2014). Electrodeposition of Au/Ag bimetallic dendrites assisted by Faradaic AC-electroosmosis flow. *AIP Adv.* 4:031329. doi: 10.1063/1.4868518
- Ji, J., Zhou, Z., Yang, X., Zhang, W., Sang, S., and Li, P. (2013). One-dimensional nano-interconnection formation. *Small* 9, 3014–3029. doi: 10.1002/smll.201201318
- Jie, S., Honghui, S., Gang, C., Yuting, Z., Yingying, Z., Tiantian, X., et al. (2015). The development of new nonenzymatic glucose biosensors using nanomaterials. *Curr. Nanosci.* 11, 736–747. doi: 10.2174/157341371166615050223620
- Jin, J., Zheng, G., Ge, Y., Deng, S., Liu, W., and Hui, G. (2015). A non-enzyme electrochemical qualitative and quantitative analyzing method for glucose, D-fructose, and sucrose utilizing Cu foam material. *Electrochim. Acta* 153, 594–601. doi: 10.1016/j.electacta.2014.11.194
- Kawasaki, J. K., and Arnold, C. B. (2011). Synthesis of platinum dendrites and nanowires via directed electrochemical nanowire assembly. *Nano Lett.* 11, 781–785. doi: 10.1021/nl1039956
- Kirsanov, D., Zadorozhnyaya, O., Krasheninnikov, A., Komarova, N., Popov, A., and Legin, A. (2013). Water toxicity evaluation in terms of bioassay with an Electronic Tongue. *Sensors Actuators B* 179, 282–286. doi: 10.1016/j.snb.2012.09.106
- Kisner, A., Heggen, M., Fernandez, E., Lenk, S., Mayer, D., Simon, U., et al. (2011). The role of oxidative etching in the synthesis of ultrathin single-crystalline Au nanowires. *Chem. Eur. J.* 17, 9503–9507. doi: 10.1002/chem.201100169
- Komkova, M. A., Karyakina, E. E., and Karyakin, A. A. (2017). Noiseless performance of prussian blue based (Bio)sensors through power generation. *Anal. Chem.* 89, 6290–6294. doi: 10.1021/acs.analchem.7b01142
- Koper, M. T. M. (2004). Electrocatalysis on bimetallic and alloy surfaces. *Surf. Sci.* 548, 1–3. doi: 10.1016/j.susc.2003.10.045
- Koposova, E., Kisner, A., Shumilova, G., Ermolenko, Y., Offenbässer, A., and Mourzina, Y. (2013). Oleylamine-stabilized gold nanostructures for bioelectronic assembly. Direct electrochemistry of cytochrome c. *J. Phys. Chem. C* 117, 13944–13951. doi: 10.1021/jp401764p
- Koposova, E., Liu, X., Kisner, A., Ermolenko, Y., Shumilova, G., Offenbässer, A., et al. (2014). Bioelectrochemical systems with oleylamine-stabilized gold nanostructures and horseradish peroxidase for hydrogen peroxide sensor. *Biosens. Bioelectron.* 57, 54–58. doi: 10.1016/j.bios.2014.01.034
- Koposova, E., Shumilova, G., Ermolenko, Y., Kisner, A., Offenbässer, A., and Mourzina, Y. (2015). Direct electrochemistry of cyt c and hydrogen peroxide biosensing on oleylamine- and citrate-stabilized gold nanostructures. *Sens. Actuators B* 207, 1045–1052. doi: 10.1016/j.snb.2014.07.105
- Ksar, F., Surendran, G., Ramos, L., Keita, B., Nadjo, L., Prouzet, E., et al. (2009). Palladium nanowires synthesized in hexagonal mesophases: application in ethanol electrooxidation. *Chem. Mater.* 21, 1612–1617. doi: 10.1021/cm80492j
- Li, M., Bo, X., Mu, Z., Zhang, Y., and Guo, L. (2014). Electrodeposition of nickel oxide and platinum nanoparticles on electrochemically reduced graphene oxide film as a nonenzymatic glucose sensor. *Sens. Actuators B* 192, 261–268. doi: 10.1016/j.snb.2013.10.140
- Liu, J., Ye, J., Xu, C., Jiang, S. P., and Tong, Y. (2007). Kinetics of ethanol electrooxidation at Pd electrodeposited on Ti. *Electrochim. Commun.* 9, 2334–2339. doi: 10.1016/j.elecom.2007.06.036
- Liu, W., Herrmann, A.-K., Bigall, N. C., Rodriguez, P., Wen, D., Oezaslan, M., et al. (2015). Noble metal aerogels—synthesis, characterization, and application as electrocatalysts. *Acc. Chem. Res.* 48, 154–162. doi: 10.1021/ar500237c
- Liu, Y., Pharr, M., and Salvatore, G. A. (2017). Lab-on-skin: a review of flexible and stretchable electronics for wearable health monitoring. *ACS Nano* 11, 9614–9635. doi: 10.1021/acsnano.7b04898
- Lowry, J. P., and O’Neill, R. D. (1992). Homogeneous mechanism of ascorbic acid interference in hydrogen peroxide detection at enzyme-modified electrodes. *Anal. Chem.* 64, 453–456. doi: 10.1021/ac00028a022
- Maistrenko, V. N., Evtugin, G. A., and Sidelnikov, A. V. (2011). “Voltammetric electronic tongue,” in *Chemical Sensors*, ed Y. G. Vlasov (Moscow: Nauka), 285–313.
- Makovos, E. B., and Liu, C. C. (1986). A cyclic-voltammetric study of glucose oxidation on a gold electrode. *Bioelectrochem. Bioenerget.* 15, 157–165. doi: 10.1016/0302-4598(86)80023-X
- Mason, H. S. (1957). Mechanisms of oxygen metabolism. *Science* 125, 1185–1188. doi: 10.1126/science.125.3259.1185

- Muratova, I. S., Mikhelson, K. N., Ermolenko, Y. E., Offenhäusser, A., and Mourzina, Y. (2016). Chemiresistors based on ultrathin gold nanowires for sensing halides, pyridine and dopamine. *Sens. Actuators B* 232, 420–427. doi: 10.1016/j.snb.2016.03.151
- Nagashima, K., Yanagida, T., Tanaka, H., and Kawai, T. (2007). Epitaxial growth of MgO nanowires by pulsed laser deposition. *J. Appl. Phys.* 101:124304. doi: 10.1063/1.2748625
- Naveen, M. H., Gurudatt, N. G., Noh, H.-B., and Shim, Y.-B. (2016). Dealloyed AuNi dendrite anchored on a functionalized conducting polymer for improved catalytic oxygen reduction and hydrogen peroxide sensing in living cells. *Adv. Funct. Mater.* 26, 1590–1601. doi: 10.1002/adfm.201504506
- Nikolaev, K. G., Ermakov, S. S., Offenhäusser, A., and Mourzina, Y. (2017). Nonenzymatic determination of glucose on electrodes prepared by directed electrochemical nanowire assembly (DENA). *J. Anal. Chem.* 72, 371–374. doi: 10.1134/S1061934817040104
- Nikolaev, K. G., Maybeck, V., Neumann, E., Ermakov, S. S., Ermolenko, Y. E., Offenhäusser, A., et al. (2018). Bimetallic nanowire sensors for extracellular electrochemical hydrogen peroxide detection in HL-1 cell culture. *J. Solid State Electrochem.* 22, 1023–1035. doi: 10.1007/s10008-017-3829-3
- Nikolaev, K., Ermakov, S., Ermolenko, Y., Averyaskina, E., Offenhäusser, A., and Mourzina, Y. (2015). A novel bioelectrochemical interface based on in situ synthesis of gold nanostructures on electrode surfaces and surface activation by Meerwein's salt. A bioelectrochemical sensor for glucose determination. *Bioelectrochemistry* 105, 34–43. doi: 10.1016/j.bioelechem.2015.05.004
- Nikolaeva, N. N., Khazova, O. A., and Vasil'ev, Y. B. (1983). Main characteristics of glucose electrooxidation on a gold anode. *Elektrokhimiya* 19, 1042–1048.
- Ozturk, B., Bret, N. F., Daniel, R. G., and Tetsuya, D. M. (2007a). Single-step growth and low resistance interconnecting of gold nanowires. *Nanotechnology* 18:175707. doi: 10.1088/0957-4484/18/17/175707
- Ozturk, B., Ishan, T., and Bret, N. F. (2007b). Directed growth of diameter-tunable nanowires. *Nanotechnology* 18:365302. doi: 10.1088/0957-4484/18/36/365302
- Panchuk, V., Lvova, L., Kirsanov, D., Goncalves, C. G., Di Natale, C., Paolesse, R., et al. (2016). Extending electronic tongue calibration lifetime through mathematical drift correction: case study of microcystin toxicity analysis in waters. *Sens. Actuators B* 237, 962–968. doi: 10.1016/j.snb.2016.07.045
- Panov, M. S., Vereshchagina, O. A., Ermakov, S. S., Tumkin, I. I., Khairullina, E. M., Skripkin, M. Y., et al. (2017). Non-enzymatic sensors based on *in situ* laser-induced synthesis of copper-gold and gold nano-sized microstructures. *Talanta* 167, 201–207. doi: 10.1016/j.talanta.2017.01.089
- Park, S., Boo, H., and Chung, T. D. (2006). Electrochemical non-enzymatic glucose sensors. *Anal. Chim. Acta* 556, 46–57. doi: 10.1016/j.aca.2005.05.080
- Pasta, M., La Mantia, F., and Cui, Y. (2010). Mechanism of glucose electrochemical oxidation on gold surface. *Electrochim. Acta* 55, 5561–5568. doi: 10.1016/j.electacta.2010.04.069
- Peris, M., and Escuder-Gilabert, L. (2013). On-line monitoring of food fermentation processes using electronic noses and electronic tongues: a review. *Anal. Chim. Acta* 804, 29–36. doi: 10.1016/j.aca.2013.09.048
- Persaud, K., and Dodd, G. (1982). Analysis of discrimination mechanisms in the mammalian olfactory system using a model nose. *Nature* 299:352. doi: 10.1038/299352a0
- Plauck, A., Stangland, E. E., Dumesic, J. A., and Mavrikakis, M. (2016). Active sites and mechanisms for  $H_2O_2$  decomposition over Pd catalysts. *Proc. Natl. Acad. Sci. U.S.A.* 113, E1973–E1982. doi: 10.1073/pnas.1602172113
- Pletcher, D. (1984). Electrocatalysis: present and future. *J. Appl. Electrochem.* 14, 403–415. doi: 10.1007/BF00610805
- Pourbeyram, S., and Mehdizadeh, K. (2016). Nonenzymatic glucose sensor based on disposable pencil graphite electrode modified by copper nanoparticles. *J. Food Drug Anal.* 24, 894–902. doi: 10.1016/j.jfda.2016.02.010
- Power, A. C., Gorey, B., Chandra, S., and Chapman, J. (2018). Carbon nanomaterials and their application to electrochemical sensors: a review. *Nanotechnol. Rev.* 7, 19–41. doi: 10.1515/ntrev-2017-0160
- Quesada-González, D., and Merkoçi, A. (2017). Mobile phone-based biosensing: an emerging “diagnostic and communication” technology. *Biosens. Bioelectr.* 92, 549–562. doi: 10.1016/j.bios.2016.10.062
- Rocchitta, G., Spanu, A., Babudieri, S., Latte, G., Madeddu, G., Galleri, G., et al. (2016). Enzyme biosensors for biomedical applications: strategies for safeguarding analytical performances in biological fluids. *Sensors* 16:780. doi: 10.3390/s16060780
- RodriGuez-Nieto, F. J., Morante-Catacora, T. Y., and Cabrera, C. R. (2004). Sequential and simultaneous electrodeposition of Pt-Ru electrocatalysts on a HOPG substrate and the electro-oxidation of methanol in aqueous sulfuric acid. *J. Electroanal. Chem.* 571, 15–26. doi: 10.1016/j.jelechem.2004.04.008
- Shabnam, L., Faisal, S. N., Roy, A. K., Haque, E., Minett, A. I., and Gomes, V. G. (2017). Doped graphene/Cu nanocomposite: a high sensitivity non-enzymatic glucose sensor for food. *Food Chem.* 221, 751–759. doi: 10.1016/j.foodchem.2016.11.107
- Shaidarova, L. G., and Budnikov, G. K. (2011). “Amperometric sensors with catalytic properties in organic voltammetry,” in *Chemical Sensors*, ed Y.G. Vlasov (Moscow: Nauka), 203–284.
- Shishov, A., Penkova, A., Zabrodin, A., Nikolaev, K., Dmitrenko, M., Ermakov, S., et al. (2016). Vapor permeation-stepwise injection simultaneous determination of methanol and ethanol in biodiesel with voltammetric detection. *Talanta* 148, 666–672. doi: 10.1016/j.talanta.2015.05.041
- Si, P., Huang, Y., Wang, T., and Ma, J. (2013). Nanomaterials for electrochemical non-enzymatic glucose biosensors. *RSC Adv.* 3, 3487–3502. doi: 10.1039/c2ra22360k
- Suib, S. L. E. (2013). *New and Future Developments in Catalysis*. Amsterdam: Elsevier.
- Talukdar, I., Ozturk, B., Flanders, B. N., and Mishima, T. D. (2006). Directed growth of single-crystal indium wires. *Appl. Phys. Lett.* 88:221907. doi: 10.1063/1.2208431
- Tee, S. Y., Teng, C. P., and Ye, E. (2017). Metal nanostructures for non-enzymatic glucose sensing. *Mater. Sci. Eng.* 70, 1018–1030. doi: 10.1016/j.msec.2016.04.009
- Thiyagarajan, N., Chang, J.-L., Senthilkumar, K., and Zen, J.-M. (2014). Disposable electrochemical sensors: a mini review. *Electrochem. Commun.* 38, 86–90. doi: 10.1016/j.elecom.2013.11.016
- Toghill, K. E., and Compton, R. G. (2010). Electrochemical non-enzymatic glucose sensors: a perspective and an evaluation. *Int. J. Electrochem. Sci.* 5, 1246–1301. Available online at: <http://www.electrochemsci.org/papers/vol5/5091246.pdf>
- Vassilyev, Y. B., Khazova, O. A., and Nikolaeva, N. N. (1985). Kinetics and mechanism of glucose electrooxidation on different electrode-catalysts: Part II. Effect of the nature of the electrode and the electrooxidation mechanism. *J. Electroanal. Chem. Interfac. Electrochem.* 196, 127–144. doi: 10.1016/0022-0728(85)85085-3
- Vlasov, Y. G., Ermolenko, Y. E., Legin, A. V., and Murzina, Y. G. (1999). Multisensor systems for the analysis of industrial solutions. *J. Anal. Chem.* 54, 476–482.
- Vlasov, Y. G., Ermolenko, Y. E., Legin, A. V., Rudnitskaya, A. M., and Kolodnikov, V. V. (2010). Chemical sensors and their systems. *J. Anal. Chem.* 65, 880–898. doi: 10.1134/S1061934810090029
- Vlasov, Y., Legin, A., Rudnitskaya, A., Di Natale, C., and D'amico, A. (2005). Nonspecific sensor arrays (“electronic tongue”) for chemical analysis of liquids (IUPAC Technical Report). *Pure Appl. Chem.* 77, 1965–1983. doi: 10.1351/pac200577111965
- Voitechovič, E., Korepanov, A., Kirsanov, D., and Legin, A. (2018). Quantification of immobilized protein in pharmaceutical production by bio-assisted potentiometric multisensor system. *J. Pharm. Biomed. Anal.* 150, 67–71. doi: 10.1016/j.jpba.2017.11.076
- Wang, D., Villa, A., Porta, F., Prati, L., and Su, D. (2008). Bimetallic gold/palladium catalysts: correlation between nanostructure and synergistic effects. *J. Phys. Chem. C* 112, 8617–8622. doi: 10.1021/jp800805e
- Wang, Y., Zhao, M., Ping, J., Chen, B., Cao, X., Huang, Y., et al. (2016). Bioinspired design of ultrathin 2D bimetallic metal-organic-framework nanosheets used as biomimetic enzymes. *Adv. Mater.* 28, 4149–4155. doi: 10.1002/adma.201600108
- Xing, W., Hu, J., Kung, S.-C., Donovan, K. C., Yan, W., Wu, R., et al. (2012). A chemically-responsive nanojunction within a silver nanowire. *Nano Lett.* 12, 1729–1735. doi: 10.1021/nl300427w
- Yang, F., Cheng, K., Wu, T., Zhang, Y., Yin, J., Wang, G., et al. (2013). Dendritic palladium decorated with gold by potential pulse electrodeposition: enhanced electrocatalytic activity for  $H_2O_2$  electroreduction and electrooxidation. *Electrochim. Acta* 99, 54–61. doi: 10.1016/j.electacta.2013.03.100

- Yi, X., Yu, G., Chang, F., Xie, Z. H., Tran, T. N., Hu, B. N., et al. (2014). Electrochemically controlled growth of Au-Pt alloy nanowires and nanodendrites. *Chemistry* 9, 2612–2620. doi: 10.1002/asia.201402442
- Yogeswaran, U., and Chen, S.-M. (2008). A review on the electrochemical sensors and biosensors composed of nanowires as sensing material. *Sensors* 8:290. doi: 10.3390/s8010290
- Zhang, A. Q., and Lieber, C. M. (2016). Nano-bioelectronics. *Chem. Rev.* 116, 215–257. doi: 10.1021/acs.chemrev.5b00608
- Zhang, H., Watanabe, T., Okumura, M., Haruta, M., and Toshima, N. (2011). Catalytically highly active top gold atom on palladium nanocluster. *Nat. Mater.* 11:49. doi: 10.1038/nmat3143
- Zhang, M., Yang, X., Zhou, Z., and Ye, X. (2013). Controllable growth of gold nanowires and nanoactuators via high-frequency AC electrodeposition. *Electrochem. Commun.* 27, 133–136. doi: 10.1016/j.elecom.2012.11.013
- Zhao, F., and Kim, J. (2016). Optical hydrogen peroxide sensor using dopamine-conjugated quantum dots as sensing medium. *Sci. Adv. Mater.* 8, 64–68. doi: 10.1166/sam.2016.2600

**Conflict of Interest Statement:** The authors declare that the research was conducted in the absence of any commercial or financial relationships that could be construed as a potential conflict of interest.

Copyright © 2018 Nikolaev, Ermolenko, Offenbäusser, Ermakov and Mourzina. This is an open-access article distributed under the terms of the Creative Commons Attribution License (CC BY). The use, distribution or reproduction in other forums is permitted, provided the original author(s) and the copyright owner(s) are credited and that the original publication in this journal is cited, in accordance with accepted academic practice. No use, distribution or reproduction is permitted which does not comply with these terms.



# Solid-Contact Potentiometric Sensors and Multisensors Based on Polyaniline and Thiacalixarene Receptors for the Analysis of Some Beverages and Alcoholic Drinks

Michail Sorvin<sup>1</sup>, Svetlana Belyakova<sup>1</sup>, Ivan Stoikov<sup>2</sup>, Rezeda Shamagsumova<sup>1</sup> and Gennady Evtugyn<sup>1\*</sup>

<sup>1</sup> Analytical Chemistry Department, A.M. Butlerov Chemistry Institute, Kazan Federal University, Kazan, Russia, <sup>2</sup> Organic Chemistry Department, A.M. Butlerov Chemistry Institute, Kazan Federal University, Kazan, Russia

## OPEN ACCESS

### Edited by:

Dmitry Kirsanov,  
Saint Petersburg State University,  
Russia

### Reviewed by:

Yuqing Miao,  
University of Shanghai for Science and  
Technology, China  
Sushmee Badhulika,  
Indian Institute of Technology  
Hyderabad, India  
Constantin Apetrei,  
Dunarea de Jos University, Romania

### \*Correspondence:

Gennady Evtugyn  
gennady.evtugyn@kpfu.ru

### Specialty section:

This article was submitted to  
Analytical Chemistry,  
a section of the journal  
Frontiers in Chemistry

Received: 08 February 2018

Accepted: 09 April 2018

Published: 24 April 2018

### Citation:

Sorvin M, Belyakova S, Stoikov I, Shamagsumova R and Evtugyn G (2018) Solid-Contact Potentiometric Sensors and Multisensors Based on Polyaniline and Thiacalixarene Receptors for the Analysis of Some Beverages and Alcoholic Drinks. *Front. Chem.* 6:134. doi: 10.3389/fchem.2018.00134

Electronic tongue is a sensor array that aims to discriminate and analyze complex media like food and beverages on the base of chemometrics approaches for data mining and pattern recognition. In this review, the concept of electronic tongue comprising of solid-contact potentiometric sensors with polyaniline and thiacalix[4]arene derivatives is described. The electrochemical reactions of polyaniline as a background of solid-contact sensors and the characteristics of thiacalixarenes and pillararenes as neutral ionophores are briefly considered. The electronic tongue systems described were successfully applied for assessment of fruit juices, green tea, beer, and alcoholic drinks. They were classified in accordance with the origination, brands and styles. Variation of the sensor response resulted from the reactions between Fe(III) ions added and sample components, i.e., antioxidants and complexing agents. The use of principal component analysis and discriminant analysis is shown for multisensor signal treatment and visualization. The discrimination conditions can be optimized by variation of the ionophores, Fe(III) concentration, and sample dilution. The results obtained were compared with other electronic tongue systems reported for the same subjects.

**Keywords:** solid-contact sensors, potentiometric sensors, electronic tongue, polyaniline, food analysis

## INTRODUCTION

Multicomponent analysis of liquid samples is one of frequently mentioned challenges of modern analytical chemistry. The determination of surface water contamination, drinking water hardness, ionic content of biological fluids, and nutritive value of foodstuffs require simultaneous determination of numerous ionic and neutral species that are naturally typical for the subject of the analysis or occasionally introduced due to contamination (Cuartero et al., 2017). Although most of the problems mentioned are successfully solved by conventional analytical equipment like ionic and high-performance liquid chromatography (Colenutt and Trenchard, 1985), some aspects of the multicomponent analysis of liquids remain in the scope of intensive investigations. Among others, two challenges call for further consideration, i.e., (i) the improvement of existing approaches in terms of higher selectivity of the analysis, and (ii) adaptation of conventional techniques to their application

outside chemical laboratory. The on-site (on-demand) application concept assumes the development of portable equipment utilizing chemical sensors with minimal sample pre-treatment and fast and reliable data processing. However, the use of individual sensors is complicated by their non-ideal selectivity toward certain analytes and unexpected influence of interferences, which existence in the sample cannot be reliably predicted. Together with a large number of analytes, this limits the application of chemical sensors to a few most important species present in the sample in moderately high quantities. The limitations mentioned can be overcome by assembling the sensor array, i.e., set of sensors with cross-reactivity/selectivity toward various sample components (Bratov et al., 2010). Their signals are processed using pattern recognition algorithms that extract information on the content of the sample or on its quality, e.g., brand name of foodstuffs (Haddi et al., 2014) or relative value of hot spirits or fresh juices (Tahara and Toko, 2013). Similar systems are utilized for estimation of taste (Ha et al., 2015), antioxidant properties (Kraujalyt et al., 2015), food adulteration (Peris and Escuder-Gilabert, 2016) and drug bitterness (Yaroshenko et al., 2016). Previous applications of sensor arrays in food analysis are reviewed in Escuder-Gilabert and Peris (2010).

Among various sensor arrays, potentiometric sensors based on ion-selective electrodes (ISEs) show undisputable advantages, e.g., fast and reversible response, sufficient reproducibility, simple measurement protocol, compatibility with portable ionometers, well elaborated theory and intuitively understandable principles of signal interpretation. In 1991–1993, C. Di Natale and Yu. Vlasov have proposed the arrays of potentiometric sensors that were defined together with the algorithms of the signal processing as “Electronic Tongue” (ET) (Di Natale et al., 1996). Since then, potentiometric ETs have been applied for classification and quantitative analysis of biological fluids (Gutiérrez et al., 2007), foodstuffs (Beullens et al., 2008), medicines (Legin et al., 2004), waste, and natural waters (Di Natale et al., 1997; Mimendia et al., 2010) and so on.

The efficiency of multisensor systems depends on performance of individual sensors. High stability of the response and variable selectivity toward various species promote discrimination of the analytes and assessment of the complex samples in accordance with quality parameters. Meanwhile previous history of ISEs was directed to the achievement of maximal selectivity of the response toward individual analytes. The potentiometric sensor arrays first involved conventional ISEs based on glass and chalcogenide glass membranes (Di Natale et al., 1996). Such an approach resulted in necessity of too many individual ISEs to establish necessary cross-selectivity and discriminate ionic species present in the sample. Later on, the ISEs with polymeric membranes containing different ionophores have been introduced to extend the performance of the multisensor systems. Porphyrin derivatives (Paolesse et al., 2003), either free or bonded to transient metal ions, were mainly applied in the potentiometric ETs. Then, conventional polymeric membranes and ionophores were substituted by semiconductor devices, e.g., field effect transistors (Ipatov et al., 2009), and planar metal electrodes directly contacted with the membranes

(Ciosek et al., 2007). Many of the ETs described were applied also in flow-through mode (Wesoly et al., 2016).

Despite obvious progress in the development of sensors and software for the ET assembling and data processing, there is a high interest to the further enhancement of the number of ionophores and to the improvement of the ISE's design. This interest is mainly related to the drawbacks of current ET systems, i.e., rather large number of individual sensors, significant correlation of their signals and limited number of problems to be solved with ET systems. Multi-purpose ET systems with lower number of ISEs will simplify their operation outside chemical laboratory and accelerate data processing based on statistical methods of data mining and pattern recognition.

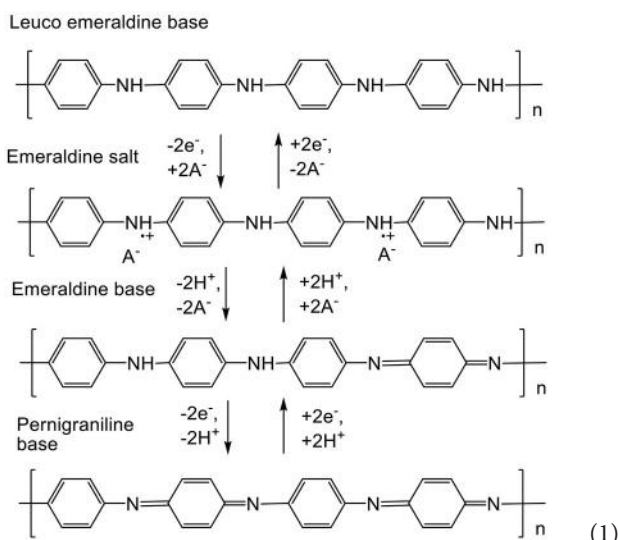
In this respect, the use of macrocyclic ionophores together with polyaniline as a platform for solid-contact potentiometric sensors is very promising in the ET systems design due to the compact and easily machining design and prospects of tuning both selectivity and sensitivity of response toward different species and complex media. In this review, own and literary data related to the use of polyaniline sensors with macrocyclic ionophores in the analysis of foodstuffs and beverages are summarized.

## POLYANILINE IN THE ASSEMBLY OF POTENTIOMETRIC SENSORS

Polyaniline is the polymer that can be obtained by chemical or electrochemical oxidation of aniline performed mainly in the presence of strong mineral acids. The reaction starts with the formation of a cation-radical, which is then coupled with initial aniline molecule with formation of the imide bond. Electrochemical deposition of polyaniline on the electrode is commonly performed by repeating cycling of the potential. In chemical synthesis,  $(\text{NH}_4)_2\text{S}_2\text{O}_8$  is commonly used. It is reduced to the sulfate anion and does not contaminate the polymer (Cirić-Marjanović, 2013). The following oligomerization involves head-to-tail binding with formation of a linear product existing in various forms, which shape and size depend on the regime of the electrolysis, presence of organic solvents and surfactants and nature of the acid added to the reaction media (Stejskal et al., 2010; Baker et al., 2017). Chemical oxidation can be performed at low temperatures (down to  $-70^\circ\text{C}$ ) to avoid the accumulation of quinoid by-products interfering with electroconductive properties of polyaniline.

The interest to polyaniline is related to its redox properties that depend on the pH and redox potential of the microenvironment. The reactions of intermolecular electron and hydrogen ion exchange (1) are supported by transfer of counter ions that balance the charge of the polymer and also change its intrinsic volume and permeability (Trivedi, 1999). The semi-oxidized form of polyaniline, emeraldine salt, exerts electroconductivity similar to that of doped semiconductors. This property can be used for electric wiring of the enzymes and nucleic acids in biosensor assembly (Dhand et al., 2011). Besides, changes in conductivity caused by the pH shift are recorded in resistive and optical sensors for the measurement

of ammonia and weak organic acids (Song and Choi, 2013; Fratoddi et al., 2015). Pure polyaniline exists in emeraldine form only in rather acidic media ( $\text{pH} < 3$ ). This region can be extended by introduction of strong insoluble organic acids in the polymer structure (Karyakin et al., 1999; Lukachova et al., 2003) or by the synthesis of polyelectrolyte complexes with sodium dodecylsulfonate (Andre et al., 2017), polystyrenesulfonate (Luo et al., 2013), carbon nanotubes (Kumar et al., 2018) or even DNA (Shamagsumova et al., 2015) as polyanionic counter ions.



The use of polyaniline in solid-contact potentiometric sensors makes it possible to avoid drawbacks typical for such devices, i.e., slow rate of electron exchange and irreversible response toward alternating analyte concentrations (Lewenstam et al., 1994). Such materials with ion-to-electron conductivity substitute internal filling of conventional ISEs. Solid-contact potentiometric ISEs are easier in manufacture and operation than the commercial ISEs with internal filling and polymer membrane containing ionophore. They do not require long conditioning in an analyte solution prior to use and do not lose workability due to leaching of internal standard solution. Regarding polyaniline, its application in the assembly of solid-contact sensors is limited by necessity in the transfer of doping anions as a part of the redox conversion. This challenge is solved by introduction of acidic groups in the side chains of the polymer (self-doped polyaniline; Jaymand, 2013) or by the addition of high-molecular anionic substances (Zhang et al., 2008). The reversibility of the polyaniline potential can be improved by implementation of conductive materials, i.e., carbon nanotubes (Bavastrello et al., 2004), graphene (Jaworska et al., 2012; Boeva et al., 2014), or noble metal nanoparticles (Shiigi et al., 2012; Lorestani et al., 2015).

Potentiometric sensors based on polyaniline were first applied for the pH measurements. In acidic media, the response is attributed to the shift of equilibrium between emeraldine and leuco-emeraldine forms (see Scheme 1) whereas in basic media the potential is sensitive to the protonation of imine groups that does not result in changes of conductivity and redox

reactions (“charge counting” mechanism of the response). In accordance with these mechanisms of potentiometric response, an intermediate pH region exists with reduced influence of the acidity on the polyaniline potential. The sensitivity of the pH measurement can be increased by addition of camphorsulfonic acid (Karyakin et al., 1999). It changes the stoichiometry of the redox reaction normally corresponded to the transfer of two electrons and two hydrogen ions per monomer unit. The over-Nernstian slope of calibration curve is observed for such pH sensors.

The polyaniline doping is a source of the potentiometric activity toward certain anions that are specifically accumulated in the polymer net. Contrary to pH measurements, the reaction with anions is less specific (Hao et al., 2010). In some cases, the addition of analytes in the polymerization mixture improves the performance of appropriate sensors. In other cases, polyaniline is covered with plasticized membrane containing anion-sensitive ionophore, preferably tetraalkylammonium salts (Shishkanova et al., 2005). The determination of nitrate (Khripoun et al., 2006), sulfate (Xing et al., 2017), salicylate (Shishkanova et al., 2014), and sulfonate anionic detergents (Karami and Mousavi, 2004) has been described with polyaniline based potentiometric sensors.

## THIACALIXARENES AND PILLARARENES AS IONOPHORES

Thiacalixarenes have found application in the ISEs predominantly for the determination on transient metal cations which are either incorporated in the pseudo-cavity formed by the substituents at the lower rim of the macrocycle or coordinated near the bridging atoms of sulfur (Yushkova and Stoikov, 2009). The inclusion of the metals to form the host-guest complex changes also the aggregation of the macrocycle via distortion of the hydrogen bonds and influences the total charge of the complex in comparison with neutral ionophore molecule. Though the factors mentioned were mostly investigated in organic solvents, they can also affect the potential of appropriate ISEs. Direct application of thiocalixarenes in potentiometric measurement of various metals has been described in rather limited number of articles. Thus, non-substituted thiocalix[4]arene and its derivative with *p*-*tert*-butyl groups at the upper rim of the macrocycle were implemented in the PVC membrane or directly deposited from vapors on Au electrode for the determination of Co(II) (Gupta et al., 2008) and Cu(II) cations (Ali et al., 2006), respectively. Here and below, roman numerals are referred to the nominal concentration of all the forms of appropriate metals including hydroxycations etc. present in aqueous solutions whereas the plus sign corresponds to a single stable form of the ion ( $\text{Na}^+$ ,  $\text{Ag}^+$ , etc.). It is interesting to note that rather high potentiometric selectivity of both sensors was announced. Mono- and bis(crown-6) thiocalix[4]arenes were successfully used for the determination of  $\text{Cs}^+$  ions in the presence of a wide range of *s*-, *p*-, and *d*-metal cations (Bereczki et al., 2006). The appropriate selectivity ( $pK_{\text{Cs}/\text{Me}}$ ) varied from  $-1.2$  for Rb to  $-5.9$  for Cu. In this case, the response is pre-determined by geometric conformity of the cation radius

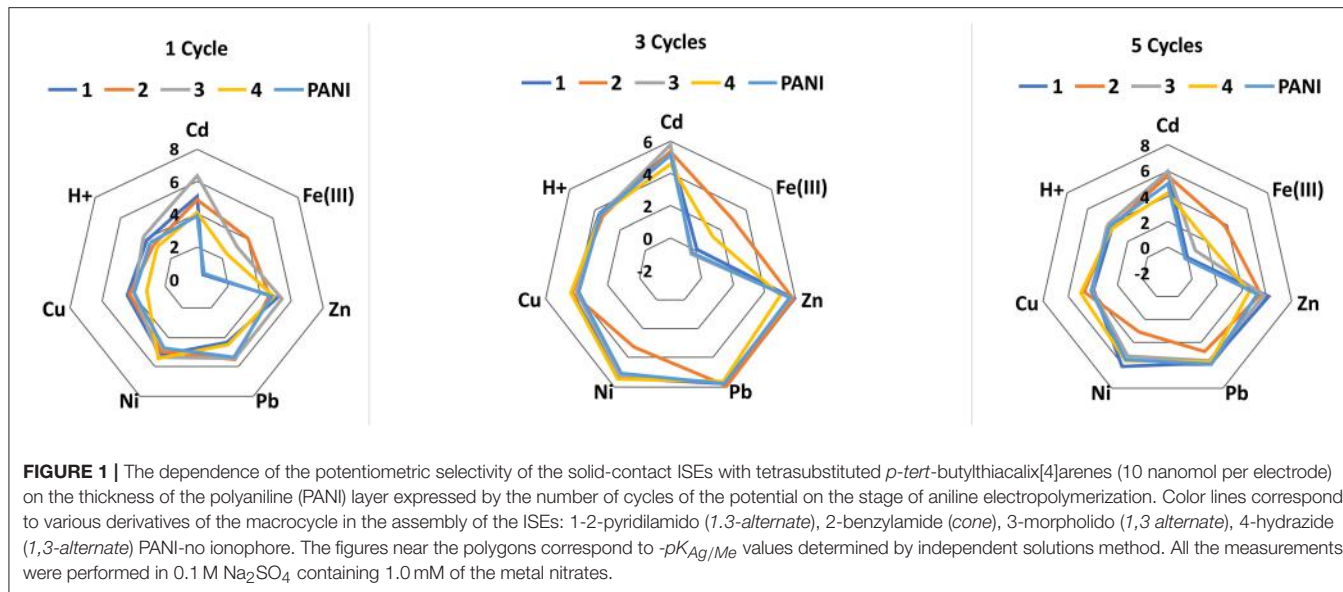


**FIGURE 1** | The dependence of the potentiometric selectivity of the solid-contact ISEs with tetrasubstituted *p*-*tert*-butylthiacalix[4]arenes (10 nanomol per electrode) on the thickness of the polyaniline (PANI) layer expressed by the number of cycles of the potential on the stage of aniline electropolymerization. Color lines correspond to various derivatives of the macrocycle in the assembly of the ISEs: 1-2-pyridilamido (1,3-alternate), 2-benzylamide (cone), 3-morpholido (1,3-alternate), 4-hydrazide (1,3-alternate) PANI-no ionophore. The figures near the polygons correspond to  $-pK_{Ag/Me}$  values determined by independent solutions method. All the measurements were performed in 0.1 M  $Na_2SO_4$  containing 1.0 mM of the metal nitrates.

and the size of the oxyethylene cycle of the crown-6 binding site of the receptor. The *p*-*tert*-butylthiacalix[4]arene with two triazole cycles at the lower rim exerted selectivity toward  $Ag^+$  ions (Omran et al., 2016). The ionophore was implemented in the PVC membrane together with a plasticizer and Na tetraphenylborate. The ISE with internal solution of 0.01 M  $AgNO_3$  showed linear response to  $Ag^+$  ions between 7  $\mu M$  and 8.0 mM [limit of detection (LOD) 3.9  $\mu M$ ].

Comprehensive consideration of selectivity of the solid-contact sensors with thiocalix[4]arene ionophores deposited onto the polyaniline film has been performed in the work of (Evtugyn et al., 2008). Tetrasubstituted thiocalix[4]arenes were synthesized from tetraacid derivatives and contained 2-pyridilamido, morpholide, pyrrolidide, and hydrazide groups responsible for cation binding. Biased potentiometric selectivity coefficients indicated that the binding properties of ionophores depended not only on the nature of the functional groups of substituents but also on the configuration of the macrocyclic core present in *cone*, *partial cone* and *1,3-alternate* configurations. The lowest LODs of 0.1  $\mu M$ –20 nM were found for *1,3-alternate* among other isomers and for pyrrolidide derivative among other substituted macrocycles. Assembling of the ion-selective layer was performed by casting the thiocalix[4]arene solution onto the polyaniline. ISEs showed rather high reproducibility of the signal (R.S.D. about 2%) and reversible response toward alternating concentrations of the analyte. The maximum shift of the potential was found for the  $Ag^+$  ions both in neutral and acidic media. Regarding other metals, the higher pH improved selectivity due to partial hydrolysis of interferences. Only Fe(III) and Hg(II) ions interfered with the  $Ag^+$  detection. However, their influence could be easily excluded by addition of fluoride and chloride ions, respectively.

Deposition of thiocalixarene ionophores partially suppressed the pH sensitivity of the response which is commonly considered as a weak point of the ISEs based on polyaniline. For the same

reason, the potentiometric selectivity of the sensors changed with the quantities of the polyaniline. **Figure 1** represents changes in the potentiometric selectivity of five ISEs with different assembly of the surface layer toward various metal cations.

The thickness of the polyaniline layer is expressed by the number of potential cycles used on the step of electropolymerization. Both the  $pK_{Ag/Me}$ -values and the influence of thiocalix[4]arenes were sensitive to the polyaniline thickness. It is interesting to note that even one cycle of the potential in acidic aniline solution was found to be sufficient for deposition of minor amounts of the oligomers providing redox reversibility of the potential and electron-to-ion conductivity. Certainly, such sensors were less stable toward external factors than those with thicker polyaniline film and showed rather a short working period within a day.

No influence of alkaline and alkaline-earth metals was found for such ISEs with no respect of the pH-value and polyaniline film thickness. The differentiation of the response by changing ionophore and measurement conditions was later used for assembling the ET system applied for the discrimination of the foodstuffs reach with oxidizable organic species (see below).

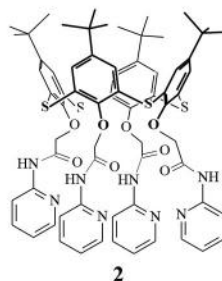
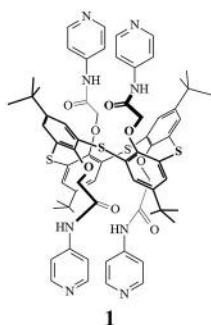
Contrary to the thiocalix[4]arenes, analogous pillar[5]arenes have found limited application in the assembly of potentiometric sensors. This might be due to lower differentiation of the signal toward metal cations involved in supramolecular interactions with this receptor. Thus, pillar[5]arenes with amide and carboxylic groups can bind  $Li^+$ ,  $Na^+$ ,  $K^+$ , and  $Cs^+$  with similar association constants determined by UV-vis spectroscopy (Yakimova et al., 2017). The binding efficiency was increased by introduction of the glycylglycide, additional amide, and carboxylic fragments in the macrocycle moiety. Similar results were reported for pillar[5]arenes bearing morpholide and pyrrolidide groups (Shurpik et al., 2014). The association constants of 100–1,000  $M^{-1}$  were determined by electron

spectroscopy for alkali metals bonded in 1:1 ratio with insignificant preference of the  $\text{Li}^+$  binding.

The only potentiometric sensor with pillar[5]arene has been described for sensitive determination of  $\text{Cu}^{2+}$  ions (Stoikova et al., 2015). The solid-contact ISE was prepared similarly to that described for functionalized thiocalix[4]arenes (Evtugyn et al., 2007). The screen-printed carbon electrode was first modified with polyaniline by repeated cycling the potential in the solution of the monomer in concentrated sulfuric acid. After that, freshly prepared solution of unsubstituted pillar[5]arene was dropped onto the working electrode and left to dry at ambient temperature. The electrode made it possible to determine from  $1 \mu\text{M}$  to  $10 \text{ mM}$  of  $\text{Cu}^{2+}$  ions (LOD  $0.3 \mu\text{M}$ ). The ISE was successfully applied for detection of  $\text{Cu}(\text{II})$  ions in the polyvitamin drops “Complivit” and Bordeaux mixture used as a fungicide in vineyards, fruit farms and gardens. Interfering effect of the  $\text{Fe}(\text{III})$  and  $\text{Ag}^+$  ions was referred to the redox reaction between the polyaniline and metal ions determined. In case of silver, the formation of metal nanoparticles in the reaction with polyaniline was also confirmed by transmission electron microscopy (Smolko et al., 2014).

## SOLID-CONTACT POTENTIOMETRIC SENSORS IN BINARY MIXTURES

Substituted thiocalix[4]arenes meet the requirement of cross-selectivity in multicomponent media required for assembling the potentiometric ET systems. This was first shown on the example of simultaneous determination of two cations [ $\text{Ag}^+ - \text{Hg}(\text{II})$  and  $\text{Ag}^+ - \text{Fe}(\text{III})$ ] in binary mixtures. Both  $\text{Hg}(\text{II})$  and  $\text{Fe}(\text{III})$  ions interfere with silver and could not be determined by a single solid-contact sensor (Evtugyn et al., 2007). The ET consisted of nine individual electrodes manufactured on the same platform of screen-printed carbon electrodes covered with electropolymerized polyaniline. Three electrodes were covered with the pyridine derivative **1** in *1,3-alternate* conformation and three others with structurally similar derivative **2** in *cone* conformation (2).



The ET described was first explored to predict the signals of individual sensors at a certain pH by modeling the response using linear and on-linear models created on a known set of binary standard solutions (Evtugyn and Stoikov, 2016). For  $\text{Ag}^+ - \text{Hg}(\text{II})$  mixture, satisfactory results have been obtained with non-linear model (3) followed from the Nikolsky-Eisenman equation and describing mutual influence of the cations in binary mixture on the ISE potential.

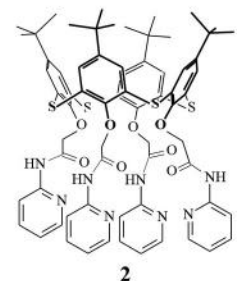
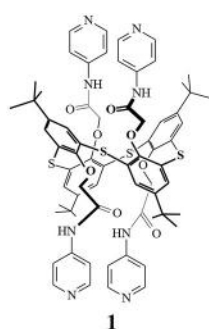
$$y_i = a_i^0 + b_i \ln(k_i c_1 + c_2 + k_{i,12} c_1 c_2) \quad (3)$$

Here  $c_1$  and  $c_2$  are the concentrations of the cations,  $i$  is the number of the ISE and  $a_i$ ,  $b_i$ , and  $k_i$  are the parameters to be extracted from the experimental data by minimization of the mean-square error function. Measurements were performed in weakly acidic media ( $\text{pH} = 1 \div 5$ ) corresponding to the real assay conditions. The pH range covers transient area corresponded to the reversible transfer of the polyaniline between the conductive emeraldine and non-conductive oxidized form. For this reason, sensor potential can be sensitive to minor pH changes and appropriate shifts of hydrolytic equilibria of  $\text{Fe}(\text{III})$  and  $\text{Hg}(\text{II})$  species. Complex pH effect was ascribed by the pH sensitivity of the above parameters  $a_i$ ,  $b_i$ , and  $k_i$  ( $i = 1 \div 3$  for three types of ISEs) (4).

$$\begin{aligned} a_i^0(\text{pH}) &= a_{10} + a_{11} \cdot \text{pH} + a_{12} \cdot \text{pH}^2 \\ b_i(\text{pH}) &= a_{20} + a_{21} \cdot \text{pH} + a_{22} \cdot \text{pH}^2 \\ k_i(\text{pH}) &= a_{30} + a_{31} \cdot \text{pH} + a_{32} \cdot \text{pH}^2 \end{aligned} \quad (4)$$

The partial coefficients  $a_{ij}$  were fitted by minimization of the mean-square error function (5).

$$F^{(i)}(a_i^0(\text{pH}), b_i(\text{pH}), k_i(\text{pH})) = \sum_j \left( \frac{y_j^{(i)} - \hat{y}_j^{(i)}}{y_j^{(i)}} \right)^2 \quad (5)$$



Last three electrodes were used as they were without additional deposition of ionophores to take into account the shift of the potential attributed to the polyaniline. The signals of the ISEs described were recorded in a set of model binary solutions of different concentrations without intermediate averaging.

Direct additive model has shown good prediction of individual responses. After that, the concentrations of  $\text{Ag}^+$  and  $\text{Hg}(\text{II})$  present in binary solutions were estimated within the range from  $10 \text{ mM}$  to  $10 \mu\text{M}$  by a number of statistical methods including

generalized additive model (GAM), partial least square (PLS) analysis, and artificial neural network (multilayer perceptron, MLP). The root-mean square error did not exceed 5.6% of logarithm of concentration of each ion. Best results were obtained with MPL consisted of two hidden layers with five and three neurons, respectively.

Similar consideration of  $\text{Ag}^+$ -Fe(III) binary solutions resulted in better prediction of the cation concentrations against  $\text{Ag}^+$ -Hg(II) mixture due to the bigger difference in the shape of the calibration curves obtained separately for each metal cation. The signal toward Fe(III) appears due to reversible redox conversion of the polyaniline and results in the S-shaped calibration curve with a rather narrow linear piece in the middle of the concentration interval.

The prediction of metal concentrations with GAM was based on the Equation (6).

$$\ln C = \text{Const} + s(1) + s(2) + s(3) + \varepsilon, \quad (6)$$

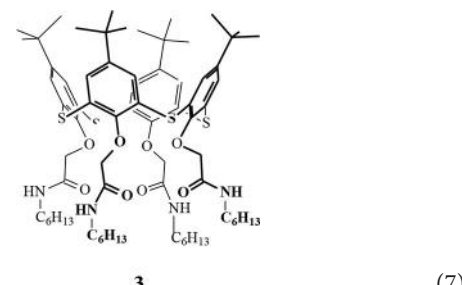
where  $s(1)$ ,  $s(2)$ , and  $s(3)$  are smooth functions describing the dependence of the individual sensor signal on the logarithm of the cation concentration, and  $\varepsilon$  is the random error with zero mean value. The GAM retains additive response summation approach but takes into account non-linear behavior of each sensor toward a certain analyte. The prediction model provided 90.6% of explained deviance for Fe(III) concentration and 70.3% for  $\text{Ag}^+$  ions. The MLP model showed better quality of prediction than linear model especially for Fe(III) concentration. The PLS regression showed that the prediction is mostly based on the signal of the sensor with the macrocycle **1** in *1,3 alternate* configuration whereas the polyaniline with no ionophore takes into account the hydrolytic instability of the cations.

## MULTISENSOR SYSTEMS FOR FOOD ASSESSMENT: CONCEPT DESCRIPTION

Solid-contact ISEs with the thiocalix[4]arene derivatives showed variable response toward many transient metal cations that depended on many factors including acidity and buffering properties of the media (Evtugyn et al., 2007, 2008). Additive model of the ISE response showed satisfactory agreement with the experimental data. However, detectable concentrations of most heavy metals were rather high for direct application of such sensors in environmental monitoring. Meanwhile, redox response of the Fe(III) ions caused by its reaction with polyaniline can be applicable for indirect characterization of many samples containing readily oxidized compounds that could affect the signal. This offers new opportunities for the use of such electrodes in the quality assessment of foodstuffs, fruits, vegetables and beverages. Indeed, ferric reducing activity measurement is a conventional parameter applied for spectrophotometric determination of "antioxidant power" (Benzie and Strain, 1996). Electrochemical analogs include ferricyanide based protocols with voltammetric signal measurements (Berker et al., 2010; Klöšeiko, 2016).

In case of solid-contact ISEs on polyaniline platform, the detection of readily oxidized species is simplified by non-linear shape of the Fe(III) calibration curve. It can be expected, that together with the antioxidants, partial hydrolysis of the Fe(III) species and their complexation with organic substances present in organic matter would alter the potential of the sensors/ This offers possibilities for extraction of new information on the sample content, origination, nutritive value etc.

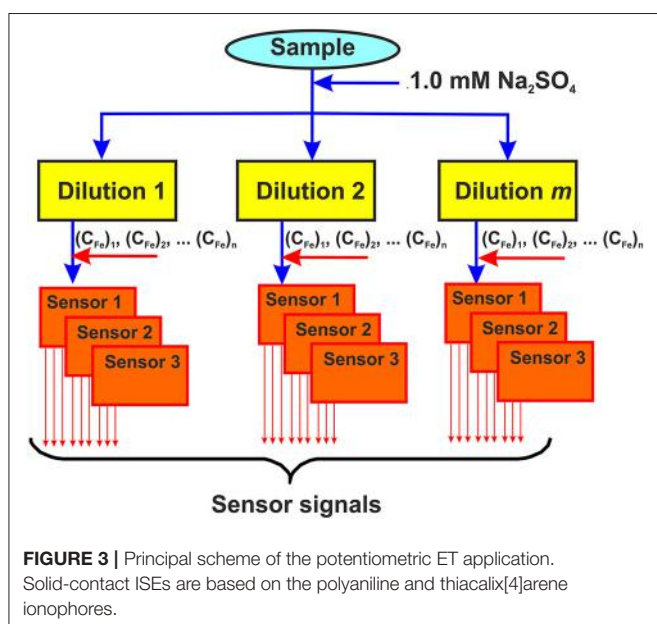
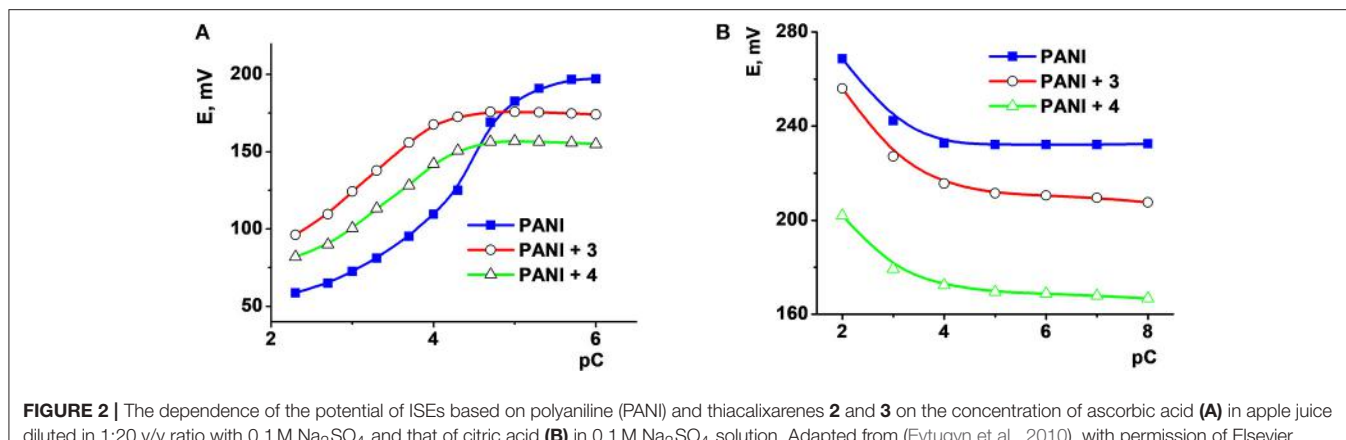
The possibility to monitor the antioxidants with the solid-contact ISEs based on polyaniline and thiocalix[4]arene ionophores in the presence of Fe(III) ions was confirmed by the analysis of some typical antioxidants like ascorbic, malic and oxalic acids, quercetin, and hydroquinone (Evtugyn et al., 2010). Their LODs varied from 2  $\mu\text{M}$  (quercetin) to 0.1 mM (oxalic acid). Thiocalix[4]arenes **2** and **3** (7) affect the sensitivity of the antioxidant determination. More lipophilic derivative **3** with long alkyl radicals in the substituents at the lower rim decreased the LODs of neutral analytes by 2–4 times against those of ascorbic, malic and oxalic acids. Meanwhile pyridine derivative **2** showed similar LOD values for all the antioxidant tested.



Different sensors respond to organic species present in the samples in a different manner. **Figure 2A** shows the signals recorded in the apple juice spiked with different amounts of ascorbic acid and a constant Fe(III) concentration. Moreover, citrate ion shifts the potential of the sensor in the opposite direction (**Figure 2B**) because of the formation of negatively charged complex with Fe(III) ions and its electrostatic accumulation onto the polyaniline surface.

Variety of the ISEs responses to various components of real samples, e.g., fruits, vegetables, foodstuffs, beverages etc., made it possible to propose the following protocol for the assessment of the above products and their discrimination in accordance with *a priori* and *a posteriori* formulated specifiers (**Figure 3**):

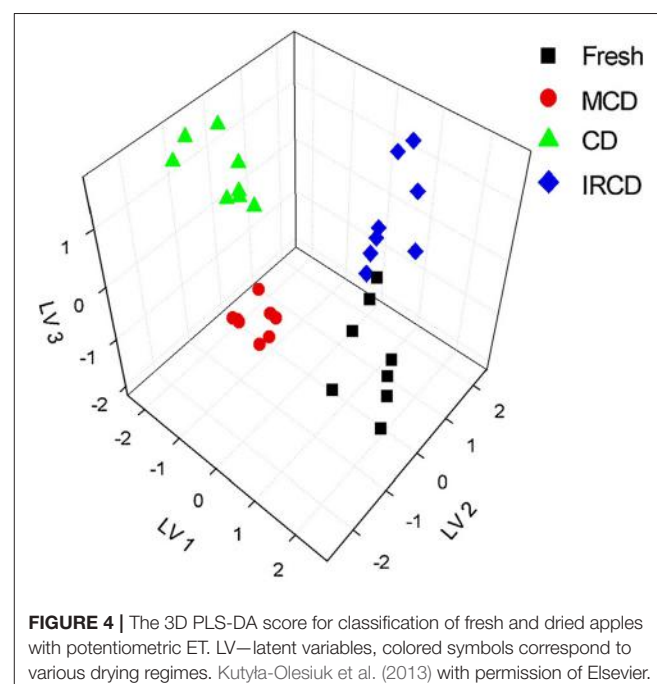
- The sample is diluted in a certain ratio with supporting electrolyte to stabilize its ionic strength and reach antioxidant concentration required;
- The aliquot of the Fe(III) salt is added into the diluted sample to reach a constant concentration in all the dilutions;
- The solid-contact ISEs based on the polyaniline and the thiocalix[4]arene ionophores are inserted in the diluted solutions and their potentials are measured against the same reference electrode ( $\text{Ag}/\text{AgCl}$ );
- A series of such measurements is performed with a certain number of sample dilutions and Fe(III) concentrations.



The number of measurements, the number of ISEs in the ET system and the choice of ionophores are the subject of investigations conducted with standard solutions (known samples). In most cases, six or nine ISEs with two or three ionophores are combined in the ET system and one or two different concentrations of Fe(III) ion are added prior to potential measurement. The signals of all the individual sensors with the same thiocalix[4]arene derivative were then processed without intermediate averaging to take into account their variability. The dilutions of the samples commonly varied from 1:1 to 1:200. The examples of the application of the ET described are given below.

## FRUIT JUICES

Fruits and fruit juices are most important natural sources of antioxidants, vitamins, and other nutrients demanded for the human health. Meanwhile the assessment of the fruits based



on the potentiometric ETs has been described only in few works. Thus, the discrimination of apple variables by the content of organic acids and sugars was demonstrated with the ET comprising of 16 potentiometric sensors in combination with Fourier transform infrared spectroscopy with attenuated total reflection (ATR-FTIR) and HPLC data (Rudnitskaya et al., 2006). The classification of the apple varieties was performed using principal component (PCA) and discriminant analysis. The calibration of organic acids and sugars was performed with PLSs regression. Peach, orange, pineapple and grapefruit juices were classified with potentiometric multisensor system consisted of copper, tin, iron, aluminum, brass, and stainless-steel wires (Lvova et al., 2006a). The classification confirmed by PCA was based on different content of organic acids. Thirty-six potentiometric sensors with PVC membranes have been

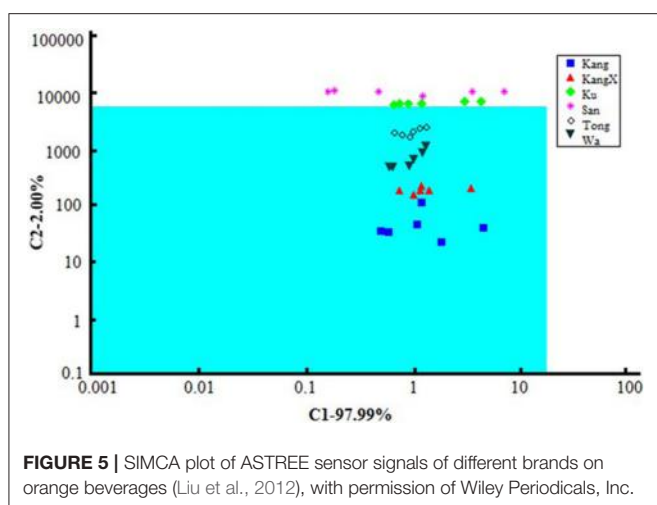


**FIGURE 5** | SIMCA plot of ASTREE sensor signals of different brands on orange beverages (Liu et al., 2012), with permission of Wiley Periodicals, Inc.

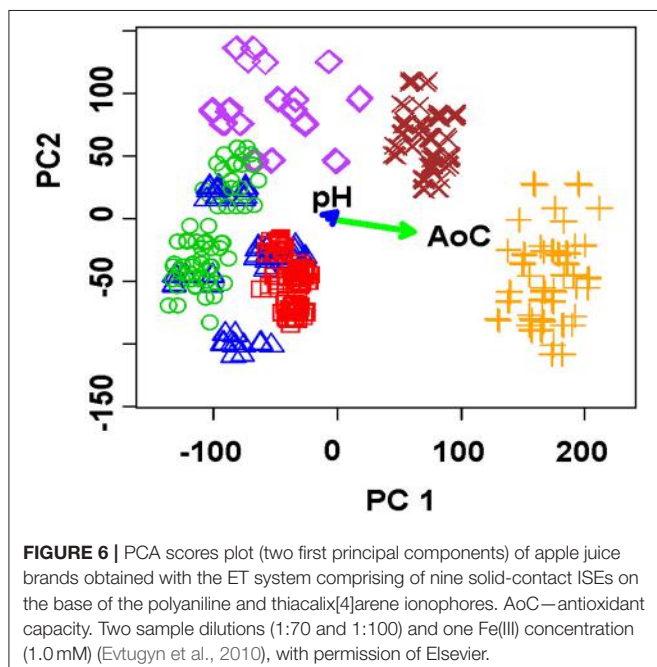


**FIGURE 6** | PCA scores plot (two first principal components) of apple juice brands obtained with the ET system comprising of nine solid-contact ISEs on the base of the polyaniline and thiocalix[4]arene ionophores. AoC—antioxidant capacity. Two sample dilutions (1:70 and 1:100) and one Fe(III) concentration (1.0 mM) (Evtugyn et al., 2010), with permission of Elsevier.

employed for classification of 16 commercial fruit juices and fruit containing non-alcoholic drinks (Dias et al., 2011). The quantitative determination of fruit content in the beverages was performed using multiple linear regression and PLS.

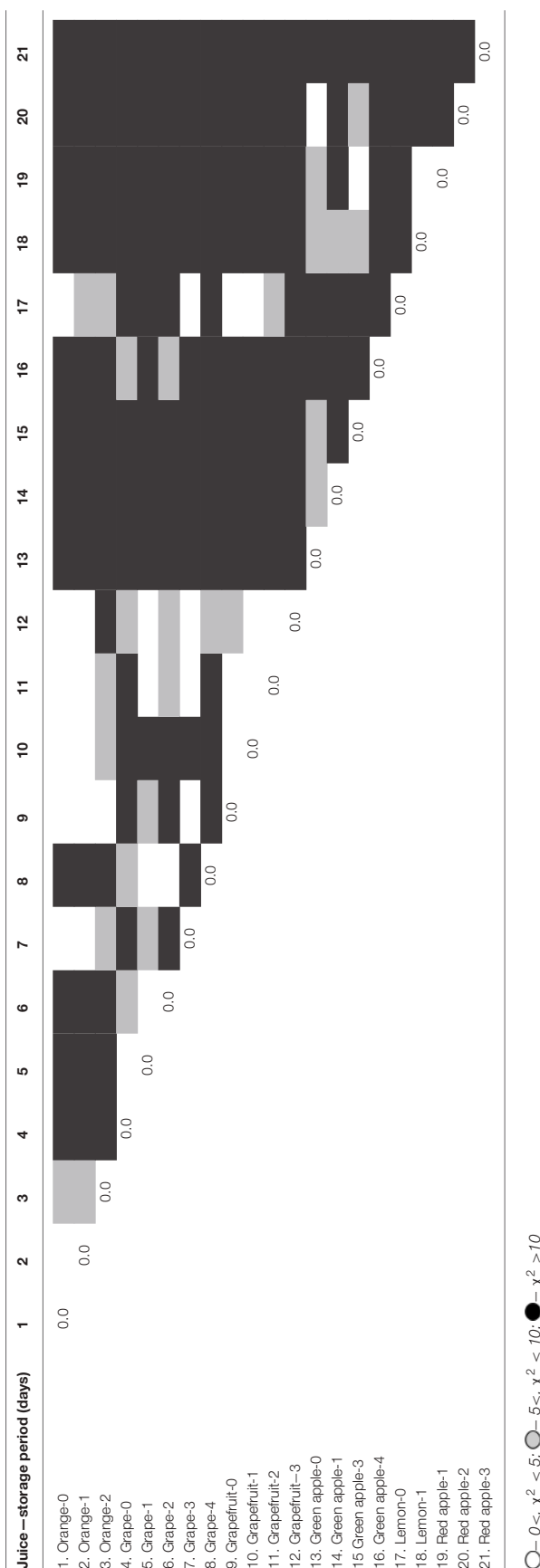
Extracts from dried apples were tested using ET consisting of  $\text{Ca}^{2+}$ ,  $\text{Na}^+$ ,  $\text{K}^+$ , cation- and anion-selective ISEs, Au voltammetric, and conductometric sensors (Kutyła-Olesiuk et al., 2013). The efficiency of qualitative and quantitative analysis was estimated by root mean squared error (RMSE) and parameters of correlation between real and PLS predicted samples. The 3D score plot obtained by PLS-DA for discrimination of fresh apples and dried ones is shown in Figure 4 for potentiometric ET. The recognition ability was estimated as percentage of correct prediction of the apple sample tested. The results obtained with potentiometric and hybrid ET showed similar sensitivity but the classification was reliable with the hybrid ET system.

Commercial sensor array based on seven field-effect transistors (FETs) with cross-selective membranes ( $\alpha$ -ASTREE, Alpha-M.O.S.) was successfully used for discrimination of beverages containing orange juice (Liu et al., 2012). The signals of the ET system were correlated with the results of reference methods. The significant parameters specifying brand of the drink were first determined by single-factor analysis of variance (ANOVA). Among them, amino acid nitrogen, reducing and non-reducing sugars, sugar-to-acid ratio, total acid, total solids, and total soluble sugar were considered. Six brands were classified by ET signal processing using a number of supervised and unsupervised methods [PCA, canonical discriminant analysis, cluster analysis, and soft independent modeling of class analogy (SIMCA)]. As an example, SIMCA plot of seven sensor signals related to different brands is shown in Figure 5. One could see, four brands (Kang, KangX, Tong, and Wa) located in the green quadrat region demonstrate high similarity. This corresponds to the PCA score that indicated two groups of similar brands classified in accordance with their physicochemical parameters.

e-Nose and ET systems were combined for discrimination of a wide number of Tunisian fruit juices (46 brands available in local market) (Haddi et al., 2014). e-Nose consisted of five commercially available MOS gas sensors and the ET of six potentiometric electrodes. The PCA showed that taken separately e-Nose and ET did not provide identification of each juice. Meanwhile its combination and the use of fuzzy ARTMAP neural nets resulted in satisfactory discrimination among samples tested except two juices.

In case of solid-contact ISEs based on polyaniline and thiocalix[4]arene derivatives, similar classification can be achieved by much lower number of sensors. Thus, the discrimination of six commercial apple juices was performed using nine sensors, three of which contained two thiocalix[4]arenes **2** and **3** and last three sensors only polyaniline (Evtugyn et al., 2010). The juices taken from 200 mL packages were diluted in 1:70 and 1:100 ratio and spiked with 0.1 and 1.0 mM  $\text{Fe}(\text{NO}_3)_3$ . Thus, the set of independent variables comprised of  $2 \times 2 \times 9 = 36$  points (signals of individual ISEs) for each juice tested. The classification in accordance with the brand name was performed using PCA. The explained variance by two first principal components was found to be 97.5% (78.8% for one  $\text{Fe}(\text{III})$  concentration and two dilutions of the juices, Figure 6).

Simultaneous determination of total antioxidant capacity confirmed the hypothesis about predominant influence of antioxidants on the sensor signals. The difference in the response toward certain juices can be referred to the minerals and vitamins added to natural fruits by producers and/or to rather small portion of natural juice in beverage tested (25%). Contrary to that, pH of the samples did not significantly affect the discrimination, probably due to rather narrow range of its variation (pH 3–4). The possibility of discrimination of apple juices and their brand name prediction were considered by linear discriminant analysis (LDA) showed 73–100% of true predictions depending on the initial learning sets.

**TABLE 1** |  $\chi^2$  statistics of freshly pressed juices (95% significance level, critical value for three sensors is 7.8 assuming normal data distribution).

The same approach was used for the discrimination of extended set of fruit juices (apple, lemon, grapefruit, grape, and orange) and fruit containing beverages (35 samples in total) that involved commercial packages and freshly pressed juices. Several samples pressed from fruits were then stored for different time (1–4 days) to estimate changes in their quality. The PCA showed satisfactory separation of all the samples by testing two juice dilutions with two different Fe (III) concentrations. Separation of samples by the ET signals was estimated with  $\chi^2$  statistics. As an example, **Table 1** represents comparison of various freshly pressed juices with different storage period. Black cells of the table correspond to full separation of appropriate juices, gray cells to their partial separation and white cells to fully concurrent classes on PCA scores.

Most of the samples are fully separated, the concurrent samples belong to congenial fruits (orange and grapefruit). It is interesting to note that the  $\chi^2$  statistics indicated different stability of the juices during the storage period. Only grapefruit and lemon kept separation of their ET signals during more than 1 day storage. This might be related to rather high acidity of these samples against other juices tested. Reduced number of parameters, i.e., application of one dilution or of one Fe(III) concentration, can be applicable for discrimination of a smaller number of samples based on simpler rules, e.g., separation of two known brands of commercial grape juices or separation of 100% fruits juices from fruit containing beverages.

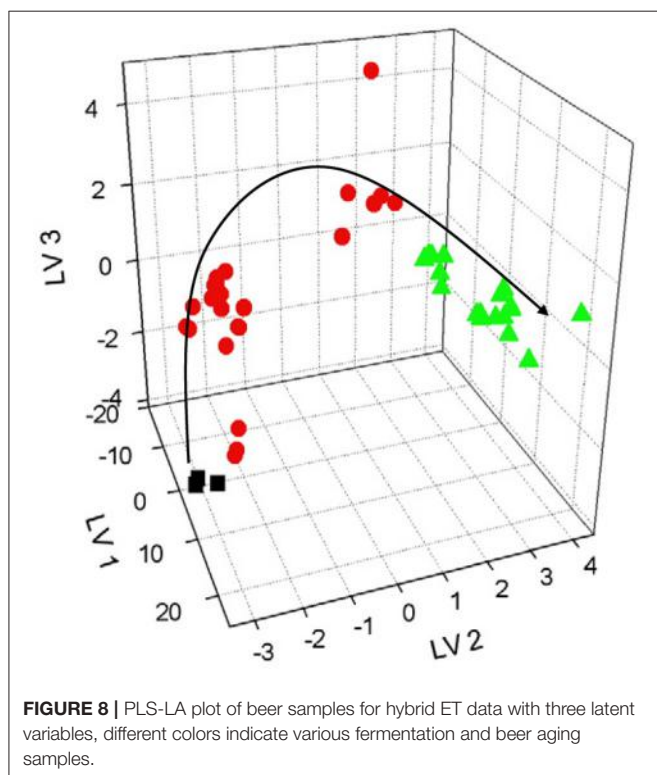
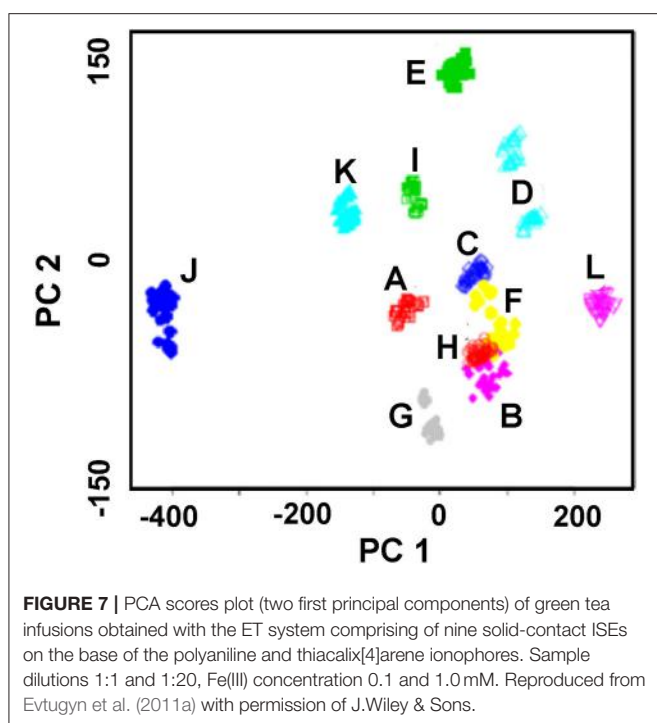
## TEA INFUSIONS

Tea is rich with antioxidants which availability and influence on taste depend on fermentation technology, tea origination, and extraction conditions. Potentiometric ETs based on PVC and polyurethane membranes were applied to distinguish black and green tea and coffee (Lvova et al., 2003). Similar plasticized membranes have been employed in the assembly of cation- and anion-selective ISEs combined together with commercial pH- and redox-sensitive electrodes in the ET system for differentiation of black and herbal tea based on PCA method (Cuartero et al., 2015).

Twenty-two potentiometric sensors including 10 anion-selective, 8 cation-selective ISEs with PVC membranes, 3 sensors made of chalcogenide glass with redox sensitivity and one standard pH electrode were applied for classification of 34 black tea samples available in Russia and Spain markets (Khaydukova et al., 2015).

Alpha M.O.S. system with six potentiometric semiconductor sensors was used for evaluation of taste sensory attributes (heavy flavor, thick flavor, sweet flavor, fresh flavor, mellow flavor, astringency, tenderness, stale flavor, purity, and fired flavor) against sensory profile test of 8 samples of black and 8 samples of green tea from different China provinces (He et al., 2009).

The use of solid-contact ISEs based on polyaniline and thiocalix[4]arene ionophores provides discrimination of green tea infusions with a small number of samples/measurements (Evtugyn et al., 2011b). The multisensor system comprised of nine screen-printed electrodes covered with polyaniline



and two thiacycl[4]arenes **2** and **3**. The dilution optimal for discrimination was much smaller than that of fruit juices described above because of much lower content of antioxidants and complexing agents in the tea infusions. The sample set involved eleven natural and flavored green tea brands and

one of oolong tea, which antioxidant capacity determined by coulometry varied from 0.45 to 5.89 Q/100 mL. **Figure 7** shows PCA score plot obtained with two dilutions and two Fe(III) concentrations. The explained variance differed from 80 to 97% for various initial data sets. No significant influence of antioxidant capacity on discrimination results was found. Probably, complexation of Fe(III) ions and direct effect of polyphenols on the polyaniline could mask such a dependency.

The LDA confirmed high efficiency of discrimination resulted in 100% prediction of the green tea brand both for the full data set (two dilutions, two concentrations of Fe(III) ions and nine sensors, 36 signals per one sample) and their reduced replicas (one dilution and one Fe(III) concentration, nine signals per one tea infusion).

## ALCOHOLIC DRINKS

Wine and beer are most frequently tested by potentiometric ETs based on various principles of signal generation (Zeravik et al., 2009). Many components influencing odor, taste, flavor and other properties directly affecting the cost of wine can alter the signals of individual sensors and hence provide discrimination of wines in accordance with qualitative and quantitative criteria. Thus, 20 samples of Barbera d'Asti and in 36 samples of Gutturnio wine were discriminated in accordance with their denomination and vintage by the ET of 23 potentiometric sensors (Legin et al., 2003). Simultaneously, quantitative parameters, e.g., total and volatile acidity, total polyphenols, glycerol, pH, ethanol, and tartaric acid concentrations were determined using multivariate calibration. Similar research has been performed with white wines using solid-contact sensors with PVC membranes containing metalloporphyrins (Verelli et al., 2007). The ET was used for classification of wines in accordance with their origin and content of some components, e.g., malic and lactic acids, SO<sub>2</sub>, polyphenols etc. ET assembled from similar sensors were applied for assessment of Madeira (Rudnitskaya et al., 2012) and New Zealand (Kirsanov et al., 2012) wines in accordance with their age (maturation). The capabilities of traditional potentiometric ET systems were extended by comparison of the results with the HPLC analysis (Rudnitskaya et al., 2010), FTIR spectroscopy (Costa et al., 2015) and humid electronic nose (Gil-Sánchez et al., 2011). Most of the ETs described offer opportunities for the wine classification and determination of common organic species like organic acids, polyphenols, other antioxidants etc. Besides, specific parameters of wine quality like bitterness (Rudnitskaya et al., 2010) or astringency (Costa et al., 2015) can be taken into account. The ETs make it possible to monitor technological processes (maceration with oak chips; Rudnitskaya et al., 2017) or wine spoilage (Gil-Sánchez et al., 2011).

Beer is another subject of the ET application mostly directed to the discrimination of certain types (light and dark beer) or brands. The discrimination is performed mostly with ISEs involving plasticized PVC membranes sensitive to inorganic cations (Na<sup>+</sup>/K<sup>+</sup>, Ca<sup>2+</sup>, NH<sub>4</sub><sup>+</sup>) and anions (H<sub>2</sub>PO<sub>4</sub><sup>-</sup>, Cl<sup>-</sup>). Cation- and anion-selective membranes containing lipophilic salt but not ionophore can be added. Contrary to wine testing,

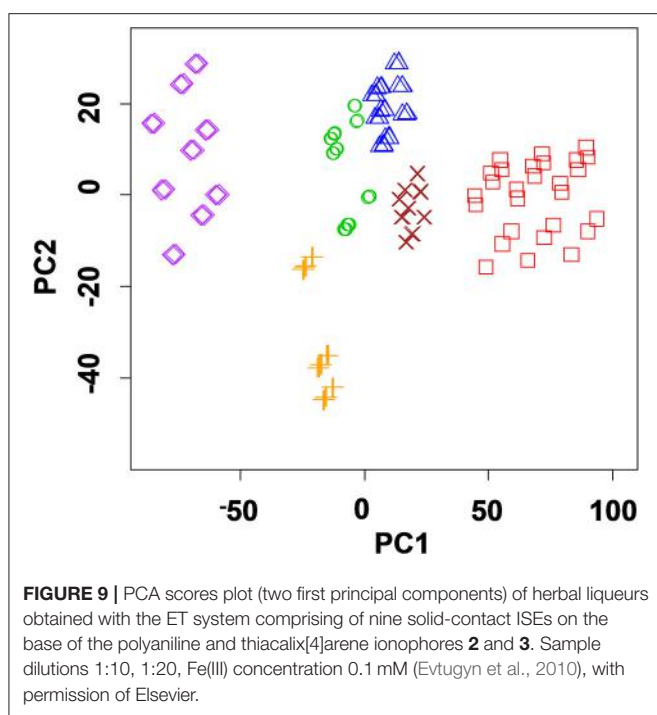


**FIGURE 9** | PCA scores plot (two first principal components) of herbal liqueurs obtained with the ET system comprising of nine solid-contact ISEs on the base of the polyaniline and thiocalix[4]arene ionophores **2** and **3**. Sample dilutions 1:10, 1:20, Fe(III) concentration 0.1 mM (Evtugyn et al., 2010), with permission of Elsevier.

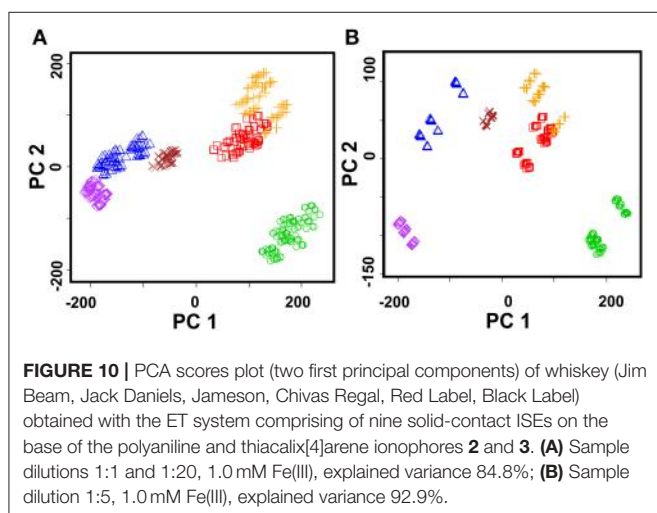


**FIGURE 10** | PCA scores plot (two first principal components) of whiskey (Jim Beam, Jack Daniels, Jameson, Chivas Regal, Red Label, Black Label) obtained with the ET system comprising of nine solid-contact ISEs on the base of the polyaniline and thiocalix[4]arene ionophores **2** and **3**. **(A)** Sample dilutions 1:1 and 1:20, 1.0 mM Fe(III), explained variance 84.8%; **(B)** Sample dilution 1:5, 1.0 mM Fe(III), explained variance 92.9%.

the response of such ISEs is not attributed to specific beer components but is indirectly influenced by lipophilic and surface-active species present in the samples. On the one hand, this makes the ET approach universal and applicable to a wide variety of beer sorts. On the other hand, such mechanism assumes quasi-reversible response and sometimes leaves room for artifacts and uncertainty in interpretation of the results.

Solid-contact ISEs with planar Au electrodes covered with the PVC membranes have been used for flow-through assessment of beer originated from different manufacture lots (Ciosek and Wróblewski, 2006). The combination of PLS and artificial neural networks resulted in 83% of true predictions.

Similar potentiometric ET combined with voltammetric sensor has been applied for characterization of beer fermentation (Kutyla-Olesiuk et al., 2012). The results obtained were processed using PLS and PLS-DA. Both methods allow tracing changes of chemical images linked with overall composition of the fermentation media leading to discrimination of individual samples and estimation of fermentation and maturation time. **Figure 8** shows typical chemical image obtained by data processing. Graphs show distinction between samples different in fermentation and aging periods. The discrimination ability was assessed the F factor. It describes the variance between different classes and variances between particular classes. For three latent variables, the variances can be expressed as Euclidean distances in the pattern space (8).

$$F = \frac{\frac{\sum_{i=1}^k \sqrt{(x - x_{ji})^2 + (y - y_{ji})^2 + (z - z_{ji})^2}}{k - 1}}{\frac{\sum_{i=1}^k \sum_{j=1}^{n_i} \sqrt{(x - x_{ji})^2 + (y - y_{ji})^2 + (z - z_{ji})^2}}{\sum_{i=1}^k (n_i - k)}} \quad (8)$$

Here  $k$  is the number of a class,  $i$  is the number of sample,  $j$  is the number of sample in  $i$ -th class,  $n$  is the number of samples in  $i$ -th class,  $x$ ,  $y$ , and  $z$  are sensor response for  $j$ -th sample in  $i$ -th class,  $x_{ji}$ ,  $y_{ji}$ , and  $z_{ji}$  are the mean values of sensor response for samples between different classes,  $x_i$ ,  $y_i$ , and  $z_i$  are mean value variances in particular class. Increasing F factor indicates bigger difference between classes. The hybrid ET showed three-fold decrease of the RMSE value against potentiometric ET.

The ET comprising of 14 ISEs with plasticized PVC and chalcogenide glass membranes was utilized for discrimination of Belgian and Dutch beers (Polshin et al., 2010). Correlation between the signals of individual sensors and several beer parameters (fermentation degree, alcohol content, pH, bitterness, color, polyphenol, and CO<sub>2</sub> content) was established and bitterness of real beer brands evaluated using PCA and canonic correlation analysis.

Most of the ET described consist of the ISEs with PVC membranes. New approaches to assembling of the multisensors have been appeared in the last years. Thus, planar microelectrodes with silver trackers have been produced from Whatman™ paper and then covered with PVC films containing various ionophores (Neru and Kubota, 2016). The discrimination of wine and beer was performed by measuring Ca/Mg and K/Na amounts together with total cation and anion concentrations and some inorganic anions present in the samples. The electrodes were impregnated in the sample to minimize the volume required for measurement. The classification was performed with PCA and multivariate calibration with principal component regression and K-nearest neighbors (KNN). Besides wine classified by different varieties of grape, the beer samples were tested by their brand and type. The ET proposed makes it possible to estimate

pH, alcohol content, carbohydrate, and caramel dye as well as fermentation type of beer.

Less attention has been paid to strong drinks like vodka or eaux-de-vie. Ethanol content was determined with the ISEs based on plasticized membranes with tetraphenylporphyrin complexes of Ni, Co, Mn, and Fe (Lvova et al., 2006b). PCA and SIMCA were applied for the discrimination of alcoholic spirits and their classification. The ET showed sensitivity toward ethanol among other aliphatic alcohols and made it possible to distinguish various beer and wine sorts.

Chalcogenide glass and plasticized anion- and cation-selective membrane electrodes have been specified for the assessment of ethanol and hot drinks (Legin et al., 2005). The ET signals were processed using PCA and PLS regression. The following samples were successfully discriminated: synthetic and alimentary grain ethanol in different degrees of purification, vodka from various Russian regions (12 samples), and cognac (six samples).

In case of solid-contact ISEs with polyaniline and thiocalix[4]arene ionophores, discrimination of alcoholic drinks can be achieved. This was first shown by discrimination of herbal liqueurs containing 28–40% of ethanol and 10–20% of sugar (Evtugyn et al., 2010). Measurements were performed with 1:1 and 1:20 dilution of the samples in the presence of 1.0 and 10 mM Fe(III) ions. Recognition of six liqueurs illustrated by PCA score plot is shown in **Figure 9**. The LDA provided 82% prediction in case of nine measurements (one dilution with one Fe(III) ion concentration) and 92% for 18 measurements (two dilutions with one Fe(III) ion concentration).

Fifteen brands of beer were classified using ET based on screen-printed electrodes covered with polyaniline and three thiocalix[4]arene receptors with long-chain alkyl- ( $-C_{18}H_{37}$ ), amino- and pyrrolidide groups in *1,3-alternate* conformation (Stoikova et al., 2014). The selection of ionophores among macrocycle derivatives was made by ranking individual sensors by prediction efficiency in accordance with the beer brands performed with LDA. Not <70% of successful prediction were obtained with the ionophores tested. In case of the above three thiocalix[4]arenes, the efficiency of the prediction with the ET system reached 100%. Simplified multisensor system with two electrodes allows reliable distinguishing between light and dark beer sorts. In this case, screen-printed carbon electrodes can be used as transducers instead of glassy carbon electrodes.

Various hot drinks were successfully discriminated using the ET system with solid-contact sensors covered with polyaniline and thiocalix[4]arenes **2** and **3** (Evtugyn et al., 2011a). The ET system was applied for discrimination of four brands of vodka from local Russian and EU distilleries, two brands of cognac, and six brands of whiskey. Besides, 40% grain ethanol of various quality was added as a model of vodka falsifications. The efficiency of discrimination was considered using PCA for different number of sample dilutions. Best results were obtained with two dilutions and one or two concentrations of the Fe(III) ions (18 and 36 points in the data set). The explained variance reaches 87–90%. Increasing number of dilutions to 3–5 decreased the explained variance of the PCA score to 70%. Similar results were obtained for particular hot drinks.

As an example, **Figure 10** shows the PCA score plot for whiskey samples.

The examples described above do not exhaust the application of potentiometric ET systems for foodstuffs discrimination based on their antioxidant properties. Thus, fermentation processes classified by potentiometric and hybrid ET systems are summarized and discussed in (Ciosek and Wróblewski, 2015). Food analysis with artificial senses based on different principles with particular emphasis to data mining protocols is considered in (Sliwinska et al., 2014). New approaches to the use of biochemical sensors for ET discrimination of complex media and data mining systems commonly used in such works are carefully considered in Cetó et al. (2016).

## CONCLUSION

Solid-contact ISEs with the macrocyclic ionophores offer broad opportunities for assessment of various foodstuffs on the base of antioxidant content and for their discrimination by brand name or origination. Such ET applications coincide well with previously published examples obtained with other potentiometric multisensors. Meanwhile the ISEs based on combination of polyaniline and macrocyclic receptors exhibit specific properties that affect the behavior of appropriate ET. First, the use of polyaniline as intermediate layer with the electron-to-ion conductivity increases the influence of the sample acidity on the signals especially in neutral and weak acidic media that is typical for many refreshments, fruit juices and vegetable extracts. The pH sensitivity of polyaniline is partially suppressed by the thiocalix[4]arene based ionophores deposited on its surface without any plastic support. This results in smoothen pH dependency of the electrode potential and of the potentiometric selectivity of sensor. Then, most of the sensors described do not assume the use of lipophilic salts and plasticizer due to rather higher plasticity of the macrocycle coverage. This simplifies assembling the ISE by casting the solution of the thiocalix[4]arene in organic solvent and its drying at ambient temperature. The response of such electrodes retains its reversibility in the series of measurements with alternating analyte concentrations. However, the formation of rather thick films of thiocalix[4]arene results in a relatively slow response of about 20 s for 95% shift of the potential.

The idea to use solid-contact potentiometric sensors based on polyaniline and thiocalix[4]arene ionophores assumes the detection of the polyaniline redox status. The interaction of the Fe(III) ions with thiocalix[4]arenes affects their surface concentration and participation in the partial oxidation of polyaniline. All the factors influencing the surface reactions change the stationary potential of the sensors. Such processes can involve:

- Direct influence of the antioxidants on the redox potential of the Fe(III)-polyaniline system;
- Changes in the pH and buffer capacity caused by the sample addition and their influence on the redox equilibria of polyaniline and hydrolytic stability of Fe(III) ions;

- Complexation of the Fe(III) ions with the sample components, e.g., citrates or polyphenolics and flavor additives;
- Adsorption of the lipophilic species on the ISE surface promoted by thiocalix[4]arene bearing long-chain alkyl radicals in the substituents.

Relative contribution of the factors mentioned depends on the analyte and discrimination parameters. Thus, in case of the fruit juices, the influence of antioxidants dominates. This is confirmed by simultaneous measurements of the antioxidant capacity of the samples. For tea infusions, higher importance of complexing agents was mentioned. Regarding the pH and buffer capacity influence, their deviation is often rather narrow within the set of the samples of the same origin, and this complicates assessment of their influence.

The application of the ET systems described requires preliminary study on the optimal number of sensors, sample dilutions, and Fe(III) ion concentration. Although such a choice might be a subject of personal preferences of an analyst, it was established for many experiments among various beverages and foodstuffs that higher difference between the dilutions improves the quality of discrimination. The absolute value of dilution varied from 1:1 to 1:200 depending on the total content of oxidizable species. The latter parameter can be expressed by antioxidant capacity (activity) determined by conventional techniques including coulometry with electrogenerated bromine.

The necessity of the Fe(III) ions for amplifying the signal is related to the S-shape of its calibration curve and hence high sensitivity of the ISE potential to the minor changes in the concentration and accessibility of reactants. In case of beer discrimination, the experiments confirmed the possibility for separation of light and dark beer types with no Fe(III) addition. The same conclusion has been made later for soya sauce discrimination (not published). Besides, similar efficiency of separation was shown for apple juices of different manufacturers with  $\text{Ag}^+$  ions. However, the results were sensitive toward content of chlorides and some other anions able to form insoluble salts with  $\text{Ag}^+$  cation.

Simple tuning of the sensor performance is another advantage of the solid-contact sensors described. Increasing amounts of polyaniline deposited by electropolymerization prior to thiocalixarene deposition as well as anodic conditioning of the electrodes improved the redox reversibility and the pH sensitivity of the signal. The slopes of appropriate calibration curves easily control the quality of the modifying layer prior to their application in the ET system. The selectivity of thiocalix[4]arenes in the assembly of the ISEs can be also modified by implementation of appropriate functional groups in the macrocycle moiety or by specifying its configuration. Although no correlation between the steric factors (configuration of thiocalix[4]arenes) and selectivity of the cation binding were found, from the basic point of view, *1,3-alternate* and *partial cone* should have advantage over *cone* configuration due to higher accessibility of the terminal groups and less dependence of recognition on the position

of the ionophore molecule on the underlaying surface. The prospects of ET systems are expected to be extended after implementation of pillar[5]arene ionophores that are more sensitive to lipophilic properties of the sample components and factors affecting hydrogen bonds and self-aggregation of the macrocycle molecules.

Most of the results reviewed were obtained with only two derivatives **2** and **3**, which provided cross-selectivity sufficient for the ET operation. Meanwhile other thiocalixarene derivatives were compared in beer testing. Among them, carboxylated and aminated thiocalix[4]arenes with lowest selectivity toward inorganic cations and acidic species were used but not proved to improve the performance of the ET system. Ranking individual sensors in accordance with the efficiency of prediction estimated by PCA or LDA is a promising way to optimize the set of ISEs combined in the ET system. This problem is often underestimated in other multisensors based on conventional ISEs but directly influences the efficiency of application and final cost of the analysis/assessment.

Summarizing the results of assembling of solid-contact sensors with thiocalix[4]arene ionophores and of their application in the ET systems, it can be concluded that this is a cost- and labor-effective way to develop the ETs intended for preliminary assessment of the quality of many products reach with antioxidants and organic acids and demanded in the food industry, environmental monitoring and medicine.

## AUTHOR CONTRIBUTIONS

GE worked under the concept of electronic tongue based on discrimination of various species on the base of their antioxidant properties and elaborated protocols for the assessment of foodstuffs and beverages in the presence of Fe(III) ions. He also performed discrimination of alcoholic drinks; MS performed experiments concerning individual potentiometric selectivity of the ISEs with thiocalix[4]arene and pillar[5]arene ionophores. Besides, he worked with the screen-printed electrodes as transducers and adapted the protocol of polyaniline polymerization to reach reversibility of its characteristics; SB has assembled solid-contact sensors with polyaniline and thiocalix[4]arene ionophores, investigated their operational and analytical characteristics and established optimal conditions for the determination of individual metals and discrimination of the metals in their binary mixtures; IS was responsible for the synthesis of substituted thiocalix[4]arenes and pillar[5]arene and their physicochemical characterization; RS conducted experiments with fruit juices and beer using electronic tongue system based on polyaniline and thiocalix[4]arenes.

## ACKNOWLEDGMENTS

Financial support of Russian Science Foundation (grant No 17-13-01208) is gratefully acknowledged.

## REFERENCES

- Ali, M. B., Chabanne, R. B., Vocanson, F., Dridi, C., Jaffrezic, N., and Lamartine, R. (2006). Comparison study of evaporated thiocalix[4]arene thin films on gold substrates as copper ion sensing. *Thin Solid Films* 495, 368–371. doi: 10.1016/j.tsf.2005.08.238
- Andre, R. S., Chen, J., Kwak, D., Correa, D. S., Mattoso, L. H. C., and Lei, Y. (2017). A flexible and disposable poly(sodium 4-styrenesulfonate)/polyaniline coated glass microfiber paper for sensitive and selective detection of ammonia at room temperature. *Synth. Metals* 233, 22–27. doi: 10.1016/j.synthmet.2017.08.005
- Baker, C. A., Huang, X., Nelson, W., and Kaner, R. B. (2017). Polyaniline nanofibers: broadening applications for conducting polymers. *Chem. Soc. Rev.* 46, 1510–1525. doi: 10.1039/C6CS00555A
- Bavastrello, V., Stura, E., Carrara, S., Erokhin, V., and Nicolini, C. (2004). Poly(2,5-dimethylaniline) - MWNTs nanocomposite: a new material for conductometric acid vapours sensor. *Sens. Actuators B Chem.* 98, 247–253. doi: 10.1016/j.snb.2003.10.020
- Benzie, I. F. F., and Strain, J. J. (1996). The ferric reducing ability of plasma (FRAP) as a measure of “antioxidant power”: the FRAP assay. *Anal. Biochem.* 239, 70–76.
- Bereczki, R., Csokai, V., Grün, A., Bitter, I., and Tóth, K. (2006). Crown bridged thiocalix[4]arenes as cesium-selective ionophores in solvent polymeric membrane electrodes. *Anal. Chim. Acta* 569, 42–49. doi: 10.1016/j.aca.2006.03.039
- Berker, K. I., Güçlü, K., Demirata, I. T., and Apak, R. (2010). Total antioxidant capacity assay using optimized ferricyanide/Prussian blue method. *Food Anal. Methods* 3, 154–168. doi: 10.1007/s12161-009-9117-9
- Beullens, K., Mészáros, P., Vermeir, S., Kirsanov, D., Legin, A., Buysens, S., et al. (2008). Analysis of tomato taste using two types of electronic tongues. *Sens. Actuators B Chem.* 131, 10–17. doi: 10.1016/j.snb.2007.12.024
- Boeva, Z. A., Milakin, K. A., Pesonen, P., Ozerin, A. N., Sergeyev, V. G., and Lindfors, T. (2014). Dispersible composites of exfoliated graphite and polyaniline with improved electrochemical behaviour for solid-state chemical sensor applications. *RSC Adv.* 4, 46340–46350. doi: 10.1039/C4RA08362H
- Bratov, A., Abramova, N., and Ipatov, A. (2010). Recent trends in potentiometric sensor arrays - A review. *Anal. Chim. Acta* 678, 149–159. doi: 10.1016/j.aca.2010.08.035
- Cetó, X., Voelcker, N. H., and Prieto-Simón, B. (2016). Bioelectronic tongues: New trends and applications in water and food analysis. *Biosens. Bioelectron.* 79, 608–626. doi: 10.1016/j.bios.2015.12.075
- Ciosek, P., Maminska, R., Dybko, A., and Wróblewski, W. (2007). Potentiometric electronic tongue based on integrated array of microelectrodes. *Sens. Actuators B Chem.* 127, 8–14. doi: 10.1016/j.snb.2007.07.015
- Ciosek, P., and Wróblewski, W. (2006). The recognition of beer with flow-through sensor array based on miniaturized solid-state electrodes. *Talanta* 69, 1156–1161. doi: 10.1016/j.talanta.2005.12.029
- Ciosek, P., and Wróblewski, W. (2015). Potentiometric and hybrid electronic tongues for bioprocess monitoring – an overview. *Anal. Methods* 7, 3958–3966. doi: 10.1039/C5AY00445D
- Cirić-Marjanović, G. (2013). Recent advances in polyaniline research: polymerization mechanisms, structural aspects, properties and applications. *Synth. Metals* 177, 1–47. doi: 10.1016/j.synthmet.2013.06.004
- Colenutt, B. A., and Trenchard, P. J. (1985). Ion chromatography and its application to environmental analysis: a review. *Environ. Pollut. Ser. B Chem. Phys.* 10, 77–96. doi: 10.1016/0143-148X(85)90007-2
- Costa, A. M. S., Sobral, M. M. C., Delgadillo, I., Cerdeira, A., and Rudnitskaya, A. (2015). Astringency quantification in wine: comparison of the electronic tongue and FT-MIR spectroscopy. *Sens. Actuators B Chem.* 207, 1095–1103. doi: 10.1016/j.snb.2014.10.052
- Cuartero, M., Carretero, A., García, M. S., and Ortúño, J. A. (2015). New potentiometric electronic tongue for analysing teas and infusions. *Electroanalysis* 27, 782–788. doi: 10.1002/elan.201400586
- Cuartero, M., Ruiz, A., Oliva, D. J., and Ortúño, J. A. (2017). Multianalyte detection using potentiometric ionophore-based ion-selective electrodes. *Sens. Actuators B Chem.* 243, 144–151. doi: 10.1016/j.snb.2016.11.129
- Dhand, C., Das, M., Datta, M., and Malhotra, B. D. (2011). Recent advances in polyaniline based biosensors. *Biosens. Bioelectron.* 26, 2811–2821. doi: 10.1016/j.bios.2010.10.017
- Dias, L. G., Peres, A. M., Barcelos, T. P., Morais, J. S., and Machado, A. A. S. C. (2011). Semi-quantitative and quantitative analysis of soft drinks using an electronic tongue. *Sens. Actuators B Chem.* 154, 111–118. doi: 10.1016/j.snb.2010.01.005
- Di Natale, C., Davide, F., Brunink, J. A. J., D'Amico, A., Vlasov, Y. u., G., Legin, A. V., and Rudnitskaya, A. M. (1996). Multicomponent analysis of heavy metal cations and inorganic anions in liquids by a non-selective chalcogenide glass sensor array. *Sens. Actuators B Chem.* 34, 539–542. doi: 10.1016/S0925-4005(96)01925-9
- Di Natale, C., Macagnano, A., Davide, F., D'Amico, A., Legin, A., Vlasov, Y. u., et al. (1997). Multicomponent analysis on polluted waters by means of an electronic tongue. *Sens. Actuators B Chem.* 44, 423–428. doi: 10.1016/S0925-4005(97)00169-X
- Escuder-Gilabert, L., and Peris, M. (2010). Review: highlights in recent applications of electronic tongues in food analysis. *Anal. Chim. Acta* 665, 15–25. doi: 10.1016/j.aca.2010.03.017
- Evtugyn, G. A., Belyakova, S. V., Shamagsumova, R. V., Saveliev, A. A., Ivanov, A. N., Stoikova, E. E., et al. (2010). Discrimination of apple juice and herbal liqueur brands with solid-state electrodes covered with polyaniline and thiocalixarenes. *Talanta* 82, 613–619. doi: 10.1016/j.talanta.2010.05.016
- Evtugyn, G. A., Dolgova, N. N., Belyakova, S. V., Stoikova, E. E., Ivanov, A. N., Stoikov, I. I., et al. (2011a). Solid-contact potentiometric sensors for discrimination of hot spirits. *Chem. Sens.* 1:6.
- Evtugyn, G. A., Shamagsumova, R. V., Stoikova, E. E., Sitzdikov, R. R., Stoikov, I. I., Budnikov, H. C., et al. (2011b). Potentiometric sensors based on polyaniline and thiocalixarenes for green tea discrimination. *Electroanalysis* 23, 1081–1088. doi: 10.1002/elan.201000586
- Evtugyn, G. A., and Stoikov, I. I. (2016). *Electrochemical (bio)Sensors Based on Supramolecular Structures (in Russian)*. Kazan University, Kazan.
- Evtugyn, G. A., Stoikov, I. I., Beljyakova, S. V., Shamagsumova, R. V., Stoikova, E. E., Zhukov, A., et al. (2007). Ag selective electrode based on glassy carbon electrode covered with polyaniline and thiocalixarene as neutral carrier. *Talanta* 71, 1720–1727. doi: 10.1016/j.talanta.2006.08.004
- Evtugyn, G. A., Stoikov, I. I., Belyakova, S. V., Stoikova, E. E., Shamagsumova, R. V., Zhukov, A., et al. (2008). Selectivity of solid-contact Ag potentiometric sensors based on thiocalix[4]arene derivatives. *Talanta* 76, 441–447. doi: 10.1016/j.talanta.2008.03.029
- Fratoddi, F., Venditti, I., Cametti, C., and Russo, M. V. (2015). Chemiresistive polyaniline-based gas sensors: a mini review. *Sens. Actuators B Chem.* 220, 534–548. doi: 10.1016/j.snb.2015.05.107
- Gil-Sánchez, L., Soto, J., Martínez-Máñez, R., García-Breijo, E., Ibáñez, J., and Llobet, E. (2011). A novel humid electronic nose combined with an electronic tongue for assessing deterioration of wine. *Sens. Actuators A Phys.* 171, 152–158. doi: 10.1016/j.sna.2011.08.006
- Gupta, V. K., Jain, A. K., Al Khayat, M., Bhargava, S. K., and Raisoni, J. R. (2008). Electroanalytical studies on cobalt(II) selective potentiometric sensor based on bridge modified calixarene in poly(vinyl chloride). *Electrochim. Acta* 53, 5409–5414. doi: 10.1016/j.electacta.2008.02.085
- Gutiérrez, M., Alegret, S., and del Valle, M. (2007). Potentiometric bioelectronic tongue for the analysis of urea and alkaline ions in clinical samples. *Biosens. Bioelectron.* 22, 2171–2178. doi: 10.1016/j.bios.2006.10.007
- Ha, D., Sun, Q., Su, K., Wan, H., Li, H., Xu, N., et al. (2015). Recent achievements in electronic tongue and bioelectronics tongue as taste sensor. *Sens. Actuators B Chem.* 207, 1136–1146. doi: 10.1016/j.snb.2014.09.077
- Haddi, Z., Mabrouk, S., Bougrini, M., Tahri, K., Sghaier, K., Barhoumi, H., et al. (2014). E-Nose and e-Tongue combination for improved recognition of fruit juice samples. *Food Chem.* 150, 246–253. doi: 10.1016/j.foodchem.2013.10.105
- Hao, Q., Lei, W., Xia, X., Yan, Z., Yang, X., Lu, L., et al. (2010). Exchange of counter anions in electropolymerized polyaniline films. *Electrochim. Acta* 55, 632–640. doi: 10.1016/j.electacta.2009.09.018
- He, W., Hua, X., Zhao, L., Liao, X., Zhang, Y., Zhang, M., et al. (2009). Evaluation of Chinese tea by the electronic tongue: correlation with sensory properties and classification according to geographical origin and grade level. *Food Res. Intern.* 42, 1462–1467. doi: 10.1016/j.foodres.2009.08.008
- Ipatov, A., Moreno, L., Abramova, N., Bratov, A., Vlasov, Y. u., and Dominges, K. (2009). “Electronic tongue” integrated sensor system based on an array of ion-selective field-effect transistors for multicomponent analysis of liquid media. *Russ. J. Appl. Chem.* 82, 1384–1389. doi: 10.1134/S1070427209080126

- Jaworska, E., Lewandowski, W., Mieczkowski, J., Maksymiuk, K., and Michalska, A. (2012). Critical assessment of graphene as ion-to-electron transducer for all-solid-state potentiometric sensors. *Talanta* 97, 414–419. doi: 10.1016/j.talanta.2012.04.054
- Jaymand, M. (2013). Recent progress in chemical modification of polyaniline. *Progr. Polym. Sci.* 38, 12387–11306. doi: 10.1016/j.progpolymsci.2013.05.015
- Karami, H., and Mousavi, M. F. (2004). Dodecyl benzene sulfonate anion-selective electrode based on polyaniline-coated electrode. *Talanta* 63, 743–749. doi: 10.1016/j.talanta.2003.12.025
- Karyakin, A., Vuki, M., Lukachova, L. V., Karyakina, E. E., Orlov, A. V., Karpachova, G. P., et al. (1999). Processible polyaniline as an advanced potentiometric pH transducer. Application to biosensors. *Anal. Chem.* 71, 2534–2540. doi: 10.1021/ac981337a
- Khaydukova, M., Cetó, X., Kirsanov, D., del Valle, M., and Legin, A. (2015). A tool for general quality assessment of black tea - retail price prediction by an electronic tongue. *Food Anal. Methods* 8, 1088–1092. doi: 10.1007/s12161-014-9979-3
- Khrpoun, G. A., Volkova, E. A., Liseenkov, A. V., and Mikhelson, K. N. (2006). Nitrate-selective solid contact electrodes with poly(3-octylthiophene) and poly(aniline) as ion-to-electron transducers buffered with electron-ion exchanging resin. *Electroanalysis* 18, 1322–1328. doi: 10.1002/elan.200603532
- Kirsanov, D., Mednova, O., Vietoris, V., Kilmartin, P. A., and Legin, A. (2012). Towards reliable estimation of an “electronic tongue” predictive ability from PLS regression models in wine analysis. *Talanta* 90, 109–116. doi: 10.1016/j.talanta.2012.01.010
- Klöšekoj, J. (2016). Cupric ferricyanide reaction in solution for determination of reducing properties of plant antioxidants. *Food Anal. Methods* 9, 164–177. doi: 10.1007/s12161-015-0177-8
- Kraujalyte, V., Venskutonis, P. R., Pukalskas, A., Cesoniene, L., and Daubaras, R. (2015). Antioxidant properties, phenolic composition and potentiometric sensor array evaluation of commercial and new blueberry (*Vaccinium corymbosum*) and bog blueberry (*Vaccinium uliginosum*) genotypes. *Food Chem.* 188, 583–590. doi: 10.1016/j.foodchem.2015.05.031
- Kumar, A., Kumar, V., and Awasthi, K. (2018). Polyaniline-carbon nanotube composites: preparation methods, properties, and applications. *Polym. Plastic Technol. Eng.* 57, 70–97. doi: 10.1080/03602559.2017.1300817
- Kutyla-Olesiuk, A., Zaborowski, M., Prokaryn, P., and Ciosek, P. (2012). Monitoring of beer fermentation based on hybrid electronic tongue. *Bioelectrochemistry* 87, 104–113. doi: 10.1016/j.bioelechem.2012.01.003
- Kutyla-Olesiuk, O., Nowacka, M., Wesoly, M., and Ciosek, P. (2013). Evaluation of organoleptic and texture properties of dried apples by hybrid electronic tongue. *Sens. Actuators B Chem.* 187, 234–240. doi: 10.1016/j.snb.2012.10.133
- Legin, A., Rudnitskaya, A., Clapham, D., Seleznev, B., Lord, K., and Vlasov, Y. (2004). Electronic tongue for pharmaceutical analytics: quantification of tastes and masking effects. *Anal. Bioanal. Chem.* 380, 36–45. doi: 10.1007/s00216-004-2738-3
- Legin, A., Rudnitskaya, A., Lvova, L., Vlasov, Y., Di Natale, C., and D’Amico, A. (2003). Evaluation of Italian wine by the electronic tongue: recognition, quantitative analysis and correlation with human sensory perception. *Anal. Chim. Acta* 484, 33–44. doi: 10.1016/S0003-2670(03)00301-5
- Legin, A., Rudnitskaya, A., Seleznev, B., and Vlasov, Y. (2005). Electronic tongue for quality assessment of ethanol, vodka and eau-de-vie. *Anal. Chim. Acta* 534, 129–135. doi: 10.1016/j.aca.2004.11.027
- Lewenstam, A., Bobacka, J., and Ivaska, A. (1994). Mechanism of ionic and redox sensitivity of p-type conducting polymers: part 1. *Theor. J. Electroanal. Chem.* 368, 23–31. doi: 10.1016/0022-0728(93)03080-9
- Liu, M., Wang, J., Li, D., and Wang, M. (2012). Electronic tongue coupled with physicochemical analysis for the recognition of orange beverages. *J. Food Qual.* 35, 429–441. doi: 10.1111/jfq.12004
- Lorestani, F., Shahnavaz, Z., Nia, P. M., Alias, Y., and Manan, N. S. A. (2015). One-step preparation of silver-polyaniline nanotube composite for non-enzymatic hydrogen peroxide detection. *Appl. Surf. Sci.* 347, 816–823. doi: 10.1016/j.apsusc.2015.04.184
- Lukachova, L. V., Shkerin, E. A., Puganova, E. A., Karyakina, E. E., Kiseleva, S. G., Orlov, A. V., et al. (2003). Electroactivity of chemically synthesized polyaniline in neutral and alkaline aqueous solutions: role of self-doping and external doping. *J. Electroanal. Chem.* 544, 59–63. doi: 10.1016/S0022-0728(03)00065-2
- Luo, J., Jiang, S., Liu, R., Zhang, Y., and Liu, X. (2013). Synthesis of water dispersible polyaniline / poly(styrenesulfonic acid) modified graphene composite and its electrochemical properties. *Electrochim. Acta* 96, 103–109. doi: 10.1016/j.electacta.2013.02.072
- Lvova, L., Legin, A., Vlasov, Y., Cha, G. S., and Nam, H. (2003). Multicomponent analysis of Korean green tea by means of disposable all-solid-state potentiometric electronic tongue microsystem. *Sens. Actuators B Chem.* 95, 391–399. doi: 10.1016/S0925-4005(03)00445-3
- Lvova, L., Martinelli, E., Mazzone, E., Pede, A., Paolesse, R., Di Natale, C., et al. (2006a). Electronic tongue based on an array of metallic potentiometric sensors. *Talanta* 70, 833–839. doi: 10.1016/j.talanta.2006.02.014
- Lvova, L., Paolesse, R., Di Natale, C., and D’Amico, A. (2006b). Detection of alcohols in beverages: an application of porphyrin-based electronic tongue. *Sens. Actuators B Chem.* 118, 439–447. doi: 10.1016/j.snb.2006.04.044
- Mimendia, A., Gutiérrez, J. M., Leija, L., Hernández, P. R., Favari, L., Muñoz, R., et al. (2010). A review of the use of the potentiometric electronic tongue in the monitoring of environmental systems. *Environ. Model. Software* 25, 1023–1030. doi: 10.1016/j.envsoft.2009.12.003
- Sliwińska, M., Wiśniewska, P., Dymerski, T., Namieśnik, J., and Wardencki, W. (2014). Food analysis using artificial senses. *J. Agric. Food Chem.* 62, 1423–1448. doi: 10.1021/jf403215y
- Neru, E. W., and Kubota, L. T. (2016). Integrated, paper-based potentiometric electronic tongue for the analysis of beer and wine. *Anal. Chim. Acta* 918, 60–68. doi: 10.1016/j.aca.2016.03.004
- Omran, O. A., Elgendi, F. A., and Nafady, A. (2016). Fabrication and applications of potentiometric sensors based on *p*-*tert*-butylthiacalix[4]arene comprising two triazole rings ionophore for silver ion detection. *Int. J. Electrochem. Sci.* 11, 4729–4742. doi: 10.20964/2016.06.35
- Paolesse, R., Di Natale, C., Burgio, M., Martinelli, E., Mazzone, E., Palleschi, G., et al. (2003). Porphyrin-based array of cross-selective electrodes for analysis of liquid samples. *Sens. Actuators B Chem.* 95, 400–405. doi: 10.1016/S0925-4005(03)00534-3
- Peris, M., and Escuder-Gilabert, L. (2016). Electronic noses and tongues to assess food authenticity and adulteration. *Trends Food. Sci. Technol.* 58, 40–54. doi: 10.1016/j.tifs.2016.10.014
- Polshin, E., Rudnitskay, A., Kirsanov, D., Legin, A., Saison, D., Delvaux, F., et al. (2010). Electronic tongue as a screening tool for rapid analysis of beer. *Talanta* 81, 88–94. doi: 10.1016/j.talanta.2009.11.041
- Rudnitskaya, A., Nieuwoudt, H. H., Muller, N., Legin, A., du Toit, M., and Bauer, F. F. (2010). Instrumental measurement of bitter taste in red wine using an electronic tongue. *Anal. Bioanal. Chem.* 397, 3051–3060. doi: 10.1007/s00216-010-3885-3
- Rudnitskaya, A., Kirsanov, D., Legin, A., Beullens, K., Lammertyn, J., Nicola, B. M., et al. (2006). Analysis of apples varieties – comparison of electronic tongue with different analytical techniques. *Sens. Actuators B Chem.* 116, 23–28. doi: 10.1016/j.snb.2005.11.069
- Rudnitskaya, A., Rocha, S. M., Legin, A., Pereira, V., and Marques, J. C. (2012). Evaluation of the feasibility of the electronic tongue as a rapid analytical tool for wine age prediction and quantification of the organic acids and phenolic compounds. The case-study of Madeira wine. *Anal. Chim. Acta* 662, 82–89. doi: 10.1016/j.aca.2009.12.042
- Rudnitskaya, A., Schmidke, L. M., Reis, A., Domingues, M. R., Delgadillo, I., Debus, B., et al. (2017). Measurements of the effects of wine maceration with oak chips using an electronic tongue. *Food Chem.* 229, 20–27. doi: 10.1016/j.foodchem.2017.02.013
- Shamagumova, R., Porfireva, A., Stepanova, V., Osin, Y., Evtugyn, G., and Hianik, T. (2015). Polyaniline-DNA based sensor for the detection of anthracycline drugs. *Sens. Actuators B Chem.* 220, 573–582. doi: 10.1016/j.snb.2015.05.076
- Shiigi, H., Morita, R., Muranaka, Y., Tokonami, S., Yamamoto, Y., Nakao, H., et al. (2012). Mass production of monodisperse gold nanoparticles in polyaniline matrix. *J. Electrochem. Soc.* 159, D442–D446. doi: 10.1149/2.071207jes
- Shishkanova, T. V., Sapurina, I., Stejskal, J., Král, V., and Volf, V. (2005). Ion-selective electrodes: polyaniline modification and anion recognition. *Anal. Chim. Acta* 553, 160–168. doi: 10.1016/j.aca.2005.08.018
- Shishkanova, T. V., Videnská, K., Antonova, S. G., nKrondák, M., Fitl, P., Kopecký, D., et al. (2014). Application of polyaniline for potentiometric recognition of salicylate and its analogues. *Electrochim. Acta* 115, 553–558. doi: 10.1016/j.electacta.2013.10.214
- Shurpik, D. N., Yakimova, L. S., Makhmutova, L. I., Makhmutova, A. R., Rizvanov, I. Kh., Plemenkov, V. V., et al. (2014). Pillar[5]arenes with morpholide and

- pyrrolidide substituents: synthesis and complex formation with alkali metal ions. *Macroheterocycles* 7, 351–357. doi: 10.6060/mhc140719s
- Smolko, V. A., Shurpik, D. N., Shamagsumova, R. V., Porfireva, A. V., Evtugyn, V. G., Yakimova, L. S., et al. (2014). Electrochemical behavior of pillar[5]arene on glassy carbon electrode and its interaction with  $\text{Cu}^{2+}$  and  $\text{Ag}^+$  ions. *Electrochim. Acta* 147, 726–734. doi: 10.1016/j.electacta.2014.10.007
- Song, E., and Choi, J. W. (2013). Conducting polyaniline nanowire and its applications in chemiresistive sensing. *Nanomaterials* 3, 498–523. doi: 10.3390/nano3030498
- Stejskal, J., Sapurina, I., and Trchová, M. (2010). Polyaniline nanostructures and the role of aniline oligomers in their formation. *Progr. Polym. Sci.* 35, 1420–1481. doi: 10.1016/j.progpolymsci.2010.07.006
- Stoikova, E. E., Dolgova, N. N., Savel'ev, A. A., Galukhin, A. V., Stoikov, I. I., Antipin, I. S., and Evtugyn, G. A. (2014). Beer classification based on the array of solid-contact potentiometric sensors with thiocalixarene receptors. *Russ. Chem. Bull.* 63, 223–231. doi: 10.1007/s11172-014-0417-x
- Stoikova, E. E., Sorvin, M. I., Shurpik, D. N., Budnikov, H. C., Stoikov, I. I., and Evtugyn, and, G. A. (2015). Solid-contact potentiometric sensor based on polyaniline and unsubstituted pillar[5]arene. *Electroanalysis* 27, 440–449. doi: 10.1002/elan.201400494
- Tahara, Y., and Toko, K. (2013). Electronic tongues - a review. *IEEE Sens. J.* 13, 3001–3011. doi: 10.1109/JSEN.2013.2263125
- Trivedi, D. C. (1999). Influence of counter ion on polyaniline and polypyrrole. *Bull. Mater. Sci.* 22, 447–455. doi: 10.1007/BF02749955
- Verelli, G., Ivova, L., Paolesse, R., Di Natale, C., and D'Amico, A. (2007). Metalloporphyrin-based electronic tongue: an application for the analysis of Italian white wines. *Sensors* 7, 2750–2762. doi: 10.3390/s7112750
- Wesoly, M., Cetý, X., del Valle, M., Ciosek, P., and Wrýblewski, W. (2016). Quantitative analysis of active pharmaceutical ingredients (APIs) using a potentiometric electronic tongue in a SIA flow system. *Electroanalysis* 28, 626–632. doi: 10.1002/elan.201500407
- Xing, L., Kang, Y., Zhou, Y., Ye, Y., Zhang, X., Huang, Y., et al. (2017). Determination of sulfate in seawater by a novel all-solid-state sulfate sensor with  $\text{H}_2\text{SO}_4$  doped polyaniline as sensitive membrane. *Int. J. Electrochem. Sci.* 12, 1506–1520. doi: 10.20964/2017.02.52
- Yakimova, L. S., Shurpik, D. N., Makhmutova, A. R., and Stoikov, I. I. (2017). Pillar[5]arenes bearing amide and carboxylic groups as synthetic receptors for alkali metal ions. *Macroheterocycles* 10, 226–232. doi: 10.6060/mhc170511s
- Yaroshenko, I., Kirsanov, D., Kartsova, L., Sidorova, A., Sun, Q., Wan, H., et al. (2016). Exploring bitterness of traditional Chinese medicine samples by potentiometric electronic tongue and by capillary electrophoresis and liquid chromatography coupled to UV detection. *Talanta* 152, 105–111. doi: 10.1016/j.talanta.2016.01.058
- Yushkova, E. A., and Stoikov, I. I. (2009). p-tert-Butyl thiocalix[4]arenes functionalized with amide and hydrazide groups at the lower rim in cone, partial cone, and 1,3-alternate conformations are “smart” building blocks for constructing nanosized structures with metal cations of s-, p-, and d-elements in the organic phase. *Langmuir* 25, 4919–4928. doi: 10.1021/la8040902
- Zeravik, J., Hlavacek, A., Lacina, K., and Skládal, P. (2009). State of the art in the field of electronic and bioelectronic tongues – towards the analysis of wines. *Electroanalysis* 21, 2509–2520. doi: 10.1002/elan.200900285
- Zhang, M., Yamaguchi, A., Morita, K., and Teramae, N. (2008). Electrochemical synthesis of Au / polyaniline-poly(4-styrenesulfonate) hybrid nanoarray for sensitive biosensor design. *Electrochim. commun.* 10, 1090–1093. doi: 10.1016/j.elecom.2008.05.021

**Conflict of Interest Statement:** The authors declare that the research was conducted in the absence of any commercial or financial relationships that could be construed as a potential conflict of interest.

Copyright © 2018 Sorvin, Belyakova, Stoikov, Shamagsumova and Evtugyn. This is an open-access article distributed under the terms of the Creative Commons Attribution License (CC BY). The use, distribution or reproduction in other forums is permitted, provided the original author(s) and the copyright owner are credited and that the original publication in this journal is cited, in accordance with accepted academic practice. No use, distribution or reproduction is permitted which does not comply with these terms.



# Graphene FET Array Biosensor Based on ssDNA Aptamer for Ultrasensitive $Hg^{2+}$ Detection in Environmental Pollutants

Jiawei Tu<sup>1</sup>, Ying Gan<sup>1</sup>, Tao Liang<sup>1</sup>, Qiongwen Hu<sup>1</sup>, Qian Wang<sup>2</sup>, Tianling Ren<sup>2</sup>, Qiyong Sun<sup>3,4</sup>, Hao Wan<sup>1\*</sup> and Ping Wang<sup>1\*</sup>

<sup>1</sup> Biosensor National Special Laboratory, Key Laboratory for Biomedical Engineering of Ministry of Education, Department of Biomedical Engineering, Zhejiang University, Hangzhou, China, <sup>2</sup> Tsinghua National Laboratory for Information Science and Technology, Tsinghua University, Beijing, China, <sup>3</sup> Key Laboratory of Healthy & Intelligent Kitchen System Integration of Zhejiang Province, Ningbo, China, <sup>4</sup> Ningbo Fotile Kitchenware CO. LTD., Bodi Centre, Hangzhou, China

## OPEN ACCESS

### Edited by:

Larisa Lvova,

Università degli Studi di Roma Tor Vergata, Italy

### Reviewed by:

Florence Lagarde,

Claude Bernard University Lyon 1, France

Ajeet Kaushik,

Florida International University, United States

### \*Correspondence:

Hao Wan

wh1816@zju.edu.cn

Ping Wang

cnpwang@zju.edu.cn

### Specialty section:

This article was submitted to Analytical Chemistry, a section of the journal *Frontiers in Chemistry*

Received: 19 March 2018

Accepted: 17 July 2018

Published: 14 August 2018

### Citation:

Tu J, Gan Y, Liang T, Hu Q, Wang Q, Ren T, Sun Q, Wan H and Wang P (2018) Graphene FET Array Biosensor Based on ssDNA Aptamer for Ultrasensitive  $Hg^{2+}$  Detection in Environmental Pollutants. *Front. Chem.* 6:333. doi: 10.3389/fchem.2018.00333

Invisible mercury ion is an extremely poisonous environmental pollutant, therefore, a fast and highly sensitive detection method is of significant importance. In this study, a liquid-gated graphene field-effect transistor (GFET) array biosensor (6 × 6 GFETs on the chip) was fabricated and applied for  $Hg^{2+}$  quantitate detection based on single-stranded DNA (ssDNA) aptamer. The biosensor showed outstanding selectivity to  $Hg^{2+}$  in mixed solutions containing various metal ions. Moreover, the sensing capability of the biosensor was demonstrated by real-time responses and showed a fairly low detection limit of 40 pM, a wide detection ranged from 100 pM to 100 nM and rapid response time below one second. These results suggest that the GFET array biosensor based on ssDNA aptamer offers a simple fabrication procedure and quite fast method for mercury ion contaminant detection and are promising for various analytical applications.

**Keywords:** biosensor, graphene FET array,  $Hg^{2+}$  detection, ssDNA aptamer, ultrasensitive detection

## INTRODUCTION

Graphene is a two-dimensional and one-atom thick sheet of  $sp^2$  hybridized carbon with exceptional electrical and physical properties, such as large detection area, ultra-high electron mobility, tunable ambipolar field-effect characteristic, and biocompatibility, compared to ones based on conventional semiconductor materials. In consequence, graphene field-effect transistor (GFET) have recently attracted much interest in sensing field (Dan et al., 2009; He et al., 2010, 2012; Huang et al., 2010, 2011; Myung et al., 2011; Kim et al., 2015; Han et al., 2017; Li et al., 2017; Kotlowski et al., 2018; Mansouri Majd and Salimi, 2018; Xu et al., 2018) for detection of DNA, protein, ions and so on. Since the first demonstrations, much progress has been achieved in the fabrication and performance of GFETs. In the sensing field, DNA aptamers combining with electrolyte-gated GFET sensor are a preferable choice, since they are smaller in size than Debye length (Maehashi et al., 2007). Therefore, the binding event between the aptamers and the targets can occur within the electric double layer in buffer solution, and as a consequence, changes in the charge distribution with proximity to the graphene can easily be detected (Guo et al., 2005; So et al., 2005). Moreover, the density of the immobilized DNA on the graphene can be controlled, and a high density of DNA can easily be prepared.

Mercury ions ( $\text{Hg}^{2+}$ ) are extremely toxic environmental pollutants, which would affect the immune and nervous systems, alter genetic expression, and cause serious damage to both mammals' health and the environment even at very low concentrations (Clarkson et al., 2003). Thus, a fast and highly sensitive  $\text{Hg}^{2+}$  detection method is of great importance in the healthcare and environmental fields. Several methods have been developed for mercury sensing, including photoelectrochemical methods (Ha et al., 2011), colorimetric analysis (Kim et al., 2012), and oligonucleotide-based sensing (Ono and Togashi, 2004). Therein, biosensing offers considerable advantages including fast response, requirement of low cost, simple equipment, and high sensitivity and selectivity. Recently, much attention has been extended to the development of optical and electrochemical techniques based on DNA for the selective  $\text{Hg}^{2+}$  detection. For example, Liu et al. (2009) developed a novel sensor for  $\text{Hg}^{2+}$  detection based on a conformational switch using ferrocene-tagged poly-thymine oligonucleotide to form thymine- $\text{Hg}^{2+}$ -thymine (T- $\text{Hg}^{2+}$ -T). A report by Zhuang et al. (2013) presented an  $\text{Hg}^{2+}$  electrochemical biosensor, which used DNA hairpins as recognition elements and exhibited a detection limit of 2.5 nM. Electrochemical strategies for mercury detection based on T- $\text{Hg}^{2+}$ -T coordination chemistry have been reported by Wang et al. (2014).

At present, the studies of GFET were basically based on a single sensor (Ohno et al., 2009; An et al., 2013; Mansouri Majd and Salimi, 2018), but single GFET has a low current that increases the difficulty of circuit design and signal acquisition. Further, due to the variation of graphene and individual FET, consistent results are hard to be obtained with a single sensor. Therefore, in this study, a common-source array design was used to obtain a large current response and reduce the impact of individual differences. To the best of our knowledge, no study based on GFET array was reported for  $\text{Hg}^{2+}$  detection with the modification of ssDNA.

Herein, a novel biosensor for  $\text{Hg}^{2+}$  ultrasensitive determination was designed and fabricated based on common-source graphene field-effect transistors array ( $6 \times 6$  GFETs) and ssDNA aptamer. The performance of biosensor was explored by analyzing the Raman spectrum, electrical properties, interferences, and so on. Furthermore, the GFET array modified by ssDNA sequences was applied to  $\text{Hg}^{2+}$  quantitative determination, which provided a promising method for fast and highly sensitive detection of  $\text{Hg}^{2+}$  in a variety of applications.

## METHODS

### System and Materials

Characterizing GFET array's current-voltage (I-V) parameters is extremely crucial to ensuring that it works properly as a sensor and meets specifications. In general, FET-type sensor characteristics testing involves the use of several kinds of instruments, including a sensitive ammeter, multiple voltage sources, and a voltmeter or an alternative approach, a turnkey semiconductor characterization system, which are either tedious or expensive. In our study, Model 2602B (Keithley Instruments Inc., USA), a two-channel source measurement unit (SMU), was utilized to perform parameter testing on the GFET array sensor.

The Model 2602B has current resolution to 0.1 fA and can be current limited to prevent damage to the sensor. **Figure 1** illustrated an I-V test configuration for an electrolyte-gated GFET sensor using a two-channel Model 2602B, and the GFET sensor had three main terminals: the electrolyte gate, the drain, and the source. A voltage applied to the gate terminal ( $V_G$ ) controlled the resulting drain current ( $I_{DS}$ ) that flowed from the drain to the source terminal. In this configuration, the Force HI terminal of Channel A was connected to the gate of the sensor and the Force HI terminal of Channel B was connected to the drain. And the source terminal of the sensor was connected to the Force LO terminals of both SMU channels. A common I-V test performed on the sensor was the drain family of curves ( $V_G$ - $I_{DS}$ ). With this test, SMU CHB stepped the drain voltage ( $V_{DS}$ ) with a step of 0.1 V from 0 to 3.0 V while SMU CHA swept the gate voltage ( $V_G$ ) from -4.0 to 4.0 V and measured the resulting drain current. An external Ag/AgCl reference electrode (saturated KCl) worked as the electrolyte gate of the sensor, which was connected to the Force HI terminal of Channel A.

Reagents used in the experiment were all of analytical grade. Deionized water ( $18.4 \text{ M}\Omega\text{-cm}$ ) used for cleaning and dilution was prepared by an ultra-pure water system Mili-Q (Millipore, USA). The mercury standard solution (100  $\mu\text{g/mL}$  in 3%  $\text{HNO}_3$ ) was purchased from the National Research Center for Certified Reference Material, China, and de-ionized water was used to dilute the standard solution into different concentrations. Other reagents were purchased from Aladdin (Shanghai, China) and used as received. Analytical grade copper chloride, lead nitrate, chromium chloride, and cadmium chloride were used to prepare stock solutions of 1,000 mg/L of the four metal ions, which were further diluted to the required concentrations before use. The ssDNA was custom-synthesized by GenScript Corp. (USA) and purified by high-performance liquid chromatography. The anti- $\text{Hg}^{2+}$  ssDNA sequence used in this study was as follows: 5'-GTT CTTTCGGCTTTGTTC-3'-C7-amino, which could easily form the T- $\text{Hg}^{2+}$ -T configuration in the present of  $\text{Hg}^{2+}$  (Lee et al., 2007; Li et al., 2008). All experiments were carried out at room temperature.

### GFET Array Fabrication

The schematic graphs of the detailed fabrication process flow of the GFET array was shown in **Figure 2**. The GFET array was fabricated with a series of photolithography methodologies. The graphene film used in the sensor was synthesized by chemical vapor deposition (CVD) on a copper foil and transferred to highly doped silicon substrate with 90 nm thick thermally grown  $\text{SiO}_2$  capping layer. After being spin-coated with polymethylmethacrylate (PMMA), the graphene/Cu film was placed on the surface of the etching solution (1 M  $\text{FeCl}_3$  and 1 M HCl) until the copper foil was completely etched away. And then, the graphene/PMMA film was rinsed by deionized water for several times before transferred onto substrates. PMMA was subsequently removed by acetone. After graphene being transferred, standard photolithography was employed to pattern the channel region of graphene and oxygen plasma etching to remove the unwanted graphene. Next, the metallic layer, which included a titanium layer of 20 nm and a gold layer of 50 nm, was sputtered by e-beam evaporation on the substrate, in which the

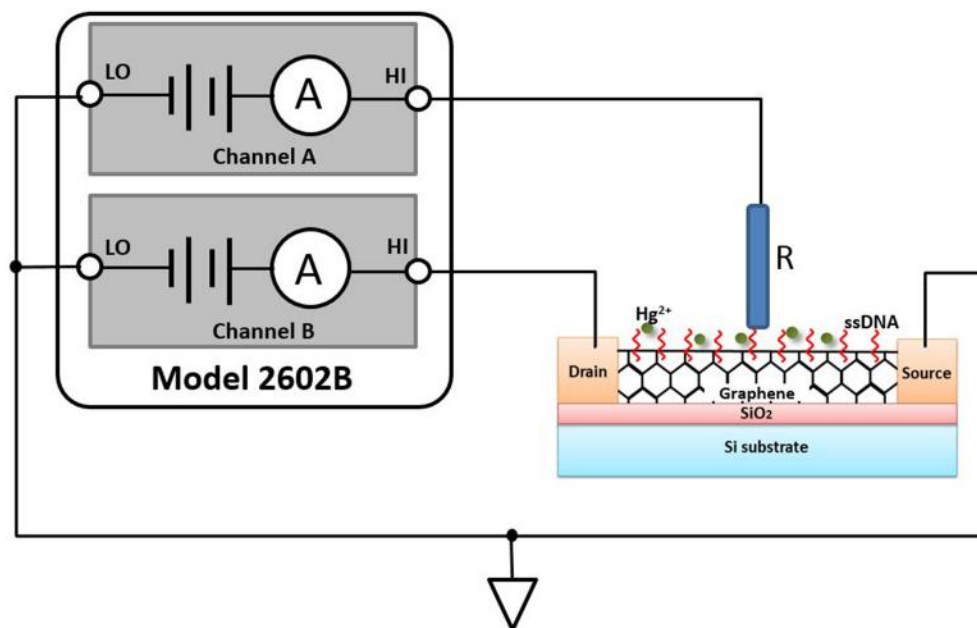


**FIGURE 1** | GFET sensor test configuration using multiple SMUs, Model 2602B: HI is short for Force HI terminal, and LO is short for Force LO terminal. R in the figure is an external Ag/AgCl reference electrode with saturated KCl.

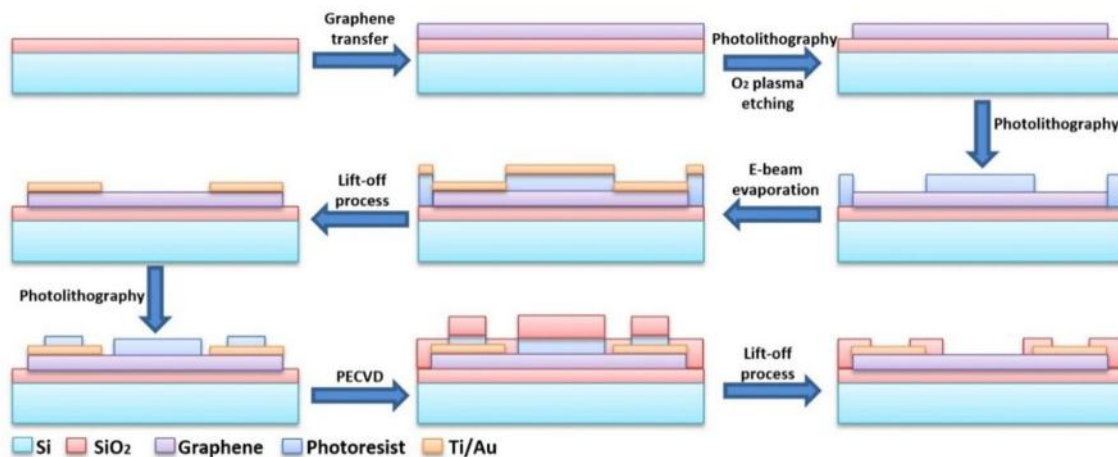


**FIGURE 2** | The schematic graphs of the fabrication process flow of the GFET array.

titanium layer acted as the adhesion layer. And, photolithography was utilized once again to define the shapes of source and drain electrodes followed by lift-off process. Afterwards, a  $\text{SiO}_2$  layer of 100 nm was deposited with plasma enhanced chemical vapor deposition (PECVD) on the metallic layer for insulation. Ultimately, partial insulation areas were etched to expose a designated gold area for spot welding to the external bonding pad and a designed graphene area as the electrolyte gate for the GFET sensor. The final structure of GFET array was seen at the lower right in **Figure 2**.

The GFET array was manufactured after all the fabrications mentioned above, the size of which was  $9.2 \times 9.2 \text{ mm}^2$ .

As shown in the **Figure 3a**, the whole packaged chip of GFET array with printed circuit board (PCB) was  $4.2 \times 4.2 \text{ cm}^2$ , consisted of  $6 \times 6$  common-source GFETs, with the exposed area of  $60 \times 80 \mu\text{m}^2$  each GFET separated by an  $800 \mu\text{m}$  gap. According to the technical processes above, the graphene was exposed as the electrolyte gate for GFET, just as the blue parts in **Figures 3b,c**, while the source and drain electrodes (the gold parts in **Figures 3b,c**) were covered by 100 nm  $\text{SiO}_2$  as the insulating layer. **Figure 3b** showed that the 36 GFETs ranked neatly in parallel, which meant all the 36 GFETs shared one source electrode. Finally, the bonding pads of GFET array chip were connected to

PCB pads by gold wires and a cell was used in chip encapsulation.

## Fabrication of Biosensor

To utilize the GFET array as an ultra-sensitive sensor for  $\text{Hg}^{2+}$  detection, DNA aptamer with plentiful thymine was functionally attached to the graphene film surface to selectively determine

the  $\text{Hg}^{2+}$ . According to the literatures (Chen et al., 2001; Kwon et al., 2012; Park et al., 2012; An et al., 2013), one of the most efficient condensing agents, 1,5-diaminonaphthalene (DAN), was stacked on the side plane of the graphene by  $\pi$ - $\pi$  interactions between the naphthalene group of DAN and its  $\text{sp}^2$ -carbon plane. Hence, the GFET array was treated with 10  $\mu\text{M}$  DAN in methanol (40  $\mu\text{L}$ ) for 3 h at room temperature and then flushed with

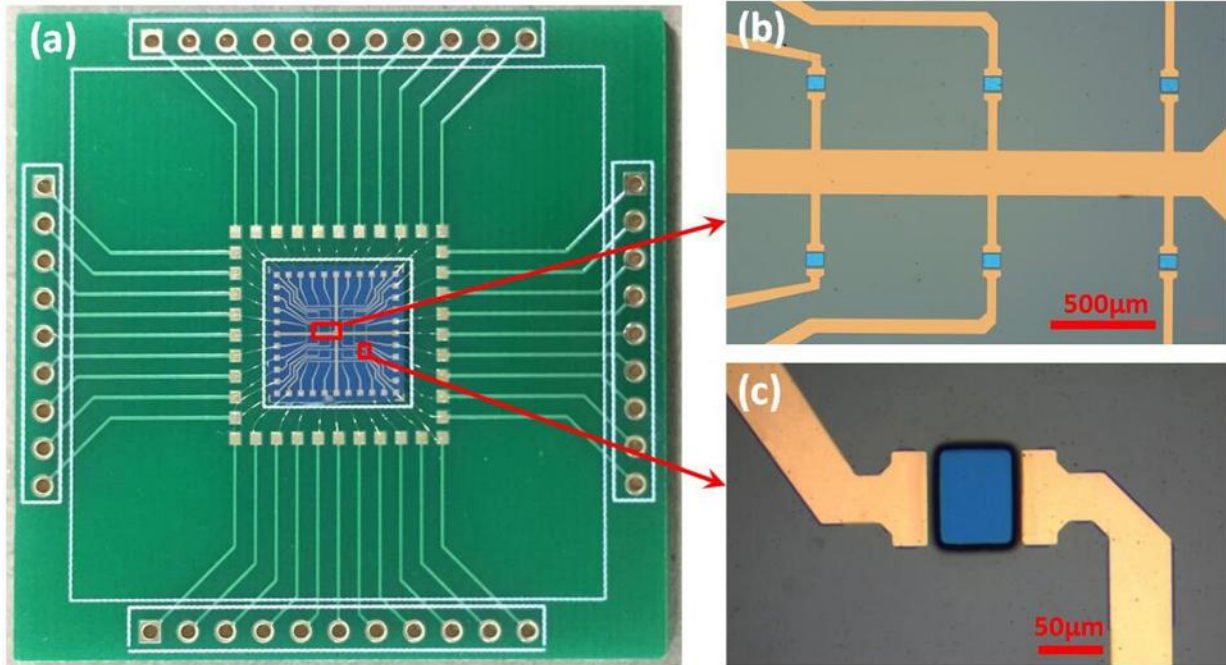


**FIGURE 3** | The photograph of the fabricated sensor: **(a)** the packaged sensor with PCB; **(b,c)** the microstructure of GFET array obtained by optical microscopy.

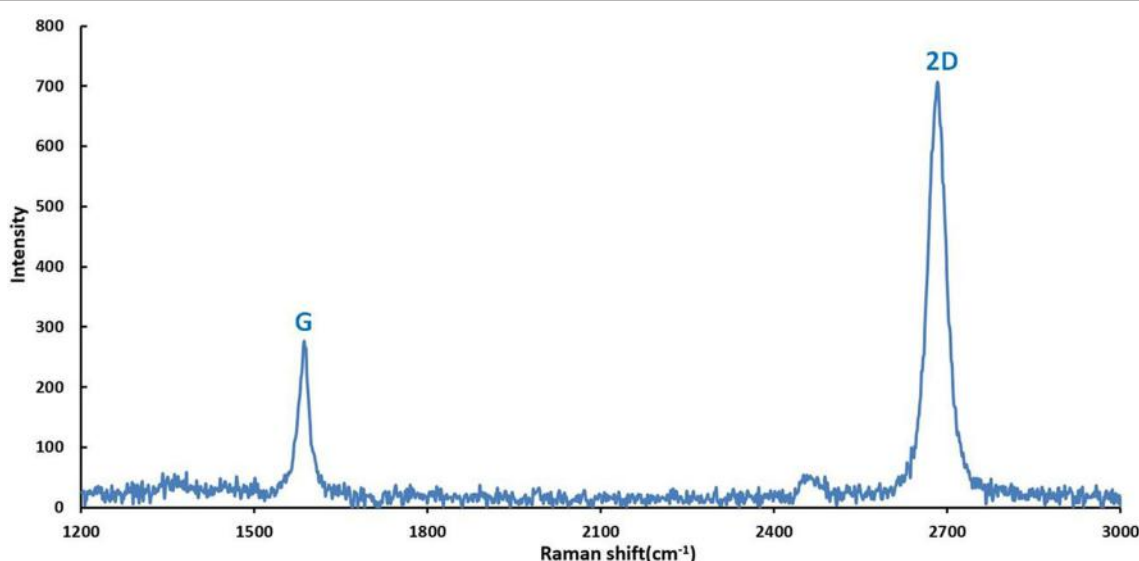


**FIGURE 4** | Raman spectrum (514.5 nm laser wavelength) obtained from the graphene film on the sensor showing the G peak and 2D band features characteristic for single-layer graphene ( $I_{2\text{D}}/I_{\text{G}} = 2.67$ ).

0.01 M phosphate buffer solution (PBS, pH 7.4). After that, 40  $\mu$ L 2% (v/v) glutaraldehyde (GA) was conjugated DAN through a Schiff-base reaction in pure environments for another 3 h. The Schiff-base reaction proceeded through chemical attachment between the aldehyde group of GA and the amine group of the DAN connected at the graphene (Lee et al., 2006). Subsequently, after flushing the chip with PBS to remove the superfluous GA, 40  $\mu$ L ssDNA (20  $\mu$ M in 0.01 M Tris-HCl buffer solution, pH 7.4) was immobilized to the GA on the graphene surface over 6 h at room temperature, which was also based on the Schiff-base reaction. Finally, the desired ssDNA-based biosensor for  $\text{Hg}^{2+}$  specific detection was fabricated and rinsed with surplus PBS.

## RESULTS AND DISCUSSION

### Characterization of Common-Source Liquid-Gated GFET Array

**Characterization of Graphene on the GFET**

According to the methods for graphene fabrication described in part 2.2 of this study, graphene film was synthesized by CVD on copper foils and patterned with proper shape after being transferred onto Si/SiO<sub>2</sub> substrates. Subsequently, the properties of graphene on the surface of GFET array were explored by Raman spectra analysis. The Figure 4 illustrated the Raman spectrum obtained from the graphene film on the GFET array sensor at 514.5 nm laser excitation. The graphene film exhibited typical monolayer graphene features with a sharp G peak and a single 2D peak with a higher intensity. The two prominent peaks appeared at approximate 1,589 and 2,683  $\text{cm}^{-1}$ , corresponding to G and 2D peaks, respectively. And, the peak intensity ratio of 2.67 between 2D and G confirmed the high percentage of monolayer with fewer multilayer islands in the graphene film on the sensor (Ferrari et al., 2006; Park et al., 2011; Zang et al., 2011; Tian et al., 2012). Meanwhile, the absence of D-band in this spectrum also confirmed the high quality of the as-grown graphene with fewer defects (Graf et al., 2007; Li et al., 2009; Tian et al., 2011).

### Characterization of Common-Source GFET Array

The signal superposition characteristics of the common-source GFET array was shown in Figure 5. The curves in the lower part of Figure 5 showed the characteristics of six independent GFETs. The red curve in the upper part of Figure 5 was the signal summation of the six independent GFETs. After connecting these six GFETs in parallel, the characteristic curve was shown as the blue curve. It can be seen that the signal intensity of the common-source GFETs had been significantly enhanced compared to a single sensor. The amplitude of superimposed current was the same as the current amplitude in the parallel condition, but the potential shifted because the reference electrode position changed. With the same reason, different single GFET had different distances from the reference electrode, so the characteristic curves of the six independent GFETs were also different. Therefore, in order to increase the response current, the array structure was effective.

### Characterization of Liquid-Gated GFET Array

For the capability test of GFET array, the electrical properties of the liquid-gated GFET array were investigated in the 0.01 M PBS (pH 7.4) at room temperature. The electrical measurements were conducted by the multiple SMUs system described above. The Figure 6 showed that gate voltage ( $V_G$ ) was swept from -0.8 to 2.0 V and the resulting drain current was measured at a gradient changing drain voltage ( $V_{DS}$ ) with a step of 0.1 V from 0 to 0.8 V. With increasing gate bias using the reference electrode, the source-drain current decreased in the beginning ( $V_G < 0.8$  V), and then increased, which indicated

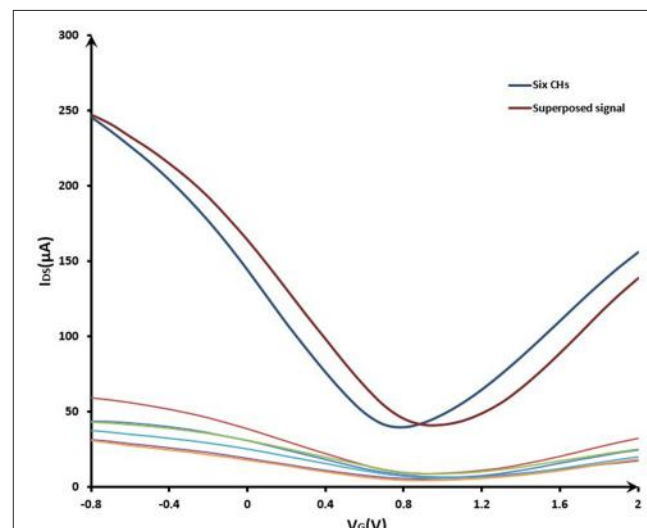


**FIGURE 5 |** The signal superposition characteristics of the common-source GFET array. VG sweeping from -0.8 to 2.0 V; VDS = 0.5 V.

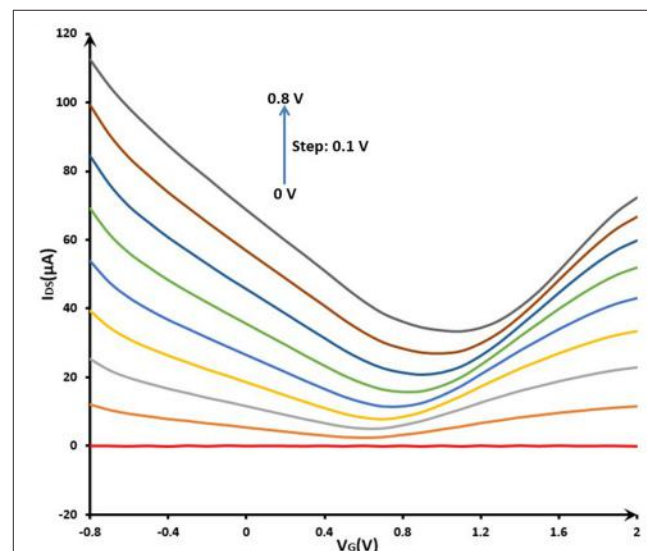


**FIGURE 6 |** Electrical properties (IDS-VG curve) of GFET array device before modification in phosphate buffer solution (0.01 M PBS, pH 7.4): VG sweeping from -0.8 to 2.0 V; VDS changing from 0 to 0.8 V with a step of 0.1 V.

significant bipolar characteristics in blank PBS. The  $I_{DS}$ - $V_G$  curve of GFET array device showed a remarkable Dirac point, which illustrated the structural integrity of common-source graphene FET array sensor. Meanwhile, a suitable quiescent bias point should be considered very cautiously in order

to obtain a high dynamic range and steady response for the sensor application. In this way, according to the  $I_{DS}$ - $V_G$  curves, this point was expected to be located around  $V_{DS} = 0.4\sim0.8$  V and  $V_G = -0.8\sim-0.4$  V for the present device.

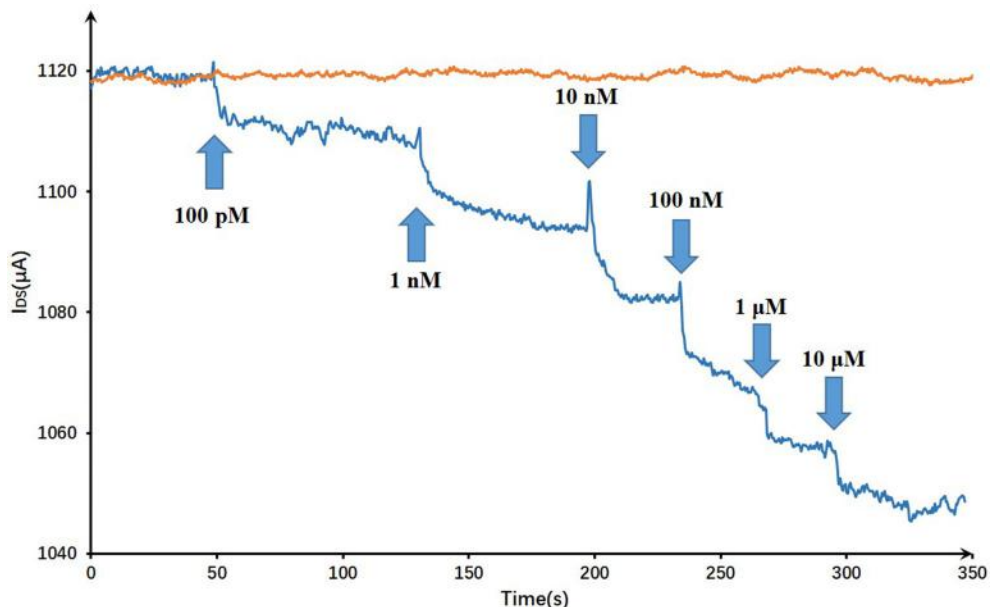


**FIGURE 7** | Dynamic responses of the DNA-based biosensor to  $\text{Hg}^{2+}$  and a blank control: the arrows pointed the adding time and corresponding concentrations.

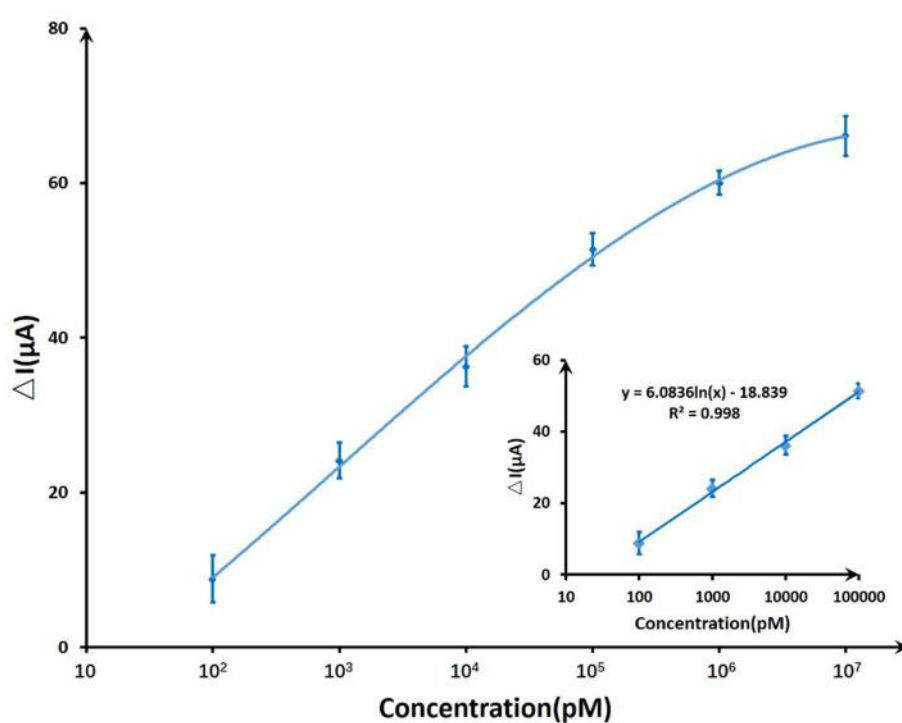


**FIGURE 8** | The sensitivity trendline of DNA-based GFET array biosensor to mercury ions ranging from 100 pM to 10  $\mu\text{M}$ . A linear fit was given for the first four concentrations.

## Analytical Figures of Merit of the GFET Biosensor Array

On account of T-Hg<sup>2+</sup>-T reaction, Hg<sup>2+</sup> ions binding to the ssDNA aptamer results electrostatic change at the interface, which will induce a change in the electrical signals. The biosensor performance was demonstrated by measuring  $I_{DS}$  upon the addition of various mercury concentrations at a constant  $V_G$  ( $V_G = -0.8$  V) and  $V_{DS}$  ( $V_{DS} = 0.5$  V). **Figure 7** displayed the real-time responses of GFET biosensor with ssDNA aptamer to different Hg<sup>2+</sup> concentrations, and  $I_{DS}$  gradually decreased when exposed to higher concentrations of Hg<sup>2+</sup> within concentrations ranging from 100 pM to 10  $\mu$ M. Moreover, the response time of the GFET array biosensor in the Hg<sup>2+</sup> determination was pretty fast (on a time scale of <1 s). The biosensor showed a concentration-dependent decrease in  $I_{DS}$  when it was exposed to the target Hg<sup>2+</sup>, and in order to further characterize the sensitivity of the ssDNA-based biosensor, the correlation between drain-source current and the logarithm of Hg<sup>2+</sup> concentration [ $\ln(\text{con})$ ] was investigated as shown in **Figure 8**. The standard deviations (SDs) in all concentrations were calculated ranging from  $\pm 1.54$  to  $\pm 3.02$   $\mu$ A, and the largest relative standard deviation (RSD) in all concentrations is 9.1%. This low RSD indicates very good repeatability of this biosensor for mercury detection. The current variation increased from 100 pM to 10  $\mu$ M of the Hg<sup>2+</sup> concentration. The saturation of the sensor was observed over 1  $\mu$ M, so the biosensor was calibrated based the

current variation of the first four samples. According to the fitting results, the correlation index ( $R^2$ ) between  $I_{DS}$  and  $\ln(\text{con})$  was 0.998, which showed a quite high correlation between them. Furthermore, the GFET biosensor array exhibited a detection limit of about 40 pM (RSD = 48.64%), which could meet the requirements for Hg<sup>2+</sup> applications.

The purpose of the experiments wanted to investigate the interference factors for the Hg<sup>2+</sup> measurements. To evaluate the selectivity of the sensing system for Hg<sup>2+</sup> ion, the responses of the ssDNA-based biosensor to various suspicious interfering metal ions, which were added in blank 0.01 M PBS (pH 7.4) as analytical samples, were recorded. As **Figure 9** showed, Cu<sup>2+</sup>, Pb<sup>2+</sup>, Cr<sup>3+</sup>, Cd<sup>2+</sup> of 10 nM and Hg<sup>2+</sup> of 100 pM were added successively in 0.01 M PBS, and the selective responses of GFET array biosensor were recorded for 200 s. From 0 to 160 s, the responses had no obvious change until the addition of Hg<sup>2+</sup> even in the case that the concentrations of competing ions were a hundred times greater than Hg ion. 100 pM Hg<sup>2+</sup> could induce a significant current reduction of the biosensor, indicating that the biosensor exhibits a high selectivity to Hg<sup>2+</sup> over other competing ones.

## Comparison

Compared to other methods and sensors for Hg<sup>2+</sup> detection, this GFET biosensor array presents high performance (**Table 1**). The first two studies are based on FET to detect Hg<sup>2+</sup>, and the third study used electrochemical impedance spectroscopy

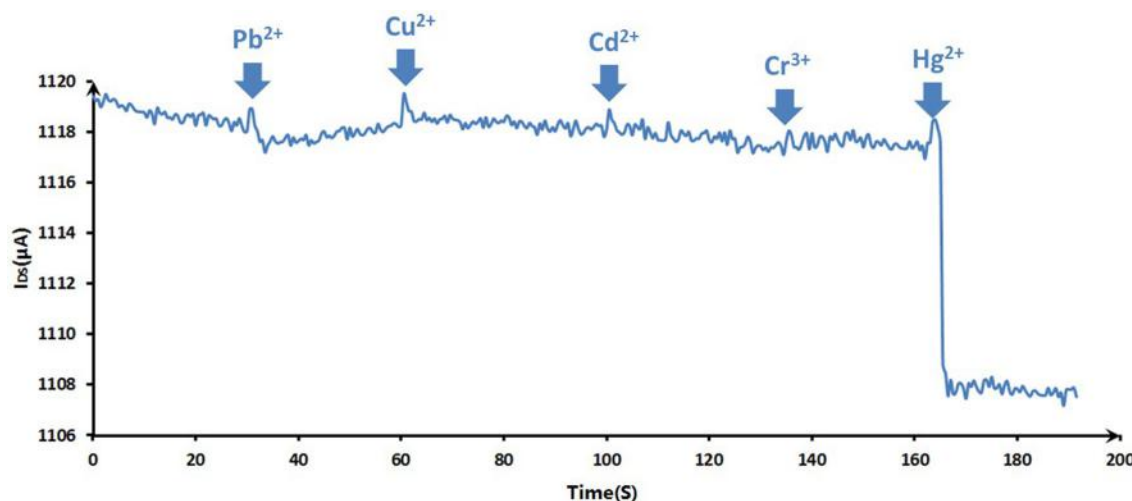


**FIGURE 9** | The selective responses of the DNA-based biosensor to various metal ions: Cu<sup>2+</sup>, Pb<sup>2+</sup>, Cr<sup>3+</sup>, Cd<sup>2+</sup> (10 nM for previous ions) and Hg<sup>2+</sup> (100 pM). The arrows pointed the adding time for corresponding ions.

**TABLE 1** | Comparison of Hg<sup>2+</sup> detection methods and sensors.

Detection method	Sensor	Detection range	Detection limit	References
Gate voltage	Alkanethiol modified GFET	Not mentioned	10 ppm (50 nM)	Zhang et al., 2010
Gate voltage	MoS <sub>2</sub> /DNA-Au NPs FET	0.1–10 nM	0.1 nM	Zhou et al., 2016
EIS	Gold disk electrode	0.1 nM–10 $\mu$ M	0.1 nM	Lin et al., 2011
Electrochemical	Au microelectrode array	10–100 nM	4 nM	Huan et al., 2012
Gate voltage	ssDNA aptamer GFET array	0.1–100 nM	40 pM	This work

(EIS) measurement based on the T-Hg<sup>2+</sup>-T principle. The fourth work used electrochemical detection for Hg<sup>2+</sup> based on Au microelectrode array. Compared to other sensors, this ssDNA aptamer GFET array presents wider detection range from 0.1 to 100 nM and the lowest detection limit of 40 pM.

Due to the very tight bonding between T-Hg<sup>2+</sup>-T, the current response would keep decreasing when bonding with more Hg<sup>2+</sup>. Thus, the response baseline would keep changing during the stability test, which is hard to be evaluated. The biosensor can be recycled before the saturation of the biosensor. Between the two measurements, the biosensor should be kept in 4°C to maintain the performance of the biosensor. When starting the measurement, the biosensor should be washed using PBS and measured in a blank sample to obtain a stable baseline. Then the biosensor can be used for the following tests.

For detecting Hg<sup>2+</sup>, the GFET array is highly sensitive, and capable for online and continuous monitoring. However, unlike detection in a buffer, water contaminant detection is usually carried out in a natural water system. In natural environment, mercury may exist as complexes which can have an effect on the results. Moreover, the suspended solid and organic and inorganic materials in water may disturb the GFET signal, leading to large uncertainties during the detection and may reduce the sensitivity and lifetime of the sensor. Therefore, to extend the GFET array into practical applications, further work is needed.

## CONCLUSION

A liquid-gated GFET array with 36 common-source FETs was fabricated and applied for Hg<sup>2+</sup> detection as a biosensor decorated with ssDNA aptamer. The characterization of GFET

array was tested and discussed based on the Raman spectrum and electrical methods on the multiple SMUs system. The array structure with common-source was effective in increasing the response current. The biosensor showed good selectivity to Hg<sup>2+</sup> in mixed solutions containing various metal ions. Moreover, the sensing capability of the biosensor was demonstrated by real-time responses and showed a fairly low detection limit of about 40 pM and quite rapid response time below 1 s. Compared with other similar detection methods and sensors, the constructed biosensor presents an excellent detection level. Overall, the simple fabrication procedure and the excellent sensing performance of the GFET array structure make it promising for contaminant detection of Hg<sup>2+</sup> in water environment.

## AUTHOR CONTRIBUTIONS

JT, QS, TR, and PW conceived the idea and designed the experiments. TL, QW, and TR designed and manufactured sensors. JT, YG, QH, and HW performed experiments. JT, YG, TL, QW, QH, and HW contributed to data analysis and interpretation. JT and PW wrote this paper. All authors discussed the results and commented on the manuscript.

## FUNDING

Financial support provided by Ministry of Science and Technology of China (973 Program) (Grant No. 2015CB352101), Natural Science Foundation of NSFCRFB Cooperation of China (Grant No. 8171101322) and Major Research and Development Program of Zhejiang Province (Grant No. 2017C03032), is gratefully acknowledged.

## REFERENCES

- An, J. H., Park, S. J., Kwon, O. S., Bae, J., and Jang, J. (2013). High-performance flexible graphene aptasensor for mercury detection in mussels. *ACS Nano* 7, 10563–10571. doi: 10.1021/nn402702w
- Chen, R. J., Zhang, Y., Wang, D., and Dai, H. (2001). Noncovalent sidewall functionalization of single-walled carbon nanotubes for protein immobilization. *J. Am. Chem. Soc.* 123, 3838–3839. doi: 10.1021/ja010172b
- Clarkson, T. W., Magos, L., and Myers, G. J. (2003). The toxicology of mercury—current exposures and clinical manifestations. *N. Engl. J. Med.* 349, 1731–1737. doi: 10.1056/NEJMra022471
- Dan, Y., Lu, Y., Kybert, N. J., Luo, Z., and Johnson, A. T. (2009). Intrinsic response of graphene vapor sensors. *Nano Lett.* 9, 1472–1475. doi: 10.1021/nl8033637
- Ferrari, A. C., Meyer, J., Scardaci, V., Casiraghi, C., Lazzari, M., Mauri, F., et al. (2006). Raman spectrum of graphene and graphene layers. *Phys. Rev. Lett.* 97:187401. doi: 10.1103/PhysRevLett.97.187401
- Graf, D., Molitor, F., Ensslin, K., Stampfer, C., Jungen, A., Hierold, C., et al. (2007). Spatially resolved Raman spectroscopy of single- and few-layer graphene. *Nano Lett.* 7, 238–242. doi: 10.1021/nl061702a
- Guo, X., Huang, L., O'Brien, S., Kim, P., and Nuckolls, C. (2005). Directing and sensing changes in molecular conformation on individual carbon nanotube field effect transistors. *J. Am. Chem. Soc.* 127, 15045–15047. doi: 10.1021/ja054335y
- Ha, D., Yu, H., Hu, N., Wu, C., Zhou, J., Kirsanov, D., et al. (2011). “Portable e-tongue based on multi-channel LAPS array with PVC membrane for rapid environment detection,” in *AIP Conference Proceedings*, AIP (New York, NY), 187–188.
- Han, D., Chand, R., and Kim, Y. S. (2017). Microscale loop-mediated isothermal amplification of viral DNA with real-time monitoring on solution-gated graphene FET microchip. *Biosens. Bioelectron.* 93, 220–225. doi: 10.1016/j.bios.2016.08.115
- He, Q., Sudibya, H. G., Yin, Z., Wu, S., Li, H., Boey, F., et al. (2010). Centimeter-long and large-scale micropatterns of reduced graphene oxide films: fabrication and sensing applications. *ACS Nano* 4, 3201–3208. doi: 10.1021/nn100780v
- He, Q., Wu, S., Yin, Z., and Zhang, H. (2012). Graphene-based electronic sensors. *Chem. Sci.* 3, 1764–1772. doi: 10.1039/c2sc20205k
- Huan, T. N., Hung, L. Q., Ha, V. T., Anh, N. H., Van Khai, T., and Chung, H. (2012). Spirally oriented Au microelectrode array sensor for detection of Hg (II). *Talanta* 94, 284–288. doi: 10.1016/j.talanta.2012.03.041
- Huang, Y., Dong, X., Liu, Y., Li, L.-J., and Chen, P. (2011). Graphene-based biosensors for detection of bacteria and their metabolic activities. *J. Mater. Chem.* 21, 12358–12362. doi: 10.1039/c1jm11436k
- Huang, Y., Dong, X., Shi, Y., Li, C. M., Li, L. J., and Chen, P. (2010). Nanoelectronic biosensors based on CVD grown graphene. *Nanoscale* 2, 1485–1488. doi: 10.1039/c0nr00142b
- Kim, H. N., Ren, W. X., Kim, J. S., and Yoon, J. (2012). Fluorescent and colorimetric sensors for detection of lead, cadmium, and mercury ions. *Chem. Soc. Rev.* 41, 3210–3244. doi: 10.1039/C1CS15245A
- Kim, J., Lee, M. S., Jeon, S., Kim, M., Kim, S., Kim, K., et al. (2015). Highly transparent and stretchable field-effect transistor sensors using graphene-nanowire hybrid nanostructures. *Adv. Mater.* 27, 3292–3297. doi: 10.1002/adma.201500710

- Kotlowski, C., Larisika, M., Guerin, P. M., Kleber, C., Kröber, T., Mastrogiacomo, R., et al. (2018). Fine discrimination of volatile compounds by graphene-immobilized odorant-binding proteins. *Sens. Actuat. B* 256, 564–572. doi: 10.1016/j.snb.2017.10.093
- Kwon, O. S., Park, S. J., Hong, J. Y., Han, A. R., Lee, J. S., and Jang, J. (2012). Flexible FET-type VEGF aptasensor based on nitrogen-doped graphene converted from conducting polymer. *ACS Nano* 6, 1486–1493. doi: 10.1021/nn204395n
- Lee, J. S., Han, M. S., and Mirkin, C. A. (2007). Colorimetric detection of mercuric ion ( $Hg^{2+}$ ) in aqueous media using DNA-functionalized gold nanoparticles. *Angew. Chem.* 119, 4171–4174. doi: 10.1002/ange.200700269
- Lee, L. M., Heimark, R. L., Baygents, J. C., and Zohar, Y. (2006). Self-aligned immobilization of proteins utilizing PEG patterns. *Nanotechnology* 17:S29. doi: 10.1088/0957-4484/17/4/006
- Li, D., Wieckowska, A., and Willner, I. (2008). Optical analysis of  $Hg^{2+}$  ions by oligonucleotide–gold-nanoparticle hybrids and DNA-based machines. *Angew. Chem.* 120, 3991–3995. doi: 10.1002/ange.200705991
- Li, X., Cai, W., An, J., Kim, S., Nah, J., Yang, D., et al. (2009). Large-area synthesis of high-quality and uniform graphene films on copper foils. *Science* 324, 1312–1314. doi: 10.1126/science.1171245
- Li, Y., Wang, C., Zhu, Y., Zhou, X., Xiang, Y., He, M., et al. (2017). Fully integrated graphene electronic biosensor for label-free detection of lead (II) ion based on G-quadruplex structure-switching. *Biosens. Bioelectron.* 89, 758–763. doi: 10.1016/j.bios.2016.10.061
- Lin, Z., Li, X., and Kraatz, H. B. (2011). Impedimetric immobilized DNA-based sensor for simultaneous detection of  $Pb^{2+}$ ,  $Ag^+$ , and  $Hg^{2+}$ . *Anal. Chem.* 83, 6896–6901. doi: 10.1021/ac2014096
- Liu, S. J., Nie, H. G., Jiang, J. H., Shen, G. L., and Yu, R. Q. (2009). Electrochemical sensor for mercury (II) based on conformational switch mediated by interstrand cooperative coordination. *Anal. Chem.* 81, 5724–5730. doi: 10.1021/ac900527f
- Maehashi, K., Katsura, T., Kerman, K., Takamura, Y., Matsumoto, K., and Tamiya, E. (2007). Label-free protein biosensor based on aptamer-modified carbon nanotube field-effect transistors. *Anal. Chem.* 79, 782–787. doi: 10.1021/ac060830g
- Mansouri Majd, S., and Salimi, A. (2018). Ultrasensitive flexible FET-type aptasensor for CA 125 cancer marker detection based on carboxylated multiwalled carbon nanotubes immobilized onto reduced graphene oxide film. *Anal. Chim. Acta* 1000, 273–282. doi: 10.1016/j.aca.2017.11.008
- Myung, S., Solanki, A., Kim, C., Park, J., Kim, K. S., and Lee, K. B. (2011). Graphene-encapsulated nanoparticle-based biosensor for the selective detection of cancer biomarkers. *Adv. Mater.* 23, 2221–2225. doi: 10.1002/adma.201100014
- Ohno, Y., Maehashi, K., Yamashiro, Y., and Matsumoto, K. (2009). Electrolyte-gated graphene field-effect transistors for detecting pH and protein adsorption. *Nano Lett.* 9, 3318–3322. doi: 10.1021/nl901596m
- Ono, A., and Togashi, H. (2004). Highly selective oligonucleotide-based sensor for mercury (II) in aqueous solutions. *Angew. Chem. Int. Edn.* 43 4300–4302. doi: 10.1002/anie.200454172
- Park, J., Xiong, W., Gao, Y., Qian, M., Xie, Z., Mitchell, M., et al. (2011). Fast growth of graphene patterns by laser direct writing. *Appl. Phys. Lett.* 98:123109. doi: 10.1063/1.3569720
- Park, S. J., Kwon, O. S., Lee, S. H., Song, H. S., Park, T. H., and Jang, J. (2012). Ultrasensitive flexible graphene based field-effect transistor (FET)-type bioelectronic nose. *Nano Lett.* 12, 5082–5090. doi: 10.1021/nl301714x
- So, H. M., Won, K., Kim, Y. H., Kim, B. K., Ryu, B. H., Na, P. S., et al. (2005). Single-walled carbon nanotube biosensors using aptamers as molecular recognition elements. *J. Am. Chem. Soc.* 127, 11906–11907. doi: 10.1021/ja053094r
- Tian, H., Ren, T. L., Xie, D., Wang, Y. F., Zhou, C. J., Feng, T. T., et al. (2011). Graphene-on-paper sound source devices. *ACS Nano* 5, 4878–4885. doi: 10.1021/nn2009535
- Tian, H., Xie, D., Yang, Y., Ren, T. L., Wang, Y. F., Zhou, C. J., et al. (2012). Single-layer graphene sound-emitting devices: experiments and modeling. *Nanoscale* 4, 2272–2277. doi: 10.1039/c2nr11572g
- Wang, W., Wang, Y., Tu, L., Klein, T., Feng, Y., Li, Q., et al. (2014). Magnetic detection of mercuric ion using giant magnetoresistance-based biosensing system. *Anal. Chem.* 86, 3712–3716. doi: 10.1021/ac404015j
- Xu, S., Jiang, S., Zhang, C., Yue, W., Zou, Y., Wang, G., et al. (2018). Ultrasensitive label-free detection of DNA hybridization by sapphire-based graphene field-effect transistor biosensor. *Appl. Surf. Sci.* 427, 1114–1119. doi: 10.1016/j.apsusc.2017.09.113
- Zang, Y., Xie, D., Wu, X., Chen, Y., Lin, Y., Li, M., et al. (2011). Enhanced photovoltaic properties in graphene/polycrystalline  $BiFeO_3/Pt$  heterojunction structure. *Appl. Phys. Lett.* 99:132904. doi: 10.1063/1.3644134
- Zhang, T., Cheng, Z., Wang, Y., Li, Z., Wang, C., Li, Y., et al. (2010). Self-assembled 1-octadecanethiol monolayers on graphene for mercury detection. *Nano Lett.* 10, 4738–4741. doi: 10.1021/nl1032556
- Zhou, G., Chang, J., Pu, H., Shi, K., Mao, S., Sui, X., et al. (2016). Ultrasensitive mercury ion detection using DNA-functionalized molybdenum disulfide nanosheet/gold nanoparticle hybrid field-effect transistor device. *ACS Sensors* 1, 295–302. doi: 10.1021/acssensors.5b00241
- Zhuang, J., Fu, L., Tang, D., Xu, M., Chen, G., and Yang, H. (2013). Target-induced structure-switching DNA hairpins for sensitive electrochemical monitoring of mercury (II). *Biosens. Bioelectron.* 39, 315–319. doi: 10.1016/j.bios.2012.07.015

**Conflict of Interest Statement:** The authors declare that the research was conducted in the absence of any commercial or financial relationships that could be construed as a potential conflict of interest.

Copyright © 2018 Tu, Gan, Liang, Hu, Wang, Ren, Sun, Wan and Wang. This is an open-access article distributed under the terms of the Creative Commons Attribution License (CC BY). The use, distribution or reproduction in other forums is permitted, provided the original author(s) and the copyright owner(s) are credited and that the original publication in this journal is cited, in accordance with accepted academic practice. No use, distribution or reproduction is permitted which does not comply with these terms.



# A Fluorescent Sensor Array Based on Heteroatomic Macrocyclic Fluorophores for the Detection of Polluting Species in Natural Water Samples

Larisa Lvova<sup>1\*</sup>, Fabrizio Caroleo<sup>1</sup>, Alessandra Garau<sup>2</sup>, Vito Lippolis<sup>2\*</sup>, Luca Giorgi<sup>3</sup>, Vieri Fusi<sup>3</sup>, Nelsi Zaccheroni<sup>4</sup>, Marco Lombardo<sup>4</sup>, Luca Prodi<sup>4</sup>, Corrado Di Natale<sup>5</sup> and Roberto Paolesse<sup>1</sup>

## OPEN ACCESS

### Edited by:

Nicole J. Jaffrezic-Renault,  
Claude Bernard University Lyon 1,  
France

### Reviewed by:

Kohji Mitsubayashi,  
Tokyo Medical and Dental University,  
Japan

Eduardo Pinilla-Gil,  
Universidad de Extremadura, Spain

### \*Correspondence:

Larisa Lvova  
larisa.lvova@uniroma2.it  
Vito Lippolis  
lippolis@unica.it

### Specialty section:

This article was submitted to  
Analytical Chemistry,  
a section of the journal  
Frontiers in Chemistry

Received: 17 March 2018

Accepted: 08 June 2018

Published: 28 June 2018

### Citation:

Lvova L, Caroleo F, Garau A,  
Lippolis V, Giorgi L, Fusi V,  
Zaccheroni N, Lombardo M, Prodi L,  
Di Natale C and Paolesse R (2018) A  
Fluorescent Sensor Array Based on  
Heteroatomic Macrocyclic  
Fluorophores for the Detection of  
Polluting Species in Natural Water  
Samples. *Front. Chem.* 6:258.  
doi: 10.3389/fchem.2018.00258

The development of a novel all-solid-state optical sensor array based on heteroatomic macrocyclic fluorophores (diaza-crown ether, metallocorrole and pyridinophans) for the photographic analysis of liquid media, is presented. The sensitivity of the new optical system toward a number of different species (cations:  $\text{Li}^+$ ,  $\text{K}^+$ ,  $\text{Na}^+$ ,  $\text{NH}_4^+$ ,  $\text{Mg}^{2+}$ ,  $\text{Ca}^{2+}$ ,  $\text{Co}^{2+}$ ,  $\text{Cu}^{2+}$ ,  $\text{Zn}^{2+}$ ,  $\text{Cd}^{2+}$ ,  $\text{Pb}^{2+}$  and anions:  $\text{NO}_2^-$ ,  $\text{NO}_3^-$ ,  $\text{Cl}^-$ ,  $\text{Br}^-$ ,  $\text{HCO}_3^-$ ) was evaluated both in single selective sensor mode and in multisensory arrangement. The satisfactory PLS1 regression models between sensor array optical response and analyte concentration were obtained for  $\text{Cd}^{2+}$ ,  $\text{Cu}^{2+}$ ,  $\text{Zn}^{2+}$ , and  $\text{NO}_2^-$  ions in all the range of tested concentrations. Among these species the highest attention was focused onto detection of cadmium and nitrite ions, for which the detection limits, DL, estimated by  $3\sigma$  method were found 0.0013 mg/L and 0.21 mg/L respectively, and these values are lower than the corresponding WHO guideline values of 0.003 mg/L ( $\text{Cd}^{2+}$ ) and 2 mg/L ( $\text{NO}_2^-$ ). The suitability of the developed sensors implemented with familiar devices for signal acquisition (Light Emitting Diode, LED, as light source and a digital camera as a signal detector), and chemometric methods for data treatment to perform fast and low-cost monitoring of species under interest, in real samples of environmental importance, is demonstrated.

**Keywords:** macrocyclic fluorophore, optical sensor, water pollutants, cadmium, nitrite

## INTRODUCTION

The use of optical techniques and optical chemical sensors for a satisfactory solution of a wide range of analytical tasks is becoming nowadays more and more popular (Askim et al., 2013; Lu, 2014; Bonifazi and Serranti, 2016; Di Natale et al., 2016). The growing interest in optical sensors implementation is due to the improved sensitivity and fast response time of such devices, simplicity in their preparation, construction, and signal acquisition. In fact, modern optical sensors often

do not require a sophisticated and high energy consuming hardware, no wire connections with the detector. Furthermore, the analytically useful signal of optical sensors can be registered even with simple wide-used electronic devices such as smartphones, or without any power supply in a “naked-eye” mode.

Among the optical detection techniques, fluorimetry is very attractive since it provides highly selective luminescence evaluation in a tunable emission range. Moreover, the optical chemical sensors based on fluorophores can be combined in sensor arrays and coupled with chemometric approach (Lvova et al., 2014), thus permitting the identification and quantitation of various analytes, such as natural water pollutants (Amatori et al., 2012; Bazzicalupi et al., 2013; Arca et al., 2014; Kang et al., 2014; Guanais Goncalves et al., 2016), toxins (Lvova et al., 2018), pesticides (Lei et al., 2016), explosives (Bolse et al., 2017; Zhu et al., 2017), agents hazardous for human skin (Moczko et al., 2016), forbidden additives and pathogens in beverages (Tan et al., 2014; Nishi et al., 2015; Han et al., 2016) and in foodstuffs (Lvova et al., 2015; Mungkarndee et al., 2015, 2016).

In particular, the accurate detection of inorganic contaminants, and heavy and transition metal ions is especially important, since these species present a severe impact and intrinsic risks for human health and environment (World Health Organization, 2017). The high amount of transition and heavy metals in environment causes their consequent accumulation in living beings, which could bring to intoxication and several serious pathologies in humans, including allergies, tumors, and genetic mutations (Vahter et al., 2002; Grigg, 2004; Lee et al., 2004). To protect humans against health risks caused by multi-metal contamination, a careful monitoring of metals content in the environment is required, and the development of low cost and easy to handle devices for in-field evaluation of heavy metal pollution represents, therefore, a challenging task. The development of analytical systems based on optical sensors for analysis of heavy metal pollution is actively investigated (Wang et al., 2008; Niu et al., 2013; Xu et al., 2014; Liu et al., 2017). Thus, Xu et al. have reported a fluorescent sensor array (Singapore Tongue, SGT) based on N, N, N', N'-tetrakis(2-pyridylmethyl)-ethylenediamine derivatives as a chelating site and quinoline, picoline and BODYPY fluorogenic fragments as signaling active unit, for rapid detection of heavy metal ions, such as  $\text{Hg}^{2+}$ ,  $\text{Fe}^{3+}$ ,  $\text{Cr}^{3+}$ ,  $\text{Zn}^{2+}$ ,  $\text{Cd}^{2+}$ ,  $\text{Cu}^{2+}$ , and  $\text{Pb}^{2+}$  (Xu et al., 2014) able to discriminate the concentration-dependent patterns of tested metals. The “safe-zone” concept was developed, which permitted to distinguish the clean water samples from those contaminated with hazardous species with Principal Component Analysis (PCA) by means of developed SGT fluorescent sensor array. The sensing materials were placed in 96-well plate and illuminated with a UV lamp at  $\lambda_{\text{ex}} = 365$  nm, the array output was measured with a standard fluorimeter. Previously, the similar concept of fluorimetric analytical system development was employed by Wang and coauthors, who tested an array composed from 9 chemosensors, both commercially available or newly synthesized, all bearing in their structure aromatic signaling units, but having different coordination chemistry and different signaling schemes, for the discrimination of 10 metal cations:  $\text{Ca}^{2+}$ ,  $\text{Mg}^{2+}$ ,  $\text{Hg}^{2+}$ ,

$\text{Cd}^{2+}$ ,  $\text{Al}^{3+}$ ,  $\text{Co}^{3+}$ ,  $\text{Zn}^{2+}$ ,  $\text{Cu}^{2+}$ ,  $\text{Ni}^{2+}$ , and  $\text{Ga}^{3+}$  (Wang et al., 2008). The possibility of metals qualitative identification by linear discriminant analysis (LDA) and quantitative analysis in the range of concentration from  $1 \times 10^{-5}$  to  $5 \times 10^{-3}$  mol/L with 90% of accuracy was also demonstrated. Selective ligands were incorporated into poly(ether)urethane matrixes and deposited onto multi-well plate by ultrasonic drilling. The sensor arrays were excited with a broadband UV lamp and the array output was recorded with Kodak Image station (440CF). Liu et al. have proposed a competitive host-guest fluorophore array for the selective discrimination of several heavy metal ions, including lanthanide and actinide salts in aqueous solution. In this system the host–metal interactions resulted in both a fluorescence enhancement and quenching, thus improving its discriminatory properties. The fluorescence assay was performed on 96-well plates and the fluorophore signal was recorded in a Microplate Reader (Liu et al., 2017). Niu et al. have developed a fluorometric sensor array based on 12 different BODYPY (4,4-difluoro-4-bora-3a,4a-diaza-s-indacene) derivatives as optically active units and multi-pyridyl ligands as the metal-binding receptors for sensitive detection of eight heavy-metal ions such as  $\text{Hg}^{2+}$ ,  $\text{Pb}^{2+}$ ,  $\text{Cd}^{2+}$ ,  $\text{Co}^{2+}$ ,  $\text{Cu}^{2+}$ ,  $\text{Ni}^{2+}$ ,  $\text{Zn}^{2+}$ , and  $\text{Ag}^+$  (Niu et al., 2013). Hierarchical clustering analysis was used for metal ions discrimination and the correct discrimination was found for all ions in concentration down to  $1 \times 10^{-7}$  mol/L. A UV LED array equipped with a 365 nm narrow band filter was used as excitation light source and Nikon D7000 digital camera served for visualization of the sensor output. The developed system was employed for the detection of metal ions in tap and marine water samples. Our group has developed optical sensor arrays for detection of diverse potential treats in water (Lvova et al., 2013; Guanais Goncalves et al., 2016) and investigated the possibility to employ a multi-transduction approach for monitoring natural waters pollution by transition metals (Lvova et al., 2015). Moreover, various modifications such as implementation of nanodots (Jing et al., 2017; Wu et al., 2017), graphene oxide (Liu et al., 2013), nanoparticles (Ambrosi et al., 2015; Peng et al., 2018), porous anodic aluminum oxide (Wang and Meng, 2017) or conjugated electrolytes (Wu et al., 2015) templates were employed in previously developed optical sensing systems in order to enhance the fluorescence signal, thus improving the identification of several heavy metal ions.

Very recently, an elegant approach employing a transparent bacterial cellulose nanopaper modified with ratiometric Carbon Dots/Rhodamine B probe for fluorescent and colorimetric analysis of heavy metal ions (i.e.,  $\text{Hg}^{2+}$ ,  $\text{Pb}^{2+}$ ,  $\text{Cd}^{2+}$ ,  $\text{Fe}^{3+}$ ,  $\text{Cu}^{2+}$ ) as a model analytes, was reported (Abbasi-Moayed et al., 2018). The color emission changes of the developed array under UV irradiation were monitored visually by naked eye or a smartphone camera; the array signal outputs were analyzed with hierarchical cluster analysis (HCA) and LDA. The applicability of the developed system to identify heavy metal ions in water and fish samples was demonstrated.

However, only few examples of multisensory fluorescent systems for analysis of anions are reported (Anzenbacher et al., 2013; Lin et al., 2015; Pushina and Anzenbacher, 2017). Thus, for instance a fluorescent sensor array based

on supramolecular metallo-gels for the identification of  $\text{CN}^-$ ,  $\text{SCN}^-$ ,  $\text{S}^{2-}$  and  $\text{I}^-$  anions in water was reported by Lin et al. (2015). The sensor array realized the anion selective response properties by the competitive coordination to the special gelator compound, of different metal ions and anions. Pushina and Anzenbacher have employed six biguanide derivatives, S1-S6, as receptors for various anions (halides, carboxylates, phosphates) binding in paper-based fluorescence-based sensor array (Pushina and Anzenbacher, 2017). The array was prepared by printing hydrophobic barriers on paper; the solutions of sensors S1-S6 in DMSO were applied on the obtained microzone plates, and their fluorescence changes upon 365 nm excitation were recorded using an UV-scanner. The aqueous solutions of 11 different analytes were correctly identified with LDA analysis. Anzenbacher et al. have also reported an anion-sensitive array based on a ratiometric calix[4]pyrrole introduced in poly(ether-urethane) hydrogel matrices with varying comonomer proportions (Anzenbacher et al., 2013). This array was used to discriminate eight different anions (acetate, benzoate, fluoride, chloride, phosphate, pyrophosphate, hydrogen sulfide, and cyanide) in urine samples and anti-inflammatory drugs with 100% classification accuracy.

Inspired by the previous works, in this study we have extended our research to the development of portable analytical system based on a fluorescent sensor array which employs familiar devices for signal acquisition (Light Emitting Diode, LED, as light source and a digital web-camera as a signal detector), in combination with chemometric methods for data treatment for fast and low-cost detection of polluting species in real samples. As sensing ligands we have used heteroatomic macrocyclic fluorophores, namely diaza-crown ethers, pyridinophanes and metallocorroles, previously studied in the group, focussing a particular attention to the application of the developed analytical system to the simultaneous accurate identification of several inorganic ions which significantly influence the toxicity index of natural water, including  $\text{Cd}^{2+}$ ,  $\text{Zn}^{2+}$ ,  $\text{Cu}^{2+}$ , and  $\text{NO}_2^-$ . Our task was also to demonstrate the applicability of the developed analytical system for rapid visual discrimination of polluted samples, which can be adapted for in field real-time monitoring purposes.

## EXPERIMENTAL

### Reagents

Membrane components, namely high molecular weight poly(vinyl chloride) (PVC), tris(2-ethylhexyl) phosphate (TOP), bis(2-ethylhexyl) sebacate (DOS), Tridodecylmethylammonium chloride (TDMACl) and potassium tetrakis-(4-chlorophenyl)borate (TpClPBK) were purchased from Fluka. The 2,8-dithia-5-aza-2,6-pyridinophane-based ligands bearing coumarin (HNCum) and naphthol-benzoxazole (HNBO), were newly synthesized and fully characterized at the “Dipartimento di Scienze Chimiche e Geologiche” of the University of Cagliari and at the Department of Pure and Applied Sciences of the University of Urbino, respectively (Lvova et al., 2016). The

1,10-bis[(5-phenyl-8-hydroxy-7-quinoliny) methyl]-1,10-diaza-18-crown-6-ether (DCHQ-Ph) was synthesized at the Chemistry Department “G. Ciamician” of Bologna University according to the previously reported procedure (Sargent et al., 2017). The ligand 5-(7-methoxy coumarin-4-methyl)-2,8-dithia-5-aza-2,6-pyridinophane (L3) was prepared at the “Dipartimento di Scienze Chimiche e Geologiche” of the University of Cagliari according to the method reported in (Bazzicalupi et al., 2013) and was already tested as  $\text{Hg}^{2+}$  selective fluorophore. The heteroatomic macrocycle [10-(4-trimethylsilylphenyl)-5,15-dimesitylcorrole] phosphorous (V) (PCorr) was synthesized in “Tor Vergata” University according to the procedure reported in (Naitana et al., 2017). Tetrahydrofuran (THF), 4-(2-hydroxyethyl)-1-piperazineethanesulfonic acid (HEPES, pH 7.5),  $\text{NaCl}$ ,  $\text{NaBr}$ ,  $\text{NaNO}_2$ ,  $\text{NaNO}_3$ ,  $\text{NaHCO}_3$ ,  $\text{KCl}$ ,  $\text{LiCl}$ ,  $\text{NH}_4\text{Cl}$ ,  $\text{MgCl}_2$ ,  $\text{CaCl}_2$ ,  $\text{CoCl}_2$ ,  $\text{Zn}(\text{NO}_3)_2$ ,  $\text{CdCl}_2$ ,  $\text{Cu}(\text{NO}_3)_2$ , and  $\text{Pb}(\text{NO}_3)_2$  salts were purchased from Sigma-Aldrich. THF was freshly distilled prior to use. Ultrapure water was used for aqueous solution preparation. All the other chemicals were of analytical grade and used without any further purification.

### Sensors Preparation

The membranes of about 100 mg weight were obtained by incorporating 1 wt% of each fluorophore, 2–10 wt% of ion exchanger, TpClPBK or TDMACl in a membrane cocktail prepared with 30–33 wt% PVC and 60–66 wt% of plasticizer (DOS or TOP) dissolved in 1 mL of THF. In total 5 membranes of different compositions were prepared, **Table 1**. The compositions of the membranes were optimized as in our previous studies for DCHQ-Ph (Lvova et al., 2009), for HNCum and HNBO (Lvova et al., 2016), and for L3 (Bazzicalupi et al., 2013) respectively; while Mb2 composition was tested for the first time.

About 7  $\mu\text{L}$  of each membrane cocktail were cast in replicate onto the same glass slide; 10 sensing spots were deposited in total, thus providing an optical sensors array. The THF solvent was allowed to evaporate overnight to form polymeric membrane films adhesive to the glass slide surface.

### Sensors Testing

All the tested membranes were photosensitive; in order to avoid photo degradation problems all of the studies were carried out on freshly prepared “disposable” optical sensors (deposited on transducer few hours prior to measurement). Membranes were kept in the dark before use. The measurements were replicated twice for each new membrane. The sensors responses toward several cations ( $\text{Na}^+$ ,  $\text{K}^+$ ,  $\text{Li}^+$ ,  $\text{NH}_4^+$ ,  $\text{Ca}^{2+}$ ,

**TABLE 1 |** Compositions of tested polymeric membranes.

Membrane	Fluorophore, wt%	Plasticizer	TpClPBK, wt %
Mb 1	DCHQ-Ph, 1 wt%	DOS	TpClPBK 5 wt%
Mb 2	PCorr, 0.5 wt%	DOS	TDMACl 5 wt%
Mb 3	HNCum, 1 wt%	TOP	TpClPBK 2 wt%
Mb 4	HNBO, 1 wt%	TOP	TpClPBK 5 wt%
Mb 5	L3, 1.3 wt%	DOS	TpClPBK 8 wt%

$Mg^{2+}$ ,  $Co^{2+}$ ,  $Cd^{2+}$ ,  $Pb^{2+}$ ,  $Cu^{2+}$ ,  $Zn^{2+}$ ) and anions ( $Cl^-$ ,  $Br^-$ ,  $NO_2^-$ ,  $NO_3^-$ ,  $HCO_3^-$ ) potentially present in real samples, and natural waters in particular, were tested in their individual solutions with a concentration range from  $3.3 \times 10^{-7}$  to  $2.2 \times 10^{-2}$  mol/L. The 1 mol/L stock solutions were prepared by dissolving corresponding amounts of sodium salts for the considered anions,  $Pb^{2+}$ ,  $Cu^{2+}$ , and  $Zn^{2+}$  nitrates, and metal chlorides for the others metal cations, in distilled water. Diluted solutions were obtained by consecutive additions of calculated amounts of the corresponding stock solution in 0.01 mol/L HEPES (pH 7.5) background solution, which was selected after a series of preliminary experiments to determine the background composition influence on the optodes response and in order to favor the pH conditions falling into the normal range of natural drinking water (that is 6.6–8.5).

In the second step the optical sensor array response was evaluated in multicomponent solutions containing four metal cations, namely  $Cd^{2+}$ ,  $Zn^{2+}$ ,  $Cu^{2+}$ ,  $Pb^{2+}$ , and nitrite ions. In total 24 multicomponent solutions with random combinations of species concentrations (<http://www.statisticshowto.com/experimental-design/#CompletelyRandomizedD>), in the range from  $1.0 \times 10^{-8}$  M to  $1.0 \times 10^{-4}$  M were prepared. The exact composition of 24 calibration solutions is given in Table 1S of Electronic Supporting Information (ESI). Two independent multivariate calibration sets, every time with a freshly deposited optode sensors were performed over a 6 month period. For each ion a working concentration interval was determined according to its level of toxicity based on the World Health Organization guidelines (World Health Organization, 2017). Since  $Cd^{2+}$  is the most toxic species, five different concentrations were tested for it, while we have limited the remaining species to three concentrations, Table 2. The sample solutions contained four different heavy metal ions:  $Cd^{2+}$ ,  $Zn^{2+}$ ,  $Pb^{2+}$ , and  $Cu^{2+}$  having randomly combined concentrations. Each new calibration solution was prepared directly prior to measurement in the measurement cuvette; for this, 3 mL of 0.01 mol/L HEPES pH 7.5 background buffer were placed in a cuvette, and the calculated amounts of  $CdCl_2$ ,  $Cu(NO_3)_2$ ,  $Zn(NO_3)_2$ ,  $Pb(NO_3)_2$ , and  $NaNO_2$  stock solutions of known concentrations ( $1.0 \times 10^{-6}$ ,  $1.0 \times 10^{-4}$ , and  $1.0 \times 10^{-2}$  mol/L) were added subsequently and stirred to obtain a homogenous solution. Sensor array was conditioned in multicomponent calibration solution for about 4 min prior the measurement, in order to allow fluorophore-analyte interaction.

Optical response of the array was measured with a photometric setup, performed in polystyrene cuvettes of 10 mm path length using a Photoassisted Technique (PT) setup (Lvova et al., 2017) in which a blue-colored InGaN LED (Roithner LaserTechnik, Austria, model H2A1-H385,  $\lambda_{ex} = 380$  nm) was employed as monochromic external light source. A frontally placed digital camera (Philips SPC900NC for notebook with a resolution of  $352 \times 288$  pixels) was used as a signal detector. The transparent cuvette was laterally illuminated with LED and the responses of the sensor array upon analyte addition were recorded from three channels representing main visible spectrum colors: red (630 nm), green (530 nm), and blue (480 nm). Additionally, for

**TABLE 2 |** Composition of multicomponent solutions and corresponding WHO guideline values.

Ion	WHO guideline value, mg/L	Concentrations, mol/L
$Cd^{2+}$	0.003 ( $2.6 \times 10^{-8}$ mol/L)	$1.0 \times 10^{-8}$ ; $3.3 \times 10^{-7}$ ; $1.6 \times 10^{-6}$ ; $3.3 \times 10^{-5}$ ; $1.0 \times 10^{-4}$
$Pb^{2+}$	0.01 ( $4.8 \times 10^{-8}$ mol/L)	$1.0 \times 10^{-8}$ ; $8.3 \times 10^{-7}$ ; $3.3 \times 10^{-5}$
$Cu^{2+}$	2 ( $3.1 \times 10^{-5}$ mol/L)	$3.3 \times 10^{-5}$ ; $6.6 \times 10^{-5}$ ; $1.0 \times 10^{-4}$
$NO_2^-$	3 ( $6.5 \times 10^{-5}$ mol/L)	$1.6 \times 10^{-6}$ ; $3.3 \times 10^{-5}$ ; $1.0 \times 10^{-4}$
$Zn^{2+}$	3 ( $4.6 \times 10^{-5}$ mol/L)*	$1.6 \times 10^{-6}$ ; $3.3 \times 10^{-5}$ ; $1.0 \times 10^{-4}$

For the full composition of calibration solutions see Table 1S in the Electronic Supplementary Information (ESI). \*A guideline value for  $Zn^{2+}$  is not established since it is not of health concern at levels found in drinking-water; however, drinking-water containing zinc at levels above 3 mg/l may not be acceptable to consumers due to the undesirable astringent taste and formation of a greasy film when boiled.

each sensing spot the luminescence intensity was calculated according to:

$$I = (R + G + B)/(3 \times 255) \quad (1)$$

where R, G, and B represent the sensing spot luminescence intensities at RGB channels, and value 255 represents the maximum intensity of optical signal measured with webcam detector. The RGB signal was evaluated after background luminosity subtraction. The duration of the overall sample illumination was 50 s, during this period 10 photographic shoots were taken every 5 s, and the final optical signal was a mean value of the records. The measurement cell was properly shielded from ambient illumination. The responses of the membranes were registered and transformed in analytically useful digital signal by in house written MATLAB (v.7.0, 2005, The MathWorks, Inc., Natick, USA) codes.

## Real Samples

The applicability of the proposed indirect method in single sensor mode was evaluated by assaying the amount of  $Cd^{2+}$  and  $NO_2^-$  ions spiked in five natural water samples: three were taken from the Rome city famous Fountains, such as Fontana di Trevi, Fontana dei Quattro Fiumi in Piazza Navona and the Fontana del Nettuno in Piazza del Popolo, one was sampled at the surface of the Tiber river that crosses the city of Rome (Isola Tiberina zone, Rome, Italy) and the other sample was a marine water sampled in the public beach area of Torvajanica, 20 km far from Rome city center (Lazio region, Italy). The standard addition method was employed, for this the additions of  $1.0 \times 10^{-8}$  mol/L and  $1.7 \times 10^{-7}$  mol/L of  $Cd^{2+}$  ions or  $3.2 \times 10^{-5}$  mol/L and  $9.6 \times 10^{-5}$  mol/L for  $NO_2^-$  ions respectively were performed to 3 mL of 1:1 mixture of water sample with 0.01M HEPES buffer at pH 7.5. The luminescence variance of the sensor array was registered with the PT technique.

## Multivariate Data Analysis

The chemometric approach was employed to treat data obtained from the optical multisensor array. The Principal Component

Analysis (PCA) and Partial Least Squares (PLS) regression method were applied to interpret the optical output of the sensor array based on membranes Mb1–Mb5 and employed for analysis of the  $\text{Cd}^{2+}$  and  $\text{NO}_2^-$  content in natural water samples. PLS1 was used to correlate the optode array output (Y-variable) with the known concentrations of  $\text{Cd}^{2+}$ ,  $\text{Zn}^{2+}$ ,  $\text{Cu}^{2+}$ , and  $\text{NO}_2^-$  ions in 24 multicomponent solutions (X-variables, see **Table 2**). Data treatment was performed with commercial Unscrambler (v. 9.1, 2004, CAMO PROCESS AS, Norway). Due to the restricted number of analyzed samples the validation was performed by using a leave-one-out cross-validation procedure. The RMSEC and RMSEV (Root Mean Square Error of Calibration and Validation, correspondingly) and the correlation coefficients,  $R^2$ , of predicted versus measured correlation lines were used to evaluate the efficiency of the applied regression model.

## RESULTS AND DISCUSSION

### Selection of Fluorophores and Fluorescent Sensor Array Construction

The chemical structures of studied fluorescent ligands are shown in **Figure 1**. All these compounds have been chosen thanks to their particular emission properties when interacting with metal cations.

The main criteria for the chemosensors selection were as following: (i) the presence in their structure of a macrocyclic chelating site which is linked to (or functions as) an the optically active fluorogenic fragment modulating (enhancing or quenching) the fluorescence emission upon the analyte binding; (ii) strong absorption around 350–450 nm in the near-UV region and high luminescence in the visible diapason; (iii) cross-sensitive properties, i.e., a strong binding ability toward several analytes; (iv) the availability in commerce or simple synthetic procedures required for their synthesis. The selected chemosensors bear in their structure different kinds of binding receptor units (pyridinophane in HNCum, HNBO and L3; diaza-crown ether in DCHQ-Ph and correlo macrocycle in PCorr), while coumarine, quinoline and naphtholbenzoxazazole serve as fluorogenic signaling fragments. Due to the different coordination properties, these compounds have different signal transduction schemes, such as fluorescence quenching or enhancement, which may vary from one analyte to another thus permitting to obtain enough information to allow to discriminate various analytes with a small number of sensing ligands. Among selected compounds, DCHQ-Ph was tested recently by our group as selective fluorophore for  $\text{Mg}^{2+}$  detection (Lvova et al., 2017). In non-complexed DCHQ-Ph, hydroxyquinoline signaling unit is poorly luminescent due to an intermolecular photoinduced proton transfer (PPT) process between the hydroxyl group

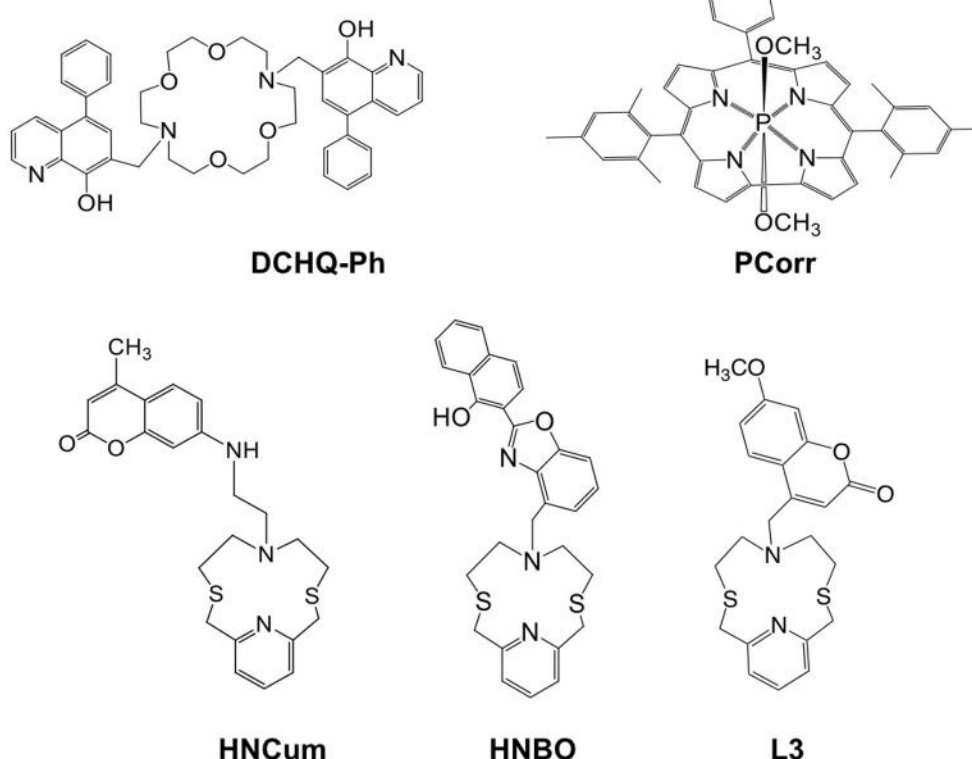


**FIGURE 1** | Molecular structures of the fluorescent ligands used inside solvent polymeric membranes optical sensor array.

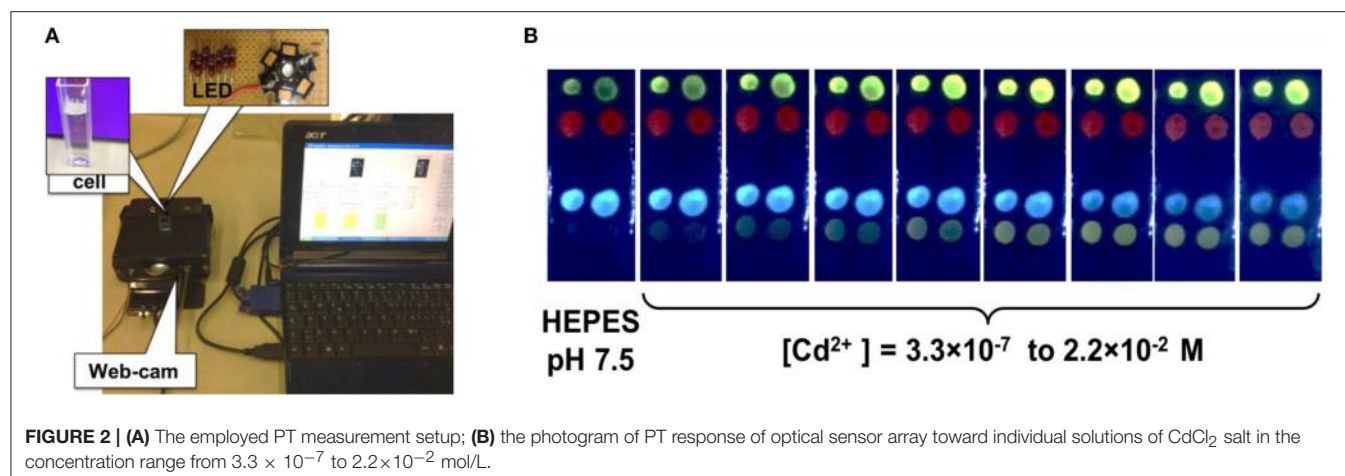


**FIGURE 2 | (A)** The employed PT measurement setup; **(B)** the photograph of PT response of optical sensor array toward individual solutions of  $\text{CdCl}_2$  salt in the concentration range from  $3.3 \times 10^{-7}$  to  $2.2 \times 10^{-2}$  mol/L.

and the quinoline nitrogen, while a significant fluorescence enhancement is observed in the DCHQ-Ph- $\text{Mg}^{2+}$  complex where both groups are involved in metal coordination and PPT is inhibited. The compound L3 was reported previously in the literature and its luminescence properties in the presence of different cations was studied (Bazzicalupi et al., 2013). As a free ligand, the coumarin signaling unit of L3 is partially quenched, and upon the coordination to metal cations a chelation enhanced fluorescence emission (CHEF effect) is observed. The HNCum and HNBO fluorophores were tested previously as selective ligands for  $\text{Cd}^{2+}$  and  $\text{Zn}^{2+}$  detection (Lvova et al., 2016). For these compounds the involvement of a large part of donor atoms of the macrocyclic receptor unit and the fluorogenic signaling unit was observed in complexation, with a photoinduced electron transfer process (PET) determining the fluorescence intensity emission change. Moreover, emission wavelength shift upon cations complexation by HNBO indicates also the contribution of an intramolecular charge transfer process (ICT) to the ligand fluorescence response. Finally, the optical properties of PCorr as anion-sensitive ligand were studied in the present work for the first time, however the physico-chemical properties (Naitana et al., 2017) and possible sensing mechanism of similar compounds have been previously discussed in the literature (Lvova et al., 2009).

As mentioned above, all the selected chemosensors exhibit a strong absorbance in the range from 350 to 450 nm, which permitted us to employ the single monochromatic light source for sensor array excitation. A commercially available blue-colored Light Emitting Diode (LED,  $\lambda_{\text{ex}} = 380$  nm) with home-made hardware was employed as an external monochromatic light source. **Figure 2A** shows a picture of the employed measurement setup and the arrangement of its major components: measurement cell with a sensor array placed inside, LED, web-camera and measurement chamber, where the sensitive substrate is placed. In this setup the webcam registers the luminescence variation of sensing spots upon the backside illumination with LED in the absence and in the presence of the analytes. In **Figure 2B** the typical PT response of the sensor array is shown during the calibration in individual solutions of

$\text{CdCl}_2$  salt in concentration range from  $3.3 \times 10^{-7}$  to  $2.2 \times 10^{-2}$  mol/L. The significant changes in the luminescence emission were recorded for the membranes Mb1, Mb3, and Mb4 based on DCHQ-Ph, HNCum and HNBO respectively.

In the same way, the response of optical sensor arrays based on Mb1–Mb5 was tested in individual solutions of 11 cations and 5 anions in 0.01 mol/L HEPES buffer at pH 7.5 and  $\lambda_{\text{ex}} = 380$  nm LED illumination, and it was found that most of tested heavy metal ions resulted in analyte-specific luminescence changes of singular sensors; while PCorr-based Mb2 was particularly sensitive to changes in nitrite-ions concentration demonstrating the luminescence quenching upon the analyte concentration growth. **Figure 3A** shows several examples of Mb1–Mb5 PT-responses toward analytes with the highest registered luminescence change. In fact, the inspection of sensing spot emission patterns indicated that Mb1 and Mb3 were most sensitive to  $\text{Cd}^{2+}$  and  $\text{Cu}^{2+}$ , Mb4 to  $\text{Cd}^{2+}$  and  $\text{Zn}^{2+}$ , while Mb5 and Mb2 to ammonium and nitrite ions, respectively. **Figure 3B** shows the comparison of fluorescence responses of membranes Mb1–Mb5 represented as the difference of luminescence intensities evaluated according to Equation (1) for all the tested analytes in concentration  $2.9 \times 10^{-4}$  mol/L into 0.01 mol/L HEPES buffer background at pH 7.5. The differences in Mb1–Mb5 responses clearly indicate the cross-sensitive response of these sensing materials to several heavy metal ions,  $\text{Cd}^{2+}$ ,  $\text{Zn}^{2+}$ ,  $\text{Cu}^{2+}$ , and nitrite-anion in particular.

According to WHO recommendations, these species are responsible for organoleptic faults ( $\text{Zn}^{2+}$  ions) and health risks ( $\text{Cd}^{2+}$ ,  $\text{Cu}^{2+}$ , and  $\text{NO}_2^-$ ) while found in environment, and in natural waters in particular (World Health Organization, 2017). As a consequence, we have decided to employ the sensor array based on Mb1–Mb5 for rapid screening of multicomponent contamination of real samples with these analytes.

## Multivariate Calibration of Optical Sensor Array

The optical response of sensor array based on Mb1–Mb5 was evaluated in 24 calibration solutions containing various concentrations of  $\text{Cd}^{2+}$ ,  $\text{Zn}^{2+}$ ,  $\text{Cu}^{2+}$ ,  $\text{Pb}^{2+}$ , and  $\text{NO}_2^-$  ions.

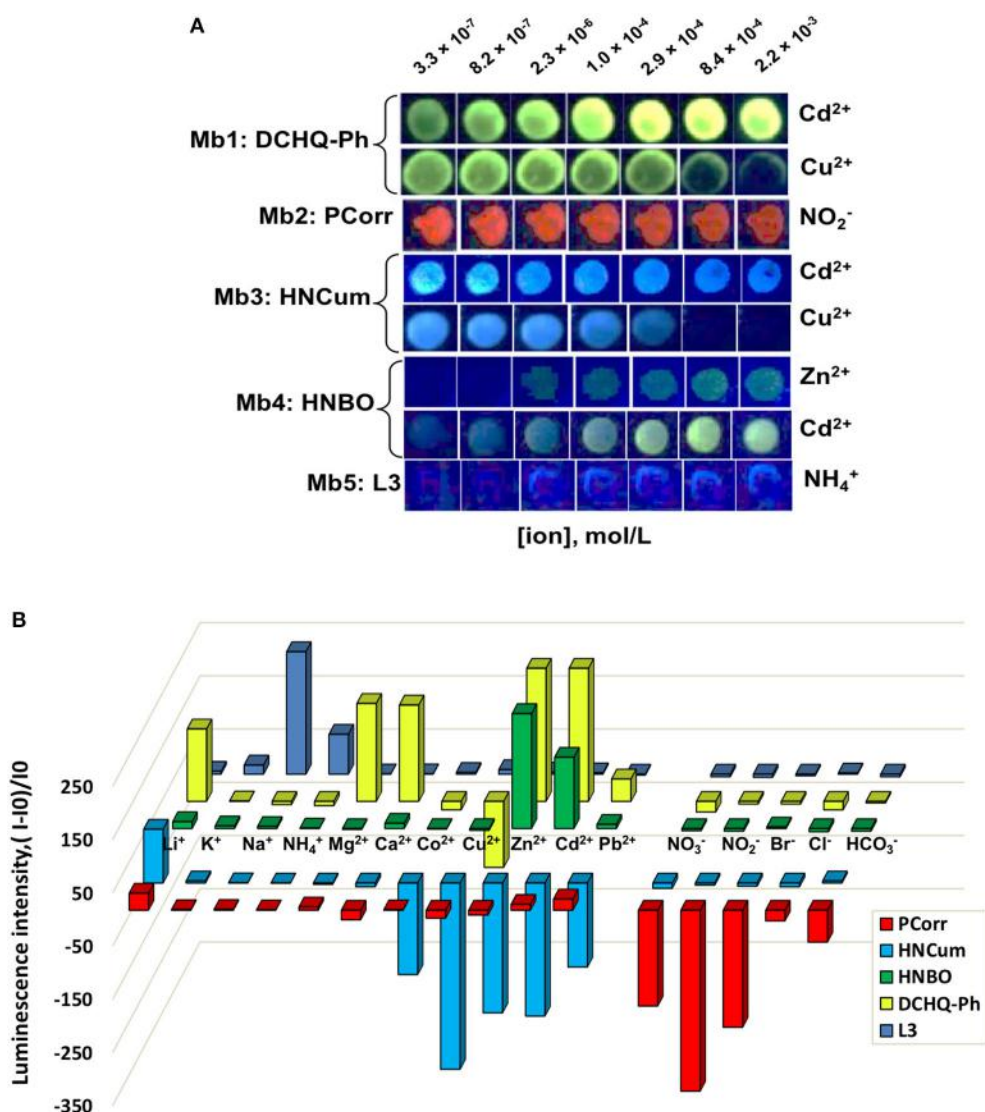


**FIGURE 3 |** Fluorescence responses of membranes Mb1–Mb5 toward several analytes in their individual solutions evaluated with PT at  $\lambda_{\text{ex}} = 380$  nm LED illumination in 0.01 mol/L HEPES buffer at pH 7.5. **(A)** Photograms of sensors PT responses with the highest registered luminescence changes; **(B)** pattern of the relative intensity changes of membranes Mb1–Mb5 toward all tested analytes at a concentration of  $2.9 \times 10^{-4}$  mol/L.

The full composition of calibration solutions is given in Table 1S of ESI, while the range of concentrations of five ions is given in Table 2. To prepare these multicomponent solutions we considered the guidelines for these ionic species in potable water established by WHO (World Health Organization, 2017), which correspond to 0.003 mg/L for Cd<sup>2+</sup>, 0.01 mg/L for Pb<sup>2+</sup>, 2 mg/L for Cu<sup>2+</sup>, and 3 mg/L for NO<sub>2</sub><sup>-</sup>, respectively. No health-based WHO guideline value for Zn<sup>2+</sup> is provided, but the drinking water containing Zn<sup>2+</sup> at concentrations above 3 mg/L ( $4.6 \times 10^{-5}$  mol/L) has an undesirable astringent taste, may appear opalescent and develops a greasy film when boiled (World Health Organization, 2017). Hence, in our tests we have used concentration values for Zn<sup>2+</sup> lower than 3 mg/L. For each ion a working concentration interval was defined according to its

level of toxicity. Since Cd<sup>2+</sup> is the most toxic species among the tested analytes, four different concentration levels were tested for it, while the concentrations of Zn<sup>2+</sup>, Pb<sup>2+</sup>, NO<sub>2</sub><sup>-</sup>, and Cu<sup>2+</sup> ions were limited to three levels. The photogram of sensor array PT response in all 24 multicomponent solutions is shown in Figure 4. The clear difference in Mb1–Mb5 responses can be observed, with especially strong emission in solutions where Cd<sup>2+</sup> and Zn<sup>2+</sup> ions are present in high concentrations.

Application of PCA analysis to the numerical outputs of sensor array luminescence response in terms of RGB intensities has permitted to identify clearly two groups of solutions corresponding to control solutions without pollutants addition (0.01 mol/L HEPES, pH 7.5) and all the multicomponent calibration solutions respectively, Figure 5. Moreover, the real

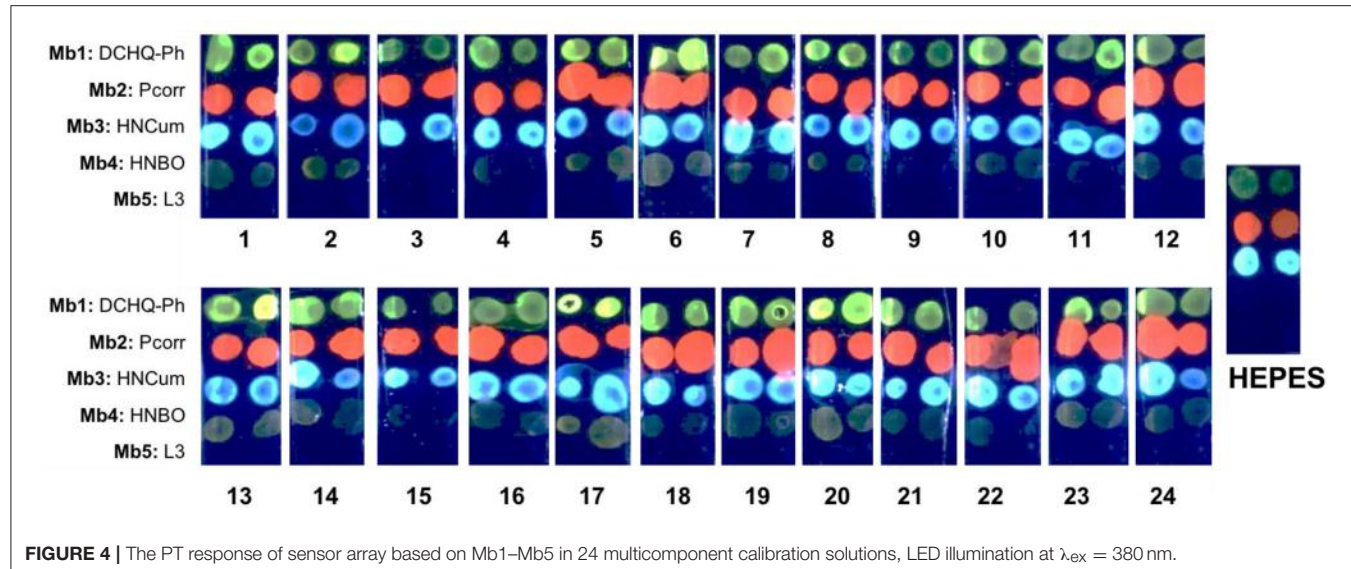


**FIGURE 4** | The PT response of sensor array based on Mb1–Mb5 in 24 multicomponent calibration solutions, LED illumination at  $\lambda_{\text{ex}} = 380$  nm.

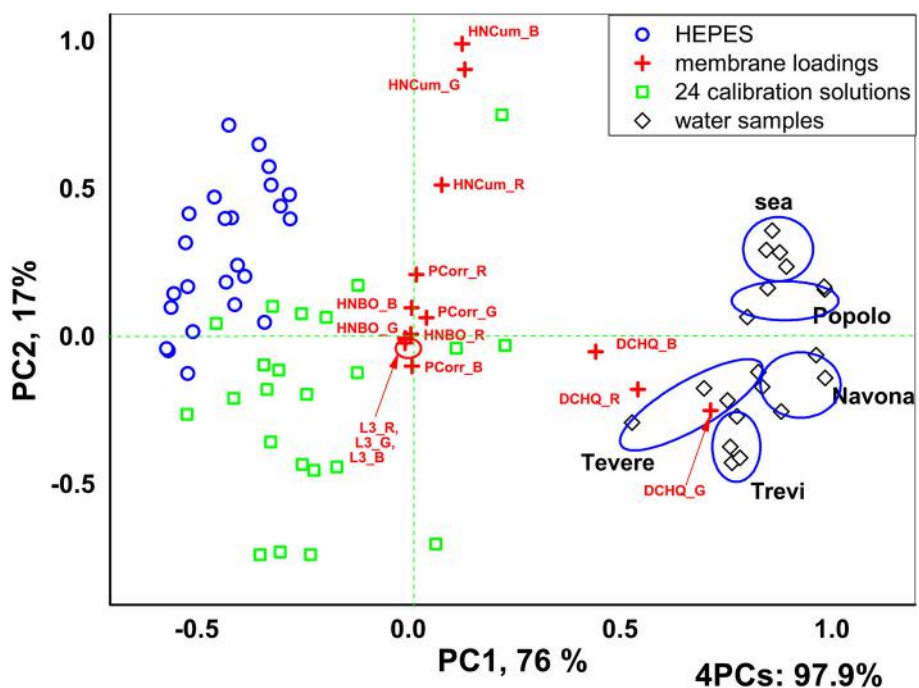


**FIGURE 5** | PCA scores and loadings plot of the Mb1–Mb5 sensor array fluorescence responses in 24 multicomponent calibration solutions.

water samples were clearly distinguished from calibration solutions and between each other. 97.9% of the total variance was explained for 4 PCs and the highest influence (highest loadings) on solutions discrimination was shown by the Mb1 and Mb3 based on DCHQ-Ph and HNCum ligands, respectively.

Furthermore, PLS1 regression models were calculated for all the polluting species employing Mb1–Mb5 sensing spots luminescence intensity calculated according to the Equation (1);

the luminescence intensities were obtained by subtraction of background luminescence intensity (the luminescence intensity of glass slide without sensing layer) and sensing spots luminescence intensity in 0.01 mol/L HEPES pH 7.5 without analytes. The linear correlations in all the range of tested concentrations with the following  $R^2$  coefficient, number of PCs representing the highest system variance, RMSEC and RMSECV values were found for  $\text{Cd}^{2+}$  ( $R^2 = 0.893$ , PCs = 4, RMSEC = 0.47 pCd, RMSEV = 0.64 pCd), for  $\text{Cu}^{2+}$  ( $R^2 = 0.906$ ,

PCs = 3, RMSEC = 0.057 pCu, RMSEV = 0.064 pCu), for  $Zn^{2+}$  ( $R^2 = 0.912$ , PCs = 3, RMSEC = 0.216 pZn, RMSEV = 0.315 pZn) and for  $NO_2^-$  ( $R^2 = 0.925$ , PCs = 3, RMSEC = 0.199 pNO<sub>2</sub>, RMSEV = 0.302 pNO<sub>2</sub>), respectively, Figure 1S. The detection limits (DL) for two polluting species of interest,  $Cd^{2+}$  and  $NO_2^-$  ions were estimated by  $3\sigma$  method (DL =  $3\sigma/S$ , where  $\sigma$  is the RMSEC recalculated in mol/L and S is the slope of the regression line at calibration stage). DL for  $Cd^{2+}$  was 0.0013 mg/L and for  $NO_2^-$  was 0.21 mg/L. Such a result is promising, considering that the obtained DL value for  $Cd^{2+}$  and  $NO_2^-$  were lower than the WHO provisional guideline values of 0.003 and 2 mg/L, respectively.

## Real Samples Analysis

We then have evaluated the added amounts of  $Cd^{2+}$  and  $NO_2^-$  ions in five natural water samples: tree samples taken from the Rome city fountains, one sample of surface water from the Tiber river and marine water sample. Since the concentrations of these two polluting species are usually low, we evaluated the real sample by introducing ions to water samples in two concentrations, one corresponding to WHO guideline value for potable water and another in several times higher of WHO limit. These concentrations were  $1.0 \times 10^{-8}$  mol/L and  $1.7 \times 10^{-7}$  mol/L for  $Cd^{2+}$ , and were  $3.2 \times 10^{-5}$  mol/L and  $9.6 \times 10^{-5}$  mol/L for  $NO_2^-$ , respectively. The luminescence variance of sensors array before and after pollutants addition was registered with PT technique and the previously calculated PLS1 regression models were used to evaluate the added pollutant amounts. The measurements were repeated twice for two disposable sensor arrays,  $n = 4$ . The obtained recoveries were in the range from 90.5 to 106.6% for  $Cd^{2+}$  and in the range from 95.1 to 105.1% for  $NO_2^-$  with the mean RSD of 3.7% ( $Cd^{2+}$ ) and 2.61% ( $NO_2^-$ ) respectively. Due to the high salinity the detection of  $NO_2^-$  ions in sea water was not possible, while satisfactory results for  $Cd^{2+}$  ions analysis in this sample were obtained (see Table 2S in the ESI).

## REFERENCES

- Abbasi-Moayed, S., Golmohammadi, H., and Hormozi-Nezhad, M. R. (2018). A nanopaper-based artificial tongue: a ratiometric fluorescent sensor array on bacterial nanocellulose for chemical discrimination applications. *Nanoscale* 10, 2492–2502. doi: 10.1039/C7NR05801B
- Amatori, S., Ambrosi, G., Fanelli, M., Formica, V., Fusi, V., Giorgi, L., et al. (2012). Multi-use NBD-based tetra-amino macrocycle: fluorescent probe for metals and anions and live cell marker. *Chem. Eur. J.* 18, 4274–4284. doi: 10.1002/chem.201103135
- Ambrosi, G., Borgogelli, E., Formica, M., Fusi, V., Giorgi, L., Micheloni, M., et al. (2015). PluS Nanoparticles as a tool to control the metal complex stoichiometry of a new thio-aza macrocyclic chemosensor for Ag(I) and Hg(II) in water. *Sens. Actu. B* 207, 1035–1044. doi: 10.1016/j.snb.2014.07.107
- Anzenbacher, P. Jr., Liu, Y., Palacios, M. A., Minami, T., Wang, Z., and Nishiyabu, R. (2013). Leveraging material properties in fluorescence anion sensor arrays: a general approach. *Chem. Eur. J.* 19, 8497–8506. doi: 10.1002/chem.201204188

## CONCLUSIONS

In this paper we have reported an optical sensor array based on heteroatomic macrocyclic fluorophores (diaza-crown ether, metallocorrole and pyridinophanes) for the photographic analysis of liquid media. The results obtained indicate a potential utility of the developed optical system for the accurate monitoring of polluting species, namely cadmium and nitrite ions, in real samples. The combination with familiar devices and the use of the PT measurement technique can allow inexpensive, rapid and accurate monitoring of heavy metals and anions pollution of natural environments that can be performed by untrained personnel.

## AUTHOR CONTRIBUTIONS

All authors listed have made a substantial, direct and intellectual contribution to the work, and approved it for publication.

## FUNDING

Fondazione di Sardegna, Regione autonoma della Sardegna, University of Urbino.

## ACKNOWLEDGMENTS

VL and AG thank Fondazione di Sardegna (FdS) and Regione autonoma della Sardegna (RAS) (Progetti Biennali di Ateneo FdS/RAS annualità 2016) for financial support. LG and VF acknowledge the Department of Pure and Applied Sciences, University of Urbino, (DiSPeA\_Fusi\_prog17) for financial support.

## SUPPLEMENTARY MATERIAL

The Supplementary Material for this article can be found online at: <https://www.frontiersin.org/articles/10.3389/fchem.2018.00258/full#supplementary-material>

- Arca, M., Caltagirone, C., De Filippo, G., Formica, M., Fusi, V., Giorgi, L., et al. (2014). A fluorescent ratiometric nanosized system for the determination of Pd(II) in water. *Chem. Comm.* 50, 15259–15262. doi: 10.1039/C4CC07969H
- Askim, J. R., Mahmoudi, M., and Suslick, K. S. (2013). Optical sensor arrays for chemical sensing: the optoelectronic nose. *Chem. Soc. Rev.* 42, 8649–8682. doi: 10.1039/c3cs60179j
- Bazzicalupi, C., Caltagirone, C., Cao, Z., Chen, Q., Di Natale, C., Garau, A., et al. (2013). Multimodal use of new coumarin-based fluorescent chemosensors: towards highly selective optical sensors for  $Hg^{2+}$  probing. *Chem. Eur. J.* 19, 14639–14653. doi: 10.1002/chem.201302090
- Bolse, N., Eckstein, R., Schend, M., Habermehl, A., Eschenbaum, C., Hernandez-Sosa, G., et al. (2017). A digitally printed optoelectronic nose for the selective trace detection of nitroaromatic explosive vapours using fluorescence quenching. *Flex. Printed Electron.* 2:024001. doi: 10.1088/2058-8585/aa6601
- Bonifazi, G., and Serranti, S. (2016). Chemical imaging: an innovative tool for particulate matter characterization and sorting. *Particul. Sci. Technol.* 34, 470–482. doi: 10.1080/02726351.2015.1115453

- Di Natale, C., Dini, F., and Scozzari, A. (2016). Non-conventional electrochemical and optical sensor systems. *Handb. Environ. Chem.* 40, 279–311. doi: 10.1007/698\_2013\_254
- Grigg, J. (2004). Environmental toxins: their impact on children's health. *Arch. Dis. Child.* 89, 244–250. doi: 10.1136/adc.2002.022202
- Guanais Gonçalves, C., Dini, F., Martinelli, E., Catini, A., Lundström, I., Paolesse, R., et al. (2016). Detection of diverse potential threats in water with an array of optical sensors. *Sens. Act. B* 236, 997–1004. doi: 10.1016/j.snb.2016.04.080
- Han, J., Bender, M., Seehafer, K., and Bunz, U. H. F. (2016). Identification of white wines by using two oppositely charged poly(p-phenyleneethynylene)s individually and in Complex. *Ang. Chem. Int. Ed.* 55, 7689–7692. doi: 10.1002/anie.201602385
- Jing, W., Lu, Y., Yang, G., Wang, F., He, L., and Liu, Y. (2017). Fluorescence sensor array based on amino acids-modulating quantum dots for the discrimination of metal ions. *Anal. Chim. Acta* 985, 175–182. doi: 10.1016/j.aca.2017.07.011
- Kang, H., Lin, L., Rong, M., and Chen, X. (2014). A cross-reactive sensor array for the fluorescence qualitative analysis of heavy metal ions. *Talanta* 129, 296–302. doi: 10.1016/j.talanta.2014.05.054
- Lee, J. Y., Friedman, J. E., Angel, I., Kozak, A., and Koh, J. Y. (2004). The lipophilic metal chelator DP-109 reduces amyloid pathology in brains of human beta-amyloid precursor protein transgenic mice. *Neurobiol. Aging* 25, 1315–1321. doi: 10.1016/j.neurobiolaging.2004.01.005
- Lei, J., Hou, C., Huo, D., Luo, X., Li, Y., Fa, H., et al. (2016). A novel detector using a fluorescent sensor array and discrimination of pesticides. *Res. Chem. Intermed.* 42, 7359–7374. doi: 10.1007/s11164-016-2541-8
- Lin, Q., Lu, T.-T., Zhu, X., Sun, B., Yang, Q.-P., Wei, T.-B., et al. (2015). A novel supramolecular metallo-gel-based high-resolution anion sensor array. *Chem. Commun.* 51, 1635–1638. doi: 10.1039/C4CC07814D
- Liu, F., Ha, H. D., Han, D. J., and Seo, T. S. (2013). Photoluminescent graphene oxide microarray for multiplex heavy metal ion analysis. *Small* 9, 3410–3414. doi: 10.1002/smll.201300499
- Liu, Y., Mettry, M., Gill, A. D., Perez, L., Zhong, W., and Hooley, R. J. (2017). Selective heavy element sensing with a simple host-guest fluorescent array. *Anal. Chem.* 89, 11113–11121. doi: 10.1021/acs.analchem.7b03377
- Lu, Y. (2014). Optical chemical sensor array based on functional nanomaterials. *Prog. Chem.* 26, 931–938. doi: 10.7536/PC131236
- Lvova, L., Di Natale, C., D'Amico, A., and Paolesse, R. (2009). Corrole-based ion-selective electrodes. *J. Porphyrins Phthalocyan.* 13, 1168–1178. doi: 10.1142/S1088424609001510
- Lvova, L., Di Natale, C., Paolesse, R., Giorgi, L., Fusi, V., Garau, A., et al. (2016). Photographic detection of cadmium(II) and zinc(II) ions. *Proc. Eng.* 168, 346–350. doi: 10.1016/j.proeng.2016.11.117
- Lvova, L., Galloni, P., Floris, B., Lundström, I., Paolesse, R., and Di Natale, C. (2013). A ferrocene-porphyrin ligand for multi-transduction chemical sensor development. *Sensors* 13, 5841–5856. doi: 10.3390/s130505841
- Lvova, L., Guanais Gonçalves, C., Prodi, L., Lombardo, M., Zaccheroni, N., Viaggiu, E., et al. (2018). Non-enzymatic portable optical sensor for Microcystin-LR. *Chem. Commun.* 54, 2747–2750. doi: 10.1039/C7CC09830H
- Lvova, L., Guanais Gonçalves, C., Prodi, L., Sgarzi, M., Zaccheroni, N., Lombardo, M., et al. (2017). Systematic approach in  $Mg^{2+}$  ions analysis with a combination of tailored fluorophore design. *Anal. Chim. Acta* 988, 96–103. doi: 10.1016/j.aca.2017.07.062
- Lvova, L., Kirsanov, D., Legin, A., and Di Natale, C., (eds.). (2014). *Multisensor Systems for Chemical Analysis - Materials and Sensors*. Singapore: Pan Stanford Publishing.
- Lvova, L., Pudi, R., Galloni, P., Lippolis, V., Di Natale, C., Lundstrom, I., et al. (2015). Multi-transduction sensing films for Electronic Tongue applications. *Sens. Act B* 207B, 1076–1086. doi: 10.1016/j.snb.2014.10.086
- Moczko, E., Mirkes, E. M., Cáceres, C., Gorban, A. N., and Piletsky, S. (2016). Fluorescence-based assay as a new screening tool for toxic chemicals. *Sci. Rep.* 6:33922. doi: 10.1038/srep33922
- Mungkarndee, R., Techakriengkrai, I., Tumcharern, G., and Sukwattanasinitt, M. M. (2016). Fluorescence sensor array for identification of commercial milk samples according to their thermal treatments. *Food Chem.* 197, 198–204. doi: 10.1016/j.foodchem.2015.10.083
- Mungkarndee, R., Tumcharern, G., Thiramanus, R., Techakriengkrai, I., and Sukwattanasinitt, M. (2015). Fluorescence sensor arrays for identification of foodborne pathogens. *Anal. Methods* 7, 7431–7435. doi: 10.1039/C5AY00797F
- Naitana, M. L., Nardis, S., Pomarico, G., Raggio, M., Caroleo, F., Cicero, D. O., et al. (2017). A highly emissive water-soluble phosphorus corrole. *Chem. Eur. J.* 23, 905–916. doi: 10.1002/chem.201604233
- Nishi, K., Isobe, S.-I., Zhu, Y., Kiyama, R. (2015). Fluorescence-based bioassays for the detection and evaluation of food materials. *Sensors* 15, 25831–25867. doi: 10.3390/s151025831
- Niu, L.-Y., Li, H., Feng, L., Guan, Y.-S., Chen, Y.-Z., Duan, C.-F., et al. (2013). BODIPY-based fluorometric sensor array for the highly sensitive identification of heavy-metal ions. *Anal. Chim. Acta* 775, 93–99. doi: 10.1016/j.aca.2013.03.013
- Peng, J., Li, J., Xu, W., Wang, L., Su, D., Teoh, C. L., et al. (2018). Silica nanoparticle-enhanced fluorescent sensor array for heavy metal ions detection in colloid solution. *Anal. Chem.* 90, 1628–1634. doi: 10.1021/acs.analchem.7b02883
- Pushina, M., and Anzenbacher, P. (2017). Biguanides, anion receptors and sensors. *Chem. Commun.* 53, 10074–10077. doi: 10.1039/C7CC05012G
- Sargentini, A., Farruggia, G., Zaccheroni, N., Marracini, C., Sgarzi, M., Cappadone, C., et al. (2017). Synthesis of a highly  $Mg^{2+}$ -selective fluorescent probe and its application to quantifying and imaging total intracellular magnesium. *Nat. Protoc.* 12, 461–471. doi: 10.1038/nprot.2016.183
- Tan, J., Li, R., and Jiang, Z. T. (2014). Discrimination of fresh fruit juices by a fluorescent sensor array for carboxylic acids based on molecularly imprinted titania. *Food Chem.* 165, 35–41. doi: 10.1016/j.foodchem.2014.05.104
- Vahter, M., Berglund, M., Akesson, A., and Liden, C. (2002). Metals and women's health. *Environ. Res.* 88, 145–155. doi: 10.1006/enrs.2002.4338
- Wang, M., and Meng, G. (2017). Fluorophores-modified nanomaterials for trace detection of polychlorobiphenyls and heavy metal ions. *Sens. Actu. B* 243, 1137–1147. doi: 10.1016/j.snb.2016.12.092
- Wang, Z., Palacios, M. A., and Anzenbacher, P. Jr. (2008). Fluorescence sensor array for metal ion detection based on various coordination chemistries: general performance and potential application. *Anal. Chem.* 80, 7451–7459. doi: 10.1021/ac801165v
- World Health Organization (2017). *Guidelines for Drinking-water Quality: Fourth Edition Incorporating the First Addendum*. Geneva: World Health Organization 2017, 631.
- Wu, Y., Liu, X., Wu, Q., Yi, J., and Zhang, G. (2017). Differentiation and determination of metal ions using fluorescent sensor array based on carbon nanodots. *Sens. Actu. B* 246, 680–685. doi: 10.1016/j.snb.2017.02.132
- Wu, Y., Tan, Y., Wu, J., Chen, S., Chen, Y. Z., Zhou, X., et al. (2015). Fluorescence array-based sensing of metal ions using conjugated polyelectrolytes. *ACS Appl. Mater. Interfaces* 7, 6882–6888. doi: 10.1021/acsami.5b00587
- Xu, W., Ren, C., Teoh, C. L., Peng, J., Gadre, S. H., Rhee, C.-L., et al. (2014). An artificial tongue fluorescent sensor array for identification and quantitation of various heavy metal ions. *Anal. Chem.* 86, 8763–8769. doi: 10.1021/ac501953z
- Zhu, Q., Xiong, W., Gong, Y., Zheng, Y., Che, Y., Zhao, J., et al. (2017). Discrimination of five classes of explosives by a fluorescence array sensor composed of two tricarbazole-nanostructures. *Anal. Chem.* 89, 11908–11912. doi: 10.1021/acs.analchem.7b04083

**Conflict of Interest Statement:** The authors declare that the research was conducted in the absence of any commercial or financial relationships that could be construed as a potential conflict of interest.

Copyright © 2018 Lvova, Caroleo, Garau, Lippolis, Giorgi, Fusi, Zaccheroni, Lombardo, Prodi, Di Natale and Paolesse. This is an open-access article distributed under the terms of the Creative Commons Attribution License (CC BY). The use, distribution or reproduction in other forums is permitted, provided the original author(s) and the copyright owner are credited and that the original publication in this journal is cited, in accordance with accepted academic practice. No use, distribution or reproduction is permitted which does not comply with these terms.



# Toward a Hybrid Biosensor System for Analysis of Organic and Volatile Fatty Acids in Fermentation Processes

Désirée L. Röhlen <sup>1†</sup>, Johanna Pilas <sup>1,2†</sup>, Markus Dahmen <sup>3</sup>, Michael Keusgen <sup>2</sup>, Thorsten Selmer <sup>1\*</sup> and Michael J. Schöning <sup>1,4\*</sup>

<sup>1</sup> Institute of Nano- and Biotechnologies, FH Aachen, Jülich, Germany, <sup>2</sup> Institute of Pharmaceutical Chemistry, Philipps-Universität Marburg, Marburg, Germany, <sup>3</sup> Institute NOWUM-Energy, FH Aachen, Jülich, Germany, <sup>4</sup> Institute of Complex Systems 8, Forschungszentrum Jülich, Jülich, Germany

## OPEN ACCESS

### Edited by:

Larisa Lvova,  
Università degli Studi di Roma Tor  
Vergata, Italy

### Reviewed by:

Pierangela Cristiani,  
Ricerca Sul Sistema Energetico, Italy  
Dongxue Han,  
Changchun Institute of Applied  
Chemistry (CAS), China

### \*Correspondence:

Thorsten Selmer  
selmer@fh-aachen.de  
Michael J. Schöning  
schoening@fh-aachen.de

<sup>†</sup>These authors have contributed  
equally to this work.

### Specialty section:

This article was submitted to  
Analytical Chemistry,  
a section of the journal  
Frontiers in Chemistry

Received: 28 March 2018

Accepted: 22 June 2018

Published: 17 July 2018

### Citation:

Röhlen DL, Pilas J, Dahmen M,  
Keusgen M, Selmer T and  
Schöning MJ (2018) Toward a Hybrid  
Biosensor System for Analysis of  
Organic and Volatile Fatty Acids in  
Fermentation Processes.  
Front. Chem. 6:284.  
doi: 10.3389/fchem.2018.00284

Monitoring of organic acids (OA) and volatile fatty acids (VFA) is crucial for the control of anaerobic digestion. In case of unstable process conditions, an accumulation of these intermediates occurs. In the present work, two different enzyme-based biosensor arrays are combined and presented for facile electrochemical determination of several process-relevant analytes. Each biosensor utilizes a platinum sensor chip (14 × 14 mm<sup>2</sup>) with five individual working electrodes. The OA biosensor enables simultaneous measurement of ethanol, formate, D- and L-lactate, based on a bi-enzymatic detection principle. The second VFA biosensor provides an amperometric platform for quantification of acetate and propionate, mediated by oxidation of hydrogen peroxide. The cross-sensitivity of both biosensors toward potential interferents, typically present in fermentation samples, was investigated. The potential for practical application in complex media was successfully demonstrated in spiked sludge samples collected from three different biogas plants. Thereby, the results obtained by both of the biosensors were in good agreement to the applied reference measurements by photometry and gas chromatography, respectively. The proposed hybrid biosensor system was also used for long-term monitoring of a lab-scale biogas reactor (0.01 m<sup>3</sup>) for a period of 2 months. In combination with typically monitored parameters, such as gas quality, pH and FOS/TAC (volatile organic acids/total anorganic carbonate), the amperometric measurements of OA and VFA concentration could enhance the understanding of ongoing fermentation processes.

**Keywords:** multi-analyte biosensor, biogas, electrochemical detection, organic acids, volatile fatty acids

## 1. INTRODUCTION

In light of the depletion of fossil fuels, the public interest of biogas production from renewable resources is steadily increasing. A particular advantage of anaerobic digestion is the ability for simultaneous utilization of industrial waste and thus, providing a promising approach for dealing with another problem of today's world (Angelidaki and Ellegaard, 2003; Komemoto et al., 2009). However, in order to realize the potential of the growing market, several technological and

economic aspects need to be improved to ensure process stability and efficient methane ( $\text{CH}_4$ ) production. Some of these important factors comprise appropriate biogas purification technologies, a suitable feedstock composition and ideal conditions inside the biogas reactor (Weiland, 2010; Andriani et al., 2014; Achinas et al., 2017). The latter is guaranteed by continuous monitoring of various physical and biochemical parameters indicating system stability [pH, alkalinity, gas quality, FOS/TAC (volatile organic acids/total anorganic carbonate)]. Process imbalances are thereby reflected by acidification of the reactor due to accumulation of volatile fatty acids (e.g., acetate, propionate, butyrate) and organic acids, like lactate, formate and alcohols (Nielsen et al., 2007; Boe et al., 2010; Li et al., 2014; Montag and Schink, 2016). Hitherto, estimation of the acid composition is conventionally carried out by gas chromatography (Diamantis et al., 2006), spectroscopy (Falk et al., 2015; Stockl and Lichti, 2018) or HPLC (high-performance liquid chromatography) (Zumbusch et al., 1994; Schiffels et al., 2011). Common disadvantages of these methods are elaborate sample pre-treatment and high costs per analysis, since these are usually executed by external service laboratories. Obviously, the main drawback is the inevitable time delay between sampling and availability of the results, making immediate intervention impossible and therefore represent an element of uncertainty for the plant operators. For these reasons, the acid content is typically only analyzed once or twice per month. In order

to overcome this problem, biosensors have been developed as reliable tools for fast and accurate analysis of several compounds.

Much attention has been paid to the development of lactate and ethanol biosensors, due to their diverse applications in food industry and healthcare (Goriuskina et al., 2009; Rathee et al., 2016). Apart from that, several studies imply an association between these intermediates and process stability of the biogas reactor (Pipyn and Verstraete, 1981; Crable et al., 2011). For this reason, the development and optimization of an organic acid (OA) biosensor, comprising enzymes for the specific detection of D/L-lactate, formate and ethanol was a subject of earlier studies (Pilas et al., 2017). In contrast, only a limited number of volatile fatty acid (VFA) biosensors have been described in the literature up to now. The detection of these analytes was accomplished with microbial fuel cells (Kaur et al., 2013), microbial electrolysis cells (Jin et al., 2017) or dissolved oxygen probes with an immobilized biofilm (Sweeney et al., 2018). On-line shock sensors, based on microbial fuel cells were also reported in the literature (Schievano et al., 2018). Specific determination of individual substrates, e.g., propionate and acetate, was realized using enzyme-based sensors (Mizutani et al., 2001; Mieliauskiene et al., 2006; Sode et al., 2008).

In the presented approach, the above mentioned OA biosensor is combined with a new established system for concurrent detection of acetate and propionate. **Figure 1A** shows the enzymatic principle of the OA biosensor for parallel

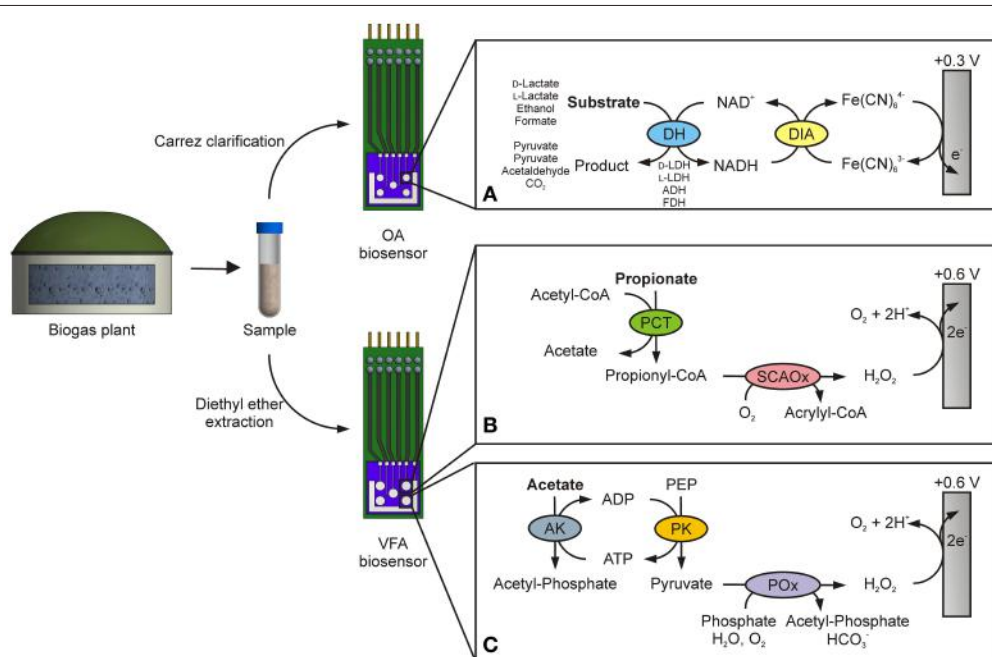


**FIGURE 1 |** Amperometric detection principles of the organic acid (OA) and volatile fatty acid (VFA) biosensor. A sample of fermentation broth is taken from a biogas plant and pretreated by either Carrez clarification or ether extraction. **(A)** Determination of ethanol, formate, D- and L-lactate is then realized by using a bi-enzymatic system, consisting of a specific dehydrogenase (DH) and diaphorase (DIA). For simultaneous detection, on each working electrode DIA with a different DH is immobilized, namely D-lactate dehydrogenase (D-LDH), L-lactate dehydrogenase (L-LDH), alcohol dehydrogenase (ADH) and formate dehydrogenase (FDH), respectively. The product  $\text{Fe}(\text{CN})_6^{4-}$  is re-oxidized at an applied potential of +0.3 V vs. Ag/AgCl. The oxidation of  $\text{H}_2\text{O}_2$  at a working potential of +0.6 V vs. Ag/AgCl is used for measurement of propionate (**B**) and acetate (**C**). For propionate quantification, propionate CoA-transferase (PCT) and short-chain acyl-CoA oxidase (SCAOx) are used. Combination of acetate kinase (AK), pyruvate kinase (PK) and pyruvate oxidase (POx) enable amperometric detection of acetate.

determination of ethanol, formate, D- and L-lactate. In each case, a specific dehydrogenase (DH) is used, which oxidizes its corresponding substrate to acetaldehyde,  $\text{CO}_2$  and pyruvate, respectively. In these reactions, reduction of the cofactor  $\text{NAD}^+$  to  $\text{NADH}$  is catalyzed. Then, diaphorase (DIA) regenerates the released  $\text{NADH}$  by reducing the electron acceptor  $\text{Fe}(\text{CN})_6^{3-}$  to  $\text{Fe}(\text{CN})_6^{4-}$ . At an applied working potential of +0.3 V vs.  $\text{Ag}/\text{AgCl}$ ,  $\text{Fe}(\text{CN})_6^{4-}$  is re-oxidized at the platinum working electrode and the generated current is proportional over a certain linear range to the particular substrate concentration. This method facilitates integration of several analyte-sensing electrodes within one biosensor array. On the contrary, the VFA biosensor works with a different principle for amperometric quantification of acetate and propionate. The working potential is set to +0.6 V vs.  $\text{Ag}/\text{AgCl}$  for anodic oxidation of  $\text{H}_2\text{O}_2$ . This compound is produced in both enzymatic reactions. For this reason, propionate CoA-transferase (PCT) and short-chain acyl-CoA oxidase (SCAOx) are immobilized on the working electrode for electrochemical sensing of propionate (**Figure 1B**). As illustrated in **Figure 1C**, acetate is indirectly determined by application of acetate kinase (AK), pyruvate kinase (PK) and pyruvate oxidase (POx).

In this work, we present for the first time a modular system for the combined amperometric detection of the OA formate, D/L-lactate and ethanol and for the VFA acetate and propionate. Each biosensor utilizes a different enzyme-based detection principle and thereby, simultaneous determination of four and two analytes was realized. The cross-sensitivity and sensor performance in spiked samples of fermentation broth were investigated. Practical application of both biosensors was demonstrated by long-term monitoring of the OA and VFA concentration in a lab-scale biogas reactor. The proposed hybrid biosensor system proved to be a promising device for rapid and facile quantification of several OA and VFAs in real samples. In this regard, the combination of various parameters enables an enhanced understanding of the process conditions within a biogas reactor and thus facilitates an efficient  $\text{CH}_4$  production.

## 2. MATERIAL AND METHODS

### 2.1. Chemicals and Reagents

For construction of the biosensors and realization of photometric assays, the following enzymes were used: Acetate kinase from *Escherichia coli* (AK, 150 U  $\text{mg}^{-1}$ ), alcohol dehydrogenase from *Saccharomyces cerevisiae* (ADH, 310 U  $\text{mg}^{-1}$ ), citrate synthase from porcine heart (CS, 100 U  $\text{mg}^{-1}$ ), diaphorase from *Clostridium kluyveri* (DIA, 51 U  $\text{mg}^{-1}$ ), formate dehydrogenase from *Candida boidinii* (FDH, 0.49 U  $\text{mg}^{-1}$ ), D-lactate dehydrogenase from *Lactobacillus leichmanii* (D-LDH, 213 U  $\text{mg}^{-1}$ ), L-lactate dehydrogenase from *Bacillus stearothermophilus* (L-LDH, 174.5 U  $\text{mg}^{-1}$ ) and pyruvate kinase from rabbit muscle (PK, 1,000 U  $\text{mg}^{-1}$ ) were each obtained from Sigma-Aldrich (St. Louis, MO, USA). Peroxidase from horseradish (HRP, 200 U  $\text{mg}^{-1}$ ) and pyruvate oxidase from *Aerococcus viridans* (POx, 25 U  $\text{mg}^{-1}$ ) were from Merck (Darmstadt, Germany).

Adenosine 5'-diphosphate sodium salt (ADP), bovine serum albumin (BSA), butyryl coenzyme A lithium salt, capronic acid, ethanol, ethylenediaminetetraacetic acid tetrasodium salt dihydrate (EDTA), flavin adenine dinucleotide disodium salt (FAD), glutaraldehyde solution (GA) (25% in  $\text{H}_2\text{O}$ ), glycerol, sodium D-lactate, potassium ferricyanide ( $\text{K}_3[\text{Fe}(\text{CN})_6]$ ), potassium ferrocyanide ( $\text{K}_4[\text{Fe}(\text{CN})_6].3\text{H}_2\text{O}$ ), propionyl coenzyme A lithium salt, sodium propionate, sodium pyruvate, thiamine pyrophosphate (TPP), Triton X-100, valeric acid and  $\text{ZnCl}_2$  were also supplied by Sigma-Aldrich. Adenosine 5'-triphosphate disodium salt (ATP), (2,2'-azino-bis(3-ethylbenzothiazoline-6-sulphonic acid) diammonium salt (ABTS), acetyl coenzyme A trilithium salt, sodium formate, sodium L-lactate, nicotinamide adenine dinucleotide ( $\text{NAD}^+$ ), oxaloacetic acid and phospho(enol)pyruvic acid monopotassium salt (PEP) were purchased from AppliChem (Darmstadt, Germany). Diethyl ether, 5,5'-dithiobis-(2-nitrobenzoic acid), potassium phosphate buffer ( $\text{K}_2\text{HPO}_4$ ,  $\text{KH}_2\text{PO}_4$ ), Tris-(hydroxymethyl)-aminomethane,  $\text{H}_2\text{SO}_4$ ,  $\text{MgCl}_2$  and NaOH were from Carl Roth GmbH & Co. KG (Karlsruhe, Germany). Dithiothreitol (DTT), sodium phosphate buffer ( $\text{Na}_2\text{HPO}_4$ ,  $\text{NaH}_2\text{PO}_4$ ), sodium acetate and sodium butyrate were acquired from Merck (Darmstadt, Germany). d-Desthiobiotin was provided by IBA (Göttingen, Germany).

### 2.2. Cloning

The propionate sensing system is composed of two recombinantly produced enzymes, a propionate CoA-transferase (PCT, EC 2.8.3.1) from *Clostridium propionicum* and a short-chain acyl-CoA oxidase (SCAOx, EC 1.3.3.6) derived from *Arabidopsis thaliana*. Fabrication of the propionate electrode involved cloning of the corresponding genes into designated expression vectors, biomass production and purification of the proteins.

Based on the published sequence (Hayashi et al., 1999), the SCAOx gene was codon-optimized for expression in *E. coli* and synthesized by Eurofins Genomics (Ebersberg, Germany). Moreover, internal restriction sites for *Esp3I* were removed. The resulting sequence was amplified by polymerase chain reaction (PCR) using two primers (SCAOx for 5'-AAGCTCTTCAATGGCGGTTCTGTCAAGCG-3' and SCAOx rev 5'-AAGCTCTTCACCCTAACAAACGAGAGCGGGTAGC-3') with incorporated *LguI* restriction sites (underlined). After analysis of the purified PCR product by chip electrophoresis (MCE-202 MultiNA; Shimadzu, Duisburg, Germany), the SCAOx gene was digested with *LguI* and cloned into a pENTRY vector (IBA, Göttingen, Germany). *E. coli* DH5 $\alpha$ -competent cells were transformed with the resultant plasmid. Following sequence analysis (Eurofins Genomics, Ebersberg, Germany), the SCAOx gene cassette was subcloned into the *Esp3I* site of a StarGate Acceptor Vector (IBA, Göttingen, Germany), containing an N-terminal-fused Strep-tag. Expression plasmids harboring propionate CoA-transferase fused to an N-terminal Strep-tag, were synthesized as previously described (Bijtenhoorn, 2005).

## 2.3. Gene Expression and Protein Purification

*E. coli* BL21(DE3) cells carrying the constructed plasmids were used for production of the recombinant proteins. Following pre-cultivation at 28°C for approx. 15 h in 100 mL LB medium (Luria-Bertani) with 50 µg/mL carbenicillin, the culture was inoculated to 500 mL of the same medium. At optical density (OD<sub>578nm</sub>) of 0.6–0.8, gene expression was initiated by treatment with 200 ng/ml AHT. Post induction, cells harboring recombinant SCAOx were incubated for 2 h at 28°C and finally harvested by centrifugation. Cell pellets were washed once with 50 mL PBS [137 mM NaCl, 2.7 mM KCl, 10 mM Na<sub>2</sub>HPO<sub>4</sub>, 1.8 mM KH<sub>2</sub>PO<sub>4</sub> (pH 7.4)] and afterwards stored at –80°C until used for protein purification. PCT-containing *E. coli* cells were cultivated for 3 h at 28°C post induction and washed with 50 mL TBS [50 mM Tris, 150 mM NaCl (pH 7.5)] prior storage.

Purification of SCAOx was accomplished by affinity chromatography with a Strep-Tactin Macroprep column (IBA GmbH, Göttingen, Germany) as outlined earlier (Röhlen et al., 2017). Briefly, cell pellets were suspended in 100 mM sodium phosphate buffer (pH 7.5, supplemented with 150 mM NaCl and 10 µM FAD) and lysed by sonication. Next, cell debris was pelleted by ultracentrifugation and the clear supernatant was loaded onto the equilibrated column. Elution of the protein was effected by addition of 2.5 mM d-desthiobiotin in aforementioned buffer. Protein concentration and purity were verified by sodium dodecyl sulfate polyacrylamide gel electrophoresis (SDS-PAGE) and Bradford analysis. Purified protein fractions were concentrated by ultrafiltration and 10 vol% glycerol was added for storage at –20°C. Similarly, recombinant PCT was purified using 100 mM Tris-HCl pH 8.0 (supplemented with 150 mM NaCl, 1.0 mM EDTA, 1.0 mM DTT) as resuspension buffer and additionally 2.5 mM d-desthiobiotin for subsequent elution. Prior enzyme immobilization, the storage buffer was exchanged with 100 mM sodium phosphate buffer pH 7.5, 1.0 mM DTT, 1.0 mM EDTA.

## 2.4. Enzyme Activity Measurements

Enzyme activities were determined spectrophotometrically at 25°C in 1 mL reaction mixture using an Ultrospec 2100 pro spectrophotometer (Amersham Biosciences, UK).

Short-chain acyl-CoA oxidase activity was measured in a coupled assay with HRP (Baltazar et al., 1999). The assay mixture included 100 mM sodium phosphate buffer (pH 7.4), supplemented with 0.05 mM FAD, 0.05 mM acyl-CoA, 2.0 mM ABTS and 5.0 U HRP. The reaction was started by addition of the enzyme and the increase in absorbance at 405 nm, due to oxidation of ABTS, was monitored. A molar extinction coefficient  $\epsilon_{405\text{nm}}$  of 18.4 mM<sup>–1</sup> cm<sup>–1</sup> was used for calculation of enzyme activities (Werner et al., 1970).

Propionate CoA-transferase activity was determined by detection of free CoA via a coupled citrate synthase-DTNB reaction (Selmer et al., 2002). The reaction mixture consisted of 100 mM sodium phosphate (pH 7.4), 0.05 mM propionyl-CoA, 20 mM sodium acetate, 1 mM DTNB (5,5'-dithiobis-(2-nitrobenzoic acid)) and 1 mM oxaloacetate and 3 U citrate

synthase. The assay was initiated by addition of PCT and the change in absorbance was followed at 415 nm. Enzyme activities were calculated using a molar extinction coefficient  $\epsilon_{415\text{nm}}$  of 14.14 mM<sup>–1</sup> cm<sup>–1</sup>.

## 2.5. Biosensor Preparation

The multi-parameter biosensor chips (14 × 14 mm<sup>2</sup>) were fabricated by thin-film technology (Pilas et al., 2018). Each biosensor array consists of five individual platinum working electrodes and an additional counter electrode (area 40.5 mm<sup>2</sup>). The diameter of each working electrode of the OA biosensor was 2 mm, whereas the working electrodes of the VFA biosensor were slightly larger (Ø 2.5 mm) for immobilization of an increased volume of enzyme solution. Before the enzymes were immobilized onto the electrodes, the biosensor chips were cleaned by electrochemical treatment in 0.5 M H<sub>2</sub>SO<sub>4</sub> until a stable signal was obtained (+2.0 V vs. Ag/AgCl for 2 min and subsequent cyclic voltammetry from –0.2 to +1.4 V vs. Ag/AgCl).

Enzymes were immobilized by chemical cross-linking with 0.4 vol% GA solution, supplemented with 10 vol% glycerol and 2% BSA. In case of the OA biosensor, each working electrode was endowed with a different DH (ADH, FDH, D-LDH and L-LDH, respectively) in combination with the DIA. Thereby, a volume of 1.5 µL of each enzyme mixture was applied on one of the working electrodes. The fifth working electrode served as a reference and was modified only with the inert protein BSA, which does not exhibit any catalytic activity. Details of exact enzyme loadings on the OA biosensor were given earlier (Pilas et al., 2017).

For construction of the VFA biosensor, GA concentrations were adjusted to 0.24 vol% (propionate electrode) and 0.7 vol% (acetate electrode) each with 2% BSA. The propionate-specific electrode contained 0.032 U PCT and 0.057 U SCAOx embedded in the BSA-GA matrix. Acetate detection was accomplished by an enzyme layer consisting of 3 U POx, 6 U PK and 6 U AK. Each electrode was equipped with 3 µL of the corresponding enzyme mixture.

## 2.6. Experimental Set-Up and Operation

All electrochemical experiments were conducted at room temperature in a three-electrode arrangement with a Ag/AgCl reference electrode (with KCl as inner electrolyte; Sensolytics, Bochum, Germany) and the biosensor, comprising the working electrode (each with five working electrodes per biosensor) and counter electrode. The set-up consisted of a custom-made measurement cell connected to a potentiostat with integrated multiplexer (EmStat3 and MUX16, PalmSens BV, Houten, Netherlands) (Pilas et al., 2018). **Figure 2** shows an image of the applied set-up. For operation of the OA biosensor, a working potential of +0.3 V vs. Ag/AgCl was applied for anodic oxidation of enzymatically produced Fe[CN]<sub>6</sub><sup>4–</sup>. Standard reaction mixture contained 2.5 mM NAD<sup>+</sup> and 2 mM Fe(CN)<sub>6</sub><sup>3–</sup> dissolved in 100 mM potassium phosphate buffer (pH 7.5).

Detection of acetate and propionate with the VFA biosensor was realized at an applied potential of +0.6 V vs. Ag/AgCl for oxidizing H<sub>2</sub>O<sub>2</sub>. Measurements were carried out in 100 mM

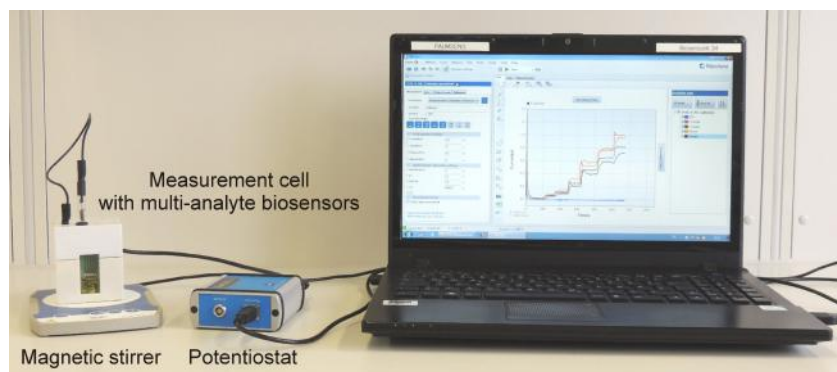


**FIGURE 2 |** Photograph of measurement set-up with biosensor and Ag/AgCl reference electrode connected to a potentiostat and software device.

potassium phosphate buffer (pH 7.0), supplemented with 5 mM MgCl<sub>2</sub>, 0.6 mM TPP, 0.02 mM FAD, 2 mM PEP, 1 mM ATP and 0.4 mM acetyl-CoA. Due to the rapid loss of enzyme activity, an additional 11.84 U PK and 2.5 U AK were added to the reaction mixture. For both biosensors, a volume of 2 mL of the corresponding measurement solution was used. Homogeneous distribution of the calibration and sample solution, respectively, was accomplished with a magnetic stirrer.

## 2.7. Analysis of Fermentation Broth From Biogas Plants

Samples of fermentation broth (approximately 50 mL) were collected one-time from three industrial continuously operated biogas plants in Germany and regularly from a lab-scale biogas reactor. Fermentation sludge from the industrial plants was stored frozen at  $-21^{\circ}\text{C}$  until further measurements, whereas samples from biogas test reactor were analyzed immediately after sampling. For application of the OA and VFA biosensor, as well as analysis by reference techniques, samples were pretreated by two different procedures (see **Figure 1**). On the one hand, samples for the OA biosensor were clarified by Carrez precipitation (Carrez, 1908). A volume of 10 mL of fermentation sludge was mixed carefully with 2 mL of 0.68 M K<sub>4</sub>[Fe(CN)<sub>6</sub>]<sub>2</sub>·3H<sub>2</sub>O and subsequently, 2 mL of 2 M ZnCl<sub>2</sub> were added and agitated again. Following precipitation was induced by addition of 5 mL of 0.4 M NaOH and the final volume was adjusted to 20 mL with deionized water. Insoluble compounds were then separated by centrifugation and the clear supernatant was used for further investigations. For comparative studies, the concentration of ethanol, formate, D- and L-lactate was as well determined with commercial photometric kits (Megazyme International, Wicklow, Ireland) following the manufacturers' instructions. On the other hand, a diethyl ether extraction method was adopted for analysis of acetate and propionate by the VFA biosensor (Schiffels et al., 2011). Therefore, 300  $\mu\text{L}$  of the fermentation broth were mixed with 0.2 g NaCl, 50  $\mu\text{L}$  concentrated HCl and 800  $\mu\text{L}$  diethyl ether. Samples were briefly centrifuged and the ether phase was diluted into 600  $\mu\text{L}$  sodium phosphate buffer pH 7.0. The content of VFA was additionally quantified by a gas chromatograph (GC-2010, Shimadzu, Duisburg, Germany)

equipped with a poly ethylene glycol column (FS-FFAP-CB-0.25, CS-Chromatographie Service GmbH, Langerwehe, Germany) and a flame ionization detector.

The OA and VFA biosensors were also applied for the long-term monitoring of a lab-scale biogas reactor (CSTR-10S, Bioprocess Control AB, Lund, Sweden) with 0.01  $\text{m}^3$  working volume, equipped with a wall jacket and an external water bath [ICC basic pro 9, IKA (Staufen, Germany)] for operation at constant temperature ( $40^{\circ}\text{C}$ ). The continuously operated reactor received a daily feeding of approximately 60 g of sugar cane silage. Analysis of the biogas composition (CH<sub>4</sub> and CO<sub>2</sub>) was performed online by an infrared sensor system (BlueSens, Herten, Germany) on a daily basis. The pH and FOS/TAC were determined offline once per week. During a period of 2 months, digestate samples (50 mL) were taken once a week, purified as described above and subsequently used for electrochemical analysis.

Prior application of the biosensors in real samples, calibration curves were obtained by monitoring the increase in the current signal after successive addition of a stock solution with defined concentration (each consisting of all analytes). Real samples were analyzed by subsequent titration to the reaction buffer, resulting in different dilutions. Based on the sensitivities of the calibration curves, the concentration of each analyte was calculated for each dilution step.

## 3. RESULTS AND DISCUSSION

### 3.1. Sensor Characteristics

The sensor performances were characterized in terms of sensitivity and linear detection range by successive addition of standard solutions with defined concentrations of each analyte. In **Figures 3A,B** the calibration curves of the OA and VFA biosensor are presented. The individual electrodes exhibited a linear relationship between current increase and analyte concentration. **Table 1** summarizes the results obtained for both biosensors. The four analyte sensing elements of the OA biosensor had a similar linear detection range with a sensitivity from 0.64 to 1.16  $\mu\text{A mM}^{-1}$ . Substantially, the different electrodes of the VFA biosensor possessed a sensitivity of 0.27

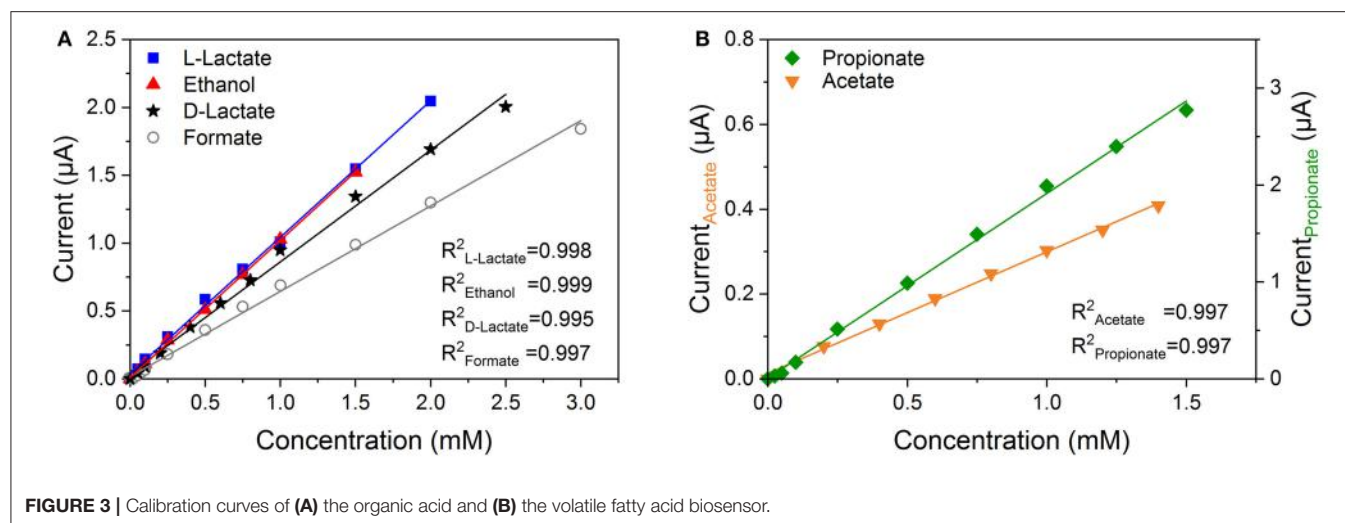


**FIGURE 3** | Calibration curves of (A) the organic acid and (B) the volatile fatty acid biosensor.

**TABLE 1** | Sensor characteristics of the volatile fatty acid (VFA) and organic acid (OA) biosensor operated at an applied potential of +0.6 and +0.3 V vs. Ag/AgCl, respectively.

Biosensor	Analyte	Sensitivity ( $\mu\text{A mM}^{-1}$ )	Linear range (mM)
VFA	Propionate	$2.11 \pm 0.41$	0–1.5
VFA	Acetate	$0.27 \pm 0.05$	0–1.4
OA	D-Lactate	$0.89 \pm 0.03$	0–2.5
OA	L-Lactate	$1.16 \pm 0.06$	0–2.0
OA	Formate	$0.64 \pm 0.02$	0–3.0
OA	Ethanol	$1.12 \pm 0.03$	0–1.5

and  $2.11 \mu\text{A mM}^{-1}$  for acetate and propionate, respectively. In literature, a propionate biosensor based on the same detection principle was reported, hereby, the enzymes were immobilized within a polymer of poly(vinyl alcohol) with styrylpyridinium groups (PVA-SbQ) (Sode et al., 2008). This biosensor displayed a linear detection range of  $10\text{--}100 \mu\text{M}$  with a sensitivity of  $1.7 \mu\text{A mM}^{-1} \text{ cm}^{-2}$ . With a normalized sensitivity of  $42.9 \mu\text{A mM}^{-1} \text{ cm}^{-2}$  the propionate electrode of the VFA biosensor shows an almost 25 times higher sensitivity over a broader linear range.

Only few electrochemical enzyme-based acetate biosensors are mentioned in literature. One of them was also a tri-enzyme system, consisting of AK, PK and POx, which were entrapped on the platinum electrode in a membrane of polydimethylsiloxane (PDMS) (Mizutani et al., 2001). Measurements were performed at an applied potential of  $-0.4$  V vs. Ag/AgCl for monitoring of the oxygen consumption. Under this condition, a linear correlation between current signal and acetate concentration was obtained in a narrow range of  $5 \mu\text{M}$  to  $0.5 \text{ mM}$  compared to the VFA biosensor of the present study ( $0.2\text{--}1.4 \text{ mM}$ ).

### 3.2. Evaluation of Interferences

Given the complex chemical composition of biogas sludges, interfering effects of different substances were investigated prior to application of the sensors in real samples. The

examined compounds were selected according to the substrate spectrum of the employed enzymes and potential occurrence in the fermentation broth. In each measurement, the respective compound was added individually to the reaction buffer and substrate-related current changes were determined. All tests were conducted in triplicate. **Table 2** summarizes the results of the influence of potential interferences on the sensor response of both biosensors. Obtained current responses were normalized against current signals monitored for the intended substrate.

The selectivity of the VFA biosensor was investigated by introduction of  $0.5 \text{ mM}$  substrate to the reaction mixture. Several different short-chain fatty acids were deployed for cross-sensitivity tests with the propionate-sensing electrode. Relevant current changes were solely observed for butyrate (28%), a natural substrate for PCT (Selmer et al., 2002) and, in the activated form (butyryl-CoA), for SCAOx (Hayashi et al., 1999). However, the combination of both enzymes strongly favors the enzymatic conversion of propionate (100%), which is consistent with data from the literature describing a propionate electrode and a photometric assay based on the same enzyme cascade (Rajashekara et al., 2006; Sode et al., 2008).

The concentration and specific ratio of volatile fatty acids in a biogas reactor is highly dependent on the feedstock and type of digestion. Although butyric acid is usually present in the biogas broth, and thus both substrates compete for the same catalytic binding site of the PCT, typical concentrations of this fatty acid are decisively lower compared to propionate (Franke-Whittle et al., 2014). Therefore, the usual ratio of the acids on the one hand and the affinity of the biosensor for the specific substrates on the other hand favor the detection of propionate in the fermentation broth. In addition, due to the thermodynamic unfavorable conditions for propionate degradation, the short-chain fatty acid persists longer in the fermentation broth than other volatile fatty acids and is therefore regarded as a reliable indicator for process monitoring (Nielsen et al., 2007).

The acetate-sensing electrode was also subjected to interference study using potential AK substrates (propionate, formate, ethanol, butyrate, and glycerol) and pyruvate, the

**TABLE 2 |** Effect of potential interferents on the different electrodes of the volatile fatty acid (VFA) and organic acid (OA) biosensor.

Interferent	VFA biosensor			OA biosensor			
	Acetate	Propionate	D-Lactate	L-Lactate	Formate	Ethanol	BSA Blank
	(%)	(%)	(%)	(%)	(%)	(%)	(%)
Acetate	100	0	–	–	0	0	0
Propionate	6	100	–	–	0	0	0
D-Lactate	–	–	100	0	0	0	0
L-Lactate	–	–	0	100	0	0	0
Formate	3	–	0	0	100	0	0
Ethanol	0	–	0	0	0	100	0
Pyruvate	117	–	0	0	0	0	0
Malate	–	–	9	12	4	7	0
Butyrate	0	28	–	–	0	–	0
Valerate	–	1	–	–	–	–	0
Capronate	–	0	–	–	–	–	0
Glycerol	0	–	–	–	–	–	0
n-Propanol	–	–	–	–	–	61	0
n-Butanol	–	–	–	–	–	43	0
Methanol	–	–	–	–	0	0	0
Ascorbate	–	–	75	53	–	–	100
Cysteine	–	–	36	29	–	–	65
Urea	–	–	1	1	–	–	6

Change in the current signal was normalized to the current obtained for the intended substrate (–, not evaluated).

main substrate of POx. While no signal response was observed with ethanol, butyrate and glycerol, slight current increase was monitored for propionate (6%) and formate (3%). Interference with propionic acid was likewise reported by different acetate biosensors using AK (Tang and Johansson, 1997; Mizutani et al., 2001). Nevertheless, our findings suggest a clear preference of AK for acetate over the other substrates tested. Apart from this, both substrates are naturally not present to the same extent and the propionate concentration is significantly lower as compared to acetate (Montag and Schink, 2016). Cross-sensitivity with propionate thereby has rather little effect on the amperometric acetate detection. Not surprisingly, the acetate sensor showed the highest sensor response upon addition of pyruvate (117%). However, as intermediate of several metabolic pathways (Zhou et al., 2018), pyruvate degrades rapidly and thus extracellular concentrations of the POx substrate are negligible compared to the acetate levels in the biogas medium. Previous studies on the accumulation of extracellular metabolites from *E. coli* under anaerobic conditions showed only minimal levels of pyruvic acid compared to the concentration of acetate and other acids (Kim et al., 2015; Yasid et al., 2016).

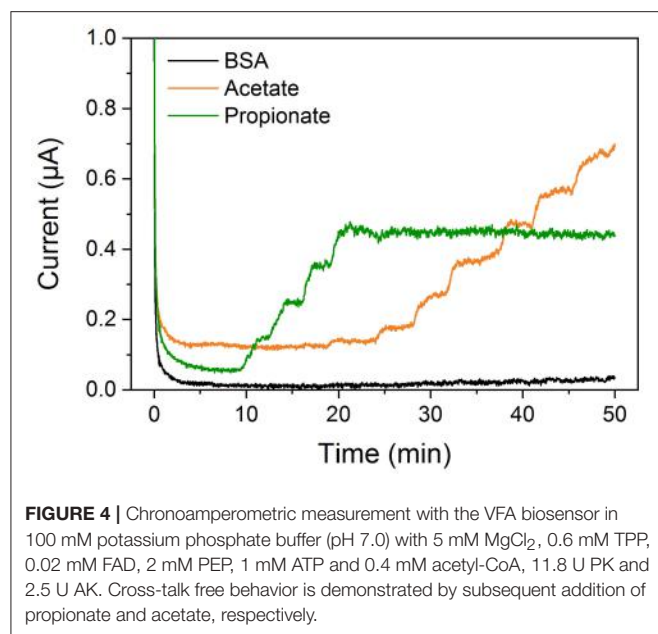
Evaluation of possible susceptibility of the OA biosensor to potential interferents was accomplished by observing the change in current signal after addition of several substrates (each 1 mM) to the measurement solution. Both lactate electrodes exhibited sensitivity toward ascorbate, cysteine and to some small extent to urea. All of these compounds are known reducing agents at the applied positive working potentials (Sprules et al., 1995; Palmisano et al., 2000). For this reason, an increase in the current signal was observed for the electrode covered with BSA. The

ethanol electrode was also sensitive to other alcohols, namely n-propanol (61%) and n-butanol (43%). This interference is mainly caused by the broad substrate spectrum of the applied ADH from *S. cerevisiae* (Plapp et al., 1993). The substrate specificity of electrochemical ethanol biosensors is generally a great challenge, since detection principles based on the enzyme alcohol oxidase show this characteristic behavior, too (Azevedo et al., 2005).

Due to the substrate range of AK on the one hand and the PCT-catalyzed formation of acetate from acetyl-CoA on the other hand, potential cross-talk between the two VFA electrodes was investigated by successive addition of the analytes. As depicted in Figure 4, only the corresponding electrode showed a current response upon introduction of the substrate. Similarly, no inadvertent interactions were observed for simultaneous determination of ethanol, formate, D- and L-lactate with the OA biosensor as described earlier (Pilas et al., 2017).

### 3.3. Evaluation of Sensor Performance in Spiked Samples

For evaluation of the sensor performance in real samples and complex matrices, sludge samples from three different biogas plants (BP1 to BP3) were collected. Biogas production in BP1 was achieved by mono-digestion of maize silage, whereas in BP2 additionally cattle slurry was applied. The feedstock of BP3 consisted of maize silage, cattle slurry and manure. The type of feedstock used for anaerobic digestion mainly influences the viscosity of the fermentation broth. In order to test the biosensors in various media compositions, biogas



plants with different feedstocks were selected. After sampling, fermentation sludges were spiked with 20 mM acetate, 5 mM propionate and each 10 mM ethanol, formate, D- and L-lactate, respectively. The concentration of VFA and OA was determined with the two biosensors and for comparative studies by gas chromatography and commercial photometric kits. **Figure 5** provides a comparison of the results obtained by the biosensors and reference techniques. For all three samples, the amperometrically determined concentrations correlate well with the corresponding conventional method. These findings demonstrate successfully the potential of simultaneous and rapid monitoring of several analytes in complex media by application of the electrochemical hybrid biosensor system.

### 3.4. Monitoring of a Lab-Scale Biogas Reactor

The formation of biogas from organic matter is a complex procedure carried out by a consortium of different microorganisms. It involves four phases: hydrolysis, acidogenesis, acetogenesis and methanogenesis. In the first step, complex polymers, like carbohydrates, fats and proteins are degraded into smaller molecules. Hydrolysis is followed by the acid-forming step, the acidogenesis. At this stage, the fermenting bacteria produce volatile fatty acids, alcohols as well as  $H_2$ ,  $CO_2$ , and  $NH_4$ . Then, acetogenic and syntrophic bacteria metabolize fatty acids and alcohols into acetate,  $H_2$  and  $CO_2$ . Finally, acetate and hydrogen are used by methanogenic archaea to produce  $CH_4$  and  $CO_2$ . In an anaerobic digester, these four processes occur concurrently. In order to successfully maintain the biogas production, suitable detection systems for specific key parameters are required. Therefore, the developed hybrid biosensor system was applied for the long-term monitoring of a lab-scale biogas reactor ( $0.01\text{ m}^3$ ), operated at mesophilic

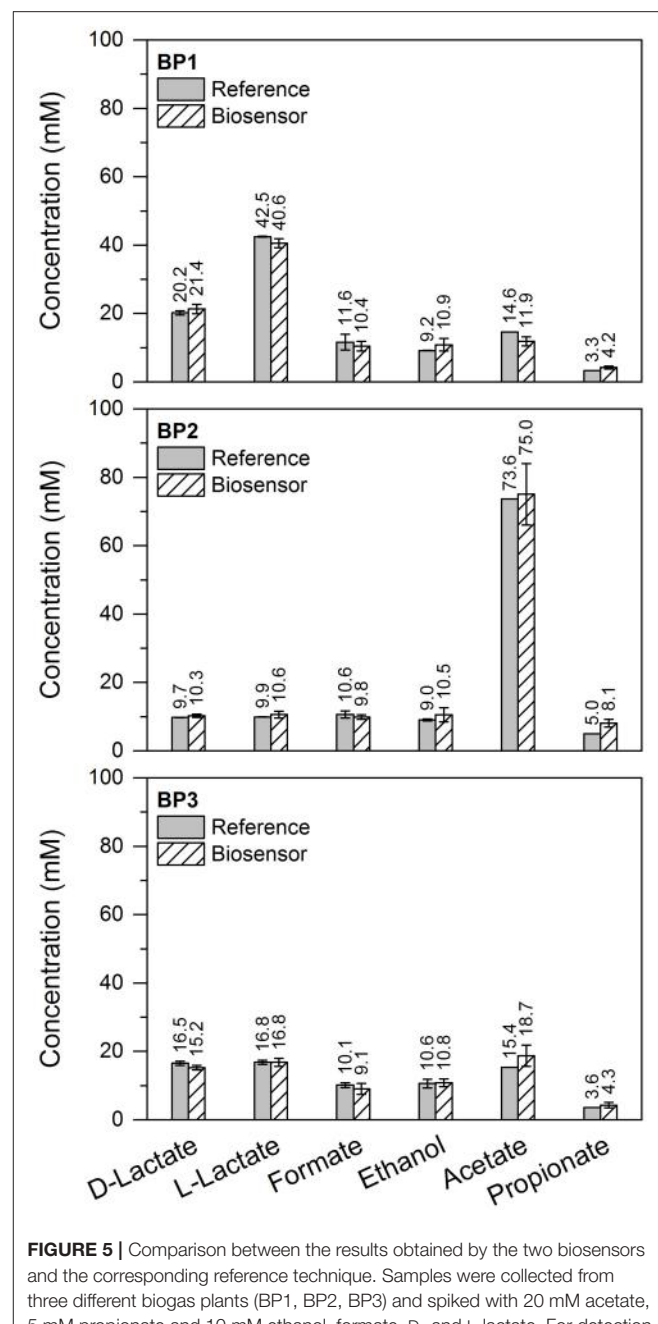
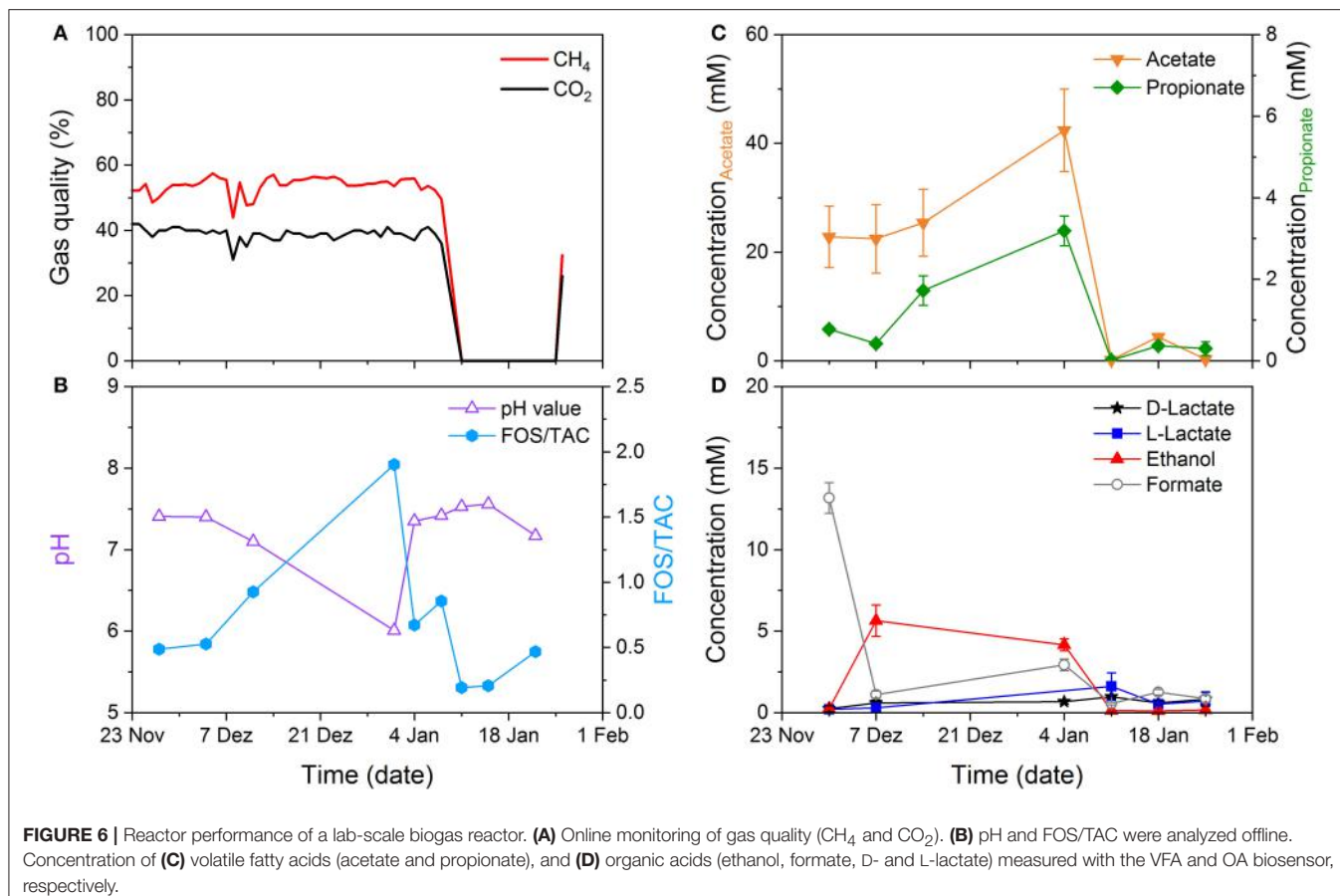


**FIGURE 5 |** Comparison between the results obtained by the two biosensors and the corresponding reference technique. Samples were collected from three different biogas plants (BP1, BP2, BP3) and spiked with 20 mM acetate, 5 mM propionate and 10 mM ethanol, formate, D- and L-lactate. For detection of ethanol, formate, D- and L-lactate a photometric reference technique was applied, and acetate and propionate were additionally quantified by gas chromatography.

conditions ( $40^\circ\text{C}$ ) with sugar cane silage as feedstock. Besides the concentration of OA and VFA, also several physical- and chemical parameters were investigated for a period of 2 months.

**Figure 6** provides an overview of all the data obtained in this time frame. The content of  $CH_4$  and  $CO_2$  in the produced biogas was analyzed online. Basically, the biogas composition was stable during the first 44 days with  $53.7 \pm 2.7\%$  and  $39.0 \pm 7.8\%$  of  $CH_4$  and  $CO_2$ , respectively (**Figure 6A**). These quantities



represent typical values reported in literature (Herout et al., 2011). Between day 45 and 47 the fermenter was temporarily shut down for technical reasons, which is reflected in the sudden loss of  $\text{CH}_4$  and  $\text{CO}_2$  release. Biogas production was resumed 5 days after restart of the digester. In addition to end-product determination, the ratio of volatile fatty acid to total alkalinity (FOS/TAC) and pH are regularly monitored process parameters and are here depicted in Figure 6B. While the pH optimum is typically defined between 6.5 and 7.5, opinions vary regarding optimum VFA concentrations and thus FOS/TAC levels, but agree on the fact, that normal VFA levels highly depend on the individual system (Angelidaki et al., 1993; Franke-Whittle et al., 2014). Therefore, stable concentrations are considered more substantial than the magnitude (Hamawand and Baillie, 2015). During the observed period, FOS/TAC concentrations fluctuated between 0.5 and 1.0 until fermenter stoppage with one peak at day 36. This sudden increase was accompanied with a drop in pH, caused by acidification of the medium due to VFA accumulation. This change in the acid composition was detectable with the hybrid biosensor, too. As depicted in Figure 6C, acetate and propionate concentrations, which have a decisive impact on FOS/TAC, showed a similar curve progress during the observed time frame. Minor changes in organic acid and alcohol content were detected by the OA sensor. For each measurement point, samples were also analyzed using the conventional techniques as described in section 3.3. Again, our

findings were in good agreement with the reference methods (data not shown). The results demonstrate a successful long-term application of the hybrid biosensor system for monitoring of acid composition changes. The detection of essential precursors and intermediates of the anoxic food chain, realized by the OA sensor, is a useful extension to established process parameters, as these are usually not covered by conventional monitoring systems. The combined determination of the different acids leads to an improved understanding of the events that occur during fermentation. Thus, potential bottlenecks of the process can be identified and eliminated immediately.

## 4. CONCLUSION

Nowadays, monitoring of organic and volatile fatty acids in anaerobic fermentation processes is only feasible by laborious techniques, such as HPLC or GC. The analysis by these methods, however, is time-consuming and results are typically provided with some delay after sampling. In this study, two different enzyme-based biosensors were demonstrated as a hybrid system for amperometric detection of several process-relevant intermediates: on the one hand, an OA biosensor for simultaneous determination of ethanol, formate, D- and L-lactate, and on the other hand, a VFA biosensor for electrochemical quantification of acetate and propionate. The

effect of various potential interferents on the sensor signal of both biosensors was investigated and results revealed only limited cross-sensitivity. The acetate electrode showed 6% response to propionate and the propionate-sensing electrode was sensitive to other volatile fatty acids (28 and 1% to butyrate and valerate, respectively). The ethanol sensor displayed sensitivity to other alcohols, such as n-propanol (61%) and n-butanol (43%). Nevertheless, both biosensors showed satisfactory cross-talk behavior and the potential for practical application in complex matrices was demonstrated. These findings were also verified by evaluation of the sensor performance in spiked samples of fermentation broth from different biogas plants. A good correlation was obtained between the biosensors and conventional reference techniques. Additionally, the electrochemical biosensor system was used for the first time for long-term monitoring of the acid composition in a lab-scale biogas reactor. Application of such a device would greatly enhance the overall understanding of complex fermentation processes. In comparison to traditional analytical procedures, the presented hybrid biosensor system offers facile, rapid and on-site determination of multiple acids, due to a portable measurement set-up.

Future work will focus on the development of a common procedure for sample preparation, which is suitable for all analytes and both biosensors. In this regard, usage of the crude extract for the electrochemical measurements is envisaged, so that sample pretreatment is not required at all. Application of such a compact monitoring device for determination of acetate, propionate, ethanol, formate, D- and L-lactate would enable early

detection of imbalances in anaerobic fermentation processes. Moreover, the broad substrate spectrum of SCAOx allows a future extension of the system by substitution of PCT with other enzymes providing activated short fatty acids. Therefore, the combination of butyrate-specific enzymes with SCAOx would permit a more precise determination of the VFA content in the biogas reactor.

## AUTHOR CONTRIBUTIONS

DR and JP designed and performed the experiments, analyzed the data and wrote the manuscript. MD contributed samples from different biogas plants. TS, MK, and MS supervised the experiments, critically reviewed and edited the manuscript.

## FUNDING

This work was supported by the German Federal Ministry of Food and Agriculture (BMEL) [grant number 22006613].

## ACKNOWLEDGMENTS

The authors thank H. Iken for fabrication of the sensor chips. We also acknowledge S. Jansen and G. Pohen from the Institute NOWUM-Energy for operating the lab-scale bioreactor, supplying the monitoring data (gas quality, pH and FOS/TAC) and performing gas chromatography analyses. DR and JP thank FH Aachen for the Ph.D. scholarship.

## REFERENCES

- Achinas, S., Achinas, V., and Euverink, G. J. W. (2017). A technological overview of biogas production from biowaste. *Engineering* 3, 299–307. doi: 10.1016/J.ENG.2017.03.002
- Andriani, D., Wresta, A., Atmaja, T. D., and Saepudin, A. (2014). A review on optimization production and upgrading biogas through CO<sub>2</sub> removal using various techniques. *Appl. Biochem. Biotechnol.* 172, 1909–1928. doi: 10.1007/s12010-013-0652-x
- Angelidaki, I., and Ellegaard, L. (2003). Codigestion of manure and organic wastes in centralized biogas plants: status and future trends. *Appl. Biochem. Biotechnol.* 109, 95–106. doi: 10.1385/ABAB:109:1-3:95
- Angelidaki, I., Ellegaard, L., and Ahring, B. K. (1993). A mathematical model for dynamic simulation of anaerobic digestion of complex substrates: focusing on ammonia inhibition. *Biotechnol. Bioeng.* 42, 159–166. doi: 10.1002/bit.260420203
- Azevedo, A. M., Prazeres, D. M. F., Cabral, J. M. S., and Fonseca, L. P. (2005). Ethanol biosensors based on alcohol oxidase. *Biosens. Bioelectr.* 21, 235–247. doi: 10.1016/j.bios.2004.09.030
- Baltazar, M. F., Dickinson, F. M., and Ratledge, C. (1999). Oxidation of medium-chain acyl-CoA esters by extracts of *Aspergillus niger*: enzymology and characterization of intermediates by HPLC. *Microbiology* 145, 271–278. doi: 10.1099/13500872-145-1-271
- Bijtenhoorn, P. (2005).  $\beta$ -Alanin-CoA-Transferase aus *Clostridium propionicum*. Diploma thesis, Philipps University Marburg, Marburg.
- Boe, K., Batstone, D. J., Steyer, J.-P., and Angelidaki, I. (2010). State indicators for monitoring the anaerobic digestion process. *Water Res.* 44, 5973–5980. doi: 10.1016/j.watres.2010.07.043
- Carrez, M. C. (1908). Le ferrocyanure de potassium et l'acétate de zinc comme agents de défécation des urines. *Ann. Chim. Anal.* 13, 97–101.
- Crable, B. R., Plugge, C. M., McInerney, M. J., and Stams, A. J. M. (2011). Formate formation and formate conversion in biological fuels production. *Enzyme Res.* 2011, 1–8. doi: 10.4061/2011/532536
- Diamantis, V., Melidis, P., and Aivasidis, A. (2006). Continuous determination of volatile products in anaerobic fermenters by on-line capillary gas chromatography. *Anal. Chim. Acta* 573–574, 189–194. doi: 10.1016/j.aca.2006.05.036
- Falk, H. M., Reichling, P., Andersen, C., and Benz, R. (2015). Online monitoring of concentration and dynamics of volatile fatty acids in anaerobic digestion processes with mid-infrared spectroscopy. *Bioprocess Biosyst. Eng.* 38, 237–249. doi: 10.1007/s00449-014-1263-9
- Franke-Whittle, I. H., Walter, A., Ebner, C., and Insam, H. (2014). Investigation into the effect of high concentrations of volatile fatty acids in anaerobic digestion on methanogenic communities. *Waste Manage.* 34, 2080–2089. doi: 10.1016/j.wasman.2014.07.020
- Goriushkina, T. B., Soldatkin, A. P., and Dzyadevych, S. V. (2009). Application of amperometric biosensors for analysis of ethanol, glucose, and lactate in wine. *J. Agricult. Food Chem.* 57, 6528–6535. doi: 10.1021/jf9009087
- Hamawand, I., and Baillie, C. (2015). Anaerobic digestion and biogas potential: simulation of lab and industrial-scale processes. *Energies* 8, 454–474. doi: 10.3390/en8010454
- Hayashi, H., De Bellis, L., Ciurli, A., Kondo, M., Hayashi, M., and Nishimura, M. (1999). A novel acyl-CoA oxidase that can oxidize short-chain acyl-CoA in plant peroxisomes. *J. Biol. Chem.* 274, 12715–12721. doi: 10.1074/jbc.274.18.12715
- Herout, M., Malaták, J., Kucera, L., and Dlabařa, T. (2011). Biogas composition depending on the type of plant biomass used. *Res. Agricult. Eng.* 57, 137–143. doi: 10.17221/41/2010-RAE
- Jin, X., Li, X., Zhao, N., Angelidaki, I., and Zhang, Y. (2017). Bio-electrolytic sensor for rapid monitoring of volatile fatty acids in anaerobic digestion process. *Water Res.* 111, 74–80. doi: 10.1016/j.watres.2016.12.045

- Kaur, A., Kim, J. R., Michie, I., Dinsdale, R. M., Guwy, A. J., and Premier, G. C. (2013). Microbial fuel cell type biosensor for specific volatile fatty acids using acclimated bacterial communities. *Biosens. Bioelectr.* 47, 50–55. doi: 10.1016/j.bios.2013.02.033
- Kim, T.-S., Jung, H.-M., Kim, S.-Y., Zhang, L., Li, J., Sigdel, S., et al. (2015). Reduction of acetate and lactate contributed to enhancement of a recombinant protein production in *E. coli* BL21. *J. Microbiol. Biotechnol.* 25, 1093–1100. doi: 10.4014/jmb.1503.03023
- Komemoto, K., Lim, Y. G., Nagao, N., Onoue, Y., Niwa, C., and Toda, T. (2009). Effect of temperature on VFA's and biogas production in anaerobic solubilization of food waste. *Waste Manage.* 29, 2950–2955. doi: 10.1016/j.wasman.2009.07.011
- Li, L., He, Q., Wei, Y., He, Q., and Peng, X. (2014). Early warning indicators for monitoring the process failure of anaerobic digestion system of food waste. *Bioresource Technol.* 171, 491–494. doi: 10.1016/j.biortech.2014.08.089
- Mieliauskienė, R., Nistor, M., Laurinavicius, V., and Csöregi, E. (2006). Amperometric determination of acetate with a tri-enzyme based sensor. *Sens. Actuat. B Chem.* 113, 671–676. doi: 10.1016/j.snb.2005.07.016
- Mizutani, F., Sawaguchi, T., Yabuki, S., and Iljima, S. (2001). Amperometric determination of acetic acid with a trienzyme/poly(dimethylsiloxane)-bilayer-based sensor. *Analyst. Chem.* 73, 5738–5742. doi: 10.1021/ac010622i
- Montag, D., and Schink, B. (2016). Biogas process parameters—energetics and kinetics of secondary fermentations in methanogenic biomass degradation. *Appl. Microbiol. Biotechnol.* 100, 1019–1026. doi: 10.1007/s00253-015-7069-0
- Nielsen, H., Uellendahl, H., and Ahring, B. K. (2007). Regulation and optimization of the biogas process: propionate as a key parameter. *Biomass Bioenergy* 31, 820–830. doi: 10.1016/j.biombioe.2007.04.004
- Palmissano, F., Rizzi, R., Centonze, D., and Zambonin, P. G. (2000). Simultaneous monitoring of glucose and lactate by an interference and cross-talk free dual electrode amperometric biosensor based on electropolymerized thin films. *Biosens. Bioelectr.* 15, 531–539. doi: 10.1016/S0956-5663(00)00107-X
- Pilas, J., Yazici, Y., Selmer, T., Keusgen, M., and Schöning, M. J. (2017). Optimization of an amperometric biosensor array for simultaneous measurement of ethanol, formate, D- and L-lactate. *Electrochim. Acta* 251, 256–262. doi: 10.1016/j.electacta.2017.07.119
- Pilas, J., Yazici, Y., Selmer, T., Keusgen, M., and Schöning, M. J. (2018). Application of a portable multi-analyte biosensor for organic acid determination in silage. *Sensors* 18, 1470–1481. doi: 10.3390/s18051470
- Pipyn, P., and Verstraete, W. (1981). Lactate and ethanol as intermediates in two-phase anaerobic digestion. *Biotechnol. Bioeng.* 23, 1145–1154. doi: 10.1002/bit.260230521
- Plapp, B. V., Green, D. W., Sun, H.-W., Park, D.-H., and Kim, K. (1993). "Substrate specificity of alcohol dehydrogenases," in *Enzymology and Molecular Biology of Carbonyl Metabolism 4*, Vol. 328, eds H. Weiner, D. W. Crabb, and T. G. Flynn (Boston, MA: Springer), 391–400.
- Rajashekhar, E., Hosoda, A., Sode, K., Ikenaga, H., and Watanabe, K. (2006). Lactate and ethanol as intermediates in two-phase anaerobic digestion. *Biotechnol. Prog.* 22, 334–337. doi: 10.1021/bp050240o
- Rathee, K., Dhull, V., Dhull, R., and Singh, S. (2016). Biosensors based on electrochemical lactate detection: a comprehensive review. *Biochem. Biophys. Rep.* 5, 35–54. doi: 10.1016/j.bbrep.2015.11.010
- Röhlen, D. L., Pilas, J., Schöning, M. J., and Selmer, T. (2017). Development of an amperometric biosensor platform for the combined determination of L-malic, fumaric, and L-aspartic acid. *Appl. Biochem. Biotechnol.* 183, 566–581. doi: 10.1007/s12010-017-2578-1
- Schiavano, A., Colombo, A., Cossettini, A., Goglio, V., D'Ardes, V., Trasatti, S., et al. (2018). Single-chamber microbial fuel cells as on-line shock-sensors for volatile fatty acids in anaerobic digesters. *Waste Manage.* 71, 785–791. doi: 10.1016/j.wasman.2017.06.012
- Schiffels, J., Baumann, M. E. M., and Selmer, T. (2011). Facile analysis of short-chain fatty acids as 4-nitrophenyl esters in complex anaerobic fermentation samples by high performance liquid chromatography. *J. Chromatogr. A* 1218, 5848–5851. doi: 10.1016/j.chroma.2011.06.093
- Selmer, T., Willanzheimer, A., and Hetzel, M. (2002). Propionate CoA-transferase from *Clostridium propionicum*: cloning of the gene and identification of glutamate 324 at the active site. *Eur. J. Biochem.* 269, 372–380. doi: 10.1046/j.0014-2956.2001.02659.x
- Sode, K., Tsugawa, W., Aoyagi, M., Rajashekhar, E., and Watanabe, K. (2008). Propionate sensor using coenzyme-A transferase and acyl-CoA oxidase. *Protein Peptide Lett.* 15, 779–781. doi: 10.2174/092986608785203737
- Sprules, S. D., Hart, J. P., Wring, S. A., and Pittson, R. (1995). A reagentless, disposable biosensor for lactic acid based on a screen-printed carbon electrode containing Meldola's Blue and coated with lactate dehydrogenase, NAD<sup>+</sup> and cellulose acetate. *Anal. Chim. Acta* 304, 17–24. doi: 10.1016/0003-2670(94)00565-4
- Stockl, A., and Lichten, F. (2018). Near-infrared spectroscopy (NIRS) for a real time monitoring of the biogas process. *Bioresource Technol.* 247, 1249–1252. doi: 10.1016/j.biortech.2017.09.173
- Sweeney, J. B., Murphy, C. D., and McDonnell, K. (2018). Development of a bacterial propionate-biosensor for anaerobic digestion monitoring. *Enzyme Microb. Technol.* 109, 51–57. doi: 10.1016/j.enzmictec.2017.09.011
- Tang, X.-J., and Johansson, G. (1997). A bioelectrochemical method for the determination of acetate with immobilized acetate kinase. *Anal. Lett.* 30, 2469–2483. doi: 10.1080/00032719708001758
- Weiland, P. (2010). Biogas production: current state and perspectives. *Appl. Microbiol. Biotechnol.* 85, 849–860. doi: 10.1007/s00253-009-2246-7
- Werner, W., Rey, H.-G., and Wielinger, H. (1970). Über die Eigenschaften eines neuen Chromogens für die Blutzuckerbestimmung nach der GOD/POD-Methode. *Fresenius' Zeitschrift für Analytische Chemie* 252, 224–228. doi: 10.1007/BF00546391
- Yasid, N. A., Rolfe, M. D., Green, J., and Williamson, M. P. (2016). Homeostasis of metabolites in *Escherichia coli* on transition from anaerobic to aerobic conditions and the transient secretion of pyruvate. *R. Soc. Open Sci.* 3, 1–12. doi: 10.1098/rsos.160187
- Zhou, M., Yan, B., Wong, J. W. C., and Zhang, Y. (2018). Enhanced volatile fatty acids production from anaerobic fermentation of food waste: a mini-review focusing on acidogenic metabolic pathways. *Bioresource Technol.* 248, 68–78. doi: 10.1016/j.biortech.2017.06.121
- Zumbusch, P. v., Meyer-Jens, T., Brunner, G., and Märkl, H. (1994). On-line monitoring of organic substances with high-pressure liquid chromatography (HPLC) during the anaerobic fermentation of waste-water. *Appl. Microbiol. Biotechnol.* 42, 140–146. doi: 10.1007/BF00170237
- Conflict of Interest Statement:** The authors declare that the research was conducted in the absence of any commercial or financial relationships that could be construed as a potential conflict of interest.
- Copyright © 2018 Röhlen, Pilas, Dahmen, Keusgen, Selmer and Schöning. This is an open-access article distributed under the terms of the Creative Commons Attribution License (CC BY). The use, distribution or reproduction in other forums is permitted, provided the original author(s) and the copyright owner(s) are credited and that the original publication in this journal is cited, in accordance with accepted academic practice. No use, distribution or reproduction is permitted which does not comply with these terms.



# SPRi-Based Biosensing Platforms for Detection of Specific DNA Sequences Using Thiolate and Dithiocarbamate Assemblies

Marcin Drozd<sup>1</sup>, Mariusz D. Pietrzak<sup>1\*</sup> and Elżbieta Malinowska<sup>1,2</sup>

<sup>1</sup> Faculty of Chemistry, The Chair of Medical Biotechnology, Warsaw University of Technology, Warsaw, Poland, <sup>2</sup> Centre for Advanced Materials and Technologies, Warsaw, Poland

## OPEN ACCESS

### Edited by:

Dmitry Kirsanov,  
Saint Petersburg State University,  
Russia

### Reviewed by:

Caifeng Ding,  
Qingdao University of Science and  
Technology, China  
Lai-Kwan Chau,  
National Chung Cheng University,  
Taiwan  
Rongxin Su,  
Tianjin University, China

### \*Correspondence:

Mariusz D. Pietrzak  
mariusz@ch.pw.edu.pl

### Specialty section:

This article was submitted to  
Analytical Chemistry,  
a section of the journal  
Frontiers in Chemistry

Received: 15 February 2018

Accepted: 30 April 2018

Published: 22 May 2018

### Citation:

Drozd M, Pietrzak MD and  
Malinowska E (2018) SPRi-Based  
Biosensing Platforms for Detection of  
Specific DNA Sequences Using  
Thiolate and Dithiocarbamate  
Assemblies. *Front. Chem.* 6:173.  
doi: 10.3389/fchem.2018.00173

The framework of presented study covers the development and examination of the analytical performance of surface plasmon resonance-based (SPR) DNA biosensors dedicated for a detection of model target oligonucleotide sequence. For this aim, various strategies of immobilization of DNA probes on gold transducers were tested. Besides the typical approaches: chemisorption of thiolated ssDNA (DNA-thiol) and physisorption of non-functionalized oligonucleotides, relatively new method based on chemisorption of dithiocarbamate-functionalized ssDNA (DNA-DTC) was applied for the first time for preparation of DNA-based SPR biosensor. The special emphasis was put on the correlation between the method of DNA immobilization and the composition of obtained receptor layer. The carried out studies focused on the examination of the capability of developed receptors layers to interact with both target DNA and DNA-functionalized AuNPs. It was found, that the detection limit of target DNA sequence (27 nb length) depends on the strategy of probe immobilization and backfilling method, and in the best case it amounted to 0.66 nM. Moreover, the application of ssDNA-functionalized gold nanoparticles (AuNPs) as plasmonic labels for secondary enhancement of SPR response is presented. The influence of spatial organization and surface density of a receptor layer on the ability to interact with DNA-functionalized AuNPs is discussed. Due to the best compatibility of receptors immobilized via DTC chemisorption:  $1.47 \pm 0.4 \cdot 10^{12}$  molecules  $\cdot$  cm $^{-2}$  (with the calculated area occupied by single nanoparticle label of  $\sim 132.7$  nm $^2$ ), DNA chemisorption based on DTCs is pointed as especially promising for DNA biosensors utilizing indirect detection in competitive assays.

**Keywords:** DNA biosensors, surface plasmon resonance imaging, DNA immobilization, self-assembled monolayers, dithiocarbamate, gold functionalization

## INTRODUCTION

Surface of gold transducers due to numerous attractive features, such as the repeatability of their preparation, excellent electrochemical properties, and unsurpassed chemical stability have gained unflagging interest as platforms for immobilization of protein- and oligonucleotide-based receptors (Sendroiu et al., 2011; Choi et al., 2014). Rapid and high-throughput detection of DNA is in high demand in many areas such as medical diagnostics (e.g. single nucleotide polymorphism, disease

markers, and pathogens detection), DNA sequencing, and environmental monitoring (Mannelli et al., 2003; Fiche et al., 2008; Kong et al., 2014; Pursey et al., 2017). Facility of preparation of ultra-thin Au-layers on glass substrates has opened up the possibility for a development of relatively simple and routine methodology of optical transducers fabrication. Capability of contactless, spatially-resolved monitoring of surface plasmon resonance (SPR) (its angle shift) on a very small area using imaging mode enabled simultaneous real-time detection and determination of various analytes with a use of different receptors spotted on a surface of transducers. Such multiplexed screening approach underlies the SPRi-based DNA biosensors and arrays (Nelson et al., 2001; Chen et al., 2009).

To take full advantage of multiplexed detection of specific DNA sequences, efforts for a development of methods of robust and regioselective tethering of oligonucleotide probes to gold have been made. Such applications require both the high durability of bioreceptor-Au transducer coupling and possibly high surface density of DNA probes (Keighley et al., 2008). The thoughtful choice of linkage chemistry is particularly important due to the need to ensure the compatibility with the methods of multispotting, typically used for fabrication of sensing platforms for high-throughput screening (Brockmann et al., 1999; Leonov and Wei, 2011; Simon et al., 2015). Among methods of gold biofunctionalization, these based on monolayers of compounds capable of chemisorption via terminal, sulfur-containing groups, mainly thiol derivatives, and more rarely other such as disulfides, sulfides, thioesters, isothiocyanates, or dithiocarbamates (DTCs) (Ulman, 1996; Mandler and Kraus-Ophir, 2011). Despite the common use of thiolate chemisorption, there is a number of reported disadvantages, limiting the use of such strategy for a construction of functional receptor layers for biosensing (Schoenfisch and Pemberton, 1998; Raigoza et al., 2012). Park et al. (2010) reported the lability of monodentate linkage of alkanethiols with gold, which negatively affects the resolution of patterns obtained via thiol self-assembly on Au substrates. Another significant difficulty in the case of direct immobilization of biologically originated compounds is a shortage (or even a total absence) of exposed thiolate moieties, which enforces the necessity of chemical modification of such receptors prior to the immobilization. Because of the listed disadvantages and due to the susceptibility of Au-thiolate bond to photochemical oxidation as well as relatively low resistance to desorption when in contact with surface-active agents (such as biogenic thiols), it seems reasonable to develop alternative, preferably one-step method to tether DNA-probes to the gold surface.

A DTC chemisorption on gold was reported as promising alternative to thiol self-assembly for the first time by Zhao et al. (2005). Since that time, bidentate anchoring of bifunctional DTC derivatives has gained interest as the elegant way of both fabrication of sensing platforms and functionalization of nanomaterials (Sharma et al., 2008; Adak et al., 2010; Wang et al., 2012). It was reported, that low-molecular weight DTCs are capable to form bonds with gold of the strength high enough to competitively desorb short thiols. It offers new possibilities to design orthogonal assemblies for further deposition of biomolecules, nanoparticles and dyes (Park et al., 2010; Leonov

and Wei, 2011). The important advantage of DTC chemistry, in terms of direct immobilization of bioreceptors, is the facility of DTC synthesis in a reaction between primary or secondary amines with carbon disulfide according to  $S_N2$  substitution mechanism (Morf et al., 2006). The common presence of receptors bearing amine moieties (proteins, oligopeptides) and commercial availability of oligonucleotides modified with terminal aminolink significantly extends the pool of available bioreceptors compatible with this immobilization method in comparison to direct immobilization of thiols.

Recently, direct immobilization of vital components of biosensors via DTC linkage was successfully demonstrated for various types of proteins: protein A (Paiva et al., 2017) and enzymes such as laccase (Almeida et al., 2017) and glucose oxidase (Almeida et al., 2012). In each case naturally occurring amine groups were converted to respective DTCs prior to direct attachment of such biomolecules to gold. Despite the increasing importance of DTC-Au chemistry for fabrication of biosensors, only two works focusing on assembly of short DNA oligonucleotides terminated with  $\omega$ -aminoalkyl moiety can be found in the literature. First of them refers to electrochemical (Wang et al., 2012), while the second one to chemiluminescent (Lou et al., 2015) DNA biosensor. Importantly, although the use of bidentate DTCs is indicated as the important advantage, no attempt was made to directly compare physicochemical and analytical performance of DTC-DNA assemblies to analogous monolayers based on thiolated DNA assemblies in the reported studies.

In the framework of presented studies we examined three different strategies of regioselective attachment of model ssDNA probes for fabrication of SPRi biosensors, including two chemical approaches: DTC and thiolate chemisorption, and physisorption of unmodified oligonucleotides. The special emphasis was put on the critical comparison of the analytical parameters of obtained biosensing platforms when detecting the target sequence. SPRi studies were performed both in the label-free format as well as applying a signal enhancement strategy with a use of DNA-functionalized AuNPs as plasmonic labels. The main aim of this work was to develop general methodologies, which are useful for preparation of receptor layers utilizing hybridization as the recognition mechanism. Biosensors constructed on their base can find applications in analytics for detection of short oligonucleotides, such as specific genomic sequences, microRNA, or PCR products.

## MATERIALS AND METHODS

### Chemicals and Oligonucleotides

6-mercaptop-1-hexanol (MCH), carbon disulfide, hexaamineruthenium(III) chloride (RuHex), and tris(hydroxymethyl)aminomethane (Tris) were obtained from Sigma-Aldrich (Poland) and used as received. Perhydrol, sulfuric acid (96%), ammonia (25%), and ethanol (96%) were purchased in Avantor S.A. (Poland). All chemicals used in this work were at least analytical grade. Milli-Q water (DI) (resistivity  $>18\text{ M}\Omega \cdot \text{cm}$ ) was used throughout experiments. DNA oligonucleotides were supplied by Metabion GmbH

(Germany). Lyophilized pellets were resuspended in 10 mM Tris-HCl buffer, pH 7.8 or DI water (in case of amino-terminated sequence) and stored at  $-20^{\circ}\text{C}$ . The corresponding sequences were listed in **Table 1**.

## Instrumentation

Two types of gold transducers have been used in the framework of this studies. Integrated SPRi-Biochips<sup>TM</sup> made of a high refractive index glass prism coated with gold thin film were purchased in Horiba Scientific (France). Gold disk electrodes were purchased in CH Instruments (USA). SPRi experiments were conducted with the use of SPRi-Lab<sup>+</sup> instrument (Horiba). Comparative studies of DNA-DNA interactions were performed with the use of homemade microfluidic system, equipped with two parallel cells integrated with optical system. Chronocoulometric and voltammetric measurements were carried out with CHI 1040A potentiostat equipped with homemade voltammetric cell adapted to measurements in nitrogen atmosphere. Apart from gold working electrode, Ag/AgCl/3.0 M KCl reference electrode and gold wire as auxiliary electrode were applied in a classical three-electrode system. Details of instrumentation used for AuNPs characterization (transmission electron microscopy and UV-Vis spectrophotometry) can be found in Supplementary Material.

## Preparation of Gold Surfaces

Prior to use, SPRi biochips were treated with “alkaline piranha” ( $\text{NH}_3/\text{H}_2\text{O}_2/\text{water} = 1:1:3$ , v/v) in  $60^{\circ}\text{C}$  for 15 min. After rinsing with DI water, 400  $\mu\text{L}$  of “acidic piranha” ( $\text{H}_2\text{SO}_4/\text{H}_2\text{O}_2 = 3:1$  v/v) was dropped on gold surface. The incubation step lasted for 2 min and then transducers were sequentially rinsed with water, ethanol, and dried in a stream of nitrogen. Gold electrodes of 2 mm diameters were polished with alumina slurry of grain size 0.3 and 0.05 nm, respectively. After mechanical polishing, electrodes were rinsed and sonicated in DI water for 2 min to remove particulate matter. Next, gold electrode surfaces were chemically cleaned by dropping of “acidic piranha” solution prepared as above. After 5 min, electrodes were thoroughly rinsed with DI water. The electrochemical treatment was performed

by registration of CV scan series for each electrode in 100 mM solution of sulfuric acid between  $-0.3$  and  $+1.6$  V, until repeatable voltammograms were observed.

## DNA Immobilization on Gold

In the framework of comparative SPRi and electrochemical studies, three DNA attachment strategies: physical adsorption (DNA-Ads), thiol chemisorption (DNA-SH), and DTC chemisorption were examined. The immobilization of single-stranded deoxyribonucleotide probes (ssDNA) on electrochemical and SPRi transducers was carried out using the same methodology. The derivatization of amine-modified ssDNA was obtained according to procedure described by Sharma (Sharma et al., 2008) with slight modifications (Drozd et al., 2016). In brief, 20  $\mu\text{M}$  solution of *Probe-NH<sub>2</sub>* in 200 mM phosphate-borate (PB) buffer pH 10.0 was mixed with aliquot of 20  $\mu\text{M}$  (equimolar) solution of  $\text{CS}_2$  in the same buffer and then sonicated in ice bath for 10 min. Then solution of DTC-modified probe was diluted to desired concentration (5  $\mu\text{M}$ ) with PB buffer. In case of thiolated (*Probe-SH*) and unmodified (*Probe*) ssDNA, respective solutions in concentrations of 5  $\mu\text{M}$  were prepared directly in 200 mM PB buffer. The immobilization was accomplished by dripping of 25  $\mu\text{L}$  of each solution on freshly cleaned gold electrodes or SPRi transducers. The topography of SPRi biochip typically consists of three separate, vertical strips. Such arrangement was aimed at obtaining of orthogonal pattern after installation of biochip in microfluidic system. The immobilization was carried out for 18 h in humid conditions and at room temperature. Then both types of Au transducers were carefully rinsed with DI water and dried under argon stream.

## Synthesis of Citrate-Stabilized Gold Nanoparticles and Their Modification With ssDNA

Spherical, citrate-capped AuNPs with mean diameter of 13.0 nm were synthesized according to Turkevich method (Turkevich et al., 1951). Modification of AuNPs with thiolated DNA was accomplished by the “salt-aging” procedure described previously by Mirkin et al. (1996). More detailed description of synthetic procedures can be found in Supplementary Material.

## Chronocoulometric Determination of DNA Surface Density

Electrochemical surface areas of gold electrodes were determined by means of cyclic voltammetry according to procedures described by Trasatti and Petrii (1992). A total surface area was given from the charge of gold oxide reduction peak, assuming 390  $\mu\text{C}\cdot\text{cm}^{-2}$  as an unit value (Tichoniuik et al., 2010). DNA density on gold were determined based on methodology by Steel et al. (1998). Electrochemical measurements were realized in six repetitions to obtain statistically meaningful results. The charge related to the amount of adsorbed redox marker was calculated according to linearized form of the Anson equation, indicating the proportionality of the charge diffusion component to the square root of time. Experimental details of voltammetric and chronocoulometric measurements and methodology of DNA

**TABLE 1** | Probes, target, and label DNA sequences (5'-3').

Functionality	Name	DNA sequence
DNA probes	<i>Probe</i>	5'-ACTTGCTCGTCTAGATCTGCTCGTTCA-3'
	<i>Probe-SH</i>	HS-C6-ACTTGCTCGTCTAGATCTGCTCGTTCA-3'
	<i>Probe -NH<sub>2</sub></i>	$\text{H}_2\text{N-C6-}$ ACTTGCTCGTCTAGATCTGCTCGTTCA-3'
Target DNA	<i>Rand</i>	5'-AACCATGTTTGGAAAGCCAAGGCCA-3'
	<i>Comp</i>	5'-TGAACGAGCAGATCTAGACGAGCAAGT-3'
AuNP labels	<i>Comp-SH</i>	HS-C6-TGAACGAGCAGATCTAGACGAGCAAGT-3'
	<i>Rand-SH</i>	HS-C6-AACCATGTTTGGAAAGCCAAGGCCA-3'

The “C6” abbreviation refers to  $\omega$ -modified *n*-hexyl chain attached to terminal 5' or 3' oligonucleotide.

coverage calculation were extensively described in Supplemental Data.

### SPRi Studies of DNA-DNA Interactions

The real-time monitoring of DNA-DNA or DNA-ssDNA-functionalized AuNPs (AuNPs@ssDNA) interactions were performed in PBS buffer pH 7.4 containing 0.25 M NaCl as running buffer (RB) under a constant flowrate of  $25 \mu\text{L} \cdot \text{min}^{-1}$  for DNA-DNA and  $10 \mu\text{L} \cdot \text{min}^{-1}$  for DNA-AuNPs@ssDNA studies, respectively. All measurements in differential mode were realized by simultaneous injection of the complementary target (*Comp*) and random sequence (*Rand*) of equal concentration (within 1 and 1,000 nM range) to separate microfluidic cells. If not stated otherwise, injections typically lasted for 7 min. Before the measurements, three separate fields (spots) for which the reflectance changes were monitored, were defined (separately for each type of receptor layer both flowcells). As regenerating agent (inducing denaturation of DNA duplexes) 50 mM aqueous NaOH was used. To obtain mixed type monolayers (MCH-blocked), repeated injection of 1 mM of MCH in RB for 10 min was carried out. All experiments were conducted in triplicate. Differential sensograms (used throughout quantitative analysis) were obtained by subtracting the normalized values of reflectance changes ( $\Delta R$ ) for the corresponding detection areas in both cells ( $\Delta R_{Comp} - \Delta R_{Rand}$ ). Values of SPRi responses used for preparation of calibration curves were typically acquired as reflectivity differences between  $\Delta R$  levels 1 min before and 10 min after beginning of target DNA injection.

## RESULTS AND DISCUSSION

Reports concerning the utilization of DNA-DTC assemblies as receptor layers usually attribute the attractiveness of analytical parameters of hybridization-based biosensors to stable, bidentate anchoring of DNA probes to gold (Sharma et al., 2008; Wang et al., 2012; Lou et al., 2015). It should be however underlined, that only indirect methods of signal generation were applied in the case of discussed solutions. Therefore, it is difficult to unequivocally assess the significance of probe density resulting from the applied immobilization strategy for a biosensor sensitivity. It should be however underlined, that the proposed approach provides a critical examination of selected methods of oligonucleotide immobilization for construction of DNA biosensing platforms. The major advantage of the SPRi technique used in this work lies in the possibility of direct measurement of the associated mass corresponding to formation of DNA duplexes in the label-free format.

### Comparative Characterization of DNA Immobilization Strategies

To comparatively examine SPRi responses corresponding to injections of a model ssDNA sequence, sensograms were registered simultaneously for three types of oligonucleotide receptor layers: thiolate (DNA-SH), dithiocarbamate (DNA-DTC), and physisorbed (DNA-Ads). To assure reliable negative control, corresponding *Rand* sequence was simultaneously injected into reference flowcell. Such approach allows for the

effective suppression of the influence of non-specific interactions of target DNA with Au on obtained real-time SPRi sensograms. The design of differential microfluidic cell used throughout our SPR studies is depicted in **Figure 1A**.

According to literature reports, conversion of oligonucleotides modified with terminal aminolink into DTCs was accomplished following to the spontaneous reaction with  $\text{CS}_2$  in a basic environment (Sharma et al., 2008). According to our previous report, slight modifications of known methodology (reaction at pH 10.0 instead of 9.0 and ultrasonic propagation) were introduced to ensure both the improvement of reaction rate and the efficiency of amine conversion (Drozd et al., 2016). The apparent pattern of immobilized ssDNA probes (dark stripes—see **Figure 1B**), may act as a proof of the successful immobilization of oligonucleotide by means of chemisorption of both thiolate and DTC as well as a direct physisorption of DNA strands on a gold chip. The details of DNA-tethering chemistry are depicted in **Figure 1C**.

The increase of differential SPRi signal was observed in the response to complementary target sequence (*Comp*) used in the concentration of 50 nM, regardless of immobilization strategy. Result of individual experiment indicating the capability of DNA-DTC for hybridization with complementary sequence, together with the specified steps of SPRi experiment is depicted in **Figure 2**. First, the reusability of obtained receptor layers was verified by fourfold repetition of target DNA injection (50 nM), each time followed by removal of hybridized strand using 50 mM of NaOH solution in the regeneration step. It is noteworthy, that in any studied case the statistically relevant drop of SPRi response along with subsequent regeneration cycles was not observed. Such result indicates the relevance of non-specific interactions between oligonucleotides and gold surface. The surprising robustness of this construct can be assigned to increased significance of multidentate, adsorptive interactions of amine moieties of nucleobases observed for DNA probes of moderate length. The mechanisms of length- and base-dependent ssDNA adsorption on gold were thoroughly investigated (Steel et al., 2000; Kimura-Suda et al., 2003). Such approach was among others successfully utilized for the development of DNA biosensors and multiplex microplatforms (Koo et al., 2015; Sina et al., 2017). Interestingly, beyond two methods based on chemisorption, also DNA adsorption approach turned out to be sufficient to assure the stable attachment of DNA receptors for further studies in a microfluidic system, where oligonucleotides are continuously exposed to shear forces.

### Analytical Performance of Various Receptor Layers Toward DNA Sensing

Due to the satisfactory reproducibility of the obtained SPRi biosensors, a full range calibration curves based on multiple injections of DNA were prepared (see **Figure 3A**). Beyond the homogeneous DNA assemblies described above, our research also focused on the determination of analytical parameters of mixed-type receptor layers obtained by backfilling the surface with 6-mercaptophexanol. Introduction of MCH was dictated

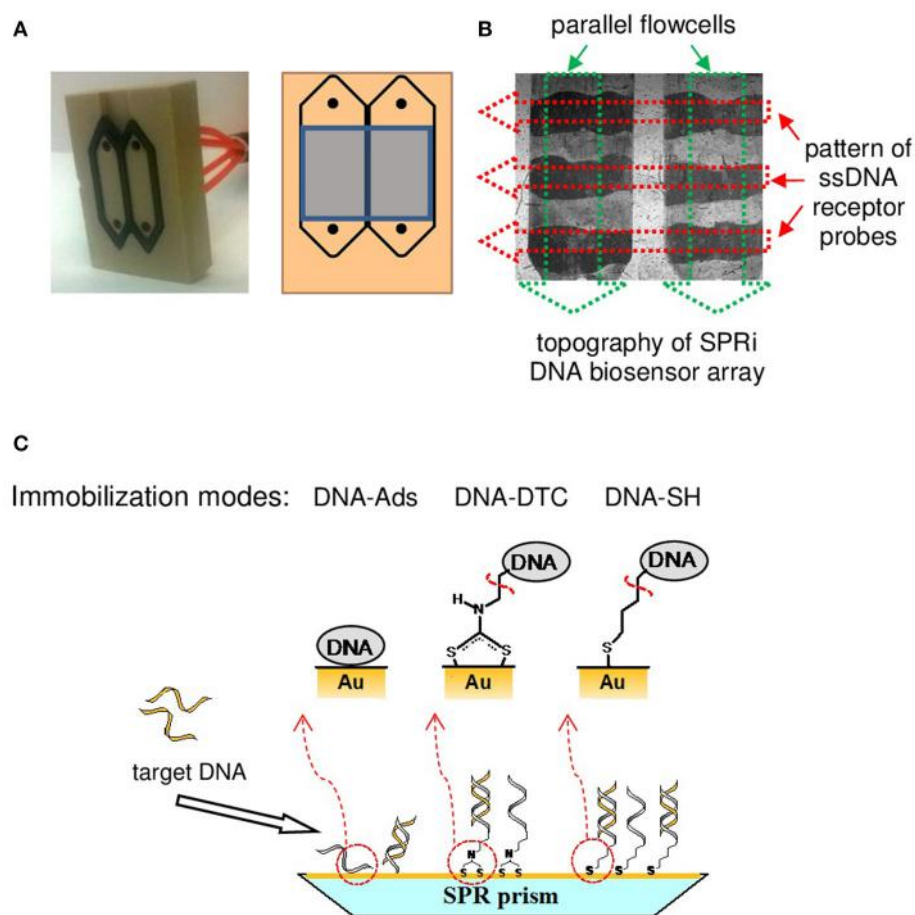


**FIGURE 1** | Schematic illustration of SPRi instrumentation and methodology utilized in this work. **(A)** Image of two-channel, homemade SPRi microfluidic cell (left). Scheme of cell design with indicated detection area of SPRi optical system (right). **(B)** Flow cell image captured by CCD camera with the schematic of orthogonal pattern of bioreceptor probes (red arrows) and microfluidic cells (green arrows). **(C)** Schematic representation of the DNA-immobilization strategies examined in the framework of presented studies (magnified side-view of SPRi biochip<sup>TM</sup>).

by its widespread use in electrochemical and SPR biosensors exploiting DNA SAMs (He et al., 2000; Tichoniu et al., 2010). Main goals of such treatment aimed at obtaining of highly ordered assemblies, backfilling of ssDNA SAM defects and pinholes, and counteracting the non-specific adsorption (Keighley et al., 2008). Schematic representation of influence of MCH on morphology of DNA-based SAM is depicted in Figure 3B.

Obtained relationships between SPR response and logarithm of the target DNA concentration were characterized by the linear course, typical for DNA sensors used in fluidic systems (Hao et al., 2017). In the case of homogeneous layers (without MCH) the highest sensitivity (defined as a slope of the linear section of calibration curve) was noted for the DNA-SH monolayer and amounted to 0.787 of resonant unit per decade. The slope of the curve for DNA-DTC was slightly smaller and was equal to 82.2% of the value obtained for DNA-SH. Surprisingly high sensitivity, which amounted to 54.4% of the value for DNA-SH monolayer was observed for DNA-Ads, taking into account the mechanism of DNA duplex formation,

which forces the repeatable conformational changes of the receptor layer. In contrary to several literature reports, this result indicates the existence of a sufficiently strong interaction between oligonucleotide probe (27 nucleobases length) and bare gold, while maintaining good availability of immobilized probes to hybridization with target DNA (Georgiadis et al., 2000; Nelson et al., 2001). It was unambiguously confirmed in a number of literature reports, that intensity of hybridization signals measured in direct format is predominantly determined by the surface density of oligonucleotide receptors (Steel et al., 1998; Peterson et al., 2001). The determined LOD values for examined biosensors amounted to 824, 725, and 615 pM, for DNA-Ads, DNA-SH, and DNA-DTC, respectively. Detection limits were calculated using three standard deviations of the reference signal (Hao et al., 2017). Despite differences in the sensitivities of the homogeneous layers, they are all characterized by wide range of linear response (see Figure 3).

It can be seen in Figure 2, that under applied conditions the time of interaction required to achieve the state of dynamic equilibrium is longer than the time applied for injection of target

DNA. The relatively short contact time of DNA probes with target sequence (7 min) is insufficient to achieve the equilibrium of the DNA-DNA duplex formation at association step. It should be stressed, that this fact opens up some possibilities for optimization of injection time in order to further improve the analytical parameters of obtained biosensors.

At the next stage of studies, the impact of MCH-backfilling on the working parameters of various DNA-based receptor layers

was revealed. DNA-SH monolayer turned out to be the most resistant to influence of 6-mercaptophexanol, which induced the loss of sensitivity by 22.7%. The observed sensitivity drop can be assigned to the partial desorption of probe DNA, caused by chemisorption of competitive surface-active agent (MCH) (Steel et al., 2000). The main difference compared to homogeneous layers was the significant decrease in the sensitivity of DNA-Ads (drop of calibration curve slope to 21.0% of the initial value) and DNA-DTC (sensitivity reached only 12.8% of the initial value obtained for the corresponding homogeneous layer). The latter result should be considered disappointing, as it indicates that the durability of the DTC-Au assembly to thiol-induced desorption turned out to be significantly lower than expected.

The introduction of backfilling agent was also reflected in the calculated detection limits. Values of LOD for developed biosensors amounted to 2.88 nM for DNA-Ads, 662 pM for DNA-SH, and 1.96 nM in the case of DNA-DTC. In the case of DNA-SH, modification with MCH induced the rearrangement and ordering of the monolayer, with a small contribution of desorption of bioreceptor. This resulted in the slight improvement of detection limit (725–662 pM). Conversely, in the case of DNA-Ads and DNA-DTC the effect of receptor desorption presumably turned out to be dominant, which was reflected in about 3.5-fold (DNA-Ads) and 3.2-fold (DNA-DTC) increase of LOD value.

Basic conclusions arising from presented research remain in opposition to few available literature reports. Comparative stability studies, which were described for DTC- and thiolate-based SAMs unequivocally indicate the higher energy of DTCs

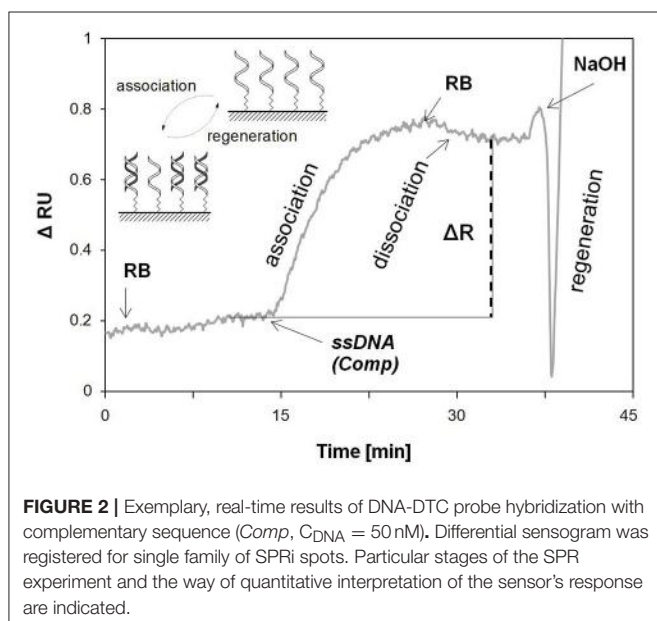


**FIGURE 2** | Exemplary, real-time results of DNA-DTC probe hybridization with complementary sequence (Comp,  $C_{DNA} = 50$  nM). Differential sensogram was registered for single family of SPRi spots. Particular stages of the SPR experiment and the way of quantitative interpretation of the sensor's response are indicated.

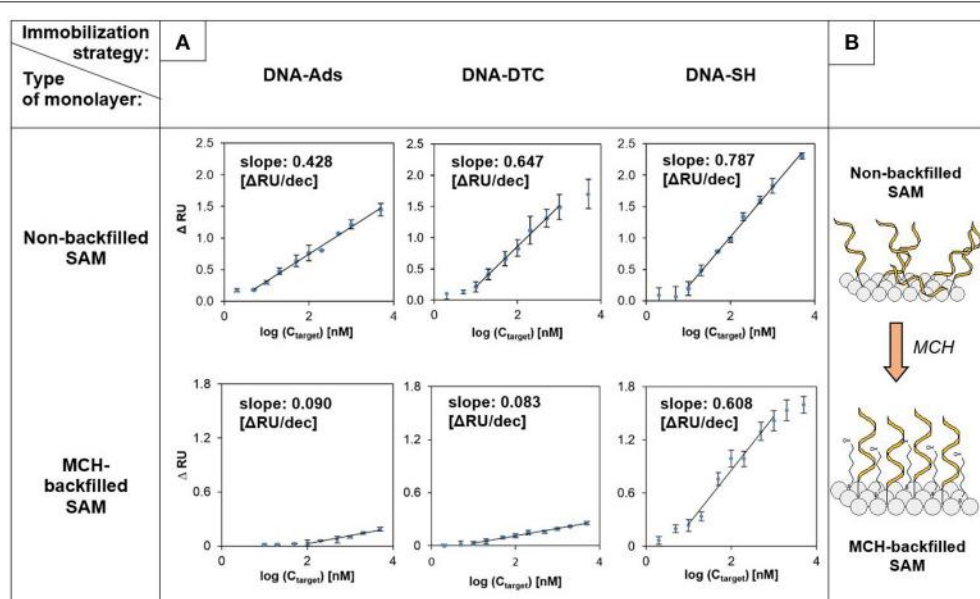


**FIGURE 3** | SPRi calibration curves and analytical parameters obtained for various immobilization strategies ( $n = 3$ ). **(A)** Comparative results for non-backfilled (top row) and MCH-backfilled (bottom row) DNA-SAMs. **(B)** Schematic illustration of DNA-monolayer reorganization induced by MCH. Random sequence (Rand) was injected into the reference cell throughout experiments. “ $n$ ” value corresponds to the number of detection areas for which reflectance changes (independent sensograms) were recorded.

chemisorption on gold in comparison to thiol assembly (Park et al., 2010; Raigoza et al., 2012). It should be however underlined, that their scope of work was limited only to simple, N,N-disubstituted DTC derivatives. Such compounds differ significantly from DTC-DNA utilized in this work in both size of side chain and the order of amine precursor. What is also important, simple, N,N-disubstituted DTCs are routinely purified before being used to form monolayers, which is not possible in the case of N-monosubstituted DTCs. Inability to isolate DNA-DTC from the reaction mixture may significantly impede the formation of monolayers on gold. The adverse effect of co-adsorption of CS<sub>2</sub> and parent amines on formation of DTC layers was already reported for simple, bifunctional DTCs (Zhao et al., 2005; Adak et al., 2010).

Process of DTC chemisorption may also be disturbed by the interaction of oligonucleotide chain with the gold surface. Assumptions drawn for DNA-DTCs are additionally supported by reports describing the mechanism of formation of thiolated DNA monolayers. The occurrence of non-specific DNA adsorption in coexistence with DNA-SH assembly was already described by Steel et al. (2000). According to this work, for thiolate monolayers composed of long oligonucleotide chains (over 24 nb), when the length of the immobilized DNA chain increased, the degree of order of obtained SAMs gradually decreased. Such phenomenon was explained by the increasing contribution of non-covalent interactions of nucleobases with Au. It should be also pointed out, that Morf et al. (2006) indicated an approximately 4-fold slower kinetics of DTC assembly compared to thiol monolayers. Low rate of Au-DTC bond formation may further enhance the interferences caused by co-adsorption of DNA chains.

## Chronocoulometric Determination of Surface Density of Immobilized DNA Probes

As postulated in section Analytical Performance of Various Receptor Layers Toward DNA Sensing, the putative explanation of diversity of biosensors sensitivity lies in the substantial differences in density of DNA immobilized on gold. For this reason, such assumption was verified by determining the surface coverage of oligonucleotide probes immobilized on Au. Chronocoulometric method of DNA quantification based on the measurement of the charge corresponding to reduction of Ru(NH<sub>3</sub>)<sub>6</sub><sup>3+</sup> adsorbed by polyanionic DNA chains bound to surface of gold electrodes was applied (Steel et al., 1998; Tichoniuk et al., 2010) (see Figure S1). To assure reliability of chronocoulometric measurements, DNA monolayer without defects and pinholes is required, therefore the scope of research was limited to MCH-backfilled, mixed monolayers.

As predicted, DNA-SH/MCH monolayer was characterized with the highest amount of immobilized DNA molecules. The obtained probe density of  $7.62 \cdot 10^{12} \text{ cm}^{-2}$  stays in accordance with values known from the literature. According to them, thiolated SAMs prepared in similar way exhibit surface density within the range of  $1\text{--}10 \cdot 10^{12} \text{ cm}^{-2}$  (Peterson et al., 2001;

Tichoniuk et al., 2010). Values within these limits are widely recognized as optimal in terms of density of oligonucleotide-based SAMs dedicated to the detection of complementary DNA sequences. On the other hand, the remaining bioreceptor layers were characterized by several times smaller surface coverage, as in the case of mixed DNA-DTC which was characterized with the lowest density ( $1.47 \cdot 10^{12} \text{ molecules} \cdot \text{cm}^{-2}$ ), over 5 times lower than in the case of corresponding DNA-SH (see Table 2). It is noteworthy, that similar trend was observed for alkyl DTC and thiolate monolayers (ferrocene-C16-DTC and ferrocene-C16-SH) by Eckermann et al. (2010), where the ratio of the surface densities calculated for thiolate and DTC monolayers was 3.46. Lower surface density of DTC derivatives is typically explained by the occurrence of steric hindrance resulting from bidentate Au-DTC chelation and thus attenuation of hydrophobic interactions of alkyl chains (Eckermann et al., 2010; Raigoza et al., 2012). It should be however noted, that surprisingly high density of DNA-Ads, together with relatively high stability of adsorbed DNA additionally confirms the assumption of large contribution of co-adsorption in the overall effect observed for DTC monolayers. Such conclusions remain in substantial discrepancy to reports concerning DNA-DTC monolayers in construction of biosensing platforms, in which the advantages of bidentate chemisorption of DTC are indicated *a priori*, without excessive verification of their superiority over thiolate chemisorption and physisorption.

## Correlation Between DNA Surface Coverage and Efficiency of AuNPs Labeling

The obtained analytical parameters of DNA-DTC based SPRi biosensors in the label-free format do not surpass the corresponding, thiol-based ones, which is attributed to lower surface density of receptors. However, the basic difference between the research presented in this work and the mentioned literature reports lies in the fact, that described DTC-DNA-based biosensors exploited indirect approach for analytical signal generation (Wang et al., 2012; Lou et al., 2015). This discrepancy became the motivation to investigate the correlation between the surface density of oligonucleotide receptors and labeling efficiency using DNA-functionalized gold nanoparticles. For this purpose, AuNPs functionalized with *Comp* (AuNPs@*Comp-SH*) and *Rand* sequence were utilized as plasmonic signal enhancers. Analysis of TEM micrographs (Figure S2) and position of LSPR maximum (519 nm, see Figure S3) confirmed, that the average diameter of the AuNPs is 13.0 nm (Haiss et al., 2007).

**TABLE 2 |** Surface densities of DNA oligonucleotides immobilized on the surface of gold disk electrodes ( $n = 6$ ).

Monolayer composition	DNA-Ads /MCH	DNA-SH/MCH	DNA-Ads/MCH
DNA surface density ( $\text{cm}^{-2}$ )	$(1.63 \pm 0.30) \cdot 10^{12}$	$(7.62 \pm 0.59) \cdot 10^{12}$	$(1.47 \pm 0.40) \cdot 10^{12}$

*"n"* value corresponds to the number of electrodes used.

It could be expected that the major difference in dimensions of AuNPs@*Comp-SH* and free *Comp* sequence would be reflected in the kinetics of their binding by capture DNA. To verify such hypothesis, investigations with the use of mixed thiol monolayers (DNA-SH/MCH) were carried out. The experiment consisted of prolonged (160 min), parallel injection of *Comp* (100 nM), and AuNPs@*Comp-SH* ( $C_{\text{AuNPs}} = 320 \text{ pM}$ ). Schematic diagram of dsDNA duplexes formation in both modes, obtained SPR sensograms and CCD image of SPRi sensor after association step are outlined in **Figure 4**. Analysis of real-time sensograms indicates the obvious, about 11.5-folds higher SPRi response caused by attachment of AuNPs labels instead of unmodified ssDNA. Observed enhancement effect derives from a double role of AuNPs, which strongly interact with the surface plasmons of gold transducer both by specific plasmonic coupling, as well as association of a relatively large mass of the nanoparticle (He et al., 2000). Significant differences in kinetics of examined interactions are indicated by character of SPRi responses. ssDNA injection resulted in reaching DNA association/dissociation equilibrium after 40 min, whereas in case of AuNPs@*Comp-SH*, such effect was not obtained within the time of experiment (See **Figure 4**).

As can be concluded from inset of **Figure 4**, binding of AuNPs labels to DNA-SH monolayer proceeds only through specific DNA-DNA interactions. Lack of observed reflectance shift for random sequence (bottom of working cell) confirms the negligible contribution of non-specific interactions between AuNPs and non-complementary DNA. A suppression of non-specific adsorption is promoted by electrostatic repulsion between polyanionic DNA chains of receptor layers and functionalized AuNPs. Similar effect was observed for mixed DNA-Ads and DNA-DTC monolayers. This observation opened the possibility of their application in indirect DNA detection using AuNPs as plasmonic labels.

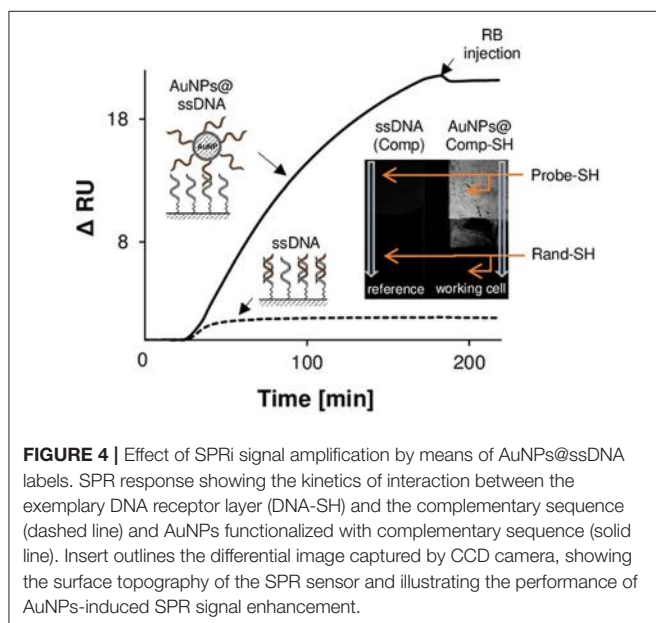


**FIGURE 4** | Effect of SPRi signal amplification by means of AuNPs@ssDNA labels. SPR response showing the kinetics of interaction between the exemplary DNA receptor layer (DNA-SH) and the complementary sequence (dashed line) and AuNPs functionalized with complementary sequence (solid line). Insert outlines the differential image captured by CCD camera, showing the surface topography of the SPR sensor and illustrating the performance of AuNPs-induced SPR signal enhancement.

The occurrence of steric hindrance and hampered transport of mass result in a slower kinetic of gold nanoparticle conjugates association and thus lowering of labeling efficiency. Therefore, it can be concluded, that the use of nanomaterial-based conjugates with the large spatial dimensions should imply the independence of the values of SPR signals from the surface coverage of DNA probes. This effect was schematically illustrated by the example of DNA-SH and DNA-DTC monolayers in **Figure 5A**.

As the next step, the thoughtful examination of relationship between spatial dimensions of AuNP labels and surface density of DNA receptor layers was carried out. Literature reports point to the stiffness of DNA double helix sufficient enough to form rigid “bridges” between solid substrate and gold nanoparticle of diameter up to 200 nm (Jones et al., 2015). Therefore, it can be expected that AuNPs used throughout the experiment form stable duplexes with immobilized DNA probes as schematically depicted in **Figure 5A**. Based on this assumption, ratios of the axial section of single Au nanoparticle and the area per

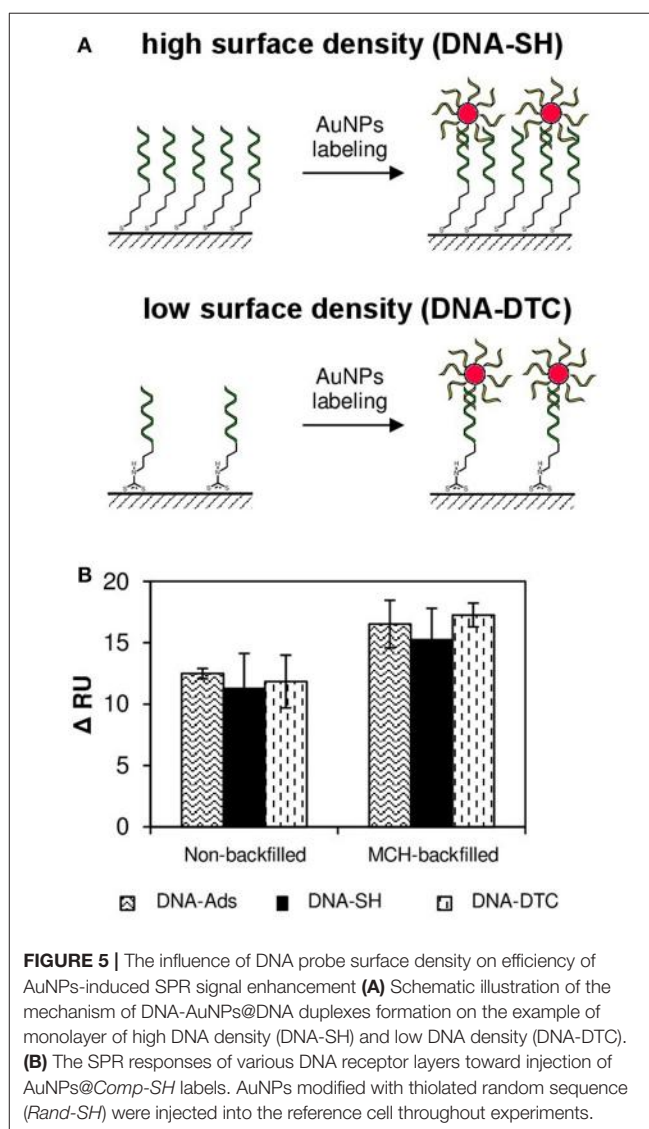


**FIGURE 5** | The influence of DNA probe surface density on efficiency of AuNPs-induced SPR signal enhancement. **(A)** Schematic illustration of the mechanism of DNA-AuNPs@DNA duplexes formation on the example of monolayer of high DNA density (DNA-SH) and low DNA density (DNA-DTC). **(B)** The SPR responses of various DNA receptor layers toward injection of AuNPs@*Comp-SH* labels. AuNPs modified with thiolated random sequence (*Rand-SH*) were injected into the reference cell throughout experiments.

immobilized ssDNA receptor were determined. The calculated area of the projection of average nanoparticle on plane (axial section of 13.0 nm diameter, assuming its sphericity) equals to 132.7 nm<sup>2</sup>. In turn, the average surface area per single DNA molecule in DNA-SH/MCH monolayer is 13.12 nm<sup>2</sup> (based on values of surface density listed in **Table 2** and assuming the uniformity of surface coverage). Obtained results (ratio = 10.11) indicate, that at least 10 *Probe-SH* molecules belong to single nanoparticle label. It is easy to notice, that for each of the mixed-type monolayers examined in this work, the number of DNA probe molecules per single label molecule is greater than one (10.11 for DNA-SH, 2.16 for DNA-Ads, and 1.95 for DNA-DTC, respectively). Obviously, such ratios are significantly underestimated, because in the calculated values complete coverage of surface with spherical nanoparticles was assumed and the contribution of oligonucleotide ligands (the increase in AuNPs hydrodynamic radius and electrostatic interactions) were not taken into account. Nevertheless, it can be stated, that in each studied case the packing density of DNA probes makes impossible to bind the theoretical number of AuNPs labels due to steric limitations. Therefore, surface density of mixed DNA-Ads, DNA-DTC, and DNA-SH layers should not significantly affect the amount of bound AuNPs labels and thus the SPRi response.

The efficiency of AuNPs@*Comp-SH* binding to all types of obtained monolayers was experimentally verified. Values of reflectance shifts ( $\Delta RU$ ) obtained on the basis of differential sensograms are presented in **Figure 5B**. As expected, response values resulting from hybridization of AuNPs@*Comp-SH* with oligonucleotide probes proved to be similar, regardless of DNA immobilization strategy. It should be underlined, that no decrease of sensitivity of mixed DNA-DTC and DNA-Ads monolayers (which was typical phenomenon in the case of

label-free formats) was not observed. Presented results point to the conclusion, that DNA monolayers of low density can compete with dense thiol monolayers in terms of sensitivity only in the case biosensors exploiting strategy of indirect signal generation, as documented in few reports regarding DNA biosensors (Sharma et al., 2008; Lou et al., 2015).

## Efficiency of SPRi Response Amplification in the Competitive Format

In the final step, proof of principle of AuNPs application in DNA detection system based on competitive format was presented. The mechanism of indirect detection in the competitive system exploits the decrease of surface density of receptors available for labeling, due to primary interaction with the analyte. The goal of this study was the verification, whether the use of receptor layer of the low density (more compatible to label dimensions, as proven above) may contribute to the improvement of labeling efficiency of receptors, which are not involved in the interaction with analytes.

**Figure 6** shows exemplary SPRi response to injection of solutions of *Comp* (1 nM), followed by competitive labeling step by means of AuNPs@*Comp-SH* for DNA-SH/MCH and DNA-DTC/MCH monolayers. As expected, in the case of such format, negative responses were obtained, which is caused by the fact, that ssDNA-functionalized AuNPs compete for receptors with ssDNA used as the model target. Inset shows values of corresponding responses obtained before and after signal amplification for all examined biosensors. As expected, the injection of AuNPs@*Comp-SH* induced significant decreases in SPRi responses for DNA-SH/MCH and DNA-DTC/MCH based biosensors. The ratio of signals before and after labeling

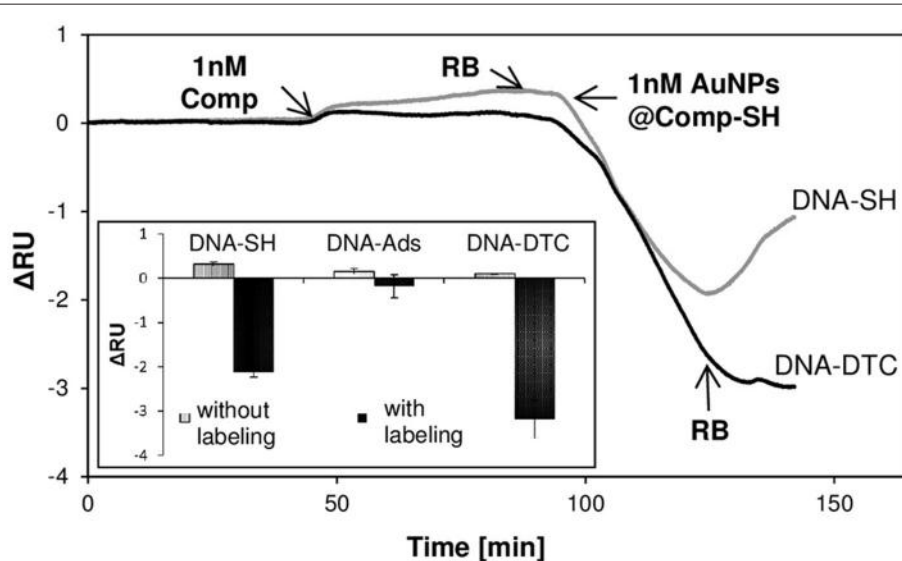


**FIGURE 6 |** The performance of SPR response enhancement by introduction of AuNPs labels in competitive assay. Exemplary SPRi sensograms illustrating the real-time responses after subsequent injection of *Comp* sequence and AuNPs@*Comp-SH* label. *Rand* sequence (1 nM) and AuNPs@*Comp-SH* label (1 nM) were simultaneously injected into the reference cell, respectively.

was 6.6 for thiolated-SAM and 32.0 for DTC-SAM, thus confirming the predicted performance of receptor layer of low surface coverage in efficient binding of AuNPs labels. It is noteworthy, that there was no noticeable enhancement effect for DNA-Ads/MCH, despite its proven ability to bind AuNP labels in the direct format (section Correlation between DNA Surface Coverage and Efficiency of AuNPs Labeling). The possible reason for such behavior of physisorbed DNA is the orientation and surroundings of free ssDNA strands. In contrary to covalently immobilized probes, adsorbed oligonucleotides tend to form more compact, and hence less exposed receptor layer, due to multiple binding sites with bare Au. Partial hybridization with *Comp* renders the remaining ssDNA probes less accessible to bulky AuNP@*Comp*-SH conjugate (Steel et al., 2000). The putative mechanism covers both the enhancement of electrostatic repulsion of polyanionic label conjugates by dsDNA, as well as emergence of a steric hindrance. Formation of helices enforces the rearrangement of monolayer and thus the override of free ssDNA probes by rigid dsDNA duplexes.

LSPR field as the evanescent wave is relatively strong in a distance not exceeding 10 nm and decays up to 30 nm (Hao et al., 2017). Therefore, AuNPs labels retain the unique capability of SPR signal enhancement by electronic coupling only at specified, small distance from Au transducer (He et al., 2004; Sendroiu et al., 2011). It should be considered, that the calculated length of double helix structure composed of 27 base pairs (length of complimentary segment in presented studies) is 7.26 nm, so it seems reasonable from the point of view of sensitivity to eliminate any redundant spacers increasing distance between transducer and plasmonic label (Ho, 1994). In this context, SPR detection in competitive mode seems to be particularly attractive. In such approach distance between AuNPs and Au transducer is usually smaller than in classical sandwich format.

## CONCLUSIONS

Three methods of immobilization of DNA oligonucleotides on gold, which find application for SPRi-based DNA biosensing in both label-free and nanoparticle-enhanced format, were critically compared. Studies focused on the evaluation of biosensors with DNA-receptor layers obtained by chemisorption (by means of DTC- and thiolate-assemblies) and physisorption. Obtained DNA receptor layers demonstrated ability to reversibly bind the model complementary sequence, thus providing the wide dynamic range of SPRi response. DNA-SH assemblies turned out to be the most attractive in terms of sensitivity, in the case of both homogeneous and

mixed monolayer. The surprising susceptibility of DNA-DTC for desorption under the influence of the surface-active MCH was explained in terms of relatively high contribution of non-specific interactions of DNA chain in during the monolayer formation. In the case of label-free DNA detection based on double helix formation, the surface coverage of immobilized DNA probes was confirmed as the crucial factor influencing the sensitivity of biosensors. Studies on interactions of receptor layers with ssDNA functionalized AuNPs contribute to the explanation of relationship between surface density of DNA receptors and the efficiency of labeling. It was shown, that the surprisingly high efficiency of AuNPs binding even by the monolayers of the low density (DNA-DTC/MCH and DNA-Ads/MCH) can be attributed to relatively low kinetics and large spatial dimensions of AuNPs in relation to the distance of oligonucleotide receptors on gold surface. In the final section, possibility of DNA-DTC/MCH application in AuNPs-amplified SPRi detection of model complementary sequence was demonstrated. We believe, that discussed immobilization approaches should facilitate the development of biosensors for simultaneous detection of multiple specific DNA targets. Due to capabilities offered by SPR measurements in imaging mode, proposed solutions also provide great potential for applications in SPRi-based DNA microarrays.

## AUTHOR CONTRIBUTIONS

MD conducted all the experiments and wrote the draft of the paper; MP provided general guidance, helped in the redaction, and revision of the final version of manuscript; EM supervised the project and reviewed the manuscript.

## FUNDING

This work has been financially supported by the Polish National Science Centre (NCN) grant PRELUDIUM 2014/15/N/ST5/02015.

## ACKNOWLEDGMENTS

Authors would like to thank Ph.D. Kamil Zukowski for the fabrication of two-channel SPRi microfluidic cell.

## SUPPLEMENTARY MATERIAL

The Supplementary Material for this article can be found online at: <https://www.frontiersin.org/articles/10.3389/fchem.2018.00173/full#supplementary-material>

## REFERENCES

- Adak, A. K., Leonov, A. P., Ding, N., Thundimadathil, J., Kularatne, S., and Low, P. S. (2010). Bishydrazide glycoconjugates for lectin recognition

- and capture of bacterial pathogens. *Bioconjugate Chem.* 21, 2065–2075. doi: 10.1021/bc100288c
- Almeida, I., Ferreira, V. C., Montemor, M. F., Abrantes, L. M., and Viana, A. S. (2012). One-pot approach to modify nanostructured gold surfaces

- through *in situ* dithiocarbamate linkages. *Electrochim. Acta* 83, 311–320. doi: 10.1016/j.electacta.2012.08.021
- Almeida, I., Henriques, F., Carvalho, M. D., and Viana, A. S. (2017). Carbon disulfide mediated self-assembly of laccase and iron oxide nanoparticles on gold surfaces for biosensing applications. *J. Colloid Interface Sci.* 485, 242–250. doi: 10.1016/j.jcis.2016.09.042
- Brockmann, J. M., Frutos, A. G., and Corn, R. M. (1999). A multistep chemical modification procedure to create DNA arrays on gold surfaces for the study of protein–DNA interactions with surface plasmon resonance imaging. *J. Am. Chem. Soc.* 121, 8044–8051. doi: 10.1021/ja991608e
- Chen, Y., Nguyen, A., Niu, L., and Corn, R. M. (2009). Fabrication of DNA microarrays with poly-L-glutamic acid monolayers on gold substrates for SPR imaging measurements. *Langmuir* 25, 5054–5060. doi: 10.1021/la804021t
- Choi, S., Seo, J. S., Bohaty, R. F., and Poulter, C. D. (2014). Regio- and chemoselective immobilization of proteins on gold surfaces. *Bioconjugate Chem.* 25, 269–275. doi: 10.1021/bc400413d
- Drozd, M., Pietrzak, M., Kalinowska, D., Grabowska-Jadach, I., and Malinowska, E. (2016). Glucose dithiocarbamate derivatives as capping ligands of water-soluble CdSeS/ZnS quantum dots. *Colloids Surf. A* 509, 656–665. doi: 10.1016/j.colsurfa.2016.09.072
- Eckermann, A. L., Shaw, J. A., and Meade, T. J. (2010). Kinetic dispersion in redox-active dithiocarbamate monolayers. *Langmuir* 26, 2904–2913. doi: 10.1021/la902839r
- Fiche, J. B., Fuchs, J., Buhot, A., Calemczuk, R., and Livache, T. (2008). Point mutation detection by surface plasmon resonance imaging coupled with a temperature scan method in a model system. *Anal. Chem.* 80, 1049–1057. doi: 10.1021/ac7019877
- Georgiadis, R., Peterlinz, K. P., and Peterson, A. W. (2000). Quantitative measurements and modeling of kinetics in nucleic acid monolayer films using SPR spectroscopy. *J. Am. Chem. Soc.* 122, 3166–3173. doi: 10.1021/ja9930824
- Haiss, W., Thanh, N. T., Aveyard, J., and Fernig, D. G. (2007). Determination of size and concentration of gold nanoparticles from UV-vis spectra. *Anal. Chem.* 79, 4215–4221. doi: 10.1021/ac0702084
- Hao, K., He, Y., Lu, H., Pu, S., Zhang, Y., and Dong, H., et. al. (2017). High-sensitive surface plasmon resonance microRNA biosensor based on streptavidin functionalized gold nanorods-assisted signal amplification. *Anal. Chim. Acta* 954, 114–120. doi: 10.1016/j.aca.2016.12.006
- He, L., Musick, M. D., Nicewarner, S. R., Salinas, F. G., Benkovic, S. J., and Natan, M. J., et. al. (2000). Colloidal Au-enhanced surface plasmon resonance for ultrasensitive detection of DNA hybridization. *J. Am. Chem. Soc.* 122, 9071–9077. doi: 10.1021/ja001215b
- He, L., Smith, E. A., Natan, M. J., and Keating, C. D. (2004). The distance-dependence of colloidal Au-amplified surface plasmon resonance. *J. Phys. Chem. B* 108, 10973–10980. doi: 10.1021/jp048536k
- Ho, P. S. (1994). The non-B-DNA structure of d(CA/TG)n does not differ from that of Z-DNA. *Proc. Natl. Acad. Sci. U.S.A.* 91, 9549–9553. doi: 10.1073/pnas.91.20.9549
- Jones, M. R., Seeman, N. C., and Mirkin, C. A. (2015). Nanomaterials. Programmable materials and the nature of the DNA bond. *Science* 347:1260901. doi: 10.1126/science.1260901
- Keighley, S. D., Li, P., Estrela, P., and Migliorato, P. (2008). Optimization of DNA immobilization on gold electrodes for label-free detection by electrochemical impedance spectroscopy. *Biosens. Bioelectron.* 23, 1291–1297. doi: 10.1016/j.bios.2007.11.012
- Kimura-Suda, H., Petrovykh, D. Y., Tarlov, M. J., and Whitman, L. J. (2003). Base-dependent competitive adsorption of single-stranded DNA on gold. *J. Am. Chem. Soc.* 125, 9014–9015. doi: 10.1021/ja035756n
- Kong, R. M., Song, Z. L., Meng, H. M., Zhang, X. B., Shen, G. L., and Yu, R. Q. (2014). A label-free electrochemical biosensor for highly sensitive and selective detection of DNA via a dual-amplified strategy. *Biosens. Bioelectron.* 54, 442–447. doi: 10.1016/j.bios.2013.11.041
- Koo, K. M., Sina, A. A., Carrascosa, L. G., Shiddiky, M. J. A., and Trau, M. (2015). DNA-bare gold affinity interactions: mechanism and applications in biosensing. *Anal. Methods* 7, 7042–7054. doi: 10.1039/C5AY01479D
- Leonov, A. P., and Wei, A. (2011). Photolithography of dithiocarbamate-anchored monolayers and polymers on gold. *J. Mater. Chem.* 21, 4371–4376. doi: 10.1039/c0jm04153j
- Lou, J., Liu, S., Tu, W., and Dai, Z. (2015). Graphene quantum dots combined with endonuclease cleavage and bidentate chelation for highly sensitive electrochemiluminescent DNA biosensing. *Anal. Chem.* 87, 1145–1151. doi: 10.1021/ac5037318
- Mandler, D., and Kraus-Ophir, S. (2011). Self-assembled monolayers (SAMs) for electrochemical sensing. *J. Solid State Electrochem.* 15, 1535–1558. doi: 10.1007/s10008-011-1493-6
- Mannelli, I., Minunni, M., Tombelli, S., and Mascini, M. (2003). Quartz crystal microbalance (QCM) affinity biosensor for genetically modified organisms (GMOs) detection. *Biosens. Bioelectron.* 18, 129–140. doi: 10.1016/S0956-5663(02)00166-5
- Mirkin, C. A., Letsinger, R. L., Mucic, R. C., and Storhoff, J. J. (1996). A DNA-based method for rationally assembling nanoparticles into macroscopic materials. *Nature* 382, 607–609. doi: 10.1038/382607a0
- Morf, P., Raimondi, F., Nothofer, H. G., Schnyder, B., Yasuda, A., and Wessels, J. M. (2006). Dithiocarbamates: functional and versatile linkers for the formation of self-assembled monolayers. *Langmuir* 22, 658–663. doi: 10.1021/la052952u
- Nelson, B. P., Grimsrud, T. E., Liles, M. R., Goodman, R. M., and Corn, R. M. (2001). Surface plasmon resonance imaging measurements of DNA and RNA hybridization adsorption onto DNA microarrays. *Anal. Chem.* 73, 1–7. doi: 10.1021/ac0010431
- Paiva, T. O., Almeida, I., Marquês, J. T., Liu, W., Niu, Y., and Jin, G., et. al. (2017). Nanostructured interfaces with site-specific bioreceptors for immunosensing. *Appl. Surf. Sci.* 412, 455–463. doi: 10.1016/j.apsusc.2017.03.180
- Park, M. H., Duan, X., Ofir, Y., Creran, B., Patra, D., and Ling, X. Y., et. al. (2010). Chemically directed immobilization of nanoparticles onto gold substrates for orthogonal assembly using dithiocarbamate bond formation. *ACS Appl. Mater. Interfaces* 2, 795–799. doi: 10.1021/am9009007
- Peterson, A. W., Heaton, R. J., and Georgiadis, R. M. (2001). The effect of surface probe density on DNA hybridization. *Nucl. Acids Res.* 29, 5163–5168. doi: 10.1093/nar/29.24.5163
- Pursey, J. P., Chen, Y., Stulz, E., Kyoung Park, M., and Kongsuphol, P. (2017). Microfluidic electrochemical multiplex detection of bladder cancer DNA markers. *Sens. Actuator B Chem.* 251, 34–39. doi: 10.1016/j.snb.2017.05.006
- Raigoza, A. F., Kolettis, G., Brandt, T. E. S., Caponigri-Guerra, G., Agostino, C., and Kandel, S. A. (2012). Coadsorption of octanethiol and dialkyldithiocarbamate on Au(111). *J. Phys. Chem. C* 116, 1930–1934. doi: 10.1021/jp2110538
- Schoenfisch, M. H., and Pemberton, J. E. (1998). Air stability of alkanethiol self-assembled monolayers on silver and gold surfaces. *J. Am. Chem. Soc.* 120, 4502–4513. doi: 10.1021/ja974301t
- Sendroiu, I. E., Gifford, L. K., Lupták, A., and Corn, R. M. (2011). Ultrasensitive DNA microarray biosensing via *in situ* RNA transcription-based amplification and nanoparticle-enhanced SPR imaging. *J. Am. Chem. Soc.* 133, 4271–4273. doi: 10.1021/ja2005576
- Sharma, J., Chhabra, R., Yan, H., and Liu, Y. (2008). A facile *in situ* generation of dithiocarbamate ligands for stable gold nanoparticle–oligonucleotide conjugates. *Chem. Commun.* 18, 2140–2142. doi: 10.1039/b800109j
- Simon, L., Lautner, G., and Gyurcsányi, R. E. (2015). Reliable microspotting methodology for peptide-nucleic acid layers with high hybridization efficiency on gold SPR imaging chips. *Anal. Methods* 7, 6077–6082. doi: 10.1039/C5AY01239B
- Sina, A. A., Foster, M. T., Korbie, D., Carrascosa, L. G., Shiddiky, M. J. A., and Gao, J., et. al. (2017). A multiplex microplatform for the detection of multiple DNA methylation events using gold-DNA affinity. *Analyst* 142, 3573–3578. doi: 10.1039/C7AN00611J
- Steel, A. B., Herne, T. M., and Tarlov, M. J. (1998). Electrochemical quantitation of DNA immobilized on gold. *Anal. Chem.* 70, 4670–4677. doi: 10.1021/ac980037q
- Steel, A. B., Levicky, R. L., Herne, T. M., and Tarlov, M. J. (2000). Immobilization of nucleic acids at solid surfaces: effect of oligonucleotide length on layer assembly. *Biophys. J.* 79, 975–981. doi: 10.1016/S0006-3495(00)76351-X
- Tichoniu, M., Gwiazdowska, D., Ligaj, M., and Filipiak, M. (2010). Electrochemical detection of foodborne pathogen *Aeromonas hydrophila* by DNA hybridization biosensor. *Biosens. Bioelectron.* 26, 1618–1623. doi: 10.1016/j.bios.2010.08.030

- Trasatti, S., and Petrii, O. A. (1992). Real surface area measurements in electrochemistry. *J. Electroanal. Chem.* 327, 353–376. doi: 10.1016/0022-0728(92)80162-W
- Turkevich, J., Stevenson, P. C., and Hiller, J. (1951). A study of the nucleation and growth processes in the synthesis of colloidal gold. *Disc. Faraday Soc.* 11, 55–75. doi: 10.1039/df9511100055
- Ulman, A. (1996). Formation and structure of self-assembled monolayers. *Chem. Rev.* 96, 1533–1554. doi: 10.1021/cr9502357
- Wang, L., Wang, X., Chen, X., Liu, J., Liu, S., and Zhao, C. (2012). Development of an electrochemical DNA biosensor with the DNA immobilization based on *in situ* generation of dithiocarbamate ligands. *Bioelectrochem.* 88, 30–35. doi: 10.1016/j.bioelechem.2012.04.003
- Zhao, Y., Pérez-Segarra, W., and Wei, A. (2005). Dithiocarbamate assembly on gold. *J. Am. Chem. Soc.* 127, 7328–7329. doi: 10.1021/ja050432f

**Conflict of Interest Statement:** The authors declare that the research was conducted in the absence of any commercial or financial relationships that could be construed as a potential conflict of interest.

Copyright © 2018 Drozd, Pietrzak and Malinowska. This is an open-access article distributed under the terms of the Creative Commons Attribution License (CC BY). The use, distribution or reproduction in other forums is permitted, provided the original author(s) and the copyright owner are credited and that the original publication in this journal is cited, in accordance with accepted academic practice. No use, distribution or reproduction is permitted which does not comply with these terms.



# Monitoring the Phenolic Ripening of Red Grapes Using a Multisensor System Based on Metal-Oxide Nanoparticles

Celia Garcia-Hernandez<sup>1</sup>, Cristina Medina-Plaza<sup>1</sup>, Cristina Garcia-Cabezon<sup>2</sup>, Yolanda Blanco<sup>2</sup>, Jose A. Fernandez-Escudero<sup>3</sup>, Enrique Barajas-Tola<sup>4</sup>, Miguel A. Rodriguez-Perez<sup>1</sup>, Fernando Martin-Pedrosa<sup>2</sup> and Maria L. Rodriguez-Mendez<sup>1\*</sup>

<sup>1</sup> Group UVaSens, Department of Inorganic Chemistry, Escuela de Ingenierías Industriales, Universidad de Valladolid, Valladolid, Spain, <sup>2</sup> Group UVasens, Department of Materials Science, Universidad de Valladolid, Valladolid, Spain, <sup>3</sup> Estacion Enologica de Castilla y Leon, Valladolid, Spain, <sup>4</sup> ITACYL, Valladolid, Spain

## OPEN ACCESS

### Edited by:

Larisa Lvova,  
Università degli Studi di Roma Tor  
Vergata, Italy

### Reviewed by:

Nicole J. Jaffrezic-Renault,  
Claude Bernard University Lyon 1,

France

Prathik Roy,  
University of Canterbury, New Zealand  
Cecilia Jimenez-Jorquera,  
Consejo Superior de Investigaciones  
Científicas (CSIC), Spain

### \*Correspondence:

Maria L. Rodriguez-Mendez  
mluz@eii.uva.es

### Specialty section:

This article was submitted to  
Analytical Chemistry,  
a section of the journal  
Frontiers in Chemistry

Received: 23 January 2018

Accepted: 09 April 2018

Published: 24 April 2018

### Citation:

Garcia-Hernandez C, Medina-Plaza C,  
Garcia-Cabezon C, Blanco Y,  
Fernandez-Escudero JA,  
Barajas-Tola E, Rodriguez-Perez MA,  
Martin-Pedrosa F and  
Rodriguez-Mendez ML (2018)  
Monitoring the Phenolic Ripening of  
Red Grapes Using a Multisensor  
System Based on Metal-Oxide  
Nanoparticles. *Front. Chem.* 6:131.  
doi: 10.3389/fchem.2018.00131

The maturity of grapes is usually monitored by means of the sugar concentration. However, the assessment of other parameters such as the phenolic content is also important because the phenolic maturity has an important impact on the organoleptic characteristics of wines. In this work, voltammetric sensors able to detect phenols in red grapes have been developed. They are based on metal oxide nanoparticles ( $\text{CeO}_2$ ,  $\text{NiO}$ , and  $\text{TiO}_2$ ) whose excellent electrocatalytic properties toward phenols allows obtaining sensors with detection limits in the range of  $10^{-8}$  M and coefficients of variation lower than 7%. An electronic tongue constructed using a combination of the nanoparticle-based sensors is capable to monitor the phenolic maturity of red grapes from véraison to maturity. Principal Component Analysis (PCA) can be successfully used to discriminate samples according to the ripeness. Regression models performed using Partial Least Squares (PLS-1) have established good correlations between voltammetric data obtained with the electrochemical sensors and the Total Polyphenolic Index, the Brix degree and the Total Acidity, with correlation coefficients close to 1 and low number of latent variables. An advantage of this system is that the electronic tongue can be used for the simultaneous assessment of these three parameters which are the main factors used to monitor the maturity of grapes. Thus the electronic tongue based on metal oxide nanoparticles can be a valuable tool to monitor ripeness. These results demonstrate the exciting possible applications of metal oxide nanoparticles in the field of electronic tongues.

**Keywords:** electronic tongue, grape, ripening, phenolic maturity, metal oxide nanoparticles

## INTRODUCTION

Grapes must be harvested at the optimal maturity point. The sugar content has a direct influence on the alcoholic degree of wines and it is the analytical indicator commonly used to decide the harvest date (OIV, 2013). It is periodically assessed using fast and simple density measurements and it is expressed as degree Brix ( $^{\circ}\text{Brix}$ ). The variation of the acidity along ripening is also an important parameter which is expressed as Total Acidity (TA) (Boss et al., 2014).

The phenolic content of grapes also changes during ripening and the phenolic maturity has a direct impact on the organoleptic characteristics of wines, and it would be desirable to assess it routinely. However, the main changes in the phenolic content take place in skins and seeds, and the assessment of phenolic maturity requires the previous separation of seeds and skins using long and complex methods (Xu et al., 2011; Meléndez et al., 2013; Nogales-Bueno et al., 2014; Sharma et al., 2015). Oenologists require new methods capable to measure the phenolic maturity of grapes with simple and direct methods.

Besides, it would be of great interest to develop new technologies able to detect simultaneously the sugar content, acidity and phenolic composition. Such a method would help to take faster decisions about the optimal harvest date. One possible approach can be the use of holistic methods, where complex signals obtained from an instrument such as GC-MS, FTIR or NMR, are processed using multivariate methods. These holistic methods have been successfully used to classify wines according to quality, to monitor fermentation, to detect wine spoilage, etc. (Buratti et al., 2011; Cozzolino et al., 2012; Godelmann et al., 2014).

Electronic tongues (ET) are a new class of instruments which are gaining interest in the food industry (Cosio et al., 2012; Kirsanov et al., 2012; Lvova et al., 2014; Rodríguez-Méndez, 2016). They are multisensor systems where an array of sensors is combined with a multivariate data software. The most common sensors used in ETs dedicated to the analysis of wines are electrochemical (amperometric or voltammetric). They have been widely used to discriminate wines according to the variety of grape, the vintage, the type of barrel used for aging etc. (Gutiérrez et al., 2010; Prieto et al., 2011; Apetrei et al., 2012; Cetó et al., 2017; Rudnitskaya et al., 2017). In spite of the interest of winemakers to have available objective methods to determine the harvesting date and the quality of grapes, ETs have been rarely applied to the quality control of grapes or their musts (Codinachs et al., 2008; Gutiérrez et al., 2011; Campos et al., 2013; Medina-Plaza et al., 2014a,b).

Nowadays, it is clear that the performance of ETs can be improved by introducing in the array sensing units specifically dedicated to a particular application. Electrodes with enhanced performances can be obtained using new sensing materials linked to nanotechnology. Metal nanoparticles have been used in the fabrication of electrochemical sensors due to their electrocatalytic properties which are related to the formation of mixed valence states on their surface (Campbell and Compton, 2010; Saha et al., 2012; Lin et al., 2013). Metal nanoparticles have demonstrated their capability to catalyze the oxidation/reduction of organic acids and phenols commonly present in wines. The oxidation of phenols occurs at lower potentials, whereas the presence of metallic nanoparticles increases the reactivity of acids and enhances the intensity of the anodic wave at negative potentials (Medina-Plaza et al., 2015a,b). In spite of this interest, metal nanoparticles have rarely been included as sensing materials in electronic tongues (Gutiérrez et al., 2013; Sharpe et al., 2014; Mercante et al., 2015). Up to now, the sensing capabilities of metal oxide nanoparticles (MONPs) have never been tested in electronic tongues.

The aim of this work was to develop an electronic tongue (ET) formed by sensors based on metal oxide nanoparticles ( $\text{CeO}_2$ ,  $\text{NiO}$ , and  $\text{TiO}_2$ ) and to evaluate their capabilities to detect phenols. Using chemometric techniques such as Principal Component Analysis (PCA), the ET was used to monitor the ripeness of 8 different varieties of grapes, from *véraison* (the onset of ripening) to post-maturity. Mathematical models were built to establish correlations between the phenolic index measured by traditional chemical techniques and the results of the ET. PLS-1 was used to predict the polyphenol index of the grapes along ripening. The possibility to obtain information about other classical indicators of maturity such as the  $^{\circ}\text{Brix}$  and Total Acidity was also analyzed.

## MATERIALS AND METHODS

Metal oxide nanoparticles of Titanium (IV), Cerium (IV), and Nickel (II) ( $\text{TiO}_2\text{NP}$ ,  $\text{CeO}_2\text{NP}$ ,  $\text{NiONP}$ ) were purchased from Sigma-Aldrich. All reagents and solvents were of high purity (Sigma-Aldrich). Deionized water ( $18.2 \text{ M}\Omega\cdot\text{cm}^{-1}$ ) was obtained from a Millipore MilliQ purifier.

Electron Microscope TEM images were recorded using a high-resolution electron microscope (HRTEM: JEOL JEM 2200) (Tokyo, Japan) operating at an accelerating voltage of 200 kV. Sample images were processed using Image J image processing software (public software).

Eight varieties of red grapes typical from the Castilla-Leon region (Spain) were included in the study: *Tempranillo*, *Garnacha*, *Cabernet-Sauvignon*, *Prieto Picudo*, *Mencia Regadio*, *Mencia Secano*, *Rufete*, and *Juan Garcia*. Grapes were grown and harvested by the Agrotechnological Institute of Agriculture of the Regional Government (ITACyL) and the cellar Bodega Cooperativa de Cigales. Berries were collected in a weekly basis from *véraison* until grapes were completely mature. Ripeness rate was different from one variety to another. For this reason, the official harvest date indicated by traditional chemical parameters, varied from one variety of grape to another. Grapes from *Tempranillo*, *Garnacha*, and *Cabernet Sauvignon* were considered matured 6 weeks after *véraison*. The rest of varieties attained the optimal ripeness 5 weeks after *véraison*. In all cases several grape bunches were left in the vine and two extra samplings were collected in successive weeks in order to analyze over-ripened grapes.

Musts were prepared from 100 berries representative of the ripening state of the vineyard. Once collected, grapes were crushed, and peels and seeds were separated by decantation. 50 mL aliquots of musts thus obtained, were frozen at  $-20^{\circ}\text{C}$  until used. Total Polyphenol Index (TPI), Brix degree ( $^{\circ}\text{Brix}$ ) and Total Acidity (TA) were analyzed following international standard methods (OIV, 2013; Boss et al., 2014). TPI was determined by diluting the samples with distilled water in a 1:100 ratio and measuring the absorbance directly at 280 nm (using a quartz cuvette of 10 mm optical path). The value of the  $I_{280 \text{ nm}}$  (TPI) was calculated by multiplying the absorbance  $\times 100$ . The total acidity is the sum of its titratable acidities when it is titrated to pH 7 against a standard alkaline solution. Carbon dioxide is not included in the total acidity. The total acidity is usually expressed in grams of tartaric acid per liter.

Brix measurements are taken with an Atago WM-7 digital refractometer.

A multisensor system consisting of 4 Carbon Paste Electrodes (CPE) was formed. Three electrodes were modified with metal oxide nanoparticles including  $\text{NiO}$  ( $\text{NiONP-CPE}$ ),  $\text{TiO}_2$  ( $\text{TiO}_2\text{NP-CPE}$ ), and  $\text{CeO}_2$  ( $\text{CeO}_2\text{NP-CPE}$ ). One unmodified carbon paste electrode (C-CPE) was also included in the array. Electrodes were prepared following the classical method by mixing graphite with the corresponding metal oxide nanoparticle (15% w/w of the MONP) Nujol was used as the binder until a paste was obtained. The paste was packed in a 1 mL plastic syringe and compressed. A metallic copper wire was used as a contact (Apetrei et al., 2011). The size of MNOPs ranged from 20 to 50 nM. **Figure 1** illustrates the shape and size of  $\text{TiO}_2$  MNPs. As observed in the TEM image, MONPs were spheric with an homogeneous distribution of sizes that coincided with the size labeled by the supplier.

Electrochemical experiments were carried out using a potentiostat (Autolab, Metrohm, USA) combined with a multiplexor system. CPEs (surface of 2 mm in diameter) served as working electrodes, with an  $\text{Ag}|\text{AgCl}/\text{KCl}$  3 mol·L<sup>-1</sup> electrode acting as a reference electrode and a platinum wire as the counter

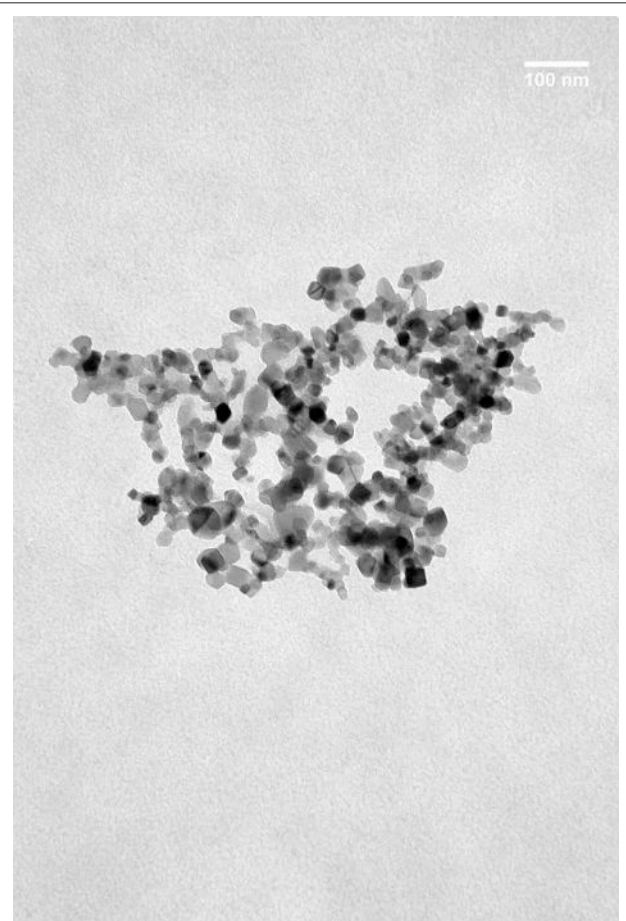


**FIGURE 1** | TEM image of the  $\text{TiO}_2$ NPs.

electrode. The MONPs sensors were able to provide responses toward aqueous solutions of phenolic acids (vanillic and caffeic acids) and polyphenols (catechol and pyrogallol) present in wines. The electrocatalytic properties and the detection limits (LD) were evaluated. The calibration curves were constructed measuring standard solutions with concentrations ranging from  $10^{-4}$  to  $10^{-6}$  mol·L<sup>-1</sup>. LDs were calculated following the 3 SD/m criterion. The reproducibility of data provided by the MONPs sensors was evaluated by comparing data provided by three sensors measuring standard solutions in different days. Cyclic voltammograms were registered at a sweep rate of 0.1 V·s<sup>-1</sup> from -0.8 to +1.0 V. Four replicas of each sample were measured. Principal Component Analysis (PCA) and Partial Least Squares (PLS) models were built using the software Matlab v5.3. (The Mathworks Inc., Natick, MA, USA).

Prior to perform the statistical analysis, the number of variables was reduced using a data reduction technique based on predefined response “bell-shaped-windowing” curves called “kernels” (Medina-Plaza et al., 2015b). In this method, each voltammogrammetric curve is multiplied by 10 smooth, bell-shaped windowing functions defined as:

$$K_i(V_j) = \frac{1}{1 + \left(\frac{V_j - c_i}{a_i}\right)^{2b_i}}$$

where  $a_i$ ,  $b_i$ , and  $c_i$  define the width, shape, and center of the different windowing functions  $K_i$ . Subsequently, data were integrated with respect to voltage. As a result, each voltammogram was reduced to a vector of 10 variables that were used as the input data source for statistical analysis.

## RESULTS AND DISCUSSION

### Monitoring Ripeness Using Chemical Parameters

Ripening was monitored by measuring  $^{\circ}\text{Brix}$ , TA, and TPI in a weekly basis (from *véraison*). These parameters were used by oenologists to establish the optimal date of harvest. The  $^{\circ}\text{Brix}/\text{TA}$  ratio was also calculated. This parameter is also commonly used to decide the optimal maturity date even if there is no biochemical relationship between the acidity loss and the sugar increase. The complete list of parameters is collected in Supplementary Table. Details can be observed in **Figure 2** for variety Tempranillo.

As observed in the **Figure 2**, TA and  $^{\circ}\text{Brix}$  followed the expected trend: TA decreased along the ripening process, while sugar content increased.  $^{\circ}\text{Brix}/\text{TA}$  ratio increased accordingly. These values were stabilized after week 5, indicating the proximity of the end of ripeness, and grapes were considered mature and harvested in week 6. Similar trends were observed in Garnacha and Cabernet-Sauvignon that also reached the maturity in week 6. Mencia Secano, Mencia Regadio, Rufete, and Juan Garcia gapes, matured at a faster rate, and were considered ripened and harvested in week 5.

In order to study the changes in over-ripened grapes, some bunches were kept in the plant during 2 more weeks. During

these 2 extra weeks, TA values were almost constant, whereas  $^{\circ}\text{Brix}$  raised drastically in Cabernet and Garnacha grapes, indicating that optimal ripening was not attained until weeks 7 or 8.

TPI values increased sharply just after the *véraison*. The following weeks, TPI varied irregularly. These results evidenced the difficulty to assess the phenolic maturity using traditional

TPI measurements in pulps. It is therefore important for wine producers to develop new methods to define the peak of ripeness and in particular of the phenolic ripeness (which nowadays is difficult to assess).

## Electrochemical Characterization of the NP-Based Electrode. Electrocatalytic Activity Toward Phenols

The objective of this work was to develop a multisensory system based on metal oxide nanoparticles to monitor the phenolic ripening. As a first task, the response of the MONP-CPE electrodes toward four phenols present in musts (vanillic acid, catechol, caffeic acid, and pyrogallol  $10^{-4}$  M), was evaluated (Figure 3). The response of the C-CPE electrode is also shown for comparison purposes.

The responses on MONP-CPEs were consistent with those already reported in bare CPE electrodes (Kilmartin et al., 2001), but the presence of MONPs caused shifts in the position of the peaks to lower potentials and/or increases in the intensity of the peaks. This effect could be attributed to the excellent electrocatalytic activity of MONPs due to the mixed valence state found at the nanoparticle surface (Medina-Plaza et al., 2015b). Depending on the nature of the MONPs used as modifiers, the responses toward a certain compound was more or less enhanced. For instance, the intensity of the redox peaks produced by the oxidation/reduction observed in vanillic

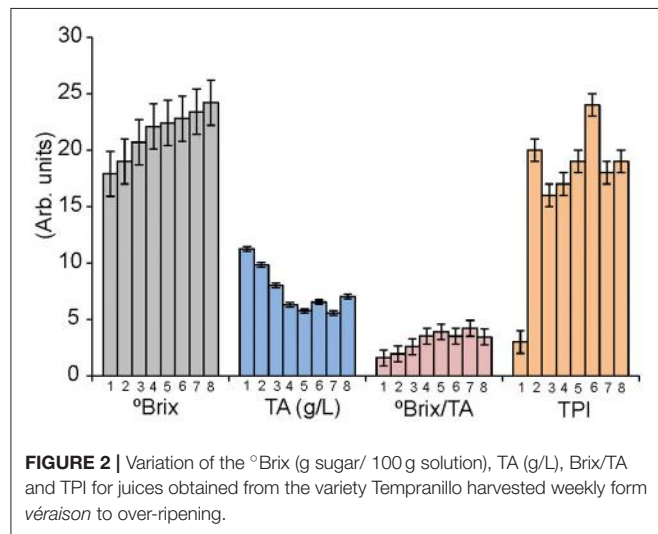


**FIGURE 2** | Variation of the  $^{\circ}\text{Brix}$  (g sugar/ 100 g solution), TA (g/L), Brix/TA and TPI for juices obtained from the variety Tempranillo harvested weekly from *véraison* to over-ripening.

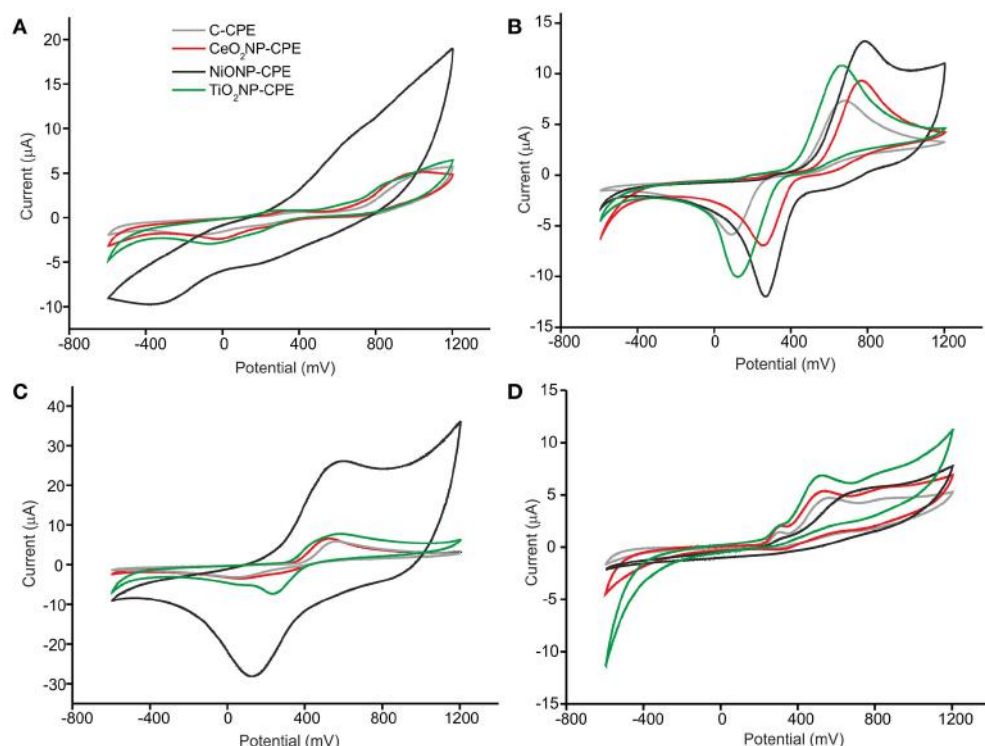


**FIGURE 3** | CV of (A) vanillic acid, (B) catechol, (C) caffeic acid, and (D) pyrogallol at C-CPE,  $\text{CeO}_2\text{NP-CPE}$ ,  $\text{NiONP-CPE}$ , and  $\text{TiO}_2\text{NP-CPE}$  electrodes. Concentration of  $10^{-4}$  M. Scan rate 100 mV·s $^{-1}$ .

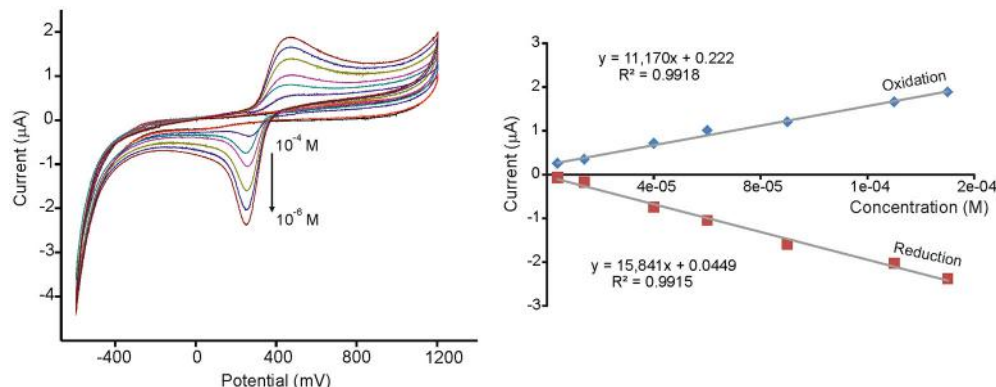


**FIGURE 4** | CVs and calibration curves of  $\text{TiO}_2\text{NP-CPE}$  immersed in increasing concentrations of caffeic acid (from  $4.0 \cdot 10^{-6}$  M to  $1.5 \cdot 10^{-4}$  M). Scan rate  $0.1 \text{ V} \cdot \text{s}^{-1}$ .

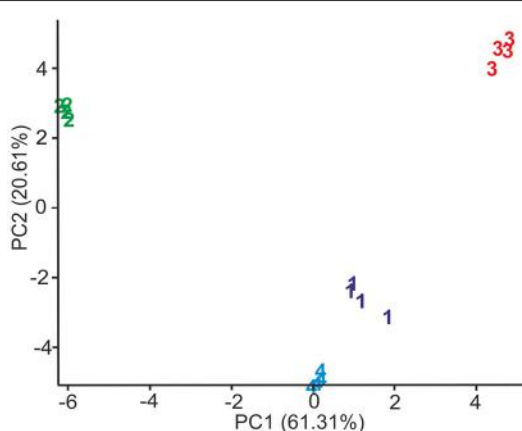


**FIGURE 5** | Scores plot of the first two principal components of the PCA model calculated from voltammograms registered when electrodes were immersed in 1: Catechol, 2: Pyrogallol, 3: Vanillic acid and 4: Caffeic acid.

acid and catechol at the graphite electrode surface increased drastically in the presence of NiONPs. The electrocatalytic effect was not so remarkable at  $\text{TiO}_2\text{NP-CPE}$  or  $\text{CeO}_2\text{NP-CPE}$  electrodes. It is also worth noting that the electrocatalytic effect was more intense in the mono-phenol (vanillic acid) or di-phenols (catechol and caffeic acid) than in the tri-phenol (pyrogallol).

Limits of detection (LD) were calculated from the slope of the curves of the redox peaks registered at concentrations ranging from  $10^{-4}$  to  $10^{-6}$  M, using  $3 \text{ SD}/\text{m}$  method, where  $\text{SD}$  is the standard deviation of the current density. LDs as low as  $10^{-8}$  M could be attained, which are much lower than those typically found in carbon electrodes (Kilmartin et al., 2001). The results are illustrated in Figure 4 for  $\text{TiO}_2\text{NP-CPE}$  immersed in caffeic acid. Reproducibility was also evaluated by measuring repeatedly the standard solutions and Variation coefficients (CV) lower than 7% were found in all cases. From the above results it can be concluded that modification with metal oxide nanoparticles drastically increases the

sensitivity of voltammetric electrodes toward phenols present in musts.

As stated before, each sensor showed a characteristic response which is linked to the electrocatalytic properties of the type of nanoparticle introduced in the carbon paste. This cross-selectivity can be used to construct a multisensor system coupled to a pattern recognition software able to provide a pattern or “digital fingerprint” for each sample studied.

Figure 5 shows the Principal Component Analysis (PCA) scores plot obtained from the responses of the array to  $10^{-4}$  M solutions of phenols. The PCA showed four distinct clusters in the plot of the two first principal components (PC1 61.31% and PC2 20.61%). The position of the clusters was related to the number of hydroxyl groups in the molecule. The monophenol (vanillic acid) was located at positive PC1 values, diphenols (catechol and caffeic acid) in the central part of the diagram and the triphenol (pyrogallol) on the left side corresponding to positive PC2 values.

## Monitoring the Ripening of Grapes With an Array of MONP-Based Electrodes

The capacity of the electronic tongue to monitor the phenolic maturity of grapes was evaluated by analyzing juices obtained from grapes collected from *véraison*, in a weekly basis, during 7–8 weeks. Due to the complexity of the samples and in order to improve the repeatability, musts were diluted 1:2 with deionized water. Coefficients of variation lower than 7% were obtained in all cases.

Figure 6 illustrates the responses obtained using the NiONP-CPE and  $\text{TiO}_2\text{NP-CPE}$  sensors immersed in musts obtained from grapes of the variety Garnacha collected during 7 weeks after *véraison*.

As illustrated in the figure, voltammograms registered in must showed peaks in the 0.6–0.8 V region, produced by components with redox activity (mainly phenols). Other components present in musts also influenced the overall response. For instance, the peaks observed at negative potentials were affected by the acidity of the samples. The array of sensors showed an interesting cross-selectivity that was due to the different catalytic properties of

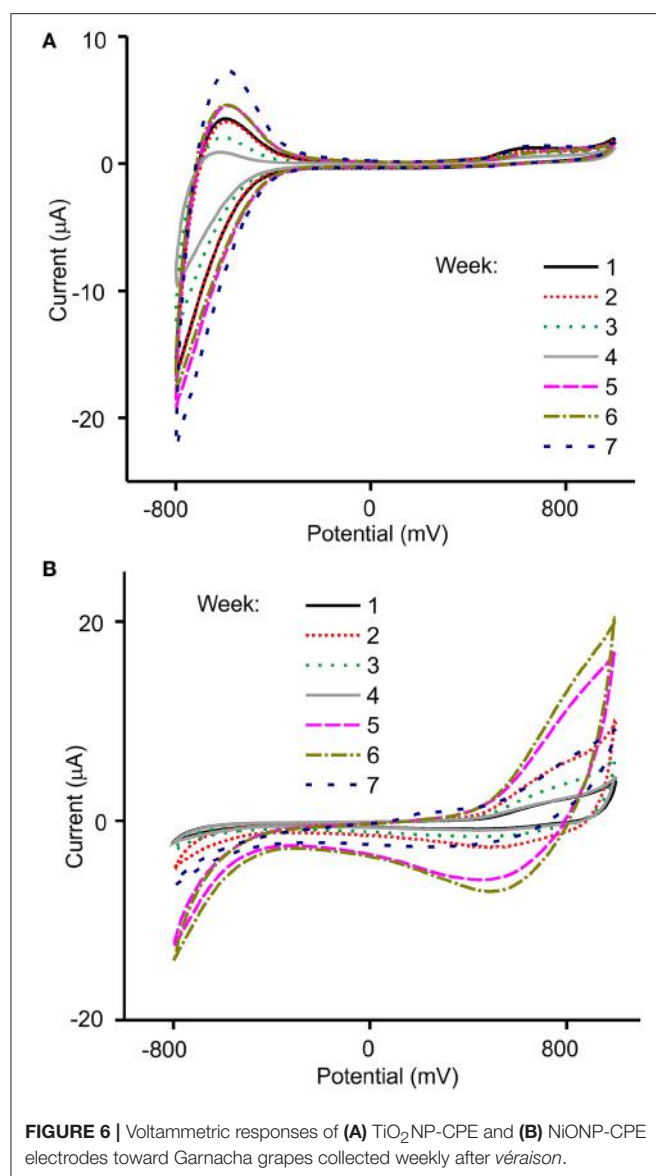


**FIGURE 6 |** Voltammetric responses of **(A)** TiO<sub>2</sub>NP-CPE and **(B)** NiONP-CPE electrodes toward Garnacha grapes collected weekly after véraison.

the MONP selected. For instance, NiONP-CPEs were highly sensitive to phenols, whereas TiO<sub>2</sub>NP-CPEs were sensitive to the acidity.

The chemical changes occurring during the ripening process could be followed using the MONP-based sensors. First, the intensity of the peaks increased, then intensity decreased and finally increased according with the tendency shown in **Figure 2** where TPI values varied similarly. The irregular increase stopped when optimal ripeness was attained. Simultaneously, a decrease in the total acidity corresponded with a progressive decrease in the intensity of the peaks at negative potentials. As already stated in the introduction, multivariate methods have demonstrated to be a good strategy for the analysis of wines. It can be expected that they can also be useful to monitor the ripeness of grapes.

When PCA was carried out using the data obtained from the electronic tongue, it was observed that clusters corresponding to grapes collected in the first 4 weeks after véraison, were positioned in a counterclockwise organization “drawing” a circle (**Figure 7A**). In sampling number 5, the circle was closed. Surprisingly, in next samplings the positions were repeated and clusters corresponding to next specimens were situated continuing the counterclockwise trend following a “screw” structure. According to PCA, grapes could be considered matured when the clusters reached the original positions. Similar results have been obtained for all the grape varieties analyzed in this work. Similar results have also been observed in previous works where ETs have been used to monitor maturity of grapes (Medina-Plaza et al., 2016).

**Figure 7B** show the contribution of the variables in a loading plot. The loadings of each sensor (ten variables per sensor) spread along the four quadrants. This graph shows the high cross-selectivity achieved by the array of sensors.

**Table 1** shows the statistical parameters obtained from the PLS-1 regression models (leave one out validation) correlating the output of the array of sensors with the chemical parameters (TPI, °Brix, TA). PLS-1 builds regression models to establish a linear relationship between the set of predictors (X-variable: Voltammetric signals obtained from the array of sensors) and the

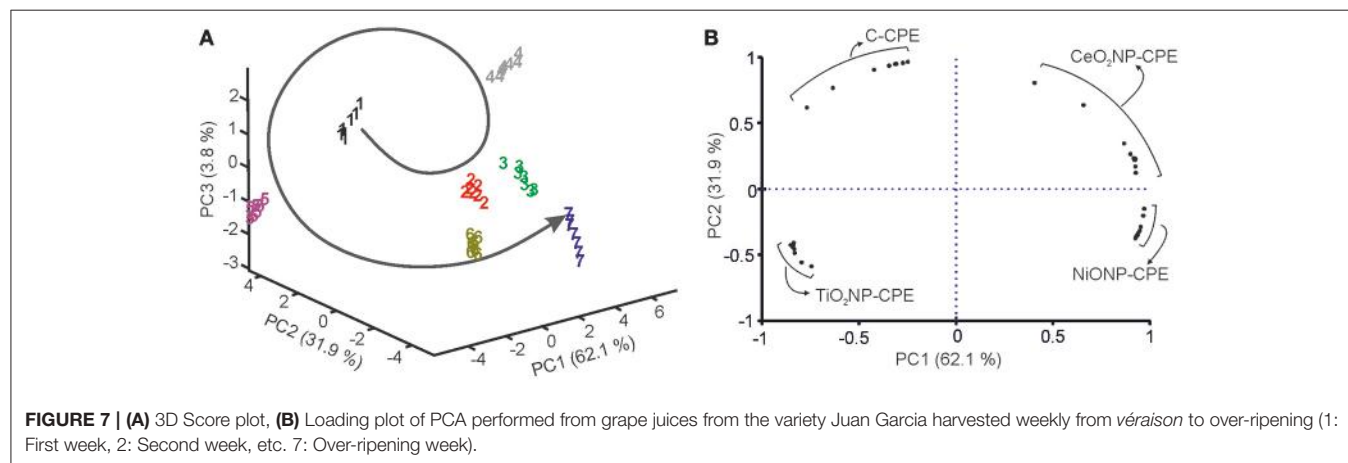


**FIGURE 7 |** **(A)** 3D Score plot, **(B)** Loading plot of PCA performed from grape juices from the variety Juan Garcia harvested weekly from véraison to over-ripening (1: First week, 2: Second week, etc. 7: Over-ripening week).

**TABLE 1** | Results of the PLS-1 regression models correlating the chemical parameters and the signals of the sensors.

Grape	Parameter	$R^2_C$ (a)	RMSE <sub>C</sub> (b)	$R^2_P$ (c)	RMSE <sub>P</sub> (d)	Number of components
Cabernet	°Brix	0.87	0.86	0.85	0.95	<b>3</b>
	TA (g/L)	0.87	0.81	0.81	1.02	7
	TPI	0.86	2.13	0.83	2.42	<b>2</b>
Garnacha	°Brix	0.92	0.91	0.82	1.40	6
	TA (g/L)	0.85	1.24	0.73	1.72	6
	TPI	0.86	2.25	0.77	3.01	<b>3</b>
Juan Garcia	°Brix	0.86	0.79	0.79	1.00	5
	TA (g/L)	0.80	1.08	0.70	1.39	6
	TPI	0.84	1.54	0.79	1.84	<b>4</b>
Mencia Regadio	°Brix	0.97	0.22	0.96	0.26	5
	TA (g/L)	0.89	0.69	0.86	0.77	5
	TPI	0.88	1.08	0.83	1.33	5
Mencia Secano	°Brix	0.86	0.58	0.79	0.74	6
	TA (g/L)	0.81	0.84	0.71	1.06	6
	TPI	0.86	1.57	0.82	1.79	<b>3</b>
Prieto Picudo	°Brix	0.87	0.73	0.63	1.25	7
	TA (g/L)	0.88	0.93	0.70	1.52	7
	TPI	0.83	1.33	0.81	1.43	<b>3</b>
Rufete	°Brix	0.85	0.49	0.83	0.53	<b>3</b>
	TA (g/L)	0.82	0.91	0.76	1.09	5
	TPI	0.91	1.51	0.90	1.64	<b>3</b>
Tempranillo	°Brix	0.81	0.89	0.76	1.01	6
	TA (g/L)	0.91	0.56	0.76	0.95	6
	TPI	0.87	2.05	0.75	2.94	<b>4</b>

Models were established for each variety of grape considered separately.

(a) Squared correlation coefficient in calibration; (b) Root mean square error of calibration; (c) Squared correlation coefficient in prediction; (d) Root mean square error of prediction.

set of responses (Y-variable: Chemical parameters obtained with traditional methods). PLS-1 finds the latent variables (indicated as number of components) in X that will best predict the latent variables in Y.

In all varieties of grapes, good correlations were found with the Total Polyphenol Index. Using a low number of components, both the calibration and the prediction showed Squared Correlation Coefficients in calibration ( $R^2_C$ ) and in prediction ( $R^2_P$ ) of ca. 0.8. Additionally, low Root Mean Square Error of calibration (RMSE<sub>C</sub>) and of prediction (RMSE<sub>P</sub>) were accomplished. These results confirm that the ET can be used to monitor the phenolic maturity of grapes. The °Brix and Total Acidity which are the parameters commonly used to evaluate the maturity of grapes, could also be predicted using the PLS-1 models but with lower correlation coefficients in prediction

(~0.7) and the models need a higher number of components. In spite of the lower correlation, the models are good enough to confirm that the electrochemical responses also reflected the acidity and the sugar concentration. This indicates that it is possible to obtain simultaneous information of the three main parameters used to monitor the maturity of grapes.

## CONCLUSIONS

The advantages of metal oxide nanoparticles as sensing materials for the detection of phenols has been evidenced. They rely on the excellent electrocatalytic properties of the metal oxide nanoparticles, that improved the sensitivity and limits of detection toward phenols with respect to unmodified sensors. Using these exceptional sensing properties, and the cross-selectivity shown by different MONPs, an electronic tongue based on metal oxide nanoparticles has been developed. The chemical changes occurring during ripening could be followed using the MONP-based multisensor system. The sensors based on different MONP show an excellent degree of cross-selectivity. Using PLS-1, correlations have been established between the signal of the multisensor system and the Total Polyphenol Index TPI, the °Brix, and the Total Acidity.

According to this, simultaneous analysis of three important markers of maturity can be achieved using a multisensory system based on MONPs. This means that the ET can be a useful tool to establish with a better accuracy the optimal harvesting date in a single experiment. This method can be used as a supplementary tool to classical analytical techniques.

The results shown here demonstrate the excellent opportunities offered by metal oxide nanoparticles as sensing materials in electronic tongues.

## AUTHOR CONTRIBUTIONS

MR-M: conceived the experiments and wrote the paper; CG-H, CM-P, CG-C, and YB: carried out the experiments; JF-E and EB-T: provided the grape samples and analyzed the grapes by chemical methods; MR-P and FM-P: carried out the chemometric analysis.

## ACKNOWLEDGMENTS

Financial support by MINECO and FEDER (AGL2015-67482-R) and the Junta de Castilla y León FEDER (VA011U16) is gratefully acknowledged. CG-H thanks for the grant of JCYL (BOCYL-D-24112015-9).

## SUPPLEMENTARY MATERIAL

The Supplementary Material for this article can be found online at: <https://www.frontiersin.org/articles/10.3389/fchem.2018.00131/full#supplementary-material>

## REFERENCES

- Apetrei, C., Apetrei, I. M., De Saja, J. A., and Rodríguez-Méndez, M. L. (2011). Carbon paste electrodes made from different carbonaceous materials: application in the study of antioxidants. *Sensors* 11, 1328–1344. doi: 10.3390/s110201328
- Apetrei, I. M., Rodríguez-Méndez, M. L., Apetrei, C., Nevares, I., del Alamo, M., and de Saja, J. A. (2012). Monitoring of evolution during red wine aging in oak barrels and alternative method by means of an electronic panel test *Food Res. Intnl.* 45, 244–249. doi: 10.1016/j.foodres.2011.10.034
- Boss, P. K., Bottcher, C., and Davies, C. (2014). Various influences of harvest date and fruit sugar content on different wine flavor and aroma compounds. *Am. J. Enology Vitic.* 65, 341–353. doi: 10.5344/ajev.2014.13137
- Buratti, S., Ballabio, D., Giovanelli, G., Dominguez, C. M. Z., Moles, A., Benedetti, S., et al. (2011). Monitoring of alcoholic fermentation using near infrared and mid infrared spectroscopies combined with electronic nose and electronic tongue. *Anal. Chim. Acta* 697, 67–74. doi: 10.1016/j.aca.2011.04.020
- Campbell, F. W., and Compton, R. G. (2010). The use of nanoparticles in electroanalysis: an updated review. *Anal. Bioanal. Chem.* 396, 241–259. doi: 10.1007/s00216-009-3063-7
- Campos, I., Bataller, R., Armero, R., Gandia, J. M., Soto, J., Martínez-Mañez, R., et al. (2013). Monitoring grape ripeness using a voltammetric electronic tongue. *Food Res. Int.* 54, 1369–1375. doi: 10.1016/j.foodres.2013.10.011
- Cetó, X., González-Calabuig, A., Crespo, N., Pérez, S., Capdevila, J., Puig-Pujol, A., et al. (2017). Electronic tongues to assess wine sensory descriptors. *Talanta* 162, 218–224. doi: 10.1016/j.talanta.2016.09.055
- Codinachs, L. M. I., Kloock, J. P., Schöning, M. J., Baldi, A., Ipatov, A., Bratov, A., et al. (2008). Electronic integrated multisensor tongue applied to grape juice and wine analysis. *Analyst* 113, 1440–1448. doi: 10.1039/b801228h
- Cosio, M. E., Benedetti, S., and Scampio, M. (2012). *Electronic Noses and Tongues in Chemical Analysis of Food: Techniques and Applications*. London: Academic Press.
- Cozzolino, D., McCarthy, J., and Bartowsky, E. (2012). Comparison of near infrared and mid infrared spectroscopy to discriminate between wines produced by different *Oenococcus oeni* strains after malolactic fermentation: a feasibility study. *Food Control* 26, 81–87. doi: 10.1016/j.foodcont.2012.01.003
- Godelmann, R., Fang, F., Humpfer, E., Schütz, B., Bansbach, M., Schäfer, H., et al. (2014). Targeted and nontargeted wine analysis by 1H NMR spectroscopy combined with multivariate statistical analysis. Differentiation of important parameters: Grape variety, geographical origin, year of vintage. *J. Agric. Food Chem.* 61, 5610–5619. doi: 10.1021/jf400800d
- Gutiérrez, J. M., Haddi, Z., Amari, A., Bouchikhi, B., Mimendia, A., Cetó, X., et al. (2013). Hybrid electronic tongue based on multisensor data fusion for discrimination of beers *Sens. Actuators B: Chem.* 177, 989–996. doi: 10.1016/j.snb.2012.11.110
- Gutiérrez, J. M., Moreno-Barón, L., Pividori, M. I., Alegret, S., and Del Valle, M. (2010). A voltammetric electronic tongue made of modified epoxy-graphite electrodes for the qualitative analysis of wine. *Microchim. Acta* 169, 261–268. doi: 10.1007/s00604-010-0351-z
- Gutiérrez, M., Domingo, C., Vila-Planas, J., Ipatov, A., Capdevila, F., Demming, S., et al. (2011). Hybrid electronic tongue for the characterization and quantification of grape variety in red wines. *Sens. Actuators B Chem.* 153, 695–702. doi: 10.1016/j.snb.2011.02.020
- Kilmartin, P. A., Zou, H. L., and Waterhouse, A. L. (2001). A cyclic voltammetry method suitable for characterizing antioxidant properties of wine and wine phenolics. *J. Agric. Food Chem.* 49, 1957–1965. doi: 10.1021/jf001044u
- Kirsanov, D., Mednova, O., Vietoris, V., Kilmartin, P. A., and Legin, A. (2012). Towards reliable estimation of an electronic tongue predictive ability from PLS regression models in wine analysis. *Talanta* 90, 109–116. doi: 10.1016/j.talanta.2012.01.010
- Lin, X. Y., Ni, Y. N., and Kokot, S. (2013). Glassy carbon electrodes modified with gold nanoparticles for the simultaneous determination of three food antioxidants. *Anal. Chim. Acta* 765, 54–62. doi: 10.1016/j.aca.2012.12.036
- Lvova, L., Kirsanov, D., Di Natale, C., and Legin, A. (2014). *Multisensor systems for chemical analysis: Materials and Sensors*. Boca Ratón, FL: CRC Press.
- Medina-Plaza, C., De Saja, J. A., Fernández-Escudero, J. A., Barajas-Tola, E., Medrano, G., et al. (2016). Array of biosensors for discrimination of grapes according to grapevariety, vintage and ripeness. *Anal. Chim. Acta* 947, 16–22 doi: 10.1016/j.aca.2016.10.032
- Medina-Plaza, C., De Saja, J. A., and Rodríguez-Méndez, M. L. (2014a). Bioelectronic tongue based on lipidic nanostructured layers containing phenol oxidases and lutetium bisphthalocyanine for the analysis of grapes. *Biosens. Bioelectron.* 57, 276–283. doi: 10.1016/j.bios.2014.02.023
- Medina-Plaza, C., García-Cabezon, C., García-Hernández, C., Bramorski, C., and Blanco-Val, Y., Martín-Pedrosa, et al. (2015a). Analysis of organic acids and phenols of interest in the wine industry using Langmuir-Blodgett films based on functionalized nanoparticles. *Anal. Chim. Acta* 853, 572–578. doi: 10.1016/j.aca.2014.10.046
- Medina-Plaza, C., Revilla, G., Muñoz, R., Fernández-Escudero, J. A., Barajas, E., Medrano, G., et al. (2014b). Electronic tongue formed by sensors and biosensors containing phthalocyanines as electron mediators. Application to the analysis of red grapes. *J. Porphyrins Phthalocyanines* 18, 76–86. doi: 10.1142/S1088424613501137
- Medina-Plaza, C., Rodríguez-Méndez, M. L., Sutter, P., Tong, X., and Sutter, E. (2015b). Nanoscale Au-In alloy–oxide core–shell particles as electrocatalysts for efficient hydroquinone detection. *J. Phys. Chem. C* 119, 25100–25107. doi: 10.1021/acs.jpcc.5b07960
- Meléndez, E., Ortiz, M. C., Sarabia, L. A., and Íñiguez, M., Puras, P. (2013). Modelling phenolic and technological maturities of grapes by means of the multivariate relation between organoleptic and physicochemical properties. *Anal. Chim. Acta* 761, 53–61. doi: 10.1016/j.aca.2012.11.021
- Mercante, L. A., Scagion, V. P., Pavinatto, A., Sanfelice, R. C., Mattoso, L. H. C., and Correa, D. S. (2015). Electronic tongue based on nanostructured hybrid films of gold nanoparticles and phthalocyanines for milk analysis. *J. Nanomat.* 16:402. doi: 10.1155/2015/890637
- Nogales-Bueno, J., Hernández-Hierro, J. M., Rodríguez-Pulido, F. J., and Heredia, F. J. (2014). Determination of technological maturity of grapes and total phenolic compounds of grape skins in red and white cultivars during ripening by near infrared hyperspectral image: a preliminary approach. *Food Chem.* 152, 586–591. doi: 10.1016/j.foodchem.2013.12.030
- OIV (2013). *Compendium of International Methods of Analysis of Wines and Musts; Organisation Internationale de la Vigne et du Vin*. Paris.
- Prieto, N., Gay, M., Vidal, S., Agaard, O., De Saja, J. A., and Rodríguez-Méndez, M. L. (2011). Analysis of the influence of the type of closure in the organoleptic characteristics of a red wine by using an electronic panel. *Food Chem.* 129, 589–594. doi: 10.1016/j.foodchem.2011.04.071
- Rodríguez-Méndez, M. L. (2016). *Electronic Noses and Tongues in Food Industry*. London: Academic Press.
- Rudnitskaya, A., Schmidke, L. M., Reis, A., Domingues, M. R. M., Delgadillo, I., Debus, B., et al. (2017). Measurements of the effects of wine maceration with oak chips using an electronic tongue. *Food Chem.* 229, 20–27. doi: 10.1016/j.foodchem.2017.02.013
- Saha, K., Agasti, S. S., Kim, C., Li, X., and Rotello, V. M. (2012). Gold nanoparticles in chemical and biological sensing. *Chem. Rev.* 112, 2739–2779. doi: 10.1021/cr2001178
- Sharma, S., Kori, S., and Parmar, A. (2015). Surfactant mediated extraction of total phenolic contents (TPC) and antioxidants from fruits juices. *Food Chem.* 185, 284–288. doi: 10.1016/j.foodchem.2015.03.106
- Sharpe, E., Bradley, R., Frasco, T., Jayathilaka, D., Marsh, A., and Andreescu, S. (2014). Metal oxide based multisensor array and portable database for field analysis of antioxidants. *Sens. Actuators B Chem.* 193, 552–562. doi: 10.1016/j.snb.2013.11.088
- Xu, Y. P., Simon, J. E., Welch, C., Wightman, J. D., Ferruzzi, M. G., Ho, L., et al. (2011). Survey of polyphenol constituents in grapes and grape-derived products. *J. Agric. Food Chem.* 59, 10586–10593. doi: 10.1021/jf202438d

**Conflict of Interest Statement:** The authors declare that the research was conducted in the absence of any commercial or financial relationships that could be construed as a potential conflict of interest.

Copyright © 2018 Garcia-Hernandez, Medina-Plaza, Garcia-Cabezon, Blanco, Fernandez-Escudero, Barajas-Tola, Rodriguez-Perez, Martin-Pedrosa and Rodriguez-Mendez. This is an open-access article distributed under the terms of the Creative Commons Attribution License (CC BY). The use, distribution or reproduction in other forums is permitted, provided the original author(s) and the copyright owner are credited and that the original publication in this journal is cited, in accordance with accepted academic practice. No use, distribution or reproduction is permitted which does not comply with these terms.



# Thermally Driven Selective Nanocomposite PS-PHB/MGC Nanofibrous Conductive Sensor for Air Pollutant Detection

**Joshua Avossa<sup>1</sup>, Emiliano Zampetti<sup>1</sup>, Fabrizio De Cesare<sup>1,2</sup>, Andrea Bearzotti<sup>1</sup>, Giuseppe Scarascia-Mugnozza<sup>2</sup>, Giuseppe Vitiello<sup>3,4</sup>, Eyal Zussman<sup>5</sup> and Antonella Macagnano<sup>1,2\*</sup>**

<sup>1</sup> Institute of Atmospheric Pollution Research-National Research Council (Ia-Cnr), Monterotondo, Italy, <sup>2</sup> Department of Innovation in Biological Systems, Food and Forestry, University of Tuscia, Viterbo, Italy, <sup>3</sup> Department of Chemical, Materials and Production Engineering, University of Naples "Federico II", Naples, Italy, <sup>4</sup> Csgl, Consorzio Interuniversitario per lo Sviluppo dei Sistemi a Grande Interfase, Sesto Fiorentino, Italy, <sup>5</sup> Faculty of Mechanical Engineering, Technion - Israel Institute of Technology, Haifa, Israel

## OPEN ACCESS

### Edited by:

Larisa Lvova,  
Università degli Studi di Roma Tor  
Vergata, Italy

### Reviewed by:

Antonio Riul Jr,  
Universidade Estadual de Campinas,  
Brazil

Dmitry Kirsanov,  
Saint Petersburg State University,  
Russia

### \*Correspondence:

Antonella Macagnano  
antonella.macagnano@cnr.it;  
a.macagnano@iia.cnr.it

### Specialty section:

This article was submitted to  
Analytical Chemistry,  
a section of the journal  
Frontiers in Chemistry

**Received:** 30 March 2018

**Accepted:** 31 August 2018

**Published:** 25 September 2018

### Citation:

Avossa J, Zampetti E, De Cesare F, Bearzotti A, Scarascia-Mugnozza G, Vitiello G, Zussman E and Macagnano A (2018) Thermally Driven Selective Nanocomposite PS-PHB/MGC Nanofibrous Conductive Sensor for Air Pollutant Detection. *Front. Chem.* 6:432. doi: 10.3389/fchem.2018.00432

The potentials to use the working temperature to tune both the sensitivity and the selectivity of a chemical sensor based on a nanostructured and nanocomposite polymer layer have been investigated and described. Thus, in a single step, a peculiar chemical layer was grown up onto IDE (Interdigitated Electrode) microtransducers by electrospinning deposition and using a single-needle strategy. The 3-component nanofibers, obtained from a mixture of polystyrene and polyhydroxybutyrate (insulating thermoplastics) and a known concentration of mesoporous graphitized carbon nanopowder, appeared highly rough on the surface and decorated with jagged islands but homogeneous in shape and diameter, with the nanofillers aggregated into clusters more or less densely packed through the fibers. The resulting sensor was conductive at room temperature and could work between 40 and 80°C without any apparent degradation. As the fibrous sensing layer was heated, the current increased and the sensitivity to some classes of VOCs such as an oxidizing gas drastically changed depending on the working temperature. More in detail, the sensor resulted highly sensitive and selective to acetic acid at 40°C but the sensitivity fell down, decreasing by 96%, when the sensor operated at 80°C. On the other hand, although an increase in temperature caused a general decrease in sensitivity to the tested VOCs (with a maximum of 14, 81, and 78% for amine, acetone and toluene, respectively) and water vapors (with a maximum of 55%), higher temperature affected only slightly the amine permeation, thus modifying the partial selectivity of the sensor to these chemicals. Conversely, when the operating temperature increased, the sensitivity to the detected gas, NO<sub>2</sub>, increased too, reporting a ~2 ppb limit of detection (LOD), thus confirming that the temperature was able to drive the selectivity of nanocomposite polymeric sensors.

**Keywords:** electrospinning technology, mesoporous graphene, hybrid and nanocomposite polymer nanofibers, gas/VOCs conductive sensor, sensor working temperature effects

## INTRODUCTION

The problem of classifying and further quantifying the chemical compounds in the air on a real-time basis is very crucial for a broad variety of activities in various fields, such as for industry (Wilson, 2012), medicine (Fitzgerald and Fenniri, 2017), food and agriculture (Srivastava et al., 2017; Basheer, 2018), indoor (Mad Saad et al., 2017) and outdoor environmental pollution (Wilson, 2012; Rai et al., 2017; Szulczynski and Gebicki, 2017), safety monitoring, and homeland security<sup>1</sup> (Sekhar et al., 2010). More recently a common aim has been based on the attempt to develop portable and easy-to-use monitoring instruments for rapid and inexpensive analysis also of complex matrices, i.e., headspaces containing various volatile and gaseous compounds, based<sup>1</sup> on sensors arrays or matrices with broad and partially overlapping sensitivity to various chemicals (olfactory machines and electronic nose systems). Each sensor has to transduce chemical information concerning multi-component gaseous mixtures into a series of measurable signals (Andrzej and Maciejewsk, 2012). As a part of these systems, sensors are exploited independently and simultaneously, and then treated as independent sensing elements. Furthermore each sensor contributes to create a multivariate response, within a sensor array, of the analyzed matrix. In order to be effective and successful, all the sensors should be characterized by as much chemical diversity as possible, on the assumption that they have not to be highly selective toward any given analyte, but highly and differently sensitive to every chemical class. On the other hand, the concept of an array of chemical sensors that can be used for any application is now outdated due to a series of difficulties, like the creation of universal databases from trained sensor arrays and the need to make the sensor array more selective to specific applications where gases or VOCs (Volatile Organic Compounds) to be revealed are present in trace amounts. For instance, in metal-oxide based sensors, that have been the most investigated and commercially used sensors, the working temperature is the main responsible of their sensitivity as well as their selectivity. Thus the same sensors, working at different working temperature values in order to detect various chemical classes with different sensitivity and selectivity, can be designed to create an array or a part of a suitable array for defined applications. For instance, SnO<sub>2</sub>-based sensors can work between 25 and 500°C but their best sensing temperatures depend on the kind of gas to be detected (Zakrzewski et al., 2006): an optimal sensing temperature of a SnO<sub>2</sub> sensor to reveal CH<sub>4</sub> has been reported to be about 400°C while that for sensing CO has been 90°C, confirming that temperature could be an effective tuner of the sensing features. Obviously in the case of MeO<sub>x</sub> semiconductors temperature is the main responsible parameter for the amount of O<sup>-</sup> distribution on the sensors surface, which is necessary for them to work properly. Vice versa,

**Abbreviations:** EPR, Electron Paramagnetic Resonance; ES, Electrospinning; IDE, Interdigitated Electrode; LOD, Limit of Detection; MGC, Mesoporous Graphene Carbon; PHB, Polyhydroxybutyrate; PS, Polystyrene; sccm, standard cubic centimeter per minutes; SEM, Scanning Electron Microscopy; TEM, Transmission Electron Microscopy; VOC, Volatile Organic Compound.

<sup>1</sup>[https://www.electrochem.org/dl/interface/wtr/wtr10\\_p035-040.pdf](https://www.electrochem.org/dl/interface/wtr/wtr10_p035-040.pdf)

sensors based on conductive polymers are designed to work at room temperature, in order to both avoid an eventual thermal degradation (Zampetti et al., 2011) of the chemical layer and to favor the adsorption and diffusion mechanisms of the analytes through the surface. Generally, the sensitivity and selectivity are commonly ruled by polymer chemical structure and arrangement within the sensing layer (Słoducho and Cabaj, 2016). In the present study, the potentials to use the working temperature to tune both the sensitivity and the selectivity of a chemical sensor based on a “soft-matter” chemical sensor have been investigated and described. Therefore a nanostructured and nanocomposite polymer sensor has been designed, fabricated, and then exposed to different chemical classes of VOCs and one gas within a range of working temperatures, compatible with the thermal stability of the polymers, to ascertain that the temperature also could be a modulator of selectivity and sensitivity such as for metal-oxide based sensors. Obviously, in the case of polymer based sensors, the temperature changes are expected to affect different chemophysical parameters of the sensing process. The chemical layer was organized as a non-woven fabric of polymeric nanofibers obtained by electrospinning technology (ES). This technology allows designing and fabricating continuous nano-microfibers when a high electrical field acts on a droplet of a polymer solution with sufficient viscoelasticity. In literature, electrospinning (ES) has been suggested as one of the most promising candidates among the various nanotechnologies for designing and creating highly sensitive and smart sensing materials, due to its cost-effectiveness, high production rate, and peculiarity of the resulting nanostructures (Macagnano et al., 2015). Commonly, several approaches have been used to impart sensing capability to nanofibers (Ding et al., 2010), such as using a polymer sensing material to electrospun nanofibers (Macagnano et al., 2011, 2016), incorporating sensing molecules into nanofibers (Han et al., 2013; Su et al., 2014), or putting sensing material on nanofiber surface via coating/grafting technique (Huang et al., 2012), etc. Conductive polymer nanofibers can be obtained by several strategies as for example blending more polymers where at least one is conductive or including conductive nanofillers along fibers.

In this paper, we present the potentials to use the working temperature to tune both the sensitivity and the selectivity of a chemical sensor based on a nanofibrous and nanocomposite polymer layer. Indeed sensors based on conductive polymers have been commonly designed to work at room temperature, to both avoid an eventual thermal degradation of the chemical layer and to favor the adsorption and diffusion mechanisms of the analytes through the surface. On the other hand, temperature can be a useful strategy for provisionally modifying the arrangement of both polymer chains and the hosted nanofillers, as well as the related electrical and sensing features. Specifically, the attention has been focused on the challenging goal of obtaining conductive fibers electrospun by a mixture of two insulating polymers, polyhydroxybutyrate (PHB) (Hankermeyer and Tjeerdema, 1999; Acevedo et al., 2018) and polystyrene (PS), hosting a conductive nanopowder of mesoporous graphitized carbon (MGC). The polymers were mainly selected for several features like their versatility (generally used to make a wide variety of consumer

products), eco-compatibility due to their biodegradability (PHB) and recyclability (PS) (Wünsch, 2000; Uyar and Besenbacher, 2008) and good environmental resistance to thermal excursion. Indeed, both the polymers are classified as thermoplastics, i.e., they can be heated to their melting point ( $T_b^{\text{PS}}$ : 240°C,  $T_b^{\text{PHB}}$ : 175°C), cooled, and reheated again without significant degradation. Further, they were both soluble in  $\text{CHCl}_3$ , meaning that a unique and easily electrospun mixture could be provided, and insoluble in  $\text{H}_2\text{O}$ , meaning that the resulting fibers could be exposed to a wide range of relative humidity percentages without undergoing structural changes. Exploiting some of the properties of electrospinning technique, nanofibers have been designed in order to be rough and porous, in order to increase the exposed surface and favoring gas and VOCs permeation. Thus, a mixing of two different organic solvents and a proper surfactant agent were used in the ES deposition mixture. Furthermore, a lot of polymer interfaces inside fibers were expected due to the incompatibility of the two polymers. About MGC, it was selected as the conductive nanofiller: its structure made of a single layer of  $\text{sp}^2$  carbon atoms bonded in a hexagonal honeycomb crystalline structure displays outstanding physical properties as high carrier mobility [up to  $350 \cdot 10^3 \text{ cm}^2/(\text{Vs})$ ], thermal stability (Bolotin et al., 2008), high mechanical strength (Young's module: 1 TPa and fracture strength: 130 GPa) and large availability of specific surface areas<sup>2</sup>. All these features were expected to provide both conductivity and a higher mechanical strength to the nanofibers. Graphitized carbon nanostructures have also been greatly investigated for their sensing features (Wang et al., 2016). Depending on the kind of application and transducer, graphene and their derivatives have been used oxidized or reduced, doped with metal-oxides - or metal-nanostructures, biomolecules or conductive polymers, etc. (Sahiner and Demirci, 2017). For these materials, gas adsorption is primarily due to physisorption on their surfaces (van der Waals forces) that can be tuned by chemical functional groups. In literature has been proven that some gases as  $\text{NO}_2$  (Novikov et al., 2016),  $\text{NH}_3$  (Karaduman et al., 2017),  $\text{H}_2\text{O}$  (Khomenko et al., 2015), and CO (Panda et al., 2016) can be detected by graphene-based sensors, too, with a partial selectivity. The latter has been explained supposing that the adsorption reactions with various gas molecules occurred at the surface of graphene, where the adsorbed molecules acted as donors or acceptors. Such a charge transfer changed carrier concentration in graphene and then the conductivity of graphene-based sensors. Depending on graphene layer arrangement and doping, a graphene based sensor can show a p-type or n-type semiconductor behavior (Meng et al., 2013). The nanofillers, adopted for being included within the planned sensor, were provided also of a mesoporous membrane that conferred a larger available surface area (50–100  $\text{m}^2/\text{g}$ ) to the nanopowder as well as the potential to get high selectivity through effects of molecular size exclusion (137 Å average pore diameter)<sup>2</sup>. The resulting MGC arrangement within the electrospun polymer nanofibers was expected to depend both on graphene/polymers mass ratio and its affinity to the hosting polymers, as well as on all the parameters of the electrospinning process. Electrical parameters are related to the quality of the MGC distribution within fibers, additionally

to the MGC amount. Therefore, a rearrangement inside the polymer nanofibers due to temperature changes is expected to tune electrical parameters such as the sensing properties of the fibrous layer, thus suggesting an easy and novel strategy of tuning of selectivity and sensitivity of the polymer based sensors.

## Materials

Mesoporous Graphitized Carbon Nanopowder, MGC (<500 nm), Hexadecyltrimethylammonium Bromide, CTAB (~99%), Polystyrene, PS (Mw = 192,000 g/mol), Chloroform (≥99%), Acetone (≥99.5%), Toluene (≥99.8%), Polyvinylpyrrolidone, PVP (Mw = 1,300,000 g/mol), Acetic Acid, AcAc (≥99%), n-Butylamine (99.5%), Poly[(R)-3-hydroxybutyric acid, PHB (natural origin) were purchased from Sigma-Aldrich. Ethanol (≥99.8%) was obtained from Honeywell-Fluka. All chemical were used without further purification. Standardized pure air (5.0) and  $\text{NO}_2$  (5.00 ppm in  $\text{N}_2$ ), were purchased from Praxair-RIVOIRA, Italy, and stored in cylinders. Interdigitated Electrodes (IDEs), provided by Micrux Technologies (Spain), were fabricated on glass substrate (IDE sizes: 10 x 6 x 0.75 mm, Pt/Ti electrodes, 120 pairs, 10  $\mu\text{m}$  wide x 5 mm long x 150 nm thick, with 10  $\mu\text{m}$  gap) and rinsed with soap and a “base piranha” mixture at 60°C for ~15 min, (3:1, v:v, ammonia water and hydrogen peroxide water solution) and finally with Milli-Q water (~18 MΩ cm) before any use.

## Electrospinning Deposition

The electrospun dispersion was prepared by mixing two different solutions: one containing the matrix of the fibers (PS and PHB) called Sol1 and the other one, called Sol2, containing the carbon nanopowder dispersion stabilized by a small amount of PVP. Sol1 solution (1:0.1:0.3 = PS:PHB:CTAB, mass ratio) was prepared, first, solubilizing 450 mg of PS pellets into 9 mL of chloroform under magnetic stirring. After completely dissolution, 60 mg of PHB were added into the solution and mixed at 45°C for 2 h. Then CTAB 150 mg and 1 mL of ethanol were poured into the system and mixed overnight at 45°C under magnetic stirring. Sol2 dispersion (1:0.4 = MGC:PVP, mass ratio) containing 50 mg of MGC, 20 mg of PVP, 1.8 mL of chloroform and 0.2 mL of ethanol were mixed and then sonicated for ~2 h. Sol1 and Sol2 (1.2 mL and 36  $\mu\text{L}$ , respectively) were mixed under magnetic stirring for 1 h (1:0.1:0.3:0.003:0.001 = PS:PHB:CTAB: MGC:PVP, mass ratio). The resulting dispersion was loaded into a glass syringe (1 cm long stainless steel tip) and connected to a syringe pump. The fibers deposition was carried out in a home-made ventilated clean box equipped at ambient condition. The electrospinning apparatus consisted of a high power AC-DC converter, a high voltage oscillator (100 V) driving a high voltage (ranging from 1 to 50 kV), a syringe pump (Model KDS 200, KD Scientific) and a rotating conductive pipe with a 45 mm diameter grounded collector. The fibrous layers were fabricated by applying 2.9 kV of electrostatic DC voltage between the syringe tip and the collector, at a pump feeding rate of 900  $\mu\text{l}/\text{h}$ . Once the potential was applied, the polymeric dispersion jet coated the IDEs placed on the grounded rotating collector (800 rpm), opposite to the syringe pump, at the distance of 8 cm. Deposition time was fixed at 2 min in order to

obtain a thin coverage of the electrodes and at 20 min for EPR (Electron Paramagnetic Resonance) analysis and water contact angle measurement.

## Material Characterization

UV-vis spectrophotometer (UV-2600 Shimadzu) was used to collect UV spectra of MGC. Samples were prepared from dilution of the electrospun dispersion (10  $\mu$ L in 1 mL CHCl<sub>3</sub>) or Sol2 (1  $\mu$ L in 1 mL of chloroform).

EPR measurements were performed by using a X-band Bruker Elexys E-500 spectrometer (Bruker, Rheinstetten, Germany). Samples (in turn,  $\sim$ 1 mg of MGC and electrospun fibers mats peel off an aluminum foil subject to rotation and deposition for 20 min) were co-axially introduced in a quartz sample tube with a diameter of 4 mm and were measured at 25°C. EPR spectra were recorded at the following settings: 100 G as sweep width, 1,024 points as resolution, 100 kHz as modulation frequency and 1.0G as modulation amplitude. Preventively, the amplitude of the field modulation was checked to be sufficiently low to avoid detectable signal overmodulation. To record the final EPR spectra, the attenuation value was fixed to 15 dB and 128 scans were accumulated with the aim to improve the signal-to-noise ratio. The specific g-factor value was determined by inserting Mg/MnO powder, as internal standard (Yordanov et al., 1999) in the quartz tube with the analyzed samples.

Optical micrographs were captured by Leitz-Wetzlar (Metallux 708082) microscope, for the evaluation of the quality coverage of the fibers deposited onto the IDE.

Fibers morphological analyses were carried out by means of micrographs from Scanning Electron Microscopy (SEM) and Transmission Electron Microscopy (TEM). The electrospun nanofibrous fabrics deposited on thin SiO<sub>2</sub> wafers and sputter-coated with gold in a Balzers MED 010 unit were analyzed for SEM by a JEOL JSM 6010LA electron microscope.

For Transmission Electron Microscopy (TEM), samples were attached onto carbon-copper grids and observed with a JEOL 1200 EX II electron microscope. Micrographs were captured by the Olympus SIS VELETA CCD camera equipped the iTEM software.

## Measurement Setup

Chemoresistors were housed in a measurement glass chamber ( $\sim$ 100 mL volume) and connected to an electrometer (Keithley 6517) capable of measuring their electrical parameters and sending data to a PC (LabVIEW Software). The current was recorded by applying potential values from  $-7.0$  to  $7.0$  V in ten steps of 0.7 V at different temperatures (20, 40, 60, 80, 100°C). Currents values vs. applied voltage were used to calculate the resistance of the fibrous coated IDE and its correlation to the temperature. All the batches of the chemoresistors fabricated in different dates but keeping the identical deposition parameters reported the same electrical features confirming the reproducibility of the deposition technique (data not shown).

Dynamic sensor measurements were carried out at different temperature (40, 60, 80°C) using: (i) 4-channel MKS 247 managing up to four MKS mass flow controllers (MFC), set in the range 0–200 sccm (standard cubic centimeter per minutes); (ii)

Environics S4000 (Environics, Inc.) flow controller, containing three MFCs supplying different flow rates (up to 500, 250, and 2.5 sccm, respectively), managed by its own software. Pure air was mixed and used as gas carrier. Different fluxes of NO<sub>2</sub> withdrawn from a cylinder at fixed concentration were mixed to pure air in order to test the dependence of IDE responses on different NO<sub>2</sub> concentrations. For evaluating the effect of water and VOCs vapors (acetone, toluene, acetic acid, and n-butylamine) on the sensor conductivity, different compounds concentrations in air were generated by a bubbler filled with liquid water or VOCs and mixed with the gas carrier (air).

## DISCUSSION AND RESULTS

The nanocomposite fibrous layer was grown up by electrospinning deposition using a single-needle. A diagram depicting the sensor development and its working is shown in **Figure 1**. The polymer drop on the needle tip, comprising PHB, PS, and MGC was subjected to an electrical field generating electric charges on the liquid surface, then repulsive electrical forces, elongation between the needle tip and collector up to the solvent evaporation and fibers formation. The transducers can be fixed onto the grounded rotating cylinder in order to collect the ejected fibers on their electrodes and then be able to measure their electric and sensing features when exposed to the selected analytes. Despite the multiplicity of the components in the mixture, the electrospun traveling liquid jet stream proceeded without interruptions, micro-drops or nozzle fillings. All the substrates, i.e., IDEs, SiO<sub>2</sub> wafers, and Al-foils, were fixed on the cylindrical collector and aligned within the deposition cone. After deposition IDEs and SiO<sub>2</sub> wafers appeared coated with a thin fibrous fabric (the inset in **Figures 3A, 4**, respectively). The heterogeneous system was collected for a few minutes on the interdigitated electrodes in order to link the metal fingers by a thin and highly porous film. Such fabrics resulted white/light gray, soft, and easy to peel off. Instead, a free-standing mat was got after at least 20 min of deposition onto the Al foil. After thermal incubation at 60°C for 12 h, the samples were investigated to outline their morphological, electrical, and sensing properties. The EPR spectra reported in **Figure 2** depicted a single and very broad Lorentzian signal at a g-factor value of  $2.0035 \pm 0.0003$ , which is typical of carbon-centered radicals (Barklie, 2003; Kausteklis et al., 2011) and associative to paramagnetic defects within the graphitic structure (Cirić et al., 2009; Kausteklis et al., 2011; Tampieri et al., 2014). Any additional resonance that would belong to frequently observed transition-metal impurities was not revealed using magnetic field scanning over broader field-range (Kausteklis et al., 2011). A quantitative analysis of the EPR spectrum was also realized by determining the signal amplitude,  $\Delta B$ . This parameter is directly obtained by the recorded spectra and is correlated to the mean distance between the radical centers (Vitiello et al., 2017), furnishing indirect information about the spatial distribution of paramagnetic centers within the whole material. For bare carbon nanopowder (**Figure 2A**), the EPR spectrum presented a  $\Delta B = 6.3 \pm 0.2$  G. A similar signal was observed in the EPR

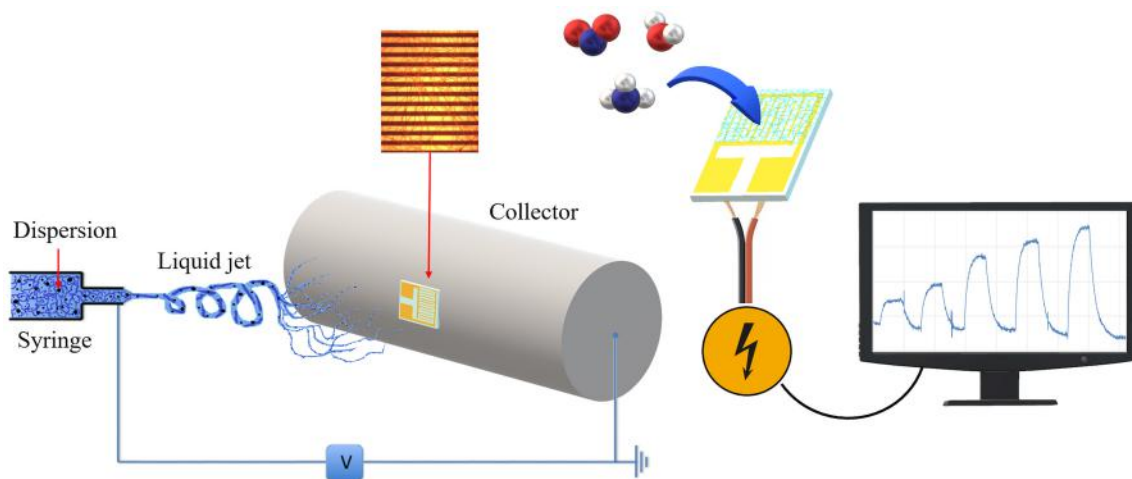


**FIGURE 1 |** Sensor developing and usage scheme. The polymer mixture loaded in the syringe (**Left**) was electrospun by applying a voltage between the tip and the cylindrical collector where an interdigitated electrode is fixed and coated with the fibers. The coated IDE was used as transducer (**Right**) and connected to a PC for sensing current changes upon interaction with gases molecules.

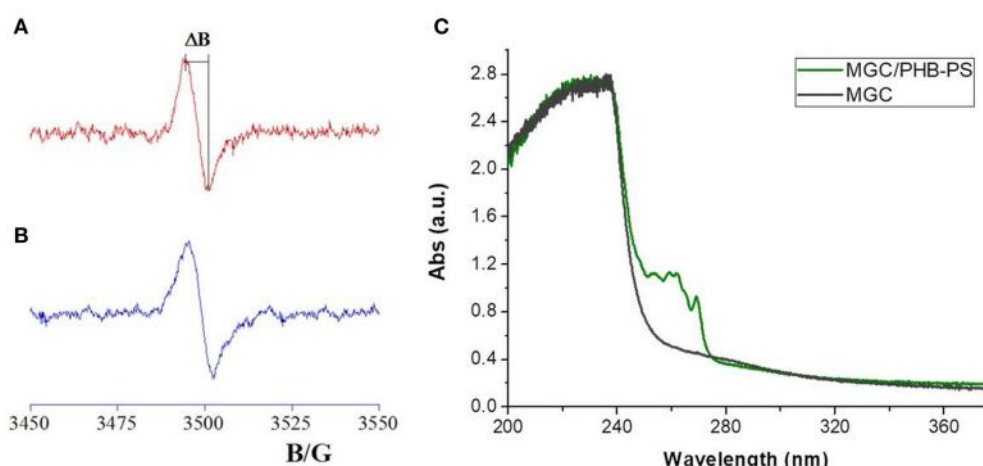


**FIGURE 2 |** EPR spectra of MGC powder (**A**) and electrospun mats (**B**).  $\Delta B$  corresponded to the distance between the maximum and the minimum within the spectra. On the right (**C**) the UV-vis adsorption spectra of diluted polymer mixture of MGC/PHB-PS (light green) and diluted Sol2 in chloroform (dark green) are reported.

spectra of the nanofibrous sample (**Figure 2B**), confirming the presence of MGC in the electrospun fibers (MGC-NFs). Here the  $\Delta B$  value reported a slight increase with respect to the value obtained from the spectrum of MGC bare ( $\Delta B = 6.7 \pm 0.2$  G), signifying that the radical centers are nearest and suggesting a more confined spatial distribution of MGC within the final electrospun materials. This result may be due to an aggregation of MGC inside the nanofibrous layer in domains with a thicker spatial density than in MGC powder. UV-Vis spectra (**Figure 2C**) of MGC (Sol2) and MGC in PHB-PS have the typical shape of graphene dispersion in chloroform except for the main peaks due to polystyrene absorbance (260 nm). The absorption band centered at 232 nm is ascribed to  $\pi-\pi^*$  transitions of aromatic

C-C bonds (signals in saturation). Instead the absorbance band at 269 nm is presumed to be due to the redshift of the graphene band due to the flakes dispersion and orientation within the polystyrene suspension (Khan et al., 2002; Ciplak et al., 2015; Uran et al., 2017).

The morphology of the electrospun fibers is summarized in **Figure 3**. The three-component nanofibers, obtained from the mixture of PS/PHB, that are immiscible polymers, and MGC, all diluted in a  $\text{CHCl}_3$  and  $\text{EtOH}$ , appeared extremely rough on the surface and decorated with jagged islands, which may indicate phase separation, but homogeneous in shape and diameter ( $d: 550 \pm 170$  nm). The long and continuous fibers as the beads absence suggested that an

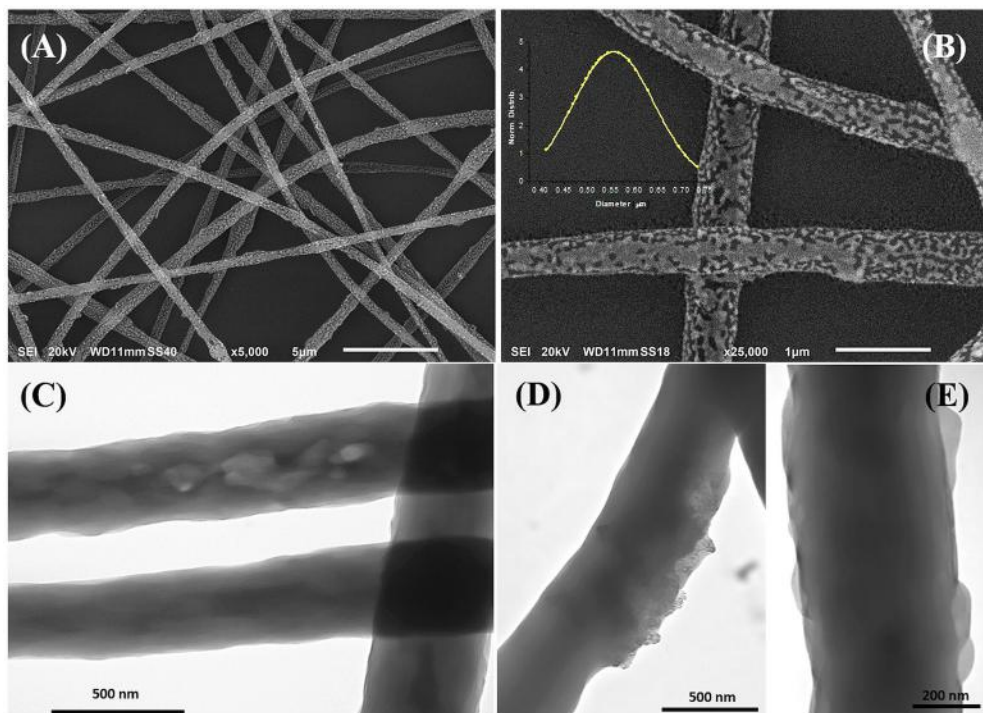


**FIGURE 3 |** SEM **(A,B)** and TEM **(C–E)** micrographs of electrospun fibers at different magnifications. The inset in **Figure B** represents the diameter distribution of the fibers collected from the SEM micrographs. SEM micrographs showed cavities and roughness on the surface while TEM highlighted protrusions **(C)**, and the MGC particles finely dispersed within the matrix **(D)**.

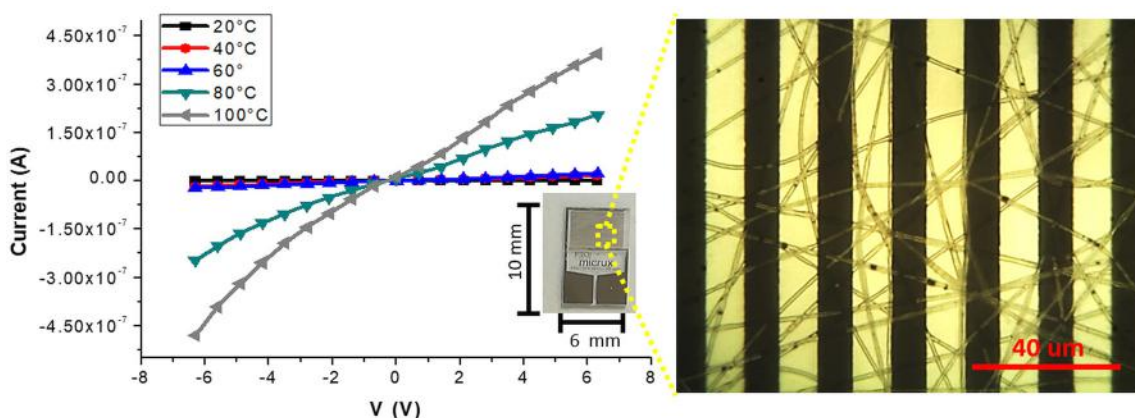


**FIGURE 4 |** Current-Voltage curves at different temperatures (20, 40, 60, 80, 100°C) for the fibers coated IDE (inset) are plotted. On the right, an optical micrograph shows a homogeneous coverage of the transparent fibers onto the interdigitated platinum bars. The optical image highlighted the presence of sub-micrometric MGC clusters.

appropriated combination of electrospinning set of parameters was achieved (e.g., potential applied, nozzle-ground distance, the feed rate, chemical combination of solvents, viscosity, molecular weight, and structure of the carrier polymers, etc.). Therefore the resulting IDE coating was a highly porous network of nanofibers with interconnected void volumes (high porosity) and high surface-to-volume ratios (specific surface area) (Zampetti et al., 2013). Several parameters are

expected to be the main responsible of the resulting fibers structure:

The use of an organic solvent combination ( $\text{CHCl}_3$ :  $\text{EtOH}$ ) whereas each component has a different rate of evaporation ( $T_b$ :  $61 < 78^\circ\text{C}$ , respectively), viscosity ( $\eta$ :  $0.57 < 1.20 \text{ cP}$ , respectively) and relative polarity ( $0.259 < 0.654$ , respectively)<sup>2</sup>

<sup>2</sup><https://sites.google.com/site/miller00828/in/solvent-polarity-table>.

The use of a mixture of chloroform and ethanol (9:1 v/v) that are solvent and non-solvent for the polymers respectively may induce a phase separation during the electrospun fibers formation. Qi *et al.* produced highly porous Poly(L-lactic acid) (PLLA) fibers by a solvent (dichloromethane) and nonsolvent mixture (Butanol), suggesting that the higher amount of nonsolvent and volatility difference between the nonsolvent and solvent the higher the porosity (Qi *et al.*, 2009). In other works, the porosity was regulated by the humidity percentage: water (acted as a non-solvent for the polymer) diffused into the polymer jet solution causing phase separation and formation of porous fibers (Megelski *et al.*, 2002; Pai *et al.*, 2009).

The use of two polymers soluble in the same solvent ( $\text{CHCl}_3$ ) but incompatible with each other, hence separating in different domains. Zhong *et al.* formed a blend of polymers by electrospinning a solution of poly(ethylene oxide) (PEO) and PS, where PEO separated in smaller domains within the PS fibers (Zhong *et al.*, 2011). Bognitzki *et al.* produced fibers possessing co-continuous phase morphologies resulted from phase separation processes occurring during fiber formation of Poly(L-lactic acid) and PVP (Bognitzki *et al.*, 2001).

The introduction of a quaternary ammonium surfactant capable of increasing polymer surface roughness. In fact, CTAB salt, increasing the charge density of the polymeric solution, can affect the average fiber diameter such as the presence of crystalline particles, can increase the surface roughness (Sarac, 2016).

**Figures 3C–E**, is a composition of TEM micrographs of fibers details, confirming an irregular edge of the fibers, with plicas and globosity. Since the mass ratio between PHB and PS is 0.13 and due to their immiscibility, the resulting fibers might be composed with a matrix of PS hosting a randomly dispersion of PHB in the form of small aggregates (Figure 3C), that may be enhanced by the clearest areas along the fibers (lighter gray). Due to the rapid stretching of the electrified jet and the fast

solvent evaporation, polymer macromolecules are forced to be oriented in the direction of elongation. This rapid event is able to inhibit the polymer chains from going back to their equilibrium conformations. As a result, electrospun nanofibers are featured by a high degree of molecular orientation. Thus PHB and PS chains were subjected simultaneously to the same electric field strengths, but since they are basically incompatible, the stretching of the PHB chains is probably limited by the incompatibility with the PS ones, as reflected by their phase. Indeed, the phase separation was distinctly apparent with small aggregates of a polymer confined in the immiscible matrix. About the distribution of MGC along fibers, due to the low contrast between MGC sheets and the polymer matrix, it is difficult to observe the MGC networks. At higher TEM magnification darker areas appear to be finely distributed within the fiber (darker areas, Figure 3D) without assembling into beads, but aggregated into clusters more or less densely packed through the fibers, where some of them protruded from the fibers. According to the MGC description provided by the supplier<sup>2</sup>, they had a sheet configuration with an approximate diameter of 35 nm, forming aggregates in the 175 nm size range and then agglomerates in the 400 nm range. Further, MGC had a 137 Å average pore diameter. The resulting fibrous layer, comprising a lot of interfaces as well as the rough fibers and pores, was expected to be an intriguing system for the development of chemical sensors, due to both the wide adsorption surface and the surface energy potentials involved. The microtransducers coated with the 2 min-deposited fibers and placed on a customized micro-heater of alumina were able to measure the electrical parameters of the resulting chemoresistor at increasing temperature values up to 100°C. Optical microscope pictures confirmed the formation of optically transparent polymeric fibers through which the electrodes of the underlying substrate can be visualized. A few of significant black MGC aggregates was found inside fibers suggesting that the graphene distribution was not completely homogeneous and probably affected too by the immiscibility of the two polymers (Figure 4, inset). Current-Voltage curves displayed a quasilinear relationship between the current changes and the increasing imposed voltage values. Such a chemoresistor reported a resistance value ( $R$ ) of about  $3.33 \cdot 10^6$  MΩ when it worked at 20°C. Obviously, electrical conductivity was strictly related to the MGC content. Changing the amount of MGC the resistance value dramatically changed (data not shown). The MGC concentration here described (0.93% mass percentage) is related to the fibrous layer containing the minimum concentration that allowed the generation of stable and reproducible electrical signals at room temperature (close to the percolation threshold). At room temperature, whereas the carbon nanopowder is dispersed inside fibers forming a non-contact mode networks, the tunneling of electrons is expected to dominate the conduction of the composite system according to the percolation theory. Such a theory (Kirkpatrick, 1973; Mutlay and Tudoran, 2014) proposes that below a critical concentration, conducting fillers are individually isolated in an insulating polymer. As the concentration of the nanofillers increases, an inter-connected network of particles distributed inside the matrix is formed. This arrangement makes the material

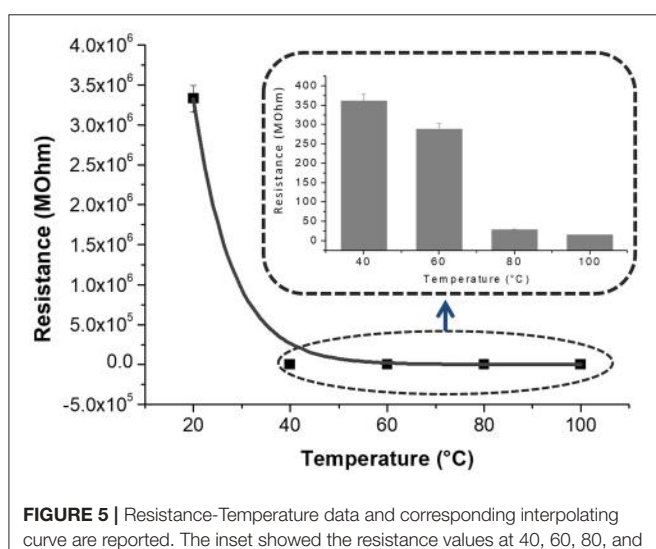


**FIGURE 5** | Resistance-Temperature data and corresponding interpolating curve are reported. The inset showed the resistance values at 40, 60, 80, and 100°C in a smaller scale.

to sharply change from insulator to semi-metal conductor. Beyond the critical concentration (percolation threshold) all the particles appear divided only by a thin polymer layer that allows the quantum mechanical tunneling. Further concentrating the particle network will generate saturation and conductivity achieves an upper limit which is quite below the conductivity of pure nanofillers (metal-like). Alekseev et al. reported that, when conductive fillers are incorporated into polymer matrices, both their state of dispersion and their orientation are also significant for determining electrical conduction of composites (Alekseev et al., 2012). The relative high resistance value of MGC in PS-PHB nanofibers suggest that the graphitic powder was organized into a network allowing the fibrous layer being conductive. Further, I-V curve shape seems to be affected by the metal-like conductivity occurring within the “darker dots” where MGC were more densely packed. However, when the transducer was microheated up to 100°C, the chemoresistor reported a nonlinear increase in the current values (resistance decrease). Specifically,  $R$  abruptly decreased  $9 \cdot 10^3$  times, i.e., from  $3.33 \cdot 10^6$  to  $3.61 \cdot 10^2$  MΩ, when temperature was increased from 20 to 40°C. The chemoresistor reached 14 MΩ resistance when the working temperature was set at 100°C (Figure 5). The temperature dependence of conductivity was non-linear but showed always a positive behavior upon heating. This result suggests the domination of the tunneling resistance in comparison with the contact one (Syurik et al., 2013) (Gao et al., 2018). The latter usually dominates in highly filled composites when physical contact between particles occurs, while the former is depending on the small dielectric barriers (insulating polymer) between the particles (Sheng, 1980). Polymer heating effects can be found in the chain reorientation due to a group rotation on the polymer backbone (Alexander, 1999), including phenyl group rotation in polystyrene (Tonelli, 1973). Such reorganization is supposed to affect the temperature dependence of conductivity due to strong  $\pi$ - $\pi$  interaction existing between aromatic organic molecules and the basal plane of the graphene. According to Cao et al., graphene sheets inside polystyrene films are able to build thermodynamically unstable networks at higher temperatures, (Cao et al., 2009), thus improving the connectivity of the conductive networks and then enhance the electrical conductivity.

Since the electrical signal at room temperature was too noisy, all sensing measurements were carried out between 40 and 80°C. Measurements at higher temperature were avoided for limiting an eventual wear of the fibers. Standard pure air with increasing percentages of water vapors was flowed throughout the measuring chamber and the changes of the sensor current were reported in Figure 6A. The humidity is everywhere in the environment, thus it is crucial to control this parameter as well as to know its effects on the designed sensor. Indeed, water molecules in the air are commonly known as potential interfering agents in the interactions between the chemical sensors and the VOCs/gases. Measurements were ranging between dry and 50% humid air. A linear relationship between humidity and current changes was reported (Figure 6B), and, specifically, the current linearly increased when humidity percentage increased, too. When the  $T_w$  was set at 40°C and relative humidity was 50%, the normalized current increased by  $7.46 \cdot 10^{-1}$  times. Similarly, the same measurements were carried out with the sensor set at increased temperature values. As previously reported, the current increased linearly with the humidity, but the sensor sensitivity to water vapor decreased at higher temperature. Therefore the normalized response to 50% of relative humidity, calculated as  $(I - I_0)/I_0$ , where  $I$  is the current value due to the reaction with the analyte and  $I_0$  is the current value when sensor is under clean air, decreased to  $3.58 \cdot 10^{-1}$  from  $7.46 \cdot 10^{-1}$  when the  $T_w$  was set at 80°C. Measuring the sensitivity values at 60 and 80°C, they diminished of about 44 and 55%, respectively. Sensitivity, defined as the ratio of the incremental change in the sensor's output ( $\Delta y$ ) to the incremental change of the measured input ( $\Delta x$ ), was calculated as the slope of the response curves (i.e., calibration curves) (Kalantar-zadeh, 2013). As a matter of fact, the fibers were designed to get a poor interaction with water molecules. Both the polymers were hydrophobic and planar structure of MGC should prefer  $\pi$ - $\pi$  interactions, despite H-bonds due to structural defects and terminal carboxyl groups. Instead, the experimental results suggested that the sensor seemed sensitive to the relative humidity. Indeed, contact angle measurement (Figure 7) showed that once a droplet of water (5  $\mu$ L) touched the surface of the ES mat (20 min deposition) a low water contact angle ( $\sim 15^\circ$ ) was formed, demonstrating that fibers possessed

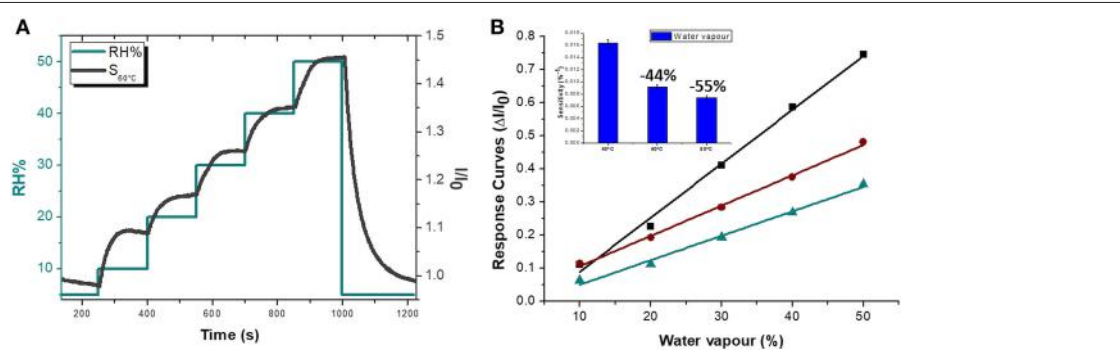


**FIGURE 6 |** Sensor electrical features at 60°C (S60°C) in dependence on %RH: the Normalized current curves ( $I/I_0$ , black) and Relative Humidity percentage (green) VS time are depicted (A). Sensor Response Curves VS Relative Humidity percentage at 40, 60, 80°C (green, brown and black, respectively) with an inset showing the Sensitivity values at 40, 60 and 80°C are reported.

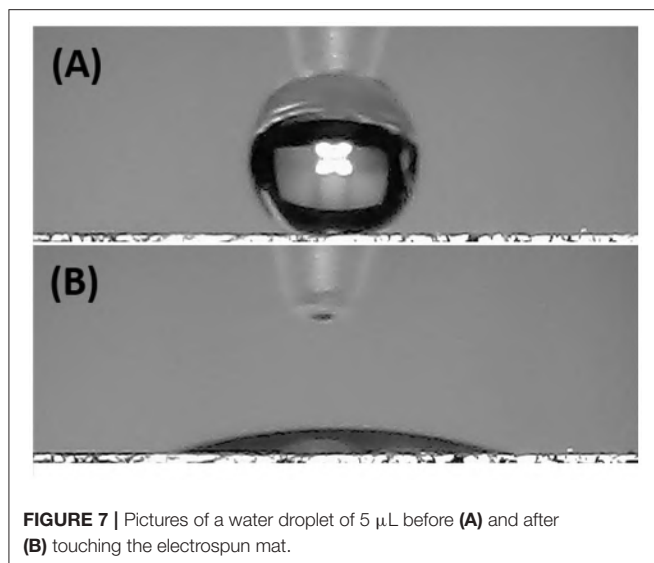


**FIGURE 7** | Pictures of a water droplet of  $5 \mu\text{L}$  before (A) and after (B) touching the electrospun mat.

an hydrophilic behavior, hence high affinity with water. More parameters were supposed to contribute to the unexpected sensor responses to the water. One of those is related to the porous and extremely wrinkled structure of the film (Zhang et al., 2012). Another one is related to the presence of numerous interfaces between MGC and the polymers (Pierleoni et al., 2018) as well as the two immiscible polymers, which facilitate the molecules permeation. Furthermore, since MGC has been designed with a mesoporous structure, it should easily entrap water molecules and interact by the oxygen atoms making part of the framework of each MGC sheet. Indeed, Boehm in his review stated that carbon black and other forms of carbon possessed a partial oxidized surface (Boehm, 1994). Finally, the salt used to allow the mixing of such a heterogeneous ES suspension, being a water soluble cationic surfactant, should favor the adsorption of  $\text{H}_2\text{O}$  molecules on to the fiber surface. On the other hand, the general decreasing in sensitivity to water molecules due to the increasing in temperature should be related to the reduction of adsorption on the nanostructured material surface and the lowering the molecules diffusion due to the backbone motion of the polymer chains (Haslam et al., 1924; Ramesh and Duda, 2000).

The sensor was then exposed to known concentrations of VOCs belonging to different chemical classes. Thus, known amounts of vapors of n-butylamine, an aliphatic amine (weak base), and acetic acid carboxylic acid (weak acid) were flowed throughout the measuring chamber and the resulting current changes were depicted in Figure 8. The shape of the transient responses indicated that the sensor responded quickly to both the analytes ( $t^{90} \approx 130 \text{ s}$ , where  $t^{90}$  is the time required by the sensor to reach 90% of the response) and it was regenerated in a few minutes ( $t^{90} \approx 150 \text{ s}$ ) by pure air. Further, the transient response shapes suggested two different VOC-surface rate of adsorption: very fast and with the reaching of a plateau in a few minutes for the amine (Langmuir-like kinetics) and linear without reaching an equilibrium phase for the acid. The kinetics of AcAc (Figure 8A) seems related to participation of multiple

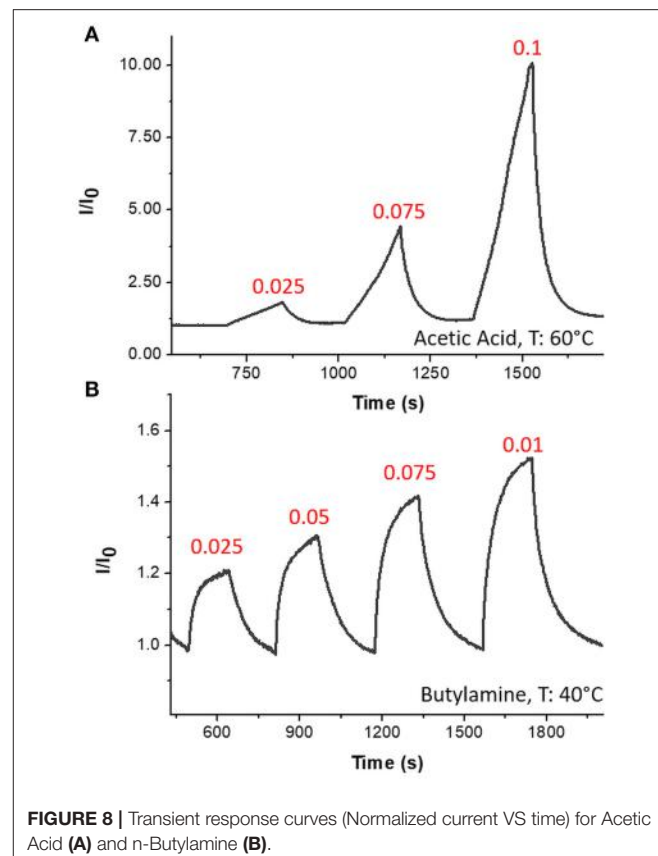


**FIGURE 8** | Transient response curves (Normalized current VS time) for Acetic Acid (A) and n-Butylamine (B).

sites of interactions, possible lateral interactions between adsorbed molecules and a multilayer formation. The response curves too (Figures 9A,C), related to the current changes when the VOCs partial pressure increased, depicted different shapes within the measured ranges, meaning different affinity between the adsorbent fibers and the two VOCs. Specifically, they were linear for n-butylamine and linear, at low concentrations, to become exponential at higher concentrations for AcAc. The response curves to the increasing vapors of toluene and acetone, respectively, have been plotted in Figures 10A,B, showing curves with linear shapes, but different slopes (sensitivities). Transient response curves as the calibration curves are related to the ad/absorbing mechanisms that result in the chemical affinity of the VOCs to the material. The fibers are a heterogeneous system where MGC are the responsible of the electrical parameter: the adsorption of both polar and apolar VOCs onto mesopores (or structural defects) and planar surfaces of graphene, respectively, determine the changes in the charges density. The mesoporous structure could work as nucleation center for entrapping and growing molecules, like AcAc, with multiple functional groups. On the other hands, these organic compounds can provide conformational changes of the hosting polymer chains, thus contributing to the redistribution of the graphene network, which is responsible for the charge flow. Since all the VOCs induced a rise in current, the effect on network distribution inside fibers could be the dominant one. A comparison of the

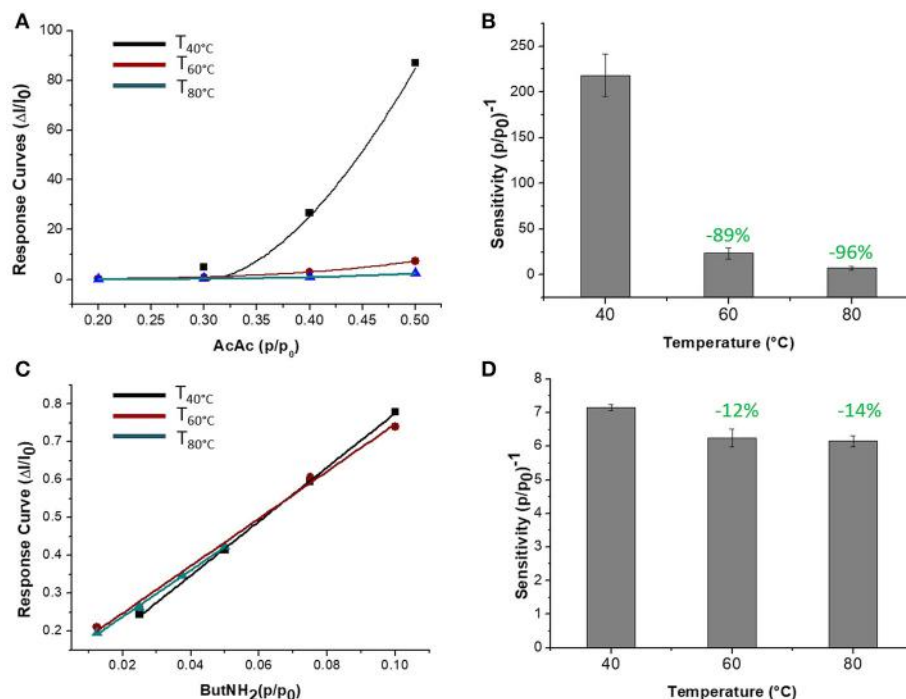


**FIGURE 9 |** Response curves VS relative partial pressure at 40, 60, 80°C for Acetic Acid (**A**) and n-Butylamine (**C**) are depicted. Sensitivity of Acetic Acid (**B**) and n-Butylamine (**D**) were estimated.

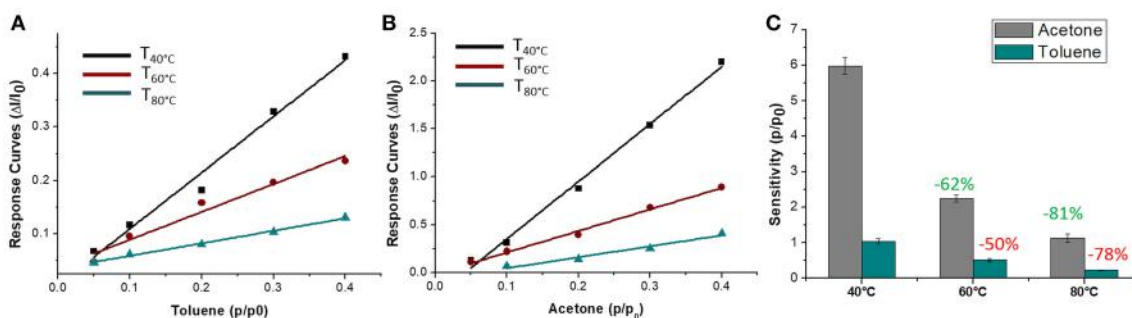


**FIGURE 10 |** Response curves VS relative partial pressure at 40, 60, 80°C for Toluene (**A**) and Acetone (**B**) and corresponding sensitivity values (**C**).

sensitivities to several VOCs and at different  $T_w$  is reported in **Figure 11**. When  $T_w$  increased to 60°C and then 80°C, the sensitivity to the amine (**Figure 9D**) decreased slightly (−12 and −14%, respectively), but enormously to the acid (**Figure 9B**) (−89 and −96%), acetone (−62 and −81%), and toluene (−50 and −78%) (**Figure 10C**). When compared to the other ones, the sensitivity to AcAc remained the highest at all temperature values, although the VOCs sensitivities ratios radically changed, reducing the global sensor selectivity (**Figures 11A,B**). Higher temperature seemed favor the permeation of amines despite the other VOCs, indeed the selectivity to n-butylamine lightly increased with the increase in the temperature, enhancing poor efficacy of a thermal role in the permeation and binding of the aliphatic amine with the fibers (**Figure 11B**).

Since graphene and overall graphene-oxide, has been investigated as highly sensitive materials to NO<sub>2</sub> (Novikov et al., 2016) the fibrous chemosensor was exposed to increasing concentrations of this gas in air, ranging between tens of ppb and a few ppm. Response and recovery time occurred in a few minutes (**Figure 12A**) showing an abrupt increase in current as the gas entered the measuring chamber and a likewise decrease until the baseline when pure air was flowed (**Figure 12A**). More specifically, response and recovery time ( $t^{90}$ ) values were measured to be <40 and <100 s, respectively. Despite to the VOCs results, when  $T_w$  increased, the sensitivity to NO<sub>2</sub> increased too, going from  $3.91 \cdot 10^{-5}$  to  $5.7 \cdot 10^{-5}$  and then to  $1.16 \cdot 10^{-4}$  ppb<sup>−1</sup> at 40, 60, and 80°C, respectively (**Figure 12B**). Here the sensitivity was calculated as the slope

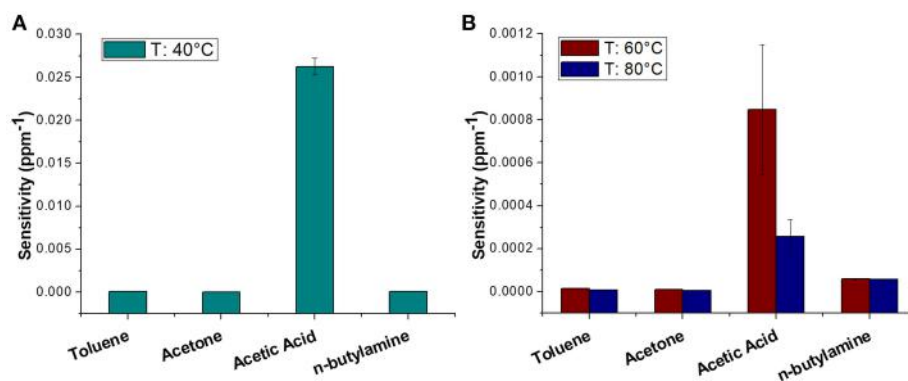


**FIGURE 11** | Diagram plotting sensitivity values ( $\text{ppm}^{-1}$ ) of Toluene, Acetone, Acetic Acid, n-Butylamine at  $40^\circ\text{C}$  (A) and  $60, 80^\circ\text{C}$  (B).

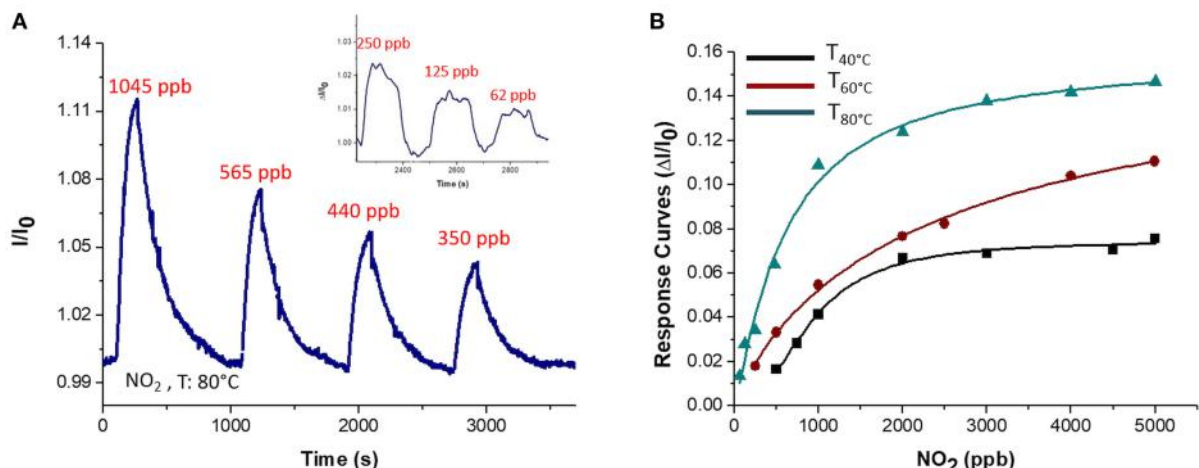


**FIGURE 12** | Transient response curve (Normalized current VS time) at  $80^\circ\text{C}$  (A) and Response curves VS concentration at  $40, 60, 80^\circ\text{C}$  for  $\text{NO}_2$  are depicted (B). The inset in A showed an increase in current at lower concentration of  $\text{NO}_2$  (150, 125, 62 ppb).

of the curves in the linear range (i.e., at lower concentrations). The affinity of the chemosensor to  $\text{NO}_2$  is depicted by the Langmuir-like calibration curves, as well as the significant effect of the temperature to the gas detection (Figure 12B). Since  $\text{NO}_2$ , that is an electron withdrawing, causes an increase in current, the MGC inside fibers is supposed to perform as a p-type semiconductor, delivering electrons to the gas molecules, leading an increase of hole concentration and leading so to an increase of graphene's conductivity. The high polymer porosity seems to allow the gas diffusion. Further the sensitivity at  $80^\circ\text{C}$  was valued to be 4 times higher than at  $40^\circ\text{C}$ . The increase in sensitivity could be due to the redistribution and orientation of graphene within polymer fibers due to the heating, allowing the gas adsorption onto a larger number of exposed binding sites, despite of the unfavorable energies involved in the phenomena of ad-adsorption. The  $\text{LOD}_{80^\circ\text{C}}$  (defined as  $3 \times$  standard deviation of the blank) has been calculated to be  $\sim 2$  ppb. In literature, chemoresistors based on graphene hybrids, reported limits of detections ranging between 10 ppm and 64 ppb at room temperature (Latif and Dickert, 2015).

## CONCLUSIONS

The present study reported the development of a conductive nanofibrous and nanocomposite polymer sensor designed so that its sensitivity and selectivity could be regulated by temperature. Electrospinning technology allowed, in one step and in 2 min, the fabrication of rough fibers comprising two thermoplastic polymers and nanopowder of mesoporous graphitized carbon. Indeed, exploiting the peculiarity of the deposition technique, through the usage of two incompatible polymers (PS and PHB), a proper mix of organic solvents and a surfactant salt, the resulting fibrous layer comprised a wide adsorption surface and a lot of interfaces that are likely features for chemical sensors. The selected amount of MGC (0.93% mass ratio), subjected to electrospun deposition together with the two polymers, appeared both finely spread inside fibers and more densely packed in some dots. Such a MGC concentration was the minimum concentration allowing the generation of stable and reproducible electrical signals at room temperature. Since the electrical conduction of nanocomposites is related also to their

state of dispersion and their orientation inside the polymer, the heating of fibers, by improving the connectivity of the conductive networks, caused a non-linear increase in current of the sensor. The sensor was able to work in a stable and reproducible way between 40 and 80°C without any significant degradation. Among the various chemical classes of the tested VOCs (aliphatic amine, aromatic hydrocarbons, ketone, and organic acid) the sensor resulted highly sensitive and selective to acetic acid. When fibers were heated, the sensitivity to the acid fell down, decreasing by 96% at 80°C if compared to that of the sensor at 40°C. On the other hand, although an increase in temperature caused a general decrease in sensitivity, higher temperature affected only slightly the amine permeation, thus modifying the partial selectivity of the sensor. Water vapors, too, were ad-absorbed by the fibrous layer, probably due to the porous and extremely wrinkled structure of the film, the number of interfaces of the heterogeneous fibers, and the mesoporous structure of MGC. An increase in temperature (from 40 to 80°C) caused a reduction in sensitivity by more than half. A completely different effect was reported when the sensor was exposed to traces of NO<sub>2</sub> and then heated. When temperature increased, the sensitivity to NO<sub>2</sub> increased too, until it achieved a LOD of about 2 ppb, when the sensor worked at 80°C. The high polymer porosity favored the gas diffusion such as the high available surface area of MGC increased the chance to bind the analyte. The further increase in sensitivity due to the heating could be presumably caused by the redistribution and orientation of graphene within polymer fibers that in turn could occupy a larger number of binding sites. The general decrease in sensitivity to all the VOCs and the relative humidity at higher temperature values despite the increasing sensitivity to NO<sub>2</sub>, means that the sensor can be tuned in order to be more selective to the gas and that the role of the potential interferents in complex environments can be significantly lowered. Further studies are needed to understand the whole mechanism of ad-absorption occurring between MGC and the VOCs/gas as well as the role of each polymer inside fibers when the working temperature changed. However, this preliminary study suggests that temperature can be a useful parameter for modulating the selectivity of defined nanocomposite polymeric sensors, letting us suppose that, as it happens for the metal oxide sensors, the same sensor could be

designed to work successfully in an array, simply changing its working temperature.

## DATA AVAILABILITY STATEMENT

The raw data supporting the conclusions of this manuscript will be made available by the authors, without undue reservation, to any qualified researcher.

## AUTHOR CONTRIBUTIONS

AM contributed to the conception and design of the study. EZ contributed to the definition of electrospun parameters. JA carried out electrospinning deposition and laboratory measurements. EZ provided the electronics of the measuring system. AB designed the water vapor measurements set-up. FD, GS-M, JA, AM, and EZ contributed to the graphics and data treatment. GV provided the EPR analysis. All authors contributed to manuscript revision, read and approved the submitted version.

## FUNDING

The present work has been funded by a 2-Year National Project, BRIC, Grant Number ID.12 2016, National Institute for Insurance against Accidents at Work (INAIL), titled: Design and development of a sensory system for the measurement of volatile compounds and the identification of job-related microorganisms.

## ACKNOWLEDGMENTS

The authors gratefully thank Dr. G. Tranfo of National Institute for Insurance against Accidents at Work for her crucial support in the BRIC ID.12 2016 Project and Dr. A. R. Taddei of High Equipment Centre, Electron Microscopy Section, University of Tuscany (VT), Italy, for providing SEM and TEM micrographs. Finally, authors thank Mr. A. Capocecera for his technical support in developing customized software for laboratory measurements.

## REFERENCES

- Acevedo, F., Villegas, P., Urtuvia, V., Hermosilla, J., Navia, R., and Seeger, M. (2018). Bacterial polyhydroxybutyrate for electrospun fiber production. *Int. J. Biol. Macromol.* 106, 692–697. doi: 10.1016/j.ijbiomac.2017.08.066
- Alekseev, A., Chen, D., Tkalya, E. E., Ghislandi, M. G., Syurik, Y., Ageev, O., et al. (2012). Local organization of graphene network inside graphene/polymer composites. *Adv. Funct. Mater.* 22, 1311–1318. doi: 10.1002/adfm.201101796
- Alexander, G. M. (1999). Anomalous temperature dependence of the electrical conductivity of carbon-poly (methyl methacrylate) composites. *Mater. Res. Bull.* 34, 603–611.
- Andrzej, S., and Maciejewsk, M. (2012). “Gas sensor array with broad applicability,” in *Sensor Array*, ed Wuqiang Yang InTech. Available online at: <http://www.intechopen.com/books/sensor-array/gas-sensor-array-with-broad-applicability>
- Barklie, R. C. (2003). Characterisation of defects in amorphous carbon by electron paramagnetic resonance (vol 10, pg 174, 2001). *Diam. Relat. Mater.* 12, 1426–1434. doi: 10.1016/S0925-9635(03)00004-9
- Basheer, A. A. (2018). Chemical chiral pollution: impact on the society and science and need of the regulations in the 21st century. *Chirality* 30, 402–406. doi: 10.1002/chir.22808
- Boehm, H. P. (1994). Some aspects of the surface chemistry of carbon blacks and other carbons. *Carbon N. Y.* 32, 759–769. doi: 10.1016/0008-6223(94)90031-0
- Bognitzki, M., Czado, W., Frese, T., Schaper, A., Hellwig, M., Steinhart, M., et al. (2001). Nanostructured fibers via electrospinning. *Adv. Mater.* 13, 70–72. doi: 10.1002/1521-4095(200101)13:1<70::AID-ADMA70>3.0.CO;2-H
- Bolotin, K. I., Sikes, K. J., Jiang, Z., Klima, M., Fudenberg, G., Hone, J., et al. (2008). Ultrahigh electron mobility in suspended graphene. *Solid State Commun.* 146, 351–355. doi: 10.1016/j.ssc.2008.02.024

- Cao, Q., Song, Y., Tan, Y., and Zheng, Q. (2009). Thermal-induced percolation in high-density polyethylene/carbon black composites. *Polymer* 50, 6350–6356. doi: 10.1016/j.polymer.2009.10.059
- Çiplak, Z., Yıldız, N., and Çalımlı, A. (2015). Investigation of Graphene/Ag nanocomposites synthesis parameters for two different synthesis methods. *Fullerenes Nanotub. Carbon Nanostruct.* 23, 361–370. doi: 10.1080/1536383X.2014.894025
- Cirić, L., Sienkiewicz, A., Náfrádi, B., Mionić, M., Magrez, A., and Forró, L. (2009). Towards electron spin resonance of mechanically exfoliated graphene. *Phys. Status Solidi Basic Res.* 246, 2558–2561. doi: 10.1002/pssb.200982325
- Ding, B., Wang, M., Wang, X., Yu, J., and Sun, G. (2010). Electrospun nanomaterials for ultrasensitive sensors. *Mater. Today* 13, 16–27. doi: 10.1016/S1369-7021(10)70200-5
- Fitzgerald, J., and Fenniri, H. (2017). Cutting edge methods for non-invasive disease diagnosis using E-tongue and E-nose devices. *Biosensors* 7:59. doi: 10.3390/bios7040059
- Gao, C., Liu, P., Ding, Y., Li, T., Wang, F., Chen, J., et al. (2018). Non-contact percolation of unstable graphene networks in poly(styrene-co-acrylonitrile) nanocomposites: electrical and rheological properties. *Compos. Sci. Technol.* 155, 41–49. doi: 10.1016/j.compscitech.2017.11.023
- Han, L., Andrade, A. L., and Ensor, D. S. (2013). Chemical sensing using electrospun polymer/carbon nanotube composite nanofibers with printed-on electrodes. *Sensors Actuators B Chem.* 186, 52–55. doi: 10.1016/j.snb.2013.05.069
- Hankermeyer, C. R., and Tjeerdema, R. S. (1999). “Polyhydroxybutyrate: plastic made and degraded by microorganisms,” in *Rev Env Contam Toxicol*, ed G. W. Ware (New York, NY: Springer), 1–24.
- Haslam, R. T., Hershey, R. I., and Kean, R. H. (1924). Effect of gas velocity and temperature on rate of absorption. *Ind. Eng.* 16, 1224–1230. doi: 10.1021/ie50180a004
- Huang, F., Wei, Q., and Cai, Y. (2012). “Surface functionalization of polymer nanofibers in functional nanofibers and their applications,” in *Functional Nanofibers and Their Applications*, ed Q. Wei (Cambridge, UK: Woodhead Publishing Series in Textiles), 92–118.
- Kalanter-zadeh, K. (2013). *Sensors*. New York, NY: Springer Science+Business Media. doi: 10.1007/978-1-4614-5052-8\_2
- Karaduman, I., Er, E., Çelikkan, H., Erk, N., and Acar, S. (2017). Room-temperature ammonia gas sensor based on reduced graphene oxide nanocomposites decorated by Ag, Au and Pt nanoparticles. *J. Alloys Compd.* 722, 569–578. doi: 10.1016/j.jallcom.2017.06.152
- Kaustecklis, J., Cevc, P., Arçon, D., Nasi, L., Pontiroli, D., Mazzani, M., et al. (2011). Electron paramagnetic resonance study of nanostructured graphite. *Phys. Rev. B Condens. Matter Mater. Phys.* 84, 1–5. doi: 10.1103/PhysRevB.84.125406
- Khan, M. S., Khan, W., Khan, S. A., and Iqbal, Y. (2002). UV absorbance studies of dilute polystyrene solutions in different solvents. *J. Chem. Soc. Pak.* 24, 237–240.
- Khomenko, V., Dittrich, R., and Joseph, Y. (2015). Graphene based chemiresistive vapor sensors. *Procedia Eng.* 120, 777–780. doi: 10.1016/j.proeng.2015.08.819
- Kirkpatrick, S. (1973). Percolation and conduction. *Rev. Mod. Phys.* 45, 574–588. doi: 10.1103/RevModPhys.45.574
- Latif, U., and Dickert, F. L. (2015). Graphene hybrid materials in gas sensing applications. *Sensors* 15, 30504–30524. doi: 10.3390/s151229814
- Macagnano, A., Perri, V., Zampetti, E., Bearzotti, A., and De Cesare, F. (2016). Humidity effects on a novel eco-friendly chemosensor based on electrospun PANi/PHB nanofibers. *Sensors Actuators B Chem.* 232, 16–27. doi: 10.1016/j.snb.2016.03.055
- Macagnano, A., Zampetti, E., and Kny, E. (2015). *Electrospinning for High Performance Sensors*. Cham: Springer Science+Business Media. doi: 10.1007/978-3-319-14406-1
- Macagnano, A., Zampetti, E., Pantalei, S., De Cesare, F., Bearzotti, A., and Persaud, K. C. (2011). Nanofibrous PANI-based conductive polymers for trace gas analysis. *Thin Solid Films* 520, 978–985. doi: 10.1016/j.tsf.2011.04.175
- Mad Saad, S., Andrew, A., Md Shakaff, A., Mat Dzahir, M., Hussein, M., Mohamad, M., et al. (2017). Pollutant recognition based on supervised machine learning for indoor air quality monitoring systems. *Appl. Sci.* 7:823. doi: 10.3390/app7080823
- Megelski, S., Stephens, J. S., Bruce Chase, D., and Rabolt, J. F. (2002). Micro- and nanostructured surface morphology on electrospun polymer fibers. *Macromolecules* 35, 8456–8466. doi: 10.1021/ma020444a
- Meng, X., Tongay, S., Kang, J., Chen, Z., Wu, F., Li, S. S., et al. (2013). Stable p- and n-type doping of few-layer graphene/graphite. *Carbon N. Y.* 57, 507–514. doi: 10.1016/j.carbon.2013.02.028
- Mutlay, I., and Tudoran, L. B. (2014). Percolation behavior of electrically conductive graphene nanoplatelets/polymer nanocomposites: theory and experiment. *Fullerenes Nanotub. Carbon Nanostruct.* 22, 413–433. doi: 10.1080/1536383X.2012.684186
- Novikov, S., Lebedeva, N., Satrapinski, A., Walden, J., Davydov, V., and Lebedev, A. (2016). Graphene based sensor for environmental monitoring of NO<sub>2</sub>. *Sensors Actuators B Chem.* 236, 1054–1060. doi: 10.1016/j.snb.2016.05.114
- Pai, C. L., Boyce, M. C., and Rutledge, G. C. (2009). Morphology of porous and wrinkled fibers of polystyrene electrospun from dimethylformamide. *Macromolecules* 42, 2102–2114. doi: 10.1021/ma802529h
- Panda, D., Nandi, A., Datta, S. K., Saha, H., and Majumdar, S. (2016). Selective detection of carbon monoxide (CO) gas by reduced graphene oxide (rGO) at room temperature. *RSC Adv.* 6, 47337–47348. doi: 10.1039/C6RA06058G
- Pierleoni, D., Minelli, M., Ligi, S., Christian, M., Funke, S., Reineking, N., et al. (2018). Selective gas permeation in graphene oxide–polymer self-assembled multilayers. *ACS Appl. Mater. Interfaces* 10, 11242–11250. doi: 10.1021/acsami.8b01103
- Qi, Z., Yu, H., Chen, Y., and Zhu, M. (2009). Highly porous fibers prepared by electrospinning a ternary system of nonsolvent/solvent/poly(l-lactic acid). *Mater. Lett.* 63, 415–418. doi: 10.1016/j.matlet.2008.10.059
- Rai, A. C., Kumar, P., Pilla, F., Skouloudis, A. N., Di Sabatino, S., Ratti, C., et al. (2017). End-user perspective of low-cost sensors for outdoor air pollution monitoring. *Sci. Total Environ.* 607–608, 691–705. doi: 10.1016/j.scitotenv.2017.06.266
- Ramesh, N., and Duda, J. L. (2000). Diffusion in polymers below the glass transition temperature: comparison of two approaches based on free volume concepts. *Korean J. Chem. Eng.* 17, 310–317. doi: 10.1007/BF02699046
- Sahiner, N., and Demirci, S. (2017). The use of graphene oxide-embedded superporous poly(2-hydroxyethylmethacrylate) cryogels for p(aniline) conductive polymer synthesis and their use in sensor applications. *Mater. Des.* 120, 47–55. doi: 10.1016/j.matdes.2017.02.004
- Sarac, A. (2016). *Nanofibers of Conjugated Polymers*. New York, NY: Pan Stanford.
- Sekhar, P. K., Brosha, E. L., Mukundan, R., and Garzon, F. (2010). Chemical sensor for environmental monitoring and homeland security. *Electrochem. Soc. Interface* 27, 35–40. doi: 10.1149/2.F04104if
- Sheng, P. (1980). Fluctuation-induced tunneling conduction in disordered materials. *Phys. Rev. B* 21, 2180–2195. doi: 10.1103/PhysRevB.21.2180
- Soloduchko, J., and Cabaj, J. (2016). “Conducting polymers in Sensor Design,” in *Conducting Polymers*, ed F. Yilmaz (London: Intech), 27–48.
- Srivastava, A. K., Dev, A., and Karmakar, S. (2017). Nanosensors and nanobiosensors in food and agriculture. *Environ. Chem. Lett.* 16, 1–22. doi: 10.1007/s10311-017-0674-7
- Su, Z., Ding, J., and Wei, G. (2014). Electrospinning: a facile technique for fabricating polymeric nanofibers doped with carbon nanotubes and metallic nanoparticles for sensor applications. *RSC Adv.* 4, 52598–52610. doi: 10.1039/C4RA07848A
- Syurik, J., Ageev, O. A., Cherednichenko, D. I., Konoplev, B. G., and Alexeev, A. (2013). Non-linear conductivity dependence on temperature in graphene-based polymer nanocomposite. *Carbon N. Y.* 63, 317–323. doi: 10.1016/j.carbon.2013.06.084
- Szulcynski, B., and Gebicki, J. (2017). Currently commercially available chemical sensors employed for detection of volatile organic compounds in outdoor and indoor air. *Environments* 4:21. doi: 10.3390/environments4010021
- Tampieri, F., Silvestrini, S., Riccò, R., Maggini, M., and Barbon, A. (2014). A comparative electron paramagnetic resonance study of expanded graphites and graphene. *J. Mater. Chem. C* 2, 8105–8112. doi: 10.1039/C4TC01383B
- Tonelli, A. E. (1973). Phenyl group rotation in polystyrene. *Macromolecules* 6, 682–683. doi: 10.1021/ma60035a007
- Uran, S., Alhani, A., and Silva, C. (2017). Study of ultraviolet-visible light absorbance of exfoliated graphite forms. *AIP Adv.* 7:4979607. doi: 10.1063/1.4979607
- Uyar, T., and Besenbacher, F. (2008). Electrospinning of uniform polystyrene fibers: the effect of solvent conductivity. *Polymer* 49, 5336–5343. doi: 10.1016/j.polymer.2008.09.025

- Vitiello, G., Pezzella, A., Zanfardino, A., Silvestri, B., Giudicianni, P., Costantini, A., et al. (2017). Antimicrobialactivity of eumelanin-based hybrids: the role of TiO<sub>2</sub> in modulating the structure and biological performance. *Mater. Sci. Eng. C* 75, 454–462. doi: 10.1016/j.msec.2016.12.135
- Wang, T., Huang, D., Yang, Z., Xu, S., He, G., Li, X., et al. (2016). A review on graphene-based gas/vapor sensors with unique properties and potential applications. *Nano-Micro Lett.* 8, 95–119. doi: 10.1007/s40820-015-0073-1
- Wilson, A. D. (2012). Review of electronic-nose technologies and algorithms to detect hazardous chemicals in the environment. *Proced. Technol.* 1, 453–463. doi: 10.1016/j.protcy.2012.02.101
- Wünsch, J. R. (2000). *Polystyrene: Synthesis, Production and Application*. Shrewsbury: Rapra Technology Ltd.
- Yordanov, N. D., Gancheva, V., and Pelova, V. A. (1999). Studies on some materials suitable for use as internal standards in high energy EPR dosimetry. *J. Radioanal. Nucl. Chem.* 240, 619–622. doi: 10.1007/BF02349422
- Zakrzewski, J., Domanski, W., Chatas, P., and Laopoulos, T. (2006). Improving sensitivity and selectivity of SnO<sub>2</sub> gas sensors by temperature variation. *IEEE Trans. Instrum. Meas.* 55, 14–20. doi: 10.1109/TIM.2005.862039
- Zampetti, E., Muzyczuk, A., Macagnano, A., Pantalei, S., Scalese, S., Spinella, C., et al. (2011). Effects of temperature and humidity on electrospun conductive nanofibers based on polyaniline blends. *J. Nanoparticle Res.* 13, 6193–6200. doi: 10.1007/s11051-011-0310-6
- Zampetti, E., Pantalei, S., Muzyczuk, A., Bearzotti, A., De Cesare, F., Spinella, C., et al. (2013). A high sensitive NO<sub>2</sub> gas sensor based on PEDOT-PSS/TiO<sub>2</sub> nanofibres. *Sensors Actuators B Chem.* 176, 390–398. doi: 10.1016/j.snb.2012.10.005
- Zhang, Z., Zhang, T., Zhang, Y. W., Kim, K. S., and Gao, H. (2012). Strain-controlled switching of hierarchically wrinkled surfaces between superhydrophobicity and superhydrophilicity. *Langmuir* 28, 2753–2760. doi: 10.1021/la203934z
- Zhong, G., Wang, K., Zhang, L., Li, Z. M., Fong, H., and Zhu, L. (2011). Nanodroplet formation and exclusive homogeneously nucleated crystallization in confined electrospun immiscible polymer blend fibers of polystyrene and poly(ethylene oxide). *Polymer* 52, 5397–5402. doi: 10.1016/j.polymer.2011.09.045

**Conflict of Interest Statement:** The authors declare that the research was conducted in the absence of any commercial or financial relationships that could be construed as a potential conflict of interest.

The handling editor and reviewer DK declared their involvement as co-editors in the Research Topic, and confirm the absence of any other collaboration.

Copyright © 2018 Avossa, Zampetti, De Cesare, Bearzotti, Scarascia-Mugnozza, Vitiello, Zussman and Macagnano. This is an open-access article distributed under the terms of the Creative Commons Attribution License (CC BY). The use, distribution or reproduction in other forums is permitted, provided the original author(s) and the copyright owner(s) are credited and that the original publication in this journal is cited, in accordance with accepted academic practice. No use, distribution or reproduction is permitted which does not comply with these terms.



# Peptide Modified ZnO Nanoparticles as Gas Sensors Array for Volatile Organic Compounds (VOCs)

Marcello Mascini<sup>1</sup>, Sara Gaggiotti<sup>1</sup>, Flavio Della Pelle<sup>1</sup>, Corrado Di Natale<sup>2</sup>,  
Sinazo Qakala<sup>3</sup>, Emmanuel Iwuoha<sup>3</sup>, Paola Pittia<sup>1</sup> and Dario Compagnone<sup>1\*</sup>

<sup>1</sup> Faculty of Bioscience and Technology for Food, Agriculture and Environment, University of Teramo, Teramo, Italy,

<sup>2</sup> Department of Electronic Engineering, University of Roma Tor Vergata, Rome, Italy, <sup>3</sup> Sensor Lab, Department of Chemistry, University of the Western Cape, Bellville, South Africa

## OPEN ACCESS

### Edited by:

Dmitry Kirsanov,  
Saint Petersburg State University,  
Russia

### Reviewed by:

Eleonora-Mihaela Ungureanu,  
Politehnica University of Bucharest,  
Romania  
Eduardo Pinilla-Gil,  
Universidad de Extremadura, Spain

### \*Correspondence:

Dario Compagnone  
dcompagnone@unite.it

### Specialty section:

This article was submitted to  
Analytical Chemistry,  
a section of the journal  
Frontiers in Chemistry

Received: 24 October 2017

Accepted: 20 March 2018

Published: 16 April 2018

### Citation:

Mascini M, Gaggiotti S, Della Pelle F, Di Natale C, Qakala S, Iwuoha E, Pittia P and Compagnone D (2018) Peptide Modified ZnO Nanoparticles as Gas Sensors Array for Volatile Organic Compounds (VOCs). *Front. Chem.* 6:105. doi: 10.3389/fchem.2018.00105

In this work a peptide based gas sensor array based of ZnO nanoparticles (ZnONPs) has been realized. Four different pentapeptides molecularly modeled for alcohols and esters having cysteine as a common spacer have been immobilized onto ZnONPs. ZnONPs have been morphologically and spectroscopically characterized. Modified nanoparticles have been then deposited onto quartz crystal microbalances (QCMs) and used as gas sensors with nitrogen as carrier gas. Analysis of the pure compounds modeled demonstrated a nice fitting of modeling with real data. The peptide based ZnONPs had very low sensitivity to water, compared to previously studied AuNPs peptide based gas sensors allowing the use of the array on samples with high water content. Real samples of fruit juices have been assayed; stability of the signal, good repeatability, and discrimination ability of the array was achieved.

**Keywords:** ZnO nanoparticles, peptides, virtual docking, quartz crystal microbalances, gas sensor array

## INTRODUCTION

In the last years, gas sensor arrays, often reported as electronic noses, have proved to be very useful tools for the analysis of foods and flavors. These tools can be applied in quality control (to control system of production, shelf-life monitoring, evaluation of the food freshness) of the product or in the study of the volatility of aromas in a wide range of food as cheese, wine, coffee, tomato, meat etc (Ampuero and Bosset, 2003; Loutfi et al., 2015). The use of gas sensor arrays in the food industry represent an opportunity considering their high sensitivity, high correlation with conventional sensory evaluation, short analysis times, low cost, non-invasive measurement, and potentiality of automation (Duran and Marcato, 2013; Vanderroost et al., 2014).

One of the simplest configurations in gas sensing is represented by quartz crystal microbalances (QCMs). These sensors have the potential for sensitive and selective target gas detection due to the ability to measure mass change, on the surface of the sensor itself, after interaction between the sensitive film and the gas (Tokura et al., 2017). The sensing surface of QCMs can be easily modified with organic compounds taking advantage of the measurement run at room temperature. Considering organic molecules as binding elements, some attempts to use proteins has been made recently with odorant binding proteins on QCMs (Sankaran et al., 2011a,b). However, either purification or production, via genetic engineering, of a pattern of odorant binding proteins for the

construction of different gas sensor arrays is costly and time consuming. The use of short peptide sequences as binding elements in the gaseous phase is particularly interesting as the peptides can easily be synthesized and designed using virtual screening to bind molecular targets. It has been recently reported that peptides exhibit a high ability to bind volatile compounds, and that main factor influencing the bond is the chemical nature of the volatile compound (Martínez-Arellano et al., 2016). The feasibility of the use of peptides onto QCMs has been already demonstrated using the glutathione tripeptide and its amino acid components to develop an array of QCM-based gas sensors (Compagnone et al., 2013). A virtual screening approach has been later developed and validated testing the response of the QCM sensors for the detection of some VOCs (Pizzoni et al., 2014). Peptides selected via molecular modeling were used different times as affinity binders in analytical detection systems (Mascini et al., 2005, 2013; Baggiani et al., 2013; Heurich et al., 2013). Peptides rationally designed have been immobilized onto piezoelectric transducers working either in liquid (Mascini et al., 2006) or in gas (Mascini et al., 2017). These short peptides have been proved to give satisfactory results in the assay of different food commodities from olive oil (Del Carlo et al., 2014) to chocolate and candies (Compagnone et al., 2015; Pizzoni et al., 2015). The ability of peptide-based gas sensors to discriminate among off-flavored and regular samples of dark, white, and milk chocolate or among candies prepared with a natural or synthetic strawberry flavor was higher than classical phorphyrin based QCMs array. In the latter works, in order to improve sensitivity and the amount of the ligand onto each sensor, the peptides have been previously immobilized onto gold nanoparticles (AuNPs) using as spacer a cysteinyl-end for each of the peptides. AuNPs represented the first choice as nanomaterial since have been extensively studied for their many different proprieties and ability to be functionalized (Saha et al., 2012; Yue et al., 2016; Della Pelle and Compagnone, 2018).

In this work, we exploit the characteristics of ZnO nanoparticles to act as carrier for the peptide binding (Vallee et al., 2010) units of a gas sensor array. ZnO, as other metal oxides has an iso-electric point in alkaline range. This is a clear advantage for non-covalent immobilization of enzymes as most of the proteins operating in physiological range have isoelectric point in acidic range. Thus, immobilization is obtained principally through electrostatic interaction. As example, glucose and cholesterol enzyme electrodes have been realized with this approach (Ahmad et al., 2009; Ren et al., 2009), and different biosensors realized using ZnO have been very well-reviewed in a recent work (Arya et al., 2012).

Here, peptide-ZnO nanoparticles have been characterized and used as gas sensing array. Four different peptides were tested as gas sensing elements. The peptides were selected from molecular modeling in order to build an array able to discriminate among alcohols and esters. Principal component analysis of the eight different alcohols and esters tested clearly indicate discrimination among the two classes. Moreover, differently from peptide-AuNPs, signal of the peptides ZnONPs was not influenced by water content, opening the possibility to work with samples with high content of water. Assay of different fruit juices was reported in this respect.

## MATERIALS AND METHODS

### Virtual Docking

A previously described docking procedure, reported in details in other works (Perez et al., 2013; Pizzoni et al., 2014), was applied to calculate the binding score between peptides and volatile compounds. Briefly, virtual binding preparation and processing was carried out using OpenEye Scientific Software package under academic license. Optimization of molecular geometries was achieved using SZYBKI with default parameterization (SZYBKI, version 1.5.7)<sup>1</sup> Ten conformers per peptide and a maximum of 200 conformers for each volatile compound were generated by means of OMEGA (Hawkins et al., 2010; Hawkins and Nicholls, 2012; OMEGA, version 2.4.6)<sup>2</sup> Multi-conformer rigid body docking was carried out using OEDocking 3.0.0, also with default parameters (OEDocking, version 3.0.0)<sup>3</sup> The entire process was automated using AutoIT V3, a freeware BASIC-like scripting language. Physicochemical properties were calculated by using VIDA version 4.1.1 (VIDA, version 4.1.1)<sup>4</sup> and an online tool for calculating peptide properties (<http://www.innovagen.se/custom-peptide-synthesis/peptide-property-calculator/peptideproperty-calculator.asp>).

### ZnONPs Characterization and Functionalization

All reagents and the eight volatile compounds used were purchased from Sigma-Aldrich (Italy). The eight volatile compounds were of analytical grade. The four peptides (IHRIC, LAWHC, TGKFC, and WHVSC) used for ZnO functionalization were purchased from Espikem (Italy, purity > 85%). ZnONPs were synthesized following the procedure used in another work (Zak et al., 2011): 0.5 M zinc acetate ethanolic solution was added with 1:1 molar ratio triethanolamine and stirred for 1 h at 60°C. The solution was then kept at room temperature 1 h and at 150°C for 18 h. The formed precipitate was dispersed in ethanol cleaned three times by centrifugation and then dried in an oven at 60°C overnight.

The nanoparticles were characterized by high resolution transmission electron microscopy (HRTEM) using (TEM, S-2400 N, HITACHI, Japan). The samples for HRTEM characterization were prepared by placing a drop of the dilute sample solution on a carbon-coated copper grid and dried at room temperature before measurements. High resolution scanning electron microscopy (HRSEM) images were recorded using a Hitachi S3000N scanning electron microscope at an acceleration voltage of 20 kV and a magnification of 100000.

ZnONPs functionalization was achieved by adding an aliquot of 100  $\mu$ L of a 10<sup>-3</sup> M aqueous solution of coating peptide to 900  $\mu$ L of ethanol/H<sub>2</sub>O 9:1 v/v suspension of ZnONPs. The ZnONPs

<sup>1</sup>SZYBKI (version 1.5.7) *OpenEye Scientific Software*, Santa Fe, NM. Available online at: <http://www.eyesopen.com>

<sup>2</sup>OMEGA (version 2.4.6) *OpenEye Scientific Software*. Santa Fe, NM. Available online at: <http://www.eyesopen.com>

<sup>3</sup>OEDocking (version 3.0.0) *OpenEye Scientific Software*. Santa Fe, NM. Available online at <http://www.eyesopen.com>

<sup>4</sup>VIDA (version 4.1.1) *OpenEye Scientific Software*. Santa Fe, NM. Available online at: <http://www.eyesopen.com>

suspensions were kept overnight at room temperature and then stored at 5°C.

Fourier Transform Infrared (FTIR) spectra of ZnONPs and ZnONPs-Peptide were recorded in the range 4,000–500 cm<sup>-1</sup> using a Perkin Elmer model Spectrum 100 series. The ultraviolet-visible (UV-Vis) spectra were recorded on a Nicolet Evolution 100 in the range 200–800 nm.

## QCM Sensors Assembly and Measurement Setup

Twenty MHz QCM sensors, were from KVG GmbH (Neckarbischofsheim, Germany). The QCM sensors modification was achieved by drop casting 5 µL of the ZnONPs-peptide suspension on each side of the crystal and let to dry for few minutes. Before the first use, the QCM were then completely dried under N<sub>2</sub> at a flow rate of 2 L/h. QCMs were stored at room temperature in the dark when not in use.

The piezoelectric measurements were carried out using a TEN 2009 E-nose (Sensor group, University of Rome Tor Vergata, Italy). Carrier gas was N<sub>2</sub> used at a flow rate of 2 L/h.

Measurements of the alcohols and aldehydes were done as described in other work (Pizzoni et al., 2014). Analysis of the real samples was run using 500 µL aliquots of juice fruit in glass lab bottles (100 mL) heated at 24°C. The sample was kept for 5 min at 24°C. This range of time was selected as the optimum time required to reach a steady state by the juice fruit volatile compounds in the headspace sample volume. The N<sub>2</sub> enriched with the volatiles present in the vapor phase of the real sample was then assayed by the E-nose for 15 min.

The stop-cocks were then opened to carry the head-space of the 100 mL glass bottle to the measuring sensor array chamber and the frequency shift ( $\Delta F$ ), taken as analytical signal, was recorded. After each measurement, a complete recovery of the signal was achieved under N<sub>2</sub> flow in about 400 s. The piezoelectric sensorgram was similar for all peptides and volatile compounds, showing a rapid decrease of the signal after the stop-cocks opening, followed by a slower raise up to the steady state. The  $\Delta F$ , was recorded for all compounds after 600 s.

In order to highlight the affinity between volatile compounds and sensors, concentration effect was removed normalizing the volatile compound response of each peptide sensor with the following equation (Di Natale et al., 2003)

$$\frac{\Delta F_i}{\sum_{i=1}^n \Delta F_i}$$

where  $\Delta F$  was the frequency shift of each sensor and  $n$  the number of sensors in the array, in this case four. Assuming valid the Sauerbrey law, such normalization is supposed to remove the effect of the concentration in the case of linearity of the sensor/signal volatile concentration.

## Multivariate Analysis

Piezoelectric responses dataset was analyzed by the unsupervised multivariate technique principal component analysis (PCA) using MatLab R2011 (Mathworks, Natick, MA, USA) Row normalized data were autoscaled (zero mean and unitary

variance) before analysis. PCA was applied to inspect the multivariate data structure by decomposing a data matrix of eight rows (the volatile compounds) and four columns (the peptides). PCA achieves this by computing the eigenvectors and eigenvalues of the covariance matrix of the dataset. PCA can be also used as a tool to reduce the dimensions of the dataset while retaining the major variation of the data. PCA has been used by many researchers for monitoring the changes in volatiles as recorded by e-nose (Baietto and Wilson, 2015).

## RESULTS AND DISCUSSION

### Virtual Docking of Peptides vs. Volatile Compounds

ZnO nanoparticles, having a high isoelectric point, provide a positive electrostatic surface suitable for interacting with negatively charged groups (Kumar and Chen, 2008; Dai et al., 2009). The peptides were immobilized by physical adsorption onto the ZnO nanoparticles taking advantage of cysteine terminal carboxyl group that in ethanol/H<sub>2</sub>O (90/10 v/v, pH~7) was negatively charged. Cysteine was also used as spacer to give orientation to the peptides binding. Peptides having aspartic or glutamic acid as residual groups were not used because it was not possible to predict the immobilization layout. As reported in **Table 1** the peptides chosen in this work had positive or neutral net charge at pH 7 with in all cases a positive formal charge.

The partition coefficient, logP, was lower than one resulting in negative logarithmic value for all peptides with slight hydrophobic tendency only for LAWHC. This peptide had also the smallest PSA (polar surface area) value reinforcing the trend of the logP. The volatile compounds tested having short or long alkyl chains were from two chemical classes; alcohols and esters. Only hex-3-en-1-ol contained a double bond and, as shown by the number of conformers, had high flexibility along with hexanol and ethyl-methyl-2-butyrate. All volatile compounds, except ethanol, had good affinity for hydrophobic phase with similar PSA.

The peptides-volatile compounds interactions cannot be correlated to a single physicochemical property, but to the contribution of each residue in the specific space occupied within the peptide. Therefore, the binding properties of the four peptides vs. the eight volatile compounds were tested considering the whole peptide as possible binding site for ligands. Molecular modeling study was addressed to reliably screen out compounds that did not fit in the binding site or that had grossly wrong electrostatic properties. In fact, the ability to distinguish between two compounds that both bind to the same active site is modest using this approach.

The percentage of the docking scores calculated over 10 conformers for each peptide are reported in **Table 2**, where higher values represent higher peptide–volatile compound affinity. All peptides had an overall trend in binding better alcohols than esters. Differences between chemical class average and single compounds of the same class were found, particularly for peptides TGKFC and WHVSC responses vs. hexen-3-en-1-ol.

**TABLE 1** | Structural and physicochemical properties of the four peptides and eight volatile compounds used in this work.

	Net charge	Isoelectric point	Formal charge	MW	LogP	PSA	Rot_B	Acc	Don
Peptides	pH 7	pH							
IHRIC	1	8.87	2	643	-1.38	277	25	7	10
LAWHC	0	7.08	1	630	-0.10	228	20	7	7
TGKFC	0.9	8.54	1	556	-1.78	232	21	7	7
WHVSC	0	7.07	1	632	-1.66	250	20	7	9
Volatile compound	Chemical class	Structure	N Confs	MW	LogP	PSA	Rot_B	Acc	Don
1-butanol	Alcohols	Short chain	5	74	0.83	20	2	1	1
1-hexanol	Alcohols	Long chain	36	104	1.82	20	4	1	1
2-methyl-1-propanol	Alcohols	Short chain	2	74	0.59	20	1	1	1
Ethanol	Alcohols	Short chain	1	46	-0.16	20	0	1	1
Hex-3-en-1-ol	Alcohols	Alkene	18	100	0.75	20	3	1	1
Ethyl acetate	Esters	Short chain	3	88	0.54	26	2	1	0
Ethyl-methyl-2-butrate	Esters	Long chain	49	130	1.82	26	4	1	0
Isopentyl acetate	Esters	Long chain	9	130	1.78	26	4	1	0

*N* confs, number of conformers; MW, molecular weight; PSA, polar surface area; RB, rotatable bond; Acc, Lipinski acceptors; Don, Lipinski donors.

**TABLE 2** | Percentage of the binding score, representing the affinity of the peptides toward the volatile compounds used in experimental part.

	IHRIC (%)	LAWHC (%)	TGKFC (%)	WHVSC (%)
1-butanol	60	61	81	66
1-hexanol	64	89	85	82
2-methyl-1-propanol	61	63	79	68
Ethanol	60	54	68	61
Hexen-3-en-1-ol	67	79	100	90
Ethyl acetate	49	63	62	37
Ethyl-methyl-2-butrate	30	68	51	28
Isopentyl acetate	33	60	48	33

The binding score average of each peptide receptor was calculated over 10 peptide conformers, the coefficient of variation ranged between 5 and 15% in all cases.

In the alcohols class, there was a clear different binding response between short and long alkyl chains with the lowest interaction for ethanol given by peptide LAWHC. This peptide was the only one having an esters binding score trend better than short alkyl chain alcohols. A relative good binding ability for esters was also exhibited by peptide TGKFC.

## ZnONPs-Peptides Characterization and Functionalization

The synthesized zinc oxide nanoparticles were characterized using transmission high resolution scanning electron microscopy (HRSEM) and transmission electron microscopy (TEM) to determine the size of the zinc oxide nanoparticles. **Figure 1** reports the classical cubic shapes obtained with an average diameter lower than 100 nm. The SEM figure indicates a homogenous shape and size for ZnONPs. It also shows that the ZnONPs are well-dispersed in the powder form.

UV/Vis absorption spectra of ethanol/ water (9:1) suspensions of ZnONPs exhibited a distinct sharp absorption band at 370 nm as reported in the literature (Zak et al., 2011); modification with the peptides did not result in any significant change of the UV spectra. A clear proof of the immobilization of peptides onto ZnONPs was obtained using FTIR spectroscopy. Changes in peak intensity and shape upon binding was observed together with the appearance of new peaks as reported in **Figure 2** for the spectra of ZnONPs vs. the TGKFC peptide modified ZnONPs.

As shown in **Figure 2**, the band appearing at 481 cm<sup>-1</sup> was assigned to the zinc oxide (Jurablu et al., 2015). The FTIR stretching frequencies observed in the spectra of unmodified ZnONP were either due to the residual of the acetate ions and ethanol solvent. These should result from the stretching frequencies of the functional groups C=O occurring in the 1,670–1,820 cm<sup>-1</sup> region, C–O in the 1,050–1,150 cm<sup>-1</sup> region, and C–H observed at 1,000–1,300 cm<sup>-1</sup>, with strong intensities.

The appearance of the band at 1,663 cm<sup>-1</sup>, can be assigned to the stretch vibration of C=O with strong intensity associated with air from the atmosphere (Djelloul et al., 2010; Dutta and Ganguly, 2012; Kumar and Rani, 2013). The band at 3,616 cm<sup>-1</sup>, is due to the stretch vibration of O–H and could be associated with the ethanol from the diluted nanoparticles (Zak et al., 2011) (Dehaghi et al., 2014).

It is expected that the thiol group of the TGKFC can interact with zinc metal to form ZnONP-TGKFC complexes. The peptide should use the thiol SH group of the peptide sequence to bind to the surface of the ZnO nanoparticles. Infact, the thiol group has high binding affinity with the metal ions (Badia et al., 2000). Looking at the peptide structure, there is a presence of  $\nu(O-H)$  at 3,612 cm<sup>-1</sup>, assigned to the stretch vibration of the O–H from the L-cysteine (C) carboxylic acid derivative of the peptide sequence.

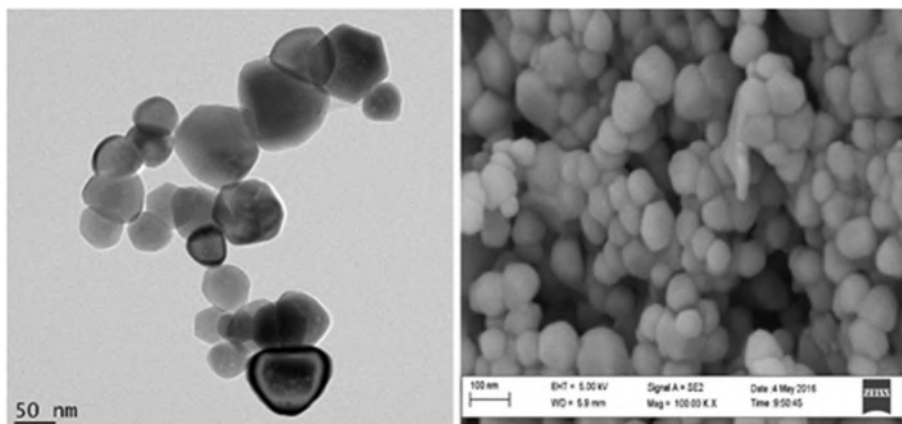


**FIGURE 1 |** HRTEM and HRSEM (100000x magnification) images of the dried ZnONP powder redissolved in ethanolic solution.

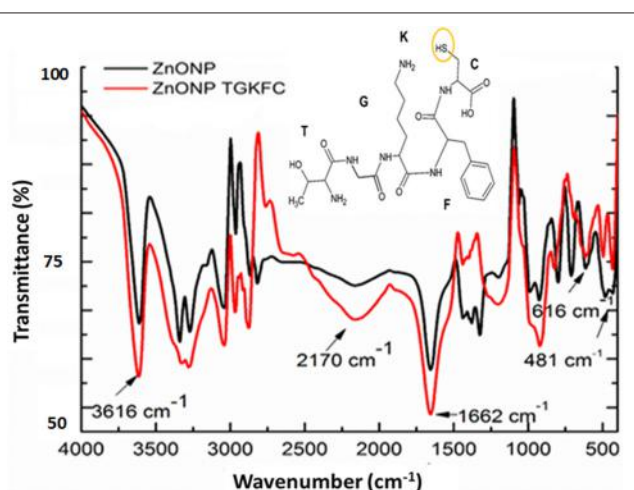


**FIGURE 2 |** Fourier transform infrared spectra of ZnONPs-TGKFC. Black line ZnONPs alone; Red line the ZnONPs bound to TGKFC. The molecular structure of the peptide was also reported highlighting the functional group involved in the stretching frequencies.

The  $\nu(\text{C=O})$  observed at  $1,662 \text{ cm}^{-1}$  with strong intensity, are stretching frequencies resulting from the peptide bond  $\text{C=O}$  functional groups between the amino acid residues overlapping with the  $\text{C=O}$  functional groups stretching frequencies of the free-carboxylic group of the L-cysteine derivatives. The weak band at  $3,200 \text{ cm}^{-1}$  was due to the peptide bond tertiary amine  $\nu(\text{N-H})$  stretching frequency. The medium band observed at  $3,350 \text{ cm}^{-1}$  was assigned to the  $\nu(\text{-NH}_2)$  primary amines of the threonine (T) and lysine (K) amino acid derivatives of the amino acid peptide sequence. Aromatic stretches;  $\nu(\text{C=C})$  of the aromatic benzene ring of the phenylalanine (F) amino acid peptide residue stretching frequencies were also observed at  $1,420 \text{ cm}^{-1}$  as multiple bands. Functionalizing the zinc oxide nanoparticles with the TGKFC peptide sequence also resulted in other unique bands formed at  $2,818 \text{ cm}^{-1}$  due to

the C-H functional group alkyl chains of the multiple amino acid residues and the stretch vibration band at  $1,339 \text{ cm}^{-1}$  assigned to the stretch vibration at C-N functional groups. In this context it can be observed that there is an influence of the peptide as the stretching mode have been shifted to higher energy state.

### Piezoelectric Array Response

The cysteine spacer, with negative carboxyl terminal group used to immobilize each peptides onto positively charged ZnO nanoparticles, was supposed to preserve the three-dimensional shape of peptides with no or very little loss of affinity properties. QCM microbalance system frequency shifts ( $\Delta f$ ) were used in order to discriminate among the eight volatile compounds and to demonstrate the matching between the predictive ability of the virtual screening with real binding data. For that reason, pure volatile compounds were tested using nitrogen as carrier gas. To evaluate the sensors affinity with respect to the affinities of other sensors in the array it was necessary to remove the information about the concentration by dividing the signal of each sensor by the sum of the signals of all sensors in the array (Pizzoni et al., 2014; Mascini et al., 2017). Then, to emphasize the contribution that each sensor brings to the total array a column normalization was carried out. The percentage of the normalized dataset response of each sensor is reported in Table 3.

The ZnO-IHRIC modified sensor had similar interactions with all the eight volatile compounds, this trend was also observed in modeling with the exception of long chain esters. The other three peptides exhibited a recognition pattern in binding the eight volatile compounds different from each other. The peptide LAWHC had strong interaction with long chain alcohols and esters but not with ethanol and surprisingly neither with hexen-3-en-1-ol, having the lowest interaction. This last behavior was not observed in modeling. With the exception of hexen-3-en-1-ol and isopentyl acetate, both peptides TGKFC and WHVSC had similar trend having better interaction with alcohols than esters, as also indicated by the modeled data. The fact

that, experimental data did not fully overlap the simulated data can be attributed to the not well-defined orientation achieved because of the physical absorption of the peptides on ZnO nanoparticles.

To better highlight the contribution of each sensor to the discrimination of the eight volatile compounds, the normalized data were analyzed making use of unsupervised PCA. The biplot of the first two principal components is shown in **Figure 3**. The first component represented 69.11% of the variance; the second 27.34% displaying together a cumulative variance of 96.45%. The

**TABLE 3** | Percentage of the normalized frequency shift of the four peptide-modified sensors vs. the eight volatile compounds.

	<b>IHRIC</b> (%)	<b>LAWHC</b> (%)	<b>TGKFC</b> (%)	<b>WHVSC</b> (%)
1-butanol	11.8 ± 1.1	15.2 ± 1.3	11.3 ± 2.6	10.1 ± 2.2
1-hexanol	11.5 ± 2.8	13.7 ± 2.1	13.8 ± 3.6	13.0 ± 2.5
2-methyl-1-propanol	10.5 ± 0.9	17.2 ± 1.7	11.2 ± 2.5	10.3 ± 2.2
Ethanol	12.6 ± 2.4	8.3 ± 1.2	19.4 ± 3.6	17.5 ± 1.0
Hexen-3-en-1-ol	14.5 ± 0.4	5.4 ± 1.0	13.4 ± 3.1	18.9 ± 3.2
Ethyl acetate	12.0 ± 0.2	16.1 ± 0.9	11.4 ± 1.4	8.1 ± 0.6
Ethyl-methyl-2-butrate	13.4 ± 0.9	13.1 ± 2.3	10.6 ± 2.6	9.6 ± 2.0
Isopentyl acetate	13.7 ± 0.3	11.1 ± 1.6	8.9 ± 1.9	12.5 ± 1.9

The standard deviation was calculated using three measurements taken in 3 different days.

behavior of volatile compounds can be appreciated looking at the scores points assuming that close distance in biplot plane is a measure of the similitude between samples. The changes of structural composition are well-captured by the PCA; in particular PC1 contributed to a clear separation between ethanol and hexen-3-en-1-ol from the others molecules. Alcohols, with the exception of hexen-3-en-1-ol, were clustered by the PC2 that scattered the esters on the fourth quadrant of PC1-PC2 plane.

The contribution of the peptides to the volatile compounds analysis can be evaluated considering the position of the loadings (the contribution of each variable to the principal components) with respect to the scores. Peptide LAWHC had a pattern recognition performance opposite to the other three peptides, contributing significantly to the separation of the esters and alcohols from ethanol and hexen-3-en-1-ol. This behavior fitted well with the simulation considering the hexen-3-en-1-ol affinity for peptides TGKFC and WHVSC. These two peptides together with IHRIC contributed to the separation of alcohols from esters on the PC2, confirming in part the trend obtained by virtual binding scores.

### Analysis in Water and Fruit Juices

Previous gas sensor arrays based on peptide modified AuNPs were used on samples with low content of water (i.e., candies, chocolate, olive oil). In fact, as already reported in the first realized peptide gas sensor arrays (Compagnone et al., 2013) pure water produced a drift of the signal. In following works,

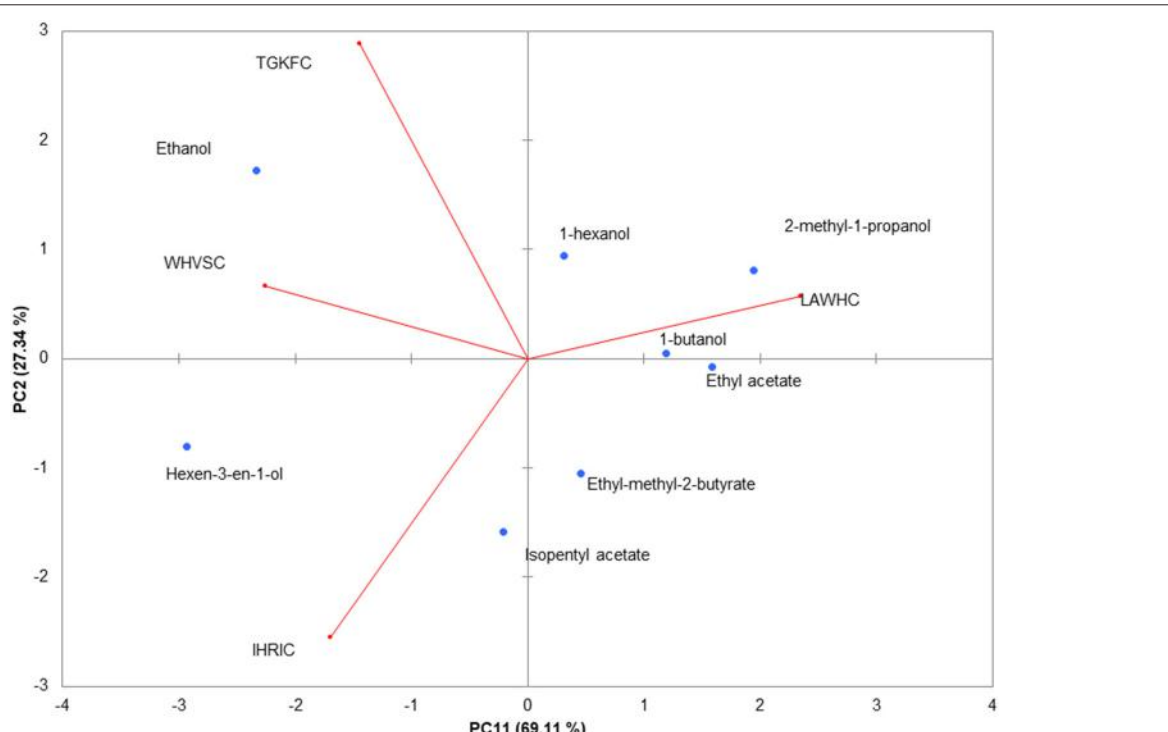


**FIGURE 3** | PCA of the piezoelectric response. The biplot (Score and loading) of the first two principal components showed 94.45% of the cumulative variance. Rows normalization were applied to the gas sensors array dataset. Data were autoscaled before PCA.

substituting citrate to borate in the production of AuNPs, drift from water was eliminated (Pizzoni et al., 2014, 2015; Compagnone et al., 2015; Mascini et al., 2017); however, high contents of water in mixture with other solvents, produced very high signals reducing the discriminating ability of the array and limited the use of the peptide based gas sensors. Peptide based ZnONPs did not interact to the same extent as AuNPs with water. Signals obtained with pure water for the four gas sensors are reported in **Figure 4**. It has to be noticed the low signal for all sensors. Stability of the signal was also evident as well as reproducibility, being the interday relative standard deviation (RSD) for all sensors tested below 10%. The small differences among the peptides can be attributed to a different degree of ZnO nanoparticles coverage that is difficult to assess accurately. The large difference between AuNPs

and ZnONPs (response in the same conditions is hundreds of Hz for AuNPs) can be attributed either to the presence of higher charge density of  $\text{Au}^{+3}$  vs.  $\text{Zn}^{+2}$  onto the nanoparticles or to the rejection effect of oxygen in the highly polar ZnONPs.

In order to demonstrate the ability of the array to carry out analysis on samples with high water content, nine different fruit juices bought at local markets were tested. E-noses based on metal-oxide gas sensors have been already successfully used for analysis of fruits (peaches) and fruit juices (apple) (Zhang et al., 2012; Wu et al., 2017). We selected this kind of samples because alcohols and esters are among the major components of the volatile fraction of juices. The aim was to demonstrate that the peptide based ZnONPs QCMs sensors can be used to classify this kind of food samples. The fruit juices were randomly tested in a period of time of 2 weeks. Interday RSDs were always below 20% for each of the samples. The PCA analysis, reported in **Figure 5A**, gave 91% of the total variance explained by the first two PCA. Loadings were well-distributed among the quadrants demonstrating that each of the peptide gas sensor contributed to the discrimination of the samples. Looking at the plot of the fruit juice scores, **Figure 5B**, differences about sugar content and the amount of fruit can be noticed. Apricot (A1 Skipper) has the highest content of fruit (%) and sugars (g) reported and is clearly separated by the other two Apricot samples (A2 Conad Bio and A3 Conad) having the same amounts of fruit and sugars. Pear fruit juices Pr2 and Pr3 (Derby Blue and Conad, respectively) have the same content of fruit and sugar and appear in the same quadrant while Pr1 (Valfrutta) contains lower sugar and is separated by the others in the PCA. Peach Fruit juices (Ph1 Yoga), (Ph2 Budget), (Ph3 Carrefour Bio) does not appear to be clearly

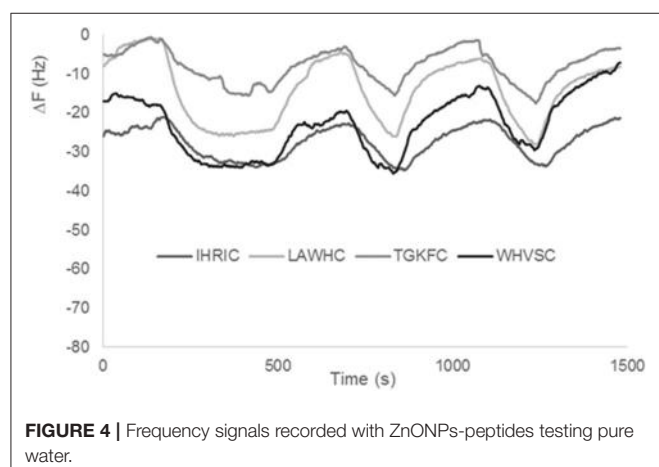


**FIGURE 4** | Frequency signals recorded with ZnONPs-peptides testing pure water.

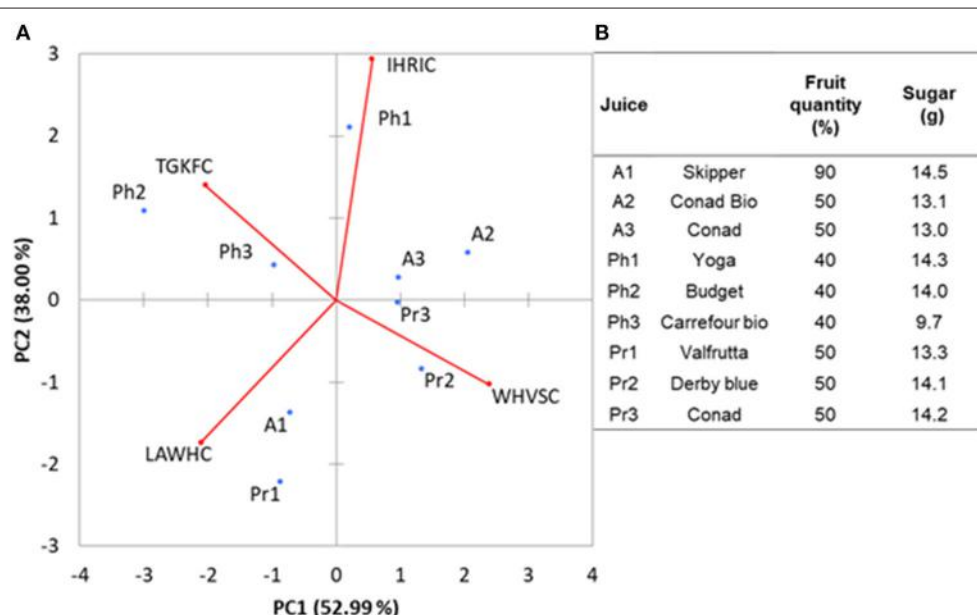


**FIGURE 5 | (A)** The biplot values (scores and loadings) for fruit juices analysis along with the percentage **(B)** of fruit quantity and sugar concentration in the different fruit juices.

discriminated by the different amount of sugars in the samples. This results demonstrated that the sensors can be used to study volatiles organic compounds of fruit juices since it is well-known that fruit content and amount of sugar influence the hedsoace pattern of these samples. Further studies including more peptide-based sensors and with homogenous type of samples will be necessary to ascertain the performance vs. other type of e-noses.

## CONCLUSIONS

The work has demonstrated the feasibility of the construction of a peptide gas sensor array based on ZnONPs. Four different peptides, selected computationally for binding alcohols and esters have been immobilized onto ZnONPs, deposited onto QCMs and tested with the pure compounds. Experimental data fitted well with modeling. The gas sensor array was then challenged with water and with fruit juices. Data demonstrated that the peptide

based ZnONPs gas sensors can be used profitably for high water content samples.

## AUTHOR CONTRIBUTIONS

MM run the molecular modeling and worked out comparison with real measurement. SG and FD prepared the sensors and run the measurements with the sensor array. CD run and interpreted multivariate data. SQ and EI run and commented characterization of the nanomaterials. PP selected the volatiles and food samples. DC supervised the work and wrote the paper collecting the different contributions.

## FUNDING

Italian Ministry of Foreign Affairs Project Materiali nanostrutturati per sistemi (bio)chimici sensibili ai pesticidi is gratefully acknowledged for funding.

## REFERENCES

- Ahmad, M., Pan, C., Gan, L., Nawaz, Z., and Zhu, J. (2009). Highly sensitive amperometric cholesterol biosensor based on Pt-incorporated fullerene-like ZnO nanospheres. *J. Phys. Chem. C* 114, 243–250. doi: 10.1021/jp9089497
- Ampuero, S., and Bosset, J. (2003). The electronic nose applied to dairy products: a review. *Sens. Actuators B Chem.* 94, 1–12. doi: 10.1016/S0925-4005(03)00321-6
- Arya, S. K., Saha, S., Ramirez-Vick, J. E., Gupta, V., Bhansali, S., and Singh, S. P. (2012). Recent advances in ZnO nanostructures and thin films for biosensor applications: review. *Anal. Chim. Acta* 737, 1–21. doi: 10.1016/j.aca.2012.05.048
- Badia, A., Lennox, R. B., and Reven, L. (2000). A dynamic view of self-assembled monolayers. *Acc. Chem. Res.* 33, 475–481. doi: 10.1021/ar9702841
- Baggiani, C., Biagioli, F., Anfossi, L., Giovannoli, C., Passini, C., and Giraudi, G. (2013). Effect of the mimic structure on the molecular recognition properties of molecularly imprinted polymers for ochratoxin A prepared by a fragmental approach. *React. Funct. Polym.* 73, 833–837. doi: 10.1016/j.reactfunctpolym.2013.03.018
- Baietto, M., and Wilson, A. D. (2015). Electronic-nose applications for fruit identification, ripeness and quality grading. *Sensors* 15, 899–931. doi: 10.3390/s150100899
- Compagnone, D., Faieta, M., Pizzoni, D., Di Natale, C., Paolesse, R., Van Caelenberg, T., et al. (2015). Quartz crystal microbalance gas sensor arrays for the quality control of chocolate. *Sens. Actuators B Chem.* 207, 1114–1120. doi: 10.1016/j.snb.2014.10.049
- Compagnone, D., Fusella, G. C., Del Carlo, M., Pittia, P., Martinelli, E., Tortora, L., et al. (2013). Gold nanoparticles-peptide based gas sensor arrays for the detection of food aromas. *Biosens. Bioelectron.* 42, 618–625. doi: 10.1016/j.bios.2012.10.096
- Dai, Z., Shao, G., Hong, J., Bao, J., and Shen, J. (2009). Immobilization and direct electrochemistry of glucose oxidase on a tetragonal pyramid-shaped porous ZnO nanostructure for a glucose biosensor. *Biosens. Bioelectron.* 24, 1286–1291. doi: 10.1016/j.bios.2008.07.047
- Dehagi, S. M., Rahmanifar, B., Moradi, A. M., and Azar, P. A. (2014). Removal of permethrin pesticide from water by chitosan-zinc oxide nanoparticles composite as an adsorbent. *J. Saudi Chem. Soc.* 18, 348–355. doi: 10.1016/j.jscs.2014.01.004
- Del Carlo, M., Fusella, G., Pepe, A., Sergi, M., Di Martino, M., Mascini, M., et al. (2014). Novel oligopeptides based e-nose for food quality control: application to extra-virgin olive samples. *Qual. Assur. Saf. Crops Foods* 6, 309–317. doi: 10.3920/QAS2013.0377
- Della Pelle, F., Compagnone, D. (2018). Nanomaterial-based sensing and biosensing of phenolic compounds and related antioxidant capacity in food. *Sensors* 18:462. doi: 10.3390/s18020462
- Di Natale, C., Macagnano, A., Martinelli, E., Paolesse, R., D'Arcangelo, G., Roscioni, C., et al. (2003). Lung cancer identification by the analysis of breath by means of an array of non-selective gas sensors. *Biosens. Bioelectron.* 18, 1209–1218. doi: 10.1016/S0956-5663(03)00086-1
- Djelloul, A., Aida, M., and Bougdira, J. (2010). Photoluminescence, FTIR and X-ray diffraction studies on undoped and Al-doped ZnO thin films grown on polycrystalline  $\alpha$ -alumina substrates by ultrasonic spray pyrolysis. *J. Lumin.* 130, 2113–2117. doi: 10.1016/j.jlumin.2010.06.002
- Duran, N., and Marcato, P. D. (2013). Nanobiotechnology perspectives. Role of nanotechnology in the food industry: a review. *Int. J. Food Sci. Technol.* 48, 1127–1134. doi: 10.1111/ijfs.12027
- Dutta, S., and Ganguly, B. N. (2012). Characterization of ZnO nanoparticles grown in presence of Folic acid template. *J. Nanobiotechnol.* 10:29. doi: 10.1186/1477-3155-10-29
- Hawkins, P. C., and Nicholls, A. (2012). Conformer generation with OMEGA: learning from the data set and the analysis of failures. *J. Chem. Inf. Model.* 52, 2919–2936. doi: 10.1021/ci300314k
- Hawkins, P. C., Skillman, A. G., Warren, G. L., Ellingson, B. A., and Stahl, M. T. (2010). Conformer generation with OMEGA: algorithm and validation using high quality structures from the Protein Databank and Cambridge Structural Database. *J. Chem. Inf. Model.* 50, 572–584. doi: 10.1021/ci100031x
- Heurich, M., Altintas, Z., and Tothill, I. E. (2013). Computational design of peptide ligands for ochratoxin A. *Toxins* 5, 1202–1218. doi: 10.3390/toxins5061202
- Jurablu, S., Farahmandjou, M., and Firoozabadi, T. (2015). Sol-gel synthesis of zinc oxide (zno) nanoparticles: study of structural and optical properties. *J. Sci. Islam. Repub. Iran* 26, 281–285. Available online at: [https://jsciences.ut.ac.ir/article\\_55316\\_a7b1e2596b6c6dc2c9ac0fcab06d9204.pdf](https://jsciences.ut.ac.ir/article_55316_a7b1e2596b6c6dc2c9ac0fcab06d9204.pdf)
- Kumar, H., and Rani, R. (2013). Structural and optical characterization of ZnO nanoparticles synthesized by microemulsion route. *Int. Lett. Chem. Phys. Astron.* 14, 26–36. doi: 10.18052/www.scipress.com/ILCPA.19.26
- Kumar, S. A., and Chen, S. M. (2008). Nanostructured zinc oxide particles in chemically modified electrodes for biosensor applications. *Anal. Lett.* 41, 141–158. doi: 10.1080/00032710701792612
- Loutfi, A., Coradeschi, S., Mani, G. K., Shankar, P., and Rayappan, J. B. B. (2015). Electronic noses for food quality: a review. *J. Food Eng.* 144, 103–111. doi: 10.1016/j.jfoodeng.2014.07.019
- Martínez-Arellano, I., Flores, M., and Toldrá, F. (2016). The ability of peptide extracts obtained at different dry cured ham ripening stages to bind aroma compounds. *Food Chem.* 196, 9–16. doi: 10.1016/j.foodchem.2015.09.023
- Mascini, M., Del Carlo, M., Compagnone, D., Cozzani, I., Tiscar, P., Mpamhang'a, C., et al. (2006). Piezoelectric sensors based on biomimetic peptides for the detection of heat shock proteins (HSPs) in mussels. *Anal. Lett.* 39, 1627–1642. doi: 10.1080/00032710600713529

- Mascini, M., Macagnano, A., Scorticini, G., Del Carlo, M., Diletti, G., d'Amico, A., et al. (2005). Biomimetic sensors for dioxins detection in food samples. *Sens. Actuators B Chem.* 111, 376–384.
- Mascini, M., Montesano, C., Sergi, M., Perez, G., De Cicco, M., Curini, R., et al. (2013). Peptides trapping cocaine: docking simulation and experimental screening by solid phase extraction followed by liquid chromatography mass spectrometry in plasma samples. *Anal. Chim. Acta* 772, 40–46. doi: 10.1016/j.aca.2013.02.027
- Mascini, M., Pizzoni, D., Perez, G., Chiarappa, E., Di Natale, C., Pittia, P., et al. (2017). Tailoring gas sensor arrays via the design of short peptides sequences as binding elements. *Biosens. Bioelectron.* 93, 161–169. doi: 10.1016/j.bios.2016.09.028
- Perez, G., Mascini, M., Sergi, M., Del Carlo, M., Roberta, C., Montero-Cabrera, L., et al. (2013). Peptides binding cocaine: a strategy to design biomimetic receptors. *J. Proteomics Bioinformatics* 6, 15–22. doi: 10.4172/jpb.1000255
- Pizzoni, D., Compagnone, D., Di Natale, C., D'Alessandro, N., and Pittia, P. (2015). Evaluation of aroma release of gummy candies added with strawberry flavours by gas-chromatography/mass-spectrometry and gas sensors arrays. *J. Food Eng.* 167, 77–86. doi: 10.1016/j.jfoodeng.2015.03.003
- Pizzoni, D., Mascini, M., Lanzone, V., Del Carlo, M., Di Natale, C., and Compagnone, D. (2014). Selection of peptide ligands for piezoelectric peptide based gas sensors arrays using a virtual screening approach. *Biosens. Bioelectron.* 52, 247–254. doi: 10.1016/j.bios.2013.08.044
- Ren, X., Chen, D., Meng, X., Tang, F., Hou, X., Han, D., et al. (2009). Zinc oxide nanoparticles/glucose oxidase photoelectrochemical system for the fabrication of biosensor. *J. Colloid Interface Sci.* 334, 183–187. doi: 10.1016/j.jcis.2009.02.043
- Saha, K., Agasti, S. S., Kim, C., Li, X., and Rotello, V. M. (2012). Gold nanoparticles in chemical and biological sensing. *Chem. Rev.* 112, 2739–2779. doi: 10.1021/cr2001178
- Sankaran, S., Panigrahi, S., and Mallik, S. (2011a). Odorant binding protein based biomimetic sensors for detection of alcohols associated with *Salmonella* contamination in packaged beef. *Biosens. Bioelectron.* 26, 3103–3109. doi: 10.1016/j.bios.2010.07.122
- Sankaran, S., Panigrahi, S., and Mallik, S. (2011b). Olfactory receptor based piezoelectric biosensors for detection of alcohols related to food safety applications. *Sens. Actuators B Chem.* 155, 8–18. doi: 10.1016/j.snb.2010.08.003
- Tokura, Y., Nakada, G., Moriyama, Y., Oaki, Y., Imai, H., and Shiratori, S. (2017). Ultrasensitive detection of methylmercaptan gas using layered manganese oxide nanosheets with a quartz crystal microbalance sensor. *Anal. Chem.* 89, 12123–12130. doi: 10.1021/acs.analchem.7b02738
- Vallee, A., Humblot, V., and Pradier, C. M. (2010). Peptide interactions with metal and oxide surfaces. *Acc. Chem. Res.* 43, 1297–1306. doi: 10.1021/ar100017n
- Vanderroost, M., Ragaert, P., Devlieghere, F., and De Meulenaer, B. (2014). Intelligent food packaging: the next generation. *Trends Food Sci. Technol.* 39, 47–62. doi: 10.1016/j.tifs.2014.06.009
- Wu, H., Wang, J., Yue, T., and Yuan, Y. (2017). Variety-based discrimination of apple juices by an electronic nose and gas chromatography–mass spectrometry. *Int. J. Food Science. Technol.* 52, 2324–2333. doi: 10.1111/ijfs.13514
- Yue, G., Su, S., Li, N., Shuai, M., Lai, X., Astruc, D., et al. (2016). Gold nanoparticles as sensors in the colorimetric and fluorescence detection of chemical warfare agents. *Coord. Chem. Rev.* 311, 75–84. doi: 10.1016/j.ccr.2015.11.009
- Zak, A. K., Razali, R., Majid, W. H., and Darroudi, M. (2011). Synthesis and characterization of a narrow size distribution of zinc oxide nanoparticles. *Int. J. Nanomedicine* 6, 1399–1403. doi: 10.2147/IJN.S19693
- Zhang, H., Wang, J., Ye, S., and Chang, M. (2012). Application of electronic nose and statistical analysis to predict quality indices of peach. *Food Bioprocess Technol.* 5, 65–72. doi: 10.1007/s11947-009-0295-7

**Conflict of Interest Statement:** The authors declare that the research was conducted in the absence of any commercial or financial relationships that could be construed as a potential conflict of interest.

The handling Editor declared a past co-authorship with one of the author CD.

Copyright © 2018 Mascini, Gaggiotti, Della Pelle, Di Natale, Qakala, Iwuoha, Pittia and Compagnone. This is an open-access article distributed under the terms of the Creative Commons Attribution License (CC BY). The use, distribution or reproduction in other forums is permitted, provided the original author(s) and the copyright owner are credited and that the original publication in this journal is cited, in accordance with accepted academic practice. No use, distribution or reproduction is permitted which does not comply with these terms.



# A Practical Method to Estimate the Resolving Power of a Chemical Sensor Array: Application to Feature Selection

Luis Fernandez<sup>1,2†</sup>, Jia Yan<sup>2,3†</sup>, Jordi Fonollosa<sup>2,4,5\*</sup>, Javier Burgués<sup>2</sup>, Agustin Gutierrez<sup>1,2</sup> and Santiago Marco<sup>1,2</sup>

<sup>1</sup> Department of Electronics and Biomedical Engineering, Universitat de Barcelona, Barcelona, Spain, <sup>2</sup> Signal and information processing for sensing systems, Institute for Bioengineering of Catalonia, Barcelona, Spain, <sup>3</sup> College of Electronic and Information Engineering, Southwest University, Chongqing, China, <sup>4</sup> Departament d'Enginyeria de Sistemes, Automàtica i Informàtica Industrial (ESAI), Universitat Politècnica de Catalunya, Barcelona, Spain, <sup>5</sup> Institut de Recerca Pediàtrica Hospital Sant Joan de Déu, Barcelona, Spain

## OPEN ACCESS

### Edited by:

Dmitry Kirsanov,  
Saint Petersburg State University,  
Russia

### Reviewed by:

Alisa Rudnitskaya,  
University of Aveiro, Portugal  
Vitaly Panchuk,  
Saint Petersburg State University,  
Russia

### \*Correspondence:

Jordi Fonollosa  
jordi.fonollosa.m@upc.edu

<sup>†</sup>These authors have contributed  
equally to this work.

### Specialty section:

This article was submitted to  
Analytical Chemistry,  
a section of the journal  
Frontiers in Chemistry

Received: 30 March 2018

Accepted: 23 May 2018

Published: 12 June 2018

### Citation:

Fernandez L, Yan J, Fonollosa J, Burgués J, Gutierrez A and Marco S (2018) A Practical Method to Estimate the Resolving Power of a Chemical Sensor Array: Application to Feature Selection. *Front. Chem.* 6:209.  
doi: 10.3389/fchem.2018.00209

A methodology to calculate analytical figures of merit is not well established for detection systems that are based on sensor arrays with low sensor selectivity. In this work, we present a practical approach to estimate the Resolving Power of a sensory system, considering non-linear sensors and heteroscedastic sensor noise. We use the definition introduced by Shannon in the field of communication theory to quantify the number of symbols in a noisy environment, and its version adapted by Gardner and Barlett for chemical sensor systems. Our method combines dimensionality reduction and the use of algorithms to compute the convex hull of the empirical data to estimate the data volume in the sensor response space. We validate our methodology with synthetic data and with actual data captured with temperature-modulated MOX gas sensors. Unlike other methodologies, our method does not require the intrinsic dimensionality of the sensor response to be smaller than the dimensionality of the input space. Moreover, our method circumvents the problem to obtain the sensitivity matrix, which usually is not known. Hence, our method is able to successfully compute the Resolving Power of actual chemical sensor arrays. We provide a relevant figure of merit, and a methodology to calculate it, that was missing in the literature to benchmark broad-response gas sensor arrays.

**Keywords:** gas sensor array, MOX sensors, Resolving Power, sensor resolution, dimensionality reduction, machine olfaction

## INTRODUCTION

Analytical figures of merit are well understood for mature chemical instrumentation (Olivieri, 2014). For univariate zero order chemical sensors, figures of merit can be estimated as well using conventional recommendations from IUPAC (Justino et al., 2010). However, the computation of figures of merit is not clear in many scenarios in which researchers and practitioners prefer to address the problems using arrays of solid-state chemical sensors, particularly in gas phase. Solid state sensors usually do not have peak shape responses as it may happen in chromatography, spectrometries, and spectroscopies. These sensors are typically characterized by very poor selectivity, non-linearities, and sensor instabilities (Hierlemann and Gutierrez-Osuna, 2008).

Similarly, conventional analytical instrumentation show degraded performance when miniaturized using microsystems technologies. Examples are the integration of Non-Dispersive Infrared Sensors with overlapping sensitivities across the spectral domain (Calaza et al., 2003; Rubio et al., 2006, 2007; Fonollosa et al., 2009) the integration of mass spectrometers in MEMS technologies (Syms and Wright, 2016) or the integration of miniature Gas Chromatographers (Zampolli et al., 2009). Figures of merit also need reconsideration for direct-sampling fast-analysis techniques, such as Ion Mobility Spectrometry (Borsdorff and Eiceman, 2006) or Direct Analysis Real Time-Mass Spectrometry (Gross, 2014). In many of these instrumental configurations, the interest is not targeted selective detection of certain analytes, but global fingerprint analysis using chemometrics (Pavlovich et al., 2016; Szymanska et al., 2016).

The definition of figures of merit for chemical sensor arrays was first considered in the pioneering work of Davide et al. (1993) and later by Snopok (Snopok and Kruglenko, 2002). In most occasions, figures of merit for chemical sensor arrays have been proposed in the context of sensor array design (Johnson and Rose-Pehrsson, 2015). The direct translation of tensorial figures of merit to sensor systems has been used by Marth (Marth et al., 1999). However, most classical definitions assume linearity of response and this limits their applicability in non-linear sensors. Recently, Burgués et al. studied the application of the Limit of Detection (LOD) definitions by IUPAC to metal oxide sensors (MOX), since most of the underlying statistical hypothesis of the theoretical development may not hold for chemical sensors (Burgués and Marco, 2017; Burgués et al., 2018). Also concerning LOD, Fonollosa et al. propose an information theory approach to weigh the uncertainty of the sensor response with the prior knowledge about the probability of analyte presence in the sample (Fonollosa et al., 2014). Similarly, Johnson and Knapp have proposed alternative definitions of selectivity based on the Cramer-Rao lower bounds (Johnson and Knapp, 2017).

Resolving Power (RP) and *Resolution* (R) are two key figures of merit in chemical instrumentation. However, there is some confusion between these two terms, and sometimes they are mixed up (Cohen et al., 2008). IUPAC has done, over the years, a tremendous effort to clarify terminology in chemical sciences.

In analytical chemistry theory, Resolving Power measures are usually defined for peak-shaped signals. Nevertheless, in sensor arrays, and due to the poor sensor selectivity, analyte discrimination is often based on the use of pattern recognition algorithms, as already acknowledged in the classic definition of electronic nose introduced by Gardner (Gardner and Bartlett, 1994). For the interested reader, the use of pattern recognition algorithms for chemical sensor arrays has been reviewed by Gutierrez-Osuna (2002) and Marco (Marco and Gutierrez-Galvez, 2012).

Today, the combination of analytical instrumentation and sensor systems for the identification of complex chemical objects using pattern recognition and machine learning techniques is widespread. One can find hundreds of examples in the literature, but just for illustration purposes, we will mention only a few. Kuske et al. used chemical sensor arrays to discriminate mold species growing on building materials (Kuske et al.,

2006). Garrido-Delgado et al. used Ion Mobility Spectrometry to classify wines according to their Certified Brand of Origin (CBO) (Garrido-Delgado et al., 2011). Cauchi et al. used Gas Chromatography Data in combination with Partial Least Squares-Discriminant Analysis (PLS-DA) for the diagnosis of diverse gastrointestinal diseases using various body samples (Cauchi et al., 2014). Vaclavik et al. have used Direct Analysis in Real Time Mass Spectrometry (DART-MS) in combination with Fisher Discriminant Analysis for authenticity assessment in olive oil samples (Vaclavik et al., 2009).

Over the years, heuristic measures of the Resolving Power of chemical sensor arrays have been proposed. In most cases, they are versions of the Fisher score that compute a ratio between the mean distance between classes and the mean dispersion of the classes (Doleman et al., 1998; Muezzinoglu et al., 2010; Xu et al., 2010; Vergara and Llobet, 2012; Magna et al., 2018).

From a formal point of view, the discrimination of classes in a multidimensional space is similar to the detection of symbols in digital communication theory. Claude Shannon, in his mathematical theory of communication in the presence of noise (Shannon, 1984), posed the problem of the number of signals (or symbols) that can be distinguished by the receiver despite the presence of noise. He proposed a ratio between the power of the signal plus noise and the power of the noise in a multidimensional setting.

Along the same lines, Gardner and Bartlett (1996) introduced the “range” as a ratio between the signal span in the input feature space and the noise hyper-volume. This concept was further developed by Pearce et al. (Pearce, 2000; Pearce and Sánchez-Montañés, 2004) and they proposed the means to calculate the hyper-volume of the signal span based on the sensor sensitivity matrix for linear sensors and the integration of the Jacobian matrix for non-linear sensors.

However, years later, no practical applications of the method can be found in the literature. We believe that this particular situation is caused by three reasons: First, their method experiences a notable increment of complexity when it is applied to arrays of non-linear sensors and/or to arrays subjected to heteroscedastic sensor noise. Second, the application of the technique is limited to discrimination tasks where the amount of sensor features does not exceed the number of pure gases. This restriction constitutes a severe shortcoming since current sensor arrays tend to provide large amounts of data per sample (LaFratta and Walt, 2008; Beccherelli et al., 2010; Marco et al., 2014). Third, it is not easy to obtain the sensitivity matrix between chemical stimuli and the sensor responses, especially for non-linear sensors. The sensitivity matrix is then used to compute the hyper-volume of the sensor space.

In this work, we present a practical approach to the estimation of the Resolving Power as defined first by Shannon and for chemical sensor arrays by Gardner and Barlett. Our method combines dimensionality reduction and proposes the use of algorithms to compute the convex hull of the empirical data to estimate the signal volume in the input feature space. We explore this concept first with synthetic data and then with empirical data from temperature modulated MOX sensors. We explore how this concept can be practically applied to

mild non-linear sensors by the partition of the input feature space.

## RESOLVING POWER AND RESOLUTION IN CHEMICAL SENSOR ARRAYS

IUPAC definitions of Resolving Power and resolution are linked to certain analytical techniques. For instance, in mass spectrometry and for a single peak made up of singly charged ions at mass  $m$  in a mass spectrum, the resolution may be expressed as

$$\frac{\Delta m}{m} \quad (1)$$

where  $\Delta m$  is usually the full width half maximum (FWHM) and  $m$  is the mass center of the peak (Todd, 1991). On the other hand, the IUPAC definition of Resolving Power is: "For two peaks of equal height with masses  $m_1$  and  $m_2$  when there is overlap between the two peaks to a stated percentage of either peak (10% is recommended), then the Resolving Power is defined as  $m_1/(m_1-m_2)$ " (Nič, 1997). Note that a smaller resolution means an enhanced figure of merit, while the contrary holds for the Resolving Power.

Instead, for chromatography, IUPAC uses the term *peak resolution* with a meaning closer to the concept of Resolving Power. In particular, peak resolution is defined in chromatography as a characteristic separation of two adjacent peaks.

$$R_{AB} = 2 \frac{|t_A - t_B|}{|w_A + w_B|} \quad (2)$$

where  $R_{AB}$  is peak resolution and  $t_A$  and  $t_B$  are the retention times for compounds A and B and  $w_A$  and  $w_B$  are the widths of the peaks at the base (Nič, 1997).

In optical spectroscopies, according to the IUPAC, the Resolving Power is the transition wavenumber (or wavelength or frequency) divided by the resolution. The transition wavenumber is the difference between two energy states and the resolution is defined as the minimum wavenumber, wavelength or frequency difference between two lines in a spectrum that can be distinguished (Nič, 1997). We can notice that in mass spectrometry resolution is a dimensionless quantity, but the definition of resolution for optical spectroscopies has physical units (wavelength, wavenumber, or frequency).

For ion mobility spectrometry, Rokushika et al. (1985) define resolution as:

$$R = \frac{t}{2W} \quad (3)$$

where  $t$  is the drift time of the ion pulse and  $W$  is the width of the ion pulse at FWHM.

On the other hand, we have to consider as well, that the term *resolution* is also used in Metrology and Measurement Science as the "smallest quantity being measured that causes a perceptible change in the corresponding indication." See, for instance, the definition issued by the Bureau International des Poids et

Measures (BIPM) in the document "International vocabulary of metrology: basic and general concepts and associated terms" (Joint committee for Guides in Metrology, 2012). This definition is commonly accepted in sensor science, where the perceptible change is related to the noise level in the sensor output. For instance, for univariate sensors, resolution is defined by D'Amico (D'Amico and Di Natale, 2001) as:

$$Res(x) = \lim_{V_{out} \rightarrow V_n} \frac{V_{out}(x)}{S(x)} \quad (4)$$

where  $Res(x)$  is the resolution,  $V_{out}(x)$  is the corresponding sensor output and  $S(x)$  the sensitivity at the working point  $x$ , being  $x$  the sensor input.  $V_n$  is the noise level and it is taken as  $k\sigma$ , where  $\sigma$  is the standard deviation of the noise and  $k$  is a multiplicative factor. In sensor science there is no consensus on the value of  $k$ , though common values are  $k = 1$ ,  $k = 3$ , or even  $k = 10$ . With these considerations in mind, when reporting resolution, it is important to state the working point for non-linear sensors and the used value of  $k$ . At this point it is easy to link the evaluation of resolution at the blank level with the definitions of the limit of detection (LOD) and limit of quantification (LOQ) in analytical chemistry (Olivieri, 2014; Desimoni and Brunetti, 2015; Burgués et al., 2018).

In this context, a related concept is the signal-to-noise ratio. Faber et al. have proposed a definition for signal-to-noise ratio in a tensorial framework (Faber et al., 1997). For first-order calibration they define the signal to noise ratio as:

$$\frac{S}{N} = \frac{r_i^{NAS}}{\sigma(r_i^{NAS})} \quad (5)$$

where the system response for analyte  $i$  is taken as the Net Analyte Signal (NAS) (Bro and Andersen, 2003; Ferré and Faber, 2003), and the noise is evaluated as the standard deviation of the measurement noise in the NAS projection. Usually, the NAS is taken to be a unidimensional vector.

In occasions, instead of the signal-to-noise ratio, the sensor community prefers to use the dynamic range ( $DR$ ), defined as the maximum concentration with respect to the LOD:

$$DR = \frac{\max(C)}{LOD} = \frac{Range}{LOD} \quad (6)$$

where  $Range$  is the maximum concentration  $C$  at which the detector is still sensitive. In other occasions, researchers prefer the term linear dynamic range, and then the maximum concentration refers to the maximum concentration of the analyte that keeps the calibration curve linear.

In this context, a different approach to the estimation of the joint discrimination power and resolution is needed. This definition should be established in the input space taking into account the span of the feature vectors and the noise intensity for each cluster.

From a formal point of view, the discrimination of classes in a multidimensional space is similar to the detection of symbols in digital communication theory. Claude Shannon, in his mathematical theory of communication in the presence of noise

(Shannon, 1984), posed the problem of the number of signals (or symbols) that can be distinguished by the receiver despite the presence of noise. He proposed that this number could be estimated as follows. If the signal has a power  $S$  and the noise has a power  $N$ , the number of signals that can be well-distinguished is:

$$K \sqrt{\frac{S+N}{N}} \quad (7)$$

where the noise is assumed to be additive.  $K$  is a constant close to 1 that depends on the allowed error to separate the different signals.

### Gardner and Barlett Proposal

Gardner and Bartlett (1996) introduced a concept that they named *range* defined as the maximum number of input conditions that can be discriminated in sensor space in the presence of noise:

$$N_n = \frac{\prod_{i=1}^n FSD(S_i)}{V_n} \quad (8)$$

From our point of view, this definition can be better described by the term “Resolving Power,” and this is how from now on, we will refer to this definition. In order to avoid confusion, we will use the term “range” only to refer to the maximum concentration at which the sensor remains sensitive.

Here, the sensor space is a space spanned by the sensor signals,  $n$  is the number of sensors,

$$V_s = \prod_{i=1}^n FSD(S_i) \quad (9)$$

is the full-scale deflection of the output  $S_i$  of the  $i$ -th sensor, and  $V_n$  is the hyper-volume of noise in the sensor space and is defined by Equation (10):

$$V_n = \frac{2\pi^{\frac{n}{2}} \prod_{i=1}^n \sigma_i}{n\Gamma\left(\frac{n}{2}\right)} \quad (10)$$

where the  $\sigma_i$  is the standard deviation of noise for  $i$ -th sensor and  $\Gamma$  is the Gamma function. It is worth noticing that  $V_n$  is a function of the sensor output and thus is not in general uniform over the whole sensor space. Gardner and Barlett just introduced the theoretical framework to quantify the ability of a chemical sensor array to discriminate sensor stimuli but did not present a methodology that can implement it. In this work, the Resolving Power of a sensor array is estimated adapting the computation of the figure of merit in case of: (a) large sensor arrays, (b) non-linear sensor, (c) heteroscedastic sensor noise.

### Estimation of the Hyper-Volume of Sensor Space

According to Pearce (2000) in order to obtain the hyper-volume of sensor space, a simple linear analytical model was used to model the mapping relationship between  $n$  such sensors, each

with potentially different sensitivity terms  $s_{ij}$  ( $i = 1, 2, \dots, n; j = 1, 2, \dots, m$ ), and  $m$  stimuli. That means the stimuli space and sensor space are related through a space transformation dictated by the sensitivity matrix  $S$ . Here, the *stimuli space* is defined as all the combinations of chemical stimuli that are possible. It must be remarked that such transformation is local if non-linearities are present in the sensors’ responses. However, for the simplified case of linear sensors,  $S$  is a matrix of constant coefficients and the transformation becomes global:

$$X = SY \quad (11)$$

where  $X$  is the response of sensors (sensor space) and  $Y$  would be defined as concentrations to every single chemical source (stimuli space). From empirical data  $S$  may be estimated by classical least squares if one knows all the constituents of the sample.

The element  $x_{ki}$  represents, the response of the  $i$ -th sensor to the  $k$ -th stimuli. Note that Pearce and Sánchez-Montañés (2004) considered only sensor arrays in which each of the individual sensors provided a single feature. This notation is not constrained to any particular type of sensor or number of elements in the sensor array. It can be extended to the case in which sensors operate under some parameter modulation (e.g., temperature in MOX sensors), since each of the working conditions can be considered as a virtual sensor in the array, and in turn, a new feature to the sensor space (or, in other words, a new column in the matrix  $X$ ).

The hyper-volume spanned by the gas mixtures in the stimuli space ( $V_o$ ) can be projected onto the sensor space, giving rise to the *hyper-volume of sensor space* ( $V_s$ ). In Pearce work (Pearce, 2000), the computation of  $V_s$  is straightforward for linear sensors. If  $S$  is a square matrix, namely if the number of pure chemical sources equals to the number of features,  $V_s$  is computed as:

$$V_s = V_o |\det(S)| \quad (12)$$

The reader is referred to Pearce (2000) for extended study of non-square matrices.

The method developed by Pearce to estimate  $V_s$  requires knowing the sensitivity matrix obtained by fitting a direct classical least squares (CLS) model that relates stimuli and sensor spaces to project  $V_o$  onto the sensor space (Equation 12). It is worth to mention that this information is not usually available. In most practical cases direct classical least squares models (CLS) are not fit, because the full set of compounds in the sample is unknown. Consequently, inverse calibration models are the preferred approach.

On the contrary, what we usually know is the set of sensor responses to a collection of mixtures, that is, the sensor space. Thus, a direct computation of  $V_s$  from the sensor space seems to be a reasonable alternative. One way to estimate  $V_s$  consists in computing the convex hull of the sensor space. The convex hull problem is one of the main issues in computational geometry. Computing the convex hull stands for creating a univocal effective representation of a convex shape. The computational cost of estimating the convex hull of a finite set of points depends on the parameters  $n$  and  $h$ , which are, respectively, the number

of points to be enclosed and the number of points on the convex hull. In this sense, the worst case scenario for convex hull computation appears when the points are distributed on a hyper-surface, since  $h$  equals  $n$ . Convex hull algorithms can be used to estimate areas, volumes and hyper-volumes. Regarding the planar case, a number of algorithms to solve the convex hull problem have been developed, including: Gift wrapping -  $O(nh)$ , Graham scan -  $O(n\log n)$ , Andrew's algorithm -  $O(n\log n)$ , Divide and Conquer -  $O(n\log n)$ , Chan's Algorithm -  $O(n\log n)$ , and Quickhull -  $O(n\log n)$ , among others (De Berg et al., 2000). For the case of spaces of dimension three or higher, the computation of volumes and hyper-volumes is generally performed using the Quickhull algorithm (Barber et al., 1996).

In this work, we compute the convex hull utilizing the Quickhull algorithm. Our choice for this algorithm is based on its ability to efficiently estimate hyper-volumes in two-dimensional spaces and in higher dimensionalities as well. Consequently, Quickhull algorithm allows computing  $V_s$  of sensor arrays comprising several sensor units, provided that sensor space contains data points properly sampled. In a nutshell, the Quickhull algorithm computes the convex hull in the following way: (1) First, it finds the  $n$  samples with the most extreme coordinates of the space (where  $n$  is the dimension of the space). (2) Next, it generates a hyper-plane using these  $n$  samples that halves the space into two subsets of samples. (3) After that, it seeks for the farthest sample with respect to the hyper-plane. The previous  $n$  samples along this one define a *facet*. (4) The samples within the *facet* are ignored by the algorithm in next steps because they do not belong to convex hull. (5) Steps (3) and (4) are repeated on the *edges* of the *facet*, with the exception of the initial hyper-plane. (6) The process continues until recursion termination and the selected samples generate the convex hull. The pseudo-code of the employed algorithm is shown in **Table 1**.

## Estimation of the Hyper-Volume of Noise

Theoretically, the value of  $V_s$  is computable in sensor spaces of any dimensionality, but it is unpractical for high-dimension

**TABLE 1** | Pseudo-code of the Quickhull algorithm, used to compute the hyper-volume.

**Algorithm 1** Estimate convex hull.

```

1: procedure QUICKHULL(A)
2:   STEP 1) Find the  $n$  samples with the most extreme coordinates of the space.
3:   STEP 2) Define hyper-plane using these  $n$  samples that splits the space in two subsets of samples.
4:   STEP 3) Find the farthest sample with respect to the hyper-plane. This sample together with the samples defining the hyper-plane form a facet.
5:   STEP 4) Ignore the samples within the facet because they do not belong to convex hull.
6:   STEP 5) Repeat steps 3) and 4) on the edges of the facet, with exception of the initial hyper-plane.
7:   STEP 6) The process continues until recursion termination and the selected samples generate the convex hull.
8: end procedure

```

spaces. This is because estimating  $V_s$  requires sampling the whole space, and the number of samples needed grows exponentially with the dimension of the space (Gutierrez-Osuna, 2002). The same applies to the estimation of  $V_n$ . Consequently, it is preferable to reduce the dimensionality of the sensor space for obtaining better estimations of  $V_s$ ,  $V_n$ , and  $N_n$ . It is worth to mention that for the case of multi-sensor platforms, in which each sensor in the array follows a different transducing mechanism, sensor auto-scaling may be necessary before reducing the dimensionality of the sensor space. The dimensionality reduction of the sensor space can be conducted applying projection techniques such as Principal Component Analysis (PCA). **Figure 1** shows the stimuli space and the corresponding responses of the sensors for different sensor and noise behaviors. In the case of linear sensor responses, the sensor space becomes an equally spaced grid. However, in the general case of non-linear responses, the grid becomes non-uniform for the same change of the input intensity. Similarly, for the case of homoscedastic noise, the dispersion caused by the noise effects is the same around any of the points in the sensor space. However, for the general case of heteroscedastic noise, the shape and size of the “cloud” change across the sensor space. Only, in the case of linear sensors under homoscedastic noise conditions, the estimation of the hyper-volume of noise is constant along the sensor space. For the general scenario of non-linear sensors, one needs another approach to estimate the hyper-volume of noise.

The estimation of the hyper-volume of noise  $V_n$  cannot in general be computed with Equation (10), because it, does not consider the correlation among sensors or features. In particular, assuming homoscedastic noise, we estimated the hyper-volume of noise from the square root of the determinant of the pooled covariance matrix.

## Proposed Methodology to Estimate the Resolving Power in a Sensor Array

Hence, our approach to estimate the Resolving power of a sensor array begins with a dimensionality reduction using Principal Component Analysis. Then, the hyper-volume of sensor space,  $V_s$ , is estimated from the convex hull that encloses the sensor responses in the new space. The pooled covariance is used to estimate the volume of noise,  $V_n$ . Finally, the Resolving power, or the number of input stimuli that can be distinguished becomes the ratio of the hyper-volume of noise over the hyper-volume of the sensor space. **Figure 2** summarizes the workflow to estimate the Resolving Power of a sensor array. It is worth to note that, in the case of non-linear sensors with heteroscedastic sensor noise, one can always split the region of interesting sub-regions, in which the Resolving Power can be estimated again. This partitioning of the region enables the estimation of the Resolving Power in non-linear scenarios.

## MATERIALS AND METHODS

### Synthetic Datasets

We generated 2001 synthetic datasets to evaluate the impact of sensor similarity on the Resolving Power of an array of sensors.

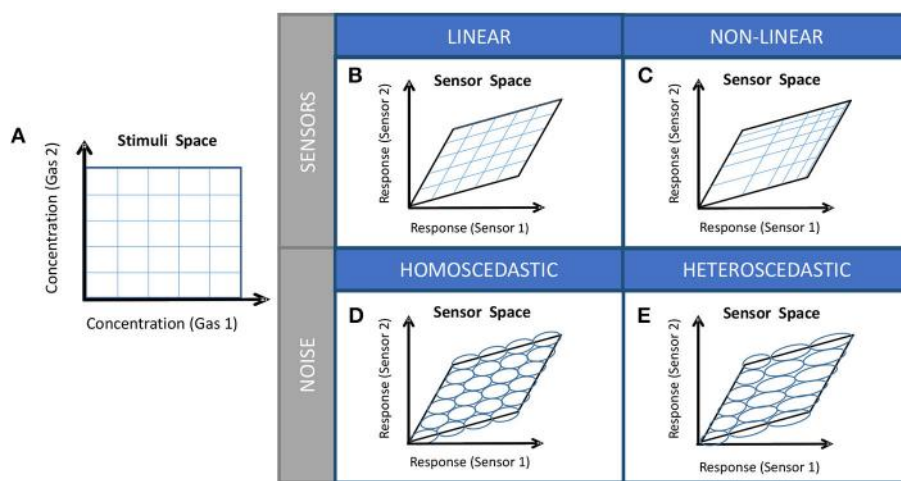


**FIGURE 1 | (A)** Stimuli space, **(B)** Image of the stimuli space (sensor space) in case of partially selective linear sensors, **(C)** Image of the sensor space in case on partially selective non-linear sensors, **(D)** Sensor space with homoscedastic sensor noise, **(E)** Sensor space with heteroscedastic noise. The computation of the Resolving Power  $N_n$  is trivial only for the combination of cases **(B,D)**.

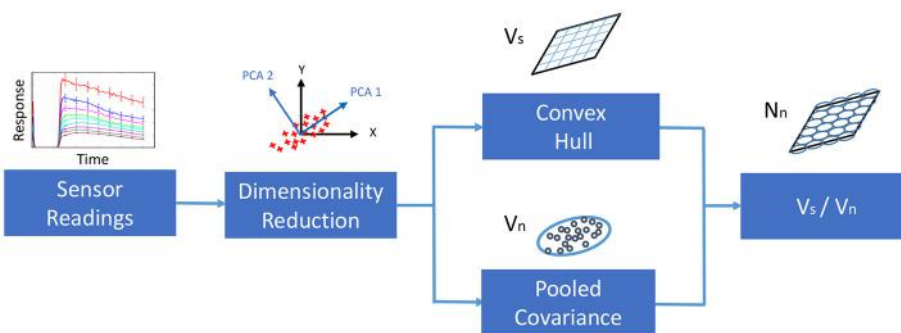


**FIGURE 2 |** Workflow for estimating the Resolving Power of an array of sensors.

To simulate the response of an array of sensors to a gas mixture, we employed the Clifford-Tuma MOX sensor model (Clifford and Tuma, 1983) (Equation 13):

$$X_i = \left( 1 + \sum_{j=1}^n K_j C_j^{\alpha_j} \right)^{-\beta} \quad (13)$$

where  $X_i$  denotes the output resistance of the  $i$ -th sensor,  $C_j$  ( $j = 1, 2, \dots, n$ ) denotes the concentration of the  $j$ -th compound of the gas mixture,  $n$  is the number of gases,  $K_j$  is the sensitivity coefficient of the sensor to the  $j$ -th compound,  $\alpha_j$  is an integer or fractional power for the concentration of the  $j$ -th compound, and  $\beta$  is a non-integer exponent for the power law nature of the MOX sensors.

In our research, we limited for convenience both the number of sensors and the number of gases ( $n$ ) to two, and we supposed that  $\alpha_1 = \alpha_2 = 1$  and  $\beta = 0.5$ . Consequently, synthetic data was computed from the simplified sensor models  $X_1 = (1 +$

$K_{11}C_1 + K_{12}C_2)^{-0.5}$  and  $X_2 = (1 + K_{21}C_1 + K_{22}C_2)^{-0.5}$ . The range of concentration was the same for the two gases:  $C_j \in [100, 1,000]$  ppm. Note that, according to their models, both sensors exhibit the same response to one mixture when  $K_{11} = K_{21}$  and  $K_{12} = K_{22}$ . Furthermore, the first and second sensors tend to be more selective, respectively, toward the first and second gases when  $|K_{11} - K_{21}| \gg 0$  and  $|K_{22} - K_{21}| \gg 0$ . Hence, the Resolving Power of the array can be modified by tuning the sensibility parameters:  $K_{11}$ ,  $K_{12}$ ,  $K_{21}$ , and  $K_{22}$ .

We changed the sensitivities of both sensors using 2001 combinations of  $K_{ij}$ , obtaining 2001 different sensor datasets. This was done by setting that the first sensor had a high sensitivity to the first gas and hardly any to the second in the beginning. Then, we decreased  $K_{11}$  and increased  $K_{12}$  according to the exponential rules  $K_{11}[k] = 0.12^{1+k-0.001}$ , and  $K_{12}[k] = 0.12^{5-k-0.001}$ , where  $k = 0, 1, 2, \dots, 2,000$ . For the second sensor, we implemented the opposite changing rule from the first sensor. That is, the second sensor was

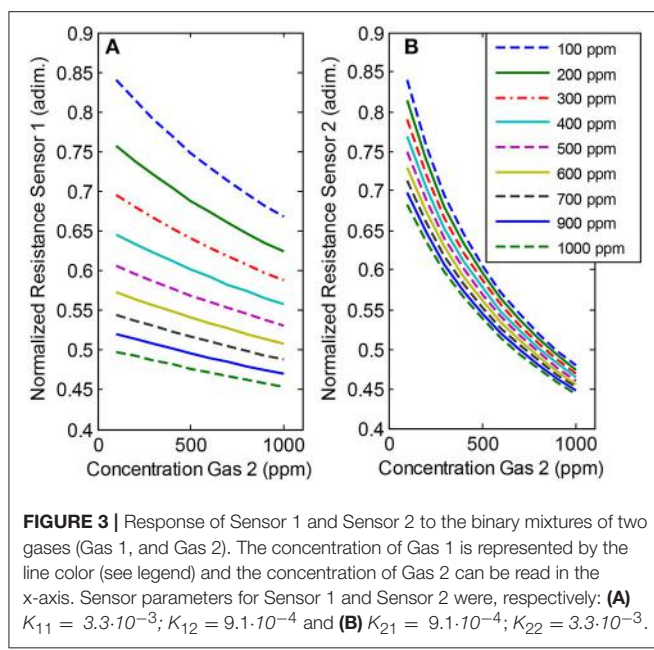


**FIGURE 3** | Response of Sensor 1 and Sensor 2 to the binary mixtures of two gases (Gas 1, and Gas 2). The concentration of Gas 1 is represented by the line color (see legend) and the concentration of Gas 2 can be read in the x-axis. Sensor parameters for Sensor 1 and Sensor 2 were, respectively: **(A)**  $K_{11} = 3.3 \cdot 10^{-3}$ ;  $K_{12} = 9.1 \cdot 10^{-4}$  and **(B)**  $K_{21} = 9.1 \cdot 10^{-4}$ ;  $K_{22} = 3.3 \cdot 10^{-3}$ .

selective to for the second gas at first, and then  $K_{21}$  and  $K_{21}$  increased and decreased, respectively, as  $K_{11}$  and  $K_{12}$ . For  $k = 2,000$ ,  $K_{11} = K_{12} = K_{21} = K_{22} = 0.12^3$ , which means that both sensor present the same sensitivities for both gases.

Figure 3 shows an example of the synthetic data for the particular combination of sensor sensitivities:  $K_{11} = K_{22} = 3.3 \cdot 10^{-3}$ ;  $K_{12} = K_{21} = 9.1 \cdot 10^{-4}$ . We can see the normalized resistance of the sensors along the concentration of first gas (First sensor on the left and second sensor on the right). For each plot, distinct colors and line types represent different concentration levels of the second gas.

## Experimental Dataset

We used a portion of the experimental dataset which is described in detail in Burgués et al. (2018). Therefore, only a brief description is given in this section. Two commercial MOX sensors (SB-500-12 and TGS 3870-A04, provided by FIS and Figaro, respectively) were exposed to dynamic mixtures of CO (0–20 ppm) and humid synthetic air (15–70% RH) in a gas chamber. The heater voltage was modulated in the range 0.2–0.9 V, following the manufacturer recommendations. The sensor output was sampled at 3.5 Hz and then interpolated to 100 sample points. We take as sensor output the full response waveform. Consequently, each sensor provides a high dimensional multivariate output (dimension 100), where each sample point is considered a feature.

The sensor resistance was measured continuously using a voltage divider with a load resistor of  $1 \text{ M}\Omega$ , once the concentration had reached the steady state in the measurement chamber. Figure 4 shows the logarithmic sensor resistance patterns of the SB-500-12 sensor under different gas conditions. It can be observed that, for certain features, the noise is

heteroscedastic because the standard deviation of the sensor response depends on the CO concentration. For example, toward the end of the heating pattern, the variance at 20 ppm is higher than at 11 ppm. Similarly, a non-linear effect of humidity at different concentration levels was found in our dataset: the cross-sensitivity to humidity varied along the heating pattern noise. Therefore, the assumption of some models that the noise has the same standard deviation for each concentration level is unrealistic in our case, and this might lead to a decrease in performance.

## Case Studies

### Case Study I: Resolving Power Against Selectivity and Noise Level

In Case Study I, we aim to analyze how the Resolving Power depends on the *selectivity* ( $sel$ ) of a sensor array. Here we are using the definition of selectivity for an array of non-specific sensors proposed by Johnson and Knapp (2017). Formally, the selectivity of a sensor array is defined as the Cramér-Rao bound analog of the Bayes' rule (Equation 14):

$$sel_{\alpha,\beta} = \frac{CRB(Y_\alpha|Y_\beta) \cdot CRB(Y_\beta|Y_\alpha)}{CRB(Y)} \quad (14)$$

where  $Y_\alpha$  and  $Y_\beta$  are, respectively, two subsets of chemical stimuli to be distinguished,  $Y$  is the whole stimuli space, and  $CRB(Y)$  is the Cramér-Rao bound analog of the Bayes' rule operator that gives the joint bound of  $Y_\alpha$  and  $Y_\beta$ . The reader is referred to Johnson and Knapp (2017) for further details.

According to the previous definition, the *selectivity* of a sensor array measures to what extent the error in the estimation of the concentration is independent of the stimuli. The *selectivity* of a sensor array ranges from 0 to 1. When the sensors of the array are fully specific, the estimation of concentration is independent among stimuli and the selectivity of the sensor array is 1. Conversely, when the sensors of the array become more and more unspecific to the set of mixtures, their responses tend to be undistinguishable and the *selectivity* value of the array decays to 0.

We corrupted the synthetic data generated in section Synthetic Datasets (2001 sensor-pair combinations) with independent Gaussian noise ( $\mu_i = 0$ ,  $\sigma_i = 0.5$ , where  $i = 1, 2$  is sensor index). Using this data we estimated  $V_s$  and  $V_n$  for each sensor-pair. Note that, since the dimensionality of the sensor space was two,  $V_s$  and  $V_n$  were areas. Finally, we computed  $N_n$ , and  $sel$  for each sensor-pair.

### Case Study II: Estimation of the Resolving Power for Multivariate Response Pattern

In Case Study II, we project a highly dimensional sensor space onto lower dimensionality space so as to obtain more accurate estimations of  $V_s$ ,  $V_n$ , and hence  $N_n$ . In particular, our sensor space is defined by the concatenation of features of two sensors units (SB-500-12 and TGS 3870-A04) modulated in temperature and exposed to the CO-H<sub>2</sub>O gas mixtures described in section Experimental Dataset. Notice that, due to the temperature profiling we obtained 100 features per sensor (200 features in total), upon which our methodology can be applied.

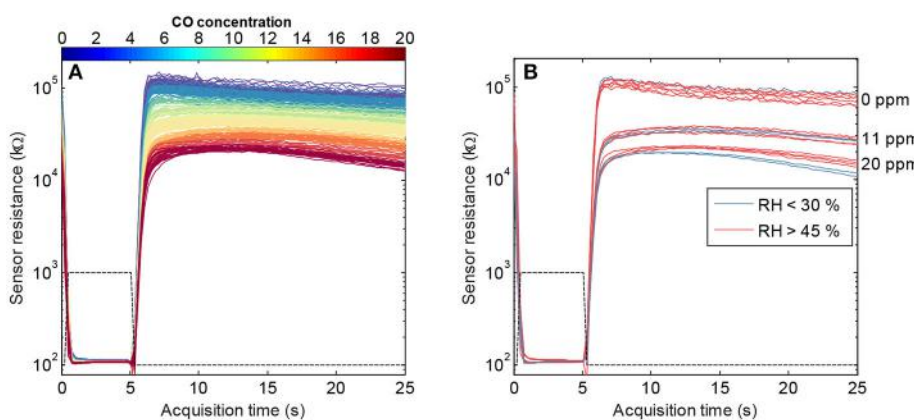


**FIGURE 4 | (A)** Collection of measurements obtained from the SB-500-12 sensor after exposing it to the experimental dataset. Data is represented as a plot of the resistance of the sensor along the acquisition time. The color of the curves represents the concentration of CO. The plot also includes the heater profile applied to the sensor. **(B)** Curves corresponding to concentrations of CO of 0, 11, and 20 ppm, colored by their level of relative humidity (RH). Observe the non-linearity introduced in the pattern due to humidity, and the heteroscedasticity of noise for different concentration levels of CO.

We used Principal Components Analysis (PCA) projection to reduce the input dimensionality of the sensor space, that is, to create a new set of sensor features (Principal Components, a.k.a. PCs) from the original ones according to their contribution to explain the variance of the dataset. We truncated the PCA model of the data to 2 PCs in order to capture the intrinsic dimensionality of the stimuli space. This criterion is also followed in the rest of sensor spaces generated along the paper (we only create 2-dimensional sensor spaces). If the dimensionality of the stimuli space is not known a priori, the optimum complexity of the PCA model can be estimated by inspecting its plot of eigenvalues against the number of PCs, looking for a “knee” on the line. Once we obtained the new reduced sensor space, we computed its Resolving Power.

### Case Study III: Feature Selection Based on Resolving Power

In Case Study III, we use the Resolving Power as a figure of merit to select the most relevant features for gas mixture discrimination from an array of two temperature modulated MOX sensors exposed to CO-H<sub>2</sub>O mixtures.

We constructed three sets of two-dimensional sensor spaces combining selected features from the TGS 3870-A04 and SB-500-12 sensors (from now on TGS and SB sensors). In the first and second sets, the two features came from the same type of sensor (TGS and SB, respectively), whereas in the third set the sensor space was generated joining one feature from each of the sensors. For the sake of simplicity, these sets were called: TGS<sub>1</sub>-TGS<sub>2</sub>, SB<sub>1</sub>-SB<sub>2</sub>, and TGS-SB. Next, we computed the Resolving Power  $N_n$  for all the pair-wise combinations of features in a set of sensor spaces.

### Case Study IV: Feature Selection Based on Resolving Power: Non-linear Sensors

In Case Study IV, we present a similar study Case study III. It is similar in the sense that we select relevant features from two

MOX for CO-H<sub>2</sub>O mixture discrimination. However, in this case we also consider the effect of non-linearity in sensor responses and the presence heteroscedastic sensor noise for estimating the Resolving Power of the array. The basic idea consists of partitioning the stimuli space in smaller regions so that their corresponding sensors spaces exhibit linearized sensor responses and homoscedastic sensor noise.

Therefore, we divided the stimuli space into four portions according to the midpoints of the concentrations of CO and the RHs, obtaining four gas mixture “subspaces” corresponding to: low concentration of CO and low RH (L-L), low concentration of CO and high RH (L-H), high concentration of CO and low RH (H-L) and high concentration of CO and RH (H-H), respectively. Then, we generated four sets of TGS-SB two-dimensional sensor spaces, one per each for each portion of the stimuli space. Finally, we computed the Resolving Power  $N_n$  for all sensor-pair combinations in a set of sensor spaces.

## RESULTS AND DISCUSSION

### Case Study I: Resolving Power Against Selectivity and Noise Level

The results of Case Study I are shown in Figure 5, where we represent the Resolving Power against selectivity for all the sensor-pairs. Additionally, we include the sensor space in three particular cases: (a) sensors are totally selective ( $sel = 1$ ), (b) sensors are totally non-selective ( $sel = 0$ ), and (c) sensors are partially selective ( $sel = 0.5$ ).

From the figure, it is evident that when the selectivity tends to 1, the Resolving Power increases dramatically, and on the contrary, when the selectivity tends to 0, the Resolving Power also tends to 0. In the case limits (a) and (b) the responses of the two sensors are, respectively, orthogonal and collinear. These two cases represent the maximum a minimum value of hyper-volume of sensor space. For the intermediate cases, the Resolving Power increases smoothly with the selectivity of the

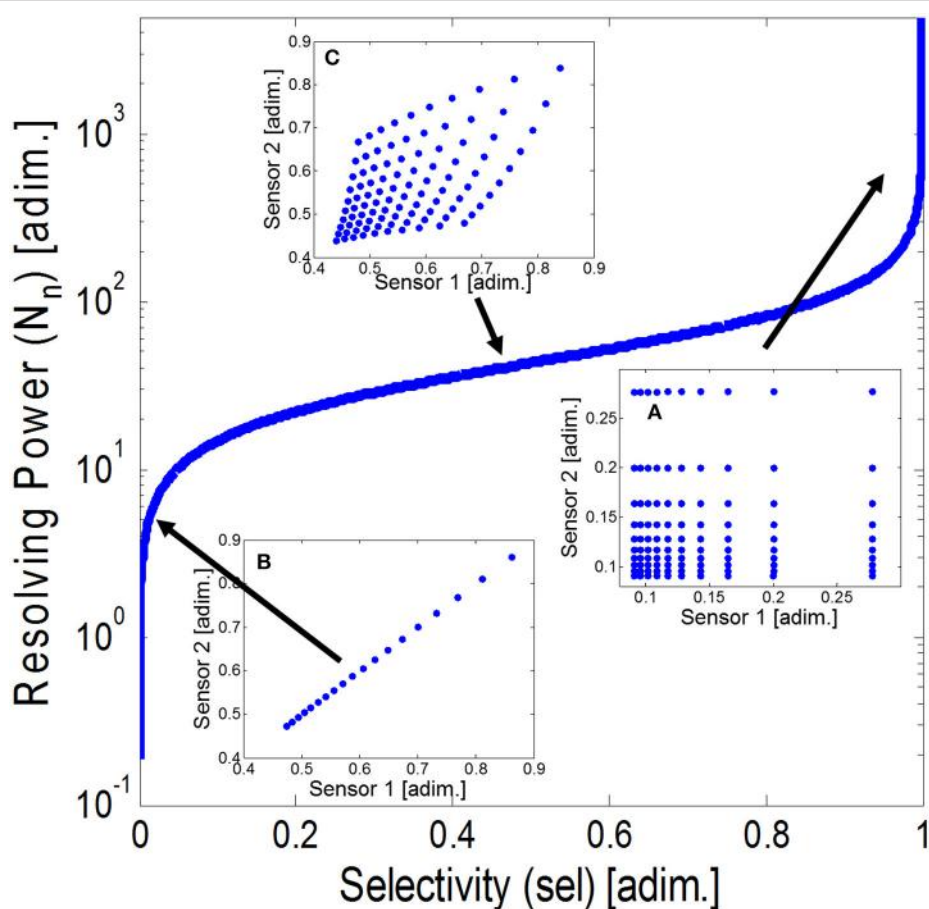


**FIGURE 5** | Resolving Power for the set of synthetic sensor-pairs against their selectivity value. The plot includes the sensor space constituted by the sensor pairs for **(A)** totally non-selective sensors, **(B)** partially selective sensors, and **(C)** totally selective sensors. Observe that the area of the sensor space strongly depends on the selectivity of the sensors.

sensor array, and so does the sensor space hyper-volume [as can be seen for case (c)]. Notice that if the Resolving Power is smaller than one no gas mixtures can be distinguished because the volume of the sensor space is smaller than the hyper-volume of noise. If the power of sensor noise was increased, we would obtain a curve with the same shape to the one of **Figure 5** but shifted toward lower values of Resolving Power (not shown). Thus, to obtain the same level of Resolving Power in both curves, we would need a higher degree of *selectivity* on the noisier one.

## Case Study II: Estimation of the Resolving Power for Multivariate Response Patterns

The highly dimensional sensor space of Case Study II (200 features) is reduced to a 2-dimensional sensor space by means of PCA projection. The result of this data transformation is shown in **Figure 6**, where we can see the scores plot of the data samples seen from the new set of sensor features (namely PC1 and PC2). We colored and selected the marker type of the samples according to respectively, their concentration of CO and

RH level. The lower/higher the concentration of CO the bluer/redder the color of the sample. Regarding the RH level, low/medium/high humidity (20–30% RH; 50–55% RH; 65–70% RH) were represented using circle/cross/diamond markers.

Observing the plot, we realize that there are two main directions for the spread of data: South-East to North-West (SE-NW), and South-West to North-East (SW-NE). Both directions have clear chemical meaning: While in SE-NW samples follow the gradient of CO concentration, in SW-NE they follow the gradient of RH level. If we turn now our attention the distribution of samples along these directions, we discover two totally different behaviors: (1) samples are distributed almost linearly and their dispersions seem constant to be independent with respect CO concentration following SE-NW direction, and (2) samples are distributed non-linearly with the RH level, and their dispersions tend to increase to high RHs. We computed the Resolving Power for this reduced sensor space obtaining  $N_n = 62$ . From the previous considerations regarding the heteroscedasticity sensor noise, it is acceptable to think that the Resolving Power of this space is underestimated.

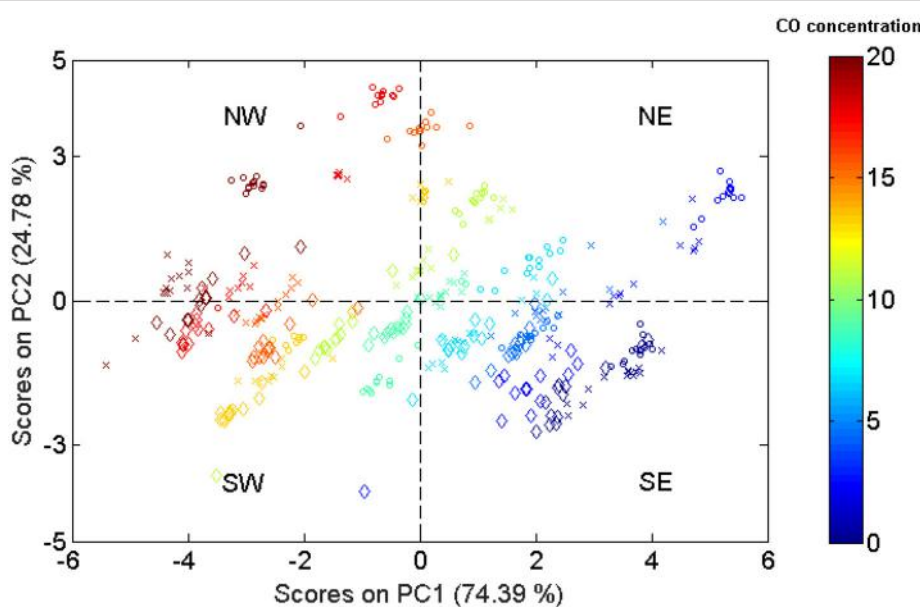


**FIGURE 6** | Reduced sensor space obtained from the projection of the original high-dimension sensor space to a 2-dimension space through a PCA projection. Samples were colored according to their concentration of CO, while the marker type represents the level of RH.

### Case Study III: Feature Selection Based on Resolving Power

Figures 7a–c shows the color maps for the collection of Resolving Power obtained from each set of sensor spaces: (a) TGS<sub>1</sub>-TGS<sub>2</sub>, (b) SB<sub>1</sub>-SB<sub>2</sub>, and (c) TGS-SB. Colors biased toward red/blue tones denote higher/lower values of the parameter. Note that the distribution of values of  $N_n$  is symmetric with respect to the swap of times for Figures 7a,b.

One can confirm similar dependencies between  $N_n$  and the features for TGS and SB sensors comparing their distributions in Figures 7a,b. For both sensors, best CO-H<sub>2</sub>O mixture discrimination occurs either combining features obtained at times below 5 s among them (high sensor temperatures) or combining one of these “early” features with another one acquired within the time range that goes from 15 to 25 s (low sensor temperatures). However, none of the sensors achieved Resolving Power above 60 by means of binary combinations of their own features.

When using features of both sensors, we can achieve much higher  $N_n$  values, as can be observed in Figure 7c. In particular, the maximum Resolving Power on the figure ( $N_n = 105$ ) was obtained for the combination of features acquired with the TGS and SB sensors at 12.5 and 1.5 s, respectively. Interestingly, combining features of both sensor types broadens the regions on the colormap where  $N_n$  presents high values and varies gracefully. That fact suggests that within these regions the sensors become more specific to the compounds of the mixture, and that they present similar *selectivity* values. Noteworthy, the Resolving Power for the best binary combination of sensor features outperforms the Resolving Power obtained in Case Study

II, where we used the full waveform and PCA projection to obtain a new 2-dimensional sensor space.

### Case Study IV: Feature Selection Based on Resolving Power: Non-linear Sensors

The Resolving Power of an array of sensor changes for different partitions of the stimuli space when sensors are non-linear (it modifies  $V_s$ ) and sensor noise is heteroscedastic and dependent on gas concentration (it modifies  $V_n$ ). This effect can be appreciated in the colormap plots of Figures 8a-d, where we show the four different collection Resolving Powers obtained from the 2-dimensional TGS-SB sensor spaces, and corresponding the stimuli space partitions: (a) L-L, (b) L-H, (c) H-L, and (d) H-H. To compare the most discriminative sensor-pair combinations among stimuli space partitions,  $N_n$  was normalized to its maximum value in each of the colormap plots. The color notation is the same as in Figure 7.

For low concentrations of CO (Figures 8a,c), feature combinations with high  $N_n$  tend to concentrate for acquisition times of the SB sensor between 0.5 and 5 s. However, when the concentration of CO increases (Figure 8b), the major part of combinations with high  $N_n$  transfer to acquisition times between 5.5 and 15 s of the same sensor (although the distribution of  $N_n$  is not unimodal along the acquisition time). Regarding the RH, low RH levels (Figures 8c,d) obtain a broader scope of features than high RH levels. This behavior is particularly evident for the TGS sensor. The maximal  $N_n$  values obtained from the four different stimuli space partitions are 47 (L-L), 21 (L-H), 64 (H-L), and 48 (H-H), respectively. It is worth noting that the sum of the Resolving Power of the four stimuli space partitions ( $N_n = 180$ ), is much higher than the

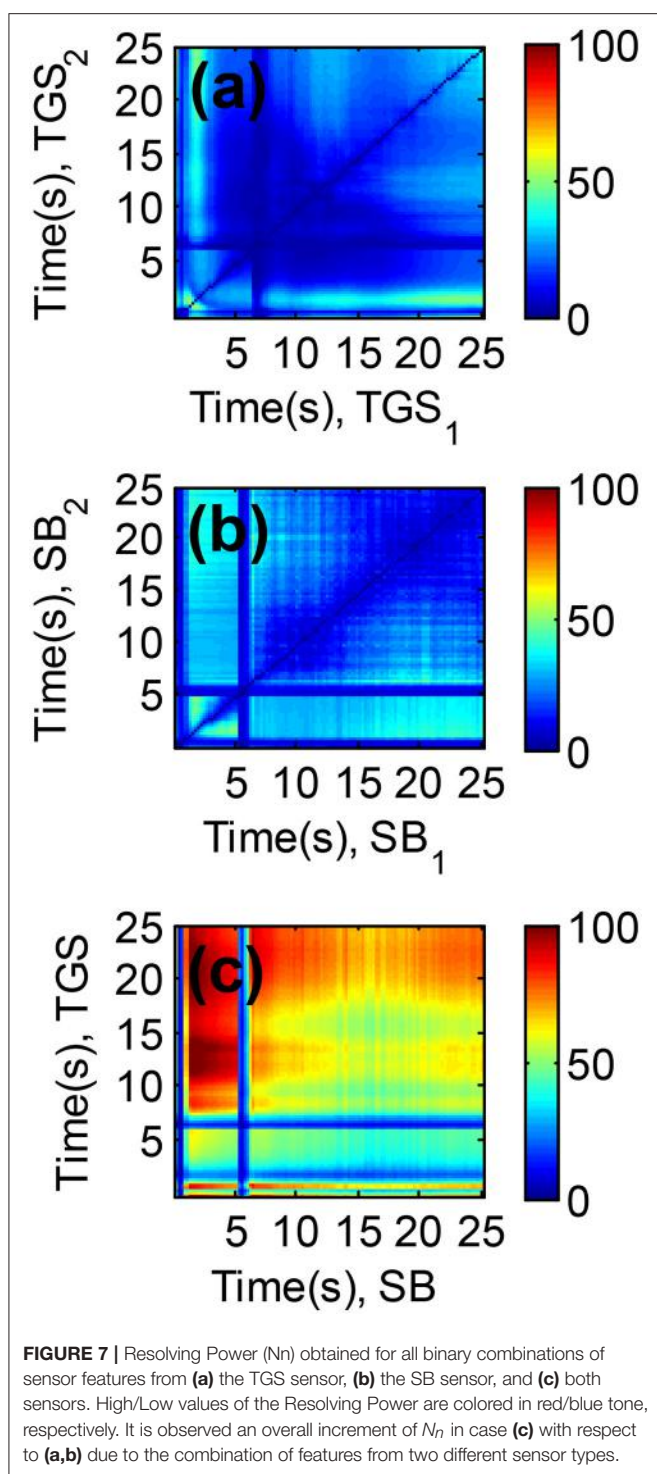


**FIGURE 7 |** Resolving Power ( $N_n$ ) obtained for all binary combinations of sensor features from **(a)** the TGS sensor, **(b)** the SB sensor, and **(c)** both sensors. High/Low values of the Resolving Power are colored in red/blue tone, respectively. It is observed an overall increment of  $N_n$  in case **(c)** with respect to **(a,b)** due to the combination of features from two different sensor types.

Resolving Power for the whole stimuli space obtained in Case Study III ( $N_n = 105$ ). That happens because the combination of features that optimizes the Resolving Power of the sensor array for the whole stimuli space is biased to the discrimination of CO-H<sub>2</sub>O mixtures with low concentrations levels of CO. It may happen too that sensor noise was overestimated for specific concentration ranges.

## CONCLUSIONS

In this paper, we have addressed from a practical point of view the relevant problem of finding a figure of merit that characterizes the Resolving Power of a chemical sensor array. The proposed figure of merit is based on the intuitive idea of computing the ratio of the hyper-volume spanned by the sensor signals and that spanned by the noise. Based on this idea, Gardner and Bartlett (1996) and Pearce (Pearce, 2000; Pearce and Sánchez-Montañés, 2004) coined the term *range* of the sensor arrays developing a theoretical framework for the application of this figure of merit to chemical sensor arrays. Since the term range has other meaning in sensor science, we propose to designate this figure of merit as Resolving Power.

Their work was an important advance, but presented significant limitations when applying the Resolving Power to actual sensor array signals. First, the intrinsic dimensionality of the sensor response is limited to the dimensionality of the stimuli space since we have as many independent sources of variance as gases. Even though the dimensionality of sensor/feature space will be higher, we have to compute the hyper-volume with a method that considers only the lower dimensional manifold spanned by the sensor responses. Second, the noise of different types represents new and independent sources of variance with respect to stimuli and makes the sensor responses to move slightly outside the manifold spanned by stimuli. Third, the non-linear nature of chemical sensor responses introduces a high degree of complexity in the transformation from stimuli to sensor space that has not been considered in depth in previous studies (Gardner and Bartlett, 1996; Pearce, 2000; Pearce and Sánchez-Montañés, 2004). Finally, the heteroscedasticity of noise in chemical sensor arrays has not been considered either in previous studies where it has been assumed to be homoscedastic (Gardner and Bartlett, 1996; Pearce, 2000; Pearce and Sánchez-Montañés, 2004).

The methodology proposed in this paper to compute the Resolving Power of the chemical sensor array overcomes these limitations in the following way. First, it finds the hyper-volume spanned by the sensor responses by computing that of its convex hull in sensor space. This captures in a natural way the hyper-volume of the lower dimensional manifold generated by sensor responses. Second, we reduce the dimensionality of the sensor space to match the intrinsic dimensionality of the stimuli space by projecting it to its first principal components. These first two steps of the method allow to successfully computing the Resolving Power of the real chemical sensor array. The fact that the dimensionality reduction is performed before the estimation of the hyper-volume makes it not necessary very intensive computational power. This has been first studied with synthetic data and then with real chemical sensor data. We used datasets with two sensors to illustrate the non-linearity of the sensor responses and the heteroscedasticity of the sensor noise, although our approach can be extended to more complex datasets. Actually, third and fourth limitations of other approaches are addressed by following a stepwise approach dividing the original stimuli space into sub-spaces that

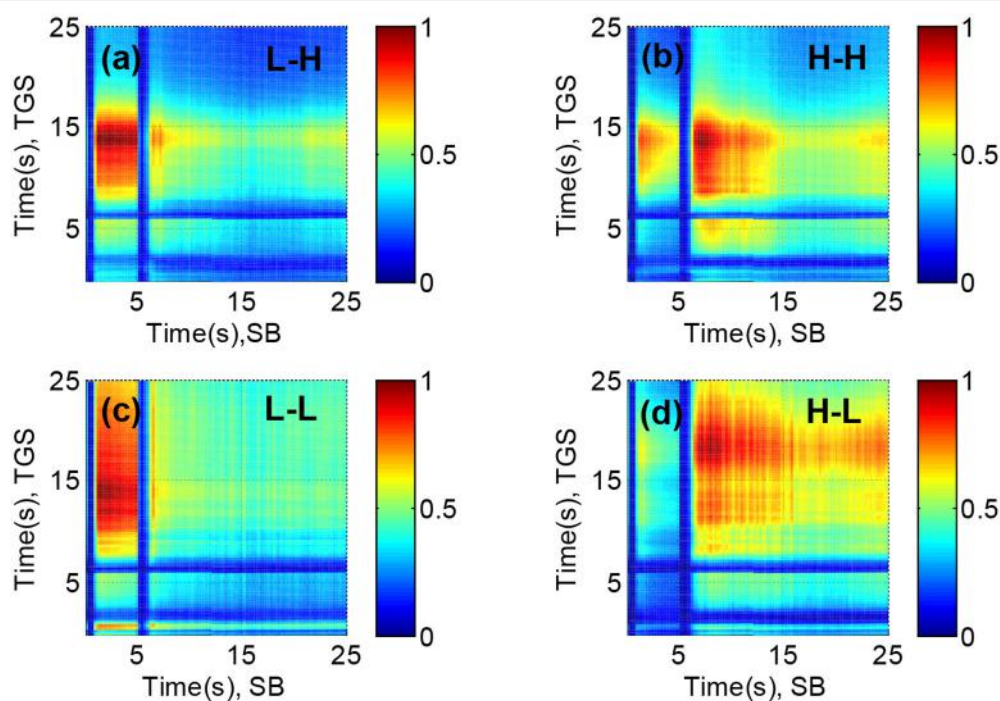


**FIGURE 8 |** Normalized Resolving Power for all pair-wise combinations of sensor features from a TGS-SB sensor space, and obtained for the partitions of the stimuli space **(a)** L-H, **(b)** H-H, **(c)** L-L, and **(d)** H-L, where L and H denote, respectively, low and high concentrations and their position for each gas type, namely, CO and  $\text{H}_2\text{O}$ . The Resolving Power is represented using the same color code as **Figure 7**. The optimum Resolving Power is obtained at different combinations of sensor features for different partitions of the stimuli space.

provide a more local measure of the Resolving Power. Due to the non-linear response of sensors to gas concentrations and the heteroscedasticity of noise it is preferable to characterize locally the Resolving Power of the chemical sensor array since this will vary with concentration. In Case Study IV, we show the need for a local measure of the Resolving Power since there are differences between the results in the four partitions.

In conclusion, the method proposed is able to successfully compute the Resolving Power of chemical sensor arrays providing a relevant figure of merit that was missing to evaluate these systems.

## AUTHOR CONTRIBUTIONS

LF and JY contributed equally to this work. LF and JY performed the formal analysis and generated the synthetic dataset. JB generated the experimental dataset with actual sensors. LF, JF, AG, and SM defined the methodology. LF, JY, JF, JB, AG, and SM participated in the writing process (preparation of the original

draft). LF and JF reviewed and edited the manuscript. LF, AG, and SM conceived the original research.

## FUNDING

This work was partially funded by the Spanish MINECO program, under grants TEC2011-26143 (SMART-IMS), TEC2014-59229-R (SIGVOL) and DPI2017-89827-R (ALPE). The Signal and Information Processing for Sensor Systems group is a consolidated Grup de Recerca de la Generalitat de Catalunya. This work received support from the Departament d'Universitats, Recerca i Societat de la Informació de la Generalitat de Catalunya (expedients 2017 SGR 1721 and 2017 SGR 952). This work has received support from the Comissionat per a Universitats i Recerca del DIUE de la Generalitat de Catalunya and the European Social Fund (ESF). Additional financial support has been provided by the Institut de Bioenginyeria de Catalunya (IBEC). IBEC is a member of the CERCA Programme/Generalitat de Catalunya. JF acknowledges the support from the Serra Húnter program.

## REFERENCES

- Barber, C. B., Dobkin, D. P., and Huhdanpaa, H. (1996). The quickhull algorithm for convex hulls. *ACM Trans. Math. Softw.* 22, 469–483. doi: 10.1145/235815.235821
- Beccherelli, R., Zampetti, E., Pantalei, S., Bernabei, M., and Persaud, K. C. (2010). Design of a very large chemical sensor system for mimicking biological olfaction. *Sens. Actuators B Chem.* 146, 446–452. doi: 10.1016/j.snb.2009.11.031
- Borsdorff, H., and Eiceman, G. A. (2006). Ion mobility spectrometry: principles and applications. *Appl. Spectrosc. Rev.* 41, 323–375. doi: 10.1080/05704920600663469
- Bro, R., and Andersen, C. M. (2003). Theory of net analyte signal vectors in inverse regression. *J. Chemom.* 17, 646–652. doi: 10.1002/cem.832

- Burgués, J., Jiménez-Soto, J. M., and Marco, S. (2018). Estimation of the limit of detection in semiconductor gas sensors through linearized calibration models. *Anal. Chim. Acta* 1013, 13–25. doi: 10.1016/j.aca.2018.01.062
- Burgués, J., and Marco, S. (2017). Multivariate estimation of the limit of detection by orthogonal partial least squares in temperature-modulated MOX sensors. *Anal. Chim. Acta* 1019, 49–64. doi: 10.1016/j.aca.2018.03.005
- Calaza, C., Meca, E., Marco, S., Moreno, M., Samitier, J., Fonseca, L., et al. (2003). Assessment of the final metrological characteristics of a MOEMS-based NDIR spectrometer through system modeling and data processing. *IEEE Sens. J.* 3, 587–594. doi: 10.1109/JSEN.2003.817672
- Cauchi, M., Fowler, D. P., Walton, C., Turner, C., Jia, W., Whitehead, R. N., et al. (2014). Application of gas chromatography mass spectrometry (GC-MS) in conjunction with multivariate classification for the diagnosis of gastrointestinal diseases. *Metabolomics* 10, 1113–1120. doi: 10.1007/s11306-014-0650-1
- Clifford, P. K., and Tuma, D. T. (1983). Characteristics of semiconductor gas sensors I. Steady state gas response. *Sens. Act.* 3, 233–254. doi: 10.1016/0250-6874(82)80026-7
- Cohen, E. R., Cvitas, T., Frey, J. G., Holmström, B., Kuchitsu, K., Marquardt, R., et al. (2008). *Quantities, Units and Symbols in Physical Chemistry, IUPAC Green Book, 3rd Edn.* Cambridge: IUPAC&RSC Publishing.
- D'Amico, A., and Di Natale, C. (2001). A contribution on some basic definitions of sensors properties. *IEEE Sens. J.* 1, 183–190. doi: 10.1109/JSEN.2001.954831
- Davide, F. A. M., Di Natale, C., and D'Amico, A. (1993). Sensor array figures of merit: definitions and properties. *Sens. Actuators B Chem.* 13, 327–332. doi: 10.1016/0925-4005(93)85393-O
- De Berg, M., Van Kreveld, M., Overmars, M. and Schwarzkopf, O. C. (2000). “Computational geometry,” in *Computational Geometry* (Berlin, Heidelberg: Springer), 1–17.
- Desimoni, E., and Brunetti, B. (2015). About estimating the limit of detection by the signal to noise approach. *Pharm. Anal. Acta* 6:355. doi: 10.4172/2153-2435.1000355
- Doleman, B., Lonergan, M. C. C., Severin, E. J. J., Vaid, T. P. P., Lewis, N. S. S., Doleman, B. J., et al. (1998). Quantitative study of the Resolving Power of arrays of carbon black polymer composites in various vapor sensing tasks0. *Anal. Chem.* 70, 4177–4190. doi: 10.1021/ac971204+
- Faber, K., Lorber, A., and Kowalski, B. R. (1997). Analytical figures of merit for tensorial calibration. *J. Chemom.* 11, 419–461. doi: 10.1002/(SICI)1099-128X(199709/10)11:5<419::AID-CEM486>3.0.CO;2-#
- Ferré, J., and Faber, N. K. M. (2003). Net analyte signal calculation for multivariate calibration. *Chemom. Intell. Lab. Syst.* 69, 123–136. doi: 10.1016/S0169-7439(03)00118-7
- Fonollosa, J., Halford, B., Fonseca, L., Santander, J., Udina, S., Moreno, M., et al. (2009). Ethylene optical spectrometer for apple ripening monitoring in controlled atmosphere store-houses. *Sens. Actuators B Chem.* 136, 546–554. doi: 10.1016/j.snb.2008.12.015
- Fonollosa, J., Vergara, A., Huerta, R., and Marco, S. (2014). Estimation of the limit of detection using information theory measures. *Anal. Chim. Acta* 810, 1–9. doi: 10.1016/j.aca.2013.10.030
- Gardner, J. W., and Bartlett, P. N. (1994). A brief history of electronic noses. *Sens. Actuators B Chem.* 18, 210–211. doi: 10.1016/0925-4005(94)87085-3
- Gardner, J. W., and Bartlett, P. N. (1996). Performance definition and standardization of electronic noses. *Sens. Actuators B Chem.* 33, 60–67. doi: 10.1016/0925-4005(96)01819-9
- Garrido-Delgado, R., Arce, L., Guamán, A. V., Pardo, A., Marco, S., and Valcárcel, M. (2011). Direct coupling of a gas-liquid separator to an ion mobility spectrometer for the classification of different white wines using chemometrics tools. *Talanta* 84, 471–479. doi: 10.1016/j.talanta.2011.01.044
- Gross, J. H. (2014). Direct analysis in real time-a critical review on DART-MS. *Anal. Bioanal. Chem.* 406, 63–80. doi: 10.1007/s00216-013-7316-0
- Gutiérrez-Osuna, R. (2002). Pattern analysis for machine olfaction: a review. *IEEE Sens. J.* 2, 189–202. doi: 10.1109/JSEN.2002.800688
- Hierlemann, A., and Gutiérrez-Osuna, R. (2008). Higher-order chemical sensing. *Chem. Rev.* 108, 641–648. doi: 10.1021/cr068116m
- Johnson, K. J., and Rose-Pehrsson, S. L. (2015). Sensor Array Design for Complex Sensing Tasks. *Annu. Rev. Anal. Chem.* 8, 287–310. doi: 10.1146/annurev-anchem-062011-143205
- Johnson, K., and Knapp, A. (2017). Selectivity measure for arrays of non-specific sensors. *Sens. Actuators B Chem.* 251, 1076–1088. doi: 10.1016/j.snb.2017.05.182
- Joint committee for Guides in Metrology (2012). *International Vocabulary of Metrology (VIM), 3rd Edn.* Sèvres: BIPM.
- Justino, C. I. L., Rocha-Santos, T. A., Duarte, A. C., and Rocha-Santos, T. A. (2010). Review of analytical figures of merit of sensors and biosensors in clinical applications. *Trends Anal. Chem.* 29, 1172–1183. doi: 10.1016/j.trac.2010.07.008
- Kuske, M., Padilla, M., Romain, A. C., Nicolas, J., Rubio, R., and Marco, S. (2006). Detection of diverse mould species growing on building materials by gas sensor arrays and pattern recognition. *Sens. Actuators B Chem.* 119, 33–40. doi: 10.1016/j.snb.2005.02.059
- LaFratta, C. N., and Walt, D. R. (2008). Very high density sensing arrays. *Chem. Rev.* 108, 614–637. doi: 10.1021/cr0681142
- Magna, G., Mosciano, F., Martinelli, E., and Di Natale, C. (2018). Unsupervised on-line selection of training features for a robust classification with drifting and faulty gas sensors. *Sens. Actuators B Chem.* 258, 1242–1251. doi: 10.1016/j.snb.2017.12.005
- Marco, S., and Gutierrez-Galvez, A. (2012). Signal and data processing for machine olfaction and chemical sensing: a review. *IEEE Sens. J.* 12, 3189–3214. doi: 10.1109/JSEN.2012.2192920
- Marco, S., Gutiérrez-Gálvez, A., Lansner, A., Martínez, D., Rospars, J. P., Beccherelli, R., et al. (2014). A biomimetic approach to machine olfaction, featuring a very large-scale chemical sensor array and embedded neuro-bio-inspired computation. *Microsyst. Technol.* 20, 729–742. doi: 10.1007/s00542-013-2020-8
- Marth, M., Maier, D., Stahl, U., Rapp, M., Wessa, T., and Honerkamp, J. (1999). Optimization of surface acoustic wave sensor arrays and application to high performance liquid chromatography. *Sens. Actuators B Chem.* 61, 191–198. doi: 10.1016/S0925-4005(99)00307-X
- Muezzinoglu, M. K., Vergara, A., Huerta, R., and Rabinovich, M. I. (2010). A sensor conditioning principle for odor identification. *Sens. Actuators B Chem.* 146, 472–476. doi: 10.1016/j.snb.2009.11.036
- Nič, M. (1997). *IUPAC Compendium of Chemical Terminology 2nd Edition* (1997). IUPAC Compend. Chem. Terminol. Gold, B, 2, 1997–1997.
- Olivieri, A. C. (2014). Analytical figures of merit: from univariate to multiway calibration. *Chem. Rev.* 114, 5358–5378. doi: 10.1021/cr400455s
- Pavlovich, M. J., Dunn, E. E., and Hall, A. B. (2016). Chemometric brand differentiation of commercial spices using direct analysis in real time mass spectrometry. *Rapid Commun. Mass Spectrom.* 30, 1123–1130. doi: 10.1002/rcm.7536
- Pearce, T. C. (2000). Odor to sensor space transformations in biological and artificial noses. *Neurocomputing* 32–33, 941–952. doi: 10.1016/S0925-2312(00)00264-2
- Pearce, T. C., and Sanchez-Montanes, M. A. (2004). “Chemical sensor array optimization?: geometri and information theoretic approaches,” in *Handbook of Machine Olfaction: Electronic Nose Technology*, eds T. C. Pearce, S. Schiffman, H. T. Nagle, and J. W. Gardner (Weinheim: WILEY-VCH Verlag), 347–376.
- Rokushika, S., Hatano, H., Baim, M., a, and Hill, H. H. (1985). Resolution measurement for ion mobility spectrometry. *Anal. Chem.* 57, 1902–1907. doi: 10.1021/ac00286a023
- Rubio, R., Santander, J., Fonollosa, J., Fonseca, L., Gràcia, I., Cané, C., et al. (2006). Exploration of the metrological performance of a gas detector based on an array of unspecific infrared filters. *Sens. Actuators B Chem.* 116, 183–191. doi: 10.1016/j.snb.2006.03.018
- Rubio, R., Santander, J., Fonseca, L., Sabate, N., Gracia, I., Cane, C., et al. (2007). Non-selective NDIR array for gas detection. *Sens. Actuators B Chem.* 127, 69–73. doi: 10.1016/j.snb.2007.07.003
- Shannon, C. E. (1984). Editorial note on “Communication in the presence of noise.” *Proc. IEEE* 72, 1713–1713. doi: 10.1109/PROC.1984.13079
- Snopok, B. A., and Kruglenko, I. V. (2002). Multisensor systems for chemical analysis: state-of-the-art in electronic nose technology and new trends in machine olfaction. *Thin Solid Films* 418, 21–41. doi: 10.1016/S0040-6090(02)00581-3

- Syms, R. R. A., and Wright, S. (2016). MEMS mass spectrometers: the next wave of miniaturization. *J. Micromech. Microeng.* 26:023001. doi: 10.1088/0960-1317/26/2/023001
- Szymanska, E., Davies, A., and Buydens, L. (2016). Chemometrics for ion mobility spectrometry data: recent advances and future prospects. *Analyst* 141, 5689–5708. doi: 10.1039/C6AN01008C
- Todd, J. F. J. (1991). Recommendations for nomenclature and symbolism for mass spectroscopy (including an appendix of terms used in vacuum technology). (Recommendations 1991). *Pure Appl. Chem.* 63, 1541–1566. doi: 10.1351/pac199163101541
- Vaclavik, L., Cajka, T., Hrbek, V., and Hajslova, J. (2009). Ambient mass spectrometry employing direct analysis in real time (DART) ion source for olive oil quality and authenticity assessment. *Anal. Chim. Acta* 645, 56–63. doi: 10.1016/j.aca.2009.04.043
- Vergara, A., and Llobet, E. (2012). Sensor selection and chemo-sensory optimization: toward an adaptable chemo-sensory system. *Front. Neuroeng.* 4:19. doi: 10.3389/fneng.2011.00019
- Xu, Z., Shi, X., and Lu, S. (2010). Integrated sensor array optimization with statistical evaluation. *Sens. Actuators B Chem.* 149, 239–244. doi: 10.1016/j.snb.2010.05.038
- Zampolli, S., Elmi, I., Mancarella, F., Betti, P., Dalcanale, E., Cardinali, G. C., et al. (2009). Real-time monitoring of sub-ppb concentrations of aromatic volatiles with a MEMS-enabled miniaturized gas-chromatograph. *Sens. Actuators B Chem.* 141, 322–328. doi: 10.1016/j.snb.2009.06.021

**Conflict of Interest Statement:** The authors declare that the research was conducted in the absence of any commercial or financial relationships that could be construed as a potential conflict of interest.

The reviewer, VP, and handling Editor declared their shared affiliation.

Copyright © 2018 Fernandez, Yan, Fonollosa, Burgués, Gutierrez and Marco. This is an open-access article distributed under the terms of the Creative Commons Attribution License (CC BY). The use, distribution or reproduction in other forums is permitted, provided the original author(s) and the copyright owner are credited and that the original publication in this journal is cited, in accordance with accepted academic practice. No use, distribution or reproduction is permitted which does not comply with these terms.



# Calibration Update and Drift Correction for Electronic Noses and Tongues

Alisa Rudnitskaya \*

Centre for Environmental and Marine Studies CESAM and Chemistry Department, University of Aveiro, Aveiro, Portugal

One of the obstacles to the wider practical use of the multisensor systems for gas and liquid analysis—electronic noses and tongues, is the limited temporal validity of the multivariate calibration models. Frequent recalibration of multisensor systems is often excessively costly and time consuming due to the large number of necessary reference sample and their limited availability. There are several circumstances that can invalidate multivariate calibration model. The most common problem in the case of sensor systems is temporarily drift or gradual change of sensor characteristics occurring during sensor exploitation. Another common situation is a change in the composition of the analyzed samples that also alters sensor response due to the matrix effects. Finally, a necessity to replace sensors in the array or to transfer calibration model from one sensor set or one type of sensors to the other can arise. As an alternative to the recalibration of the sensor system using full set of calibration samples, drift correction and calibration update has been proposed. The main approaches can be summarized as follows:

- Drift correction that consists in modeling sensor temporarily drift or drift direction using a series of measurements and then using it for correcting new data.
- Calibration standardization that aims to correct new measured data by eliminating new variation. For this purpose, a relationship between two experimental conditions is established using a reduced set of samples measured at both conditions (standardization subset).
- Calibration update that consists in incorporation of new sources of variance in the calibration model by recalculating it using initial calibration samples and reduced set of samples measured at new conditions. The latter can be either standard or unknown samples.

This paper presents an overview of different methods reported for the drift correction and calibration update of the electronic noses and tongue and discussion of the practical aspects of their implementation.

**Keywords:** calibration update, calibration transfer, drift correction, electronic nose, electronic tongue

## OPEN ACCESS

### Edited by:

Dmitry Kirsanov,  
Saint Petersburg State University,  
Russia

### Reviewed by:

Santiago Marco,  
University of Barcelona, Spain  
Carmen Horrillo,

Consejo Superior de Investigaciones  
Científicas (CSIC), Spain

### \*Correspondence:

Alisa Rudnitskaya  
alisa@ua.pt

### Specialty section:

This article was submitted to  
Analytical Chemistry,  
a section of the journal  
*Frontiers in Chemistry*

**Received:** 16 March 2018

**Accepted:** 31 August 2018

**Published:** 25 September 2018

### Citation:

Rudnitskaya A (2018) Calibration  
Update and Drift Correction for  
Electronic Noses and Tongues.  
*Front. Chem.* 6:433.  
doi: 10.3389/fchem.2018.00433

## INTRODUCTION

The electronic noses and electronic tongues are multisensor systems based on arrays of cross-sensitive or partially selective chemical sensors and data processing tools. They have been shown to be promising analytical instruments for a wide range of applications including environmental, food and clinical analysis among others (Schaller et al., 1998; Winquist et al., 2002; Legin et al., 2003).

Chemical sensors as any analytical instruments require regular calibration to account for the changes in their response and ensure their proper functioning. Alterations in the instrumental response may result from the changes of the environmental conditions, composition of the measured samples or device characteristics. The latter is of particular relevance for the chemical sensors that are prone to gradual change of their characteristics or temporarily drift occurring during their exploitation. While regular re-calibration using standards is an established procedure for the individual sensors, as e.g., calibration of pH glass electrode using a series of buffer solutions, it becomes problematic in the case of multisensor systems. Both electronic noses and tongues include partially specific sensors that produce non-selective signals in the multicomponent media, such as almost all real world samples. Therefore, they rely on multivariate calibration models for interpreting their responses and relating them to concentration or property of interest. Multivariate calibration requires large number of standard samples, some of which could be of limited availability. Consequently, frequent recalibration of sensor arrays is prohibitively costly both with respect to the necessary time, availability of standard samples and labor. Alternatively, calibration transfer or update requiring small number of standard samples or no standard samples at all can be implemented.

Impracticability of re-calibration also applies to other analytical techniques that produce non-specific signals in multicomponent samples, the most common example of these being near infrared (NIR) spectroscopy. As NIR spectroscopy is widely applied to the industrial monitoring, significant efforts have been directed to the development of the calibration transfer and update techniques for the NIR spectroscopic instruments (Feudale et al., 2002). However, fewer works addressed this issue for the chemical sensor arrays. In the field of gas sensor arrays main efforts have been directed to the drift filtering and compensation (Marco and Gutierrez-Galvez, 2012; Deshmukh et al., 2015; Liang et al., 2018) while very few papers dealt with calibration update for the electronic tongue systems.

It should be noted that several measures have been recommended to prolong validity of the calibration models. These include optimization of the sensor manufacturing procedures and tighter sensor quality control, which improve stability of the sensing layer, and development of the measuring procedures, including sensor cleaning and conditioning for sensing surface regeneration, and controlled measuring conditions, which improve repeatability of the sensor signal (Korotcenkov and Cho, 2011). Notwithstanding importance of these factors for the proper functioning of the sensors, in practice they are not sufficient to completely avoid recalibration.

This paper will focus exclusively on the calculation based techniques of the drift reduction and calibration update and will present an overview of different methods reported for the drift compensation, calibration update and transfer for the electronic noses and tongues and discussion of the practical aspects of these methods' implementation. Described methods are summarized in the **Table 1**.

## FACTORS INVALIDATING CALIBRATION MODELS

There are several circumstances that can invalidate multivariate calibration model comprising changes in the sensor characteristics due to the drift or sensor replacement, changes of the environmental conditions or composition of measured samples. The most common problem in the case of sensor systems is temporarily drift or gradual change of sensor characteristics occurring during its exploitation. Causes of the drift vary depending on the employed transducer and sensing material with each type of sensor having its particular Achilles' heel.

Conductometric metal oxide gas sensors (MOX) are the most commonly applied in the electronic nose systems due to their low cost and sensitivity to a wide range of gases (Meixner and Lampe, 1996). Sensing layer of MOX sensors is n-type semiconducting metal oxides, of which tin dioxide is the most common. Sensing mechanism of MOX sensors is based on catalytic oxidation of analyte gases on the sensing layer consisting of contiguous small metal oxide grains. Oxygen absorption by the grains creates depletion layer on their surface, increasing their resistance and, consequently, resistance of the entire sensing layer. MOX sensors respond to the volatiles capable of absorbing and undergoing redox reaction on the sensor surface. Stability of the sensor response is thus conditioned by the two main effects: changes of the morphology of the sensing layer and its poisoning (Korotcenkov and Cho, 2011). Structural changes may include changes of the size and geometry of the metal oxide grains leading to the alterations in their conductivity and catalytic properties. Cracking of the metal oxide film after large number of operation cycles (Sharma et al., 2001) and phase separation between metal oxide and additives when they are used are other factors affecting sensor stability (Wang et al., 2007). Finally exposure to the compounds capable to irreversibly bind to metal oxides results in the inhibition of the catalytic activity or poisoning (Meixner and Lampe, 1996; Pijolat et al., 1999). Nitrogen, phosphorus and sulfur containing compounds are typical examples of such inhibitors.

Another group of sensing materials commonly employed in the electronic noses are conducting polymers, such as polypyrrole (PPy), polyaniline (PANI), polythiophene (PTh) and their derivatives (Bai and Shi, 2007; Bernabei et al., 2016). Wide adoption of intrinsically conducting polymers in gas sensing is due to their high sensitivity, good mechanical properties allowing for easy sensor device manufacturing and low operation temperature. Conducting polymers also prone to temporal changes of both baseline and sensitivity (Schaller et al., 2000; Kondratowicz et al., 2001; Kemp et al., 2006). Irreversible changes of response are typically attributed to de-doping and consequent decrease of conductivity of the polymer, which can be provoked by the nucleophilic attack on the carbon back backbone by some volatile compounds (Kondratowicz et al., 2001; Kemp et al., 2006) or oxidation (Schaller et al., 2000). Similar process i.e., partial conversion of the polymer from electrically conducting into non-conducting state have been

**TABLE 1** | Summary of calibration transfer and drift reduction methods.

Method	Sensor technology	Task	Model	N transfer samples	References
<b>COMPONENT CORRECTION</b>					
PCA	MOX gas sensors Voltammetric metal liquid sensors	Classification, recognition Recognition			Artursson et al., 2000; Holmin et al., 2001
ICA	QMB, MOX and polymeric gas sensors	Recognition	PCA		Di Natale et al., 2002; Kermitt and Tomic, 2003
CPCA	Polymeric gas sensors	Classification, recognition			Ziyatdinov et al., 2010
CCA and PLS	MOX gas sensors	Classification			Gutierrez-Osuna, 2000
OSC	Polymeric gas sensors	Classification	k-NN		Padilla et al., 2010
<b>DRIFT MODELING</b>					
DWT	MOX gas sensors	Recognition	PCA		Zuppa et al., 2007
ARMA	MOX gas sensors	Sensor response			Zhang and Peng, 2016
Kalman filter	MOX gas sensors	Drift prediction			Zhang and Peng, 2016
Chaotic time series	MOX gas sensors	Drift prediction			Zhang et al., 2013
<b>SIGNAL STANDARDIZATION–CALIBRATION TRANSFER BETWEEN INSTRUMENTS</b>					
SWS	Potentiometric liquid sensors	Quantification	PLS	10	Khaydukova et al., 2017b
DS + PLS	QMB gas sensors	Recognition	PCA	72	Tomic et al., 2002
DS + Robust regression	MOX gas sensors	Classification	ANN	27	Deshmukh et al., 2014
DS + MLR	Polymer gas sensors MOX gas sensors Potentiometric and voltammetric liquid sensors Potentiometric liquid sensors	Classification Quantification Quantification Quantification	DFA SVR PLS PLS	8 5 3 10	Balaban et al., 2000; Fonollosa et al., 2016; Khaydukova et al., 2017a,b
DS + ANN	QMB and polymer gas sensors	Recognition	PCA	138	Shaham et al., 2005
PDS + MLR	MOX gas sensors	Quantification	SVR PLS	5 5	Fernandez et al., 2016; Fonollosa et al., 2016
WPDS + SEMI + robust regression	MOX gas sensors	Classification and quantification		6	Yan and Zhang, 2015
DS + RWLS	MOX gas sensors	Quantification	BPNN	5	Zhang et al., 2011
Tikhonov regularization	Potentiometric liquid sensors	Quantification	PLS	10	Khaydukova et al., 2017b
<b>SIGNAL STANDARDIZATION–CALIBRATION UPDATE</b>					
SWS	Potentiometric liquid sensors	Classification and quantification	LDA, LR, PLS-DA, PLS	3 10	Sales et al., 1999; Panchuk et al., 2016
DS + MLR	Potentiometric liquid sensors	Classification and quantification	LDA, LR, PLS-DA, PLS	3	Panchuk et al., 2016
DS + PLS	Potentiometric liquid sensors	Quantification	PLS	4–7	Rudnitskaya et al., 2017
DS + ANN	Potentiometric liquid sensors	Quantification	PLS	4–7	Rudnitskaya et al., 2017
PDS + PLS	Potentiometric liquid sensors	Quantification	PLS	3–10	Sales et al., 1999, 2000
<b>MODEL EXPANSION–CALIBRATION TRANSFER</b>					
TCTL	MOX gas sensors	Classification and quantification	LR, RR	6	Yan and Zhang, 2016a
TCTL + SEMI					
<b>MODEL EXPANSION–CALIBRATION UPDATE</b>					
Weighting	Potentiometric liquid sensors	Quantification	PLS	4–7	Rudnitskaya et al., 2017
Tikhonov regularization	Potentiometric liquid sensors	Quantification	RR	4–7	Rudnitskaya et al., 2017
Joint-Y PLS	Potentiometric liquid sensors	Quantification	PLS	4–7	Rudnitskaya et al., 2017; Cruz et al., 2018
TCTL	MOX gas sensors	Classification and quantification	LR, RR	10	Yan and Zhang, 2016a
TCTL + SEMI					
DAELM-S	MOX gas sensors	Classification		20–30	Zhang and Zhang, 2015

(Continued)

**TABLE 1 |** Continued

Method	Sensor technology	Task	Model	N transfer samples	References
SAELM-T	MOX gas sensors	Classification		40–50	Zhang and Zhang, 2015
DCAE	MOX gas sensors	Classification		10	Yan and Zhang, 2016b
<b>ADAPTIVE MODEL EXPANSION</b>					
SOM	MOX gas sensors Simulated data with drift	Classification Classification	SOM SOM		Di Natale et al., 1995; Marco et al., 1998
mSOM	Polymeric gas sensors	Classification	mSOM + LVQ		Distante et al., 2002; Zuppa et al., 2004
A <sup>2</sup> INET	MOX gas sensors and simulate data	Classification	k-NN		de Castro and von Zuben, 2002; Martinelli et al., 2013, 2014
Unsupervised selection	QMB gas sensors	Classification	LDA		Magna et al., 2018
Semi-boost, COREG	MOX gas sensors	Classification	BPNN		De Vito et al., 2012
System identification	MOX gas sensors	Classification	Box-Jenkins model + recursive LS	150	Holmberg et al., 1996, 1997
Classifier ensembles	MOX gas sensors	Classification	SVM		Vergara et al., 2012
<b>GLOBAL CALIBRATION</b>					
Fuzzy inference system	MOX gas sensors	Quantification	PLS		Šundić et al., 2002
	MOX gas sensors	Classification	PLS-DA + k-NN		Solórzano et al., 2018

identified as a source of irreproducibility of potentiometric chemical sensors employing conducting polymers as a solid inner contact (Lindfors and Ivaska, 2004; De Marco et al., 2008, 2009; He et al., 2015). Polymer conversion in this case is caused by the protonation/deprotonation and red-ox reactions occurring in the water layer forming between sensitive membrane and inner solid contact (De Marco et al., 2008).

Two main types of sensors employed in the electronic tongues are potentiometric and voltammetric. Voltammetry is based on the measurements of current generated by reduction and oxidation of species on the electrode surface. Fouling of the electrode surface by the reaction products leads to its inhibition and frequent renewal of the electrode surface is required to maintain its active state (Šulík, 1992). Mechanical, thermal and electrochemical pre-treatment procedures were shown to be effective for the restoration of the electrode surface properties (Holmin et al., 2004; Olsson et al., 2006). Thorough polishing of the metal electrodes is effective for restoration of electrode surface and drift removal (Cavanillas et al., 2015). When mechanical polishing is not feasible, i.e., in the case of thin film sensors, flow-through set-ups, etc., mathematical methods to account for the drift are necessary (Holmin et al., 2001).

Fouling is less critical for the potentiometric chemical sensors that function in the zero-current measuring set-up, however, it may still occur upon sensor exposure to certain substances. For example, poisoning of the solid sensors through formation of insoluble compounds on their surface or absorption of lipophilic compounds by the polymeric membranes have been reported (Vlasov and Bychkov, 1987; Lisak et al., 2016). Potentiometric

sensors with polymeric membranes, mainly plasticized polyvinyl chloride (PVC), typically display rapid drift of their signal during first days of their use, which is attributed to the equilibration processes between water and membrane phases. Further, gradual leaching of the active compounds, ionophores, from the sensing membrane, may induce low long-term drift (Lindfors and Ivaska, 2004). In the potentiometric sensors with glass membranes potential-generating processes occur at the interface between solution and modified surface layer, which is formed as a result of oxidation and partial destruction of glass network by solution (Vlasov and Bychkov, 1987). Interaction with compounds present in the analyzed media may lead to changes in the modified surface layer, which provokes alteration of the sensor response or drift (De Marco et al., 2003).

Another factor affecting sensor characteristics is fluctuations of the temperature and humidity in the environment, in which sensors are deployed. Effect of these two parameters is especially pronounced in the case of gas sensors. In particular, at some temperature ranges change of the baseline conductivity of conducting polymer sensors provoked by the change of the temperature for 1°C may be comparable of the sensor response to the analyte (Schaller et al., 2000). Liquid sensors are less sensitive to the temperature fluctuations. For example, while response of potentiometric sensors is dependent on the temperature according to the Nernst equation, potential changes provoked by temperature alterations within ca. 4°C are considered negligible, therefore less strict temperature control during measurements is required.

Clearly as drift causes are different, its manifestation in the sensor system response will also differ. Therefore, several strategies were put forward to deal with sensor drift.

## DRIFT CORRECTION FOR KNOWN INTERFERENCES

When factors causing sensor drift are not only known but can also be easily quantified, as is the case with effects of humidity and to the less extent temperature fluctuation on the MOX gas sensors response, these factors can be measured and used to compensate for drift they induce. Temperature and humidity sensitivity of the sensors may be calculated and used for sensor signal correction (Kashwan and Bhuyan, 2005; Hossein-Babaei and Ghafarinia, 2010; Mumyakmaz et al., 2010; Huerta et al., 2016).

## DRIFT COMPENSATION AND MODELING

Drift compensation and modeling methods presume that drift can be separated from the analytical signal and modeled and obtained model can be used for the correction of the sensor array response in new samples.

Group of methods called Component Correction (CC) is based on the assumption that sensors of the array have similar (correlated) behavior with the respect to drift and drift of sensor array has a specific direction, which is the same for all measured samples and reference gas. Therefore, drift correction can be done by identifying and modeling drift direction in the reference samples and subtracting it from the new data. CC was implemented using a number of techniques with PCA and Partial Least Square regression (PLS) being the most common (Artursson et al., 2000; Gutierrez-Osuna, 2000).

A very simple linear drift correction of sensor signals using regularly measured standard sample has been proposed in Haugen et al. (2000). This approach was tested on the data of the monitoring of fish and milk spoilage using the MOX sensor array. The advantage of this method is its obvious simplicity, though for its proper functioning sensor drift should be linear over time.

PCA applications to drift modeling is straightforward: if the sensor responses in the reference samples have significant drift, the first components in a PCA model calculated using only measurements in reference sample will describe the direction of the drift (Artursson et al., 2000). Therefore, loading vector  $p_d$  of the PCA model calculated in reference sample is attributed to the noise and used to calculate projection  $t_d$  of the new measurements  $X_n$ . Drift correction is performed by subtracting drift component from the new measurement matrix:

$$X_n^{\text{corr}} = X_n - t_d p_d' \quad (3.1)$$

Similar reasoning is underlying PLS application for drift compensation but instead of considering direction of the maximum variance of the sensor responses in the reference samples as a drift, changes in the sensor array response in reference samples are modeled as a function of time. PLS model is calculated using sensor responses in the reference samples as

an  $X_d$  matrix and time as Y matrix. Resulting loadings  $p_d$  and weights  $w_d$  are used to calculate projection of new measurements:

$$t_d = X_n w_d (p_d' w_d)^{-1} \quad (3.2)$$

New measurements are corrected for drift by extracting drift component:

$$X_n^{\text{corr}} = X_n - t_d p_d' \quad (3.3)$$

Both PCA and PLS model for drift correction may include one or several latent variables. Important issues for the CC are scaling and transformation, which must be the same for both reference and analyzed samples. Outliers, which can skew drift direction, should be detected and removed prior to the drift model calculations.

CC has been successfully applied to the drift correction of MOX sensor array exposed to the 4 gases (hydrogen, ammonia, ethanol, and ethene) and their mixtures during 2 months period. Mixture of 4 gases at their mean concentration levels was measured throughout experiment as a reference. Both recognition and classification performance of the electronic nose was improved after drift correction compared to the uncorrected or corrected by multiplicative drift correction data (Artursson et al., 2000).

CC is based on an assumption that drift directions of sensors in reference gas and all measured samples are highly correlated. If this assumption does not hold, drift correction will be inefficient and, furthermore, some analytical information will be removed together with drift. A generalization of PCA to several classes called Common Principal Component Analysis (CPCA) has been proposed to take into account different behavior of sensors in different samples (Ziyatdinov et al., 2010). CPCA calculates loading vector  $p$  so that it expresses common covariance for all classes (gases) instead of variance observed in the reference gas. Detailed description of CPCA can be found in (Flury, 1984). CPCA was applied to the drift correction of the data set measured in ammonia, n-butanol and propanoic acid at different concentration levels by an array of 17 polymeric sensors over the period of 7 months. The first 1,000 and 1,200 measurements out of 3,484 were used for drift modeling by CPCA and PCA. Better results were obtained using larger calibration data set with CPCA performing better than both PCA and uncorrected data.

Drift correction using PLS and Canonical Correlation Analysis (CCA) that employs both measurements in washing and reference gas sample has been described in Gutierrez-Osuna (2000). Drift reduction algorithm consisted in three steps:

1. Find linear projections  $\tilde{x}$  and  $\tilde{y}$  of measurements in wash and reference gas,  $x$ , and samples,  $y$ , that are maximally correlated:  $\{A, B\} = \text{argmax} [\rho(A_x B_x)]$ ;
2. Fit a regression model  $y_{\text{pred}} = W\tilde{y}$  by ordinary least squares:

$$W = \text{argmin} (y - W\tilde{y})^2;$$

3. Deflate  $y$  and use the residual  $z$  as a drift corrected data for classification purposes:

$$z = y - y_{\text{pred}} = y - WBy.$$

PLS and CCA were used to find projection matrices A and B in the first step of the algorithm. Drift correction was applied to the measurements made by an array of 10 MOX sensors in four splices' headspace during 3 months. Success of drift correction depended on the size of the calibration data set and on the period of time elapsed between last calibration measurement and test. Both PLS and CCA could maintain correct classification rate of 95% for up to 10 consecutive measurement sessions when at least 5 days of measurements were used for calibration. This was significant improvement in comparison to uncorrected data, for which classification rate varied between 70 and 80% in the same settings. However, increase of the time elapsed between calibration and test measurements was shown to have detrimental effect on the efficiency of drift correction.

CC using PCA was employed for the drift reduction of the voltammetric electronic tongue and compared to the additive correction (Holmin et al., 2001). Additive correction consisted in subtraction of the sensor signal measured in the reference sample from the signals measured in the analyzed samples. An electronic tongue comprising 4 metal electrodes (gold, iridium, platinum, and rhodium) was used for measurements in the green and black tea brews, apple juice and process water from pulp and paper plant. Solution of potassium hexacyanoferrate(II) in phosphate buffer was used as a reference solution for drift modeling. Both CC and additive drift correction were effective in drift reduction for the studied data set as sensor drift in this experiment was linear.

Modification of PCA called correlated information removing based interference suppression (CIRIS) has been suggested for background correction of the electronic nose in (Liang et al., 2017). CIRIS consists in applying PCA to the measurements in reference gas and analyzed samples individually. The 1st PC calculated in the reference gas describes to the interference/drift of the sensor signals and corresponding loading vector corresponds to the main direction of this interference. Loading vector calculated in the analyzed samples, which is most correlated with that interference direction, is used for data correction. CIRIS was applied for correction of measurements with an array of 30 tin oxide sensors in the headspace 8 cultured bacteria, which are commonly associated with wound infections. Headspace of aqueous ethanol solution was used as a reference gas. CIRIS improved correct classification rate compared to the uncorrected data from 85 to 93%.

Drift filtering using OSC has been reported in (Padilla et al., 2010). The main idea of OSC consists in removal of the variance not correlated to a vector (or matrix) Y. This is done by constraining the deflation of non-relevant information of X in such a way that only information orthogonal to Y is removed (Wold et al., 1998). OSC filtering was applied to the data set consisting of measurements with an array of 17 conductive polymer sensors in ammonia, propanoic acid and n-butanol over the period of 10 months. Measurements made during the first 15 days were used for calculation of OSC model and optimization of a number of components to remove, and for calculation of classification model using k-NN. Use of OSC filter permitted to maintain correct classification rate between 80 and 98% for the test data set compared to 64–93% for uncorrected data.

PCA correction performed slightly worse than OSC with correct classification rate between 78 and 97% for test data.

Another method for compensation of the drift that has a specific direction is Independent Component Analysis (ICA) (Di Natale et al., 2002; Kermit and Tomic, 2003; Tian et al., 2012). Similarly to PCA, ICA decomposes matrix of sensor signals X as  $X = AS$ , where A is called mixing matrix and S is a matrix of independent components or source signals (Hyvärinen and Oja, 2000). ICA differs from the orthogonal methods such as PCA in that extracted latent variables are statistically independent, i.e., information contained in one independent component cannot be inferred from the others. In practice it means that matrix of sensor array signals can be decomposed into a series of components, some of which are correlated with analytical signal and some with drift. Therefore, independent components mostly correlated with known drift source can be removed.

Removal of independent components correlated with temperature and humidity fluctuations was demonstrated to improve capability of an arrays of quartz microbalance (QMB) sensors with metalloporphyrine membranes to discriminate between two types of peaches (Di Natale et al., 2002). Limitation of this work is that measurements were done during only 4 days.

The same approach was applied to the background removal from the responses of an array of 30 metal oxide gas sensors in the headspace of the infected mouse wounds (Tian et al., 2012). Signal correction by ICA was found to be more effective than PCA and permitted to improve correct classification rates for three bacterial species compared to uncorrected data from 85 to 96%.

ICA can be also used for removal of drift of unknown origin in unsupervised mode (Kermit and Tomic, 2003). After pre-processing of the raw electronic nose data by PCA, obtained square matrix with number of principal components equal to the number of sensor signals was decomposed by ICA. Some of the Independent Components are expected to be highly correlated with sensor drift while other components are expected to be largely free of drift and, thus, can be used for classification purposes. This approach was tested on the data from the mixed sensor array comprising 10 MOSFET and 12 MOS sensors. Sensor signals were collected in two measuring sessions: in headspace of solutions of 5 organic compounds (1% cyclohexanal, 1% ethanol, 5% ethanol, 1% hexanal, and 1% isopropanol) and 5 sample of propanol and butanol at different concentrations, with 200 and 90 measurements acquired, respectively. Unfortunately, no information about timeframe of the measurements was provided. Only sensors responding to some of the analytes were retained for the analysis, resulting in 9 and 6 variables for the 1st and 2nd measuring session, respectively. In both cases combination of PCA and ICA permitted to separate drift from analytical signal improving discrimination performance of the sensor array.

Another group of drift filtering methods is based on the premises that drift of a sensor array resides in low frequency of the signal contrary to the response to analytes, which is high frequency. Sensor signals are split into low and high frequency components, and the slowest signal component is considered drift and removed from the data.

Application of one of such methods - Discrete Wavelet Transform (DWT) was described in Zuppa et al. (2007). The procedure of the drift removal using DWT consist of three steps: decomposition of the signal, thresholding, and reconstruction of the signal. In the decomposition step, a signal is decomposed into a set of orthonormal wavelet functions that constitute a wavelet basis. After that small wavelet coefficient associated to the noise are removed and signal is reconstructed using remaining coefficients. Detailed description of DWT algorithm can be found in Mallat (1989); Ergen (2012). Efficiency of DWT for drift removal was demonstrated on the artificially generated drifting sensor responses.

Methods developed for time series analysis such as Autoregressive moving average (ARMA), Kalman filter (Zhang and Peng, 2016) and chaotic time series analysis (Zhang et al., 2013) have been adopted for drift modeling. These methods are used to analyze time series of signals, in which the present signal value depends on its preceding values. ARMA and Kalman filter algorithms have been tested on data set consisting of the same sample measured by an array of 4 MOX sensors for 10 months. Composition of measured samples was unfortunately unspecified. Measurements carried out during the first month of experiment were used to model drift of each sensor of the array sensor and the rest of the data for model testing. ARMA was found to be more efficient with prediction errors of sensor drift about an order of magnitude lower compared to Kalman filter. Detailed description of ARMA and Kalman filter algorithms can be found in Navarro-Moreno (2008) and Faragher (2012), respectively.

The same group has applied a chaotic time series analysis to the sensor drift modeling (Zhang et al., 2013). Drift extraction was done using discrete Fourier Transform with an assumption that sensor drift belongs to low frequency part of the signal. Further drift modeling included two steps: phase space reconstruction of the drift and training of the Radial Based Function (RBF) neural network for the prediction of the sensor baseline. This approach was tested on the data set described above. Increase of the number of measurements used for the modeling was demonstrated to improve baseline prediction. Using at least 1,000 points measured during 3 weeks period was enough to achieve the best performance in prediction of the sensor baseline for the data measured in the following ca. 9 months.

It is important to note that in Zhang et al. (2013) and Zhang and Peng (2016), drift modeling methods were applied to the prediction of the portion of the sensor signals separated as drift, efficacy of the methods of time series analysis to maintain initial calibration performance in prediction of new samples has not been demonstrated.

Obvious problem with drift modeling methods is that a relatively long series of measurements is required to produce a drift correction model. Measurements made during several weeks are typically used. Furthermore, it can be expected that after some time of the sensor system functioning, drift correction model would become invalid and would need an update, which logically requires another worth of several weeks of measurements.

## MULTIVARIATE CALIBRATION UPDATE

Calibration update methods rely on the regular sensor array measurements in a small number of standards that are used for correction of sensor responses in new unknown samples or for re-calculation or update of calibration model.

### Data Standardization

This group of methods aims to correct new measured data by eliminating new variation. For this purpose, a relationship between two experimental conditions is established and measurements made in new experimental conditions are corrected by this relationship and used for concentration prediction in new samples using initial calibration model. Reduced set of standards measured at both conditions also called standardization or transfer data set is used to for such correction. Two approaches are possible for data standardization: correction of the concentrations predicted at new conditions correction of signals measured in the new conditions.

#### Slope and Bias Correction of the Predicted Values

The slope and bias correction adjusts concentrations predicted in unknown samples using a relationship between concentrations predicted by the calibration model in the standardization subset measured initially and in new conditions (Sales et al., 1999). The relationship between two sets of prediction concentrations,  $c_i$  and  $c_n$ , corresponding to the initial and new conditions, respectively, is calculated by the univariate regression:

$$c_i = \text{Intercept} + \text{Slope} \times c_n \quad (4.1)$$

Concentrations of the samples measured in new conditions are predicted using initial calibration model and corrected using slope and bias determined using update sample set as described above:

$$c_n^{\text{corr}} = \text{Intercept} + \text{Slope} \times c_n, \quad (4.2)$$

where  $c_n^{\text{corr}}$  is corrected concentrations measured in new conditions.

Slope and bias correction has been applied to the data from the potentiometric sensor arrays: an array of 7 sensors with plasticized PVC membranes used for quantification of potassium and calcium in the synthetic ground water (Sales et al., 1999) and an array of 7 sensors with chalcogenide glass and plasticized PVC membranes used for quantification of copper and lead in the model solutions (Rudnitskaya et al., 2017). In both cases slope and bias correction was compared to the other calibration update techniques and was found to be the least less efficient (Sales et al., 1999; Rudnitskaya et al., 2017).

### Signal Standardization

Signal standardization is by far the most widely used approach among calibration update methods. It was applied to drift removal and calibration transfer from one instrument to the other for both electronic nose and electronic tongue. Signal standardization consists in using a relationship between sensor

responses in the initial (at the time of calibration) and new conditions in standardization sample set for correction of the data measured in unknown samples in new conditions. Methods used for data standardization differ in the way the relationship between two sets of sensor signals is calculated (Wang et al., 1991; Bouveresse et al., 1996; Feudale et al., 2002). Single wave standardization (SWS) calculates relationship between each signal individually, piecewise direct standardization (PDS) between groups of signals and direct standardization (DS) between all signals. Both SWS and PDS are linear methods, i.e., they account for the linear shifts of the sensor signals. PDS was proposed as an improvement over SWS with the rational that spectroscopic signals at the adjoin wavelengths are highly correlated, which allows to take into account not only vertical but also horizontal shifts, i.e., shifts of the wavelengths. Both SWS and PDS have been applied to the standardization of the potentiometric sensor data and PDS was found to produce better results (Sales et al., 1999). However, responses of sensors in an array can be independent or partially correlated depending on the array composition, sensor arrangement in the array and analyzed samples, which contradict rational of PDS of high correlation between adjoin signals. Considering this, standardization method that corrects all signals simultaneously, the DS, is more commonly used for the calibration transfer for sensor arrays. Relationship between signals measured in the initial and new conditions can be calculated by means of various multivariate techniques, such as the Multiple Linear Regression (MLR), Partial Least Square 2 regression (PLS2) or auto-associative artificial neural network (ANN), among others.

Calibration transfer from one “master” to four “slave” identical electronic noses equipped with 8 polymer coated QMB sensors has been performed using univariate and multivariate methods, namely linear regression and PLS2 regression (Tomic et al., 2002). Measurements were carried out in the individual solutions of anisole, cyclohexanone, propanol, and toluene during 50 weeks. Calibration transfer was done using the first 72 measurement points acquired over the period of ca. 1 month for each instruments with the rest of the data used for testing. Both linear regression and PLS2 were demonstrated to be successful in removing shifts between instruments according to the RMSEP of the predicted sensor response.

Calibration transfer from one electronic nose to the other using robust regression has been proposed in Deshmukh et al. (2014). Electronic nose instruments were identical and each was equipped with an array of 6 MOX sensors. Calibration model was calculated using back-propagation ANN and measurements in gas samples collected at the pulp and paper production sites. Transfer of the calibration model to the other instrument was done using 27 transfer samples comprising 27 mixtures of four target compounds (hydrogen sulfide, dimethyl sulfide, dimethyl disulphide e methyl mercaptan).

Comparison of the four methods of data standardization has been done using two electronic noses of different models each equipped with identical 12 conducting polymer sensors and measurements in milk samples stored for different periods. Data standardization was done by ANN, MLR, and least squares individually for each sensor with and without intercept, of which

MLR produced the best results for the storage time prediction (Balaban et al., 2000).

Calibration transfer between two electronic noses employing different types of sensors, one with QMB sensors and another with conducting polymer sensors, has been described (Shaham et al., 2005). Measurements in vapors of 23 organic compounds were used for both calibration and data standardization. Performance in data standardization of MLR, PLS2, Principal Component regression (PCR), ANN and a method introduced in this work called Tessellation-based linear interpolation (TLT) was compared. The TLT is a local method that uses for prediction only calibration samples near unknown one. The TLT consists of two stages: tessellation and prediction. First, tessellation of the calibration data, i.e., sensor responses,  $X$ , for which class labels  $Y$  are known, is performed. Tessellation is done in such a way that all vertices of all simplexes are calibration set  $X$  points. Prediction of class membership of a new sample is done by first locating simplex enclosing vector of sensor responses and calculating barycentric coordinates of this sample relative to the vertices of simplex that encloses it. The barycentric coordinates of a point  $p$  within a simplex can be defined as weights, which, if placed at the simplex's vertices, will have their center of mass coincide with  $p$ . After normalization of sum of coordinates to 1, unique coordinates are obtained that are used as interpolation weights. The value of the  $Y$  is when predicted as the average of  $Y$  values of the simplex's vertices, weighted according to the barycentric coordinates. Among all data standardization methods, ANN was found to be the most effective for the studied data. Unfortunately, no comparison with uncorrected data was shown. Another observation is that mapping from quartz microbalance sensor array to conducting polymer ones was more complicated and yielded higher classification errors than vice versa.

In the works described above successful calibration transfer between electronic noses using data standardization has been demonstrated, though relatively large data sets (Balaban et al., 2000; Tomic et al., 2002; Deshmukh et al., 2014) or even entire calibration sets were necessary for the efficient calibration transfer (Shaham et al., 2005).

Comparison of different approaches to the data standardization for the calibration transfer from one sensor array to the other and for calibration update for the same sensor array were reported in Fernandez et al. (2016) and Fonollosa et al. (2016).

In the first series of experiments, measurements were made with five identical arrays of 8 MOX sensors in the individual vapors of ethanol, ethylene, carbon monoxide, or methane, each at 10 concentration levels (Fonollosa et al., 2016). Calibration transfer from the “master” to four “slave” instruments has been carried out as well as calibration update for the same instrument. Calibration was done using measurements from the same measuring session, of which 20 samples were used for calibration and other 20 as tests. Standardization data set comprised 2 concentration levels for each gas, i.e., 8 samples in total. Four methods were evaluated for both calibration transfer and update: DS and PDS, both employing PLS2 regression for mapping, OSC and Generalized Least Squares Weighting (GLSW). GLSW is a data selection method as it identifies

and “shrinks” instrument channels (sensors or sensor response features) that are responsible for the main sources of variance between initial and new conditions (Martens et al., 2003).

In the second series of experiments, 12 identical arrays composed of three MOX sensors were used for measurements in individual vapors of ethanol, acetone and butanone at 7 concentration levels. Measurements at 0 °C were considered as initial condition and used for calibration while measurements at  $\pm 10^{\circ}\text{C}$ ,  $\pm 20^{\circ}\text{C}$ ,  $\pm 30^{\circ}\text{C}$ ,  $\pm 40^{\circ}\text{C}$ , and  $\pm 50^{\circ}\text{C}$  were considered new conditions. Data correction is performed for an increasing number of transfer samples, from 2 to 12 (Fernandez et al., 2016). In both experiments data standardization improved performance of the calibration model with DS and PDS producing lower prediction errors for the new conditions/new instrument. It was also found that PDS needs less standardization samples to achieve lower error, i.e., 5 vs. 11 necessary for DS (Fernandez et al., 2016).

A combination of two standardization methods—Windows Piecewise Direct Standardization (WPDS) and Standardization Error based Model Improvement (SEMI) was proposed for the electronic nose calibration transfer in Yan and Zhang (2015). WPDS is a modification of PDS that weighs a subset of initial sensor signals used for standardization of new signals. Data standardization by WPDS was implemented using ridge regression algorithm. SEMI works similarly to GLSW by weighing down variables that had highest standardization errors, i.e., sensors that drifted most, before feeding standardized new data to the calibration model for prediction. This approach was tested on the data from three identical portable electronic noses equipped with 8 MOX sensors, one of which was considered “master” instrument. Seven groups of samples were measured: acetone, hydrogen and ammonia at different concentration levels, air exhaled by healthy people and air exhaled by healthy people and spiked by three aforementioned compounds, 248 samples in total. All available measurements were used for calculating classification and calibration model for prediction of gas concentrations. Six samples, three individual compounds at two concentration levels, were used as transfer set for calibration transfer from “master” to two “slave” instruments. Combination of WPDS and SEMI was effective for the calibration transfer particularly in the case of the regression models, where RMSEP of concentrations decreased, in some cases 3-fold compared to uncorrected data. Improvement of the correct classification rate for classification models was more modest, which indicates higher tolerance of the classification model to drift.

Application of the Robust Weighted Least Square (RWLS) to the data standardization was described in Zhang et al. (2011). RWLS belongs to the robust regression algorithms that owe their name to the property of being less sensitive or more “robust” in the presence of outliers in the data. Detailed description of RWLS algorithm implemented in Zhang et al. (2011) can be found elsewhere (Heiberger and Becker, 1992). Calibration transfer was done from one “master” to five “slave” electronic noses, all equipped with 3 MOX sensors, using measurements in the individual vapors of formaldehyde, benzene and toluene at different concentration levels. Transfer data comprising 5 samples of formaldehyde, which was considered a reference gas, were selected by Kennard-Stone algorithm. Data standardization

by RWLS allowed to achieve lower concentration prediction errors compared to uncorrected data. It was also observed that efficiency of data standardization varied between “slave” instruments.

Signal standardization was applied to both calibration transfer and update for the electronic tongue sensor system (Panchuk et al., 2016; Debus et al., 2017; Khaydukova et al., 2017a,b).

Calibration update was applied to the potentiometric electronic tongue comprising 10 sensors with plasticized PVC and chalcogenide glass membranes (Panchuk et al., 2016). Measurements were made in the tap water spiked with different amount of cyanobacteria growth media from both nontoxic and toxic, i.e., microcystin producing, strains over the period of 74 days. Tap water and two solutions of inorganic salts in HEPES buffer at different concentration levels, which were used as standardization samples, were measured at each measuring session. Data were standardized by SWS and DS, employing LS regression and MLR for the data mapping, respectively. Both standardization methods were effective in drift removal in classification model, allowing to maintain correct classification rate throughout the experiment. SWS performed better in microcystin quantification achieving lower errors compared to both DS and uncorrected data though ca. 2-fold increase of RMSEP was observed along the time. Surprisingly, no improvement was found for data standardization by DS as RMSEP of microcystin concentration was the same with uncorrected and DS corrected data.

The same two techniques, SWS and DS with MLR and Tikhonov regularization were used for the calibration transfer between two identical arrays of potentiometric sensors (Khaydukova et al., 2017b). Arrays comprising 17 sensors with plasticized PVC membranes was used for measurements in mixed solutions of 6 lanthanides. Ten solutions selected by Kennard-Stone algorithm were used for standardization. DS with Tikhonov regularization performed better producing lowest RMSEP for all tested models, i.e., prediction of sum of all, light and heavy lanthanides, which were close to the errors obtained using the “master” instrument. SWS and DS showed unstable behavior with DS producing highest errors for prediction of sum of all and light lanthanides and SWS producing highest errors for the prediction of heavy lanthanides and an error slightly lower than DS for the prediction of light lanthanides.

Results reported in Panchuk et al. (2016) and Khaydukova et al. (2017b) indicate that performance of data standardization methods is dependent on the data and, probably, composition of standardization data sets.

An ambitious task of calibration transfer between two different types of sensor systems was described in Khaydukova et al. (2017a). Two electronic tongues, potentiometric one comprising 26 sensors with plasticized PVC and chalcogenide glass membranes and voltammetric one comprising 4 carbon paste electrodes modified with metal nanoparticles, were used for measuring 8 samples of must of different grape varieties. Three samples were selected for the calibration transfer using Kennard-Stone algorithm. Transfer of the PLS regression models for the prediction of tartaric acid content, pH and total phenolics was done by DS. Transfer of the calibration model from voltammetric

to potentiometric sensor array worked better than vice versa, which is in agreement with the results reported for the two electronic noses based on different types of sensors (Shaham et al., 2005). RMSEP values close to the “master” electronic tongue were obtained for tartaric acid and total phenolics when calibration was transferred from voltammetric electronic tongue to the potentiometric one. In other cases calibration transfer was not successful. The authors point to the importance of the standardization samples for calibration transfer to work considering that Kennard-Stone algorithm may be not be optimal for this purpose. Another culprit can be limited number of calibration samples that were available in this work.

## Model Expansion

This group of methods is based on the expansion of calibration model by joining initial calibration data set and measurements made in new conditions in the subset of standardization or transfer samples, and recalculating calibration model. In this way, new sources of variance are incorporated in the updated calibration model, which allows to decrease prediction errors for the samples measured in new conditions.

Application of three methods of calibration model expansion, namely weighting, Tikhonov regularization and Joint-Y PLS, to the calibration update of potentiometric sensor array has been reported in Rudnitskaya et al. (2017).

Weighting is the most straightforward approach to the model expansion consisting in simply adding newly measured standardization samples to the calibration data set and recalculating the model (Stork and Kowalski, 1999; Capron et al., 2005).

Initial calibration model can be expressed as:

$$y_i = X_i b_i + e, \quad (4.3)$$

where  $X_i$  is a matrix of sensor responses and  $y_i$  is concentrations.

Regression coefficients  $b_i$  are calculated according the following expression:

$$b_i = X_i' y_i \quad (4.4)$$

Model update is performed by adding measurements in standardization samples made in new conditions to the initial sensor response matrix and recalculating calibration model according to the equation:

$$b_n = \left[ \begin{matrix} X_i \\ W X_n \end{matrix} \right]' \times \left[ \begin{matrix} y_i \\ W y_n \end{matrix} \right], \quad (4.5)$$

where  $X_n$  is a matrix of responses in the transfer samples,  $y_n$  is respective reference values and  $W$  is a weighting factor that may be applied to the transfer data set. Number of samples in the transfer data set is typically significantly smaller than in the initial calibration set. Thus, increasing weight of added samples is necessary to avoid that initial calibration data dominate updated model. Sample weighting is usually done by including multiple copies of the standard update samples. Value of  $W$  has to be determined empirically.

Tikhonov regularization is a variant of a ridge regression adapted to the calibration update purposes (Kalivas et al., 2009; Kunz et al., 2010).

Standard form of TR or ridge regression can be expressed as follows:

$$\begin{bmatrix} X \\ \lambda I \end{bmatrix} b = \begin{bmatrix} y \\ 0 \end{bmatrix}, \quad (4.6)$$

where  $I$  is identity matrix and  $\lambda$  is a regularization meta-parameter.

Regression coefficients  $b$  can be calculated according to the following equation:

$$\hat{b} = (X'X + \lambda^2 I)^{-1} X'y \quad (4.7)$$

Modification of Tikhonov regularization to make it applicable to the calibration update consists in introduction of an additional meta parameter  $\tau$ :

$$\begin{bmatrix} X_i \\ \tau I \\ \lambda X_n \end{bmatrix} b_n = \begin{bmatrix} y_i \\ 0 \\ \lambda y_n \end{bmatrix} \quad (4.8)$$

Parameter  $\tau$  enhances the degree of nonsingularity of the covariance matrix in the inverse operation. Regression coefficients  $b_n$  for the updated calibration model can be calculated using the following expression:

$$\hat{b}_n = (X_i'X_i + \tau^2 I + \lambda^2 X_n'X_n)^{-1} (X_i'y_i + \lambda^2 X_n'y_n). \quad (4.9)$$

Both parameters  $\lambda$  and  $\tau$  need to be optimized.

Joint-Y Partial Least square regression (JYPLS) has been developed to solve a product transfer problem from one plant to the other while maintaining the same quality of the final product (Jaekle and Macgregor, 1998; García Muñoz et al., 2005). When applied to calibration update, JYPLS consists in modeling common latent variable space of the response matrices in initial (i) and transfer (n) calibration samples,  $X_i$  and  $X_n$ , and corresponding concentrations,  $Y_i$  and  $Y_n$ . JYPLS models joint Y matrix combining  $Y_i$  and  $Y_n$  using matrices  $X_n$  and  $X_n$  (García Muñoz et al., 2005):

$$Y_j = \begin{bmatrix} Y_i \\ Y_n \end{bmatrix} = \begin{bmatrix} T_i \\ T_n \end{bmatrix} Q_j' + E_{Y_j} \quad (4.10)$$

$$X_i = T_i P_i' + E_{X_i} \quad X_n = T_n P_n' + E_{X_n} \quad (4.11)$$

$$T_i = X_i W_i^* \quad T_n = X_n W_n^* \quad (4.12)$$

$$W_i^* = W_i (P_i' W_i)^{-1} \quad W_n^* = W_n (P_n' W_n)^{-1} \quad (4.13)$$

Where  $P_i$ ,  $W_i$ ,  $T_i$ ,  $P_n$ ,  $W_n$ , and  $T_n$  are weights, loadings and scores for the  $X_i$  and  $X_n$  matrices () that have the same interpretation as in the PLS regression model, and  $Q_j$  is a common loading matrix of  $Y$ . JYPLS is very flexible as response matrices  $X_i$  and  $X_n$  can have different number of both variables and samples and matrices  $Y_i$  and  $Y_n$  can have different number of samples. However, matrices  $Y_i$  and  $Y_n$  must have the same number of variables and matrices  $X_i$  and  $X_n$  should have the same covariance structure.

Comparison of model expansion methods, weighting, Tikhonov regularization and JYPLS, and data standardization methods, slope and bias correction of predicted values and DS with PLS2 regression and ANN for data mapping, has been done for the electronic tongue (Rudnitskaya et al., 2017). An array of 7 potentiometric sensors with chalcogenide glass and plasticized PVC membranes was used for measurements in copper, lead and cadmium mixed model solutions during 3 months. Calibration model was calculated using samples measured during first experimental session and used for prediction of copper and lead concentrations in samples measured in consequent sessions. A set of transfer samples, from 4 to 7, was selected using Kennard-Stone algorithm. Model expansion methods generally performed better achieving lowest RMSEP of lead concentrations and the same RMSEP of copper concentration but with smaller number of transfer samples compared to the data standardization.

Furthermore, JPLS was used to account for the matrix effect for the potentiometric electronic tongue (Cruz et al., 2018). Electronic tongue constituted by 6 sensors with plasticized PVC membranes was calibrated in the mixed solutions of four paralytic shellfish toxins. Afterwards, 4 mixed solutions prepared in bivalve extracts were used as transfer samples for the calibration recalculation. Updated calibration model was applied to the quantification of three toxins in contaminated bivalve extract. Results obtained using updated calibration model were close to the reference method, while without update calibration model was unusable.

Model expansion by a variant of ridge regression called by the authors transfer sample-based coupled task learning (TCTL) has been reported for an electronic nose (Yan and Zhang, 2016a). Two tasks were addressed: calibration transfer using data set described in Yan and Zhang (2015) and calibration update using long-term drift data set described in Vergara et al. (2012). Calibration update for the long-term drift data set was done using 10 transfer samples selected using Kennard-Stone algorithm, as it was found that smaller number of samples did not ensure the best performance. For both tasks and data sets, TCTL allowed to obtain better results compared to the uncorrected data and performed similarly to the combination of variable standardization with SEMI (Yan and Zhang, 2015), TCTL with SEMI and DAELM (Zhang and Zhang, 2015).

An important issue in model expansion methods is validation of the updated calibration models for optimization of the model parameters. Cross-validation is not a viable option as number of transfer samples is typically limited while validation using initial calibration samples would not reflect model performance in new unknown samples. Several approaches to model diagnostics that do not require use of validation data set has been proposed to deal with this issue. These tools mainly focus on finding a trade-off between bias and variance of the updated calibration model, i.e., finding number of latent variables or model parameter values (transfer sample weights, Tikhonov regularization parameters  $\lambda$  and  $\tau$ ) that minimizes both. Graphic diagnostic tools such as plots of b-coefficients errors of the updated calibration model vs. RMSEC or RMSE in calibration samples vs. RMSE in transfer samples, have been demonstrated to be efficient (Stork

and Kowalski, 1999; Green and Kalivas, 2002; Kalivas et al., 2009).

## Selection of Standardization Samples

In practice it is preferable to avoid using large data sets for the data standardization or calibration transfer. Thus, efforts were directed to decrease number of standardization samples. This can be achieved by careful selection of standardization samples with the aim to identify samples describing enough variation to allow successful calibration transfer while keeping number of samples necessary to measure in new conditions or by new instrument to the minimum. In some instances standardization samples can be selected on the basis of the previous knowledge or convenience, i.e., each analyte at two concentration levels, when the task is discrimination of individual gases' vapors at different concentration levels. In other cases, leverage (Hoaglin and Welsch, 1978) and Kennard-Stone algorithm (Kennard and Stone, 1969) were proposed for identification of the most relevant samples for the calibration transfer. Leverage matrix is calculated as a covariance matrix of the sensor array mean-centered responses. Maximum diagonal elements of the leverage matrix correspond to the most relevant samples in the training data set. Kennard-Stone algorithm is commonly used for selection of samples uniformly distributed over the object space. This is sequential procedure consisting of selecting as the next sample the one that is most distant from those already selected. Two samples that are the most distant from each other serve as a starting point. The distance is usually the Euclidean distance.

## Adaptive Learning

Adaptive drift correction methods are based on the idea of continuous update of the classifier using unknown samples measured during routine functioning of the sensor array. This approach is attractive for practical applications as it does not require reference samples beyond the calibration data set and does not require long-term measurements as drift modeling methods. At the first stage calibration is performed by using a set of calibration samples with known class membership to calculate and optimize classification model. In the following testing stage new unknown samples are used for correction/recalculation of the classification model after they have been assigned to the class. Adaptive drift correction can be performed in supervised, unsupervised and semi-supervised mode depending on the employed method.

First implementations of adaptive drift correction used unsupervised neural network—Self-Organizing Map (SOM) (Di Natale et al., 1995; Marco et al., 1998). SOM consists of a rectangular single layer of neurons, whose weight vectors have the same dimensionality as input data (Kohonen, 1996). During calibration step a known sample is presented to the net and distances between this sample and all neurons are calculated using Euclidean or other metrics. Weights of the winning neuron, i.e., neuron closest to the particular calibration sample, and its neighbors are updated to decrease even further their distance to the calibration sample. Learning rate decreases monotonically with the increase of the neuron distance to the winning neuron and along the training. Trained network forms clusters of

neurons corresponding to the same class, i.e., to the similar calibration samples. This process is unsupervised, however, after its completion, user intervention is necessary to label clusters according to the classes and define criterion to avoid cluster overlapping, i.e., allocate neurons corresponding to more than one class. During routine operation, training of the SOM can continue with a slow learning rate to account for the sensor drift and resulting cluster displacement. Continuously adapting SOM has been shown to be more robust in the presence of the drift compared to the static one (Marco et al., 1998).

Use of multiple self-organizing maps or mSOM, one for each modeled class, has been proposed with the aim to increase user influence over training process (Distante et al., 2002; Zuppa et al., 2004). mSOM have been tested using data from an array of 32 polymeric conducting sensors measured in 6 gases (acetonitrile, methanol, propanol, acetone, butanol, and water) over the period of 4 weeks. Use of continuous net training permitted to decrease error rate from 9% to less than 3%.

Similar modification of unsupervised technique for the purpose of semi-supervised classification has been proposed for the other type of the network—Artificial Immune Network (AINET). AINET is an algorithm inspired by the adaptive immune system (de Castro and von Zuben, 2002). Modified algorithm called Adaptive Artificial Immune Network (A<sup>2</sup>INET) consists in training separate AINET for each class (Martinelli et al., 2013, 2014). Calibration starts by initiation of a set of processing units or network cells. Distances or affinities between network cells and calibration sample are calculated and a cell closest to this sample is selected. Then selected cell is replicated or cloned and cells with less affinity are changed or mutated. Both number of clones to add and mutation rate being are functions of the affinity of particular cell to the calibration sample. Cells with less affinity are eliminated and a pool of the cells is updated. Detailed description of both original AINET and adapted algorithms can be found in de Castro and von Zuben (2002) and Martinelli et al. (2013). For the purpose of pattern recognition outputs of the trained network are used as inputs into classifier such as e.g., k nearest neighbors (k-NN). A<sup>2</sup>INET is continuously adapted during sensor operation as after new unknown sample is assigned to the class, it is used to clone and mutate network cells.

A<sup>2</sup>INET performance in drift compensation has been assessed using synthetic and experimental data. The latter included measurements with an array of four MOX sensors in five individual gasses (acetaldehyde, acetone, ammonia, ethanol, and ethylene) during 18 months and in 3 gases (acetaldehyde, ethylene, and toluene) during 12 months. A<sup>2</sup>INET permitted to improve classification rate compared to the standard classifier from 81 to 95% (de Castro and von Zuben, 2002; Martinelli et al., 2013) and from 90 to 99% (Martinelli et al., 2014), respectively. Adaptive classifier was also robust in the presence of artificially added noise and faults.

Algorithm of unsupervised on-line selection of training features (UOL) was described in (Magna et al., 2018). This method performs selection of the features of the sensor response matrix that afford better class separation during initial calibration step and after each new sample is measured. Features here refer

to the parameters of the response of QMB sensors, for which frequency shifts at different time periods, response integral at different time frames, etc. are measured. After new sample is measured, feature selection from the calibration set is performed in such a way as to avoid that new sample is considered an outlier (far from all classes) or ambiguous (between several classes). Thus, UOL “adapts” calibration data set to new unknown samples. Selected features are used to recalculate classification model. Any classifier, e.g., LDA, PLS-DA, or k-NN can be used in combination with UOL. Feature selection is done using two criteria, MR and PR. MR is the ratio between Mahalanobis distances from the new sample to the two nearest class distributions M<sub>1</sub> and M<sub>2</sub>. MR is calculated for each feature *i* according to:

$$MR_i = M_1 \frac{M_1}{M_2}$$

Feature is not included in the calibration model when MR<sub>i</sub> is bigger than a fixed value, i.e., 0.9. PR evaluates probabilities of a new sample to belong to known class distribution:

$$PR_i = \max_j \left( \frac{1}{\sigma_j \sqrt{2\pi}} \exp \left( -\frac{(x - \mu_j)^2}{2\sigma_j^2} \right) \right),$$

where  $\mu_j$  and  $\sigma_j$  are the standard deviation and the mean of the *i*th feature for the *j*th class. A large value of PR<sub>i</sub> means that new sample has a low probability to be an outlier for at least one class. Thus, features with PR<sub>i</sub> lower than certain threshold are rejected.

UOL has been applied to the synthetic and experimental data sets, the latter consisted of measurements made in ethanol, toluene and their mixture with an array of seven QMB sensors with metalloporphyrin coatings. Measurements were carried out during two measuring sessions 45 days apart. For the best performing classification method, LDA, use of unsupervised on-line selection allowed to improve classification rate from 88 to 100%. Classification improvement was even more drastic when noise was added to the data: from 66 to 92% without calibration update to 88–100% after using unsupervised on-line selection.

Adaptive drift correction for back-propagation neural network (BPNN) classifier was implemented using two semi-supervised algorithms: semi-boost and Semi-Supervised Regression with Co-Training (COREG) (De Vito et al., 2012). The crucial step in both algorithms is selection of unlabeled samples from the pool for classifier recalculation. Semi-boost selects unlabeled samples with highest relevance, which is estimated by taking into account their classification confidence and the presence of labeled samples in their neighborhood. Thus, COREG algorithm selects unlabeled samples that decrease classification error for the calibration data set when included in it. Both methods have shown improvement of the correct classification rates compared to BPNN without recalculation. Semi-boost classifier update applied to the measurements with an array of 5 MOX sensors in head-space of ground coffee samples improved classification rate from 89 to 93%. COREG was used for model correction for 1 yearlong city air pollution

monitoring data measured using the same electronic nose system. Performance gain of 11% was obtained when employing optimal data split into 6% of the data as calibration, 10% as unlabeled sample pool and the rest as test samples.

A method based on system identification theory that models responses of each of the individual sensors of the array in new samples using responses of the other sensors in new and previously measured samples has been proposed (Holmberg et al., 1996, 1997). Dynamic sensor response is described by the linear Box-Jenkins model in the following form:

$$\hat{y}_i(t) = G(q, \theta^A) u(t) + v(t)$$

where  $\hat{y}_i(t)$  is the value of the modeled output of the sensor  $i$  in discrete time;  $u(t)$  are the inputs (signals from the other sensors of the array),  $G$  is the linear function of the sensor dynamics;  $q$  is the time shift operator,  $qy(t) = y(t+1)$ ;  $\Theta^A$  are parameters of the model of the class A; and  $v(t)$  is disturbance or noise. Model parameters  $\Theta$  for each class are estimated using calibration data set. When new (unknown) sample is measured, estimates of each sensor response in this sample  $\hat{y}(t)$  are calculated using actual and previous responses of all other sensors of the array for all possible classes (gases). Overall square error  $E$  is calculated according to an expression:

$$E = \sum_{i=1}^N (y_i(t) - \hat{y}_i(t|\hat{\theta}_i^A))^2$$

Unknown sample at a time  $t$  is assigned to the class, for which the lowest error  $E$  was found.

At the same time with each new measurement, classification models are updated using recursive least squares (RLS) algorithm, which assigns exponentially decreasing weights to the older measurements:

$$\hat{\theta}_i^A(t) = \hat{\theta}_i^A(t-1) + L_i(t) \varepsilon_i(t),$$

where  $\varepsilon_i(t)$  is the prediction error for the sensor  $i$  calculated according to the previous equation and  $L_i(t)$  is a gain vector estimated by the RLS algorithm. To avoid updating wrong model due to misclassification of the new (unknown) samples, model parameters are updated only in the case of significant difference between the prediction error of the model of the recognized gas and the prediction errors of the other models. This approach has been applied to the data set consisting of the measurements of three MOX sensors in 1-propanol, 2-propanol, 1-butanol and 2-butanol during 45 days. Measurements collected during the first 10 days (150 measuring cycles) have been used for calculating classification models, while measurements collected during consequent 35 days (730 measuring cycles) were used for model testing and update. Adaptive model displayed lower prediction errors compared to the static model with average classification rates 91 and 85%, respectively (Holmberg et al., 1997).

An approach named classification ensembles was proposed for continuous update of the calibration model during functioning of the electronic nose system (Vergara et al., 2012). First, a Support

Vector Machine (SVM) classifier is trained on a set of calibration data. When the next batch of calibration data is available, the next classifier is trained and the final classifier  $h_{t+1}(x)$  at time step  $(t+1)$  is a weighted combination of all classifiers. Thus, drift correction is performed by gradually including it in the calibration model. Classifier ensembles were applied to the very large data set consisting of measurements in 6 individual gases (ammonia, acetaldehyde, acetone, ethylene, ethanol, and toluene) at different concentration levels by an array of 16 MOX sensors during 36 months. Classification ensembles were shown to be effective as a drift reduction strategy though the more time elapsed between the last calibration and new unknown samples, the more classification rate deteriorated.

Domain regularized component analysis (DRCA) has been proposed for the adaptive drift correction in Zhang et al. (2017). DRCA finds a common subspace for both reference and new data. Its algorithm can be summarized as follows:

1. Calculate matrix  $A = ((\mu_r - \mu_n)(\mu_r - \mu_n)')^{-1} (X_r X_r' + \lambda X_n X_n')$ , where  $\mu$  is a mean vector,  $X$ -matrix of sensor responses, indexes  $r$  and  $n$  refer to reference and new data, correspondingly.  $\lambda$  is a regularization parameter, which is used since less new data are typically available compared to the reference data.
2. Perform eigenvalue decomposition of the matrix  $A$  and consider eigenvector corresponding to the first  $d$  largest eigenvalues an optimum subspace:  $P = [p_1, p_2, \dots, p_d]$ .
3. Correct data by calculating subspace projection:  $X_r' = P' X_r$  and  $X_n' = P' X_n$ .

Performance of DRCA combined multi-class SVM with RBF kernel was evaluated using publicly available data set (Ziyatdinov et al., 2010) and it compared favorably with other classification and drift correction approaches.

Calibration model expansion by inclusion of the transfer samples in the calibration model was described in Zhang and Zhang (2015). Two approaches based on extreme learning machines or back-propagation neural network were employed. The first one named source domain adaption extreme learning machine (DAELM-S) uses transfer samples for regularization or update of the calibration model. The second one named target DAELM or DAELM-T works similarly to a semi-supervised adaptive neural network described in (De Vito et al., 2012; Martinelli et al., 2014). Both algorithms were shown to be more successful in drift reduction compared to CC by PCA and Support Vector Machine classification models as they maintained correct classification rate close or above 90%. It is worth to note that relatively large number of transfer samples were necessary for these algorithm functioning: 20 to 30 for DAELM-S and 40 to 50 for DAELM-T.

An ANN with three hidden layers, which combines drift removal and calibration model update using both new unknown and transfer samples has been described in Yan and Zhang (2016b). This method named drift correction autoencoder (DCAE) includes the following steps:

1. The first denoising layer is pre-trained with new unknown data (or data measured on the "slave" instrument) in unsupervised mode followed by fine-tuning of the network

- weights using calibration data set (or data measured on the “master” instrument).
2. The second layer is initialized using weights of the denoising layer.
  3. The domain vector  $d$  ( $d \in X$ ) is created for each calibration, transfer and unknown sample such as  $d_i = 1$  if the sample is from the  $i$ th device and 0 otherwise. The acquisition time  $t$  can also be added into  $d$ .
  4. The second layer is trained to minimize the expression  $\sum_{p=1}^P \|f(x_p^c d_p^c) - f(x_p^n d_p^n)\|^2$ , where  $P$  is the number of transfer samples,  $x^c$  and  $d^c$  are transfer samples from the calibration data set or “master” instrument and its respective domain vector, and  $x^n$  and  $d^n$  are transfer samples measured at new conditions or “slave” instrument and their respective domain vectors.
  5. Using output of the second layer, the third layer is trained as classifier using calibration data set and consequently used to predict class membership for the new unknown data.

DCAE performance was evaluated using public data set described in Vergara et al. (2012) DCAE performed similarly to the other drift reduction methods such as CC by PCA, OSC and classification ensembles for the second data batch, i.e., data measured in the month following calibration. However, contrary to the other methods DCAE was able to maintain this performance for the consequent batches due to the use of transfer samples. DCAE also performed slightly better than DAELM-S.

Obvious attraction of adaptive methods of drift reduction and model update is that no reference samples are required, instead unknown samples measured during routine sensor array operation are used. However, no strategy has been proposed to deal with the situation when due to the sensor drift or condition change newly measured samples began to be allocated to the wrong classes. It also should be noted that the best performance of the adaptive correction is achieved when all sensors of the array display similar behavior with respect to drift.

## GLOBAL MODELS

Instead of being modeled, known sources of variation can be also included in the calibration model, which in this case becomes global or general calibration. Combination of the data pre-treatment and variable selection by fuzzy inference system with linear multivariate regression was proposed to account for the effects of humidity on the response of an array of gas MOS sensors (Šundić et al., 2002). Measurements with an array of 5 sensors were carried out in carbon monoxide, methane and their mixtures at three humidity levels. Nonlinearity of the sensor responses caused by varying humidity as well as sensor cross-sensitivity at low gas concentrations could be taken into account by the fuzzy inference algorithm.

Global calibration can be applied to the calibration transfer between electronic nose instruments, in which case source of undesirable variation is differences in response characteristics between sensors of the same composition (Solórzano et al., 2018).

General calibration model is calculated using measurements made with several replicas of sensor array and is expected to include variations between different sensor arrays of the same composition. This approach was evaluated on 5 arrays constituted by 24 MOX sensors, which were used for measurements in six gases (acetaldehyde, methane, ethanol, propane, nitrogen dioxide, and carbon monoxide) at 3 concentration levels each at varying humidity. General classification models were calculated using multiclass Partial Least Squares-Discriminant Analysis (PLS-DA), followed by k-NN in the latent variable (LV) subspace. Calibration and validation data sets were composed by the measurements of 4 sensor arrays, while measurements with fifth were used to test classification model performance. While individual calibration requires less samples and gives better prediction results compared to the general calibration, the latter is capable to provide significant cost-reduction for mass-produced sensor array ensuring acceptable performance.

## CONCLUSIONS

Calibration update is essential for the practical use of the electronic nose and electronic tongue sensor systems. Several methods discussed in this review have been successfully applied to tackle issues of temporarily sensor drift, matrix effects or calibration transfer between instruments. Performance and consequently choice of the calibration update method depends on the data at hand, i.e., on the behavior of the particular sensors in analyzed samples. In practice multivariate calibration update methods may be preferable to the drift modeling as they require only few transfer samples to be measured regularly to maintain calibration model indefinitely. Special attention should pain to the provision of the adequate transfer samples matching matrix of the analyzed media and with reproducible compositions.

As transfer samples in some cases can be of limited availability or have high costs, even if only few of them are necessary, adaptive drift correction methods may be of interest. It is difficult to envisage that adaptive correction can function without any standard samples at all after calibration completion, but it may serve as a mean to decrease even further number of transfer samples or frequency, at which they need to be measured.

Though drift reduction and calibration update are very important issues for practical applications of the sensor systems, they are not routinely used yet. With exception of Component Correction and Direct Standardization, a typical situation for the most methods described in the review is that they were reported only once in an article dedicated to a novel approach to the calibration update, which was tested on the available data set, often public or artificial one. It is important to note that nothing precludes application of methods developed for one type of sensor system to the other.

Finally, while a wide number of algorithms of both drift reduction and calibration update were described, they were mostly tested in the model samples. Only few works dealt with

analysis of the real world samples and none of the methods was tested in the real world setting and for long periods of time. More applications of calibration update techniques to the sensor systems deployed in real world scenarios are called for.

## AUTHOR CONTRIBUTIONS

The author confirms being the sole contributor of this work and approved it for publication.

## REFERENCES

- Artursson, T., Eklöv, T., Lundström, I., Mårtensson, P., Sjöström, M., and Holmberg, M. (2000). Drift correction for gas sensors using multivariate methods. *J. Chemometr.* 14, 711–723. doi: 10.1002/1099-128X(200009/12)14:5/6<711::AID-CEM607>3.0.CO;2-4
- Bai, H., and Shi, G. (2007). Gas sensors based on conducting polymers. *Sensors* 7, 267–307. doi: 10.3390/s7030267
- Balaban, M. O., Korel, F., Odabasi, A. Z., and Folkes, G. (2000). Transportability of data between electronic noses: mathematical methods. *Sens. Actuators B Chem.* 71, 203–211. doi: 10.1016/S0925-4005(00)00617-1
- Bernabeij, M., Pantalei, S., and Persaud, K. C. (2016). “Large-scale chemical sensor arrays for machine olfaction,” in *Essentials of Machine Olfaction and Taste*, ed T. Nakamoto (Singapore: John Wiley and Sons, Singapore Pte Ltd.), 49–85. doi: 10.1002/9781118768495.ch3
- Bouveresse, E., Hartmann, C., Massart, D. L., Last, I. R., and Prebble, K. A. (1996). Standardization of near-infrared spectrometric instruments standardization of near-infrared spectrometric instruments. *Anal. Chem.* 68, 982–990. doi: 10.1021/ac9510595
- Capron, X., Walczak, B., De Noord, O. E., and Massart, D. L. (2005). Selection and weighting of samples in multivariate regression model updating. *Chemometr. Intelligent Lab. Syst.* 76, 205–214. doi: 10.1016/j.chemolab.2004.11.003
- Cavanillas, S., Winquist, F., and Eriksson, M. (2015). A self-polishing platinum ring voltammetric sensor and its application to complex media. *Analyt. Chim. Acta* 859, 29–36. doi: 10.1016/j.aca.2014.11.039
- Cruz, M. G. N., Ferreira, N. S., Gomes, M. T. S. R., Botelho, M. J., Costa, S. T., Vale, C., et al. (2018). Determination of paralytic shellfish toxins using potentiometric electronic tongue. *Sens. Actuators B Chem.* 263, 550–556. doi: 10.1016/j.snb.2018.02.158
- de Castro, L. N., and von Zuben, F. J. (2002). Learning and optimization using the clonal selection principle. *IEEE Trans. Evol. Comput.* 6, 239–251. doi: 10.1109/TEVC.2002.1011539
- De Marco, R., Jee, E., Prince, K., Pretsch, E., and Bakker, E. (2009). Synthesis and characterization of high-integrity solid-contact polymeric ion sensors. *J. Solid State Electrochem.* 13, 137–148. doi: 10.1007/s10008-008-0600-9
- De Marco, R., Pejcic, B., Prince, K., and van Riessen, A. (2003). A multi-technique surface study of the mercury(ii) chalcogenide ion-selective electrode in saline media. *Analyst* 128, 742–749. doi: 10.1039/b212914k
- De Marco, R., Veder, J.-P., Clarke, G., Nelson, A., Prince, K., Pretsch, E., et al. (2008). Evidence of a water layer in solid-contact polymeric ion sensors. *Phys. Chem. Chem. Phys.* 10, 73–76. doi: 10.1039/B714248j
- De Vito, S., Fattoruso, G., Pardo, M., Tortorella, F., and Di Francia, G. (2012). Semi-supervised learning techniques in artificial olfaction: a novel approach to classification problems and drift counteraction. *IEEE Sensors J.* 12, 3215–3224. doi: 10.1109/JSEN.2012.2192425
- Debus, B., Kirsanov, D. O., Panchuk, V. V., Semenov, V. G., and Legin, A. (2017). Three-point multivariate calibration models by correlation constrained MCR-ALS: a feasibility study for quantitative analysis of complex mixtures. *Talanta* 163, 39–47. doi: 10.1016/j.talanta.2016.10.081
- Deshmukh, S., Bandyopadhyay, R., Bhattacharyya, N., Pandey, R. A., and Jana, A. (2015). Application of electronic nose for industrial odors and gaseous emissions measurement and monitoring—an overview. *Talanta* 144, 329–340. doi: 10.1016/j.talanta.2015.06.050
- Deshmukh, S., Kamde, K., Jana, A., Korde, S., Bandyopadhyay, R., Sankar, R., et al. (2014). Calibration transfer between electronic nose systems for rapid *in situ* measurement of pulp and paper industry emissions. *Analyt. Chim. Acta* 841, 58–67. doi: 10.1016/j.aca.2014.05.054
- Di Natale, C., Davide, F. A. M., and D’Amico, A. (1995). A self-organizing system for pattern classification: time varying statistics and sensor drift effects. *Sensors and Actuators B: Chemical*, 27(1–3), 237–241. doi: 10.1016/0925-4005(94)01593-7
- Di Natale, C., Martinelli, E., and D’Amico, A. (2002). Counteraction of environmental disturbances of electronic nose data by independent component analysis. *Sens. Actuators B Chem.* 82, 158–165. doi: 10.1016/S0925-4005(01)01001-2
- Distante, C., Siciliano, P., and Persaud, K. C. (2002). Dynamic cluster recognition with multiple self-organising maps. *Pattern Analysis Appl.* 5, 306–315. doi: 10.1007/s100440200027
- Ergen, B. (2012). “Signal and image denoising using wavelet transform,” in *Advances in Wavelet Theory and Their Applications in Engineering, Physics and Technology*, ed D. Baleanu (IntechOpen), 495–514. doi: 10.5772/36434
- Faragher, R. (2012). Understanding the basis of the kalman filter via a simple and intuitive derivation [lecture notes]. *IEEE Signal Process. Magazine* 29, 128–132. doi: 10.1109/MSP.2012.2203621
- Fernandez, L., Guney, S., Gutierrez-Galvez, A., and Marco, S. (2016). Calibration transfer in temperature modulated gas sensor arrays. *Sens. Actuators B Chem.* 231, 276–284. doi: 10.1016/j.snb.2016.02.131
- Feudale, R., Woody, N., Tan, H., Myles, A., Brown, S., and Ferre, J. (2002). Transfer of multivariate calibration models: a review. *Chemometr. Intelligent Lab. Syst.* 64, 181–112. doi: 10.1016/S0169-7439(02)00085-0
- Flury, B. N. (1984). Common principal components in k groups. *J. Am. Stat. Assoc.* 79, 892–898. doi: 10.2307/2288721
- Fonollosa, J., Fernández, L., Gutiérrez-Gálvez, A., Huerta, R., and Marco, S. (2016). Calibration transfer and drift counteraction in chemical sensor arrays using direct standardization. *Sens. Actuators B Chem.* 236, 1044–1053. doi: 10.1016/j.snb.2016.05.089
- García Muñoz, S., MacGregor, J. F., and Kourtzi, T. (2005). Product transfer between sites using Joint-Y PLS. *Chemometr. Intelligent Lab. Syst.* 79, 101–114. doi: 10.1016/j.chemolab.2005.04.009
- Green, R. L., and Kalivas, J. H. (2002). Graphical diagnostics for regression model determinations with consideration of the bias/variance trade-off. *Chemometr. Intell. Lab. Syst.* 60, 173–188. doi: 10.1016/S0169-7439(01)00194-0
- Gutierrez-Osuna, R. (2000). “Drift reduction for metal-oxide sensor arrays using canonical correlation regression and partial least squares,” in *Proceedings of the 7th International Symposium On Olfaction & Electronic Nose*, 1–7. Available online at [http://research.cs.tamu.edu/prism/publications/isoen00\\_gutierrez.pdf](http://research.cs.tamu.edu/prism/publications/isoen00_gutierrez.pdf)
- Haugen, J. E., Tomic, O., and Kvaal, K. (2000). A calibration method for handling the temporal drift of solid state gas-sensors. *Analyt. Chim. Acta* 407, 23–39. doi: 10.1016/S0003-2670(99)00784-9
- He, N., Höfler, L., Latonen, R. M., and Lindfors, T. (2015). Influence of hydrophobization of the polyazulene ion-to-electron transducer on the potential stability of calcium-selective solid-contact electrodes. *Sens. Actuators B Chem.* 207, 918–925. doi: 10.1016/j.snb.2014.10.048
- Heiberger, R. M., and Becker, R. A. (1992). Design of an S function for robust regression using iteratively reweighted least squares. *J. Comput. Graph. Stat.* 1, 181–196. doi: 10.2307/1390715

## ACKNOWLEDGMENTS

Thanks are due for the financial support to CESAM (UID/AMB/50017-POCI-01-0145-FEDER-007638), to FCT/MCTES through national funds (PIDDAC), and the co-funding by the FEDER, within the PT2020 Partnership Agreement and Compete 2020, to FCT for post-doctoral fellowship SFRH/BPD/104265/2014 and to MAR 2020 (MAR-02.01.01-FEAMP-0025).

- Hoaglin, D. C., and Welsch, R. E. (1978). The hat matrix in regression and anova. *Am. Statist.* 32, 17–22.
- Holmberg, M., Davide, F. A. M., Di Natale, C., D'Amico, A., Winquist, F., and Lundström, I. (1997). Drift counteraction in odour recognition applications: lifelong calibration method. *Sens. Actuators B Chem.* 42, 185–194. doi: 10.1016/S0925-4005(97)80335-8
- Holmberg, M., Winquist, F., Lundström, I., Davide, F., DiNatale, C., and D'Amico, A. (1996). Drift counteraction for an electronic nose. *Sens. Actuators B Chem.* 36, 528–535. doi: 10.1016/S0925-4005(97)80124-4
- Holmin, S., Krantz-Rücker, C., and Winquist, F. (2004). Multivariate optimisation of electrochemically pre-treated electrodes used in a voltammetric electronic tongue. *Analyt. Chim. Acta* 519, 39–46. doi: 10.1016/j.aca.2004.03.070
- Hosseini-Babaei, F., and Ghafarinia, V. (2010). Compensation for the drift-like terms caused by environmental fluctuations in the responses of chemoresistive gas sensors. *Sensors Actuat. B Chem.* 143, 641–648. doi: 10.1016/j.snb.2009.10.006
- Huerta, R., Mosqueiro, T., Fonollosa, J., Rulkov, N. F., and Rodriguez-Lujan, I. (2016). Online decorrelation of humidity and temperature in chemical sensors for continuous monitoring. *Chemometr. Intelligent Lab. Syst.* 157, 169–176. doi: 10.1016/j.chemolab.2016.07.004
- Hyvärinen, A., and Oja, E. (2000). Independent component analysis: algorithms and applications. *Neural Netw.* 13, 411–430. doi: 10.1016/S0893-6080(00)00026-5
- Jaeckle, C. M., and Macgregor, J. F. (1998). Product design through multivariate statistical analysis of process data. *AICHe J.* 44, 1105–1118. doi: 10.1002/aic.690440509
- Kalivas, J. H., Siano, G. G., Andries, E., and Goicoechea, H. C. (2009). Calibration maintenance and transfer using Tikhonov regularization approaches. *Appl. Spectr.* 63, 800–809. doi: 10.1366/000370209788701206
- Kashwan, K. R., and Bhuyan, M. (2005). “Robust electronic-nose system with temperature and humidity drift compensation for tea and spice flavour discrimination,” in *2005 Asian Conference on Sensors and the International Conference on New Techniques in Pharmaceutical and Biomedical Research- Proceedings* (Kuala Lumpur), 154–158. doi: 10.1109/ASENSE.2005.1564528
- Kemp, N. T., Kaiser, A. B., Trodahl, H. J., Chapman, B., Buckley, R. G., Partridge, A. C., et al. (2006). Effect of ammonia on the temperature-dependent conductivity and thermopower of polypyrrole. *J. Polymer Sci. Part B Polym. Phys.* 44, 1331–1338. doi: 10.1002/polb.20792
- Kennard, R., and Stone, L. A. (1969). Computer aided design of experiments. *Technometrics* 11, 137–148. doi: 10.1080/00401706.1969.10490666
- Kermitt, M., and Tomic, O. (2003). Independent component analysis applied on gas sensor array measurement data. *Sensors J. IEEE* 3, 218–228. doi: 10.1109/JSEN.2002.807488
- Khaydukova, M., Medina-Plaza, C., Rodriguez-Mendez, M. L., Panchuk, V., Kirsanov, D., and Legin, A. (2017a). Multivariate calibration transfer between two different types of multisensor systems. *Sens. Actuat. B Chem.* 246, 994–1000. doi: 10.1016/j.snb.2017.02.099
- Khaydukova, M., Panchuk, V., Kirsanov, D., and Legin, A. (2017b). Multivariate calibration transfer between two potentiometric multisensor systems. *Electroanalysis* 29, 2161–2166. doi: 10.1002/elan.201700190
- Kohonen, T. (1996). *Self-Organizing Maps*, Kohonen.pdf.
- Kondratowicz, B., Narayanaswamy, R., and Persaud, K. C. (2001). An investigation into the use of electrochromic polymers in optical fibre gas sensors. *Sens. Actuators B. Chem.* 74, 138–144. doi: 10.1016/S0925-4005(00)00723-1
- Korotcenkov, G., and Cho, B. K. (2011). Instability of metal oxide-based conductometric gas sensors and approaches to stability improvement (short survey). *Sens. Actuators B. Chem.* 156, 527–538. doi: 10.1016/j.snb.2011.02.024
- Kunz, M. R., Kalivas, J. H., and Andries, E. (2010). Model updating for spectral calibration maintenance and transfer using 1-norm variants of tikhonov regularization. *Analytical Chem.* 82, 3642–3649. doi: 10.1021/ac902881m
- Legin, A., Rudnitskaya, A., and Vlasov, Y. (2003). Chapter 10 electronic tongues: new analytical perspective for chemical sensors. *Compr. Anal. Chem.* 39, 437–486. doi: 10.1016/S0166-526X(03)80115-0
- Liang, Z., Tian, F., Yang, S. X., Zhang, C., Sun, H., and Liu, T. (2018). Study on interference suppression algorithms for electronic noses: a review. *Sensors* 18:1179. doi: 10.3390/s18041179
- Liang, Z., Tian, F., Zhang, C., Sun, H., Liu, X., and Yang, S. X. (2017). A correlated information removing based interference suppression technique in electronic nose for detection of bacteria. *Analyt. Chim. Acta* 986, 145–152. doi: 10.1016/j.aca.2017.07.028
- Lindfors, T., and Ivaska, A. (2004). Stability of the inner polyaniline solid contact layer in all-solid-state K+-selective electrodes based on plasticized poly(vinyl chloride). *Analyt. Chem.* 76, 4387–4394. doi: 10.1021/ac049439q
- Lisak, G., Arnebrant, T., Lewenstam, A., Bobacka, J., and Ruzgas, T. (2016). *In situ* potentiometry and ellipsometry: a promising tool to study biofouling of potentiometric sensors. *Anal. Chem.* 88, 3009–3014. doi: 10.1021/acs.analchem.5b04364
- Magna, G., Mosciano, F., Martinelli, E., and Di Natale, C. (2018). Unsupervised on-line selection of training features for a robust classification with drifting and faulty gas sensors. *Sens. Actuators B Chem.* 258, 1242–1251. doi: 10.1016/j.snb.2017.12.005
- Mallat, S. G. (1989). A theory for multiresolution signal decomposition: the wavelet representation. *IEEE Trans. Pattern Analysis Machine Intelligence* 11, 674–693. doi: 10.1109/34.192463
- Marco, S., and Gutierrez-Galvez, A. (2012). Signal and data processing for machine olfaction and chemical sensing: a review. *IEEE Sens. J.* 12, 3189–3214. doi: 10.1109/JSEN.2012.2192920
- Marco, S., Ortega, A., Pardo, A., and Samitier, J. (1998). Gas identification with tin oxide sensor array and self-organizing maps: adaptive correction of sensor drifts. *IEEE Trans. Instrument. Meas.* 47, 316–321. doi: 10.1109/19.728841
- Martens, H., Høy, M., Wise, B. M., Bro, R., and Brockhoff, P. B. (2003). Pre-whitening of data by covariance-weighted pre-processing. *J. Chemometr.* 17, 153–165. doi: 10.1002/cem.780
- Martinelli, E., Magna, G., De Vito, S., Di Fuccio, R., Di Francia, G., Vergara, A., et al. (2013). An adaptive classification model based on the artificial immune system for chemical sensor drift mitigation. *Sens. Actuators B Chem.* 177, 1017–1026. doi: 10.1016/j.snb.2012.11.107
- Martinelli, E., Magna, G., Vergara, A., and Di Natale, C. (2014). Cooperative classifiers for reconfigurable sensor arrays. *Sens. Actuators B Chem.* 199, 83–92. doi: 10.1016/j.snb.2014.03.070
- Meixner, H., and Lampe, U. (1996). Metal oxide sensors. *Sens. Actuators B. Chem.* 33, 198–202. doi: 10.1016/0925-4005(96)80098-0
- Mumyakmaz, B., Özmen, A., Ebeoglu, M. A., Taşlantı, C., and Gürol, I. (2010). A study on the development of a compensation method for humidity effect in QCM sensor responses. *Sens. Actuators B Chem.* 147, 277–282. doi: 10.1016/j.snb.2010.03.019
- Navarro-Moreno, J. (2008). ARMA prediction of widely linear systems by using the innovations algorithm. *IEEE Trans. Signal Process.* 56, 3061–3068. doi: 10.1109/TSP.2008.919396
- Olsson, J., Winquist, F., and Lundström, I. (2006). A self polishing electronic tongue. *Sens. Actuators B. Chem.* 118, 461–465. doi: 10.1016/j.snb.2006.04.042
- Padilla, M., Perera, A., Montoliu, I., Chaudry, A., Persaud, K., and Marco, S. (2010). Drift compensation of gas sensor array data by orthogonal signal correction. *Chemometr. Intelligent Lab. Syst.* 100, 28–35. doi: 10.1016/j.chemolab.2009.10.002
- Panchuk, V., Lvova, L., Kirsanov, D., Gonçalves, C. G., Di Natale, C., Paolesse, R., et al. (2016). Extending electronic tongue calibration lifetime through mathematical drift correction: Case study of microcystin toxicity analysis in waters. *Sens. Actuators B Chem.* 237, 962–968. doi: 10.1016/j.snb.2016.07.045
- Pijolat, C., Pupier, C., Sauvan, M., Tournier, G., and Lalauze, R. (1999). Gas detection for automotive pollution control. *Sens. Actuators B. Chem.* 59, 195–202. doi: 10.1016/S0925-4005(99)00220-8
- Rudnitskaya, A., Costa, A. M. S., and Delgadillo, I. (2017). Calibration update strategies for an array of potentiometric chemical sensors. *Sens. Actuators B. Chem.* 238, 1181–1189. doi: 10.1016/j.snb.2016.06.075
- Sales, F., Callao, M. P., and Rius, F. X. (1999). Multivariate standardization techniques on ion-selective sensor arrays. *Analyst* 124, 1045–1051. doi: 10.1039/a902585e

- Sales, F., Pilar Callao, M., and Xavier Rius, F. (2000). Multivariate standardization for correcting the ionic strength variation on potentiometric sensor arrays. *Analyst* 125, 883–888. doi: 10.1039/a909500d
- Schaller, E., Bosset, J. O., and Escher, F. (1998). 'Electronic noses' and their application to food. *LWT* 316, 305–316.
- Schaller, E., Bosset, J. O., and Escher, F. (2000). Instability of conducting polymer sensors in an electronic nose system. *Analisis* 28, 217–227. doi: 10.1051/analisis:2000113
- Shaham, O., Carmel, L., and Harel, D. (2005). On mappings between electronic noses. *Sens. Actuators B. Chem.* 106, 76–82. doi: 10.1016/j.snb.2004.05.039
- Sharma, R. K., Chan, P. C. H., Tang, Z., Yan, G., Hsing, I. M., and Sin, J. K. O. (2001). Investigation of stability and reliability of tin oxide thin-film for integrated micro-machined gas sensor devices. *Sens. Actuators B. Chem.* 81, 9–16. doi: 10.1016/S0925-4005(01)00920-0
- Solórzano, A., Rodríguez-Pérez, R., Padilla, M., Graunke, T., Fernandez, L., Marco, S., et al. (2018). Multi-unit calibration rejects inherent device variability of chemical sensor arrays. *Sens. Actuators B. Chem.* 265, 142–154. doi: 10.1016/j.snb.2018.02.188
- Stork, C. L., and Kowalski, B. R. (1999). Weighting schemes for updating regression models-A theoretical approach. *Chemometr. Intell. Laboratory Syst.* 48, 151–166. doi: 10.1016/S0169-7439(99)00016-7
- Štulík, K. (1992). Activation of solid electrodes. *Electroanalysis* 4, 829–834. doi: 10.1002/elan.1140040902
- Šundić, T., Marco, S., Perera, A., Pardo, A., Hahn, S., Bársan, N., and Weimar, U. (2002). Fuzzy inference system for sensor array calibration: Prediction of CO and CH4 levels in variable humidity conditions. *Chemometr. Intelligent Laborat. Syst.* 64, 103–122. doi: 10.1016/S0169-7439(02)00069-2
- Tian, F., Yan, J., Shan, X., Feng, J., He, Q., Shen, Y., et al. (2012). Background interference elimination in wound detection by electronic nose based on reference vector-based independent component analysis. *Information Technol. J.* 11, 850–858. doi: 10.3923/itj.2012.850.858
- Tomic, O., Ulmer, H., and Haugen, J. E. (2002). Standardization methods for handling instrument related signal shift in gas-sensor array measurement data. *Anal. Chim. Acta* 472, 99–111. doi: 10.1016/S0003-2670(02)00936-4
- Vergara, A., Vembu, S., Ayhan, T., Ryan, M. A., Homer, M. L., and Huerta, R. (2012). Chemical gas sensor drift compensation using classifier ensembles. *Sens. Actuators B. Chem.* 166–167, 320–329. doi: 10.1016/j.snb.2012.01.074
- Vlasov, Y. G., and Bychkov, E. A. (1987). Ion-selective chalcogenide glass electrodes. *Ion-Selective Electrode Review* 9, 5–93.
- Wang, Q., Varghese, O., Grimes, C. A., and Dickey, E. C. (2007). Grain boundary blocking and segregation effects in yttrium-doped polycrystalline titanium dioxide. *Solid State Ionics* 178, 187–194. doi: 10.1016/j.ssi.2006.12.006
- Wang, Y., Veltkamp, D. J., and Kowalski, B. R. (1991). Multivariate instrument standardization. *Anal. Chem.* 63, 2750–2756. doi: 10.1021/ac00023a016
- Winquist, F., Krantz-Rücker, C., and Lundström, I. (2002). Electronic tongues and combinations of artificial senses. *Sensors Update* 11, 279–306. doi: 10.1002/seup.200211107
- Wold, S., Antti, H., Lindgren, F., and Öhman, J. (1998). Orthogonal signal correction of near-infrared spectra. *Chemometr. Intelligent Lab. Syst.* 44, 175–185. doi: 10.1016/S0169-7439(98)00109-9
- Yan, K., and Zhang, D. (2015). Improving the transfer ability of prediction models for electronic noses. *Sens. Actuators B. Chem.* 220, 115–124. doi: 10.1016/j.snb.2015.05.060
- Yan, K., and Zhang, D. (2016a). Calibration transfer and drift compensation of e-noses via coupled task learning. *Sens. Actuators B. Chem.* 225, 288–297. doi: 10.1016/j.snb.2015.11.058
- Yan, K., and Zhang, D. (2016b). Correcting instrumental variation and time-varying drift : a transfer learning approach with autoencoders. *IEEE Trans. Instrument. Meas.* 65, 2012–2022. doi: 10.1109/TIM.2016.2573078
- Zhang, L., Liu, Y., He, Z., Liu, J., Deng, P., and Zhou, X. (2017). Anti-drift in E-nose: a subspace projection approach with drift reduction. *Sens. Actuators B Chem.* 253, 407–417. doi: 10.1016/j.snb.2017.06.156
- Zhang, L., and Peng, X. (2016). Time series estimation of gas sensor baseline drift using ARMA and Kalman based models. *Sensor Rev.* 36, 34–39. doi: 10.1108/SR-05-2015-0073
- Zhang, L., Tian, F., Kadri, C., Xiao, B., Li, H., Pan, L., et al. (2011). On-line sensor calibration transfer among electronic nose instruments for monitoring volatile organic chemicals in indoor air quality. *Sens. Actuators B. Chem.* 160, 899–909. doi: 10.1016/j.snb.2011.08.079
- Zhang, L., Tian, F., Liu, S., Dang, L., Peng, X., and Yin, X. (2013). Chaotic time series prediction of E-nose sensor drift in embedded phase space. *Sens. Actuators B Chem.* 182, 71–79. doi: 10.1016/j.snb.2013.03.003
- Zhang, L., and Zhang, D. (2015). Domain adaptation extreme learning machines for drift compensation in e-nose systems. *IEEE Trans. Instrumentation Meas.* 64, 1790–1801. doi: 10.1109/TIM.2014.2367775
- Ziyatdinov, A., Marco, S., Chaudry, A., Persaud, K., Caminal, P., and Perera, A. (2010). Drift compensation of gas sensor array data by common principal component analysis. *Sens. Actuators B Chem.* 146, 460–465. doi: 10.1016/j.snb.2009.11.034
- Zuppa, M., Distante, C., Persaud, K. C., and Siciliano, P. (2007). Recovery of drifting sensor responses by means of DWT analysis. *Sens. Actuators B Chem.* 120, 411–416. doi: 10.1016/j.snb.2006.02.049
- Zuppa, M., Distante, C., Siciliano, P., and Persaud, K. C. (2004). Drift counteraction with multiple self-organising maps for an electronic nose. *Sens. Actuators B Chem.* 98, 305–317. doi: 10.1016/j.snb.2003.10.029

**Conflict of Interest Statement:** The author declares that the research was conducted in the absence of any commercial or financial relationships that could be construed as a potential conflict of interest.

The handling editor declared a past co-authorship with the author.

Copyright © 2018 Rudnitskaya. This is an open-access article distributed under the terms of the Creative Commons Attribution License (CC BY). The use, distribution or reproduction in other forums is permitted, provided the original author(s) and the copyright owner(s) are credited and that the original publication in this journal is cited, in accordance with accepted academic practice. No use, distribution or reproduction is permitted which does not comply with these terms.



# Advances in the Electronics for Cyclic Voltammetry: the Case of Gas Detection by Using Microfabricated Electrodes

Giorgio Pennazza<sup>1</sup>, Marco Santonico<sup>1</sup>, Luca Vollero<sup>2</sup>, Alessandro Zompanti<sup>1</sup>, Anna Sabatini<sup>1</sup>, Nandeesh Kumar<sup>3,4</sup>, Ivan Pini<sup>3</sup>, William F. Quiros Solano<sup>5</sup>, Lina Sarro<sup>5</sup> and Arnaldo D'Amico<sup>3\*</sup>

<sup>1</sup> Unit of Electronics for Sensor Systems, Department of Engineering, Campus Bio-Medico University of Rome, Rome, Italy,

<sup>2</sup> Unit of Computational Systems and Bioinformatics, Department of Engineering, Campus Bio-Medico University of Rome, Rome, Italy, <sup>3</sup> Department of Electronic Engineering, University of Rome Tor Vergata, Rome, Italy, <sup>4</sup> Lintes Research Laboratory, Teramo, Italy, <sup>5</sup> Laboratory of Electronic Materials, Devices and Components, DIME, Delft University of Technology, Delft, Netherlands

## OPEN ACCESS

### Edited by:

Dmitry Kirsanov,  
Saint Petersburg State University,  
Russia

### Reviewed by:

António Manuel Peres,  
Polytechnic Institute of Bragança,  
Portugal

Ashok K. Sundramoorthy,  
SRM University, India

### \*Correspondence:

Arnaldo D'Amico  
damico@eln.uniroma2.it

### Specialty section:

This article was submitted to  
Analytical Chemistry,  
a section of the journal  
Frontiers in Chemistry

Received: 07 March 2018

Accepted: 12 July 2018

Published: 10 August 2018

### Citation:

Pennazza G, Santonico M, Vollero L, Zompanti A, Sabatini A, Kumar N, Pini I, Quiros Solano WF, Sarro L and D'Amico A (2018) Advances in the Electronics for Cyclic Voltammetry: the Case of Gas Detection by Using Microfabricated Electrodes. *Front. Chem.* 6:327. doi: 10.3389/fchem.2018.00327

This paper presents an advanced voltammetric system to be used as electronic tongue for liquid and gas analysis. It has been designed to be more flexible and accurate with respect to other existing and similar systems. It features improved electronics and additional operative conditions. Among others these include the possibility to optically excite the solution and to treat the output signal by a differentiation process in order to better evidence the existence of small details in the response curve. Finally by the same type of tongue preliminary results are shown dealing with O<sub>2</sub> and CO<sub>2</sub> concentration measurements in appropriate solutions.

**Keywords:** voltammetry, lock-in, gas sensors, electronic interface, multivariate analysis, multivariate pattern analysis, oxygen, carbon dioxide

## INTRODUCTION

Cyclic voltammetry (CV) is one of the most-important and most-widespread applied electrochemical techniques (Legin et al., 1997; Tahara and Toko, 2013). This technique has been also utilized in the design and development of the so-called Electronic Tongue (ET), as multisensory system for liquids.

An ET can be imagined as an ensemble of chemical sensors able to mainly operate in liquids and give chemical images of them. As we know the different tastes that humans can detect by the tongue are five in number and are called as follows: saltines, bitterness, sweetnes, sournes, and umami; for each of them about 100 receptors are available in humans for redundancy purpose.

The ET has been employed to discriminate mainly chemical species in liquids (Legin et al., 1995, 1997, 1999a; Vlasov et al., 2005) by an array of chemically sensitive devices such as ion-selective electrodes characterized by different specificity and through a typical statistical analysis such as Principal Component Analysis (PCA) and Partial least Square (PLS) or specific neural networks (Krantz-Rücker et al., 2001; Legin et al., 2004; Rudnitskaya and Legin, 2008). In this case the total specificity (one sensor for one chemical specie) for each sensor is proved to be not necessary at all. As a matter of fact, in practice it happens that most of the employed sensors for the matrix are

characterized by a rather low specificity (each sensor sensitive to more than one chemical species). On the other hand it is possible to develop specific taste sensors (biosensors) (Rudnitskaya et al., 2008) that only respond to a specific taste type (Vlasov et al., 2000). It is worth pointing out that also for the human tongue, although characterized by sufficiently well localized taste bio-receptors, they seem to be non-perfectly specific.

The (ET) looks like an electronic nose (Legin et al., 1999b; Winquist et al., 2000; Santonico et al., 2013) whose typical ambient is gaseous in character but at the end also in this case a compound image is obtained.

Although many papers have been written so far on ET, technical aspects that are dealing with electronic interface performance, especially with respect to accuracy and versatility have not sufficiently been addressed. For this reason we have oriented the content of this paper toward those technical aspects that are dealing with electronic interface performance when the accuracy and versatility are among the most important parameters to take into account.

Essentially three are the main detection techniques employed for the liquid investigation when an ET is used: (a) Matrix ion selective electrodes, (b) Amperometric analysis, and (c) Voltammetric analysis.

Referring to point (a) we have to consider the use of multi-metal head as an ions multi-sensors system where chemical potentials are measured and associated to the chemical species in solution (Rudnitskaya et al., 2008). In this case techniques such as the PCA-PLS can be advantageously used for the determination of the chemical species present in solution.

Point (b) refers to a technique where red-ox reactions are put in evidence by the measure of the current once a suitable voltage is applied to the electrodes.

Among the different possibilities to deal with this problem, we will confine our attention to the last one, and illustrate the new voltammetric system.

In particular, we will consider along this paper aspects dealing with the improved (ET) related to:

- small signal detection by very highly selective filters;
- low noise amplifiers;
- optical systems for the injection of light power in the proximity of the working electrode;
- high input dynamic range (IDR);
- improved input flexibility including DC bias and ramp together;
- possibility to zoom inside the IDR;
- gas detection in suitable liquids (example with O<sub>2</sub> and CO<sub>2</sub>) (Pennazza et al., 2017; Santonico et al., 2017);
- technology for miniaturized electrodes;
- differentiation of the output signal for higher resolution analysis;

Moreover, In this paper we illustrate some advanced features included in the designed system and comment on the versatility of the information that can be gained by its applications. The possibility of measuring different types of gas (O<sub>2</sub> and CO<sub>2</sub>) fluxed through liquids is also shown.

## MATERIALS AND METHODS

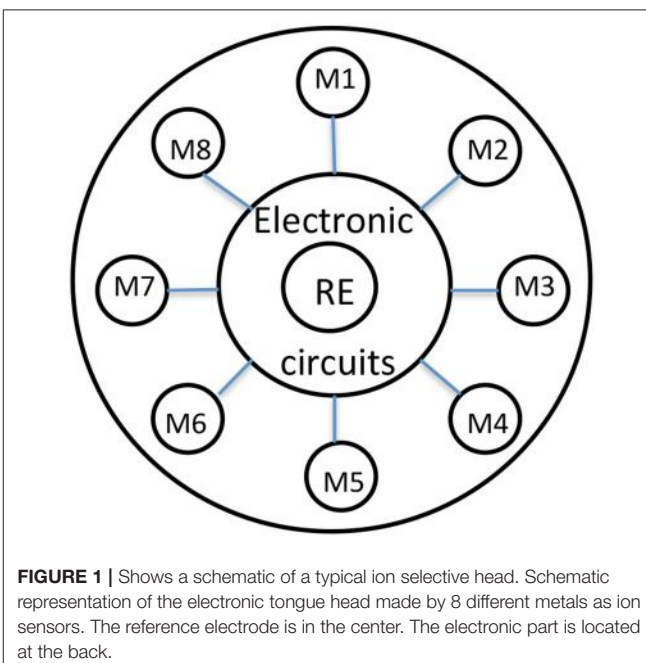
In this section the designing and development of the last sensor system here used is presented. The description starts by the introduction to the sensing system, passing through the innovative device realized by an advanced cyclic voltammetric structure. The interface developed for liquid analysis is illustrated and the sub-section devoted to the electrodes and to the calibration procedure closes the experimental section.

### The Sensing System

The sensing system is based on an electrochemical analytical technique called cyclic-voltammetry, usually used to study a compound, a biological material, or an electrode surface. In voltammetry a time-dependent potential is applied to an electrochemical cell and the resulting current is measured as a function of this potential.

The electrochemical cell used in voltammetry is, in most cases, made of three electrodes, respectively called **working (WE)**, **reference (RE)**, and **counter (CE)** electrode (Figure 1). A time-dependent potential excitation signal is applied between the working electrode and the reference electrode and the current that flows between the working and auxiliary electrodes is measured. Current peaks, observed at specific applied voltages, are due to specific redox reactions running on the working electrode surface. Cyclic Voltammetry (CV) consists of cycling the potential of the reference electrode. The sensing system essentially consists of the following elements: electrochemical cell, electronic interface, microcontroller unit, PC for data analysis.

The signal conditioning stage applies the time-dependent potential between the working and reference electrodes and



converts the current flowing between the working and the auxiliary electrodes into a voltage signal, then digitally acquired by the ADC conversion stage (Figure 2).

## The Advanced Cyclic Voltammetric Structure

Figure 3 represents an advanced and rather complete voltammetric electronic system characterized by high resolution, operating with three conventional electrodes (WE), (CE), and (RE).

$V_{DC}$  represents a bias voltage,  $V_{AC}$  represents a very small amplitude sinusoidal voltage which is added to  $V_{DC}$  and  $V_r$  represents both the positive and negative time dependent ramp function. These three types of signals can be applied one at the

time or coupled to each other in order to give rise to different analysis methodologies. Finally a lock-in amplifier is used to measure the output of the trans-impedance low noise amplifier ( $A_1$ ) The low noise amplifier  $A_2$  has the duty to inject current into the solution by the (CW) and to apply, as an example, both a  $V_{DC}$  voltage to the reference electrode and the ramp voltage  $V_r$ .

The voltage ramp is designed to have a variable slew rate from 0.1 up to 10 mV/s. The system can be programmed through the microcontroller to infer a zoom action in particular points of interest, determined by a significant polarization value of the (RE).

Another important strategy that can be adopted in the system represented in Figure 3 is the presence of an electronic block (B4) able to perform the first time derivative of the output voltage. This is proved to be useful in those cases (complex solutions) where varieties of red-ox reactions can take place, in order to better evidence hidden details of the current changes. Block B2 does represent the output of the trans-impedance amplifier  $A_1$ , while B1 represents the generator of suitable light pulses.

A further strategy considers the output voltage divided in many samples (from 500 up to 1,000) according to the selected division in the time domain. This strategy allows the transformation of an (ET) in a huge number of equivalent sensors with the advantage associated to the matrixes methodology.

## Electronic Tongue for Liquid Analysis: Interfaces

It has been demonstrated that the ET is a practical tool for the investigation of red-ox reaction phenomena in different kind of liquids.

Here we will enter some details aiming at exploring the intrinsic mechanisms of the varieties of electronic circuit behavior in real operative conditions.

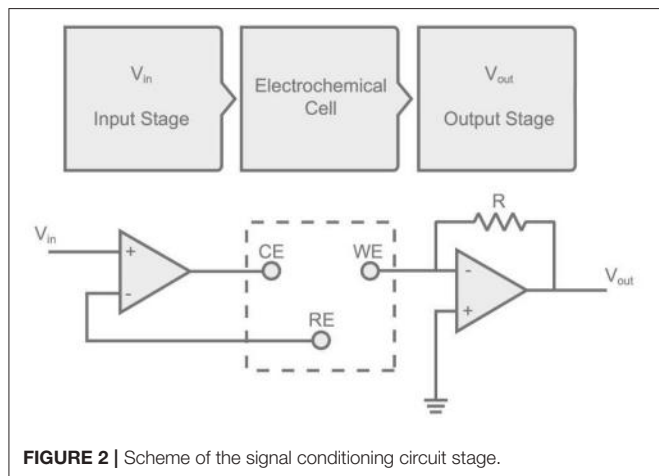


FIGURE 2 | Scheme of the signal conditioning circuit stage.

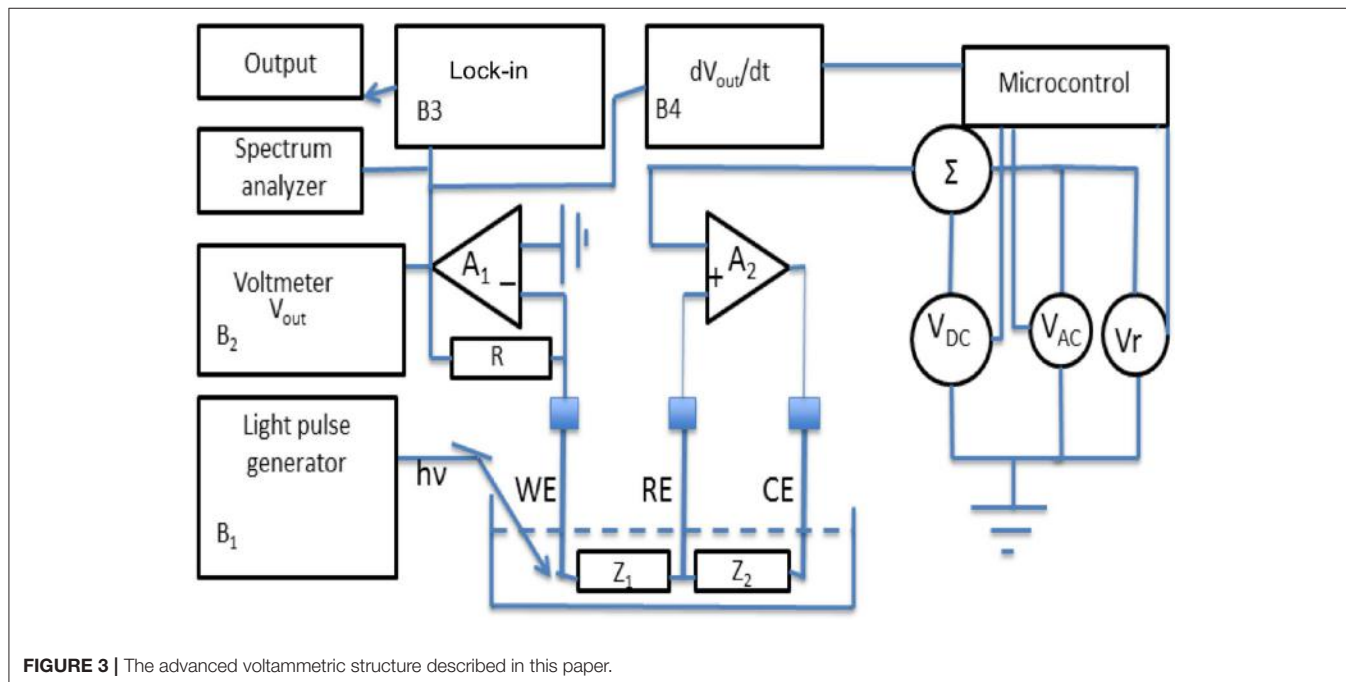
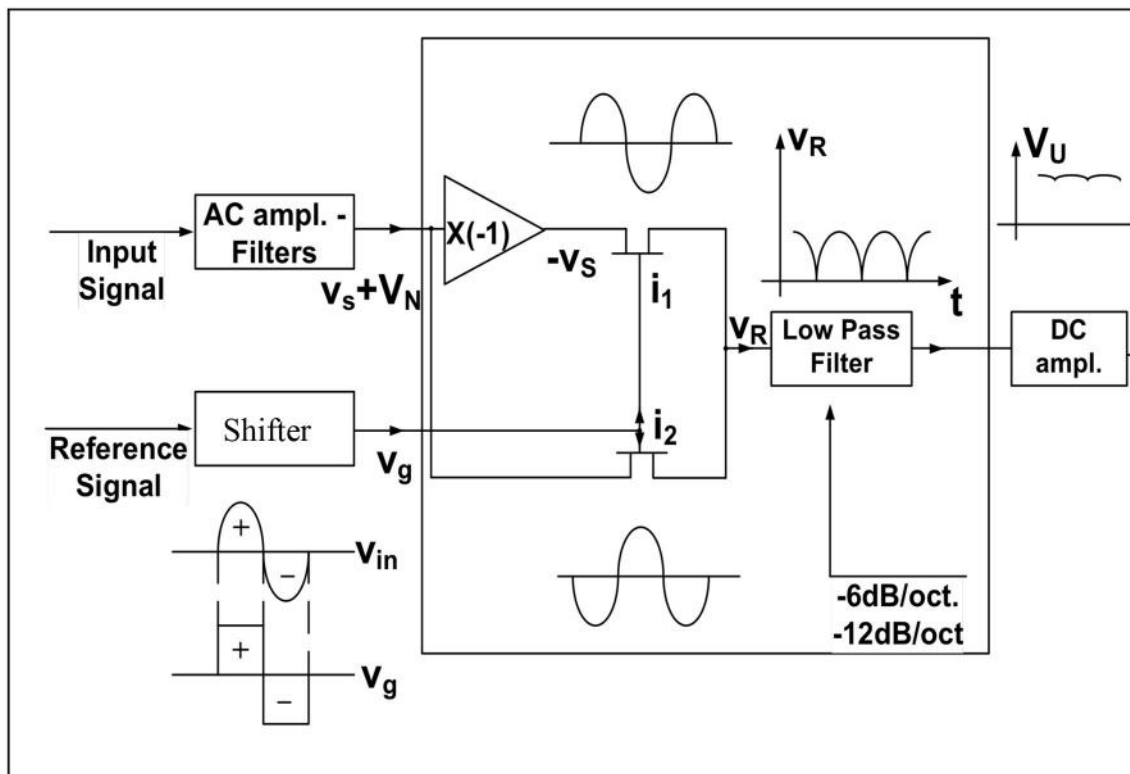
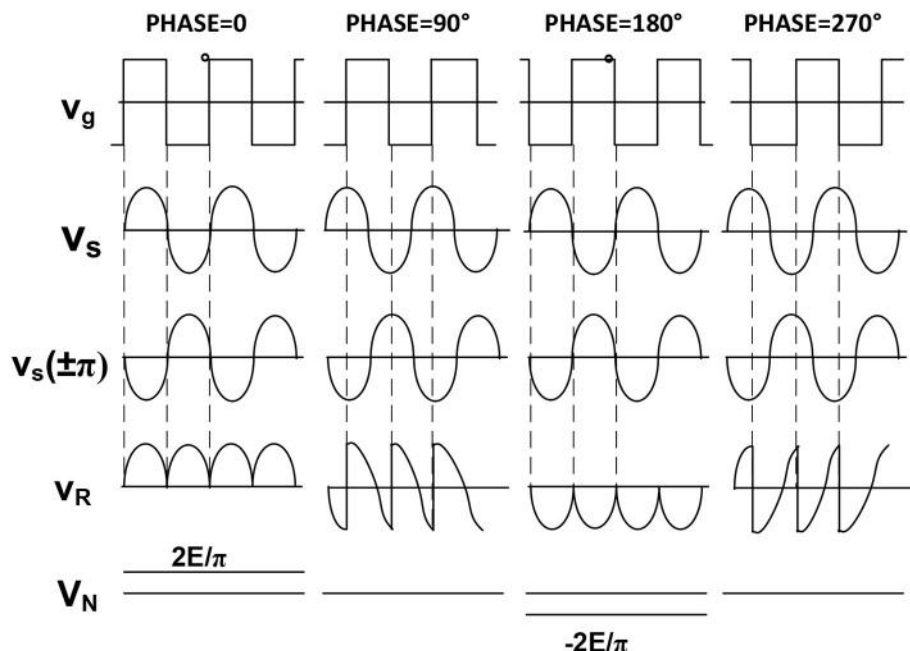


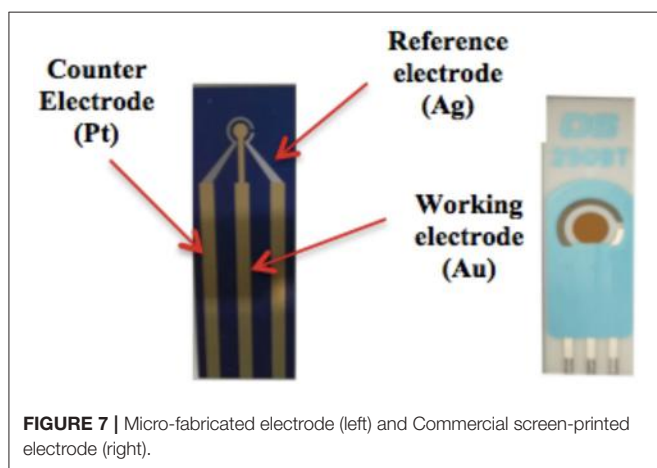
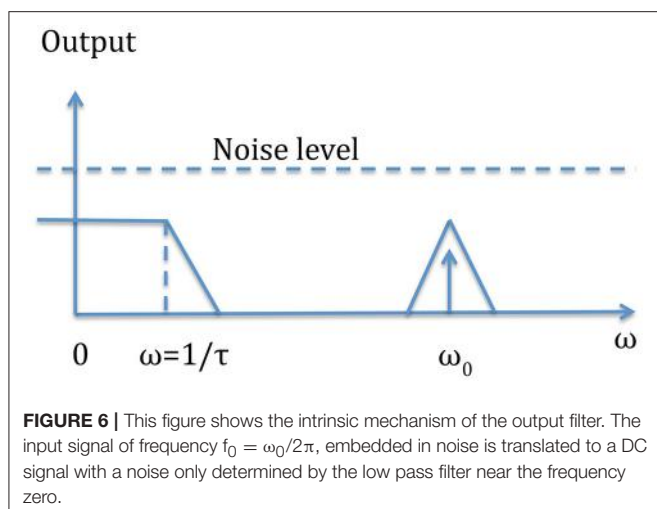
FIGURE 3 | The advanced voltammetric structure described in this paper.



**FIGURE 4** | Schematic of a lock-in amplifier.



**FIGURE 5** | Phase implication on the detection procedure. The output can be positive or negative according to the phase difference between signal and reference. Two are the input signals:  $V_i$  of which it is desirable to measure the amplitude, and  $V_r$  which represents the reference signal.



Furthermore, we will comment on the main results obtained so far by this technique, indicating the possible technical improvements that are necessary to achieve better results in terms of sensitivity and resolution.

Any time that the design involves processing lines for small signals analysis, made by amplification steps, filtering, conversions, all embedded in noise, it is of up most importance a careful characterization of the source of signals in terms of output current or voltage.

This is normally done estimating the impedance value, defining its structure (differential with or without common mode voltages or currents or unbalanced with respect to a reference point, etc.) and the signal to noise (S/N) ratio. This would allow to face the most convenient measurement strategy. In those cases where the S/N is greater than one, usual techniques of amplification and filtering can be employed taking care that the small S/N perturbation should be the main concern. In those cases where the S/N ratio is less than one it is necessary to consider particular techniques listed below and easy to find in the technical notes:

- (1) Lock-in amplifiers (analog or digital) with only one reference frequency.
- (2) Waveform averagers such as for instance the “box car integrators.”
- (3) Autocorrelators and crosscorrelators.

In this paper only the lock-in amplifier operating with a single reference signal is taken into a brief consideration, because it is the most utilized in the sensor context especially when the noise introduces measurement problems.

The Lock-in amplifier can be seen as a very narrow filter whose central frequency can be selected according to the operating frequency of the experiment under test.

It is basically a phase sensitive ac frequency selective voltmeter that compares the input signal against a reference signal in a phase sensitive circuit, producing a dc level proportional to the part of the input signal which is synchronous with the input and in phase with the reference.

The basic principle of a lock-in amplifier is shown in the following Figure 4.

The reference signal is the input of a phase shifter which has the duty to form two output signals able to drive the two gates  $I_1$  and  $I_2$  in order to get the full rectification of the sinusoidal input signal, as shown in the node  $V_R$ . Of course the noise level can be well above this rectified signal. Only after the low pass filter action the noise will be reduced leaving the average output value with a signal to noise ratio larger than one as expected.

Figure 5 shows the paramount importance of having a phase shifter in the reference block. In fact, only if this phase between the input signal and the reference one is  $0^\circ$  or  $270^\circ$  we have a sound meaning of the DC output which reaches the maximum amplitude.

The output  $V_o$  of the synchronous detector is given by the following product:

$$V_R = V_i * V_g$$

$$\text{where } V_i = V_s + V_n$$

The low pass filter located at the output of the synchronous detector will reduce the noise leaving a DC component representing the average value of the rectified sinusoid.

$$V_{\text{OUTPUT}} = \frac{1}{T} \cdot \int_0^T (V_N + V_S) dt = \frac{1}{T} \cdot \int_0^T V_S dt + \text{residual.noise} \quad (1)$$

where  $T$  is the averaging time, i.e., the time necessary to perform the measurement and to reduce the noise.

The higher  $T$  the most effective the noise reduction is.

So a longer waiting time results in a more accurate measurement.

The S/N ratio improvement achievable through the use of a lock-in amplifier can be expressed by the ratio of the signal to noise ratio at the output to the signal to noise ratio at the input.

This improvement can also be expressed as the square root of the signal source bandwidth divided by the equivalent noise bandwidth of the lock-in amplifier, which is given by  $1/4\tau$  ( $\tau = RC$ ) in the case of 6 db/octave output filter.

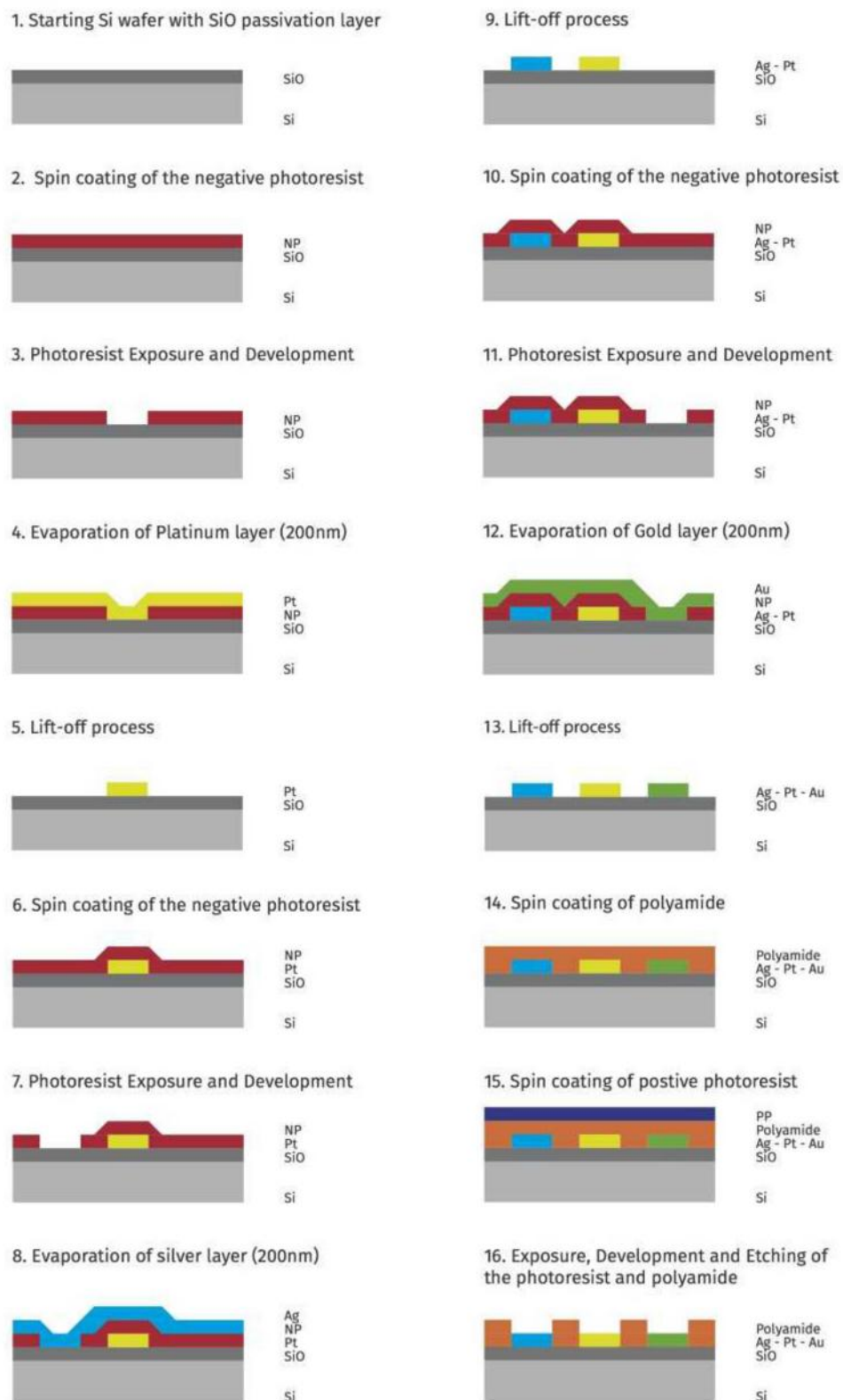
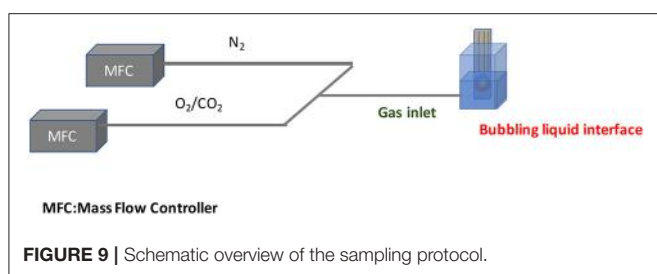


FIGURE 8 | Main fabrication steps for the microfabricated electrodes.



**TABLE 1 |** Comparison of the two electrode models.

Screen-printed electrodes (SPE)	
Interpolating function	$2.93 \cdot 10^{-6}x^2 + 3.28 \cdot 10^{-6}x + 2.36 \cdot 10^{-6}$
R-square factor	0.9839
Sensitivity function	$5.86 \cdot 10^{-6}x + 3.278 \cdot 10^{-6}$
LOD (noise current 10 nA)	0.0031 M
Micro-fabricated electrodes (MFE)	
Interpolating function	$9.51 \cdot 10^{-7}x^2 + 1.13 \cdot 10^{-5}x + 3.54 \cdot 10^{-6}$
R-square factor	0.9939
Sensitivity function	$1.9 \cdot 10^{-5}x + 1.13 \cdot 10^{-5}$
LOD (noise current 10 nA)	0.0009 M

So in order to increase the improvement ratio by a factor of 10, it is necessary to increase the output filter time constant by a factor 100.

It is worth mentioning that a lock-in amplifier can be seen as a narrow filter whose Q (quality factor of the filter) can be expressed as  $Q = \frac{f_0}{\Delta f}$  where  $f_0$  is the operating frequency and  $\Delta f$  is the bandwidth of the output filter given by  $\Delta f = \frac{1}{4\tau}$  and centered in the origin of the frequency axes.

The higher the operating frequency is, the higher both the Q and the noise rejection are.

In some applications the signal is modulated at a given frequency so integrated lock-in amplifiers can be advantageously used to achieve a better S/N ratio. **Figure 6** schematically shows how the lock-in filter works: the equivalent filter is that of a low pass filter whose width can be reduced increasing the time constant. So in order to have a high Q filter we have to increase the measuring time. This means that a trade-off must be reached between a low signal to noise ratio and the measurement time.

The system has been tested from the noise point of view, especially as far as the trans-amplifier (A1) is concerned. It has been designed and constructed by assembling discrete bipolar transistors. The measured noise spectral density in the bandwidth ranging from 1 Hz up to 100 KHz has been as low as  $1 \text{ nV}/(\text{Hz})^{1/2}$ . This has permitted to reach high resolution values during the measurements.

## Electrodes

The sensing system was tested with two types of electrodes (reported in **Figure 7**):

- A Micro-fabricated electrode,
- A commercial screen-printed electrode.

## Commercial Screen-Printed Electrodes (SPE)

The system can use commercial screen printed electrodes made by Dropsens (ref. code 250BT). The working electrode is made of gold and has a diameter of 4 mm, the counter electrode is made of platinum, the reference electrode is made of silver and all the other electric contacts are made of silver.

The supporting material is ceramic and the total thickness of the electrode is 1 mm. The thickness of the metal material screen-printed on the electrode is about 1  $\mu\text{m}$ . The surface roughness is quite high.

## Micro-Fabricated Electrodes (MFE)

Micro-fabricated electrodes were designed to improve the performances of the sensing system. The main aim was to have a more effective control on the fabrication of the electrodes. In fact, using a micro-fabrication process it is possible to control the thickness of each metal layer, the purity of the materials and the surface roughness.

The electrodes were fabricated in the Else Kooi Laboratory of the Delft University of Technology.

The metals used in the micro-fabricated electrode are the same as those of the SPE. Two batches of the MFE were fabricated: one with a 4 mm-long working electrode (in practice with geometry and size identical to the SPE type); another with the same geometry of the SPE, but with a smaller working electrode diameter, namely 1 mm. In the following we will refer to the first and to the second respectively as MFE-4 and MFE-1.

The fabrication process is schematically illustrated in **Figure 8**. The starting substrate is a 4" diameter silicon wafer on which 300 nm of thermal oxide for substrate isolation is grown (**Figure 8.1**). The first metal electrode, the counter electrode, is formed using a lift-off process (**Figures 8.2–8.5**). First, a 1.5  $\mu\text{m}$ -thick photoresist layer is spun and pre-baked at 100°C for 60 s. The electrode pattern is then exposed using contact exposure and developed using MF-300 series developer. After development, a deep UV post-exposure and an oxygen plasma flash to clean are performed to condition the photoresist for the lift-off process and to remove any residue from the surface where the metal is to be deposited, respectively. Subsequently, a 200 nm-thick platinum layer is deposited by thermal evaporation. The lift-off (removal of the photoresist and the undesired platinum) is done in an ultrasonic bath of NMP (N-Methyl-2-pyrrolidone) at 70°C. The substrate is rinsed in DI water and dry with a spin dryer to guarantee a clean surface prior the following second and third metal electrodes deposition and patterning.

To fabricate the reference electrode (Ag) and working electrode (Au), a 200 nm-thick layer is evaporated for both metals. The patterning and lift-off process is performed as previously described (**Figures 8.6–8.13**).

Finally a 5  $\mu\text{m}$  polyimide layer is deposited by spin coating (**Figure 8.14**) and patterned to expose the contact areas to the solution and to isolate the metal lines. The polyimide is patterned (**Figures 8.15, 8.16**) using conventional lithography. The unwanted polyimide layer is etched in 25% TMAH (Tetramethylammonium hydroxide) solution.

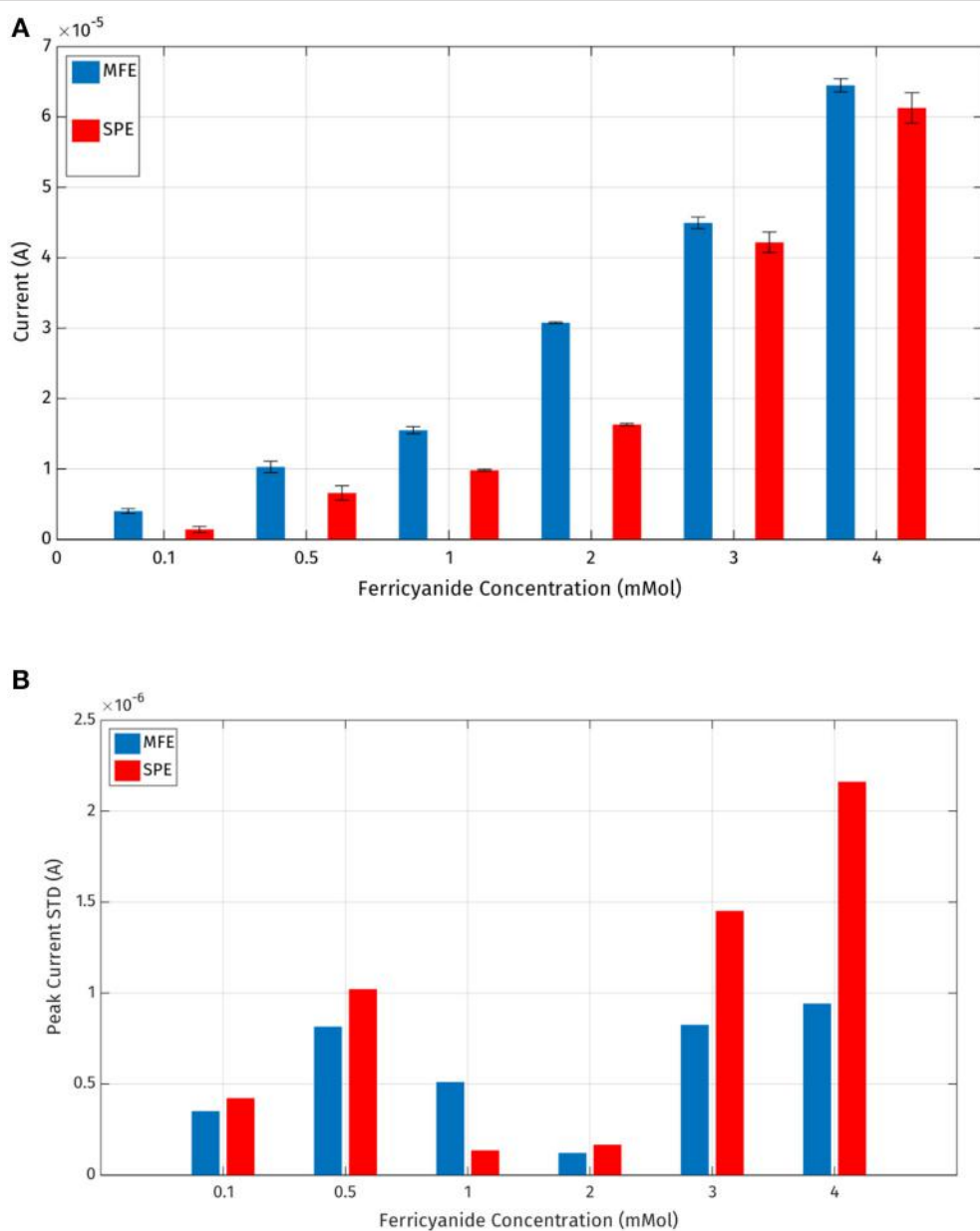


**FIGURE 10 | (A)** Mean values and standard deviations of the output current peaks registered by the MFE and SPE reported in **Table 1**; **(B)** standard deviations of the output current peaks.

Finally, the masking photoresist is stripped in oxygen plasma and the polyimide is thermally cross-linked in a vacuum oven at 350°C more details can be found in the **Supplementary Material**.

## Calibration Procedure

In order to compare different behaviors of the electrodes described before, a dedicated electronic interface has been designed, based on a comparator coupled with a trans-impedance circuit. The system provides signals to an ADC device and the acquisition board is based on an ATMEL 328 microprocessor

with a 12 bit converter. The input signals are generated by an internal function generator which can provide different periodic waves (square, triangular, sine) at different frequencies.

The sensor system has been calibrated via a specific sampling procedure. In order to reduce the effects of sampling errors an apparatus composed of a mass flow controller (MFC) with a minimum dilution of 1:400 was used.

In **Figure 9** a schematic drawing of the experimental set-up is shown.

The *MFC* was used in the sensor calibration to provide different concentrations of gases (in this work CO<sub>2</sub> and O<sub>2</sub>).

The output of each MFC device is mixed in order to obtain different percentage of  $N_2$  as carrier gas and of the target gas ( $O_2$ ,  $CO_2$ ). Both commercial electrodes and custom micro fabricated electrodes described before were immersed in a target solution of 4 ml in volume. The solution has to be bubbled with a one of the gas target for 30s. The high-resolution of the system allowed the

analysis of even small charge changes in the solution (Pennazza et al., 2017).

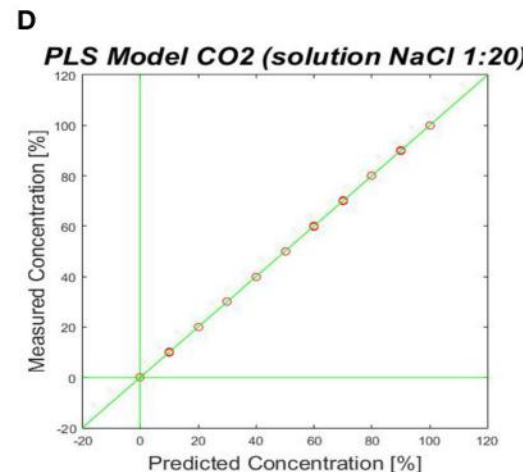
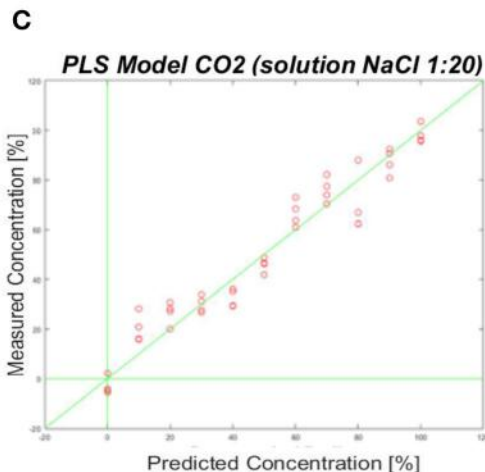
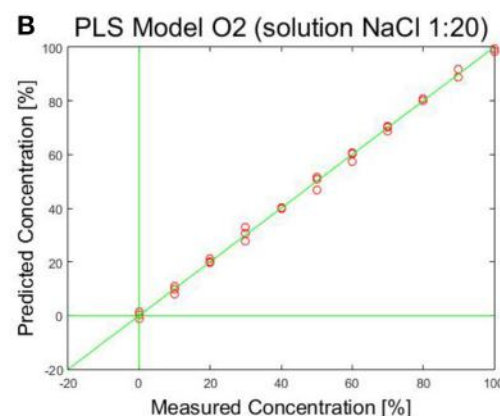
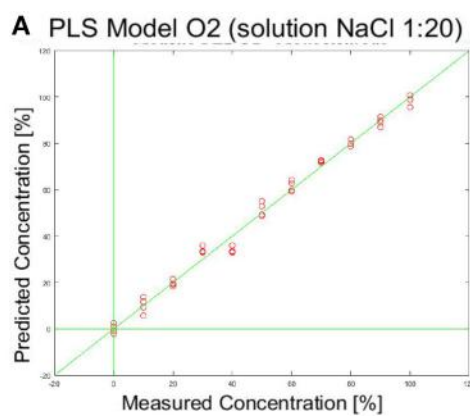
In particular the tested solutions are: (1) physiological solution; (2) a mixture of a suitable physiological solution in distilled water with 1:20 ratio. This ratio has been experimentally determined in order to give a sufficient conductivity to the solution.

When the electrodes are immersed into the solution, the electronic interface activates the electrodes by applying one of these three wave forms: triangular, sine and square.

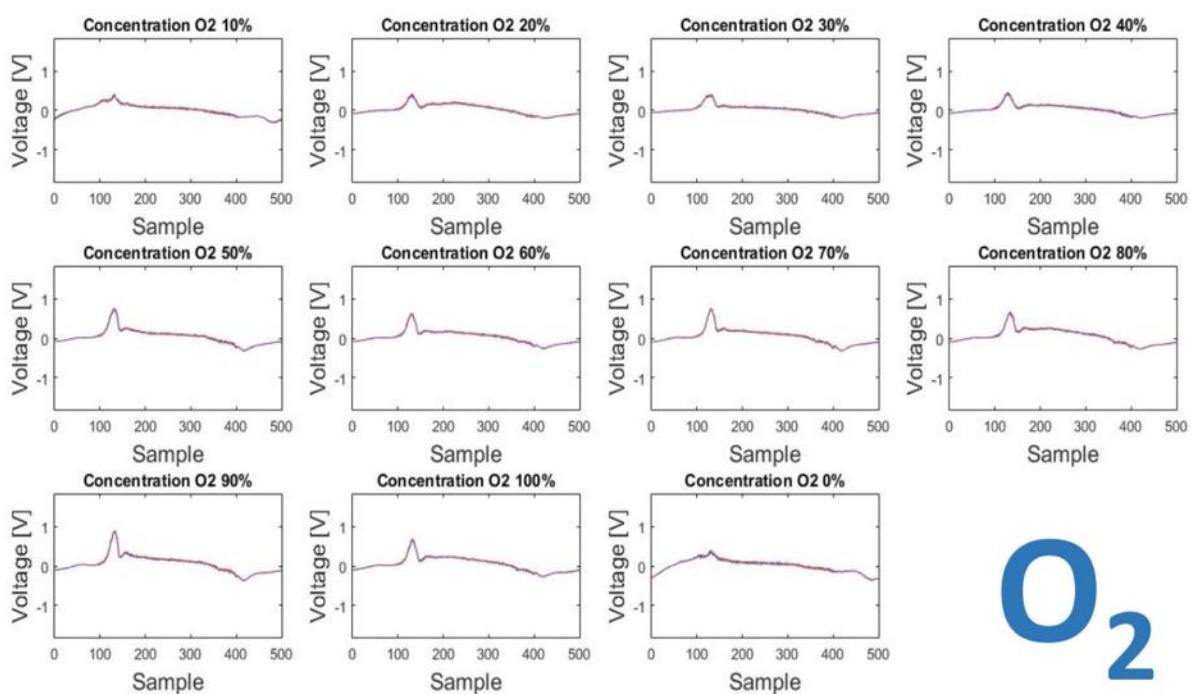
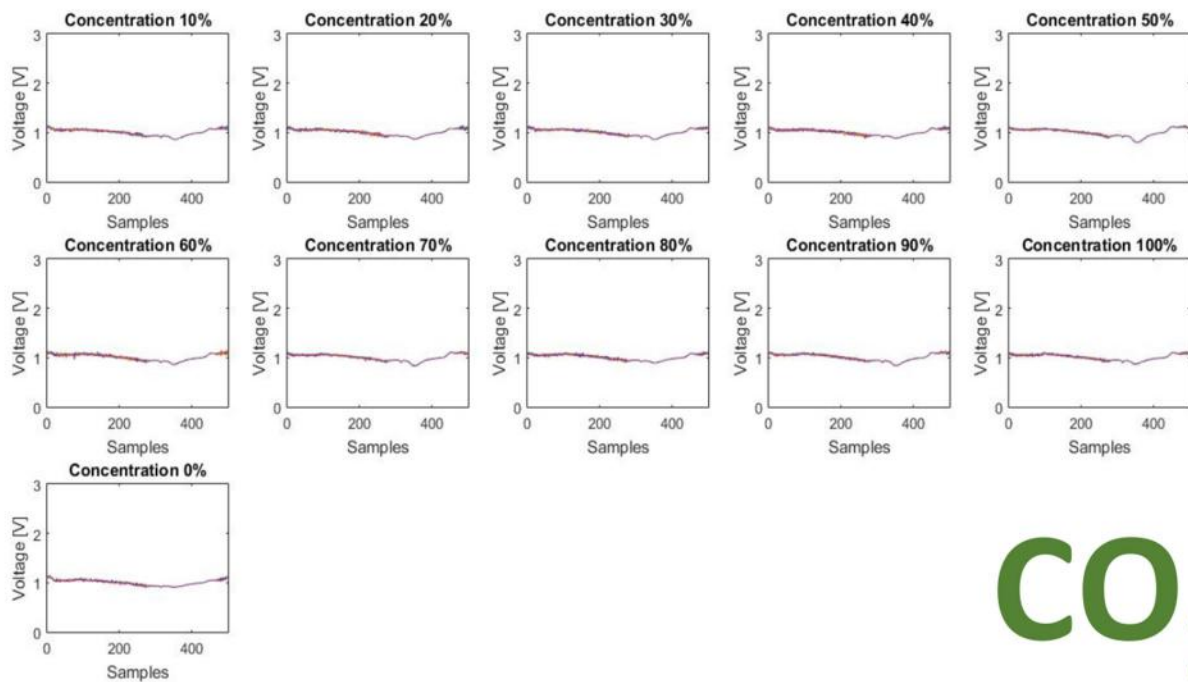
The gas targets used for the calibration ( $O_2$  and  $CO_2$ ) have been considered with concentration levels in the range of [0–100%].

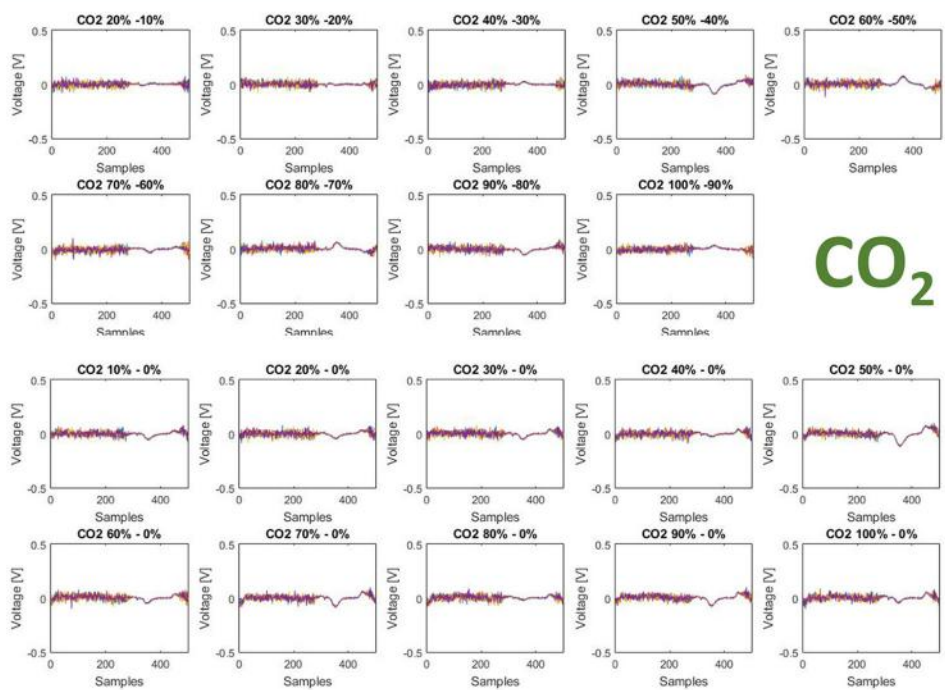
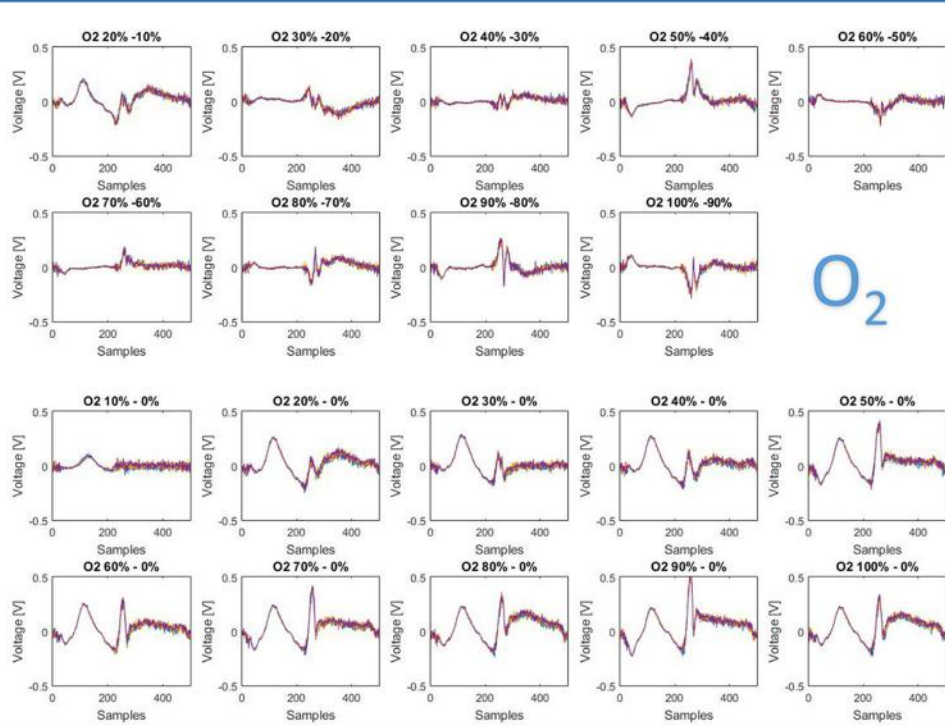
## RESULTS: PRELIMINARY TESTS ON SPE, MFE4 AND MFE1

A preliminary set of tests was performed by the different electrodes in order to verify their affordability and the correct functionality of the electrochemical working principle.



**FIGURE 11** | Shows the prediction ability of the calculated PLS-Model. **(A,B)** PLS-DA model obtained by fingerprinting of SPE (Figure 7 right) and MFE1 (Figure 7 left); **(C,D)** PLS-DA model obtained by fingerprinting of SPE (Figure 7 right) and MFE1 (Figure 7 left).

**A****O<sub>2</sub>****CO<sub>2</sub>****FIGURE 12 |** (Continued)

**B****CO<sub>2</sub>****O<sub>2</sub>**

**FIGURE 12 | (A)** The fingerprints here presented show two important features of the sensor: (1) measurable differences are present for different concentration level of CO<sub>2</sub> and different concentration levels of O<sub>2</sub>; (2) measurable differences are indeed present for different gases: CO<sub>2</sub> and O<sub>2</sub>. These two aspects account for a useful intra-gas and inter-gas fingerprint variability, which permits gas identification and calibration. **(B)** Difference of finger printings among different responses to gas concentration [CO<sub>2</sub> green panel (above), O<sub>2</sub> blue panel (below)].

**TABLE 3** | Comparison table of the proposed gas sensor with some reference standard at the state of the art.

	TR250Z Oxygen sensor	SST LuminOx	LFO2-A2 Oxygen sensor	Device presented in this work
Technology	Zirconium dioxide ( $\text{ZrO}_2$ )	Fluorescence-based optical technology	Electrochemical	Electrochemical
Dimensions	89 × 70 × 13 mm	20 × 20 × 12.5 mm	20 × 20 × 17.4 mm	40 × 40 × 18 mm
LOD	0.01% $\text{O}_2$	0.01% $\text{O}_2$	0.1% Oxygen	round 10% for both $\text{O}_2$ and $\text{CO}_2$
$\text{CO}_2$ and $\text{O}_2$ sensitivity	Oxygen	Oxygen	Oxygen	BOTH
Power consumption	24 VDC	4.5–5.5 VDC	0.6 VDC	±1.8 VDC

To this purpose, the electrodes were tested using a high-end potentiostat by Metrohm, the Autolab PGSTAT302N. SPE and MFE4 were compared by using a solution of DI water containing concentrations (0.1, 0.5, 1, 2, 3, 4 mM) of ferrocyanide ions  $\text{Fe}(\text{CN})_4^-$ . This kind of ion was chosen because it produces a reversible redox reaction and it is widely used in electrochemical experiments. The experiments were done applying a triangular wave ranging from  $-0.25$  and  $0.6$  V with a scan rate of  $0.04$  V/s to the reference electrode.

The output current data have been interpolated by a quadratic function and the sensor characteristics have been evaluated as shown below in **Table 1**.

It is also possible to evaluate the precision of the experimental data generated with the two types of electrodes. Considering **Figures 10A,B**, it is possible to compare standard deviations of five repeated measurements per concentration for each electrode: it's evident that micro-fabricated electrodes produce more precise measurements with a lower standard deviation error and a higher current peak mean value.

Thus, it has been demonstrated experimentally that the micro-fabricated electrodes should allow a slightly lower LOD (Limit of Detection) also producing more repeatable measurements.

At this point the effectiveness of MFEs was demonstrated. Thus, a further cyclic voltammetry experiment was conducted using a solution of DI water containing a concentration of 4 mM of ferrocyanide ions  $\text{Fe}(\text{CN})_4^-$ , in order to verify MFE1 applicability. The principal electrical and fabrication parameters calculated for SPE, MFE1, and MFE4 are reported in **Table 2**.

Gas sensor calibration has been performed in two steps, only using MFE-1 because the main interest related to this technological step was size reduction. In the first step a regression model has been built for both electrodes. The measurement sequence was randomized in order to avoid memory effects.

The best results were evaluated considering the root mean square error in cross validation (RMSECV) relative to different responses of sensors to specific wave form signal inputs. A RMSECV of about 10% for MFE1 and a RMSECV 9.65% for SPE were obtained.

For the  $\text{CO}_2$  sensor, the best results were obtained using a sine wave form as input signal. The same procedure has been adopted for  $\text{O}_2$  sensor. In **Figure 11** the prediction ability of the calculated PLS-DA model is represented.

Also in this case the best results were evaluated considering the root mean square error in cross validation (RMSECV) relative to different responses of sensors to specific wave form signal inputs. A RMSECV of about 10% for MFE1 and a RMSECV 21.3% for SPE were obtained.

All the measurements have been executed in triplicate for each concentration. The best performance of MFE1 has been obtained by analyzing the multidimensional fingerprinting outputs. In **Figures 12A,B** the fingerprints for each concentration of  $\text{O}_2$  and  $\text{CO}_2$  are reported.

Two different finger printings can be easily observed for the two gases. This aspect is interesting because, on this basis, it is possible to characterize a specific gas elaborating the multidimensional informative content provided by each fingerprinting. Another advantage could come by adopting a feature extraction strategy of on the raw data. In particular, the system provides 500 current values corresponding to the interaction of the sensor with the solution modified with gas. By selecting a reduced number of features (less than 500), which is useful for a specific target application, it is possible to optimize the measurement time, thus reducing the exposition of the electrode to the gas. This last point could also improve sensor repeatability, reproducibility and life time.

It is worth comparing the performance of this prototype gas sensor with the commercial solution currently available. This comparison is well illustrated in **Table 3**.

From this table it is evident that the proposed solution is competitive in terms of dimensions and power consumption, and it is interesting its ability of measuring both oxygen and carbon dioxide. Regarding the Limit of Detection, the results obtained must be improved.

## CONCLUSIONS

In this work we have described a more complete voltammetric system called electronic tongue for the determination of the features related to red-ox reaction of analytes in solutions and compare it with the state of the art (Legin et al., 1995, 1997, 1999a; Arrieta et al., 2004; Vlasov et al., 2005; Rudnitskaya and Legin, 2008; del Valle, 2012; Tahara and Toko, 2013). Technical improvements of the system have been illustrated in order to indicate possible measurement paths allowing better performances in terms of resolution and flexibility. The main additional characteristics are: the inclusion of a lock-in amplifier for the detection of signals when the signal to noise ratio is less

than one; the presence of bias and sinusoidal input voltages for the reference electrode polarization; the possibility to divide the output signal in a high number of parts (till 1,000) in order to improve the resolution; the possibility to zoom in any point inside the response curve; the possibility to differentiate the output voltage in order to evidence details of the response; the use of light to change the sensitivity of the response (feature not utilized in this paper); the possibility to increase the input voltage dynamic range. An electronic chain comprising a spectrum analyzer has been included in the overall measurement system in order to evaluate the noise spectral density of the output amplifier with and without signals. Custom microfabricated electrodes were designed and realized to improve the performances of the sensing system.

A complete flow chart of the technological steps for the fabrication of miniaturized three electrode sensor has also been developed and reported.

The flexibility of the new ET system related to the utilization of these new miniaturized electrodes has been confirmed by showing the system performance/behavior/response in an application dealing with the detection of  $O_2$  and  $CO_2$  into a given solutions.

## REFERENCES

- Arrieta, A. A., Apetrei, C., Rodríguez-Méndez, M. L., and De Saja, J. A. (2004). Voltammetric sensor array based on conducting polymer-modified electrodes for the discrimination of liquids. *Electrochimica Acta* 49, 4543–4551. doi: 10.1016/j.electacta.2004.05.010
- del Valle, M. (2012). Sensor arrays and electronic tongue systems. *Int. J. Electrochem.* 986025:2012. doi: 10.1155/2012/986025
- Krantz-Rücker, C., Stenberg, M., Winquist, F., and Lundström, I. (2001). Electronic tongues for environmental monitoring based on sensor arrays and pattern recognition: a review. *Analyt. Chim. Acta* 426, 217–226. doi: 10.1016/S0003-2670(00)00873-4
- Legin, A. V., Bychkov, E. A., Seleznev, B. L., and Vlasov, Y. G. (1995). Development and analytical evaluation of a multisensor system for water quality monitoring. *Sens. Actuat. B Chem.* 27, 377–379. doi: 10.1016/0925-4005(94)01621-N
- Legin, A., Kirsanov, D., Rudnitskaya, A., Iversen, J. J. L., Seleznev, B., Esbensen, K. H., et al. (2004). Multicomponent analysis of fermentation growth media using the electronic tongue (ET). *Talanta* 64, 766–772. doi: 10.1016/j.talanta.2004.04.001
- Legin, A., Rudnitskaya, A., Vlasov, Y., Di Natale, C., Davide, F., and D'Amico, A. (1997). Tasting of beverages using an electronic tongue. *Sens. Actuat. B Chem.* 44, 291–296. doi: 10.1016/S0925-4005(97)00167-6
- Legin, A., Rudnitskaya, A., Vlasov, Y., Di Natale, C., Mazzone, E., and D'Amico, A. (1999a). Application of electronic tongue for quantitative analysis of mineral water and wine. *Electroanalysis* 11, 814–820. doi: 10.1002/(SICI)1521-4109(199907)11:10/11<814::AID-ELAN814>3.0.CO;2-7
- Legin, A., Smirnova, A., Rudnitskaya, A., Lvova, L., Suglobova, E., and Vlasov, Y. (1999b). Chemical sensor array for multicomponent analysis of biological liquids. *Analyt. Chim. Acta* 385, 131–135. doi: 10.1016/S0003-2670(98)00690-4
- Pennazza, G., Santonico, M., Zompanti, A., Parente, F. R., Ferri, G., and D'Amico, A. (2017). Design and development of an electronic interface for gas detection and exhaled breath analysis in liquids. *IEEE Sensors J.* 18, 31–36. doi: 10.1109/JSEN.2017.2771565
- Rudnitskaya, A., and Legin, A. (2008). Sensor systems, electronic tongues and electronic noses, for the monitoring of biotechnological processes. *J. Indus. Microbiol. Biotechnol.* 35, 443–451. doi: 10.1007/s10295-007-0298-1

## AUTHOR CONTRIBUTIONS

GP: manuscript writing, electronic design, data interpretation; MS: manuscript writing, electronic design, device fabrication; LV: data analysis, data interpretation, manuscript revision; AZ: manuscript writing, device fabrication, data acquisition; AS and NK: device fabrication, data acquisition; IP: data analysis, manuscript revision; WQ: device fabrication; LS: electronic design, device fabrication, manuscript writing; AD: manuscript writing, electronic design, data interpretation.

## FUNDING

This work was partially funded by the 2016 FLAG-ERA project: (Frictionless Energy Efficient Convergent Wearables for Healthcare and Lifestyle Applications).

## SUPPLEMENTARY MATERIAL

The Supplementary Material for this article can be found online at: <https://www.frontiersin.org/articles/10.3389/fchem.2018.00327/full#supplementary-material>

- Rudnitskaya, A., Legin, A., Seleznev, B., Kirsanov, D., and Vlasov, Y. (2008). Detection of ultra-low activities of heavy metal ions by an array of potentiometric chemical sensors. *Microchim. Acta* 163, 71–80. doi: 10.1007/s00604-007-0900-2
- Santonico, M., Pennazza, G., Grasso, S., D'Amico, A., and Bizzarri, M. (2013). Design and test of a biosensor-based multisensorial system: a proof of concept study. *Sensors* 13, 16625–16640. doi: 10.3390/s131216625
- Santonico, M., Pennazza, G., Parente, F. R., Grasso, S., Zompanti, A., Stornelli, V., et al. (2017). “A gas sensor device for oxygen and carbon dioxide detection,” in *Multidisciplinary Digital Publishing Institute Proceedings*, Vol. 1 (Paris: Eurosensors 2017), 447.
- Tahara, Y., and Toko, K. (2013). Electronic tongues—a review. *IEEE Sens. J.* 13, 3001–3011. doi: 10.1109/JSEN.2013.22263125
- Vlasov, Y. G., Legin, A. V., Rudnitskaya, A. M., D'Amico, A., and Di Natale, C. (2000). “Electronic tongue”—new analytical tool for liquid analysis on the basis of non-specific sensors and methods of pattern recognition. *Sens. Actuat. B Chem.* 65, 235–236. doi: 10.1016/S0925-4005(99)00323-8
- Vlasov, Y., Legin, A., Rudnitskaya, A., Di Natale, C., and D'Amico, A. (2005). Nonspecific sensor arrays (“electronic tongue”) for chemical analysis of liquids (IUPAC Technical Report). *Pure Appl. Chem.* 77, 1965–1983. doi: 10.1351/pac200577111965
- Winquist, F., Holmin, S., Krantz-Rücker, C., Wide, P., and Lundström, I. (2000). A hybrid electronic tongue. *Analyt. Chim. Acta* 406, 147–157. doi: 10.1016/S0003-2670(99)00767-9
- Conflict of Interest Statement:** The authors declare that the research was conducted in the absence of any commercial or financial relationships that could be construed as a potential conflict of interest.
- Copyright © 2018 Pennazza, Santonico, Vollero, Zompanti, Sabatini, Kumar, Pini, Quiros Solano, Sarro and D'Amico. This is an open-access article distributed under the terms of the Creative Commons Attribution License (CC BY). The use, distribution or reproduction in other forums is permitted, provided the original author(s) and the copyright owner(s) are credited and that the original publication in this journal is cited, in accordance with accepted academic practice. No use, distribution or reproduction is permitted which does not comply with these terms.



# 3D Printed e-Tongue

**Gabriel Gaál<sup>1</sup>, Tatiana A. da Silva<sup>1</sup>, Vladimir Gaál<sup>1</sup>, Rafael C. Hensel<sup>1</sup>, Lucas R. Amaral<sup>2</sup>, Varlei Rodrigues<sup>1</sup> and Antonio Riul Jr.<sup>1\*</sup>**

<sup>1</sup> Applied Physics Department, University of Campinas, Campinas, Brazil, <sup>2</sup> School of Agricultural Engineering, University of Campinas, Campinas, Brazil

Nowadays, one of the biggest issues addressed to electronic sensor fabrication is the build-up of efficient electrodes as an alternative way to the expensive, complex and multistage processes required by traditional techniques. Printed electronics arises as an interesting alternative to fulfill this task due to the simplicity and speed to stamp electrodes on various surfaces. Within this context, the Fused Deposition Modeling 3D printing is an emerging, cost-effective and alternative technology to fabricate complex structures that potentiates several fields with more creative ideas and new materials for a rapid prototyping of devices. We show here the fabrication of interdigitated electrodes using a standard home-made CoreXY 3D printer using transparent and graphene-based PLA filaments. Macro 3D printed electrodes were easily assembled within 6 min with outstanding reproducibility. The electrodes were also functionalized with different nanostructured thin films via dip-coating Layer-by-Layer technique to develop a 3D printed e-tongue setup. As a proof of concept, the printed e-tongue was applied to soil analysis. A control soil sample was enriched with several macro-nutrients to the plants (N, P, K, S, Mg, and Ca) and the discrimination was done by electrical impedance spectroscopy of water solution of the soil samples. The data was analyzed by Principal Component Analysis and the 3D printed sensor distinguished clearly all enriched samples despite the complexity of the soil chemical composition. The 3D printed e-tongue successfully used in soil analysis encourages further investments in developing new sensory tools for precision agriculture and other fields exploiting the simplicity and flexibility offered by the 3D printing techniques.

## OPEN ACCESS

**Edited by:**

Dmitry Kirsanov,  
Saint Petersburg State University,  
Russia

**Reviewed by:**

Hugo Oliveira,

Laboratório Ibérico Internacional de  
Nanotecnologia (INL), Portugal  
Carmelo Sgarlata,  
Università degli Studi di Catania, Italy

**\*Correspondence:**

Antonio Riul Jr.  
riul@ifi.unicamp.br

**Specialty section:**

This article was submitted to  
Analytical Chemistry,  
a section of the journal  
Frontiers in Chemistry

**Received:** 12 February 2018

**Accepted:** 16 April 2018

**Published:** 03 May 2018

**Citation:**

Gaál G, da Silva TA, Gaál V, Hensel RC, Amaral LR, Rodrigues V and Riul A Jr. (2018) 3D Printed e-Tongue. *Front. Chem.* 6:151.  
doi: 10.3389/fchem.2018.00151

## 1. INTRODUCTION

The continuous increase for food demand and limited productive crop areas have stimulated the development of new precision agriculture tools to avoid excessive and/or insufficient use of fertilizers and pesticides in soil management. Therefore, high-detailed data for soil characterization is fundamental for a precise soil management. However, current soil chemical analysis protocols are time-consuming and expensive procedures demanding alternative approaches for rapid and on-site soil characterization (Adamchuk and Viscarra Rossel, 2010).

There are basically two approaches for point-of-care soil characterization, one of them based on chemical extraction of specific soil macro-nutrients and then its detection by ion-selective electrodes (ISE) or ion selective field effect transistors (ISFET) (Artigas et al., 2001; Kim et al., 2007; Shaw et al., 2013). Despite the precise quantitative characterization, some parameters need to be

tuned for each ion present on the soil sample, making it complicated for measurements of various nutrients or even the use of several instruments. The other approach is the direct measurement of the soil fertility parameters, and the most used techniques are optical spectroscopy (An et al., 2014; Vohland et al., 2014), capillarity electrophoresis (Smolka et al., 2017) and electronic tongues (Mimendia et al., 2014; Braunger et al., 2017). Optical spectroscopy provides several soil properties through rapid and simple measurements, but the lack of correlation between spectral bands and concentration of soil nutrients leads to models with high prediction errors. Electrophoresis is an interesting approach as it uses high electrical potential in order to separate ions based on their net charge. It provides accurate qualitative measurements of certain ions presented on samples, and also quantitative estimations of their concentrations. However, the need of high electrical potentials ( $\sim 2000$  V) may hamper some on-site applications. On the other hand, electronic tongue (e-tongue) sensors detect variations of the analyte dielectric constant, ensuring high sensitivity with no need of specific interactions (Riul et al., 2010). They have been widely used in quality control of foodstuff, beverages and pharmaceuticals, in addition to clinical and environmental analysis. Moreover, e-tongue devices provide rapid and continuous analysis of complex systems and fast experiments for either qualitative, semi-quantitative or quantitative analyses (Legin et al., 2003; Citterio and Suzuki, 2008; Shimizu et al., 2017).

One kind of e-tongue sensor uses interdigitated electrodes (IDEs) which are arrays of parallel plates capacitors in order to measure the analyte dielectric constant. The IDE geometry maximizes the capacitor effective area and then it increases its overall sensitivity (Olthuis et al., 1995; Igrela and Dias, 2011). The electrode fabrication usually involves expensive, complex and multistage micro-fabrication processes which still involves the use of toxic reagents. In that sense, there are great efforts to develop alternative techniques such as ink-jet printing, screen-printing and direct drawing processes exploiting conductive inks for electrode fabrication (Tomazelli Coltro et al., 2004; Coltro et al., 2010; Cummins and Desmulliez, 2012; Nakashima et al., 2012; Perinka et al., 2013; Chagas et al., 2015; Paula et al., 2018). However, these techniques still require further steps to integrate the electrodes to assemble a functional device. The use of 3D printers in such task permits an easy integration of the electrodes to complex and intricate 3D structures in order to build up sensors in a straightforward manner (Gaal et al., 2017). Recent advances in thermoplastic materials used as filaments for Fused Deposition Modeling (FDM) 3D printing allowed an easy fabrication of 3D printed electrodes using a commercial conductive filament for electrochemical applications (Foster et al., 2017).

In this work we aim the development of planar 3D printed IDEs in order to assemble a proof of concept e-tongue. We have exploited this simple 3D-printed e-tongue sensor to discriminate soil samples enriched with important nutrients for crop production. Planar IDEs were printed in a home-made FDM 3D printer, being further functionalized with nanostructured Layer-by-Layer (LbL) films to be used as sensing units (Riul

et al., 2003). Soil samples diluted in ultra-pure water were characterized via Principal Component Analysis (PCA) of the Electrical Impedance Spectroscopy (EIS) and a clear distinction among all samples was obtained.

## 2. MATERIALS AND METHODS

### 2.1. 3D Printer

A two nozzle home-made CoreXY FDM 3D printer was built based on the RepRap open hardware, displayed in **Figure 1**. It uses two commercial hot nozzles of  $400\ \mu\text{m}$  in diameter to extrude thermoplastics filaments of  $1.75\ \text{mm}$  in diameter. The molten filament is deposited over a hot bed to ensure a good adhesion of the first layer and to maintain a constant temperature gradient along the printed layers avoiding delamination. The hot bed is formed by a commercial heated plate coupled with a mirror, which provides a smooth and flat printing surface with building area of  $200\ \text{mm} \times 200\ \text{mm}$ . The printing heads are moved in the XY plane by two stepper motors following the H-frame type XY-positioning system (Itoh et al., 2004; Sollmann et al., 2010) and the hot bed is moved in the z-axis by another couple of stepper motors. The printer control is done by an open source Arduino microcontroller board Mega 2560, interfaced with a commercial RepRap Arduino Mega Pololu Shield (RAMPS).

The design of the interdigitated electrodes were done with Autodesk Inventor 2015 Student Edition and were further converted to STereoLithography (STL) format. The STL models were sliced using the free license software Slic3r optimized for two extruders. The slicing procedure converts the STL 3D models and transforms them into stacks of 2D printing planes, further interpreted by the printer hardware.

Planar IDEs, **Figure 2a** of several geometries were 3D-printed in order to verify the limits of our system and demonstrate the facility to tune the device geometry. For the e-tongue system planar IDEs were designed to have 3 pairs of fingers  $9\ \text{mm}$  long,  $1\ \text{mm}$  width and  $1\ \text{mm}$  spaced each other. The IDE

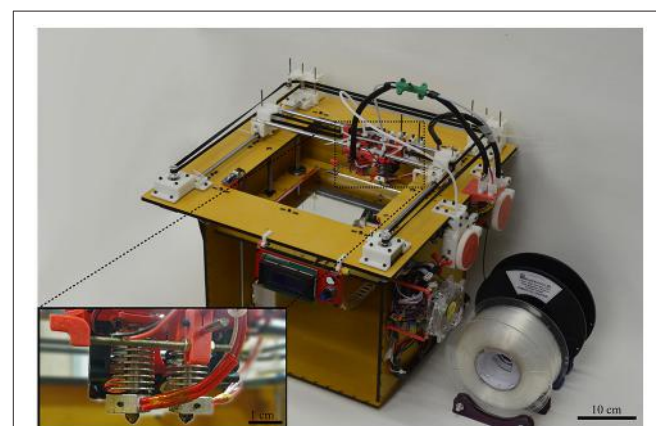


**FIGURE 1 |** Two nozzle home-made CoreXY 3D printer used to produce the planar IDEs. Inset:  $0.4\ \text{mm}$  in diameter two nozzles setup.

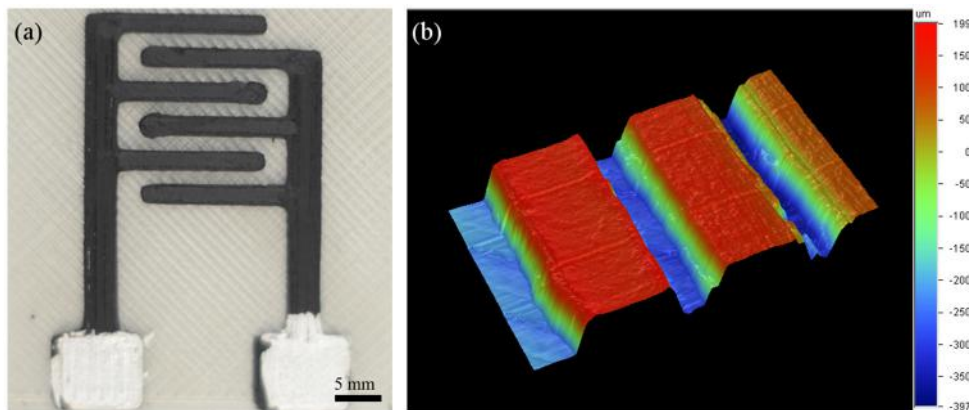


**FIGURE 2 | (a)** 3D printed IDE with 2 mm finger thick and 1.4 mm of finger separation. **(b)** 3D profilometry mapping of a printed IDE.

base was comprised of 2 planes having 0.4 mm thickness that were printed with transparent Poly Lactic Acid (PLA) purchased from e3D. The conductive filament is a commercial PLA-based thermoplastic doped with graphene fibers, purchased from BlackMagic 3D. A profilometer Dektak 150 was used to estimate the root-mean-square (RMS) surface roughness of the printed conductive tracks.

### 2.1.1. Chemical Treatment

Before the dip-coating deposition, it was applied a chemical treatment on the surface of the printed IDEs in order to ensure the adhesion of the polyelectrolytes. The printed IDEs were placed in a solution of  $\text{KMnO}_4\text{-H}_2\text{SO}_4$  (50 mL), prepared from  $\text{KMnO}_4$  (194 mg) dissolved in  $\text{H}_2\text{SO}_4$  (1 M). They were maintained in ultrasonic bath for 3 hours, and then washed with 1 L of ultra-pure water and  $\text{HCl}$  (1 M) (Martins et al., 2014). To remove the  $\text{MnO}_2$  adhered to the surface of the IDEs a further cleaning process was performed with a 1 M  $\text{H}_2\text{SO}_4$  (25%) solution, and a 30%  $\text{H}_2\text{O}_2$  (75%) solution. Ultra-pure water was provided from an Arium Comfort Sartorius system that was used also to prepare all polyelectrolyte solutions described below.

### 2.1.2. LbL Dip-Coating

The LbL polymer film deposition was made in a home-made setup based on an Arduino board UNO and stepper motors. This setup allows a fully automated LbL film mounting with precise control of a large number of parameters for the LbL film deposition such as dipping velocities, time of immersion in each polyelectrolyte, wash and dry times (Hensel et al., 2018).

It was used three different LbL films in which the anionic layers used were copper phthalocyanine-3,4',4'',4'''-tetrasulfonic acid tetrasodium salt ( $\text{CuTsPc}$ ), montmorillonite K (MMt-K), poly(3,4-ethylenedioxothiophene)-poly(styrenesulfonate) (PEDOT:PSS), and for all three LbL architectures poly(diallyldimethylammonium chloride) (PDDA) was used as the cationic layer. The aqueous  $\text{CuTsPc}$  solution was used at 0.5 mg/mL and pH 8, the MMt-K water solution was used at 1 mg/mL and pH 3, and the PEDOT:PSS solution was used at 0.2 mg/mL and pH 3. The cationic PDDA solution was

prepared at 10  $\mu\text{L}/\text{mL}$  and the pH was adjusted to be the same as the corresponding anionic polyelectrolyte forming the LbL film. The immersion time was 10 min for both anionic and cationic layers, and it was kept the same for all films deposited. 50 bilayers were deposited on each 3D-printed IDE and the LbL deposition was confirmed by the difference of the coated IDE impedance spectrum in air compared with that of the bare electrode also in air.

## 2.2. Electronic Tongue

The e-tongue sensor was comprised of 4 sensing units, one bare IDE and three coated with nanostructured films described above. The sensor is based on the impedance measurement of the IDEs immersed in the liquid system, comparing the electrical response at a fixed frequency of different samples via Principal Component Analysis (PCA). Briefly, PCA is a multivariate statistical tool that reduces the dimensionality of the original data set facilitating correlation and visualization. This procedure is based on a linear transformation that maximizes the variance of the initial matrix and plot the new data on a new set of orthogonal axis called Principal Components without losing information (Rencher, 2012).

### 2.2.1. Soil Samples

The soil samples were extracted from the same location and separated into seven pots with 1 L capacity. Each of them was added  $\text{NH}_4\text{NO}_3$ ,  $\text{NH}_4\text{H}_2\text{PO}_4$ ,  $\text{KCl}$ ,  $\text{CaCl}_2(\text{H}_2\text{O})_2$ ,  $\text{MgCl}_2(\text{H}_2\text{O})_6$ , or  $(\text{NH}_4)_2\text{SO}_4$ , in order to separately fertilize six soil samples with nitrogen (N), phosphorus (P), potassium (K), calcium (Ca), magnesium (Mg) or sulfur (S), respectively. A seventh sample was kept unfertilized as the control. All pots were maintained for 40 days in a greenhouse with daily irrigation to allow chemical reactions and full fertilization of the soils. To quantify the amount of macro-nutrients available to the plants, a portion of the samples was sent to a commercial laboratory for traditional chemical analysis.

The samples used for the 3D printed e-tongue analysis were diluted in 25 mL of ultra-pure water at 1 mg/mL. It was used a commercial Frequency Response Analyzer (FRA)

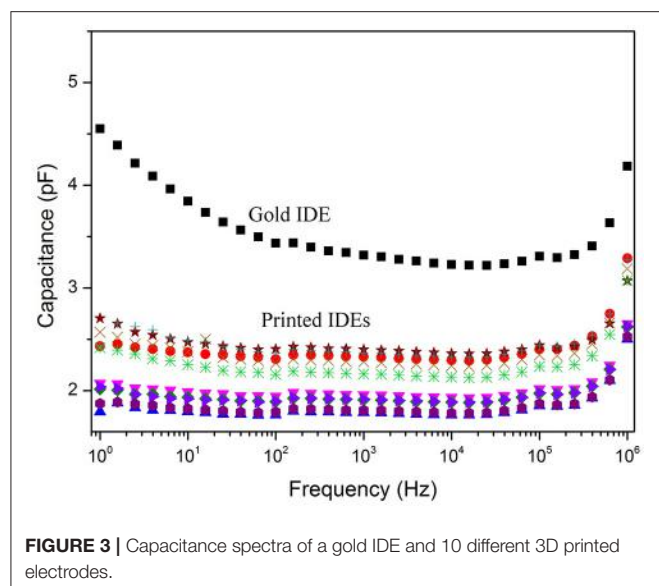


**FIGURE 3** | Capacitance spectra of a gold IDE and 10 different 3D printed electrodes.

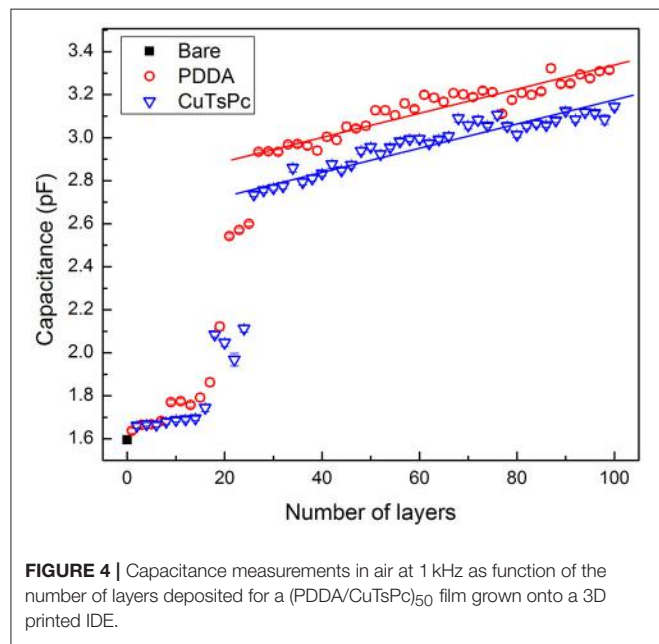


**FIGURE 4** | Capacitance measurements in air at 1 kHz as function of the number of layers deposited for a  $(\text{PDDA/CuTsPc})_{50}$  film grown onto a 3D printed IDE.

Solartron 1260A with a Dielectric Interface 1269A to acquire the impedance spectra in ambient conditions. The data was analyzed at 1 kHz, as at the kHz frequency region the impedance of the system is known to be dominated by the film/electrode interface (Riul et al., 2003). The impedance spectrum was acquired for each soil sample and after the measurement the IDEs were thoroughly washed in ultra-pure water. A control EIS was then performed in ultra-pure water to verify cross-contamination of the electrodes.

### 3. RESULTS AND DISCUSSION

#### 3.1. 3D Printed IDEs

An iterative process was used to optimize the printer parameters in order to print different planar IDEs. Figure 2a illustrates

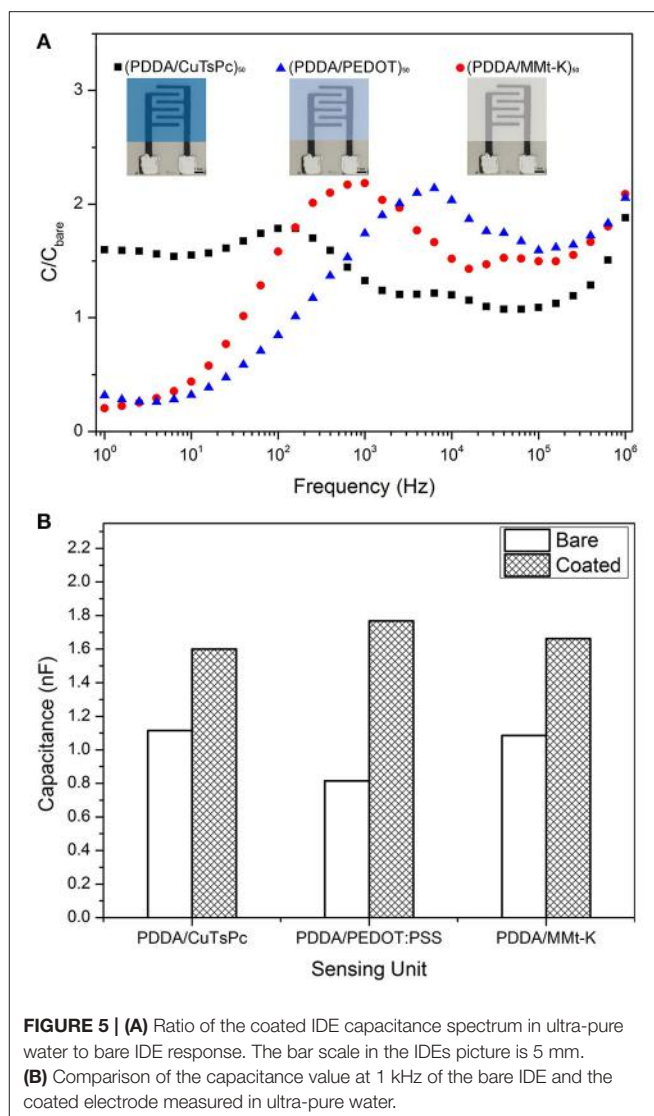


**FIGURE 5** | (A) Ratio of the coated IDE capacitance spectrum in ultra-pure water to bare IDE response. The bar scale in the IDEs picture is 5 mm.

(B) Comparison of the capacitance value at 1 kHz of the bare IDE and the coated electrode measured in ultra-pure water.

a particular IDE configuration that were printed within less than 10 min. It is worth mentioning that the geometry can be easily modified by simply changing the computational 3D model design, thus facilitating the prototyping process. Profilometry of a printed IDE finger showed a 6  $\mu\text{m}$  RMS surface roughness on a square region on the top of the printed conductive track, Figure 2b.

Figure 3 illustrates the capacitance response in air among ten different 3D printed IDEs when compared with a gold IDE onto glass substrate with similar geometric parameters. As expected, the frequency response of the printed IDEs is analogous to the gold electrode. Moreover, besides the rapid prototyping offered by the 3D-printing technique it was observed an outstanding reproducibility of the geometric parameters of the printed devices as their capacitance spectra deviated in 1 pF range.

#### 3.2. LbL Deposition

In order to verify the layer-by-layer growth of the nanostructured films onto the polymeric substrate, the capacitance at 1 kHz was

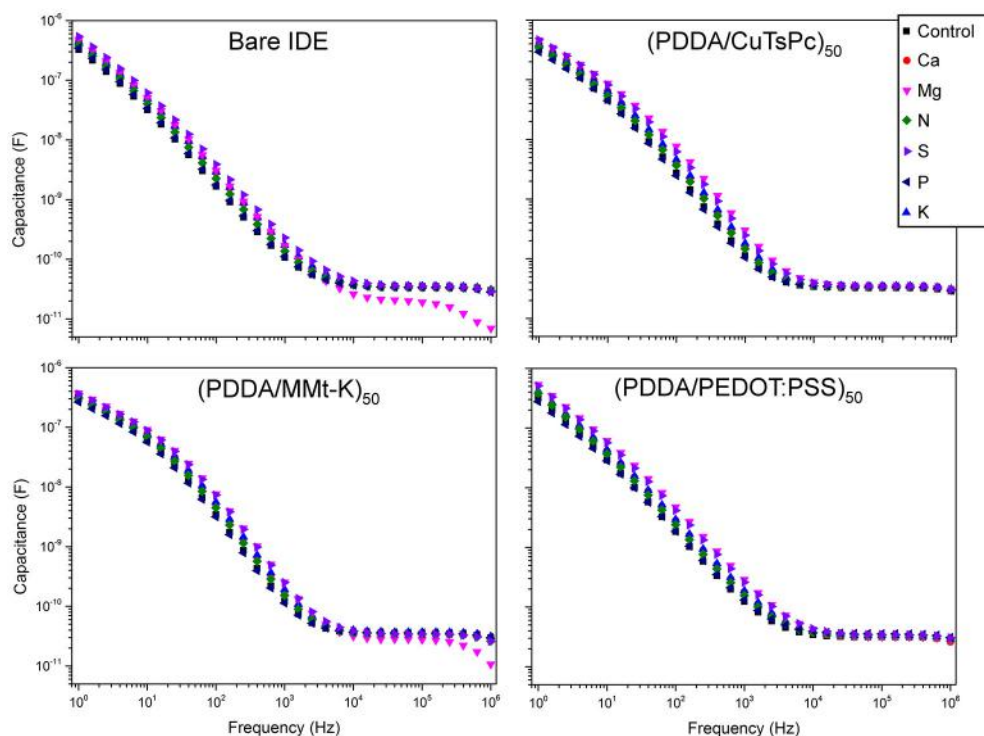


**FIGURE 6** | Capacitance spectra of each macro-nutrient solution of all four sensing units.

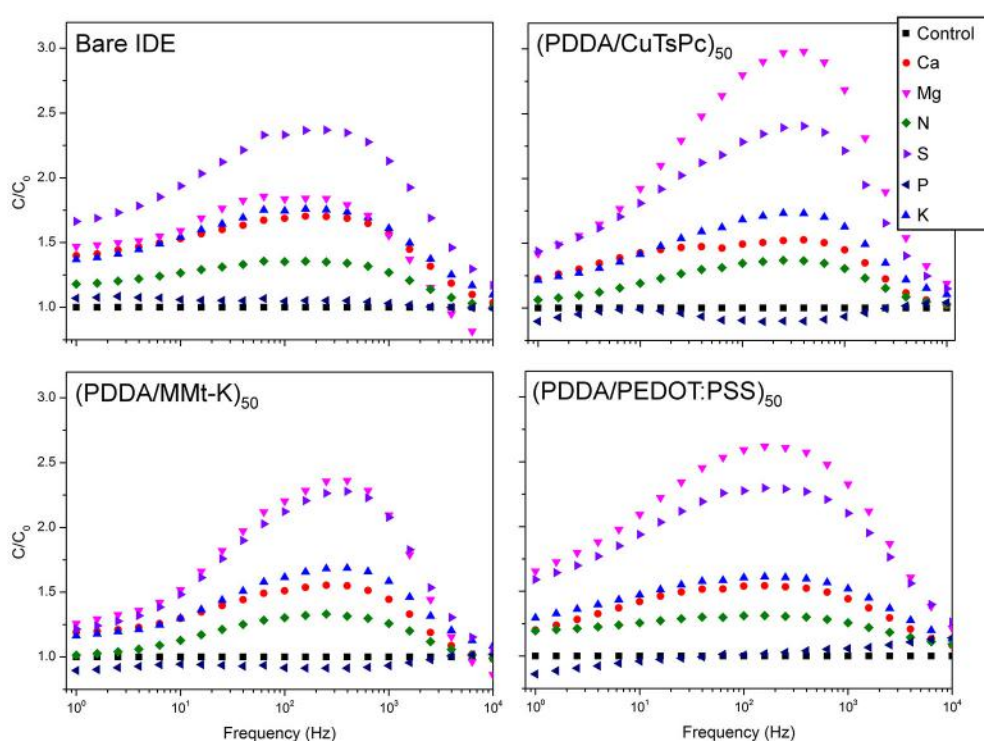


**FIGURE 7** | Ratio of the capacitance spectrum of each macro-nutrient solution ( $C$ ) to the spectrum of the control sample ( $C_0$ ) of all the four sensing units.

measured in air after each deposition step, **Figure 4**. Firstly, it was observed an initial non-linear trend in the measured capacitance between two different polyelectrolytes, attributed to the starting adsorption process of materials on the plastic electrodes in the LbL film build-up (Poghossian et al., 2006, 2013; Daikuzono et al., 2015). A linear trend growth was observed only after the twentieth five deposited layer, thus indicating a homogeneous adsorption process of materials on the electrode interface. The  $(\text{PDDA/CuTsPc})_{50}$  film deposition was chosen to such analysis as it is easier to compare with recent ongoing studies on the capacitance change in the LbL dipping process made in our research group (Ferreira, 2016; Hensel et al., 2018).

The final deposition process was confirmed by the difference between the impedance spectrum of the bare electrode and the coated IDE. **Figure 5A** illustrates the ratio of the real capacitance spectrum of a coated IDE to a bare IDE measured in ultra-pure water. Such graph indicates a change of the capacitive response of the coated IDE in comparison with the bare electrode in all the spectrum range. In particular, **Figure 5B** shows the comparison of the real capacitance values of the bare IDE and the coated electrodes at 1 kHz measured in ultra-pure water. As discussed previously, this frequency has a major contribution from the film/electrolyte interface (Riul et al., 2003), rendering easy the verification of the presence of thin films onto the printed IDEs.

### 3.3. e-Tongue Analysis of Soil Samples

**Figure 6** shows the frequency response of the real capacitance of a single measurement for each soil sample and each sensing unit. As expected at mid to low frequency region ( $10^4$  Hz to 1 Hz) it can be observed a dispersion of the samples response, moreover, at this frequency range each sensing unit has a different shape of the spectra. It was also evaluated the relative capacitance spectra, **Figure 7** which is the ratio between the real capacitance of the sample enriched with a nutrient (C) to the real capacitance of the control sample ( $C_0$ ). This analysis allows one to easily identify samples enriched with Mg and S, presenting good distinction from the control, while the phosphorus sample is grouped quite close to the control. This would be expected, since on tropical and poor soils, practically all the applied P must be retained by soil colloids (adsorbed and unavailable to the plants), which causes the similarity between P and control solutions.

PCA analysis was applied to a set of three independent real capacitance measurements at 1 kHz from all seven samples, **Figure 8A**. A good correlation of the rough data and PCA decomposition was observed as the two first principal components add up to 99.36%. Moreover, a good distinction was achieved among the enriched aliquots even considering the high complexity involved in soil analysis. Nevertheless, an expected superposition between the phosphorus and the control samples was observed hindering their distinction as discussed above. One can overcome this superposition considering the third principal component, which accounts for 0.49% of the data variance creating a 3D extension of the PCA plot, **Figure 8B**. The data projection into the  $\text{PC3} \times \text{PC1}$  plane shows clearly the separation of the control and phosphorus clusters. Finally, the 2D score plot is often used over the 3D extension because it is easier

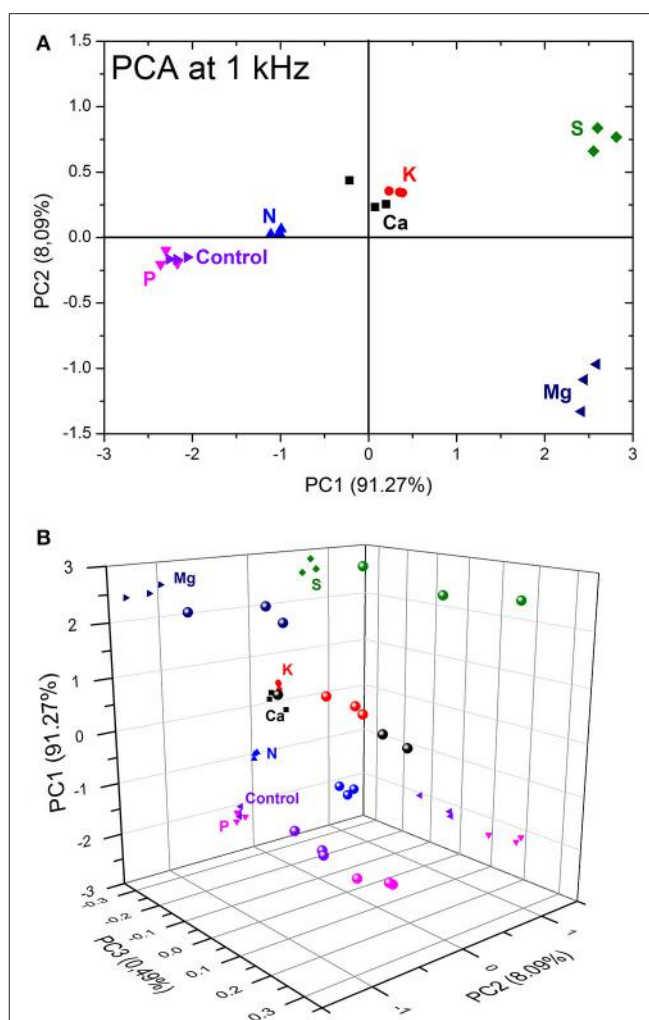


**FIGURE 8 |** PCA score plot (A) 2D  $\text{PC1} \times \text{PC2}$ , and (B) 3D plot, evaluated at 1 kHz of the 3D printed e-tongue applied to soil analysis of seven distinct samples.

to see the data clustering, but in some cases it can hide important information and lead to false conclusions.

It is important to stress that this e-tongue system can contribute in the future for point-of-care systems applied in soil analysis and management. There is no need of complicated apparatus as impedance measurements can be taken at a fixed frequency simplifying the development of portable devices. Moreover, statistical analysis that does not require high computational demand can be easily integrated to create a portable tool for soil management. Despite the lack of quantitative information about the soil nutrients, the system can be used as a simplified apparatus to control deviations from the standard soil composition.

## 4. CONCLUSIONS

Using a home-made Core-XY FDM 3D printer and a commercial conductive filament, 3D printed IDEs have been successfully

fabricated within 6 min with outstanding reproducibility. The electrodes were further functionalized with different nanostructured thin films via dip-coating LbL technique in order to develop a proof of concept 3D printed e-tongue. This system was then applied to soil analysis to discriminate soil aliquots enriched with different macro-nutrients (N, P, K, S, Mg, and Ca). The frequency response of the soil samples diluted in water were verified by electrical impedance spectroscopy, and then compared via PCA analysis. A good distinction of all samples was obtained despite the complexity of the soil chemical composition. Our results show that 3D printing technology potentiates the field of sensor fabrication with cost-effective and alternative materials for a rapid prototyping as well as greater flexibility in design, paving the way for more abundant developments.

## AUTHOR CONTRIBUTIONS

GG: Fabrication of the printed electrodes, growth of the nanostructured LbL films for the e-tongue sensor and PCA

analysis of the EIS of the soil samples. TdS: EIS measurements of the soil samples. VG: Project and setup of the Core-XY 3D printer. RH: Growth analysis of the nanostructured polymer films. LA: Preparation of the soil samples, discussions during the writing and revision of the manuscript. VR: Project of the Core-XY 3D printer, discussions during the writing and revision of the manuscript. AR: Principal investigator in this subject.

## FUNDING

Authors are grateful for the financial support by the Brazilian research founding agencies FAPESP (Grants no 2014/03691-7, 2015/14836-9, 2015/21616-5, and 2017/06985-0), CAPES and CNPq.

## ACKNOWLEDGMENTS

Authors also thank LNNano/CNPEM (LMF project no 21340) for the fabrication of the gold IDEs.

## REFERENCES

- Adamchuk, V. I., and Viscarra Rossel, R. A. (2010). "Development of on-the-go proximal soil sensor systems," in *Proximal Soil Sensing*, eds R. A. Viscarra Rossel, B. Minasny, and A. B. McBratney (Sydney: Springer), 15–28.
- An, X., Li, M., Zheng, L., Liu, Y., and Sun, H. (2014). A portable soil nitrogen detector based on NIRS. *Precis. Agricult.* 15, 3–16. doi: 10.1007/s11119-012-9302-5
- Artigas, J., Beltran, A., Jiménez, C., Baldi, A., Mas, R., Domínguez, C., et al. (2001). Application of ion sensitive field effect transistor based sensors to soil analysis. *Comput. Electron. Agricult.* 31, 281–293. doi: 10.1016/S0168-1699(00)00187-3
- Braunger, M. L., Shimizu, M., Jimenez, M. J. M., Amaral, L. R., de Oliveira Piazzetta, M. H. Gobbi, A. L. (2017). Microfluidic electronic tongue applied to soil analysis. *Chemosensors* 5:14. doi: 10.3390/chemosensors5020014
- Chagas, C. L. S., Costa Duarte, L., Lobo-Júnior, E. O., Piccin, E., Dossi, N., and Coltro, W. K. T. (2015). Hand drawing of pencil electrodes on paper platforms for contactless conductivity detection of inorganic cations in human tear samples using electrophoresis chips. *Electrophoresis* 36, 1837–1844. doi: 10.1002/elps.201500110
- Citterio, D., and Suzuki, K. (2008). Smart taste sensors. *Analyst. Chem.* 80, 3965–3972. doi: 10.1021/ac086073z
- Coltro, W. K. T., De Jesus, D. P., Da Silva, J. A. F., Do Lago, C. L., and Carrilho, E. (2010). Toner and paper-based fabrication techniques for microfluidic applications. *Electrophoresis* 31, 2487–2498. doi: 10.1002/elps.201000063
- Cummins, G., and Desmuliez, M. P. Y. (2012). Inkjet printing of conductive materials : a review. *Circ. World* 38, 193–213. doi: 10.1108/03056121211280413
- Daikuzono, C. M., Dantas, C. A. R., Volpati, D., Constantino, C. J. L., Piazzetta, M. H. O., Gobbi, A. L., et al. (2015). Microfluidic electronic tongue. *Sens. Actuat. B. Chem.* 207, 1129–1135. doi: 10.1016/j.snb.2014.09.112
- Ferreira, R. C. H. (2016). *Growth Study of Self-Assembled Nanostructured Films Using Capacitance Measurements*. PhD thesis, Universidade Estadual de Campinas.
- Foster, C. W., Down, M. P., Yan, Z., Ji, X., Rowley-neale, S. J., Smith, G. C., et al. (2017). 3D printed graphene based energy storage devices. *Sci. Rep.* 7, 1–11. doi: 10.1038/srep42233
- Gaal, G., Mendes, M., Almeida, T. P. D., Piazzetta, M. H. O., Gobbi, A. L., Riul, A., et al. (2017). Simplified fabrication of integrated microfluidic devices using fused deposition modeling 3D printing. *Sens. Actuat. B. Chem.* 242, 35–40. doi: 10.1016/j.snb.2016.10.110
- Hensel, R., Rodrigues, K., Pimentel, V., Riul, A., and Rodrigues, V. (2018). Automated self-assembly and electrical characterization of nanostructured films. *MRS Commun.* doi: 10.1557/mrc.2018.47. [Epub ahead of print].
- Igreja, R., and Dias, C. J. (2011). Extension to the analytical model of the interdigital electrodes capacitance for a multi-layered structure. *Sens. Actuat. A Phys.* 172, 392–399. doi: 10.1016/j.sna.2011.09.033
- Itoh, K., Iwasaki, M., and Matsui, N. (2004). Robust fast and precise positioning of ball screw-driven table system on machine stand," in *The 8th IEEE International Workshop on Advanced Motion Control, 2004. AMC '04* (Kawasaki), 511–515.
- Kim, H.-J., Hummel, J. W., Sudduth, K. A., and Motavalli, P. P. (2007). Simultaneous analysis of soil macronutrients using ion-selective electrodes. *Soil Sci. Soc. Am. J.* 71:1867. doi: 10.2136/sssaj2007.0002
- Legin, A., Rudnitskaya, A., Lvova, L., Vlasov, Y., Natale, C. D., and Amico, A. D. (2003). Evaluation of Italian wine by the electronic tongue : recognition, quantitative analysis and correlation with human sensory perception. *Analyst. Chim. Acta* 484, 33–44. doi: 10.1016/S0003-2670(03)00301-5
- Martins, M. V., Pereira, A. R., Luz, R. S., Iost, R. M., and Crespilho, F. N. (2014). Evidence of short-range electron transfer of a redox enzyme on graphene oxide electrodes. *Phys. Chem. Chem. Phys.* 16, 17426–17436. doi: 10.1039/C4CP00452C
- Mimendia, A., Gutiérrez, J. M., Alcañiz, J. M., and del Valle, M. (2014). Discrimination of soils and assessment of soil fertility using information from an ion selective electrodes array and artificial neural networks. *Clean - Soil Air Water* 42, 1808–1815. doi: 10.1002/clen.201300923
- Nakashima, H., Higgins, M. J., O'Connell, C., Torimitsu, K., and Wallace, G. G. (2012). Liquid deposition patterning of conducting polymer ink onto hard and soft flexible substrates via dip-pen nanolithography. *Langmuir* 28, 804–811. doi: 10.1021/la203356s
- Olthuis, W., Streekstra, W., and Bergveld, P. (1995). Theoretical and experimental determination of cell constants of planar-interdigitated electrolyte conductivity sensors. *Sens. Actuat. B Chem.* 25, 252–256. doi: 10.1016/0925-4005(95)85053-8
- Paula, K., Gaál, G., Almeida, G., Andrade, M., Facure, M., Correa, D., et al. (2018). Femtosecond laser micromachining of poly(lactic acid)/graphene composites for designing interdigitated microelectrodes for sensor applications. *Opt. Laser Technol.* 101, 74–79. doi: 10.1016/j.optlastec.2017.11.006
- Perinka, N., Kim, C. H., Kaplanova, M., and Bonnassieux, Y. (2013). Preparation and characterization of thin conductive polymer films on the base of PEDOT:PSS by ink-jet printing. *Phys. Proc.* 44, 120–129. doi: 10.1016/j.phpro.2013.04.016
- Poghossian, A., Abouzar, M. H., Sakkari, M., Kassab, T., Han, Y., Ingebrandt, S., et al. (2006). Field-effect sensors for monitoring the layer-by-layer adsorption of charged macromolecules. *Sens. Actuat. B Chem.* 118, 163–170. doi: 10.1016/j.snb.2006.04.013
- Poghossian, A., Weil, M., Cherstvy, A. G., and Schöning, M. J. (2013). Electrical monitoring of polyelectrolyte multilayer formation by means of

- capacitive field-effect devices. *Analyt. Bioanalyt. Chem.* 405, 6425–6436. doi: 10.1007/s00216-013-6951-9
- Rencher, A. C. (2012). *Methods of Multivariate Analysis, 2nd Edition*. Provo, UT: John Wiley & Sons.
- Riul, A., Soto, A. M., Mello, S. V., Bone, S., Taylor, D. M., and Mattoso, L. H. (2003). An electronic tongue using polypyrrole and polyaniline. *Synthet. Metals* 132, 109–116. doi: 10.1016/S0379-6779(02)00107-8
- Riul, A. J., Dantas, C. A. R., Miyazaki, C. M., and Oliveira, O. N. Jr. (2010). Recent advances in electronic tongues. *Analyst* 135, 2481–2495. doi: 10.1039/c0an00292e
- Shaw, R., Williams, A., Miller, A., and Jones, D. (2013). Assessing the potential for ion selective electrodes and dual wavelength UV spectroscopy as a rapid on-farm measurement of soil nitrate concentration. *Agriculture* 3, 327–341. doi: 10.3390/agriculture3030327
- Shimizu, F. M., Todão, F. R., Gobbi, A. L., Oliveira, O. N., Garcia, C. D., and Lima, R. S. (2017). Functionalization-free microfluidic Electronic tongue based on a single response. *ACS Sens.* 2, 1027–1034. doi: 10.1021/acssensors.7b00302
- Smolka, M., Puchberger-Engel, D., Bipoun, M., Klasa, A., Kiczkajlo, M., Smiechowski, W., et al. (2017). A mobile lab-on-a-chip device for on-site soil nutrient analysis. *Precis. Agricult.* 18, 152–168. doi: 10.1007/s11119-016-9452-y
- Sollmann, K., Jouaneh, M., Member, S., and Lavender, D. (2010). Dynamic Modeling of a Two Axes, Parallel, H- Frame Type XY-positioning System. *IEEE/ASME Trans. Mechatron.* 15, 1–12. doi: 10.1109/TMECH.2009.2020823
- Tomazelli Coltro, W. K., Fracassi da Silva, J. A., Torres da Silva, H. D., Richter, E. M., Furlan, R., Angnes, L., et al. (2004). Electrophoresis microchip fabricated by a direct-printing process with end-channel amperometric detection. *Electrophoresis* 25, 3832–3839. doi: 10.1002/elps.200406091
- Vohland, M., Ludwig, M., Thiele-Bruhn, S., and Ludwig, B. (2014). Determination of soil properties with visible to near- and mid-infrared spectroscopy: effects of spectral variable selection. *Geoderma* 223–225, 88–96. doi: 10.1016/j.geoderma.2014.01.013

**Conflict of Interest Statement:** The authors declare that the research was conducted in the absence of any commercial or financial relationships that could be construed as a potential conflict of interest.

Copyright © 2018 Gaál, da Silva, Gaál, Hensel, Amaral, Rodrigues and Riul. This is an open-access article distributed under the terms of the Creative Commons Attribution License (CC BY). The use, distribution or reproduction in other forums is permitted, provided the original author(s) and the copyright owner are credited and that the original publication in this journal is cited, in accordance with accepted academic practice. No use, distribution or reproduction is permitted which does not comply with these terms.

# Advantages of publishing in Frontiers



## OPEN ACCESS

Articles are free to read for greatest visibility and readership



## FAST PUBLICATION

Around 90 days from submission to decision



## HIGH QUALITY PEER-REVIEW

Rigorous, collaborative, and constructive peer-review



## TRANSPARENT PEER-REVIEW

Editors and reviewers acknowledged by name on published articles

### Frontiers

Avenue du Tribunal-Fédéral 34  
1005 Lausanne | Switzerland

Visit us: [www.frontiersin.org](http://www.frontiersin.org)

Contact us: [info@frontiersin.org](mailto:info@frontiersin.org) | +41 21 510 17 00



## REPRODUCIBILITY OF RESEARCH

Support open data and methods to enhance research reproducibility



## DIGITAL PUBLISHING

Articles designed for optimal readership across devices



FOLLOW US  
[@frontiersin](https://twitter.com/frontiersin)



## IMPACT METRICS

Advanced article metrics track visibility across digital media



## EXTENSIVE PROMOTION

Marketing and promotion of impactful research



## LOOP RESEARCH NETWORK

Our network increases your article's readership